The effect of physical processes and the chemical feedback on the evolution of molecular clouds

by

Philip Deane George Cox

Thesis

Submitted to the University of Kent

for the degree of

Master of Philosophy

School of Physical Sciences

September 2017

University of Kent

CONTENTS

LIST OF TABLES

LIST OF FIGURES

ACKNOWLEDGMENTS

Firstly, and very importantly, I should like to thank my supervisor, Dr. Jingqi Miao, for giving me the opportunity to work on the physics and mathematics which lay behind this PhD thesis. Her support and encouragement, and valued discussions and suggestions, during the research has helped me see patterns behind some of the randomness of the subject.

My thanks also extend to the academic and administrative staff of the School of Physical Sciences and the Centre for Astrophysics and Planetary Science in particular.

I also have to thank my parents, Ursula and Robert Cox. I owe the progress I have made over the years and my personal and academic achievements to their tireless and unconditional support provided over the period of work for my PhD and, indeed, during all the time leading up to it. I also thank them for having the foresight to have lived during the early years of my life in Belgium and France and for making it possible for me to have Germany as a second homeland. In any event I would not have got this far without their care. I also have to thank my partner, Lizzi Standing, for her support and for conversations on topics widely separated from molecular clouds which have helped to keep my feet on the ground - although sometimes my mind was among the stars. Also to my friends I have made during my time at Kent. It is impossible to list all your names and to name some would be unfair on the others.

This thesis was typeset with $\LaTeX 2_\varepsilon$[1] by the author.

---

[1]$\LaTeX 2_\varepsilon$ is an extension of $\LaTeX$. $\LaTeX$ is a collection of macros for $\TeX$. $\TeX$ is a trademark of the American Mathematical Society. The style package *warwickthesis* was used in an adapted format for the University of Kent thesis guidelines.

Declarations

This thesis was organised and written by the Author, and has not been submitted for the purposes of a qualification at any other institution or for any other degree.

The content comprising Chapters 1 and 2 are based on generally available knowledge of the development of the state of the art in the area of astrophysics addressed by this thesis. The section on the Objectives of this work was written following discussions with the Author's supervisor on defining the major areas of interest and the approach to be used.

The content comprising Chapter 3 was adapted and extended from work which has been published as Nelson and Langer (1997, 1999) and others.

The content comprising Chapter 4 was adapted and extended from work which has been published as Nelson and Langer (1997, 1999) and others, the Author's contributions are identified. The data reported are the Author's own.

The content comprising Chapter 5 is the Author's own based on discussions with his supervisor.

All data reported in Chapters 6 and 7 are the Author's own, unless explicitly stated otherwise. The data, comments and suggestions given in Chapter 8 are the Author's own, unless explicitly stated otherwise.

All instances where use has been made of other work have been cited.

Abstract

How the prospect of star formation in molecular clouds is affected by different physical and chemical processes is still not clearly understood, although various theoretical models have considered some of the possible processes in the investigation of stellar evolution. Nevertheless, the roles of many very basic physical and chemical processes in the evolution of molecular clouds have not been fully evaluated. The main objective of the work presented in this thesis is to carry out the first quantitative investigation on the importance of chemical cooling, cosmic ray heating, gas-dust interaction and photo-electric heating by FUV radiation on cloud evolution.

First, the effect of micro-physical and chemical cooling on the evolution of molecular clouds are investigated by numerical simulations based on Smoothed Particle Hydrodynamics (SPH) involving various physical or chemical feedback mechanisms. Based on the classical concept of Jeans Mass, which is used to predict the potential for gravitational collapse of a molecular cloud at hydrostatic equilibrium, a newly defined quantity called Modified Jeans Mass (MJM) is used to describe the minimum mass needed for a cloud to collapse under a certain set of initial physical conditions. Comparison of MJMs can reveal the extent of the roles played by the micro-physical and chemical cooling processes in the evolution of molecular clouds.

A set of intensive numerical simulations using different combinations of the basic micro-physical processes and chemical feedback was designed. Various models of simulation which include different physical or chemical feedback mechanisms result in a range of MJMs, to isolate these effects from those influenced by externally imposed

FUV radiation these models were run with zero FUV input. Comparison of the MJMs as well as following the evolution of the physical properties of molecular clouds enables a quantified description of the importance of the individual physical and chemical feedback processes, as well as combinations of these, on the prospect of star formation.

Secondly, the model which represented the conditions observed in nature, that is with all the microphysical and chemical processes activated, was subjected to FUV radiation and the effects of the resulting photo-electric heating on the cloud's evolution was tracked. This set of simulations studied the variation of MJMs resulting from molecular clouds with a range of initial densities being subjected to a range of different intensities of FUV radiation. It is found that a power law fitting can be applied to describe the behaviour of MJM vs initial density, i.e., $M_{MJM} = a\, n_i^b$ with a and b being different for different simulation models.

The detailed description for the evolution of the physical properties is presented for a representative molecular cloud in each set of simulations, and the general evolutionary features of all of the molecular clouds in the same set of simulation are summarised. The analysis on the calculated mass left in the condensed core formed when a cloud collapses, essentially the 'seed' for potential star formation, is also performed. It can be concluded that: a) the different microphysical and chemical cooling processes do indeed contribute to the dynamic evolution of a molecular cloud toward star formation, although chemical cooling is the most important of these; b) the effect of FUV radiation on the evolution of molecular clouds depends strongly on the initial density and on the intensity of the FUV. For low density clouds the loss of material because of photo-evaporation is the major effect reducing the chances of star formation, in high density clouds shock propagation is the predominant effect promoting the formation of protostar seeds.

CHAPTER 1

INTRODUCTION

1.1 EARLY HISTORY

That there were differences in the appearance of heavenly bodies was known to the Ancients, in about 140AD the Greek astronomer and geographer Claudius Ptolemaeus of Alexandria (Ptolemy) noted in his *Mathematike Syntaxis*, sometimes called the *Almagest*, that five stars had a cloudy appearance and were not as sharply defined as others in the sky. Over the years the number of these diffuse objects slowly increased until the development of the astronomical telescope in the 17th century significantly increased the number of such objects being identified.

In the 18th century Charles Messier was the first to compile a systematic catalogue of nebulae and star clusters visible from Paris which he began in 1760 so that he could better distinguish between nebulae and comets which looked alike when viewed with the small telescopes then available. In Messier's time a nebula, derived from the Latin word for 'cloud', was a term used to denote any diffuse celestial light source. The first version of his catalogue was published in 1774 and the third and final published edition in 1781 included 103 objects. He and his collaborators subsequently added more nebulae in manuscript making a total of 109 but a later edition was not published partially due to the disruption caused by the French Revolution (Jones, 1968, 1991).

Since then many astronomers have been active in listing and classifying nebulae using data obtained by telescopes with greater light gathering capability and more accurate optics.

Allied with the observational activity attempts were made to explain the evolution of nebulae and these efforts were aided by the availability towards the end of the 19th century of higher resolution photography. Examination of these photographs showed that although many of the nebulae did appear to be amorphous clouds some of these objects had, in fact, structure. Some of those with structure appeared to be clusters of stars and others had a spiral form. The terms used to describe these objects became more specific, the structured objects with individual stars were known as galaxies and the curtains of dark matter obscuring some stars were known as clouds.

From their formation, their diversity and beauty, to their role in stellar and planetary formation nebulae have provided mankind with a source of endless interest, speculation and analysis leading to momentous discoveries about the history of the Universe and Man's place within it. Fascinated by the processes, the size and the beauty of the nebulae, the work reported in this thesis continues, in a small way, this long tradition of inquiry.

1.2 INITIAL THEORIES AND STUDIES OF NEBULAE

Theories to explain the origins of these diffuse and structured objects on a scientific basis were developed from the mid-18th century onwards and in the last quarter of the 19th century, one of these postulated that the bright lines in spiral and rotating nebulae were clusters or clouds of meteors (then called meteorites) with irregular motions moving out of the main streams, colliding with each other and so becoming hot and emitting light.

At the same time there was great interest in understanding the way that the solar system had been formed and two incompatible theories explaining its formation were developed. One was the nebula theory in which the primitive nebula was taken to be a rotating mass of fluid which at successive epochs became unstable from excess of rotation and shed a ring from the equatorial region which formed the planets. The other was the meteorite theory which postulated that the planets in the solar system had been formed as accretions of meteors so there was considerable interest in the study of the behaviour of meteor clouds.

Darwin (1889) published a paper entitled 'On the Mechanical Conditions of a swarm of Meteorites, and on Theories of Cosmogony', 'Cosmogony' being the word then used

to describe the branch of science that deals with the origin of the universe, especially of the solar system. He proposed a model which treated the solid meteors as a gas and showed that the two competing models could be aligned. In his model the central core is isothermal but the outer layers are adiabatic and the 'atmosphere' is maintained by convection. This conclusion was reached by numerical calculations rather than from a purely analytical approach.

Although the mathematical approach was original it should also be remembered that at the time nebulae were thought to lie within the Milky Way and so were involved with the formation of planets. The identification of some of the nebulae as extra-galactic objects lay 30 years in the future including the spiral nebula in Andromeda, a 'very remarkable photograph' of which Darwin refers to in his paper. With the development of better telescopes and careful observation Edwin Hubble showed in the late 1920s that many star clusters and spiral nebulae were in fact separate galaxies and lay outside the local galaxy. In doing so he started a new branch of astronomy and astrophysics.

Darwin observed in the summary of this paper that no mathematical studies of the stability of rotating masses of gas had been done to date. An understanding of the properties of these structures was, however, essential in demonstrating the validity of the nebula hypothesis. Studies of this topic were continued by Jeans (1902) who discussed the different characteristics of a rotating liquid and a rotating self-gravitating mass of gas but still with the ultimate aim of describing the formation of a planetary system. He reported on analytical studies of a uniform isothermal model of a spherical gas cloud leading to the concepts of the Jeans Length and the Jeans Mass or Jeans Instability which are the conditions needed for the collapse of such a cloud, the collapse being initiated by instabilities in all or part of the cloud. A study of vibration modes showed that the cloud is in equilibrium if small disturbances are damped and is unstable if they are amplified. The Jeans Length is the radius of a gas cloud below which the cloud will not collapse and above which the cloud will collapse and the magnitude of which depends on the temperature, density and the mass of the particles making up the cloud. A cloud that is smaller than its Jeans length will not have sufficient self-gravity to overcome the repulsive gas pressure forces and will therefore not collapse, whereas a cloud that is larger than its Jeans length will have sufficient self-gravity and will collapse.

Jeans also formulated the equation for the Jeans Mass which may be written as

$$M_J = \left(\frac{5kT}{G\mu}\right)^{3/2} \left(\frac{3}{4\pi\rho}\right)^{1/2}, \tag{1.1}$$

where M_J is the Jeans mass, k is Boltzmann's constant, G is the gravitation constant,

μ is the mean mass per particle, and ρ is density.

1.3   Limits to the Classical Approach

Jeans' 1902 paper studied a uniform isothermal model of a nebula. Later work by others extended the concept, for example Bonnor and Ebert (Ebert (1955); Bonnor (1956)) independently developed a model for the greatest mass that an isothermal gas sphere embedded in a external medium can have without collapsing. Observations however showed that stars and gas clouds are more complex than simple spheres making full analytical treatments of this and similar problems involving influences such as radiation of various energies, magnetic fields, turbulence and chemical reactions not feasible due to the difficulties in describing the highly anisotropic cloud and gas formations observed, non-linear fluid dynamics and large systems of interconnected variables in a form which could lead to a solution. Analytical solutions for some of the simpler configurations can be and have been constructed but it is not practical to do so easily for arbitrary geometries and complex density structures. A more comprehensive set of modelling tools is required to solve such problems.

1.4   Modern Developments in Star Formation Theory

1.4.1   Observational and Theoretical Astrophysics

Attempts by astronomers and astrophysicists to identify and quantify the processes concerned with star formation may be considered as two linked areas of endeavour: on the one hand are the observations and measurements of the objects in the Universe and on the other the development of hypotheses to explain the observations and possibly also to suggest new observations. Both activities support each other in attempting to explain the mechanisms by which the Universe not only started but also reached the state now observed. The process of star formation is complex and involves many variables and processes and takes place in time scales outside human experience.

The observational basis of modern astrophysics is represented by the data generated by measurements made using ground and satellite carried instruments operating over the broadest possible electro-magnetic frequency range measurable with current

technologies. Examples of recent developments are the satellite based measuring instruments such as the recently launched space telescopes *Spitzer*, launched in 2003, and *Herschel*, launched in 2009, which opened new windows enabling a deeper understanding of the evolution of molecular clouds in the Photo-Dissociation Region (PDR), a transition region between the ionised H II and molecular regions in a gas cloud predominantly illuminated by far ultra-violet (FUV) photons (6 eV $< hv <$ 13.6 eV). The ever-increasing quantity of high resolution data over infrared and sub-millimetre wavelengths revealed the in-depth structures and physical properties of molecular clouds in PDRs (e.g. Shimajiri et al., 2013; Köhler et al., 2014; Stock et al., 2015).

Theoretical considerations based on first principles are used to identify and explain the features, effects and magnitudes of the processes involved in star formation and numerical modelling attempts to quantify these effects. Although a broad picture has been established, the processes on these different spatial scales - at least 10^{31} orders of magnitude - influence one another making it currently impossible to obtain a complete picture of star formation although a broad outline is discernible. Because the physics required to study these systems differs from one topic to another, the topics including quantum mechanics, gravitation, thermodynamics, hydrodynamics, electromagnetism and chemistry - and the effects of each are interdependent - finding solutions is non-trivial. As a result the analysis of processes at the different scales is the subject of separate areas of study - and within each of these there are a multitude of issues and unanswered questions - but the results of each of these, however, illuminates and informs the others. As a result, theoretical modelling faces challenges to develop comprehensive models to interpret the observational data but as far as the star forming processes are concerned two broad, but overlapping, thrusts can be identified:

- those concerned with much larger scales covering the mechanics of the formation of Giant Molecular Clouds (GMC) from the very diffuse Interstellar Medium (ISM), the creation of star clusters from the GMCs, the coming together of individual stars and clusters to form galaxies and clusters of galaxies and the subsequent life cycles of the galaxies

- those concentrating on the formation and evolution of individual stars (including binary and multiple systems) and, by extension, any associated planets.

1.4.2 Early Universe

Identifying and understanding the processes implicit in the creation of stars, both as it now occurs and as it occurred in the early period of the Universe is essential in describing the history of the Universe. In the early universe there were no stars and

the only elements present were hydrogen and helium with trace quantities of lithium and beryllium. As the Universe cooled gas was able to collapse and coalesce. Stacy et al. (2010) suggest that the formation of the first stars in an environment with low metallicity was probably very different to the formation of stars today. The addition of the heavier elements such as oxygen, silicon and the metals (collectively known as 'metals') to the ISM by nuclear fusion in the interior of the first generation of stars created dust and increased the efficiency of the cooling of the gas clouds. Stars are therefore the primary source of the elements heavier than the hydrogen and helium that were produced in the aftermath of the Big Bang, these heavier elements are necessary for life as we understand it and it is clear that to reach the chemical abundances observed today many cycles of star creation and destruction, for the heavier elements in particular through supernovae, have been necessary.

1.4.3 INTERSTELLAR MEDIUM AND MOLECULAR CLOUDS

The starting point of a description of star formation may be taken as the ISM; even though it is very tenuous the quantity of matter distributed over the vast distances between the stars is immense. In abundances the ISM is now known to be composed of approximately 70% hydrogen, 28% helium, and 2% 'metals' by mass. Some of the 'metals' is in the form of dust. These dust particles are composed of silicates, carbon, ice, and iron compounds and are small and irregularly shaped with dimensions which scatter blue light so it can be deduced that they typically have sizes in the order of the wavelength of blue light, that is of around 450 to 500 nanometres. Other elements can exist in atomic or in molecular form such as carbon compounds. The ISM is pervaded by magnetic fields and electromagnetic radiation covering the entire spectrum; its density varies depending on its position relative to other objects, it being denser closer to the stars, protostars and planetary systems and less dense when far from any of these bodies. As an example the particle number density in molecular clouds, of interest for this thesis, typically ranges from 10^2 to 10^5 cm^{-3}, in comparison the Earth's atmosphere has a number density of approximately 3.0×10^{19} cm^{-3} at sea level. Going further out from the edge of a galaxy the void between the galaxies is called 'intergalactic space' where the Intergalactic Medium is almost completely empty and very close to a total vacuum.

The bulk of the ISM is in motion and eventually, due to a combination of the actions of supernova explosions causing supersonic motion, the effect of magnetic fields, the time dependent gravitational field due to spiral density waves in the stellar disc of the galaxy, the ensuing turbulence and shock fronts and with enough gravitational attraction between the particles, clouds stretching across parsecs can form. These

were first observed within our local Galaxy and have since also been identified in neighbouring galaxies. If the clouds are sufficiently dense at optical wavelengths they absorb the light from the stars behind them and are known as 'dark nebulae', an example being the Horsehead Nebula.

Most molecular gas is found in Giant Molecular Clouds (GMCs) which typically have dimensions of 10 to 100 pc, and masses of 10^3 to 10^6 $M_\odot$, but some molecular gas is found in smaller clouds known as Bok Globules (Bok and Reilly, 1947). An interstellar cloud can collapse due to its self-gravity if it is large enough but, in the ordinary interstellar medium, this can only happen if the cloud has a mass of several thousand solar masses - which is a much greater value than that of any known star. It is concluded that there must be some process, or processes, that causes the cloud to fragment into smaller, higher density, clouds whose masses are in the same range as that of stars. Self-gravity acting by itself cannot do this, but this fragmentation can occur if the magnetic pressure within the cloud is much larger than the thermal pressure so compressing the gas.

These processes rely on the interaction of magnetohydrodynamic waves - which are possible due to the conductive nature of the ionised hydrogen making up the bulk of the ISM - with a thermal instability. A magnetohydrodynamic wave in a medium in which the magnetic pressure is much larger than the thermal pressure can produce dense regions, but not sufficiently dense for self-gravity to be effective. The gas in these denser regions is, however, also heated by cosmic rays and cooled by radiative processes. The net result is that although the gas is in thermal equilibrium it can exist in three different phases at the same pressure: ionised (H II), atomic (H I), and molecular (H_2) depending on its temperature. Thus the ISM in potential star-forming regions can be broadly divided into three phases:

- the hot ISM with temperatures $T > 10^4$K which contains mainly HII

- the warm ISM with temperatures between about 100K and 10^4K containing HI

- the cold ISM at $T < 100$K containing mainly H_2.

An increase in pressure, due to a supernova or a spiral density wave can move the gas from the warm phase into an intermediate unstable phase and a magnetohydrodynamic wave can then produce denser fragments whose self-gravity is strong enough for them to collapse to form clumps in the cold phase.

Stars can form in the cold phase of molecular clouds (MCs) as the temperature is sufficiently low to allow molecules to form. MCs have high column densities, shielding them from the interstellar radiation field with the result that their temperatures can

become very low (typically about 10K) allowing the formation of molecular hydrogen and other molecular species. Although the clouds demonstrate high absorption for visible light the dust becomes increasingly transparent at far-infrared, sub-millimetre, and radio wavelengths and observations at these frequencies reveal complex morphological and kinematic structures. Within the MCs the gas is not distributed evenly, instabilities lead to a transient, filamentary yet clumpy structure, there being cold high-density regions interspersed between warmer regions of very low density material.

The cold areas of molecular hydrogen - the objects of interest for this thesis - are very hard to observe. In the optical range they are only observable as 'dark clouds' as MCs can have tens of magnitudes of optical extinction meaning it is impossible to see their contents or anything behind them. Protostars embedded within MCs may be observed in the infrared, but not the MCs themselves. Although it would be useful to observe the structure and kinematics of the cold gas within MCs, cold molecular hydrogen ($T < 100K$) has no easily excited states so remains directly unobservable. The only possibility of observing cold H_2 directly is to measure the ultraviolet absorption along the line of sight from a massive star behind the cloud, the limitation is that there are very few of these lines of sight available. Therefore 'tracers' must be used, these are other molecules or dust in the MC which are assumed to have a similar distribution to the underlying H_2 distribution although McKee & Ostriker (McKee and Ostriker, 2007) refer to a method of using scattered IR to obtain density distributions (Foster and Goodman, 2006), (Padoan et al., 2006).

1.4.4 Physical Processes in Molecular Clouds

The volumes of the ISM associated with star formation consist overwhelmingly of molecular, rather than atomic or ionised, gas and the issue is to understand the several physical processes that govern the behaviour of the ISM and how the molecular gas is formed, maintained and transformed into stars. The microphysics of the ISM may be grouped as

- the thermodynamics of the molecular gas

- the chemical processes present in the molecular gas.

Observations show that the internal temperature of molecular clouds can be low, dropping to minima of about 10K, which implies that the various heating and cooling processes have to be in equilibrium to allow these temperatures to be maintained. In these colder, denser, non-ionised molecular regions, magnetohydrodynamics has a less significant influence of the evolution of the cloud.

In the ISM and in the outer layers of an MC the major heating process is due to the interaction of FUV with dust grains. Photons with energies in the range of 6 eV $< h\nu < 13.6$ eV strike dust grains and eject fast electrons which eventually deposit their energy as heat in the gas. The heating rate is proportional to the radiation field strength, the dust abundance and the rate at which the radiation field is attenuated with penetration (Tielens, 2005). Thus in the interiors of molecular clouds, if the cloud is of sufficient size and density, photoelectric heating is strongly suppressed because of the absorption of the FUV photons, the cloud is self-shielding and the central regions will be cool.

An additional source of heating in molecular clouds is H_2 formation on dust grains. Some fraction of the 4.48eV binding energy of the H_2 molecule formed on the surface goes into kinetic energy of the dust grain and if the dust grain is 'hotter' than the gas then this energy is transferred to the gas as heat.

Cosmic rays are also a source of heat input into the MC. As the cosmic rays are relativistic particles they have low interaction cross-sections and therefore are able to penetrate into regions where light and FUV is already absent because of absorption. The first step in the process of cosmic ray heating is the interaction of a cosmic ray with a hydrogen molecule which ejects an electron:

$$cr + H_2 \longrightarrow H_2{}^+ + e^- + cr.$$

The free electron's energy depends only weakly on the energy of the incident cosmic ray and is typically 30eV but it cannot easily directly transfer its energy to other particles in the gas because its small mass means that most collisions are elastic and therefore do not transfer energy. However, the electron also has enough energy to ionise or dissociate other hydrogen molecules thus providing an inelastic reaction that can convert some of the 30 eV to heat. There are several further mechanisms by which heat transfer can occur which are discussed in Glassgold et al. (2012). In the deep interior of molecular clouds cosmic rays provide the majority of the heat input.

There are two main cooling processes in molecular clouds: dust radiation and molecular line emission. Dust can cool the gas efficiently because, being solids, they are thermal emitters. However, dust is only able to cool the gas if collisions between dust grains and hydrogen molecules occur with sufficient frequency to keep them thermally well-coupled. If the collision frequency is too low the grains cool off but the gas stays hot. The density at which grains and gas become well-coupled is around 10^4 to 10^5 cm^{-3}, which is higher than the typical density in a GMC but it does become important as the density of a collapsing object increases. The other cooling process is molecular line emission and the most important molecule for this purpose is CO. The physics is fairly simple: CO molecules are excited by inelastic collisions with hydrogen molecules

and such collisions convert kinetic energy to potential energy within the molecule. If the molecule de-excites radiatively, and the resulting photon escapes from the cloud, the cloud loses energy and cools.

The most significant chemical processes are concerned with hydrogen, carbon and oxygen. In the case of hydrogen the molecular form has a lower energy state than than atomic hydrogen but the transformation in the gas phase is extremely slow due to the symmetry of the hydrogen molecule. The dominant formation process is formation on the surfaces of dust grains where the excess energy released by forming the molecule is transferred into vibrations in the dust grain lattice. The molecular hydrogen can also be split into the atomic form via various pathways and the balance between the two forms depends on the shielding offered by the MC at that point.

Carbon-oxygen chemistry is important in understanding cooling processes as CO is the most significant molecule. The main reason for this is abundances: the most abundant elements in the universe after H and He are O, C, and N. CO is the simplest and, under the conditions found in the ISM, the most energetically favourable molecule that can be made from these elements. There are two main pathways to CO, one passes through the OH molecule via a series of reactions and the other is through the CH molecule. Both of these reaction chains require the presence of H_2.

The final result of all these processes working together is that clouds tend to have a layered structure. In poorly-shielded regions near the surface where the FUV has not yet been attenuated, the photo-dissociation region, HI and C^+ dominate. Further in, where the FUV has been partly attenuated, H_2 and C^+ dominate and at the centre H_2 and CO are the most significant chemical states.

1.4.5 STAGES IN STAR FORMATION

From this starting point current thinking, such as that given by (Goodwin, 2013), is that conceptually star formation can be divided into several main stages:

1. Molecular cloud formation: a large (10^3 to 10^6 $M_\odot$) cloud of gas forms within the ISM. The high column and volume densities allow the cloud to cool, and remain cool, thus allowing molecular hydrogen and other molecules to form.

2. Prestellar core formation: the molecular cloud fragments into self-gravitating condensations known as 'clumps' and, on smaller scales, 'cores'. 'Prestellar' cores are the birth places of stars.

3. Embedded star formation: prestellar cores collapse and form a protostar, often a binary or a multiple system, surrounded by a disc of gas. Initially these pro-

tostars are large, astronomical unit (AU) sized hydrostatically supported objects embedded in the gas of the core.

4. Pre-main sequence stars: most of the mass in the core is collected by accretion by the star or, in the case of multiple systems, stars. Young stars on the pre-main sequence are observed to be surrounded by massive discs, these discs may well be in the process of planet formation and disappear quite quickly. Eventually the star will reach the main sequence and become a 'normal' main sequence star.

5. Star clusters: in the second stage listed above, a molecular cloud usually fragments into many cores, forming a star cluster of between 10^2 and 10^6 stars in only a few pc^3 in a few Myr.

6. The end of star formation: once one or more massive (> 10 M$_\odot$) stars form, the energy from their UV radiation fields (and associated HII regions), stellar winds and eventual supernovae will expel any gas that has not already been formed into stars. This reduction in the available quantity of gas prevents further star formation and can result in the destruction of any nearby star clusters.

The stages listed above do not necessarily happen sequentially but some stages have to happen before the next, for example stars cannot form before a molecular cloud has formed. This thesis is concerned with processes occurring in the second of these stages, that of individual prestellar core formation, specifically looking at the significance of microphysical and chemical processes on the evolution of the core from the initial cloud.

Astrophysics covers a vast range of topics and areas of studies both observational and theoretical and it is impossible to give a comprehensive description of star formation in a few words. However many review papers such as (McKee and Ostriker, 2007; Klessen et al., 2009; Goodwin, 2013), have been published which, with their references, give a clear summary of the current state of knowledge.

1.5 Modelling

As mentioned in Section 1.3, strict analytical methods are not appropriate in describing the complex interplay of processes inherent in star formation and numerical simulations, based on fundamental physical principles, enable more realistic models to be constructed. There are many different types of computational fluid dynamics models that may be used to study different aspects of star formation but these may be grouped into two broad families - grid-based (Eulerian) and particle-based (Lagrangian). Both

types have their own advantages and disadvantages when it comes to simulating the evolution of MCs but generally grid-based codes are sometimes more suitable when gravity is not being considered whereas the Lagrangian-based technique of Smoothed Particle Hydrodynamics (SPH), originally introduced by Lucy (1977) and Gingold and Monaghan (1977), is more appropriate when studying flows where gravity dominates.

Some of the issues with SPH and differences between it and grid-based techniques are explored by Price (2011). Advances have been made in both types over the years and modifications and additions to the code sets have been made to extend their capabilities and ameliorate some of their limitations. For example for grid-based simulations the size of the mesh in the grid may be changed while the simulation is running (adaptive mesh refinement, see for example Berger and Colella (1989)) to cope with changes in flows and densities and issues with discretisation of the equations of self-gravitational hydrodynamics can be avoided if the ratio of cell size to Jeans' length can be kept under 0.25 (Truelove et al., 1997).

Similarly in SPH models some of the issues with significant increases in local particle densities may be counteracted using 'sink particles', Bate et al. (1995). Both grid-based and particle-based approaches can be adapted to allow for relativistic and magneto-hydrodynamics (MHD) effects as well as chemical reactions occurring in the computing space.

All of these different types of modelling help analyse certain parts of the star formation process or other astrophysical problems. They can help, for example, in making simulations of PDR regions (Andree-Labsch et al., 2014) or of the Pillars of Creation in the Eagle nebula or of bright rimmed clouds (Miao et al., 2009; McLeod et al., 2015) and also permits the analysis of certain aspects in more detail such as geometry of clouds (Kinnear et al., 2015) or modelling the chemical reactions occurring in the MCs (Seifried and Walch, 2016).

1.6 Computing Considerations

A number of software packages covering a variety of end uses are readily available for both grid and particle based computational fluid dynamics. A sub-set of these are designed to simulate astrophysical processes such as galaxy, star and planet formation.

The use of mesh-based solvers for terrestrial mechanical and hydrodynamics problems is well known. In the last decade or so interest in SPH techniques to solve mechanical and hydraulics problems has been increasing and several open source and commercial SPH-based packages are now available for these areas. Examples of open

source codes are AQUAgpusph, (Cercos-Pita, 2015) an SPH solver, DualSPHysics (Crespo et al., 2015) for free-surface flow phenomena such as waves or impact of dam-breaks on off-shore structures.

For astrophysics, apart from the CLOUD code used for the numerical calculations which are the subject of this thesis, other examples of SPH code packages which are freely available are:

- GADGET (Springel et al., 2001) which evolved into

- GADGET-2 (Springel V., 2005, MNRAS, 364, 1105)

- PHANTOM (Price et al., 2017)

- SEREN (Hubber et al., 2011) which evolved from the earlier DRAGON code (Goodwin et al., 2004) .

In addition ndspmhd (Price, 2012) is a 'home brew' code which is intended for experiments with algorithms and which arose from work in modelling magnetohydrodynamics using SPH.

Examples of grid-based codes for astrophysics applications are:

- Athena (Stone et al., 2008)

- RAMSES (Teyssier, 2002)

- ZEUS which is a family of codes covering 2D and 3D cases (Stone and Norman, 1992; Clarke, 1996).

An open source code designed for a specific purpose in astrophysics is Cloudy (Ferland et al., 2013). This is a plasma simulation code designed to simulate conditions in a non-equilibrium gas and to predict its spectrum.

Both Athena and ZEUS are intended for magnetohydrodynamic studies, the original version of ZEUS is a two-dimensional code that includes ideal magnetohydrodynamics and radiative transfer (Stone and Norman, 1992). Several three-dimensional versions have been developed, for example (Clarke, 1996) and (Clarke, 2010). RAMSES is intended for general purpose simulations in self-gravitating fluid dynamics, it is a grid-based solver with adaptive mesh refinement.

Descriptions of these codes and examples of their use may be found in the associated references and other published work such as Walch et al. (2013).

In view of the very large number of particles - in the order of one million - necessary to achieve reliable simulations of very large scale events, these codes have been adapted or written to run on parallel processors and supercomputers, e.g., (Bate et al., 2014)

to obtain results at a suitably high resolution for that study. In view of the computing resources available for this work such large scale modelling was not possible but it was felt that a closer study of the effects of a limited range of microphysical processes during the, for star formation, critical period of the creation of a clump would be of interest and would be compatible with the resources available. Therefore the investigations into the interplay between the microphysical processes reported in this thesis have been modelled using SPH as the self-gravity of the particles in the molecular clouds is an important consideration.

1.7   Objectives of this work

Gorti and Hollenbach (2002) have presented results of simulations on effects of FUV radiation from nearby hot, massive stars of type OB on the evolution of clumps in star-forming molecular clouds. They discussed the various effects and processes which affect clump evolution with a very much simplified analytical model as well as with one-dimensional numerical simulations. Radiation is considered to affect the clouds in two ways. The first mechanism is seen to assist the collapse of the cloud by inducing shocks that propagate through the cloud. These can then cause local clumps of higher density to form which act as kernels for mass accretion. The other assumption is that it hinders the cloud's collapse by photoevaporation. That is, the radiation feedback heats material on the cloud's surface layer thereby increasing the average velocity of the constituent particles. This enables some of those with outwardly directed velocity vectors to escape thus causing the cloud to lose mass which in turn reduces its net gravitational energy and therefore its tendency to collapse.

This study is intended to understand these mechanisms in more detail. To do so it is necessary to understand the relative importance of the physical factors involved and in this study the effects of:

- FUV photo-electric heating

- cosmic ray heating

- gas-dust thermal exchange

- molecular line cooling

- basic chemistry

acting in a molecular cloud were simulated. Other factors such as turbulence and magnetic fields were not included in the models simulated due to limitations in available computer time; it was also considered that their effects were less significant in cooler molecular clouds than in the hot, ionised interstellar medium.

This study reports on extensive SPH numerical simulations of the evolution of a simplified spherical model of a molecular cloud and attempts to describe the physical processes in order to:

1. Identify and compare the roles of the physical and chemical processes listed above in the evolution of molecular clouds in photo-dissociation regions (PDRs) with specific interest in the formation of prestellar cores. It is hoped that the investigation will provide a data point for astrophysicists on the importance of including different microphysical and chemical processes in constructing models of star formation in different environments.

2. Reveal the dynamic region of the evolution of molecular clouds in terms of initial physical conditions of the clouds and the external radiation fields, which can provide astronomers with useful tools to decide the origin of the observed objects.

The aim of the simulations is to identify the relative importance of these different microphysical and chemical processes under different conditions of cloud densities and temperatures which can occur during a cloud's evolution. The model is intentionally simplified, for example momentum is conserved but the particles are considered stationary at the start, as the object is to understand these processes and their interactions and not to model the complete evolution of a star.

To achieve this aim simulations were run with different combinations of the radiation and chemical processes active and isolated. In some cases these combinations do not reflect real conditions but the results are intended to form a baseline against which the significance of the individual processes can be judged.

For all the simulations, the corresponding 'Modified Jeans Mass' caused by the radiation and the chemical feedback was found for each of the different combinations. The evolution of the physical properties of the simulated objects in all the simulated molecular clouds are analysed and categorised according to their dynamic behaviour. An overall picture of the effect of the radiation and chemical feedback on the evolution of molecular clouds will be presented.

As outlined in Section 1.2, Jeans' model for the collapse of interstellar gas clouds assumes that, at a given temperature and radius, the cloud is stable if its internal gas pressure is sufficient to withstand the self-gravity of the particles making up the cloud, that is it must be in hydrostatic equilibrium. However the models used in the numerical

simulations discussed in this thesis do allow for random instabilities, this 'clumping' can initiate collapse of parts of the cloud without the Jeans Mass for the whole cloud being reached. As these 'clumps' do not contain all the mass of the cloud the gravitational attraction is less than would be expected for the case of the Jeans mass; this effect can lead to the differences seen in the predictions made by the numerical models. In particular the mass required for cloud collapse is significantly reduced in the case of an isothermal cloud. Further reduction in the mass required for cloud collapse can be seen if an non-isothermal cloud is exposed to externally incident FUV. These simulations also show that collapse is accelerated with increasing FUV flux.

1.8 Layout

This Thesis is organised as follows. The issues which have to be addressed in modelling a tenuous gas cloud and the concepts behind the SPH code used to simulate the molecular cloud are described in Chapter 2. The chemical networks and micro-physical processes outlined in Section 1.4.4 with specific reference to the models adopted in the SPH code are described in Chapter 3. The setup and initial conditions of the cloud and the choice of the number of particles used in the model and subsequent testing are described and discussed in Chapter 4.

Chapter 5 discusses thermal effects and introduces the concept of the Modified Jeans Mass as an indicator of the effect the thermal processes have on a cloud's collapse. The simulation results obtained for different combinations of active micro-physical and chemical processes are shown in Chapter 6 and the results for a range of FUV flux levels are included in Chapter 7 again using the Modified Jeans Mass as an indicator of the significance of the effects of the micro-physical and chemical process on a cloud's evolution. A summary of the significance of the simulation results and a discussion of some of the issues raised is included in Chapter 8. The final Chapter 9 describes some initial investigations on the effects of FUV intensities on the time required for a protostar 'seed' to form and also lists some fields of investigations which could extend the area of study covered in this thesis. The Appendices A to C include plots of the results of the simulations for all the different combinations of processes, cloud densities and flux levels studied.

Chapter 2

Smoothed Particle Hydrodynamics

2.1 Introduction

The dimensions of objects in the observable universe, from comets and planets, through stars, star clusters to galaxies and nebulae, molecular clouds and the intergalactic medium vary by many orders of magnitude. All these objects have been formed or shaped by interactions between their components and with each other and these processes can largely be explained by the discipline of fluid dynamics. Only in the case of interactions between solid bodies are other disciplines appropriate.

The range of time scales is also very large as are the number and strengths of the interactions which can occur, these often involving spatial and temporal dimensions which are very different from those encountered with simple gas flows. The resulting clouds, nebulae and stars are shaped by the gravitational attraction between the constituent particles, the dynamics of moving particles and bodies and interactions with other physical processes such as electromagnetic radiation of different energies, energetic particles from other sources, chemical and fusion reactions, shocks and magnetic fields. To explain these processes requires a multi-disciplinary approach which can also deal with time scales ranging from sub-second to mega-years. Except for the simplest

of bodies analytical methods are not suitable, there being a lack of symmetry in many cases and the processes involved being complex.

As a result numerical methods are the only tools which can be used to study the evolution of the bodies in the observable universe - and because of the way matter is mostly distributed, in the form of gas, gas clouds and stars, with only some relatively very small solid objects, fluid dynamics, sometimes also called hydrodynamics, is the most appropriate. Techniques developed in this discipline are also used in the study of flows in many technical applications, the aerodynamics of aircraft and automobiles and liquid sloshing in tanks are examples, and as a result computational fluid dynamics is a well understood field. As indicated in Section 1.6 there are a number of computational fluid dynamics code packages which have been written to solve fluid flow problems, no single code package deals with the types of materials and fluid flows seen in terrestrial problems and the materials and flows seen in astrophysics. Astrophysics sets some very specific requirements on the way that the analysis is performed, the method adopted has to be able to deal with conditions such as:

- there being no fixed boundaries. This implies that flows are determined by interactions within the medium itself and are not given by the presence of fixed structures

- the mutual gravitational attraction between particles

- the conservation of properties, e.g., angular momentum

- physical quantities that can vary by many orders of magnitude within the region being studied

- step changes in properties, such as shocks

- the objects can be exposed to external influences, e.g., electromagnetic radiation

- magnetic fields, both internal and external

- heat balance

- chemical reactions.

2.2   The Hydrodynamic Equations

The evolution of objects formed from the interstellar medium is assumed to be described by the fluid dynamic equations. In a simple case of a self-gravitating fluid

the hydrodynamic equation for the conservation of mass, also known as the continuity equation, and those for momentum and energy are given here in Lagrangian form.

The continuity equation may be written as

$$\frac{d\rho}{dt} + \rho \nabla \cdot \boldsymbol{v} = 0 \tag{2.1}$$

where $\boldsymbol{v}$ is velocity and ρ is density.

The momentum equation may be written as

$$\frac{d\boldsymbol{v}}{dt} = -\frac{1}{\rho}\nabla P - \nabla \Phi + \boldsymbol{S}_{visc} \tag{2.2}$$

where P is pressure and Φ is the gravitational potential. $\boldsymbol{S}_{visc}$ is added to the basic Euler equation to represent the force due to viscosity which is important where there are sharp gradients due to shocks.

The energy equation may be written as

$$\frac{du}{dt} + \frac{P}{\rho}\nabla \cdot \boldsymbol{v} = \frac{\Gamma - \Lambda}{\rho} \tag{2.3}$$

where u is the internal energy per unit mass. Γ and Λ represent non adiabatic heating and cooling rates respectively. The derivative d/dt is the Lagrangian time derivative

$$\frac{d}{dt} = \frac{\partial}{\partial t} + \boldsymbol{v} \cdot \nabla \tag{2.4}$$

The evolution of a given fluid can be simulated using a hydrodynamic algorithm to solve these equations.

2.3 The Hydrodynamic Equations in Smoothed Particle Hydrodynamics

As mentioned in the Introduction section 1.5, numerical methods developed for finding approximate solutions to the fluid equations may be divided into two broad groups, Eulerian (grid based) and Lagrangian (particle based). In both cases the main problem domain, which is treated as continuous, is sub-divided into an array of simpler parts, and a solution for each part is found. These part solutions are then combined to yield a solution for the original problem domain. In the Eulerian method the problem domain is divided into a fixed grid where the properties of the boundaries are shared

with the neighbour and, using a finite difference method, a solution is found for each individual grid element. In the Lagrangian method the fluid is sub-divided into a series of 'mass-particles' which possess properties which interact with the neighbouring 'mass-particles' and solutions found for each particle. In essence in a simple grid the Eulerian method keeps volume constant and the Lagrangian method keeps mass constant. In a sense the Eulerian method can be equated to an observer observing the grid and the fluid from the outside, in the Lagrangian approach the observer may be treated as travelling with a particle in the fluid.

Both the Eulerian and Lagrangian approaches are equally valid, each has its advantages and disadvantages for the treatment of a given problem domain in computational fluid dynamics. The most significant of these are discussed in this section in terms of their suitability in reaching solutions for astrophysical problems. The use of these approaches in modelling other physical processes such as the response of materials to large deformations, fluid dynamics, coupled fluid-structure problem domains and non-linear solid mechanics are not considered.

Grid-based systems are limited by the size of the grid set initially, the fluid being studied cannot exist outside the grid. Because of the dimensional magnitudes of astrophysical problems a large number of grid elements are required, and therefore much computational time may be needed to process each set of calculations. As a consequence, the grid approach is not suitable for modelling fluid evolution with high spatial resolution unless specialised techniques are adopted, such as Adaptive Mesh Refinement. On the other hand a grid system enables magnetic fields and shock fronts to be easily modelled and is suited to 2-D simulations.

In the Lagrangian approach the 'mass-particles' are associated with a spatial distance, the smoothing length, over which their properties are smoothed by a kernel function. The physical quantity under investigation for any particle can then be obtained by summing the relevant properties of all the particles which lie within the range of the kernel. Thus the resolution of the Lagrangian method can be changed with respect to variables such as the density by altering the smoothing length. Similar to the grid-based approach a high particle density can also affect the necessary computer processing time adversely, but the use of 'sink' particles - where an agglomeration of particles can be represented by one 'sink' particle - can ease this issue. Being a particle-following, i.e., a mass-following, method the effects of chemical processes are easier to compute as the reactions, and therefore heat absorption or emission occurs where the particles are found. A Lagrangian approach permits the simple calculation of the effects of self-gravity in combination with a particle-based gravity solver, an important consideration for the study of astrophysical clouds, as well as the use of

structures of arbitrary shape. One artefact of the smoothing length in the Lagrangian approach which can affect the results is the 'smearing out' of features such as shocks which are infinitely thin.

It is difficult to integrate magnetic fields and their effects into a Lagrangian approach, work has been done in this area in recent years (Tricco and Price, 2012; Hopkins and Raives, 2016). However in view of the particle densities and species present in the molecular clouds being studied and reported on in this thesis, it is considered that magnetic effects will not be significant compared to the effects of other inputs such as ionisation and heat. As a first approximation they may be disregarded.

Both approaches can treat the effects of externally incident radiation fairly efficiently - as mentioned above the grid-based analysis can give clean shock front results and a Lagrangian approach can use ray-tracing to solve for arbitrarily arranged multiple sources.

Whether a grid-based or Lagrangian approach is selected depends on which is the most efficient system for the computational problem being addressed. As has already been stated, a grid-based approach is well suited for studying flows and shocks and 2-D slices, Lagrangian for 3 dimensional objects with self-gravity. Smoothed Particle Hydrodynamics (SPH) is a particular implementation of a Lagrangian approach and was originally specifically developed by Gingold and Monaghan (1977) and Lucy (1977) to solve astrophysical problems such as binary star formation. This approach has been developed further by many contributors and as a result it is the preferred method for studying the evolution of astrophysical clouds and star formation - this is the numerical method selected for the modelling presented in this thesis.

2.3.1 Fundamentals of SPH

In SPH the interpolation points called particles are moved with the local fluid velocity and are evaluated in a coordinate system attached to the particle. The particles have a spatial volume based on a smoothing length (h) with properties that are smoothed by a kernel function. Derivatives are calculated via a kernel approximation without the need for finite differences; in this way the partial differential equations of Lagrangian fluid dynamics are transformed into ordinary differential equations. To ensure that the physically conserved properties are also conserved in the construction of the discretised particles, the particle equations need to possess the correct symmetries. This ensures momentum conservation during interactions of particle pairs. Inside the simulation region there is a constant number of neighbouring particles (N_{neib}) overlapping each other. Their properties (mass, velocity, position, density and temperature) are smoothed by a kernel function.

The smoothing kernel defines the extent of a particle's influence. Commonly used are the Gaussian function and the cubic spline. The latter function is zero for particles further away than two smoothing lengths as distinct from the Gaussian function where particles at any finite distance away make a small contribution to the gravity field affecting the particle under study.

2.3.1(a) SPH Representation of Physical Quantities

SPH uses a kernel approximation in which a function $f(\boldsymbol{r})$ is approximated by

$$\langle f(r) \rangle = \int f(r')W(|\boldsymbol{r} - \boldsymbol{r'}|, h)\mathrm{d}^3 r', \tag{2.5}$$

where W is the smoothing kernel and the smoothing length h determines the width of the kernel.

In order to recover the original function at the limit of an infinitely small smoothing region, the kernel should fulfil

$$\lim_{h \to 0} f_h(\boldsymbol{r}) = f(\boldsymbol{r}) \tag{2.6}$$

and

$$\int W(\boldsymbol{r_i} - \boldsymbol{r_j}, h)\mathrm{d}^3 r = 1 \tag{2.7}$$

so apart from being normalised, the kernel should have the Dirac δ-function in the limit of vanishing smoothing length. To arrive at a discrete approximation, which can be written as

$$f_h(\boldsymbol{r}) = \int \frac{f(\boldsymbol{r})}{\rho(\boldsymbol{r})}W(|\boldsymbol{r} - \boldsymbol{r'}|, h)\rho(\boldsymbol{r})\mathrm{d}^3 r, \tag{2.8}$$

where ρ is the mass density, one can replace the integral by a sum over a set of interpolation points, i.e. particles, whose masses, m_j, result from the term $\rho(\boldsymbol{r})\mathrm{d}^3 r$ which can be written as

$$f(\boldsymbol{r_i}) = \sum_{j=1}^{N} \frac{m_j}{\rho_j} f(r_j)W(\boldsymbol{r}_i - \boldsymbol{r}_j), h). \tag{2.9}$$

2.3.1(b) SPH Representation of the Gradient of Physical Quantities

In the general case in SPH the properties for any arbitrary particle i are calculated as a function of the sum of the product of the properties of each of the neighbouring

particles j with the value of the smoothing kernel at the separation r_{ij}. The gradient of the smoothing kernel at each location is also computed and is used to ensure the correct calculation of the pressure forces on each particle. Thus any property A at the position of an arbitrary particle i, $\boldsymbol{r}_i$ is made up by the sum of the contributions from all the particles j within a distance $2h$ of particle i. Making the assumption that it is possible to make both first and second order differentials of the smoothing kernel, it is therefore possible to define the gradient and the Laplacian of any property A. So the partial derivative of the x-component becomes

$$\frac{\partial}{\partial x} A_i(r_i) = \frac{\partial}{\partial x}\left(A_j \frac{m_j}{\rho_j} W(r_i - r_j, h)\right) \tag{2.10}$$

Using the product rule on (2.10) gives for the RHS

$$\frac{\partial}{\partial x}\left(A_j \frac{m_j}{\rho_j} W(r_i - r_j, h)\right) = \frac{\partial}{\partial x}\left(A_j \frac{m_j}{\rho_j}\right) W(r_i - r_j, h) + A_j \frac{m_j}{\rho_j}\frac{\partial}{\partial x} W(r_i - r_j, h)$$

$$= 0 \cdot W(r_i - r_j, h) + A_j \frac{m_j}{\rho_j}\frac{\partial}{\partial x} W(r_i - r_j, h)$$

$$= A_j \frac{m_j}{\rho_j}\frac{\partial}{\partial x} W(r_i - r_j, h) \tag{2.11}$$

It can be seen from (2.11) that $A_j \frac{m_j}{\rho_j}$ is neither dependant on the x-component nor on any other component of coordinate space, and hence the product can be considered a constant. The x-component therefore only affects the smoothing kernel and so the summation also only affects the smoothing kernel. The gradient of the smoothed property becomes

$$\nabla A_i(r_i) = \sum_j A_j \frac{m_j}{\rho_j} \nabla W(r_i - r_j, h) \tag{2.12}$$

A specific way of writing the symmetrised form is

$$\frac{\nabla A}{\rho} = \nabla \frac{A}{\rho} + \frac{A}{\rho^2}\nabla \rho \tag{2.13}$$

$$\nabla A = \rho\left(\nabla\left(\frac{A}{\rho}\right) + \frac{A}{\rho^2}\nabla \rho\right) \tag{2.14}$$

in SPH term this becomes

$$\nabla A_i(r_i) = \rho \sum_j \left(\frac{A_j}{\rho_j^2} + \frac{A}{\rho^2}\right) m_j \nabla W(r_i - r_j, h) \tag{2.15}$$

2.3.1(c)   THE SMOOTHING FUNCTION AND SMOOTHING LENGTH

To reduce the computational cost it is advantageous to reduce the number of contributing particles in the sum of equation (2.21) to a subset of local particles. To do this the kernel should have a finite width otherwise the summation would extend to all the N particles in the simulation and create a numerically expensive task where the method would be $\mathcal{O}(N^2)$.

The smoothing length, h, determines the width of this kernel. The quantity $2h$ is chosen to be the radius of the influence of the kernel function, which is the definition of the SPH particle size. The number of nearest neighbours, N_{neib}, is constant so h varies depending on the fluid density, see Figure 2.1. This means the smoothing length varies with each SPH particle and also varies with time as the simulations progress.

The cubic spline SPH kernel by Monaghan and Lattanzio (1985) is used in this SPH simulation where

$$W(u,h) = \frac{1}{\pi h^3} \begin{cases} 1 - \frac{3}{2}\left(\frac{u}{h}\right)^2 + \frac{3}{4}\left(\frac{u}{h}\right)^3 & 0 \le u/h \le 1, \\ \frac{1}{4}\left[2 - \left(\frac{u}{h}\right)\right]^3 & 1 \le u/h \le 2, \\ 0 & u/h \ge 2, \end{cases} \tag{2.16}$$

where $u = |r_i - r_j|$. The smoothed functions are used throughout in the SPH code used for these simulations such as in equation (2.21). The visual representation of the cubic spline can be seen in Figure 2.2.

When variable smoothing lengths are used, it is usual practice to symmetrise the equation of pressure force so that momentum conservation through pairwise interactions is ensured. Two different methods of symmetrisation have been proposed (Evrard, 1988; Hernquist and Katz, 1989), but for the case of a barotropic equation of state, as considered by the SPH code, the pressure force is no longer derived from a potential function and so it does not strictly lead to conservation of energy. An alternative method has been derived to determine the smoothing length as a function of the particles positions permitting the conservative equations of motion to be written.

Assume h_i to be of the general form

$$h_i = \mathcal{G}\left[\sum_{j=1}^{N} \chi_{in} H\left(|r_i - r_j|\right)\right] \tag{2.17}$$

where $\mathcal{G} = \mathcal{G}_i$ and $H = H_{in}$ are arbitrary functions and the χ_{in} are arbitrary numbers that are zero when $i = j$. The subscripts i, j denote that the arguments of functions
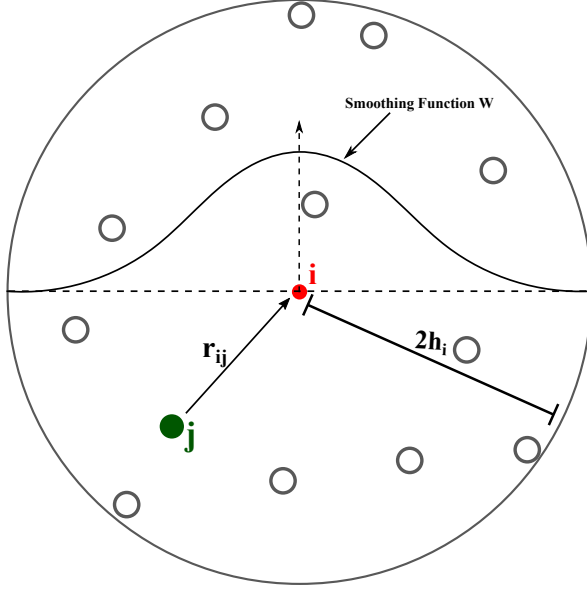
Figure 2.1: This diagram is a 2D representation of a 3D smoothed particle. The smoothing length h of a particle is varied to keep the number of nearest neighbours within a distance of $2h$ constant at a number given by N_{TOL}. A representation of the smoothing function shows how it weights the contribution of particles at different distances. Particles at distances greater that $2h$ do not contribute to the smoothing length calculation.

relate to particles i and j. The smoothing length is symmetrised based on

$$h_{ij} = \frac{h_i + h_j}{2}. \tag{2.18}$$

The method chosen to calculate the smoothing length, h_i, for each particle must meet two basic conditions. Firstly h_i has to be some function of the particle's position. Secondly the number of nearest neighbours that h_i encompasses should be approximately constant with each particle it affects, this ensures that each point in the fluid is treated with similar accuracy. A three-step approach similar to that proposed by Hernquist and Katz (1989) has been adopted.

1. An estimate of h_i^n, particle i's smoothing length at time-step n, is obtained using the relation

$$h_i^n = \frac{1}{2} h_i^{n-1} \left[1 + \left(\frac{N_{\text{TOL}})}{N^{n-1}} \right)^{1/3} \right] \tag{2.19}$$

where N_{TOL} is a parameter that determines the desired number of nearest neighbours, and N^{n-1} is the number of nearest neighbours at the previous time step.

2. A nearest neighbour search is performed using the method described in Section

25
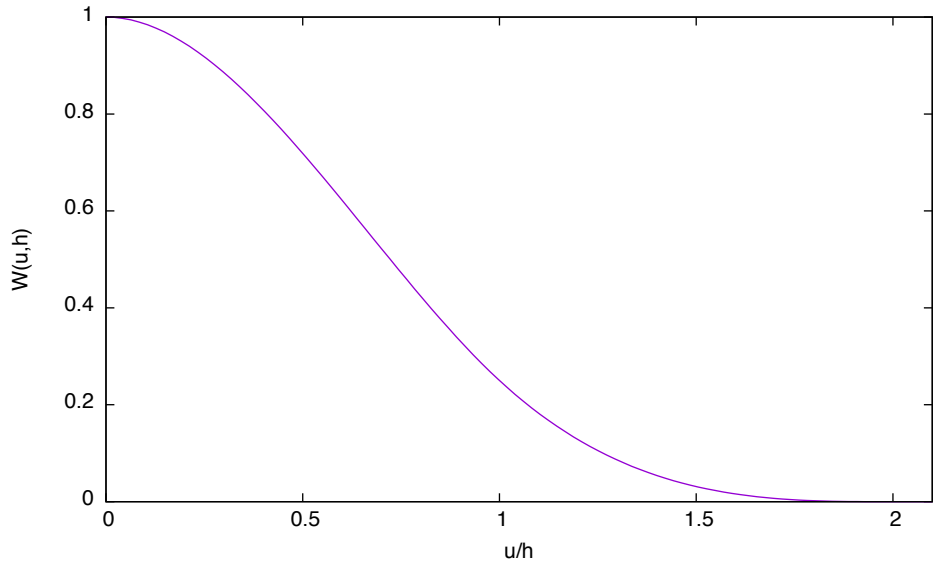
Figure 2.2: Cubic Spline (Monaghan and Lattanzio, 1985)

2.4.1 and the number of particles lying within $2h_i^n$ is counted. If the number of neighbours lies within a small range either side of N_{TOL} then it proceeds to the next stage of the algorithm. Otherwise, h_i^n is adjusted so the number of neighbours falls within the required range.

3. The most distant nearest neighbour of particle i is selected, and the new h_i is set to

$$h_i = \frac{1}{2} |r_i - r_{i_{\max}}| \tag{2.20}$$

where $r_{i_{max}}$ is the position of particle i's furthest neighbour. In terms of the general equation (2.17), the functions $\mathscr{G}(x) = x$ and $H(x) = {}^x\!/_2$, with $\chi_{in} = \delta_{ni_{\max}}$.

2.3.2 THE DENSITY

The summation can be written as (Monaghan, 1992),

$$\rho(\boldsymbol{r}) = \sum_{j=1}^{N} m W(\boldsymbol{r}_i - \boldsymbol{r}_j), h). \tag{2.21}$$

Here the particle j has mass m_j, position r_j and density ρ_j.

26

2.3.3 THE PRESSURE FORCE

An inviscid fluid with a barotropic equation of state is a Hamiltonian system. When modelling such a system the particle equations of motion in SPH therefore can be treated as a Hamiltonian system. Nelson and Papaloizou (1993) Nelson and Papaloizou (1994) write the thermal contribution to the total energy as

$$U = \int_V F(\rho)\rho d^3 r, \tag{2.22}$$

where

$$\frac{dF}{d\rho} = \frac{P}{\rho^2}. \tag{2.23}$$

This has the Monte Carlo representation

$$U = \sum_{k=1}^{N} m_k F(\rho_k). \tag{2.24}$$

U, as the potential function, can be used for deriving the pressure force on a particle i with

$$F_{P,i} = -\frac{\partial U}{\partial \boldsymbol{r}_i} \tag{2.25}$$

The same equation holds for an adiabatic system for which the entropy of each particle is conserved. One only replaces the $F(\rho)$ in equation (2.24) with the internal energy per unit mass, $\mathscr{U}(S, \rho)$ as a function of entropy and density. The Monte Carlo representation with the internal energy per unit mass for the pressure potential function is

$$U = \sum_{k=1}^{N} m_k \mathscr{U}(S_k, \rho_k), \tag{2.26}$$

where S_k denotes the entropy per unit mass for particle k. The qualities that $\mathscr{U}$ needs are given by

$$\left(\frac{\partial \mathscr{U}}{\partial \rho}\right)_S = \frac{P}{\rho^2}. \tag{2.27}$$

For an adiabatic flow S_k is constant, so that in both adiabatic and barotropic cases the pressure force on a particle i are found after differentiating either equations (2.24) or (2.26) and using (2.21) so

$$\boldsymbol{F}_{P,i} = -\sum_{k=1}^{N}\sum_{j=1}^{N} m_k m_j \left(\frac{P_k}{\rho_k^2}\right)$$
$$\times \frac{\partial}{\partial \boldsymbol{r}_i} \frac{1}{2} \left[W(|r_k - r_j|), h_k) + W(|r_k - r_j|, h_j)\right] \tag{2.28}$$

where $\boldsymbol{r}_{kj} \equiv \boldsymbol{r}_k - \boldsymbol{r}_j$ (Hernquist and Katz, 1989).

$$\frac{\partial W_{jk}}{\partial r_i} = \frac{\partial W_{jk}}{\partial |r|_{jk}} \frac{r_{jk}}{|r_{jk}|} (\delta_{ij} - \delta_{ik}) + \frac{1}{2}\frac{\partial W_{jk}}{\partial h_{jk}}\left(\frac{\delta h_j}{\delta r_i} + \frac{\delta h_k}{\delta r_i}\right) \tag{2.29}$$

The pressure force obtained on particle i can be written as

$$\boldsymbol{F}_i = -\sum_{k=1}^{N} m_i m_k \left(\frac{P_i}{\rho_i^2} + \frac{P_k}{\rho_k^2}\right) \frac{\partial W_{ik}}{\partial r_i}\bigg|_{h_{ik}\text{constant}}$$
$$-\frac{1}{2}\sum_{n=1}^{N}\sum_{k=1}^{N} m_i m_k \left(\frac{P_i}{\rho_i^2} + \frac{P_k}{\rho_k^2}\right) \frac{\partial W_{ik}}{\partial h_{ik}} \chi_{in} H'_{in} \mathscr{G}'_i \frac{r_{in}}{|r_{in}|}$$
$$-\frac{1}{2}\sum_{k=1}^{N}\sum_{j=1}^{N} m_j m_k \frac{P_k}{\rho_k^2} \frac{\partial W_{jk}}{\partial h_{jk}} \times \left(\chi_{ji} H'_{ji} \mathscr{G}'_k \frac{r_{ij}}{|r_{ij}|} + \chi_{ji} H'_{ki} \mathscr{G}'_k \frac{r_{ik}}{|r_{ik}|}\right) \tag{2.30}$$

As mentioned previously $\mathscr{G}$ and H are arbitrary functions and χ are arbitrary numbers, being zero when $k = n$. As equation (2.30) is derived from a potential which only relies on the distances between particles, the global conservation of energy, momentum and angular momentum are conserved. However it should be noted that in pairwise interactions momentum is not conserved.

By using the three-step approach described in Section 2.3.1(c) and the equations therein (2.19), (2.20), the pressure force on particle i from (2.30) can be expressed as

$$F_{P,i} = -\frac{1}{2}\sum_{j=1}^{N} m_i m_j \left(\frac{P_i}{\rho_i^2} + \frac{P_j}{\rho_j^2}\right)$$

$$\times \left[\frac{\partial W(\boldsymbol{r}_{ij}, h_i)}{\partial \boldsymbol{r}_i}\bigg|_{h_i\text{const}} + \frac{\partial W(\boldsymbol{r}_{ij}, h_j)}{\partial \boldsymbol{r}_i}\bigg|_{h_j\text{const}}\right]$$

$$-\frac{1}{2}\sum_{j=1}^{N} m_i m_j \left(\frac{P_i}{\rho_i^2} + \frac{P_j}{\rho_j^2}\right) \frac{\partial W(\boldsymbol{r}_{ij}, h_i)}{\partial h_i} \frac{r_{i\,\text{imax}}}{|r_{i\,\text{imax}}|}$$

$$-\frac{1}{2}\sum_{j=1}^{N} m_k \frac{P_k}{\rho_k^2} \mathscr{G}'_k \chi_{ki} H'_{ki} \frac{\boldsymbol{r}_{ik}}{|\boldsymbol{r}_{ik}|} \sum_{j=1}^{N} m_j \frac{\partial W(\boldsymbol{r}_{kj}, h_k)}{\partial h_k}$$

$$-\frac{1}{2}\sum_{j=1}^{N} m_k \frac{P_k}{\rho_k^2} \mathscr{G}'_k \chi_{ki} H'_{ki} \frac{\boldsymbol{r}_{ik}}{|\boldsymbol{r}_{ik}|} \sum_{j=1}^{N} m_j \frac{P_j}{\rho_j^2} \frac{\partial W(\boldsymbol{r}_{kj}, h_k)}{\partial_k} \tag{2.31}$$

2.3.4 ARTIFICIAL VISCOSITY

In the case of modelling the behaviour of an astrophysical cloud, viscosity plays a very much less important role than is the case in modelling terrestrial flows. As a result the equations used as the starting point are the Euler equations for an inviscid fluid rather than the more complete Navier-Stokes equations, solutions for the Euler equations being less compute intensive. Nevertheless viscosity does play a role in describing the evolution of features such as shocks in the clouds under study so it is necessary to add a term to the equations derived above for an inviscid system to describe the dissipative force but, if it is included, then the system will no longer be a Hamiltonian. The Navier-Stokes implementation for SPH implementation of the standard artificial viscosity is

$$S_{i,\text{visc}} = -\sum_{j=1}^{N_i} = m_j \Pi_{ij} \nabla W(r_{i,j}, h_{i,j}) \tag{2.32}$$

Adding a term by which the energy dissipated through the viscosity term is converted into thermal energy can be done by ensuring that the net rate of energy input into the system is equal to the time rate of change of the Hamiltonian. A suitable artificial viscous pressure term is given by Π_{ij}, where Π is

$$\Pi_{ij} = \frac{1}{\bar{\rho}_{ij}}(-\alpha\, u_{ij}\bar{c}_{ij} + \beta\mu_{ij}^2) \tag{2.33}$$

where $\bar{\rho}_{ij} = (\rho_i + \rho_j)/2$, $\bar{c}_{ij} = (c_i + c_j)/2$, α and β are free parameters and control

the strength of the viscous terms these have been set to be 0.5 and 1.0 respectively.

$$\mu_{ij} = \begin{cases} \overline{h}_{ij} \dfrac{\boldsymbol{v}_{ij} \boldsymbol{r}_{ij}}{r_{ij}^2 + \eta^2} & \text{if } \boldsymbol{v}_{ij} \cdot \boldsymbol{r}_{ij} < 0 \\ 0 & \text{otherwise.} \end{cases} \tag{2.34}$$

In this case $\boldsymbol{v}_{ij} = (\boldsymbol{v}_i - \boldsymbol{v}_j)$, and $\eta = 0.01\overline{h}_{ij}^2$ prevents the denominator from disappearing.

The entropy equation for a given particle i can be written as

$$\left. \frac{\partial \mathscr{U}_i}{\partial S_i} \right|_{\rho_i} \frac{dS_i}{dt} = \mathscr{H}_i \tag{2.35}$$

2.3.5   The Total Energy

For a strictly adiabatic or a barotropic inviscid flow, the total energy, E, must be conserved. This can be written as

$$E = T_k + U + \Omega \tag{2.36}$$

where T_k is the kinetic energy, U is the potential function of thermal energy, which is used for the pressure force, and Ω is the gravitational energy. A more detailed examination of the energy conservation with respect to the chemical processes modelled will be given in Chapter 3.

2.4   Gravity

Modelling the mutual gravitational attraction between particles is an important part of understanding the evolution of a gas cloud. This mutual attraction is implicit in equation (2.2). For a given particle i the gravitational force applied on it by particle j can be shown to be

$$-\nabla \boldsymbol{\Phi}_i = -G \frac{M(|\boldsymbol{r}_i - \boldsymbol{r}_j|)}{|\boldsymbol{r}_i - \boldsymbol{r}_j|^2} \frac{(\boldsymbol{r}_i - \boldsymbol{r}_j)}{|\boldsymbol{r}_i - \boldsymbol{r}_j|}, \tag{2.37}$$

where

$$M(|\boldsymbol{r}_i - \boldsymbol{r}_n|) = 4\pi m \int_0^{|\boldsymbol{r}_i - \boldsymbol{r}_n|} u^2 W(u, h_g) \mathrm{d}u \tag{2.38}$$

An obviously simple solution is to do a pair-wise calculation of the gravitational force on each particle i for all values of r_{ij} for all N particles within the problem

domain. The sum of the individual results will give the net force on a particle i, $\boldsymbol{F}_i$ and will give an accurate result without any approximations. The general case is

$$\boldsymbol{F}_i = \sum_{j=1}^{N} (j \neq i)\boldsymbol{F}_{ji}. \tag{2.39}$$

This disadvantage of this approach is that, for large values of N, it requires a very large number of calculations which can be described as $\mathcal{O}(N^2)$.

One method of reducing the number of calculations is to use an 'Octree' approach and produce a list of near-neighbours to the particle i of interest. The assumption is that most of the net force on a particular particle is generated by those particles closest to it and the contributions of the other particles will either be largely mutually cancelled or they are so far away that their contribution is minimal because of the inverse square effect. By using an Octree approach, described in Section 2.4.1, the computational complexity for gravitational effects can be reduced to $\mathcal{O}(NlogN)$. So for a calculation using, say, 10^5 particles the calculation complexity can be reduced by a factor of about 10^4 at the cost of greater inaccuracies but these will be within the errors set by other approximations made in the model and calculations.

However in an SPH analysis it is also necessary to be able to calculate local variations of some properties or effects around any particle i in order to be able to calculate the effect of these variations on the selected particle. This may also be achieved by using a 'near-neighbour' list for particle i so the same list may be used for more than one purpose with obvious savings in computer time.

2.4.1 Octrees

An Octree (a compressed form of Octant-Tree) is a method used to partition a three dimensional space by recursively subdividing it into eight equal octants. Barnes and Hut (1986) describe the implementation of an Octree analysis by the division of a virtual cubic bounding box into eight sub-cells with the linear dimensions of these cells being exactly half of that of their parent. A tree of occupied cells is then constructed starting from the bounding box by firstly discarding empty sub-cells, secondly by accepting sub-cells with one particle and then finally by recursively dividing any sub-cells containing more than one particle into a higher level of 8 sub-sub-cells. A visual depiction of a two-dimension analogue, a Quadtree, by which a space may be partitioned by recursively subdividing it into four equally sized squares is shown in Figure 2.3 where an area is subdivided until each square contains only one particle.

The dynamic analysis is performed by assigning to every cell containing one particle, as well as to higher level cells containing more than one particle, a pseudo-particle that

(a) Quadrant representation (b) Quadtree representation
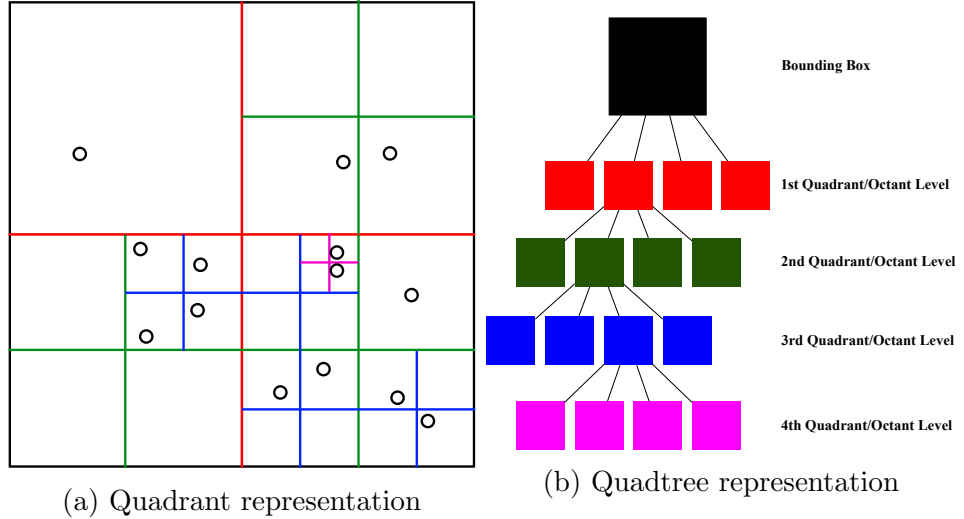
Figure 2.3: Representation of a Quadtree, the 2-D analogue of an Octree. The left diagram is the visual representation of the quadrant recursive subdivision. The circles represent particles.The subdivision of Quadrants continues until a maximum of one particle is in a Quadrant. The right hand diagram is a representation of the associated Quadtree. The colours correspond to the level of each Quadrant.

contains the total mass in the cell located at the centre-of-mass of all the particles it contains. Starting at the bounding box cell, the force on any particle p can be approximated by a recursive calculation where l is the dimension of the cell under consideration and D is the distance from the cell's centre-of-mass to p. If $l/D < \theta$, where θ is a fixed accuracy parameter $\simeq 1$, then the interaction between this cell and p is included in the total. If $l/D = \theta$, then the cell is subdivided into its 8 sub-cells and the process repeated for each of these sub-cells. A new tree is then constructed for each time step.

Barnes and Hut have shown that results are accurate to $\simeq 1\%$ with little dependence on the number of particles and that empirically the force error scales approximately as the -1.5 power of the computing time. The errors are also only weakly correlated from one time step to the next so there is little or no accumulation of the errors in one direction.

2.4.2 SPLINE SOFTENING

Because the fluid continuum is represented by a finite set of particles it is necessary to avoid the situation where the gravitational attractions between closely spaced particles lead to numerical divergence in the simulation. To avoid this occurring it is essential to soften the gravitational potential of the particles, this also avoids the SPH particles

from acting as 'solid' particles. The method described by Hernquist and Katz (1989) uses the expressions (2.37) and (2.38) for the gravitation force between particle i and a node in the oct-tree structure at $\boldsymbol{r}_n$ with a mass m. In the spline softening, the value of h_g used is chosen such that it will be large enough to prevent small scale Jeans instabilities from occurring but at same time not so small that it is smaller than the smallest h_i attained throughout all the calculations. It is kept constant for all the calculations. This approach does not permit calculations to have sufficient spatial resolution for hierarchical fragmentation to occur, but conversely will result in good conservation of the total energy of the system.

2.5 INTEGRATION CONSIDERATIONS

The processes involved with the evolution of a molecular cloud are continuous and solutions to the equations describing their evolution require integration over time. However the computer model of this evolution needs a discretised world as it advances through time. The process of advancing through time in the computer model is a non-trivial problem, it requires the discretising of time and, by extension, the properties of the cloud that are time-dependent in order that the computational model can achieve a solution.

2.5.1 DISCRETISATION

The basic problem can be explained by considering a single moving particle in one-dimensional space which is subject to some acceleration dependent on its position x. At any moment it will have a velocity v appropriate to its particular position. If time is stepped discretely by δt then the particle's position at the end of that time interval will be x_{n+1}, that is its position is given by $x_{n+1} = x_n + v_n \delta t$. But as the acceleration and velocity of a particle are both functions of position then all of the changes in the acceleration and velocity of the particle occurring within that discrete time interval are not calculated and are therefore lost. Considering the path of the particle over many such time intervals can therefore lead to the dynamic calculations giving very different outcomes in the final position and acceleration of the particle than would have been the case if the time step chosen had been smaller. The optimal goal for the modelling is to chose a method that keeps the changes in acceleration of the particle to a minimum and in finding a suitable size for the time step and, and the same time, ensuring that both these criteria keep the results within a reasonable margin of error.

To be able to keep the margins of error to an acceptable level a method which uses adaptive timestep sizes is more efficient than a fixed time interval. It is necessary to ensure that the size of the timestep chosen will allow the convergence of the equations and in this case the calculation of the size of any given timestep uses an extension of the Courant-Friedrichs-Lewy condition (Courant et al., 1928) for the majority of the simulations.

At the start of the simulation the modelled cloud has a uniform temperature and the constituent particles have position but no velocity and in addition no heating or cooling has occurred due to chemical reactions. This implies that a 'set-up' step is required so the particles acquire values for these variables which are then used in subsequent iterations. These are obtained by using a very small timestep value for the first iteration, that is from step '0' to step '1', by defining an artificial Courant number. Subsequently the timestep size calculations were made according to equation (2.40) below.

2.5.2 Leapfrog Scheme

Leapfrog integration is a method for numerically integrating differential equations, essentially values for position and velocity are updated at interleaved time points. These are staggered in such a way that they 'leapfrog' over each other, for example, the particle position is updated at integer time steps and the particle's velocity is updated at integer-plus-a-half time steps as can be seen in figure 2.4. To integrate the momentum and the particle-shift equations for the studies reported here, a standard second order leapfrog scheme with modifications recommended by Hernquist and Katz (1989) was used for predicting time-centred velocities in the viscous pressure term. The time step size was determined by

$$\delta t = \mathscr{Q}\min_i \frac{h_i}{1.5|\boldsymbol{v}|_i + c_i + 1.2(\alpha c_i + \beta\max_j|\mu_{ij}|)} \tag{2.40}$$

The factor $\mathscr{Q}$ is a constant, usually taken to be in the range of (0.2-0.3), the $1.5|\boldsymbol{v}|_i$ term helps keep the stability of the time integration, c_i is the speed of sound, α and β are the viscosity coefficients.

2.5.3 Heating and Cooling Terms

With the incorporation of heating and cooling terms there are differences in the timescales between the thermal and dynamic processes. This makes it necessary to integrate the
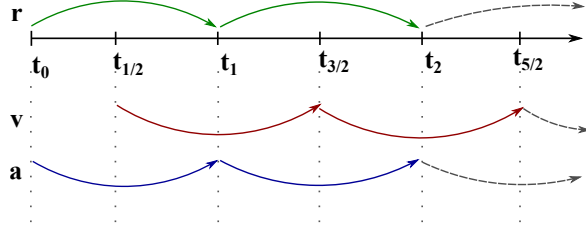
Figure 2.4: This diagram represents the leapfrog scheme. A particle's position, r, is updated every full timestep. The particle's velocity, v, is updated every half timestep, this is then used to calculate the new position of the particle. The acceleration, a, is updated every timestep so as to be able to update the velocity at the next half timestep.

energy equation implicitly, so the energy equation is written in the form.

$$f(T_i^{n+1}) = u_i(T_i^{n+1}) - u_i(T_i^n) - \delta t Q_i^n + \delta \left[\frac{\Lambda(T_i^n, n_i^n) - \Gamma(n_i^n)}{\rho_i^n} \right] \qquad (2.41)$$

where Q_i^n is the PdV work and the viscous dissipation. The superscripts n and $n+1$ denote the nth and the $n^{\text{th}} + 1$ time steps (Nelson and Langer, 1997).

This equation is non-linear in T_i and so must be solved iteratively. In this SPH code bracket the root of this equation and then iterate until the condition

$$\left| \frac{f(T_i^{n+1})}{u_i(T_i^n + \delta t Q_i^n)} \right| < 0.001 \qquad (2.42)$$

has been met.

CHAPTER 3

MODELLING THE THERMAL AND CHEMICAL NETWORKS

3.1 INTRODUCTION

The evolution of molecular clouds is affected not only by self-gravitation and viscosity as described in the previous chapter but also by heating and cooling of the cloud, or regions of the cloud, by incident radiation, chemical reactions and micro-physical processes within the cloud. This chapter examines the physical effects of these phenomena on the evolution of the cloud and the way in which they are modelled in the computer code. The computational modelling program used is CLOUD which is that described by Nelson and Langer (1997, 1999) and which in turn is based on earlier work reported by Goldsmith and Langer (1978). The model was originally written to investigate the stability of molecular clouds in an isotropic far ultra-violet radiation (FUV) field representing the interstellar background.

The code contains two numerical solvers, one for the hydrodynamic equations and the other is a set of differential equations for 12 chemical networks. The chemical network and the heating and cooling processes are described separately in the following sections but in practice the reactions and effects caused by each are interdependent, changes in one phenomenon will induce changes in another. The CLOUD code permits
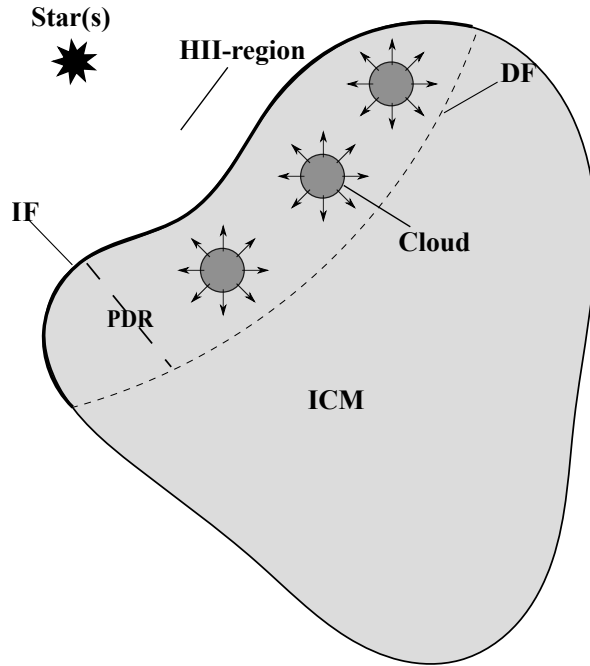
Figure 3.1: This diagram shows the cloud setup for the simulation. HII region is the ionised hydrogen region lying just outside the simulation space. The IF is the Ionisation Front, ICM stands for Interclump Material and DF shows the Dissociation Front. PDR is the Photodissociation region. The star represents a source of radiation such as an OB star.

each section of code modelling these various effects to be switched off or on independently. A process for which the code is switched on is described as 'activated'.

Types of incident radiation considered by the SPH code used here are cosmic ray and FUV originating from sources external to the cloud. Extreme ultra-violet radiation (EUV) is not considered as the cloud is assumed to be at a sufficient distance from an H II region containing OB stars that this radiation does not affect the cloud.

The conceptual arrangement of the molecular cloud and nearby radiation sources is shown in Figure 3.1.

3.2 CHEMICAL NETWORK

There are two main reasons for modelling chemical reactions as part of a more complete numerical model of a molecular cloud. Firstly since different species heat and cool at different rates, the temperature of the cloud, or regions of the cloud, can vary. In turn this affects the dynamical evolution of the cloud in that the balance between the thermal pressure, which tends to cause the cloud to expand, and the cloud's self-gravity,

causing collapse, will change. External influences, such as cosmic rays and FUV, are instrumental in the conversion of one chemical species to another and local flux levels can affect these reactions. Secondly the distribution of the various atomic, ionic, or molecular species can be used as tracers to track the evolution of the different regions of the cloud.

The chemical model adopted in CLOUD is intended to represent the key intermediate reactions involving carbon and oxygen occurring in a molecular cloud rather than tracking all the possible individual reactions. This simplification is possible because many of the intermediate reactions occur very quickly, not only compared to the typical timescales involved in a cloud's evolution but also absolutely.

The chemical species that are tracked are He^+, H_3^+, OH_x, CH_x, CO, C I, C^+, HCO^+, O I, M^+ and e^-. Some species have been grouped in order to keep the chemical network manageable. Thus O_2, H_2O and OH are all treated as OH_x, CH and CH_2 are grouped as CH_x and the species M is used to describe the metals Mg, Fe, Ca and Na which provide a background source of electrons in the shielded regions of the cloud. These simplifications are permissible because of the similar chemical pathways and reaction rates within each group.

An example of this approach can be demonstrated in one of the important series of carbon and hydrogen reactions where the overall reaction can be described as

$$2\,C^+ + 2\,H_2 \longrightarrow CH_x + H \tag{3.1}$$

where $CH_x = CH + CH_2$ and although a series of reactions take place between the start and the finish they occur quickly and they are therefore not explicitly followed in the model. The start of this series is one of the most significant reactions for converting carbon ions to molecules in regions with high photon flux and is written as

$$C^+ + H_2 \longrightarrow CH_2^+ + h\nu. \tag{3.2}$$

Subsequently the CH_2^+ product quickly converts via ion-molecule reactions with molecular hydrogen and via dissociative recombination with electrons as shown by

$$CH_2^+ + H_2 \longrightarrow CH_3^+ + H. \tag{3.3}$$

In turn the molecular ion CH_3^+ rapidly reacts with free electrons and dissociates into CH and CH_2 which are the products shown in the RHS of equation (3.1). Thus the model can describe a three step process as a single reaction as the intermediate reactions occur very quickly.

The model used also incorporates the treatment of self-shielding using the program of Bergin et al. (1995) but it does not explicitly track the species H I and H$_2$ because, at low temperatures, they do not affect the hydrogen chemistry.

The complete set of reactions and coefficients used are shown in Table 3.1 and the initial conditions and abundances and the conservation conditions can be found in Table 3.2.

Reactions	Reaction Rate Coefficients[a]	Number[b]
Cosmic-ray ionisation:		
$cr + H_2 \longrightarrow H_3^+ + e + H + cr$	1.2×10^{-17}	k_1
$cr + He \longrightarrow He + e + cr$	6.8×10^{-18}	k_2
Ion-molecule reactions:		
$H_3^+ + C\,\textsc{i} \longrightarrow CH_x + H_2$	2×10^{-9}	
$H_3^+ + O\,\textsc{i} \longrightarrow OH_x + H_2$	8×10^{-10}	k_{11}
$H_3^+ + CO \longrightarrow HCO^+ + H_2$	1.7×10^{-9}	
$He^+ + H_2 \longrightarrow He + H + H^+$	7×10^{-15}	k_{13}
$He^+ + CO \longrightarrow C^+ + O + He$	1.6×10^{-9}	
$C^+ + H_2 \longrightarrow CH_x + H$	4×10^{-16}	
$C^+ + OH_x \longrightarrow HCO^+$	1×10^{-9}	
Neutral-neutral reactions:		
$O\,\textsc{i} + CH_x \longrightarrow CO + H$	2×10^{-10}	
$C\,\textsc{i} + OH_x \longrightarrow CO + H$	$5.8 \times 10^{-12}T^{0.5}$	
Electron recombination:		
$He^+ + e \longrightarrow He + hv$	$9 \times 10^{11}T^{0.64}$	k_{200}
$H_3^+ + e \longrightarrow H + H_2$	$1.9 \times 10^{6}T^{0.54}$	k_{201}
$C^+ + e \longrightarrow C\,\textsc{i} + hv$	$1.4 \times 10^{10}T^{0.61}$	
$HCO^+ + e \longrightarrow CO + H$	$3.3 \times 10^{5}T^{1.0}$	
$M^+ + e \longrightarrow M + hv$	$3.8 \times 10^{10}T^{0.65}$	
Charge-transfer reactions:		
$H_3^+ + M \longrightarrow M^+ + e + H_2$	2×10^{9}	
Photoreactions:		
$hv + C\,\textsc{i} \longrightarrow C^+ + e$	$3 \times 10^{10}\,G_0 e^{3A_v}$	
$hv + CH_x \longrightarrow C\,\textsc{i} + H$	$1 \times 10^{9}\,G_0 e^{-1.5A_v}$	
$hv + CO \longrightarrow C\,\textsc{i} + O$	$10^{-10}\,\mathscr{S}(N(CO), N(H_2))G_0 e^{-3A_v}$ [c]	
$hv + OH_x \longrightarrow O\,\textsc{i} + H$	$5 \times 10^{-10}\,G_0 e^{-1.7A_v}$	
$hv + M \longrightarrow M^+ + e$	$2 \times 10^{-10}\,G_0 e^{-1.9A_v}$	
$hv + HCO^+ \longrightarrow CO + H$	$1.5 \times 10^{-10}\,G_0 e^{-2.5A_v}$	

Table 3.1: Chemical reactions and reaction rates. Cosmic ray is represented by 'cr', photon contribution in the chemical equations is represented by hv.

[a] Rate coefficients are taken from the UMIST catalog (Bergin et al., 1995). Two-body reactions are in units of cm^3 s^{-1} molecule^{-1}, while photoreactions and cosmic ray reaction are in units of s^{-1} molecule^{-1}.

[b] Numbers for reactions are noted in the few cases which are used to define equations for initial conditions which can be seen in Table 3.2.

[c] $\mathscr{S}(N(CO), N(H_2))$ is the ^{12}CO self-shielding factor of van Dishoeck and Black (1988) taken from Bergin et al. (1995)

Initial conditions:

$n(\mathrm{C\,I}) = n(\mathrm{CO}) = n(\mathrm{CH}_x) = n(\mathrm{HCO}^+) = 0$

$n(\mathrm{C}^+) = n(\mathrm{C}_{\mathrm{total}})$

$n(\mathrm{O\,I}) = n(\mathrm{O}_{\mathrm{total}})$

$n(\mathrm{M}^+) = n(\mathrm{M}_{\mathrm{total}})$

$n(\mathrm{He}^+) = \left(\dfrac{k_2}{k_{200}n(\mathrm{e}) + k_{13}n(\mathrm{H}_2)} \right) n(\mathrm{He}_{\mathrm{total}})$

$n(\mathrm{H}_3^+) = \left(\dfrac{k_1}{k_{201}n(\mathrm{e}) + k_{11}n(\mathrm{O\,I})} \right) n(\mathrm{H}_2)$

$n(\mathrm{e}) = n(\mathrm{C}^+) + n(\mathrm{He}^+) + n(\mathrm{M}^+)$

Initial fractional abundances:

$n(\mathrm{C}_{\mathrm{total}}) = 10^{-4}n(\mathrm{H}_2)$

$n(\mathrm{O}_{\mathrm{total}}) = 2 \times 10^{-4}n(\mathrm{H}_2)$

$n(\mathrm{He}_{\mathrm{total}}) = 0.28n(\mathrm{H}_2)$

$n(\mathrm{M}_{\mathrm{total}}) = 10^{-7}n(\mathrm{H}_2)$

Conservation conditions:

$n(\mathrm{e}) = n(\mathrm{C}^+) + n(\mathrm{He}^+) + n(\mathrm{M}^+) + n(\mathrm{HCO}^+)$

$n(\mathrm{He}_{\mathrm{total}}) = n(\mathrm{He}) + n(\mathrm{He}^+)$

$n(\mathrm{M}_{\mathrm{total}}) = n(\mathrm{M}^+) + n(\mathrm{M})$

Table 3.2: The initial conditions, initial fractional abundances and the conservation conditions which are used for the chemical network calculations.

3.3 THERMAL PROCESSES

The total thermal process is made up of several constituent heating, cooling and heat transfer processes. The sum of all the individual processes determines the temperature of the SPH particles that are included in the cloud.

Three separate heating processes are considered:

- Far ultraviolet and dust grain photoelectric heating

- H_2 formation on surfaces of dust grains

- Background cosmic ray flux.

The cooling process considered is that caused by atomic and molecular line emission and the heat transfer process considered is the gas-dust thermal interaction.

A more detailed description of these processes is given in the following sections, but to give an initial understanding of the relative contribution of these processes each acting alone the results of calculations of the variation in these effects is shown in

Figure 3.2 which shows different heating and cooling functions as a function of density for six different temperatures. For high density CO is the main cooling channel as can be seen in Figure 3.2.

3.3.1 FUV AND DUST GRAIN PHOTOELECTRIC HEATING

A major contribution to the heating of the gas in the cloud under consideration is through the ejection of electrons from dust grains by the incident FUV portion of the interstellar radiation. It should be noted that incident UV is both scattered and absorbed as it penetrates the cloud and the model has to allow for both these effects. In the following the calculation for energy absorption is first presented followed by considerations of absorption and scattering. In the first instance it has been assumed that the radiation is isotropic but some calculations have been made with directional sources for the FUV.

Nelson and Langer (1999) adopted the formula presented in Falgarone and Puget (1985) but modified to include the effects of grain-charging on the grain work function. Thus the heating rate is given by:

$$\Gamma_{pg} = 4.86 \times 10^{-26} \mathrm{G}_0 n f(T, n(e), \tau_{\mathrm{uv}}) \mathrm{e}^{-\tau_{\mathrm{uv}}} \, \mathrm{ergs} \, \mathrm{cm}^{-3} \, \mathrm{s}^{-1} \tag{3.4}$$

where $f(T, n(e), \tau_{\mathrm{uv}})$ is a factor that accounts for the effects of grain charging (Hollenbach et al., 1991), and G_0 is a factor that determines the flux of FUV, τ_{uv} is the uv extinction.

In principle the absorption and scattering, or visual extinction, of the incident FUV to any arbitrary point in the cloud may be calculated by interpolating the density of the SPH particles onto the chosen ray path extending from the cloud's surface to the particle's position. In principle there are an infinite number of possible ray paths so a simplification is made to reduce the number of possible paths so reducing the computing overhead. The FUV heating rate at that point is taken as an average of the heating rates along each direction. This approach is appropriate when the geometry of the cloud surface is of a simple form, as is the case with the initial conditions of the clouds considered here. If a cloud of arbitrary shape is being considered the ray tracing approach is more appropriate.

In general the ultraviolet extinction at an arbitrary point τ_{uv} has to be calculated where $\tau_{\mathrm{uv}} = \langle K \rangle \tau_v$. The usual form of the equation for τ_{uv} is

$$\tau_{\mathrm{uv}}(r) = 1.25 \times 10^{-21} \int_r^R 2n(r') \, \mathrm{d}r' \tag{3.5}$$

which is of a form suitable for integrating along the radial direction in a spherically
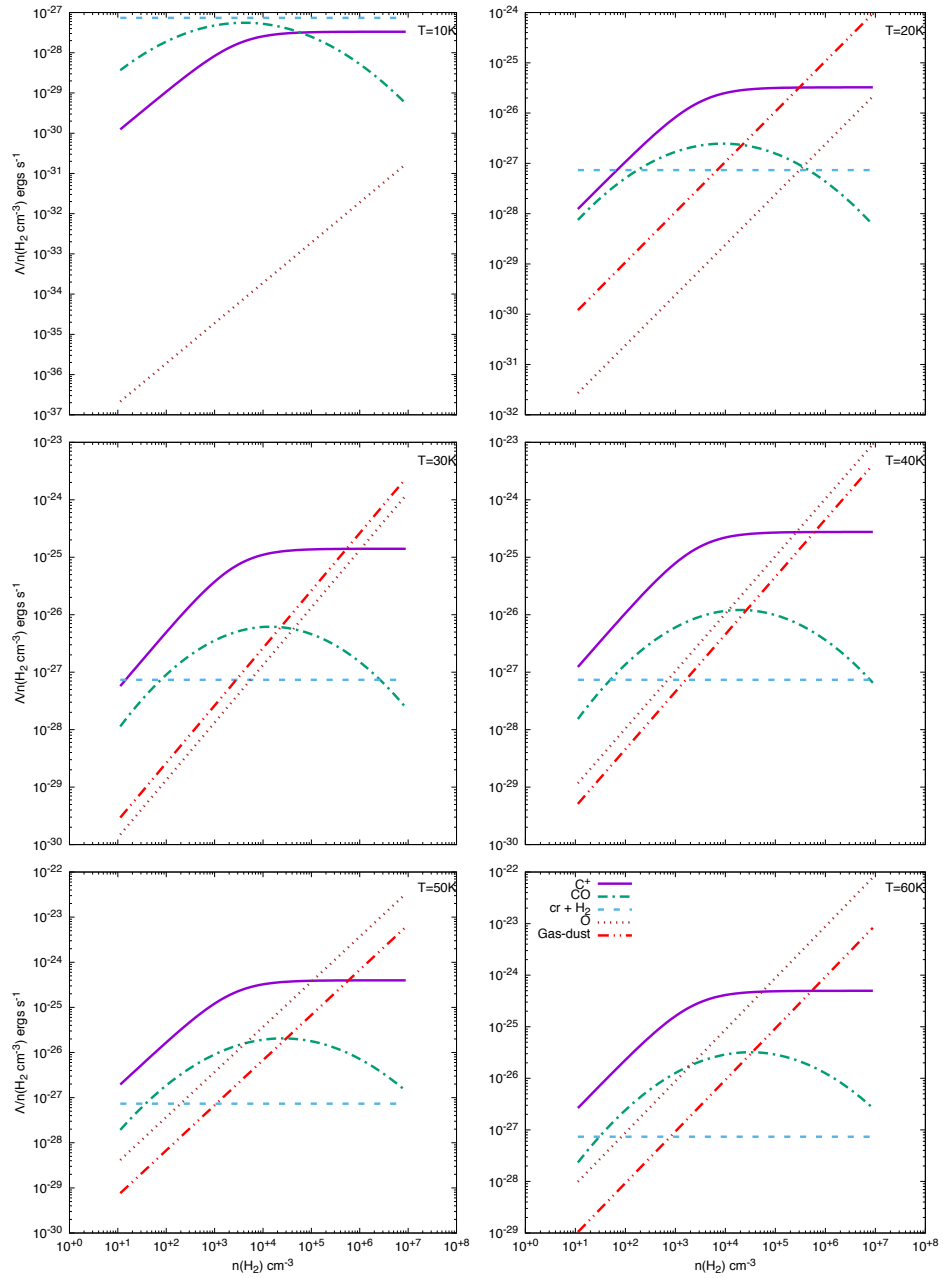
Figure 3.2: This graph shows different heating and cooling function as a function of density for six different temperatures. The fractional abundance for $n(CO) = n(C^+) = 5 \times 10^{-5}$ and the temperature of the dust grains is set to $T_d = 10K$. The C^+ cooling is the solid purple line, the CO cooling is represented by the green dash-dotted line. The combined cosmic-ray and H_2 formation heating by the blue long dashed line, the oxygen by the brown short dashed line. The gas dust cooling represented by the red double dotted dashed line.

symmetric distribution of matter. This expression has to be modified to permit an arbitrary distribution of matter in three dimensions as is the case with the clouds being studied. Consider a plane orthogonal to the line of sight to the centre of the cloud. The plane is then rotated through 45° relative to the centre, this is then repeated until the cloud is completely surrounded, the planes are aligned to the surfaces of a small rhombicuboctahedron which is a good approximation to a sphere for this purpose. A total of 26 iterations is necessary and the optical depth therefore has to be calculated along each of these directions. From an arbitrary point x', y' and z', in three dimensional space the 26 optical depths are calculated by integrating outwards from the starting point, these are identified as $\tau_{x-,y-,z-}$, $\tau_{x-,y-}...\tau_{x+,y+,z+}$ where τ_{x+} represents the optical depth calculated along the positive x direction to the surface of the cloud at X_{max}, y', z' and similarly for the other directions.

In order to be able to compute the values for the UV extinction the cloud is discretised by sub-dividing it using a regular cubic grid extending to the cloud's surface. The density in each cell is then calculated by taking the mean density of the particles contained within that cell. Cells that do not contain particles have their density calculated by taking the average density of the six adjacent cells in the x, y and z directions. The optical depth along a given coordinate direction from the cloud's surface to a given particle position is then approximated by summing over cells along that direction from the particle position to the surface. The value for the UV extinction along the positive x-direction for a particle located at r_i is then given by the expression

$$\tau_{x+} = 1.25 \times 10^{-21} \sum_{k=1}^{N_{\text{grid}}} 2n_k \Delta x \qquad (3.6)$$

where N_{grid} is the number of cells along the positive x axis from the particle's position r_i to the cloud's surface, n_k is the number density of cell k and Δx is the grid size. This calculation is made for all 26 directions.

The UV heating rate is calculated as an average of the heating rates along each of

the 26 axes which can be shown to be given by

$$\Gamma_{pg} = 4.86 \times 10^{-26} G_0 n(H_2) \frac{1}{26} [e^{-\tau_{x+,y+,z+}} + e^{-\tau_{x+,y+}} + e^{-\tau_{x+,y+,z-}}$$
$$+ e^{-\tau_{x+,z+}} + e^{-\tau_{x+}} + e^{-\tau_{x+,z-}}$$
$$+ e^{-\tau_{x+,y-,z+}} + e^{-\tau_{x+,y-}} + e^{-\tau_{x+,y-,z-}}$$
$$+ e^{-\tau_{y+,z+}} + e^{-\tau_{y+}} + e^{-\tau_{y+,z-}}$$
$$+ e^{-\tau_{z+}} + e^{-\tau_{z-}}$$
$$+ e^{-\tau_{y-,z+}} + e^{-\tau_{y-}} + e^{-\tau_{y-,z-}}$$
$$+ e^{-\tau_{x-,y+,z+}} + e^{-\tau_{x-,y+}} + e^{-\tau_{x-,y+,z-}}$$
$$+ e^{-\tau_{x-,z+}} + e^{-\tau_{x-}} + e^{-\tau_{x-,z-}}$$
$$+ e^{-\tau_{x-,y-,z+}} + e^{-\tau_{x-,y-}} + e^{-\tau_{x-,y-,z-}}] \, \mathrm{ergs\,cm^{-3}\,s^{-1}} \tag{3.7}$$

In the limit of the optical depth going to zero, the heating rate converges to the value obtained using equation 3.4.

Not only the interior of a cloud is heated by the incident FUV, the surface will also be heated on timescales that could be either fast or slow compared to the sound crossing time within the cloud. Impulsive heating implies that the FUV heats the cloud's surface layer. In this case, the temperature of the outer region rises more quickly than the temperature increase can propagate through the entire cloud and as a result this region attains a much higher pressure than the cold central volume. A shock propagates inward and a heated, energetic photo-evaporative gas flow leaves the surface.

3.3.2 Cosmic Ray Heating

Cosmic ray interaction is a significant heating process for the interior regions of the clouds shielded from the FUV flux. The heating due to cosmic-rays is given by:

$$\Gamma_{cr} = \zeta_p(H_2) \Delta Q_{cr} \, \mathrm{ergs\,cm^{-3}\,s^{-1}} \tag{3.8}$$

where $\zeta_p(H_2)$ is the primary cosmic-ray ionisation rate of H_2 and ΔQ_{cr} is the energy deposited as heat as a result of this ionisation. Following Goldsmith and Langer (1978), values of $\zeta_p(H_2) = 2.0 \times 10^{17} \mathrm{s^{-1}}$ and $\Delta Q_{cr} = 20\mathrm{eV}$ have been used, giving a total cosmic-ray heating rate of $\Gamma_{cr} = 6.4 \times 10^{-28}$ n ergs cm^{-3} s^{-1}.

3.3.3 H_2 Formation Heating

A source of heating in molecular clouds that is not directly due to external influences is H_2 formation on dust grains from the combination of monatomic hydrogen. Some fraction of the 4.48eV binding energy of the released H_2 molecule goes into kinetic energy and is thus transferred to the gas as heat. In a steady state, that is under those conditions where only cosmic rays split H_2 molecules into the atomic form, and at high densities where most of the hydrogen is in molecular form, the H_2 formation heating can be considered as another term in the cosmic-ray heating term (see discussion in (Goldsmith and Langer, 1978))

$$\Gamma_{H_2} = \left(\frac{\Gamma_{cr}}{3} \right) \left(\frac{Q_{H_2}}{4.48\text{eV}} \right) \text{ergs cm}^{-3}\,\text{s}^{-1} \tag{3.9}$$

where Q_{H_2} is the energy released as heat, $Q_{H-2} = 2.0\,\text{eV}$ in the SPH code.

3.3.4 Cooling by Atomic and Molecular Line Emission

A gas may be cooled if a molecule, previously excited by radiation or collision, returns to its de-excited state by the emission of a photon which then escapes from the immediate vicinity. The temperature of the gas locally then falls. The model used for these simulations is that proposed by Nelson and Langer (1997, 1999) which assumes that the cloud is essentially composed of molecular hydrogen, with a few trace species. The discussions of the molecular line cooling effect in these papers considers that contributions provided by the main cooling species, including local radiative trapping and by the fine-structure emission of O I, C I and C^+, are appropriate to the conditions found in the clouds modelled whereby T $<$ 200K, $n(H_2) < 10^8$ cm^{-3} and column densities are given by $N(H_2) < 2 \times 10^{22}$ cm^{-2}. As a result the assumption that most of the cloud is composed of molecular hydrogen, the equality n = $n(H_2)$ holds throughout.

The CO cooling function used in Nelson and Langer (1997, 1999) is an analytical fit to the cooling curves presented by Goldsmith and Langer (1978), it has the correct limiting behaviour in both the optically thin and optically thick limits of the cloud. The cooling formulae for C^+ and O I were originally developed by Chieze and Pineau Des Forets (1987).

The cooling due to CO can be written as

$$\Lambda_{CO} = \alpha \left(\frac{T}{10} \right)^{\beta} (n)^{\delta}\, n(CO)\, 10^4, \tag{3.10}$$

where $\alpha = 5.0 \times 10^{-30} \text{ergs cm}^{-3}\text{s}^{-1}$, $\beta = 0.6 + 0.41 \log_{10}(n)$, $\delta = 2.3 - 0.18\log_{10}(n)$, and $n = n(H_2)$ cm^{-3}.

The cooling due to C^+ which takes into account collisional de-excitation can be written as

$$\Lambda_{C^+} = \frac{2.2 \times 10^{-23} n_H (1 - f/2) n(C^+) e^{-92/T}}{1 + (n/n_{crit}) \left(1 + 2e^{-92/T}\right)} \, \text{ergs cm}^{-3} \, \text{s}^{-1} \tag{3.11}$$

where the number density of hydrogen $n_H = n(\text{H\,I}) + 2n(\text{H}_2)$, $f = 2n(\text{H}_2)/n_H$, and the critical number density, $n_{crit} = 3 \times 10^3 \, \text{cm}^{-3}$.

The cooling due to O\,I is written as

$$\Lambda_{O\,I} = 10^{-26} n_h (1 - f/2) n(\text{O\,I}) [24 e^{-228/T} + 7 e^{-326/T}] T^{1/2} \text{ergs cm}^{-3} \, \text{s}^{-1} \tag{3.12}$$

where $n(\text{O\,I})$ is the number density of oxygen.

The C\,I cooling is written as

$$\Lambda_{C\,I} = 1.38 \times 10^{-16} (e_{10} A_{10} f_1 \beta_{01} + e_{21} A_{21} f_2 \beta_{21}) n(\text{C\,I}) \tag{3.13}$$

where A are Einstein coefficients, e is the energy between levels f_1 and f_2 which describes the fractional level populations, β is the escape probability and $n(\text{C\,I})$ is the number density of C\,I.

In the low-density regions the cooling is dominated by C^+, C\,I, as well as ^{12}CO and O^+. In the high density regions ^{12}CO has high opacity but the isotopic molecular lines that contribute to most of the cooling have low opacities so it is felt that the (Nelson and Langer, 1997) cooling function allows reasonably accurate modelling of the effects of opacity in the cloud.

Some plots of molecular line cooling with respect to density and cloud temperature can be seen in Figures 3.3b, 3.3c and 3.3d which show how these parameters affect the cooling process for the species C^+, C\,I and O\,I. There are more variables that affect the cooling of the cloud, or regions of the cloud, than are shown in these plots but the intention here is to show the complexity of the problem and how the total cooling is made up the sum of these individual effects.

3.3.5 Gas-dust Thermal Exchange

If the temperature of the gas present in the cloud is different from that of the dust in the same region, there will be a transfer of thermal energy between these two constituents when they collide: hot gas will transfer energy to cool dust and vice versa. An estimation of the rate of energy exchange can be made if is assumed that when a molecule hits a dust grain it is adsorbed and reemitted later with energy $\sim 3/2 T_d$,
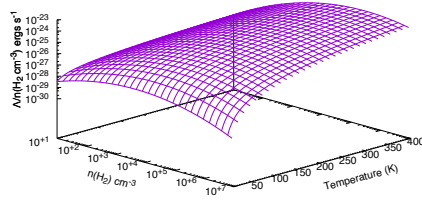
(a) CO based cooling.
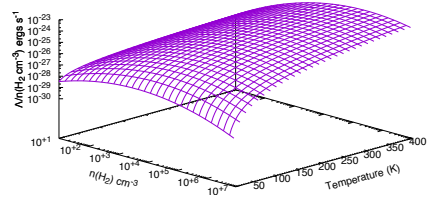
(b) C$^+$ based cooling.
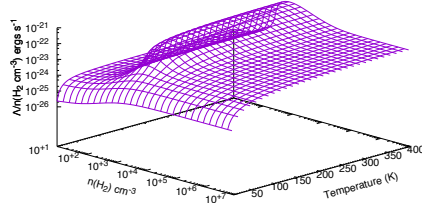
(c) C I based cooling.
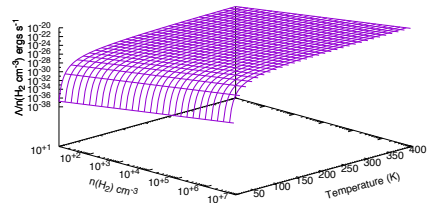
(d) O I based cooling.

Figure 3.3: Molecular Line cooling as a function of density and gas temperature for the species CO, C$^+$, C I and O I.

where T$_d$ is the dust temperature. From this Goldsmith and Langer (1978) derived an equation to give the energy exchange rate:

$$\Gamma_{gd} = 2.4 \times 10^{-33} T_g^{1/2} \left(T_g - T_d \right) n^2 \, \text{ergs cm}^{-3} \, \text{s}^{-1} \tag{3.14}$$

Gas-dust interactions play a major role in the thermal evolution of the cloud only when the number density is rather high because of their quadratic dependence on n. That is they become significant when $n \geq 10^5$ cm^{-3} and where T_d is quite low, up to about 10K. These are the conditions prevailing in the central volumes of a collapsing cloud. In the outer layers of the cloud, although dust temperature may be higher, dust plays a negligible role in both thermal and dynamic evolution due to the very low local density (Nelson and Langer, 1997).

White et al. (1999) reports that dust temperatures are kept down due to interactions with cool gas in the shielded inner regions of a cloud and are about T$_d$ = 20K which matches observation. The model used is in this study incorporates the calculation of dust temperature using a formula suggested by Hollenbach et al. (1991).

The cooling rate with respect to cloud temperature and opacity can be seen in Figure 3.4.

In the outer regions of the cloud, where the incident radiation flux is high, dust temperatures will be considerably higher but because of the lower densities the role of dust in the cloud's evolution, both thermal and dynamic, is not so significant.
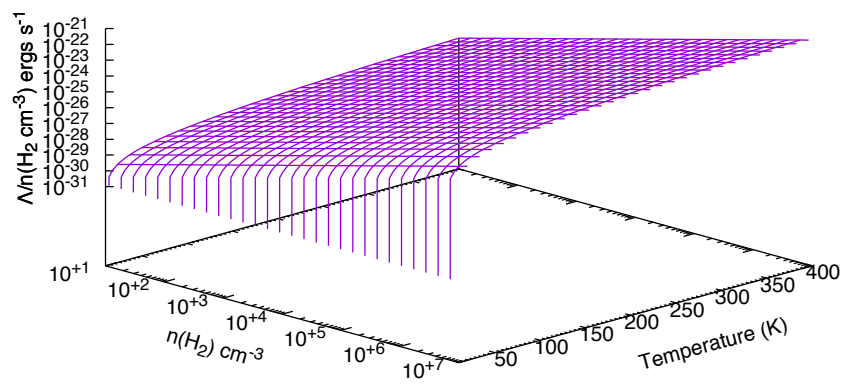
Figure 3.4: This graph shows gas dust interactions and their cooling effect as a function of two of the variables, temperature and density.

CHAPTER 4

INITIAL CONDITIONS AND TESTING

4.1 INTRODUCTION

The previous chapters have described the selection of Smoothed Particle Hydrodynamics as a particular implementation of a Lagrangian approach to achieving numerical solutions to the type of problem presented by the evolution of interstellar gas clouds. Inside the simulation domain the physical properties, such as the velocity, density, temperature, etc., of each SPH particle at a location (x_i, y_i, z_i) are calculated as an average over a fixed number of neighbouring SPH particles, with a distance weighted kernel function. The evolution of a cloud due to the effects of its self-gravity and its viscosity can be followed. In addition to these effects the CLOUD code has been extended, as described previously, to allow for the thermal effects of incident FUV and cosmic ray radiation and the heating and cooling effects of chemical reactions which can occur. These are based on the atomic and molecular species known to be present in the interclump material, dust grains, hydrogen, carbon, oxygen and their various compounds.

All the simulations run in the main body of the thesis adopt an initially uniform mass distribution. This chapter describes how the boundary conditions and initial conditions for the simulations were selected and set by the Author. The factors considered are the initial distribution of particles in the volume of interest and the method used to

populate this volume, the issues raised by a purely random positioning of the particles which can lead to premature collapse of the molecular cloud and methods chosen to mitigate this effect. In addition the effects of varying the number of particles on the length of time calculated as needed for collapse are discussed and the reasons for the selection of the number of particles used in the simulations are given.

4.2 Boundary Conditions

There are two boundary conditions to be considered. One is concerned with the limits of the computing space and the other concerns the way the molecular cloud relates to the ICM within which it is positioned. All the simulations of the evolution of molecular clouds discussed in this thesis use the same boundary conditions.

The evolution of the cloud is taken to occur within a cubic simulation space at the centre of which is placed the initial spherical cloud. The cube is sized to be larger than the cloud so any expanding cloud can be accommodated, the cube can be up to several parsecs larger than the cloud's initial dimensions. Some small number of particles will inevitably reach the limits of the simulation space and these are considered 'captured' and although their motion takes no further part in the simulation of the cloud's evolution they continue to be included in other particles' 'nearest neighbour' lists.

For the physical model of the molecular cloud an outflow boundary is set which is confined by a weak pressure equivalent to that produced by a warm (100K) and tenuous interstellar medium with a density of 10 $n(H_2)\,\mathrm{cm}^{-3}$.

4.3 Initial Particle Distributions

The initial conditions in SPH simulations need careful consideration to avoid artefacts being introduced into the numerical results. A particle's fluid properties are expressed as a linear combination of all the nearest neighbour particles which contribute to a particle's position and motion. Diehl et al. (2012) point out that in order that the SPH codes give accurate results it is essential that the computation starts with initial conditions whose interpolation properties are as accurate as possible.

In addition the initial particle arrangement has to be a good fit to the concepts on which SPH is based, that is it should be as close as possible to a particle arrangement

(a) Uniform   (b) Random   (c) Glass like
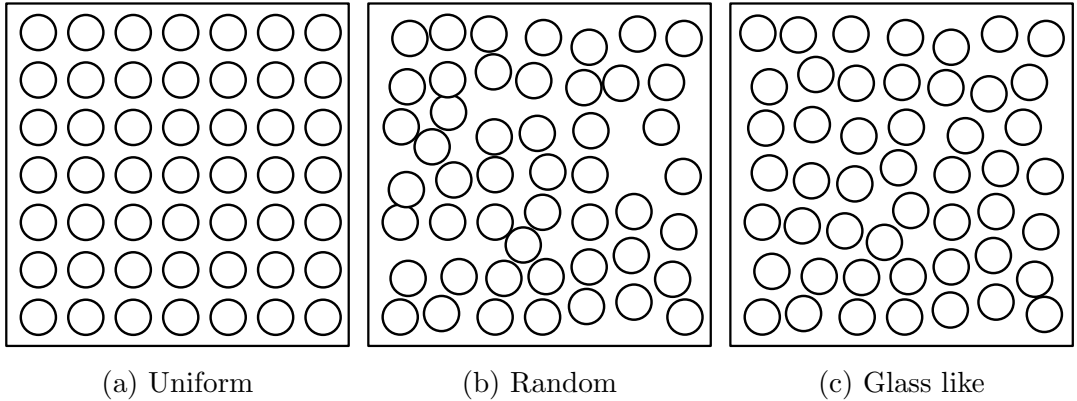
Figure 4.1: 2-D representation of three different initial particle arrangements.

that would arise in an SPH simulation. The arrangement should also be locally and globally isotropic as the cloud being modelled has no preferred axes or directions.

There are essentially two main approaches to arranging the starting positions of the particles within the problem domain - one is as a regular lattice and the other is essentially a random arrangement.

Lattice structures, for example a cubic lattice or an hexagonal close packed structure, are easy to set up and show good interpolation accuracies. However the artificial alignments of the lattice planes can introduce artefacts in the results.

A random arrangement of the particles corresponds more closely to the arrangement of the real particles in the inter-clump material and offers a good model for the initial conditions. However ensuing simulations suffer from the effect that random initial positions give Poisson noise in the particles' distribution resulting in high-frequency noise in the results for density and particle accelerations (Hubber et al., 2011). Random positioning could also give localised volumes of high number density at the start of the simulation which are close to the value which has been taken as that signifying imminent cloud collapse: these high values would then affect the rate of collapse. However the aim of these studies is not to start the model with high density clumps which could trigger collapse in a short space of time but to follow over a longer period the evolution of a cloud which exhibits no such volumes. In order to achieve this aim, and to reduce the noise in the results, the spread of values of the particles' separations was reduced to produce a 'glassy' arrangement, the position of the particles was still essentially random but the spread in the values of the separations between the particles was reduced.

The difference between the three different arrangements, a uniform lattice, random and 'glass-like', is shown in Figure 4.1 using two dimensional images to represent three dimensional arrangements.

4.4 PSEUDO POTENTIAL

Code was written by the Author to set up the initial positions of the particles which worked in the following manner. The clouds were initially populated with particles by randomly positioning the particles within a normalised sphere representing the molecular cloud under study. The sphere is taken to be placed in a cube such that the six faces of the cube formed tangents to the sphere's surface.

Three pseudo-random numbers were generated for each particle to represent its position on the x, y and z axes of the cube. If the particle was found to lie within the volume defined by the sphere the particle count was incremented by one and the position stored. If the particle's position lay outside the sphere the result was discarded and three new pseudo-random numbers were generated: the process was repeated until 100k particles were positioned within the sphere.

After the sphere was populated the glass-like arrangement of the particles was produced by subjecting them to pseudo-repulsive and pseudo-attractive forces. The pseudo-potential of each particle may be represented by

$$v_{j,\text{pseudo}} = \sum_{i=1}^{N-1} -\frac{1}{r_i} + \frac{\bar{r}^2}{r_i^3}, \tag{4.1}$$

where

$$\bar{r} = \sum_{i=1}^{N} \frac{\bar{r}_{sep}}{N}, \tag{4.2}$$

and where $v_{j,\text{pseudo}}$ is the net velocity of the focus particle j, N is the total number of particles in the simulation, $\bar{r}_{sep}$ is the mean separation of the 10 nearest particles and r_i is the separation between the particle i and the focus particle j.

The average separation $(\bar{r}_{sep})$ of the 10 nearest particles to a focus particle was calculated and then repeated for all the particles taking each in turn to be a focus particle. The mean of the $\bar{r}_{sep}$ values for all the focus particles was then calculated and this was taken to be the average inter-particle separation $(\bar{r})$.

To minimise computational time this process was run fifteen times using very small time steps: the separations were not calculated to produce zero net force on each particle as reported by Diehl et al. (2012). The smoothing effect that this procedure has can be seen in Figure 4.2 which shows the initial, more clumpy, distribution of particles in a random arrangement and the smoothed pseudo-potential setup.
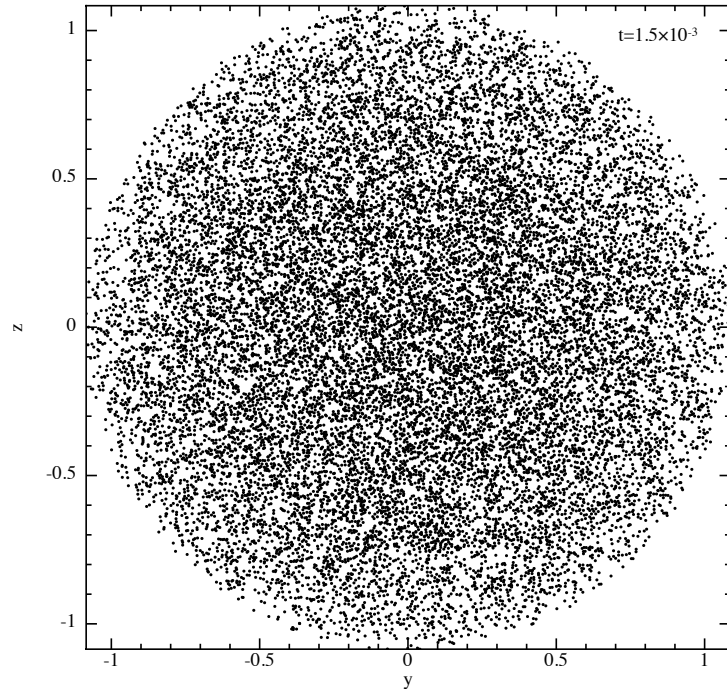
(a) Random initial distribution of SPH particles
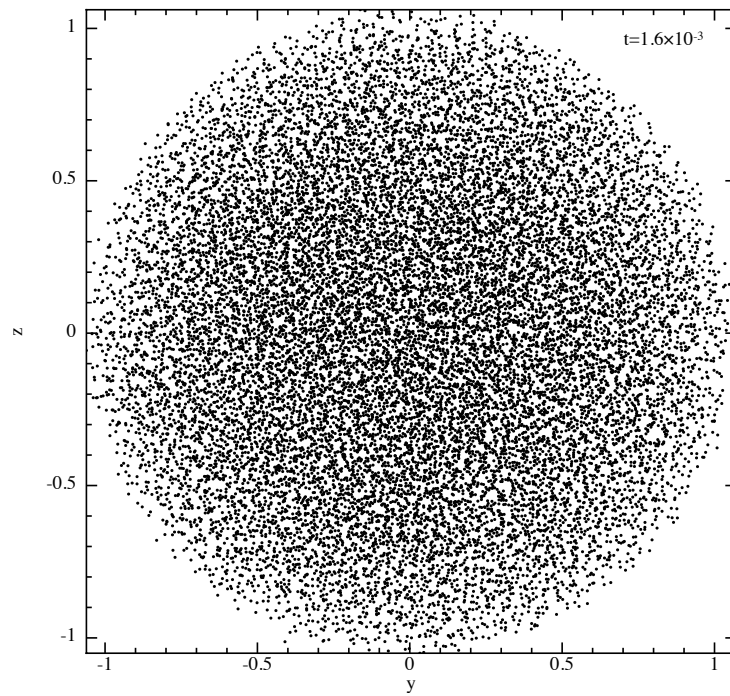
(b) Pseudo potential initial distribution of SPH particles

Figure 4.2: Initial distribution of SPH particles

4.5 Effect of different initial distribution of SPH particles

After the pseudo-potential code was written, it was determined that other hydrodynamic codes, such as Gadget-2 (Springel, 2005) and Seren (Hubber et al., 2011), existed which can be used to produce glass-like distribution under specified settings. Therefore it is possible to compare the glass-like distribution generated by the pseudo-force or pseudo-potential approach with those produced by the Gadget-2 and Seren codes. This was done by running the simulation codes using the same conditions, except for the initial particle arrangement, and plotting the particle number density against time. The initial particle number density was set at $n_i = 100$ cm^{-3}, the cloud mass as 27M$_\odot$ and the external FUV radiation flux is set to 1G$_0$, with all of the micro-physical and chemical processes being activated. This value of the mass is chosen because the cloud under the given settings is just at a critical initial state to, or not to, collapse. This means it will be dynamically sensitive for any small changes in the initial particle distribution.

A simple method to identify if a molecular cloud would collapse or not after a period of time is to trace the mean density evolution of the simulated cloud. The results are plotted in Figure 4.3. The plots correspond to a starting structure analogous to that of 'glass' produced by (i) the Gadget-2 code and (ii) the Seren code , (iii) a 'glass-like' structure resulting from the method described above and (iv) random positioning.

Figure 4.3 shows the evolution of the mean density of the simulated clouds with the initial particle distributions generated by the different codes. It may be seen that in the clouds with the initial particle distribution generated by the pseudo potential, the Gadget-2 and the Seren codes, the mean density rises sharply from the initial value of 100 cm^{-3}, to 10^{10} cm^{-3}, a sign of collapse of the cloud, after $t > 3.0$ Myr. However a cloud with an initially random distribution did not collapse, but dispersed after 4.5 Myr. This is due to the random distribution of particles creating more uneven gaps between small clumps, so that FUV radiation could penetrate deeper into this cloud than into the clouds generated by the other three codes. Therefore the temperature in these gaps increases which creates higher thermal pressure gradients, consequently the cloud disperses.

Comparing the time required for collapse for the three collapsed clouds, the difference between the Gadget-2 and Seren setups is about 1.5 Myr, while that between the pseudo-potential code and Gadget-2 is less than 0.3 Myr, and 1.2 Myr from that of
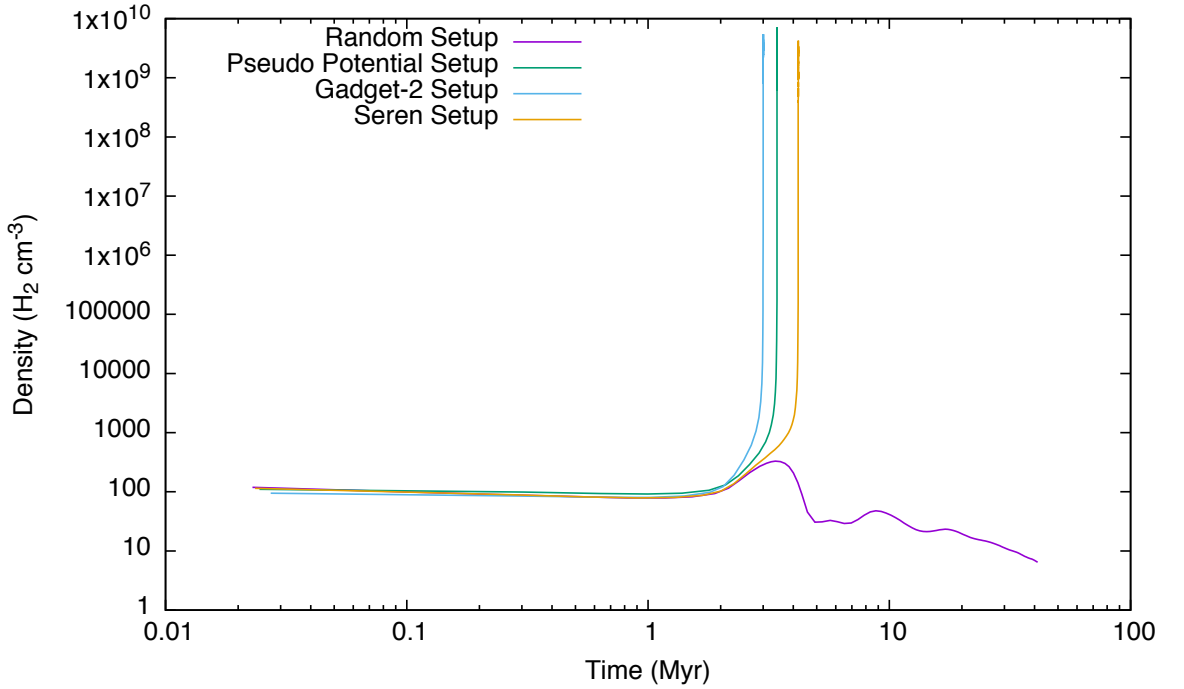
Figure 4.3: The evolution of mean cloud number density with computational time for four different starting assumptions for the cloud particle arrangements. The cloud is set to be of density $n_i = 100$ cm^{-3} and with mass 27M$_\odot$ and with a cosmic ray flux of 1G$_0$. The plots correspond to a structure analogous to that of 'glass' produced by (i) Gadget-2 (Springel, 2005) and (ii) Seren (Hubber et al., 2011), a 'glass-like' structure resulting from the method described above (iii) and (iv) random positioning.

the Seren code. Therefore the initial distribution of particles generated by the pseudo potential code is reliable to use, and is consistent with the other two codes.

Due to the geometric shape of the molecular cloud under investigation being a simple sphere, any improvement to a purely random distribution of particles by making it more glassy reduces not only the Poisson noise in the results but also the risk of random clumping. The pseudo-potential approach to smooth the separation between the particles' positions yields a more uniform distribution of particles but introduces no directionality bias although, as stated in Section 4.4, no attempt was made to achieve zero net force on the particles. This is a concern for the Gadget-2 and the Seren codes as they are intended that arbitrary shapes can be generated and for these cases it is important that zero net force exists between the particles otherwise the shapes will not be stable. For a simple shape like a sphere, where multiple density nodes will not form, this is not a concern.

The pseudo-potential approach to obtain an initial glass-like distribution of particles was subsequently used for all the simulations reported here.

4.6 NUMBER OF PARTICLES AND TIME CONVERGENCE

An important consideration is the choice of the number of SPH particles, N, which are used to represent the simulated object and tracked during the simulation. In principle, simulations using larger numbers of particles will provide results of higher resolution than that using fewer particles, for the volume element in the simulation domain represented by each of the SPH particles can be small enough so as not to lose any detailed characteristics in the simulated region. However the cost of achieving high resolution is the extended simulation time because to track the dynamic behaviour of the whole system the hydrodynamic equations described in Chapter 2 are solved N times at each time step. In order to find the minimum number of SPH particles needed to get convergent simulation results it is necessary to investigate the effect of the number of SPH particles on the dynamic evolution of molecular clouds.

Nelson and Langer (1999) used 24,021 particles in the simulation work for investigation of the stability of a Bok molecular cloud of mass of 35 $M_\odot$, which leads to a resolution of 1.45×10^{-3} $M_\odot$ per SPH particle. The Author ran a set of simulations using 20,000, 50,000, 100,000 and 150,000 SPH particles to track the evolution of molecular clouds using the same initial particle positioning method described in Section 4.4. All these simulations used the same starting conditions with a particle density $n_i = 100$ cm^{-3}, cloud mass $30M_\odot$, R=1.13 and a cosmic ray flux of $1G_0$. These give resolutions of 1.35×10^{-3}, 5.4×10^{-4}, 2.7×10^{-4} and 1.8×10^{-4} $M_\odot$ per SPH particle respectively. The time for collapse of the cloud is taken as being the time at which the extremely high particle density occurs and the results are presented in Figure 4.4. It may be seen that the behaviour of the clouds at collapse is the same for any of the selected particle numbers, however the collapsing times are different, being 3.15, 3.2, 3.48 and 3.45 Myr respectively.

In order to see the trend of the variation of the collapsing time, T_i, with increased number of SPH particles in the cloud more clearly, a parameter, q, is defined to measure the change in the collapsing time per thousand particles,

$$q = \frac{T_i - T_{i-1}}{N_i - N_{i-1}}, \qquad (4.3)$$

with N_i the SPH particles for the ith simulation, where $i = 2$, 3, 4. The differences in the time to collapse between one simulation and the preceding are 0.05, 0.28 and -0.03 Myr respectively, and the differences in the numbers of SPH particles are 30K, 50K and 50K. The calculation gives $q_2 = 0.0017$, $q_3 = 0.0056$ and $q_4 = -0.0006$
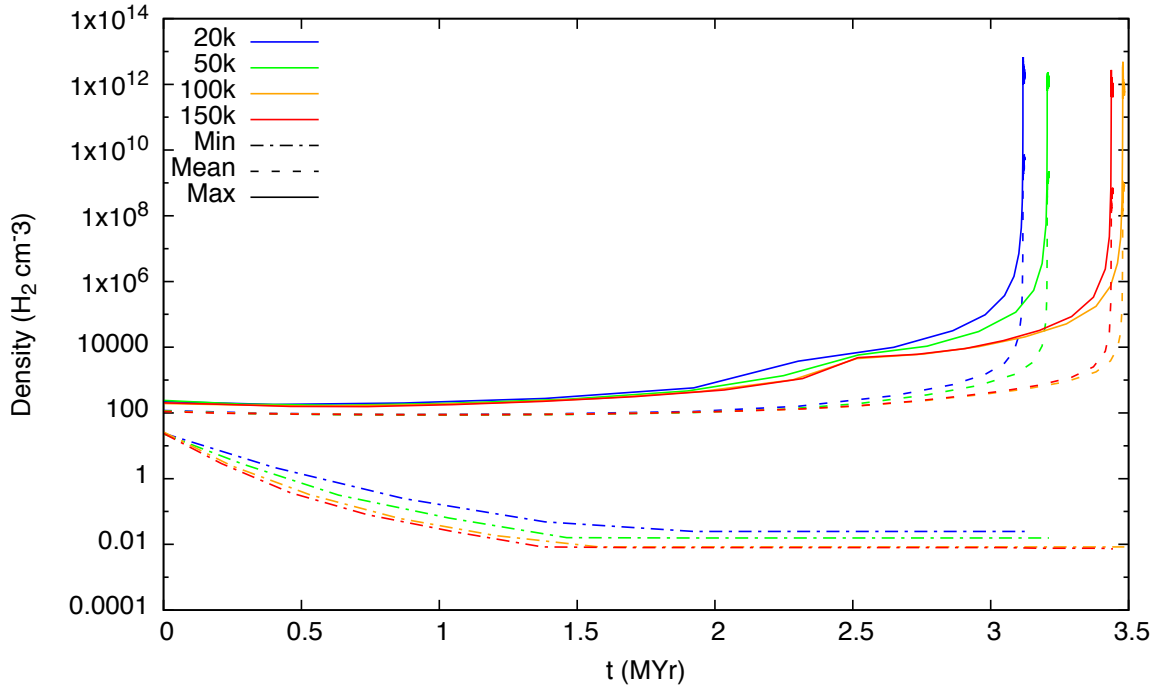
Figure 4.4: The time evolution of a molecular cloud in simulations with different initial particle numbers are shown. The colours indicate the number of initial particles, blue corresponds to 20,000 particles, green to 50,000, orange to 100,000 and red to 150,000. A dashed and dotted line represents the minimum cloud density, a dashed line indicates mean density and a solid line indicates the maximum density calculated during the simulation.

Myr per thousand particles respectively. This suggests that the result converges well after $N \geq 100,000$ at which point an increase per thousand particles only varies the collapsing time by 0.0006 Myr, that is a relative variation of $0.0006/3.45 \times 100\% = 0.017\%$. Therefore the choice of $N = 100,000$ is a good guarantee of the validity of the simulation results.

Before this analysis was undertaken a number of full simulations had been run using 20,000 particles. Based on this analysis it was decided to repeat these simulations using 100,000 particles. Using 150,000 particles would have given a slightly more accurate results but the closeness to the time convergence using 100,000 particles was deemed acceptable without incurring the additional computational time cost and it would align the number of particles used in this thesis to other work published in the more recent past. All the results reported in this thesis use 100,000 particles.

4.7 Data Handling

To be able to handle efficiently the quantities of data produced by the large number of simulations being run, the Author made changes to the CLOUD code regarding the data output and storage with the intention of improving the storage efficiency and speed of access to the data. The storage format selected was the Hierarchical Data Format version 5 supported by the HDF Group (The HDF Group, 1997). The HDF5 file structure includes only two major types of object, *datasets*, which are multidimensional arrays of a homogeneous type and *groups*, which are container structures which can hold datasets and other groups, resulting in a hierarchical, filesystem-like data format.

The original CLOUD code output the results as ASCII, the changes made to the code formatted the output directly in the HDF5 format.

CHAPTER 5

SIMULATION STRUCTURE AND PARAMETERS

5.1 INTRODUCTION

In order to understand the significance of each contribution to the evolution of the cloud of the different sources of heat energy, thermal transfer and cooling caused by the interplay of the different mechanisms discussed in Section 3.3, it is necessary to define a baseline from which the different results can be compared. It is also useful to define a 'figure of merit' to quantify the contributions that the different effects have on a cloud's evolution. For this purpose the concept of the Modified Jeans Mass has been adopted.

To recapitulate, the heat sources external to the cloud are the FUV and cosmic ray fluxes. The energy from these sources is considered to be converted to heat via ionisation processes and dust grain photoelectric heating. Hydrogen molecule formation from monatomic hydrogen also releases heat within the cloud. The cloud is considered to be cooled by photon emission from changes in atomic and molecular energy states, generally grouped as molecular line cooling (MLC). The gas-dust thermal exchange process transfers heat energy between gas and dust particles depending on their relative temperatures.

To identify which of these micro-physical and chemical processes are the most significant in the evolution of molecular clouds the effects of each of the processes acting singly and in various combinations together and with different levels of the FUV flux was examined on an idealised molecular cloud. An indicator of the effectiveness of these influences was required and for this the concept of the 'Modified Jeans Mass' was developed.

5.2 Modified Jeans Mass

Much of the work which has been done over the last century in modelling the evolution of molecular clouds has been in refining the analytical model proposed by Jeans (1902). The concept of the Jeans Mass, the mass of a cloud in equilibrium under the effects of gravity and thermal pressure only, is still useful as a check on the stability or otherwise of a idealised molecular cloud. The effect of including thermal inputs and the chemical pathways modelled in the simulation will be to produce a variation in the minimum initial cloud mass required for collapse from that predicted by Jeans' model. The changed mass is called in this thesis the 'Modified Jeans Mass' (MJM) and the variation in the MJM caused by including different physical and chemical processes in a cloud of a certain initial density, directly reflects the effects of these processes on the dynamics of a molecular cloud. Therefore finding MJM in different circumstances is one of the major objectives in the simulations.

The MJM for a given start density and a given FUV flux was determined by a form of interval halving. Expected upper and lower limits for the minimum mass of the cloud were selected by trial-and-error, but in the first instance based on values given by Nelson and Langer (1999), as start points for the simulation. Subsequent runs used the half-way point between the maximum non-collapsing mass and the minimum collapsing mass until the difference between the two was equivalent to 1 Solar Mass at which point the calculation was taken to be complete. Commonly between 10 and 20 simulation runs were required to identify the collapsing point for each of the combinations of particle density, FUV flux and other processes selected. This approach resulted in cloud masses used in the simulations ranging from 0.5 to 2,050$M_\odot$; the simulations needed to identify these limits covered a wider range, from 0.1 - 5000$M_\odot$.

5.3 Criteria for data analysis

In view of the numbers of individual simulations made and to ensure a consistent classification of the results it is necessary to define some criteria to decide whether a cloud has reached its MJM. This requires a definition for collapse as well as for some other relevant parameters. By setting limits for these relevant parameters it is possible to compare the results of the simulations with each other. The criteria chosen are:

- Definition for the collapse of a cloud

- Definition of the dynamic radius of the cloud during its evolution

- Definition of the dynamic mass of the cloud during its evolution

- Definition of the mass of the core of the cloud.

To judge if a cloud either eventually collapses to form a dense core or evaporates, the following criteria have been defined:

1. The maximum density at a snapshot of the simulated evolution of the cloud satisfies $n \geq 10^7$ cm^{-3}

2. There are at least 10 particles whose density is higher than 10^7 cm^{-3} .

3. The dynamic mass should be a stable value at the end of the simulation.

It should be emphasised that the formation of a highly condensed core from a collapsing cloud in these simulations does not mean that a real star has been created. To follow the evolution sufficiently to identify if this would be the case would take much time since the simulation would progress extremely slowly due to lack of 'sink particle' implementation in the CLOUD code (Nelson and Langer, 1999).

The dynamic radius of a cloud is defined here as the distance between the centre of the cloud and the furthest point r from the centre where the radial velocity is 0. Positive values for velocity mean that the particles are moving outward along the radial direction (that is they are 'evaporating') and negative values indicate inward motion, the cloud (or that region of the cloud) is collapsing. The radius at which $v_r = 0$ is taken as the point which distinguishes between the cloud and the evaporated material. The dynamic mass of the cloud is defined here as all the material contained within the sphere of radius r. For ease, these two parameters are referred to here as the radius and the mass of the cloud.

The core mass of the cloud is defined as the mass of all the particles at the centre of the cloud where the density is $\geq 10^7$ cm^{-3}. This mass is sometimes referred to as the 'seed' for star formation.

5.4 GROUPING OF SIMULATIONS

A number of different Models have been identified in order to be able to investigate the effects of each of the component thermal and chemical processes. The Models are not meant to represent physically real or observed molecular clouds. They are designed to be able to analyse the roles that each of the component processes and identify their effect, either singly or in combination, on the evolution of molecular clouds.

The simulations were divided into two major groups:

- A group with the FUV flux set to zero and with various combinations of the physical and chemical processes active. The results and discussion for this group are to be found in Chapter 6.

- A group with various set levels of FUV flux and with all the chemical and physical processes active. The results and discussion for this group are to be found in Chapter 7.

In order to obtain a sufficient number of data points to give conclusive results a total of some 1,350 separate simulations were run using 100,000 particles. Each of these runs could take up to 20 hours of computer time without including the subsequent post-processing. In addition many simulations were made using 20,000 particles before, as referred to in Section 4.6, the decision was made to standardise on 100,000.

CHAPTER 6

THE EFFECT OF MICRO-PHYSICAL AND CHEMICAL COOLING PROCESSES ON THE EVOLUTION OF MOLECULAR CLOUDS

6.1 INTRODUCTION

Various theoretical models exist for the investigation of the evolution and star formation in molecular clouds under different astrophysical environments. As mentioned earlier in Section 1.4 the Jeans model (Jeans, 1902) defined the minimum mass of a self-gravitating system balanced by thermal pressure, such as seen in Bok globules (Vainio and Vilja, 2015). Micro-turbulence was first taken into account in the evolution of galaxies and stars by von Weizsäcker (1951) and Chandrasekhar (1951), this work was recently extended by Federrath et al. (2011). On the other hand Mestel and Spitzer (1956) found that magnetic fields could prevent the collapse of an initially unstable Jeans system. The model proposed by Shu (1983) further investigated the ambipolar diffusion of magnetic fields in self-gravitating layers of a neutral isothermal system

under quasi-magnetohydrostatic and local ionisation equilibrium. Recently the effect of the radiation feedback from massive young stars on the evolution of molecular clouds surrounding H II regions (Bertoldi, 1989; Lefloch and Lazareff, 1994; Bisbas et al., 2011; Gritschneder et al., 2009) or in PDRs (Gorti and Hollenbach, 2002; Motoyama et al., 2013) are investigated both semi-analytically and numerically.

It is well acknowledged that on the evolutionary path from molecular clouds to star(s), micro-physical processes such as photo-electric heating, cosmic ray heating and chemical line cooling also play important role (Klessen and Glover, 2016) in addition to turbulence, magnetic field and ionisation radiation feedback as mentioned above. Micro-physical and chemical processes have recently been included in various hydrodynamical simulations, e.g., the evolution of Bok globules in PDRs (Nelson and Langer, 1999) and the radiation driven implosion in molecular clouds around H II regions (Miao et al., 2006, 2009; Kinnear et al., 2014, 2015; Kusune et al., 2015; Bisbas et al., 2015). They have also been included in the modelling of chemistry of star forming filaments (Seifried and Walch, 2016), in the recent hydrodynamic simulation of the life cycle of molecular clouds (Walch et al., 2015) and in the simulation of star formation in dwarf galaxies (Hu et al., 2016). Although the importance of including of the micro-physics and chemistry in simulating the expansion of D-type ionisation front has been quantitatively explored by Haworth et al. (2015), the importance of them in the dynamic evolution of molecular clouds where the effects vary depending on the local densities, temperatures and FUV intensities has not yet been investigated in detail.

Therefore it is the intention in this chapter to evaluate the roles of some of the micro-physical processes and chemistry in the evolution of molecular clouds, based on extensive numerical simulation results obtained by using a comprehensive hydrodynamic code written by Nelson and Langer (1999) as described earlier in Chapters 2 and 3. All the data reported in this chapter and their discussion are original. It is hoped that these early results could at least provide astrophysicists with a set of benchmarks to assist in deciding whether or not these basic physical and chemical processes should be included in their particular models of the evolution of molecular clouds and star formation so increasing the realism of their simulations.

6.2 Effects of combinations of activated processes without FUV input

This series of simulations is not intended to follow a cloud's evolution for its own sake but to identify the significance of the different physical and chemical processes acting either singly or, in different combinations, together. As mentioned in Section 3.1, if more than one of the micro-physical and chemical processes are activated at the same time the reactions and effects caused by each of them are interdependent, changes in one phenomenon will induce changes in another. To identify the significance that each part of the thermal model has in changing the minimum initial cloud mass required for collapse, that is resulting in different values for the MJM, simulations were made with each process isolated in turn as well as with all of them activated. To achieve this aim, six combinations, called Models in this thesis, of activated and inactive micro-physical and chemical processes were defined; these are listed in Table 6.1. Simulations were made of the evolution of clouds of various initial densities.

Model	Chemical Cooling	Gas-dust	Cosmic-ray
A	No	No	No
B	No	Yes	Yes
C	Yes	No	Yes
D	Yes	Yes	No
E	Yes	Yes	Yes
F	Yes	No	No

Table 6.1: The activated physical processes included in the different models.

To simplify the study of the effects that these processes have working singly or together on a cloud's evolution, FUV photoelectric heating is excluded by switching off the FUV radiation input in the computer model. Thus, with no incident FUV, the results obtained from this group of simulations can be applied to the evolution of a molecular cloud in an environment without significant incident stellar radiation. Results with different levels of FUV are reported and discussed in 7.

In all cases the evolution was tracked by following the change in cloud density with time until the collapsing point was reached. In addition the abundances of selected chemical species were tracked as a function of radius.

6.3 Different Models and the Overall Result

Model A covers the case for the isothermal evolution of a molecular cloud which is not subject to any internal or external influences, it is intended to give a baseline for comparison with the results of other simulations. For this simulation the FUV and cosmic ray fluxes were set to zero and the molecular line cooling and gas-dust thermal exchange mechanisms were inactivated.

Model B is designed for exploration of the effect of the basic internal gas-dust thermal exchange and background cosmic ray heating, chemical cooling is not included. In Models C, D, E and F chemical cooling is taken into account, but with the gas-dust exchange and the cosmic ray heating being switched off in turn, then with both on or both off.

For each model, five different simulations are performed with molecular clouds of different initial densities $n_i = 50$, 100, 500, 1000 and 5000 cm^{-3}, these are named as Cloud type 1, 2, 4, 5 and 7 respectively for the convenience of identification in the discussion that follows. (The missing numbers 3 and 6 as well as 8 are reserved for additional densities reported in Chapter 7). The cloud temperature was set at 60K as it represents a warm medium which has been subjected to incident radiation. It may be observed that lower temperatures, down to 10K, are to be expected in the centres of dense MCs where much incident radiation has already been absorbed but the initial densities of the model clouds are not sufficiently high for these low temperatures to be reached.

For a specified initial density, the mass and radius of a cloud are found through simulations, these are defined as MJM and radius for a particular set of simulations. For example, Cloud Type 4 with an initial density of 500 cm^{-3} will correspond to six different MJMs found from the six models defined in Table 6.1.

Figure 6.1 presents an overall picture of the variation of MJMs with initial densities obtained through the simulation of the cloud evolution for each of the six different Models given in Table 6.1. In general, it can be seen that the MJM decreases with increasing initial density of the molecular cloud, which is the consequence of the increase of the cloud's gravitational potential energy with increasing initial density. The results for each Model are discussed individually in each of the following sections, for each Model the relation between the MJM and initial density of the cloud will be examined and the dynamical evolution of one representative cloud, a Cloud Type 4 with $n_i = 500$ cm^{-3}, will be analysed in detail. To conclude the chapter, in the final two sections the concept of the 'normalised core mass' will be introduced and then a summary given of
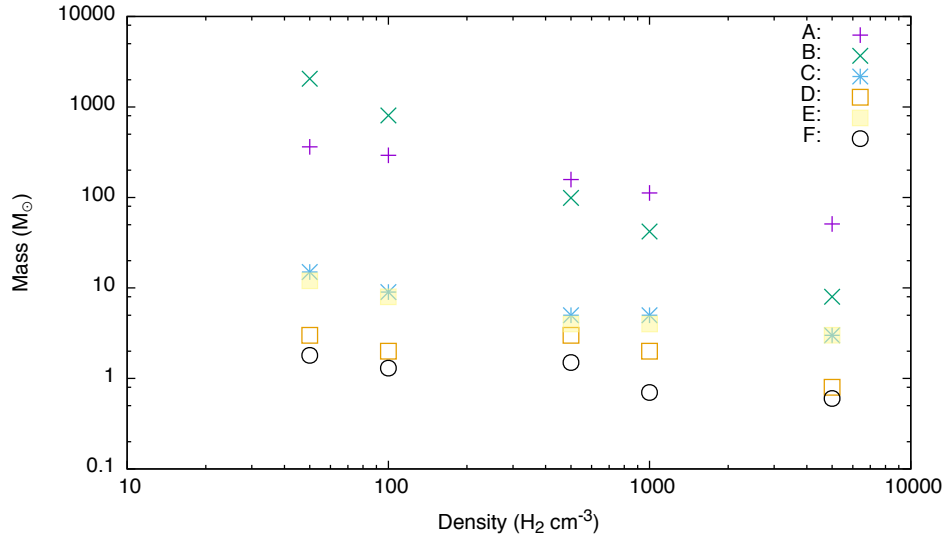
Figure 6.1: The variation of MJM with initial density of a molecular cloud, when different micro-physical and chemical processes are activated. The letters in the legend have the same meaning as in Table 6.1.

the general evolutionary features of the molecular clouds with reference to the different Models.

6.4 MODEL A: ISOTHERMAL EVOLUTION

6.4.1 VARIATION OF MJM WITH n_i

In the five simulations in Model A of clouds with five different initial densities no micro-physical or chemical processes are activated, as is shown in Table 6.1, so the evolution of a cloud is controlled only by self-gravity and thermal pressure. The latter is caused by the density gradient in the cloud at the point when evolution starts. Therefore the energy evolution equation is not solved and the temperature is kept the same as the initial temperature of 60K. This is the so-called isothermal model and appears frequently in astrophysical simulations. As shown by the purple cross symbols in Figure 6.1, the MJM decreases from 384 $M_\odot$ at $n_i = 50$ cm^{-3} to 50 $M_\odot$ at $n_i = 5000$ cm^{-3}. The best fit line gives

$$M_{MJM} = 2.04 \, n_i^{-0.43} (10^3) M_\odot \qquad (6.1)$$

This relationship of MJM with density can be qualitatively explained by pointing out that the lower the initial density, the weaker is the gravitational binding of a cloud

and therefore a higher initial mass is required for a cloud to collapse.

In order to obtain an overall picture on the dynamic evolution of the clouds in this model, the characteristics of the evolution of Cloud Type 4 are analysed in some detail and reference is made to other cloud types where appropriate. The simulation results of the other four cloud types can be found in Appendix A.1.

6.4.2 THE DYNAMIC EVOLUTION OF CLOUD TYPE 4

Figure 6.2a and 6.2b describe the evolution of the density and radial velocity of the cloud of an initial density $n_i = 500$ cm^{-3}, with different scales. Simulations show that an initial mass of 158 M$_\odot$ is needed for the cloud to collapse, which corresponds to an initial radius of 1.15 pc. Figure 6.2a shows the full range of velocities on the y-axis, the scale is changed in Figure 6.2b in order to reveal the inward motion in the very central part of the cloud. As mentioned in Section 5.3, in the velocity profile, positive values mean that the particles are moving outward along the radial direction (that is they are 'evaporating') and negative for inward motion, the cloud (or that region of the cloud) is collapsing. It can be seen that the central part of the cloud always moves inwards while the evolution of the outer layers of the cloud can be divided into two phases, an early expanding phase and a later collapsing phase.

6.4.2(a) EXPANDING PHASE

From the top left panel in Figure 6.2a, it can be seen that at $t = 0.31$ Myr, the expansion of the outer layer leads to the formation of a boundary layer with decreasing density in which the radial velocity increases with the radial distance due to the decreasing gravitational acceleration with radial distance r. In the central part of the core, although there has not been significant change in the density distribution from that initially set, the velocity profile in top-left panel of Figure 6.2b indicates that the inner part of the cloud has developed a inward motion with a peak speed of 0.1 km s^{-1}. When $t = 1.17$ Myr, the centre part of the cloud becomes denser with a peak density of about 10^3 cm^{-3} while the outer layer keeps expanding with a peak speed of 18 km s^{-1} at the outmost boundary of the cloud. The next few panels in both figures show that the centre density keeps increasing (up to 10^5 cm^{-3}) and the inward motion in the central part slows down when the mass is being accumulated to the centre. At the same time the outer layer keeps expanding with a peak speed up to 30 km s^{-1} at the boundary, when $t = 2.10$ Myr.

The evolution of the radius and the total mass of the cloud described above is presented in Figure 6.3 and the corresponding mass loss rate is presented in Figure

6.4. It is clearly shown that both the radius and the mass of the cloud decrease during the expanding phase which lasts about 2.45 Myr, after which time the mass loss rate changes from negative to zero. The radius and mass of the cloud have dropped to 0.55 pc and 58 $M_\odot$ respectively.

6.4.2(b) COLLAPSING PHASE

After the central particle density has increased to a value greater than 10^5 cm^{-3} the gravitational force in the inner part of the cloud becomes so strong after $t > 2.45$ Myr that part of the expanding layer is suddenly pulled back. This inverse motion of the material may be seen by the deep velocity drop of -0.32 km s^{-1} at $r = 2$ pc in the bottom-left panel of Figure 6.2b. When the inward moving gas collides with the high density central core, it is bounced back, as shown by the small positive velocity hump in the same panel. The accumulation of the gas in the central part of the cloud further increases the gravitational force on the gas in the outer layer which results in an accelerated inward motion. This is shown in the bottom-right panel in Figure 6.2b. The maximum speed of inward motion reaches 0.7 km s^{-1} and the peak density in the centre is higher than 10^{12} cm^{-3} at $t = 3.13$ Myr while expanding velocity of the outermost layers is still approximately 30 km s^{-1}.

This collapsing phase can be better observed through the evolution of the mass and radius of the cloud as shown in Figure 6.3 and the mass change rate in Figure 6.4. During the first 2.45 Myr, although both the radius and mass of the cloud decrease with time due to the initial expansion of the outer layer, the mass change rate gradually changes from negative towards zero at $t \sim 2.45$ Myr. At this point the mass change rate then turns positive and reaches a value of 1190 $M_\odot$ Myr^{-1} when $t \sim 2.48$ Myr as a result of the return of the evaporating outer layer toward the centre. Consequently the radius and mass of the cloud increase sharply to 2pc and 150 $M_\odot$ at $t = 2.5$ Myr. Afterwards, the size and the mass of the cloud continuously increase but at a much lower rate. When $t = 3.13$ Myr, the central density reaches an extremely high value of $> 10^{13}$ cm^{-3} which is often taken as indication of the formation of a 'seed', that is a small high density collection of gas and dust around which further material can coalesce leading to the formation of a star (Nelson and Langer, 1999), when the simulation almost stopped running. From this point onwards tracing the further evolution of the cloud leading to formation of a real star is difficult with the current version of the code.

6.4.3 EVOLUTIONARY FEATURES OF CLOUDS IN MODEL A

The evolutionary features of the physical properties of the other four clouds of initial densities of 50, 100, 1000 and 5000 cm^{-3} in Model A simulations follow a similar dynamic sequence to that described above, the plots of these can be found in Appendix A.1. The central density always gradually increases and then satisfies the criteria for the formation of a seed of a protostar. The outer layers of the clouds more or less follow the two phase evolutionary path. Although it is not necessary to discuss the evolution of each one in detail, a summary of the general features of their evolution is presented.

1) The two-phase evolutionary path toward collapse as described in Section 6.4.2(b) is most obviously observed in molecular clouds of lower initial densities such as $n_i = 50, 100$ and 500 cm^{-3} and the maximum speed of the inward motion in a cloud decreases with the increase of the initial density of the cloud, from -7 km s^{-1} for Cloud Type 1 to -0.7 km s^{-1} in Cloud Type 4. When $n_i \geq 1000$ cm^{-3} the evolution of the velocity does not show any very obvious two-phase pattern, the collapse is a rather smooth process and occurs in a much shorter time, as shown in Figure 6.5 which describes the evolution of the maximum density in the five clouds in Model A. It is clear that the lower the initial density, the longer is the time needed for a cloud to collapse, although the lower density cloud has a higher initial mass as described in Equation (6.1). The collapsing time (t_{col}) can be fitted into an exponential function of the initial density: $t_{col} = 355.3 \, n_i^{-0.715}$ (Myr).

2) The evolution of the mass and radius of a cloud with different particle densities n_i is more or less similar to that of Cloud Type 4, that is they first decrease and then increase. In Cloud types 1, 2 and 4 this pattern is seen most clearly. Particularly in Cloud Type 1 this pattern appears periodically almost as if an oscillation has set in. In Cloud Types 6 and 7, with $n_i = 1000$ and 5000 cm^{-3}, mass and radius decrease with a superposed periodic change with time before stable values are reached.
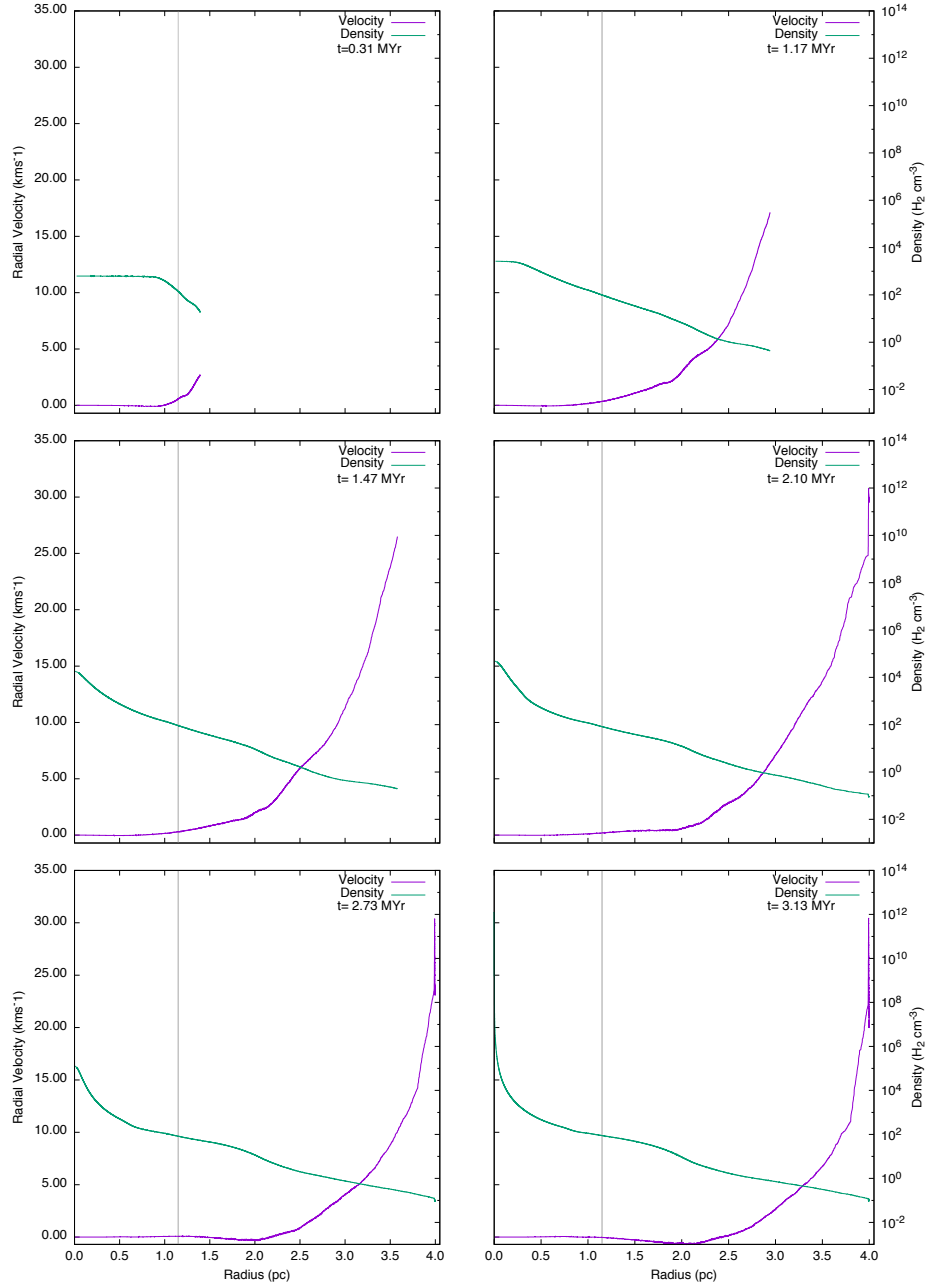
(a) The evolution of the mean density and mean radial velocity snapshots over radial distance in a Cloud Type 4 (initial density $n_i = 500$ cm^{-3}). The grey vertical line shows the initial radius of the cloud.

Figure 6.2: Model A simulations (cont.)
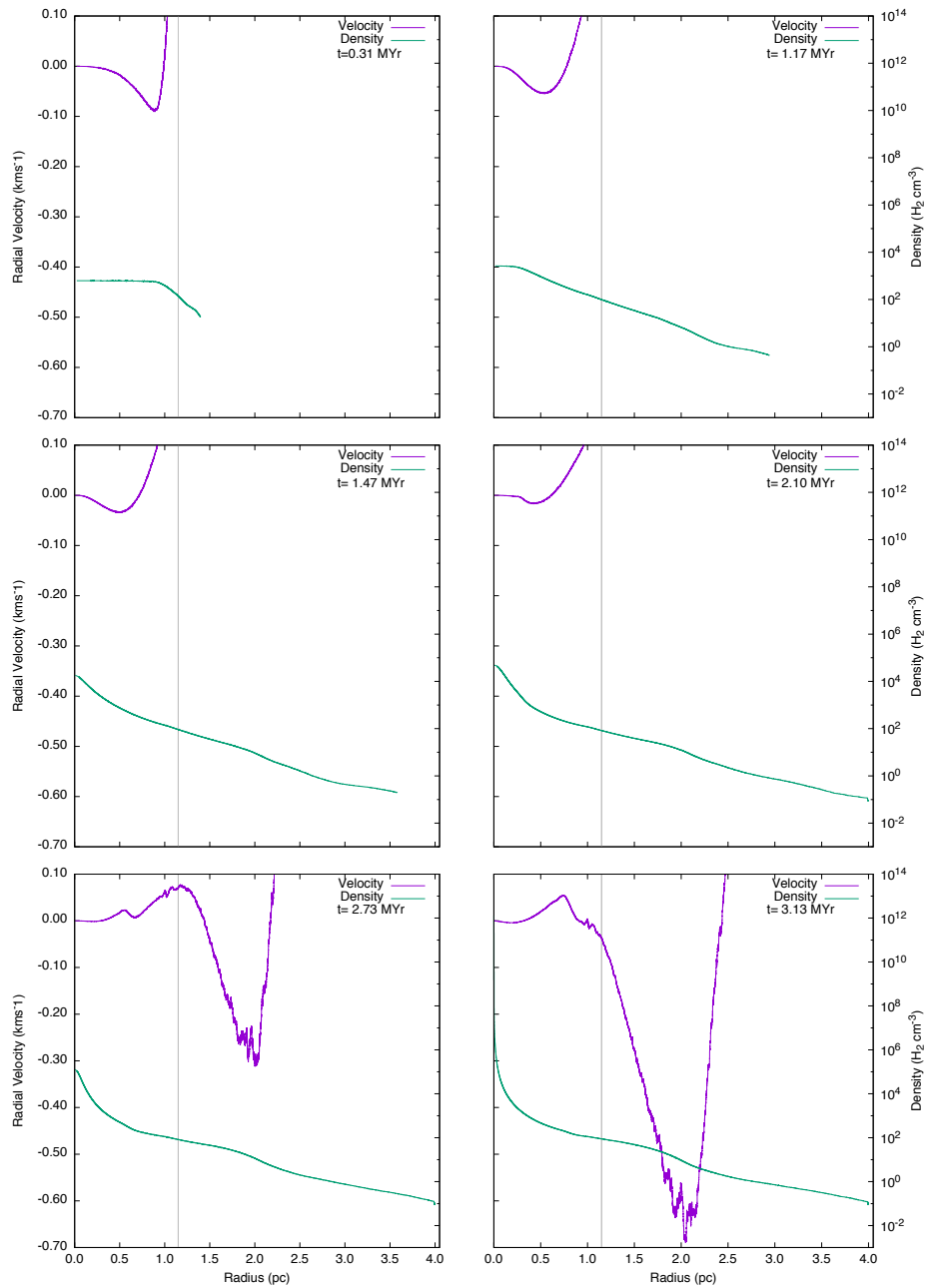
(b) The same as in Figure 6.2a but with the velocity scale being matched to that in the inner part of the cloud.

Figure 6.2: Model A simulations
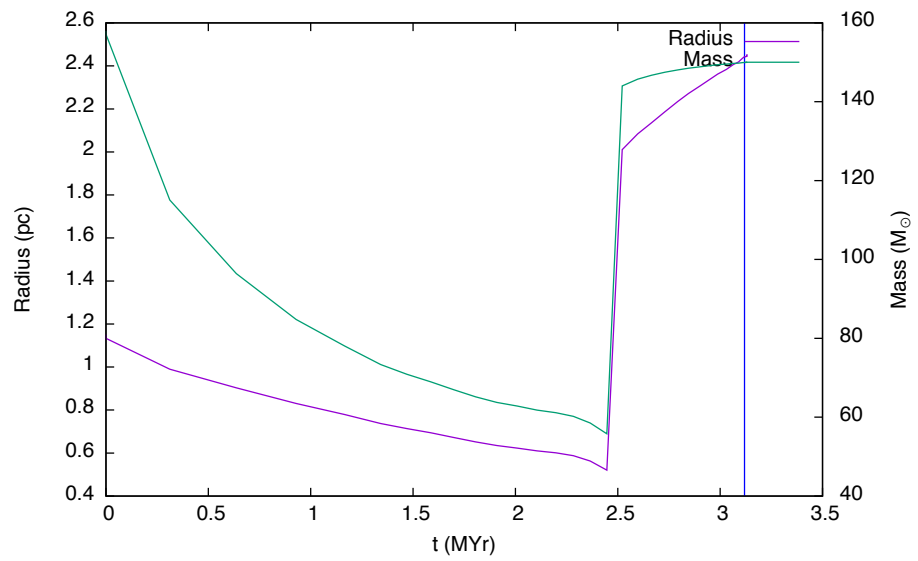
Figure 6.3: Model A: the evolution of the radius and the mass with respect to time of a Cloud Type 4

.
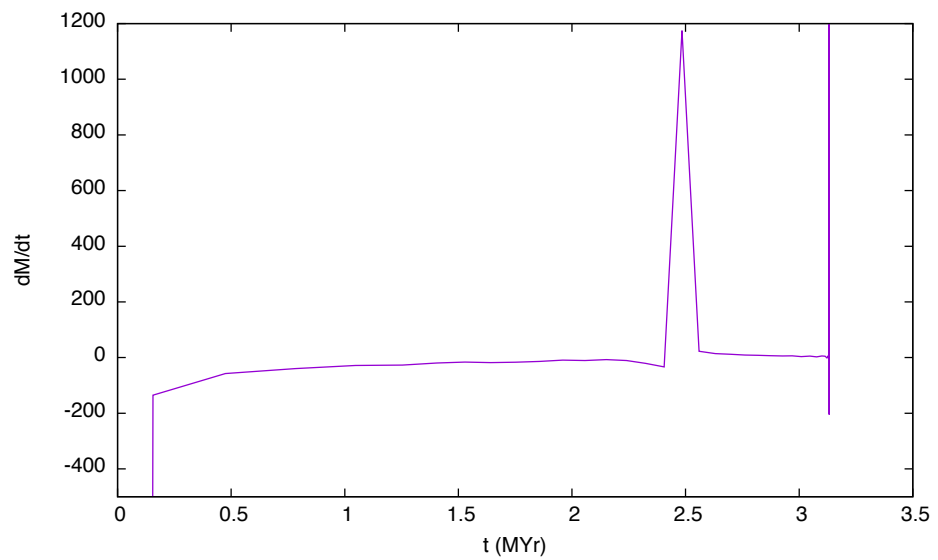
Figure 6.4: Model A: the evolution of the mass change rate of a Cloud Type 4

.
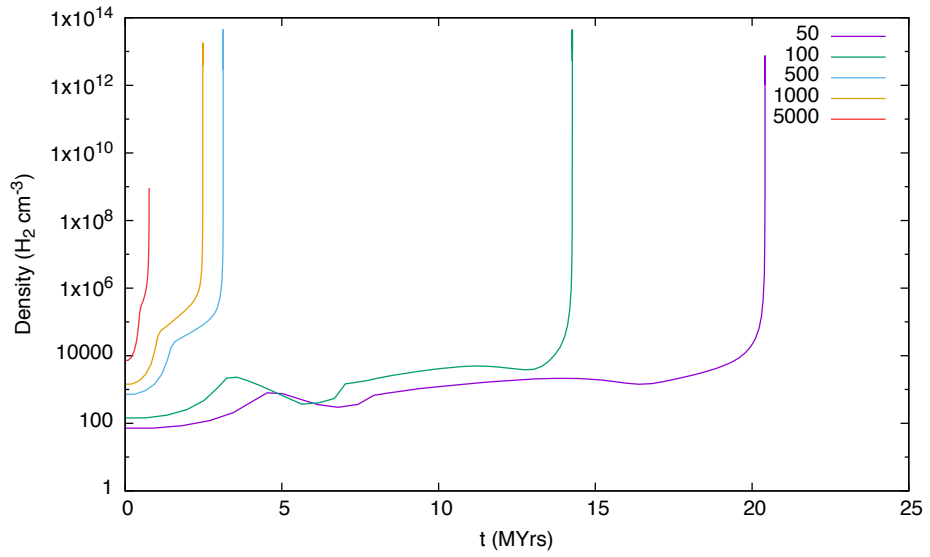
Figure 6.5: Model A: the evolution of the maximum density in the simulated clouds of different initial densities.
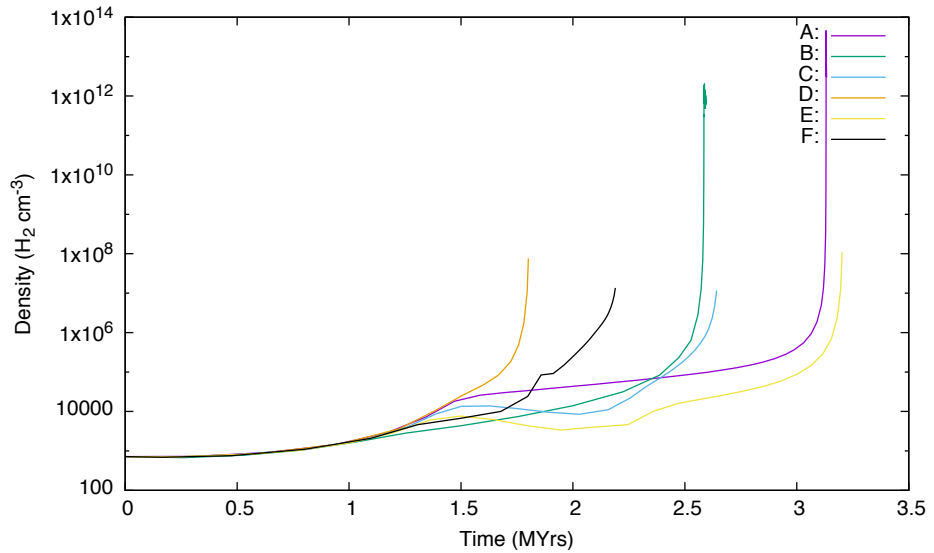
Figure 6.6: Models A - F: the variation of maximum density with time for each of the six Models. The starting condition for all is a Cloud Type 4.

6.5 MODEL B: MICRO-PHYSICAL PROCESSES ACTIVATED

6.5.1 THE NET THERMAL ENERGY EXCHANGE

This Model of simulations is intended to examine the effects of some of the micro-physical processes on the evolution of clouds and is based on the results from the Model A simulations. This being the case the external cosmic-ray ionising heating is activated as is the internal gas-dust energy exchange while the molecular line cooling remains inactive as shown in Model B in Table 6.1. The external FUV input is inactive. The same set of initial densities are used for comparison.

As described in Chapter 3, the cosmic-ray heating rate is linearly proportional to the local gas density n. The gas-dust energy exchange rate is proportional to n^2 and linearly to the difference of the gas and dust temperatures $T_g - T_d$.

Combining equations (3.8) and (3.14) the net energy exchange contributed by the two processes at any point inside the simulation domain can be written as:

$$\Gamma_{\text{net}} = 2.4 \times 10^{-28} n [2.73 - 10^{-5} T_g^{1/2} (T_g - T_d) n] \tag{6.2}$$

where Γ_{net} is in unit of erg cm^{-3} s^{-1}. Further analysis of the density dependence of Γ_{net} on the number densities n in the middle of the range studied can provide more detailed information on its thermal effect. If it is assumed that $T_g = 60$K and $T_d = 10$ K, it can be shown that

$$\Gamma_{\text{net}} \begin{cases} = 0 & \text{for} \quad n_1 = 0 \text{ and } n_2 = 700 \text{ cm}^{-3} \\ > 0 & \text{for} \quad 0 < n < 700 \text{ cm}^{-3} \\ = \text{Maximum}(> 0) & \text{for} \quad n_m = 350 \text{ cm}^{-3} \\ < 0 & \text{for} \quad n > 700 \text{ cm}^{-3} \end{cases} \tag{6.3}$$

where n_1 and n_2 are the density points at which $\Gamma_{\text{net}} = 0$, and n_m is the point for Γ_{net} to become the maximum.

Therefore the net effect of the thermal exchange is to heat the gas in low density regions and cool it in high density regions, though the values of density (n_1, n_2 and n_m) at which the transitions occur vary with the local gas and dust temperatures and these can also vary with time t. In this section the results of the Model B simulations are examined and compared with the Model A results to identify the effect of these micro-physical processes on the dynamics of a molecular cloud.

6.5.2   Variation of MJM with n_i

It can be seen from the green cross symbols in Figure 6.1 that the MJMs for different initial densities n_i are spread over a much wider range than those in the Model A simulations and lie between 2000 M$_\odot$ at $n_i = 50$ cm^{-3} and 7 M$_\odot$ at $n_i = 5000$ cm^{-3}. This can be qualitatively understood by looking at the behaviour of the net thermal exchange rate Γ_{net} with density. Although during the dynamic evolution of a cloud, both the density n and the gas temperature T_g vary with time and the radial distance from the centre of a cloud, a general physical picture of the variation of the MJMs with density can still be derived based on Equation (6.3). At low density, such as for $n_i = 50$ and 100 cm^{-3}, the role of Γ_{net} in the evolution of a cloud is to heat the gas (similar to that is described in the second line of Equation (6.3)) therefore the cloud needs a higher initial mass than its counterpart in the Model A simulations to be able to collapse. This is shown in Figure 6.1. The difference in the MJMs of the pair of clouds of same initial density in Models B and A decreases with n_i when $n_i < 175$ cm^{-3}, similar to that described in Equation (6.3). At $n_i \sim 175$ cm^{-3}, $\Gamma_{\mathrm{net}} \sim 0$, the difference disappears and the pair of clouds with that initial density have similar MJMs of 385 M$_\odot$. With the initial density increasing to such values as $n_i = 500, 1000$ and 5000 cm^{-3}, the net effect of the two micro-physical processes is to cool the gas, so that a cloud in Model B requires a lower initial mass to collapse than its counterpart in Model A. However the difference in MJMs between the corresponding (same initial density) clouds in Model A and Model B simulations increases with the initial density n_i, which is due to the gas-dust cooling rate being proportional to n^2. Overall, the variation of MJM with the initial density n_i can be fitted into a law of the following form

$$M_{\mathrm{MJM}} = 2.1\, n_i^{-1.22}(10^5)\mathrm{M}_\odot \tag{6.4}$$

6.5.3   Dynamic Evolution of Cloud Type 4

Because the physical properties of the central part of the cloud are decisive in deciding whether the cloud collapses or not, in the Figures following the radial distribution of the physical properties of the cloud are plotted on a scale which best shows the behaviour of this region. For example, if the inwardly directed velocity in the central part of the cloud is less than a hundredth of the evaporation velocity in the outer layers of the envelope, the velocity scale is chosen to reveal the variation in the velocity in the core of the cloud.

In Figures 6.7 and 6.8, six snapshots of the density, velocity and temperature profiles of Cloud Type 4 (initial density $n_i = 500$ cm^{-3}) are presented. The MJM of the cloud
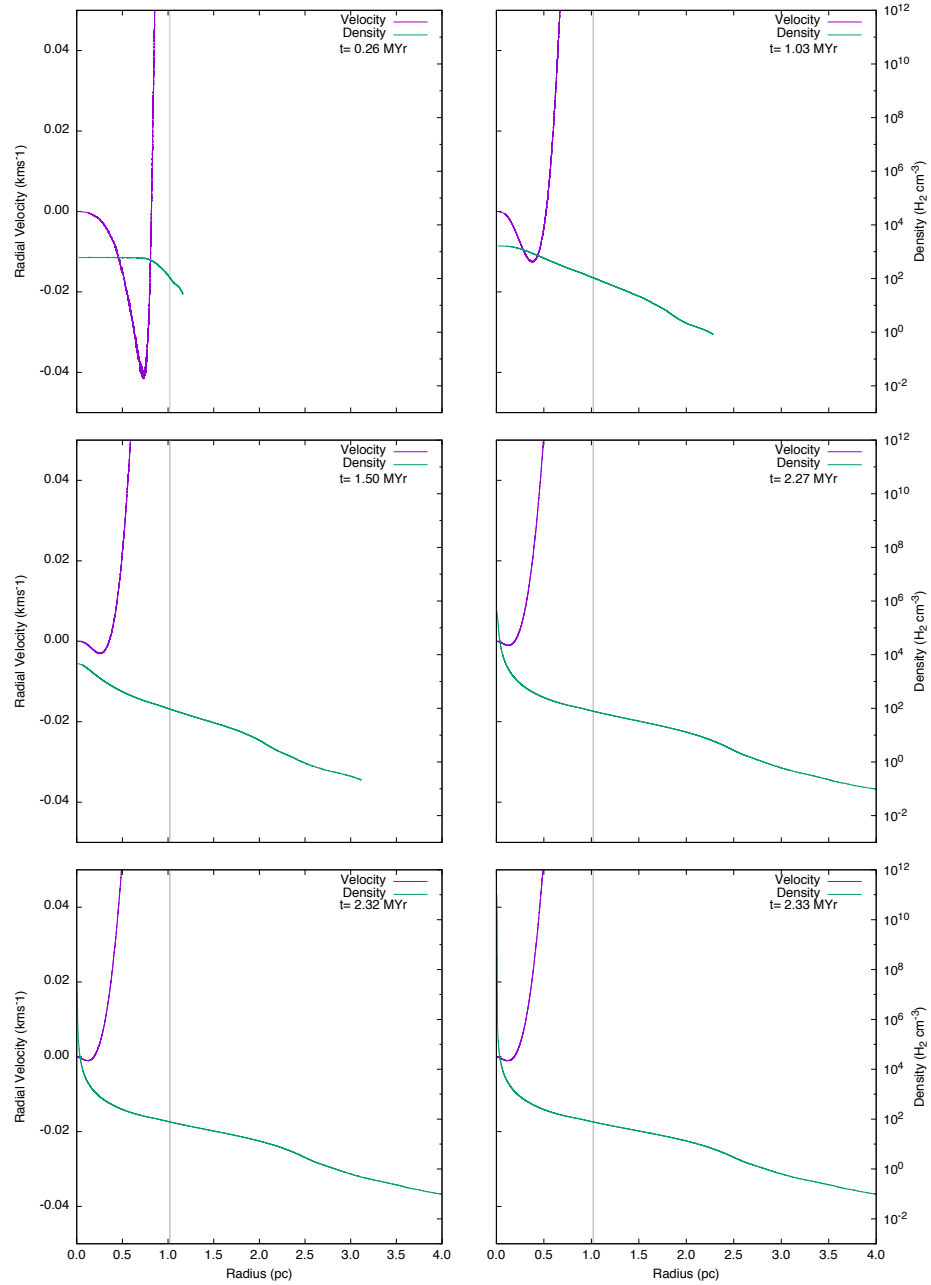
Figure 6.7: Model B: the evolution of the mean density and mean radial velocity distribution with radial distance in a Cloud Type 4. The velocity scale is expanded in order to show the collapsing high density core. The grey vertical line shows the initial radius of the cloud.

is 99 $M_\odot$ and initial radius is 0.985 pc. The thermal energy evolution is controlled, on the one hand, by the net thermal energy exchange Γ_{net}, which provides a weak heating effect at least at the beginning of the evolution (when $T_g = 60\,K$, $T_d = 10\,K$ and $0 < n_i = 500 < 700$ cm^{-3}, $\Gamma_{net} > 0$) and on the other hand by the work done by the gas expanding into the surrounding volume through evaporation which reduces the internal energy of the system.

In the early moments of the cloud's evolution at $t = 0.26$ Myr, as shown in Figure 6.7, an inward motion (with a maximum inward velocity of 0.04 km s^{-1}) appears in the interior together with an outer layer evaporating with a speed of > 18 km s^{-1} (not shown in the figure). The density profile in the interior has not yet changed except for a drop at the boundary due to the outward expansion. The temperature inside the cloud is still around the initial 60K meaning that an almost balanced thermal energy budget is still maintained. However in the outer layer the gas does work as its volume expands quickly outwards by converting its internal energy. As the heating effect from Γ_{net} is not sufficient to compensate for this energy loss a temperature drop results at the boundary layer which can be seen in the top left panel of Figure 6.8.

When $t = 1.03$ Myr, as shown in the top-right panel of Figure 6.7, the inward velocity in the central region of the cloud falls as the density increases toward the centre. The outer layer continues to expand so that its density decreases with radius. With a density distribution profile as shown in the top-right panel, the net thermal energy exchange function Γ_{net} exhibits different heating or cooling effects at different radial distances, in a qualitatively consistent way with what is described by Equation (6.3), although the density points for the transitions are different from the values given by the equation. At least it could be expected that

i) There should exist a point of r_m with a density n_m, at which $\Gamma_{net} > 0$ shows a maximum net heating effect which would increase the internal energy, and therefore the temperature of this region, after compensating for the work done by expanding outwards;

ii) In a higher density region such as in the central part of the cloud, Γ_{net} is negative, therefore its role is to cool the gas and the local temperature should decrease from the initial of 60K.

The temperature profile in the top-right panel of Figure 6.8 exactly presents what is expected above, a qualitatively consistent temperature variation over $n(r)$ with Equation (6.3). The peak temperature of around 80K appears at a radius of $r_m \sim 1.7$ pc with $n_m \sim 100$ cm^{-3}, determined by the density and gas/dust temperature evolution

of this region in the cloud. The temperature decreases slightly toward the centre due to a noticeable increase in the central density.

The further evolution of the cloud is presented in the four subsequent panels in Figure 6.7. The density in the central region continues to increase and at $t = 2.60$ Myr $n_{\mathrm{C}} > 10^{12}$ cm^{-3} which leads to an increased cooling effect of Γ_{net}. Consequently the central temperature keeps decreasing, down to a few degrees Kelvin as may be seen in the final panel. In the expanding outer layer the gas temperature (T_{g}) keeps rising which makes the n_{m} decrease, because $n_{\mathrm{m}} \propto T_g^{-1/2}(T_g - T_d)^{-1}$ which is derived from Equation (6.2). Consequently the corresponding radial distance r_{m} keeps moving outward. While a seed of protostar forms in the cooled centre at $t = 2.6$ Myr, the maximum temperature in the outer later of the cloud rises to 450 K at $r_m \sim 2.25$pc. It may be seen from Figure 6.11 that the fractional abundance of the C$^+$ species decreases by 5 orders of magnitude from its starting value (10^{-5}) with decreasing temperature towards the centre of the cloud and increases by one order of magnitude in the outer layers. The abundance remains sensibly constant at radii $\gtrsim 1.5$pc for the remainder of the cloud's evolution, there being little correlation to the gas temperature which reaches 450K at ≈ 2.2pc as the collapsing point is reached. The fractional abundance of the CO species rises slightly close to the origin as the temperature falls, at 2.28 Myr the fall is close to two orders of magnitude. From this time to the collapsing point in the expanding outer layers there is a temperature peak of approximately 150K at a radius of $\gtrsim 2.2$pc, at which point a minimum in the CO species abundance may be identified. At greater radii the temperature fall to 120K and the CO species abundance increases by a factor of 2. These effects may be considered in conjunction with Figure 3.2 where it can be seen that C$^+$ cooling is less effective by some 4 orders of magnitude at lower densities and CO cooling is at a peak at densities at 10^{-4} and declines at greater and lower densities.

6.5.4 Comparison with Cloud Type 4 in Model A

Different evolutionary features can be found by comparing the simulation results for Cloud Type 4 in Model B with those in the Model A simulations, examination shows two features of note. Firstly, the outer layer of Cloud Type 4 in Model B keeps expanding with high thermal energy through the net heating effect of Γ_{net}, the gravitational field of the core not being strong enough to reverse the expansion of the outer gas layers. As a result in Model B the cloud's mass and radius monotonically decrease with time as shown in Figure 6.9 and the rate of change of mass ($\frac{dM}{dt}$) shown in Figure 6.10 describes a quick decrease then tends to zero at about $t = 2.5$ Myr. This is unlike the 'two-phase' evolution effect seen in the Model A simulations as shown in Figure

6.4 where the rate of change of mass in Cloud Type 4 exhibits a positive peak after reaching a zero, explained by the gravitational pull of the expanding gas in the outer layer of the cloud.

Secondly, it is also observed that the time to collapse of the centre of Cloud Type 4 is shorter in the Model B simulations than that found in the Model A simulations. This may be explained by the cooling effect of the gas-dust thermal exchange in the highly condensed central region, This is shown by the green solid line in Figure 6.6, which describes the evolution of the maximum density in Cloud Type 4 in all six models.

6.5.5 Evolutionary Features of Cloud Types 1, 2, 5 and 7 in Model B

The evolutionary features of the physical properties of other four clouds in the Model B simulations do not show qualitatively different behaviour from that observed in Cloud Type 4. The details can be found in the relevant sections of Appendix A.2.

Firstly, the central density in all the clouds increases gradually and forms a highly condensed seed of a protostar. The evolution of the peak density with respect to time in the five clouds of different initial densities follows a very similar pattern to that shown in Figure 6.5 and the time for the maximum density to become greater than 10^7 cm^{-3} decreases with increasing initial density. This is because the initial self-gravitational potential increases with the initial density of a cloud. It may also be seen that the time to collapse (t_{col}) of every cloud in Model B is shorter than that found in the Model A simulations. For example it is 10.49 Myr in Model B and 20.42 Myr in Model A simulations for Cloud Type 1, while for Cloud type 5 it is 0.6 Myr and 0.75 Myr in Model B and Model A simulations. This can be attributed to the cooling effect of Γ_{net} at the high density centre of a cloud in the Model B simulations which helps to condense the gas at the centre, in turn this then speeds up the gravitational collapse of the cloud. The collapsing time in Model B simulations over the initial density can be fitted into a power law, $t_{col} = 118.6 n_i^{-0.62}$ Myr.

Secondly, the outer layer expansion is accelerated by the net thermal heating effect, $\Gamma_{\mathrm{net}} > 0$, at low density compared to that in Model A simulations. At the start of the simulation the initially defined cloud mass and radius decrease with time and subsequently reach a stable value. The percentage mass finally left in the cloud $\left[M(t = t_{col}) / M(t = 0) \right]$ also increases with the initial density.

Thirdly, the evolution of temperature distribution over radial distance in all of the 5 clouds are similar to each other. When a density distribution over radial distance is built up (decreasing with radiation distance), the temperature decreases toward the centre and increases outward, then reaches a maximum at some point in the expanding

outer layer, and then falls further away. This variation pattern of temperature distribution is governed by the thermal function Γ_{net} over the local density distribution, just as described by Equation (6.3). The final structure of the cloud is a very cold high density small core surrounded by a warm envelope. For the same reason, the maximum temperatures in the envelope in the 5 clouds in Model B simulations also show a non-monotonic variation with the initial density of a cloud, these are 590, 1200, 450, 350 and 80K in Cloud types 1, 2, 4, 5 and 7 respectively.

Figure 6.8: Model B: the evolution of the mean temperature distribution with the radial distance in a Cloud Type 4. The grey vertical line shows the initial radius of the cloud.

Figure 6.9: Model B: The evolution of the mass and radius of a Type 3 cloud (initial density of 500 cm^{-3}).

Figure 6.10: Model B: the evolution of the mass change rate of Cloud Type 4.
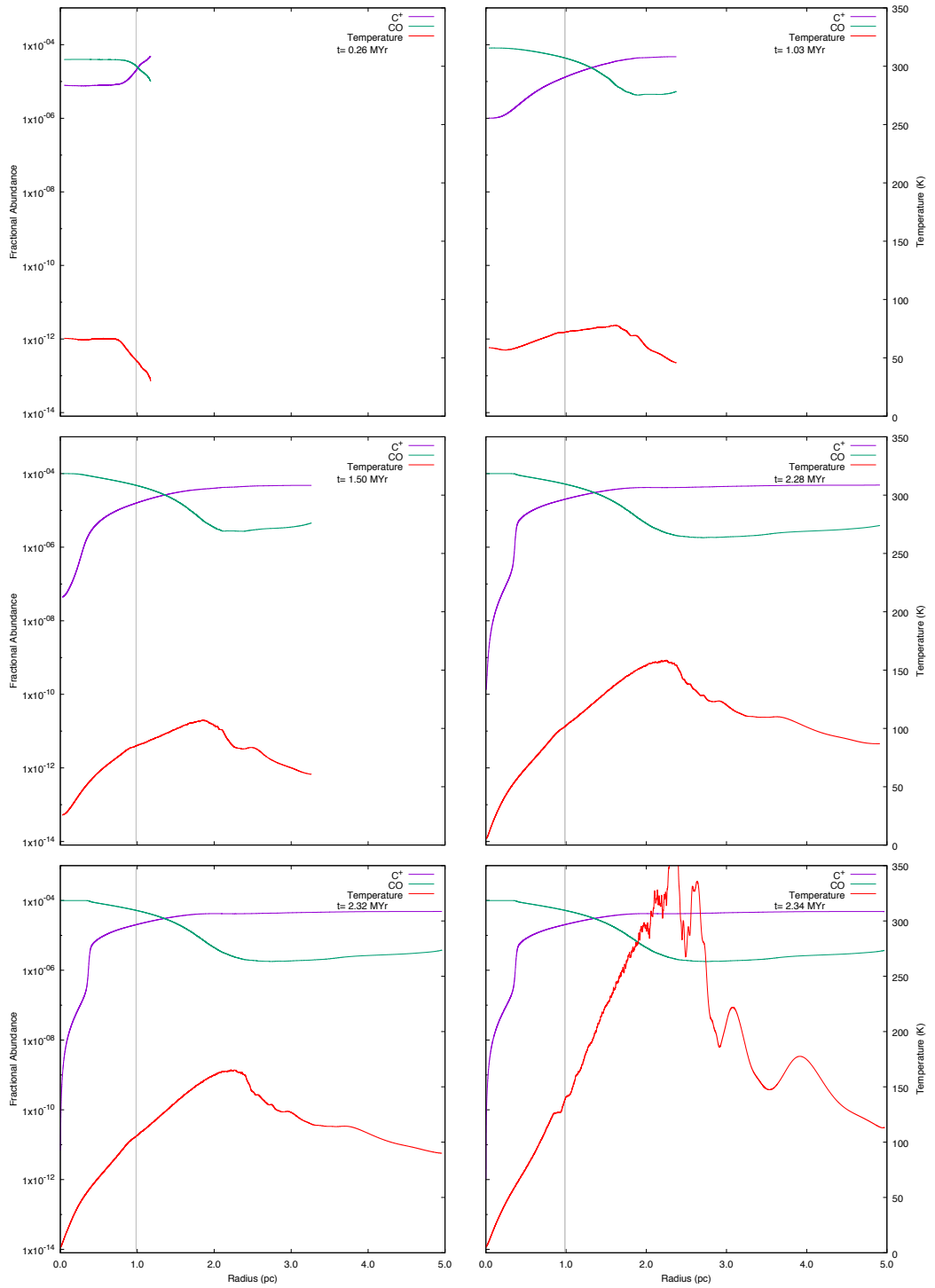
Figure 6.11: Model B: six snapshots showing the chemical abundances of CO and C$^+$ for a cloud with an initial density of 500 cm^{-3}, a mass of 99 M$_\odot$ and a radius of 0.99 pc.

6.6 Model F: Chemistry and Molecular Line Cooling Activated

In this section the net effect of the chemical reactions and associated molecular line cooling on the evolution of molecular clouds of Types 1, 2, 4, 5 and 7 is studied to identify the variations of MJMs, and the associated physical properties, and their dependencies on the initial densities of the clouds. In addition these results are compared to those obtained from the Model A simulations. This set of simulations includes only the effects of the chemical network and molecular line cooling as described in Model F in Table 6.1, the internal gas-dust thermal interchange mechanism is not activated nor are there any external influences due to FUV and cosmic ray radiation. The evolution of each of the chemical species is traced by a numerical solver for a set of differential equations based on the chemical reaction chain of converting C II to CO, see table 3.1. The consequent chemical cooling is contributed by CO, C, C II and O emission lines excited by collisions.

6.6.1 Variation of MJM with n_i

The black circles in Figure 6.1 describe the variation of the MJM with different initial densities, this variation can be fitted into the power law of

$$M_{MJM} = 4.37\, n_i^{-0.23}\, M_\odot.$$

(6.5)

The MJM values are dramatically lower, being two orders of magnitude lower than the corresponding ones in Model A and three orders of magnitude lower than for the Model B simulations. In addition the dependency of the MJMs on the initial density of a cloud is much weaker. The values of the MJMs lie in the range from $1.72 M_\odot$ to $0.65 M_\odot$ corresponding to the initial density range of $n_i = 50\,\mathrm{cm}^{-3}$ to $n_i = 5000\,\mathrm{cm}^{-3}$. The MJMs obtained from this set of simulations performed with this model demonstrate that chemical cooling is an efficient mechanism in helping interstellar gas condense and as a result improves the chances of star formation in a molecular cloud.

6.6.2 Dynamic Evolution of Cloud Type 4

Figures 6.12 and 6.13 describe the evolution of the density, radial velocity and temperature profiles as a function of the radius in a Cloud Type 4 with an initial mass of $1.5 M_\odot$ and radius of 0.244 pc obtained from this model.
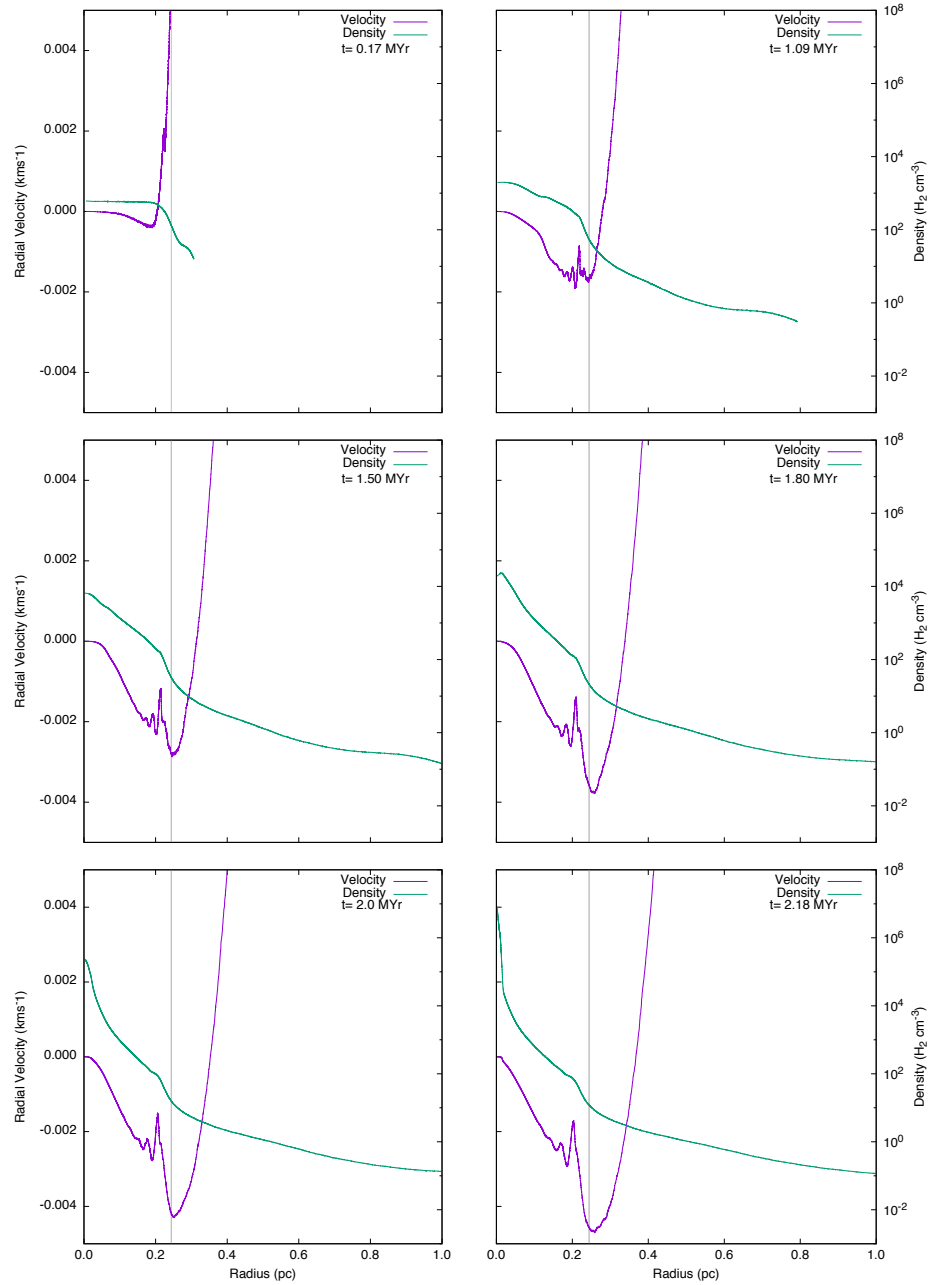
Figure 6.12: Model F: the evolution of the mean density and mean radial velocity distribution with radius r in a Cloud Type 4. The velocity scale is expanded in order to show the collapsing high density core in more detail. The grey vertical line shows the initial radius of the cloud.
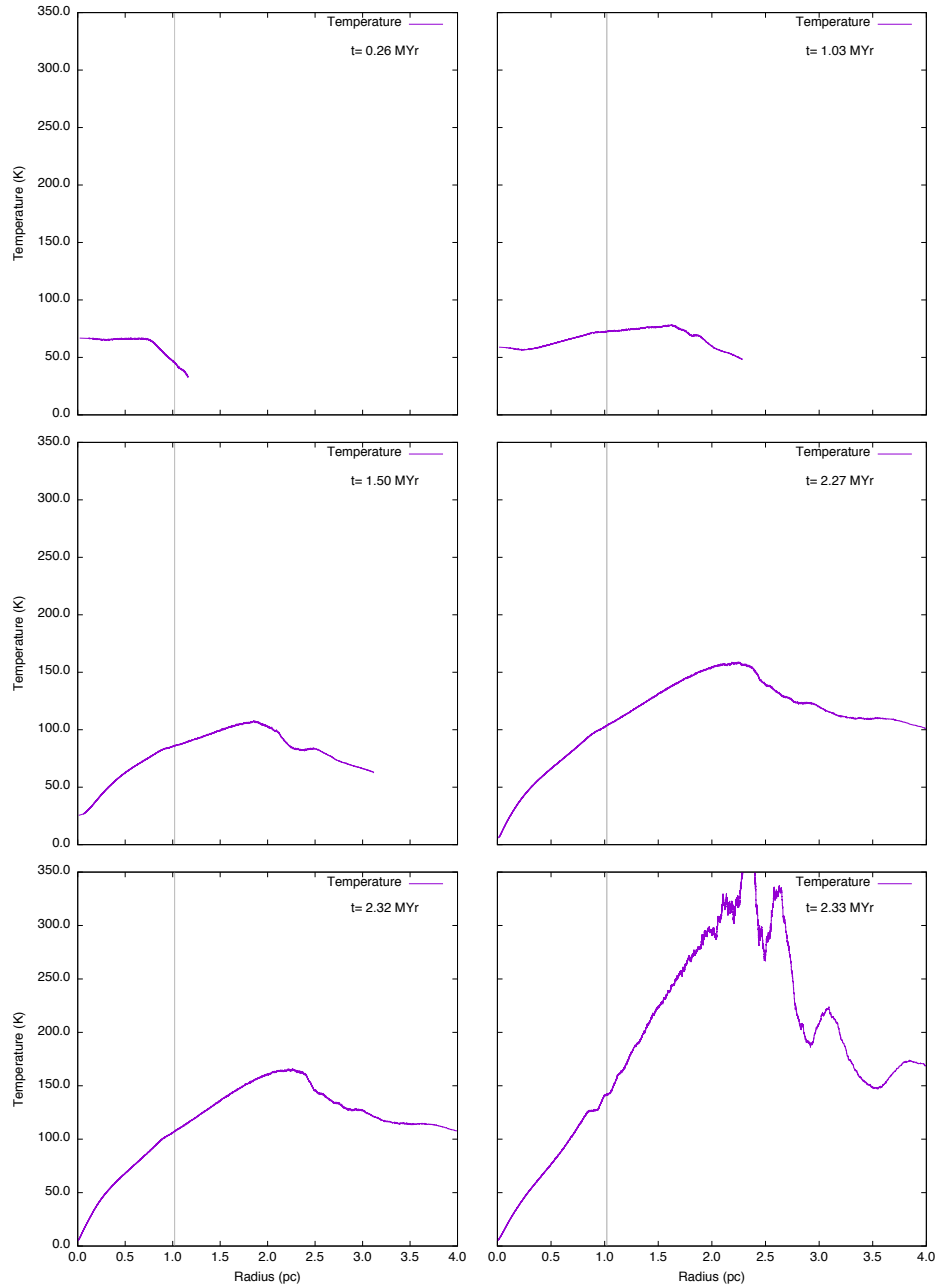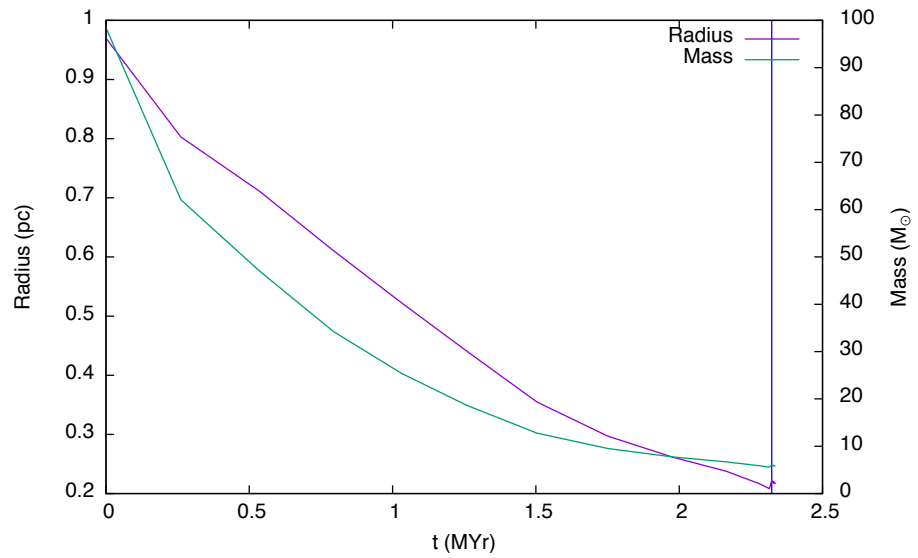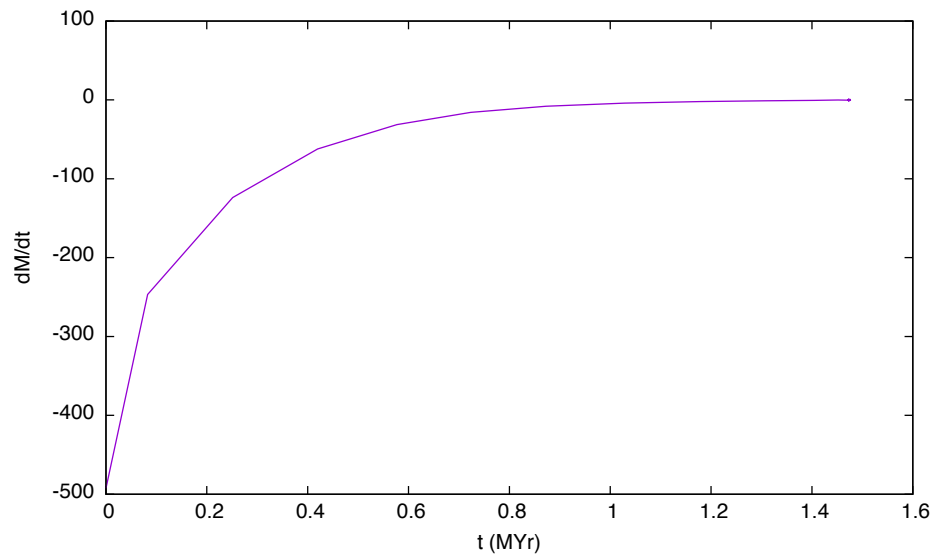
Figure 6.13: Model F: The evolution of the mean temperature distribution with radius r in a Cloud Type 4. The grey vertical line shows the initial radius of the cloud.
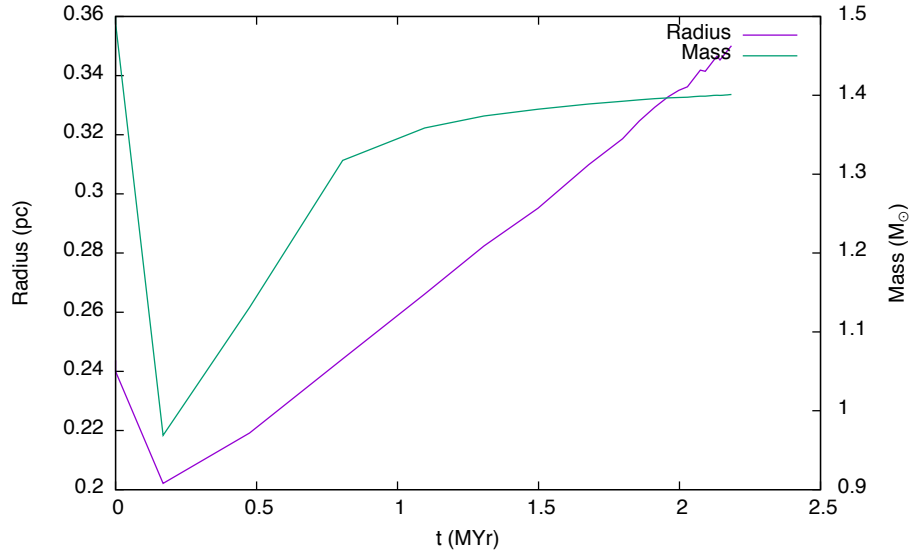
Figure 6.14: Model F: the evolution of the mass and radius of a Cloud Type 4.

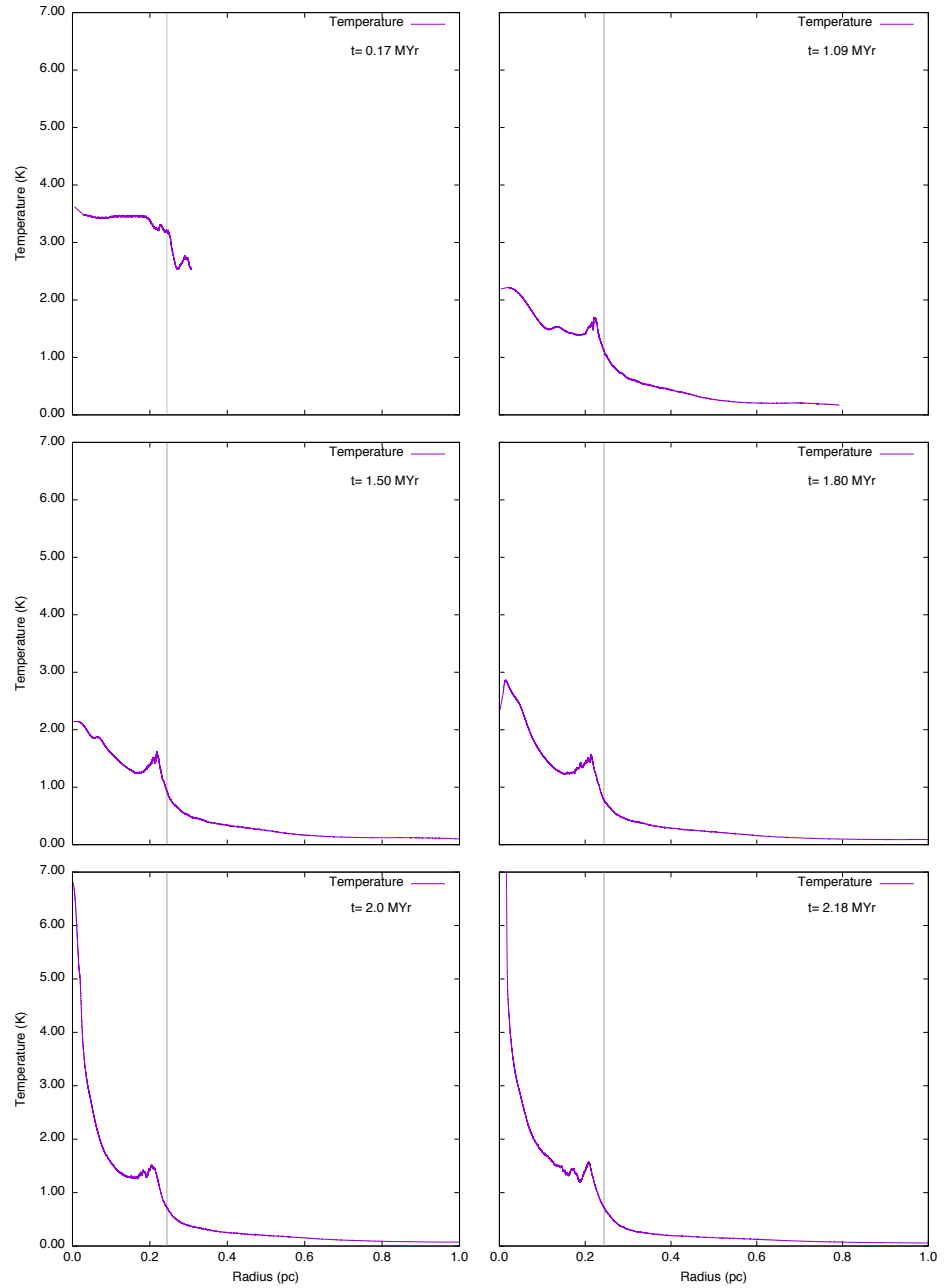During the first 0.17 Myr, the central region of the cloud exhibits an almost uniform density together with an expanding outer layer in which the density gradually decreases with increasing radius. The velocity distribution shows a slow inward motion at the edge of the central region of the cloud, further out the velocity vector is more strongly away from the centre. The evolution of the internal energy of the system, which can be inferred from the temperature since $\frac{dU}{dt} \propto \frac{dT}{dt}$, is governed by the system work rate function and the chemical cooling rate which can be expressed as $\Gamma'_{net} = -\frac{P}{\rho}\nabla \cdot \nu - \frac{\Lambda}{\rho}$. At an initial temperature of 60K, the chemical cooling term is dominated by the CO line emission and is about 10 times stronger than that at temperature of 10K (Nelson and Langer, 1997), while the work rate function term is much lower than the cooling term during the same period of time because of the lower value of $\nabla \cdot \nu$, meaning that $\Gamma'_{net} < 0$. Therefore the temperature of the cloud quickly drops from 60K to 3.5K in the major central part of the cloud as shown in the top left panel of Figure 6.13. When the molecular cloud gets cooled so dramatically, the inward motion of the particles is accelerated under the influence of the increasing self-gravity of the cloud.

From the subsequent panels in Figure 6.12, an accelerated inward motion can be seen which results in condensed core with continually increasing density, the simulation stops at $t = 2.18$ Myr when the central density $> 10^7$ cm^{-3}, at this point the maximum inward velocity reached >3 ms^{-1}. During the same time period the temperature profile in Figure 6.13 shows that the temperature at the centre decreases further to 2.15K at $t = 1.5$ Myr due to the dominant cooling effect. However the temperature in the central core then increases to 2.9K at $t = 1.8$ Myr, and continues to increase to 7K at $t = 2.18$Myr. This slightly raised central temperature is the result of the competition

between the work rate function and the chemical cooling term involved in the internal energy evolution. This phenomena can be qualitatively understood in that after $t > 1.5$ Myr the central density is $n > 10^4$ cm^{-3} and the central temperature is so low, 2.15K, that the cooling term is dominated by C II line emission. This decreases in strength with local density and increases when the local density $n > 10^4$ cm^{-3}, see Table 3.1. On the other hand, a steep inward radial velocity gradient has built up in the central region after $t > 1.5$ Myr, which makes the work rate function term $-\frac{P}{\rho}\nabla \cdot \nu$ a positive value and whose order of magnitude is slightly larger than that of the cooling term in the same region given by $\Gamma'_{\text{net}} > 0$. Therefore the temperature in the central region of the cloud increases. The higher the central density the lower the chemical cooling rate which results in a higher central temperature, this rising to 7K at $t = 2.18$Myr.

Considering the outer layer, the expansion velocity increases with radial distance $(\nabla \cdot \nu > 0)$, which makes the work rate function term a negative value as $\Gamma'_{\text{net}} < 0$. Therefore the temperature in the low density outer layer keeps decreasing to almost zero. Although the temperature at the centre is slightly increased to a few Kelvin as discussed above, the thermal pressure gradient is not high enough to compensate for the self-gravity which continuously pulls gas toward the centre, where a seed of a protostar forms.

Figure 6.14 presents the evolution of the mass and radius of the same Cloud Type 4 which starts, as mentioned above, with an initial mass of 1.5 M$_\odot$ and a radius of 0.244 pc. During the first 0.17 Myr the radius of the cloud decreases to 0.205 pc, the mass decreases to 0.97 M$_\odot$ due to the loss of particles to the expanding outer layer and the central region of the cloud is cooled by the dominant chemical cooling mechanism. After $t > 0.17$ Myr the cloud becomes very cold, with a temperature of a few Kelvin, and the self-gravity of the cloud starts to influence the evolution by attracting back the particles in the previously expanded low density outer layer. The mass shows a rapid increase to 1.35 M$_\odot$ at $t = 0.8$ Myr while the radius also increases nearly linearly as well. The radius of the cloud continues to increase at a constant rate after $t = 0.8$ Myr but after this time the rate of increase of the cloud's mass falls. This is because the outer layer has a very low density so any reduction in its radius does not contribute much mass. The mass and radius increase to 1.4 M$_\odot$ and 0.35 pc respectively at $t = 2.18$ Myr at which point the simulation stops.

It may be seen from Figure 6.15 that the development of the fractional abundance of the chemical species C$^+$ and CO follows a similar pattern to that seen in Model B although the values are slightly different and distinct changes of gradient exist in the plots at the original cloud radius which remain throughout the evolution. The fractional abundance of C$^+$ decreases in the low temperature region towards the centre of the

cloud and increases at radii greater than the original radius although the maximum value remains close to that set originally. The fractional abundance of the CO at the origin increases at each time step, over the complete evolution by approximately one order of magnitude, as the temperature increases from very low values. From the origin out to the initial cloud radius of $\gtrsim 0.24$pc the species tracks the falling temperature. For values of the radius $\gtrsim 0.24$pc the fractional abundance of CO then increases for increasing values of the radius in the low temperature and density regions predicted in this Model.

6.6.3 COMPARISON BETWEEN MODEL A AND MODEL F SIMULATIONS

Modelling the effects of the different activated internal and externally imposed influences on a Cloud Type 4 with the same initial conditions it may be seen that the evolution of the cloud during the first 0.17 Myr is very similar regardless of whether it is exposed to Model F or Model A influences. In both cases the central region has not yet been significantly affected with the particle density remaining close to the initial value of $n_i = 500$ cm^{-3}; an initial inward motion is just starting and the outer layer also starts expanding. After $t = 0.17$ Myr in Model F the cloud is noticeably cooler and almost the whole cloud starts moving inwards as shown in the top-right panel of Figure 6.12. In comparison after the same time only the very central part, that lying within a third of the initial radius, of the Cloud Type 4 in the Model A simulations starts moving inwards. As a result a Cloud Type 4 in the Model F simulations takes much less time to form a potential seed of a protostar than that with Model A. This may be seen in Figure 6.6.

On the other hand, at same initial density and temperature, the MJM is two orders of magnitude lower in Model F than in Model A simulations. The big difference in the two MJMs, 158 M$_\odot$ in Model A and 1.5 M$_\odot$ in Model F emphasises the importance of including chemical cooling in models of molecular evolution and star formation.

6.6.4 THE GENERAL EVOLUTIONARY FEATURES OF MODEL F SIMULATION

As shown in Figures A.85 - A.99 in Appendix A, the evolution of the density, velocity, and temperature distributions in Cloud types 1, 2, 5 and 7 qualitatively follow similar routines to the Cloud Type 4 described above. The chemical cooling at the initial temperature of 60K is most efficient in Cloud Type 7 with an initial density of $n_i = 5000$ cm^{-3} (Nelson and Langer, 1997) and least efficient in Cloud Type 1 with an

initial density of $n_i = 50$ cm^{-3}. As a consequence, Cloud type 7 takes only 0.06 Myr to be cooled to 4K but a Cloud Type 1 requires about 1.5 Myr. All the five clouds are able to collapse to form a seed of a protostar, but it should be noted they all have a slightly warm central volume with a temperature of $T_c < 20$K due to the decreased cooling effect of C II line emission at high densities and low temperature in the later stage of the clouds' evolution (Nelson and Langer, 1997).

The time to the formation of a seed of a protostar, that is the time to collapse (t_{col}), is therefore closely related to the efficiency of the cooling, which in turn is dependent on the initial particle density. This time can be given by the power law of the form

$$t_{col} = 175 n_i^{-0.16} \text{Myr} \tag{6.6}$$

and is 19.28 Myr for Cloud Type 1 and 1.41 Myr for Cloud type 5.

Due to the efficiency of molecular line cooling, the temperature of the central region of the clouds shown in the simulations performed with this model drops very quickly which in turn decreases the thermal pressure inside the clouds. This has the result that 90% of clouds' initial mass is attracted towards the centre by the dominant self-gravity after which the central seed of a protostar forms.
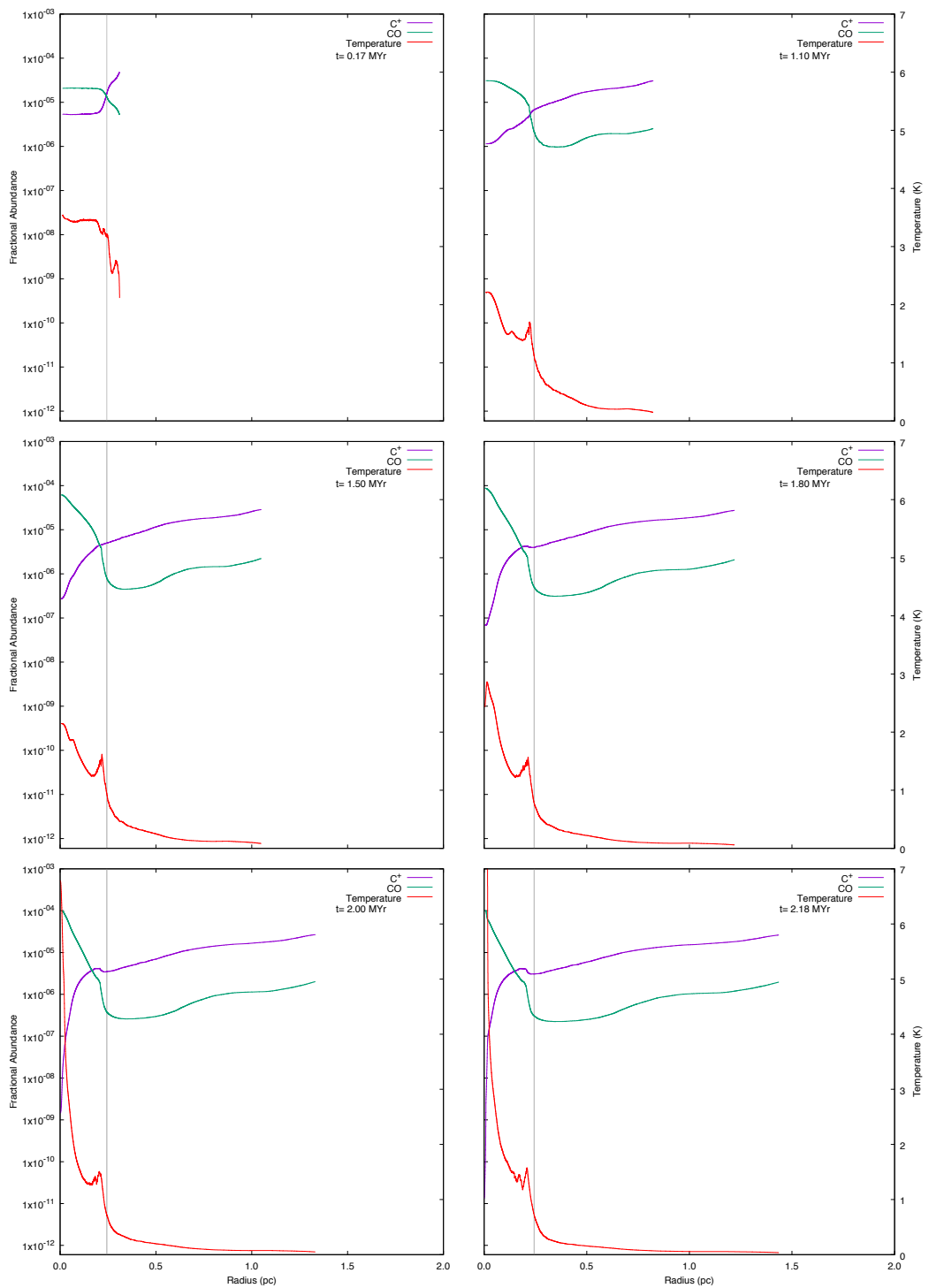
Figure 6.15: Model F: six snapshots showing the chemical abundances of CO and C^+ for a cloud with an initial density of 500 cm^{-3}, a mass of 1.5 M$_\odot$ and a radius of 0.24 pc.

6.7 Model C: Chemical Cooling and Cosmic-ray Heating Activated

The Model F simulation results demonstrate the importance of including molecular line cooling in modelling gas clouds. The next step is to to study to what extent cosmic-ray heating offsets the influence of chemical cooling in the evolution of a molecular cloud by adding the background cosmic-ray heating to the Model F simulations. These are the Model C simulations as listed in Table 6.1. Clouds of the same five initial densities as previously described are used.

6.7.1 Variation of MJM with n_i

The blue star symbols in Figure 6.1 present the MJMs found from the Model C simulations. Inspection shows that over the whole range of the initial cloud densities cosmic ray heating has partially offset the chemical cooling effect as can be seen from the MJMs in the Model C simulations which are, on average, 6.22 $M_\odot$ higher than those found in the Model F simulations. The values of the MJMs derived from Model C decrease from 14 $M_\odot$ to 1.8 $M_\odot$ when the density increases from 50 cm^{-3} to 5000 cm^{-3}. It should also be noted that the MJMs in the simulations performed with this model are still, on average, 209 times lower than those calculated in the Group A simulations. It may be deduced that the role of cosmic ray heating is limited and chemical cooling is still the dominant factor in the thermal evolution of molecular clouds in an interstellar medium. The variation of MJMs with n_i found with this model may be fitted into a power law of the form

$$\mathrm{M}_{MJM} = 45.86\, n_i^{-0.33} \mathrm{M}_\odot. \tag{6.7}$$

6.7.2 The Evolution of Cloud Type 4

Again, for simplicity and ease of understanding, the evolution of physical properties of a Cloud Type 4 under Model C conditions are described and compared with those found in the Model F simulations. The results for clouds of other initial densities are discussed in Section 6.7.3.

Figures 6.16 and 6.17 show a series of snapshots of n, v and T taken during the evolution of a Cloud Type 4 with an initial mass of 5 $M_\odot$ and radius of 0.364 pc.

In Figure 6.18 it can be seen that in the first 0.23 Myr, the outer layer of the

cloud starts to expand, therefore the cloud mass and radius both decrease with time as shown although the physical properties of the inner part of the cloud have not changed significantly. At the initial temperature of 60K and the initial particle density of $n_i = 500$ cm^{-3} chemical cooling dominates over cosmic ray heating, so the temperature of the cloud drops from 60K to about 7 - 10K, which is about 3K higher than that found in Cloud Type 4 after a similar time in the Model F simulations. This temperature increase may be explained by the inclusion of cosmic ray heating.

After the whole cloud has been cooled by the predominant chemical cooling effect, cosmic ray heating becomes more significant than chemical cooling in the outer layers where both density and temperature are low (Nelson and Langer, 1997). As a consequence after $t = 1.07$ Myr the temperature in the outer layers rises to 50K as shown in the top-right panel of Figure 6.17. Then a steep pressure gradient is built up at the interface between the cool central region and the expanding warm outer layer which creates a maximum inward velocity of about 25 ms^{-1} at the interface as shown in the top-right panel of Figure 6.16. The gas is then pushed toward the centre, where the density increases to a few 10^3 cm^{-3}. In the centre, with the temperature lower than 7K and the density lying between $n = 10^2 - 10^3$ cm^{-3}, the chemical cooling is almost balanced by the cosmic ray heating (as can be seen in the top-left panel of Figure 1 of Nelson and Langer (1997)). Although the work rate function of the collapsing atmosphere contributes to heating in the central regions, it is at least two orders of magnitude lower then both the cosmic ray heating and the chemical cooling rates and so does not make an observable change in the temperature in the centre, which remains at about 7K.

As the gas density in the warm outer layer between 0.5 and 1.0 pc from the centre further decreases to $n < 10$ cm^{-3} the chemical cooling become less efficient than the cosmic ray heating as shown in the bottom-right panel of Figure 1 in Nelson and Langer (1997). Therefore the temperature reaches about 100K at $t = 1.89$ Myr and the maximum inward particle velocity at a radial distance of 0.6 pc increases to 60 ms^{-1} as shown in the bottom-left panels of Figures 6.17 and 6.16. The latter also shows that the central density increases to $n = 10^4$ cm^{-3}.

The bottom right panels in Figures 6.16 and 6.17 show that at $t = 2.63$ Myr the maximum density in the central core of radius of 0.06 pc increases to $n = 10^7$ cm^{-3} while the maximum temperature in the warm expanding outer layer reaches 170K. At this higher density and low temperature of about 7K, the cosmic ray heating rate is slightly more efficient than the chemical cooling, so a small temperature spike, up to 20K, appears at the central point. In the spherical shell between 0.06 - 0.35 pc where the density is $10^3 < n < 10^4$ cm^{-3} the cosmic ray heating and chemical cooling rates

are almost equally efficient with the result that the temperature in this narrow range remains unchanged. At the final stage of the evolution, the inward radial velocity gradually decreases because of the high density static core in the centre so the inward motion of the particles to the centre is slowed down.

The Cloud Type 4 exposed to the conditions of this model evolves into a structure consisting of a cool and high density core surrounded by a warm envelope, while in the Model F simulations, Cloud Type 4 ends with a high density but slightly warm core which is embedded in a cool and very low density medium.

Figure 6.18 reveals that after an initial decrease in both mass and radius during the first 0.23 Myr of the evolution, the mass included in the cloud gradually increases up to $t = 0.8$ Myr, as does the radius. The density outside the radial distance of 0.95 pc is very low afterward, so the cloud mass does not change significantly with an increasing radius. The apparent dip in mass and radius at $t = 2.3$ Myr show the cloud is at a critically stable state, it undergoes expansion and contraction oscillations with small a amplitude around the stable state. This does not affect the formation of a very small seed of a protostar in the centre of the cloud. The evolution of the cloud mass and radius in Cloud Type 4 exposed to Model F conditions follows a similar routine to that described above.

The evolutionary time for Cloud Type 4 to develop a high density and cool seed of a protostar under Model C conditions takes 2.63 Myr, which is 0.45 Myr longer than in the Model F simulations due to the added cosmic ray heating effect, and 0.5 Myr less than that found in the Model A simulations. This effect can be explained by the inclusion of the chemical cooling effect which is dominant in most regions of the dense core in the cloud being counterbalanced to some extent by the effect of cosmic ray heating.

With regard to the fractional abundancies of the chemical species C^+ and CO it may be seen from Figure 6.19 that their development follows a similar pattern to those seen in Models B and F although, again, the values are slightly different. The distinct changes of gradient which exist in the plots at the original cloud radius, the same effect seen in Model F, remain throughout the evolution. The fractional abundance of C^+ decreases in the low temperature region towards the centre of the cloud and increases at radii greater than the original radius. The CO species does the reverse, the fractional abundance increases at the centre, falls to the original radius (0.36 pc), then recovers slightly. At a radius of $\gtrsim 0.5$ pc there is a temperature peak and although the temperature declines at greater radii the fractional abundances of both species remain at almost constant levels, and close to the start values, for the rest of the evolution.

6.7.3 The General Evolutionary Features

The detailed evolution of physical properties derived from simulations of Cloud types 1, 2, 5 and 7 under Model C conditions can be found in Figures A.21-32 but no qualitatively different features can be seen from the plots. The qualitative difference in the evolution of the physical properties can be summarised. Initially the time for the formation of a seed for a protostar decreases with initial density due to the increasing initial gravitational potential per unit mass with increasing density. The collapsing time (t_{col}) can be fitted into a power law of the form $t_{col} = 29.65 n_i^{-0.4}$ Myr. For Cloud Types 1 and 7 this is 6.20 and 0.98 Myr respectively.

The thermal evolution of all the clouds starts with an initial cooling stage, because the chemical cooling dominates over the cosmic ray heating in the initial density range of $n_i = 50$ - 5000 cm^{-3} at the initial temperature of 60K. Afterward, the expanding low density outer layer is heated by cosmic ray heating which is more effective under these conditions than the molecular line cooling. The temperature in the warm expanding outer layer consequently decreases with the initial density, due to the sensitivity of the chemical cooling to the local temperature and density, so that the significance of cosmic ray heating in the evolution of a cloud also changes with the local physical conditions. The maximum temperatures are calculated to be 450K, 375K, 170K, 78K and 42K for Cloud types 1, 2, 4, 5 and 7 respectively.

The steep pressure gradient built up between the cool core and warm expanding outer layer in each of the clouds initiates an inward motion of the gas inside the cloud with its velocity decreasing with density, which is attributed to the maximum temperature decreasing with the initial density as explained above. The maximum velocities calculated are is 150, 100, 60, 40 and 10 ms^{-1} for Cloud types 1, 2, 4, 5 and 7 respectively.
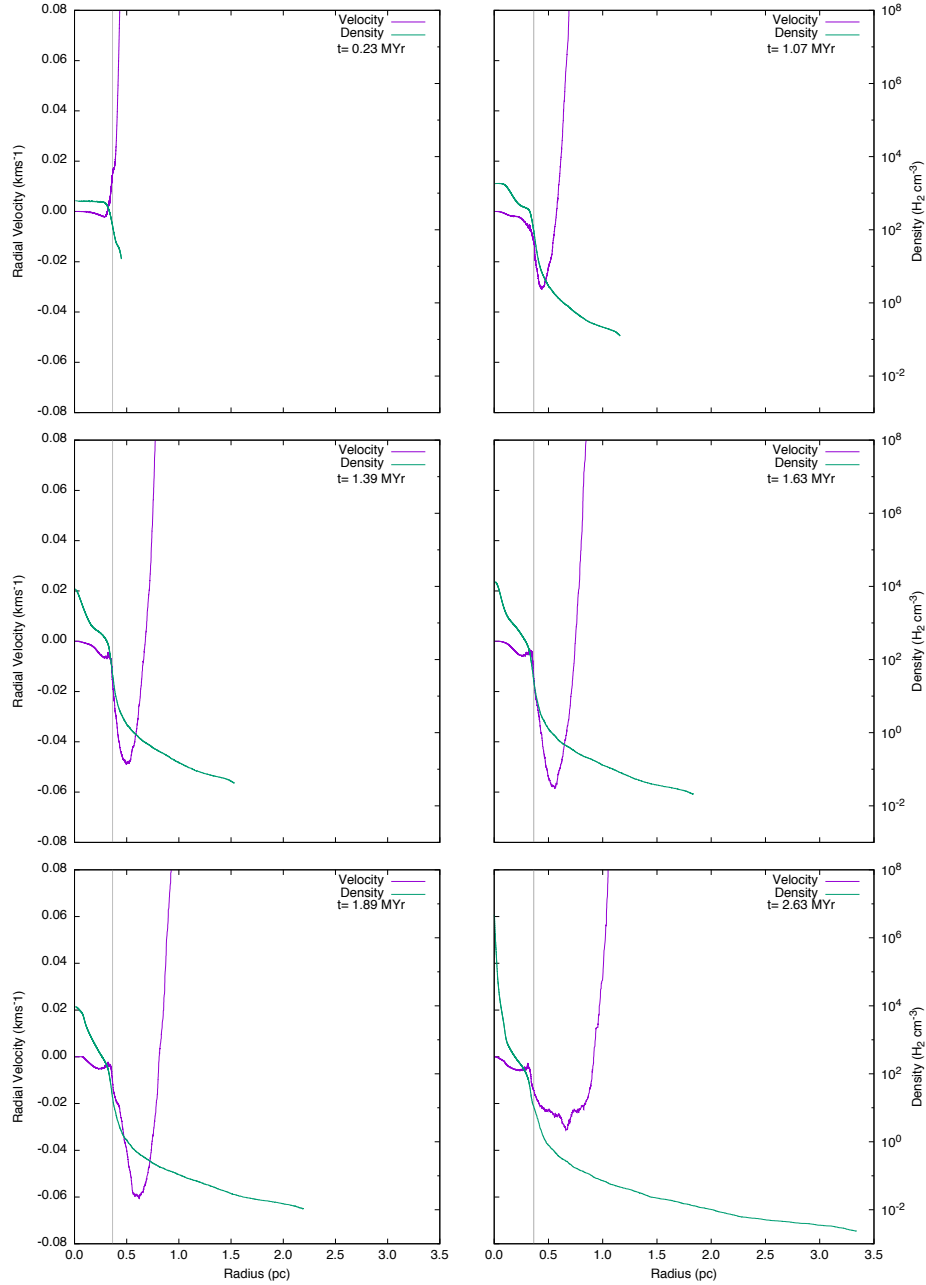
Figure 6.16: Model C: the evolution of the mean density and mean radial velocity distribution with radius r in Cloud Type 4. The velocity scale is expanded in order to show the collapsing high density core in more detail. The grey vertical line shows the initial radius of the cloud.
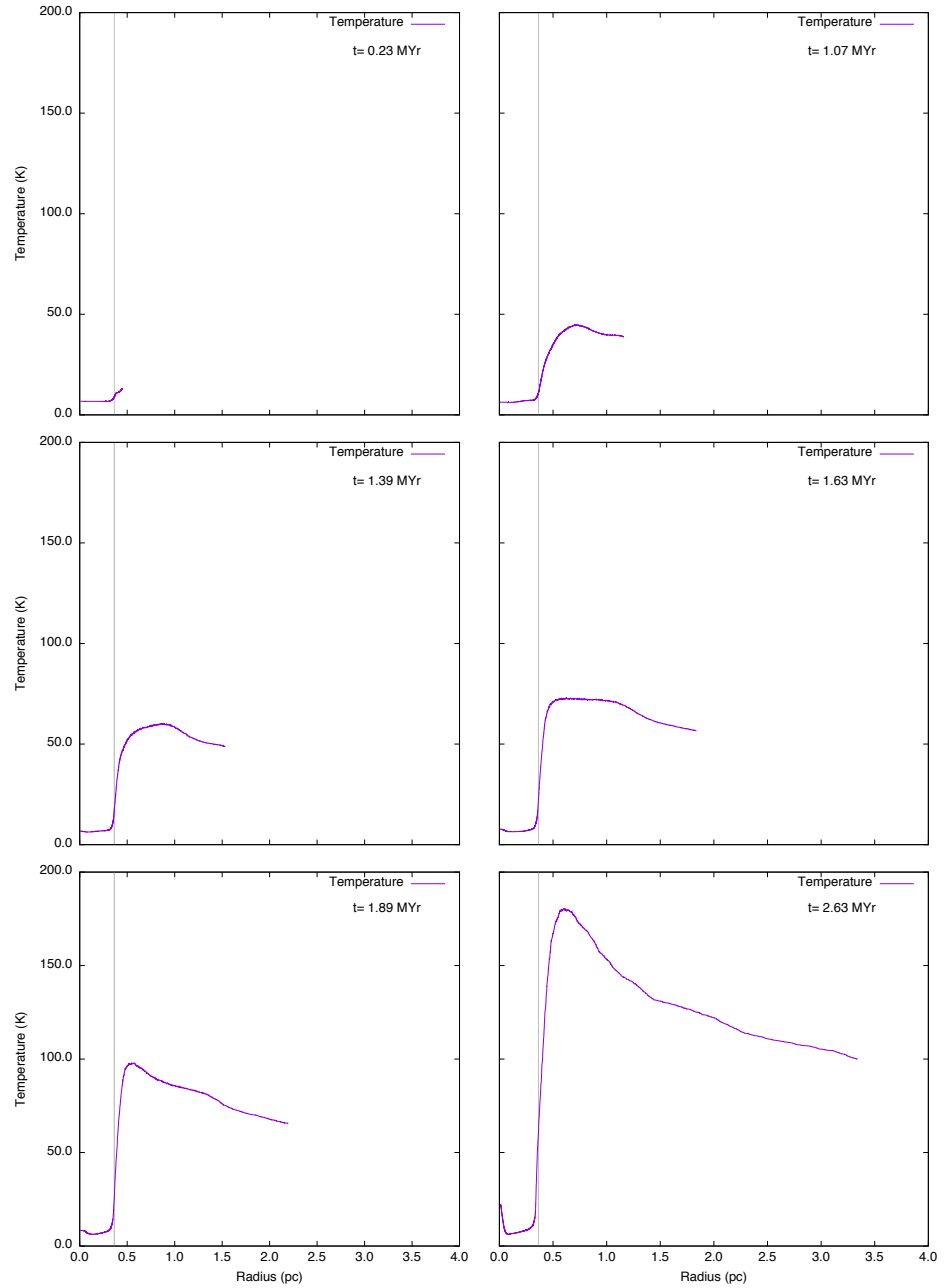
Figure 6.17: Model C: the evolution of the mean temperature distribution with radius r in Cloud Type 4. The grey vertical line shows the initial radius of the cloud.
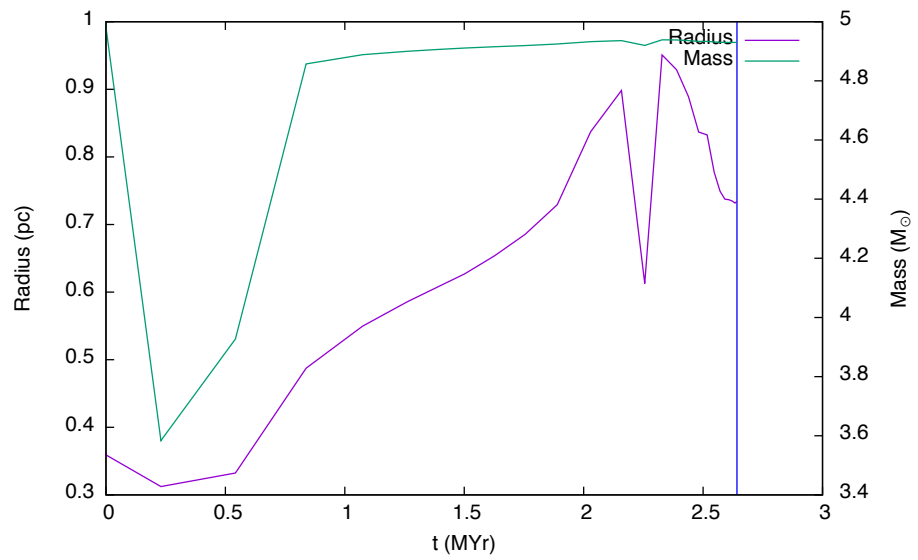
Figure 6.18: Model C: the evolution of the mass and radius of Cloud Type 4.
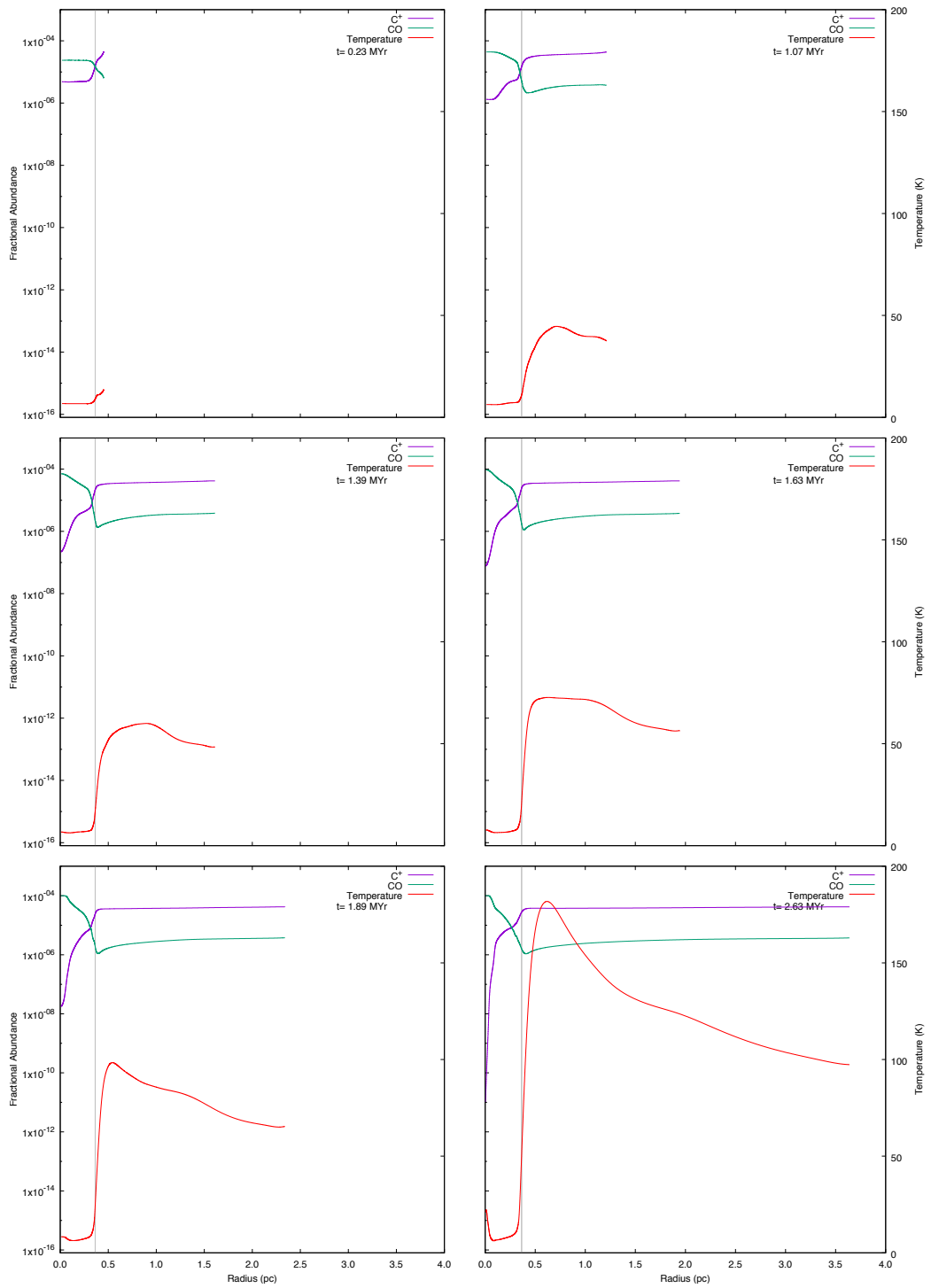
Figure 6.19: Model C: six snapshots showing the chemical abundances of CO and C^+ for a cloud with an initial density of 500 cm^{-3}, a mass of 5 M$_\odot$ and a radius of 0.36 pc.

6.8 Model D: Chemical Cooling and Gas-dust Thermal Exchange Activated

From the analysis of the simulation results presented in Section 6.7 it has been demonstrated that cosmic ray heating could offset a small fraction of the chemical cooling effect and in so doing increase the MJMs by a factor of 5.4 compared to those determined in the Model F simulations. The next step of the investigation is to determine whether the physical process of gas-dust thermal exchange would play a similar role to cosmic ray heating in the evolution of the same clouds. This model, Model D, therefore contains both chemical cooling and the gas-dust thermal exchange, as described in Table 6.1. Both external influences, FUV and cosmic ray, are inactive.

In this Section the evolution of physical properties of a Cloud Type 4 under Model D conditions are described and compared with those found in the Model F simulations.

6.8.1 Variation of MJM with n_i

The unfilled orange square symbols in Figure 6.1 show that the MJMs found for a cloud exposed to the conditions of this model are all higher than those found in the Model F simulations but by, on average, only 0.98 $M_\odot$. In contrast the MJMs were 4.84 $M_\odot$ lower than those found in the Model C simulations. It would appear therefore that gas-dust thermal exchange plays a similar role to that played by cosmic ray heating, the gas being heated by the transference of thermal energy from dust grains to the gas, although its effect is weaker than that of cosmic ray heating. The MJM decreases with increasing initial density and is 3 $M_\odot$ at $n_i = 50$ cm^{-3} and 0.8 $M_\odot$ at $n_i = 5000$ cm^{-3}. The relationship of the MJM with n_i can be described by a power law of the form

$$\mathrm{M}_{MJM} = 7.69\, n_i^{-0.23} \mathrm{M}_\odot. \tag{6.8}$$

6.8.2 Evolution of Cloud Type 4

It is known that gas-dust interactions only play an important role when the local density is higher than 10^5 cm^{-3} as noted in Section 3.3.5. This is confirmed by the fact that the mean difference in the MJMs in the Models D and F simulations is only 0.98 $M_\odot$. Therefore it would not be expected that the dynamic evolution of Cloud Type 4 exposed to the conditions of this model is significantly different from that described in the Model F simulations. Therefore it is only necessary to summarise the aspects that

are different in the evolution of the physical properties to avoid unnecessary repetition.

For this model, the Cloud Type 4 has a mass of 3 $M_\odot$ and radius of 0.307 pc and the evolution of the physical properties of the cloud are presented in Figures 6.20, 6.21 and 6.22. These plots are all very similar to those in the Model F simulations.

At an initial density of $n_i = 500$ cm^{-3} and an initial temperature of 60K, the gas-dust interaction in principle cools the cloud although its value is one order of magnitude lower than that of chemical cooling. Therefore the density, velocity and temperature distributions as functions of the radius are almost same as those found in Model F. Only when $t > 1.41$ Myr and the central density n is greater than 10^5 cm^{-3} does a difference appear as the gas-dust interaction starts to play a noticeable role. The temperature of the central region then rises from 3.2K at $t = 1.22$ Myr to 4.3K, due to the gas-dust heating effect ($T_{\mathrm{gas}}(\sim 3.2K) < T_{\mathrm{dust}}(\sim 10K)$). This is about 2K higher than the same cloud in the Model F simulations. Subsequently the central temperature reaches 5.5K at $t = 1.80$ Myr, while Model F reached 2.9K after the same time. Because the central density in Cloud Type 4 in this Model D simulation is almost $n = 10^8$ cm^{-3} further changes are extremely small, so that a direct comparison with Model F is not possible.

The small change in the temperature of the central region does not cause any discernible change in the evolution of mass and radius. The shorter high density core formation time in Model D, 1.8 Myr compared to 2.18 Myr in Model F, is due to the gas-dust cooling effect in the initial stage of evolution in Model D. The higher MJM in Model D required for Cloud Type 4 to collapse to form a protostar seed, may be attributed to the gas-dust heating being more effective in the later stages of the evolution of the cloud.

The changes in the fractional abundancies of the chemical species C$^+$ and CO follow a similar pattern to those seen in Models B, F and C although, again, the absolute values are slightly different as may be seen Figure 6.23. The distinct changes of gradient in the curves of the fractional abundances at the original cloud radius (0.31 pc) as seen previously remain throughout the cloud's evolution. The fractional abundance of C$^+$ is lower than the start value in the region close to the centre of the cloud, where the temperature is 4K higher than the 1K at the original radius at the final time step, and increases with the falling temperatures at radii greater than the original radius. The CO species does the reverse, the fractional abundance increases at the centre, falls to the original radius, then recovers slightly. The fractional abundances of both species then increase at similar rates for the rest of the evolution.

6.8.3 General Evolutionary Features

The evolution of physical properties of Cloud types 1, 2, 4 and 7 can be found in Figures A.33-45. Not only are there no qualitatively different features among the five clouds in this model, but they also share great similarities with those of Model F. The power law describing the relationship of time to dense core formation as a function of initial density is of the form

$$t_{col} = 112.28\, n_i^{-0.46} Myr \qquad (6.9)$$

which gives 18.57 Myr for a Cloud Type 1 and 2.19 Myr for a Cloud type 7. An initially higher density cloud takes less time to develop a protostar seed due to the higher initial self-gravitational attraction of the gas in the cloud. The other evolutionary features described in Section 6.6 are also valid for these Model D simulations.
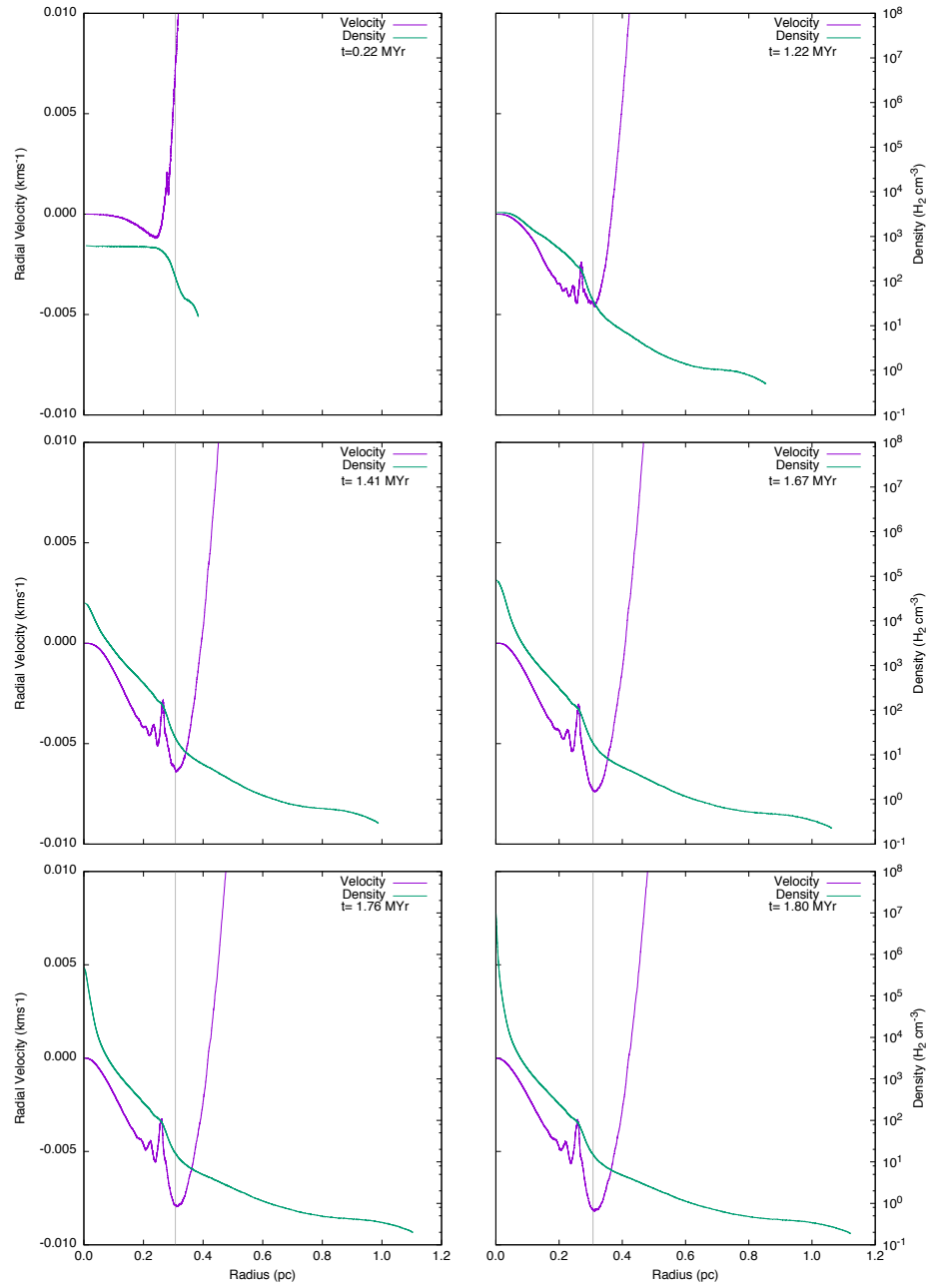
Figure 6.20: Model D: the evolution of the mean density and mean radial velocity distribution with radius r in Cloud Type 4. The velocity scale is expanded in order to show the collapsing high density core in more detail. The grey vertical line shows the initial radius of the cloud.
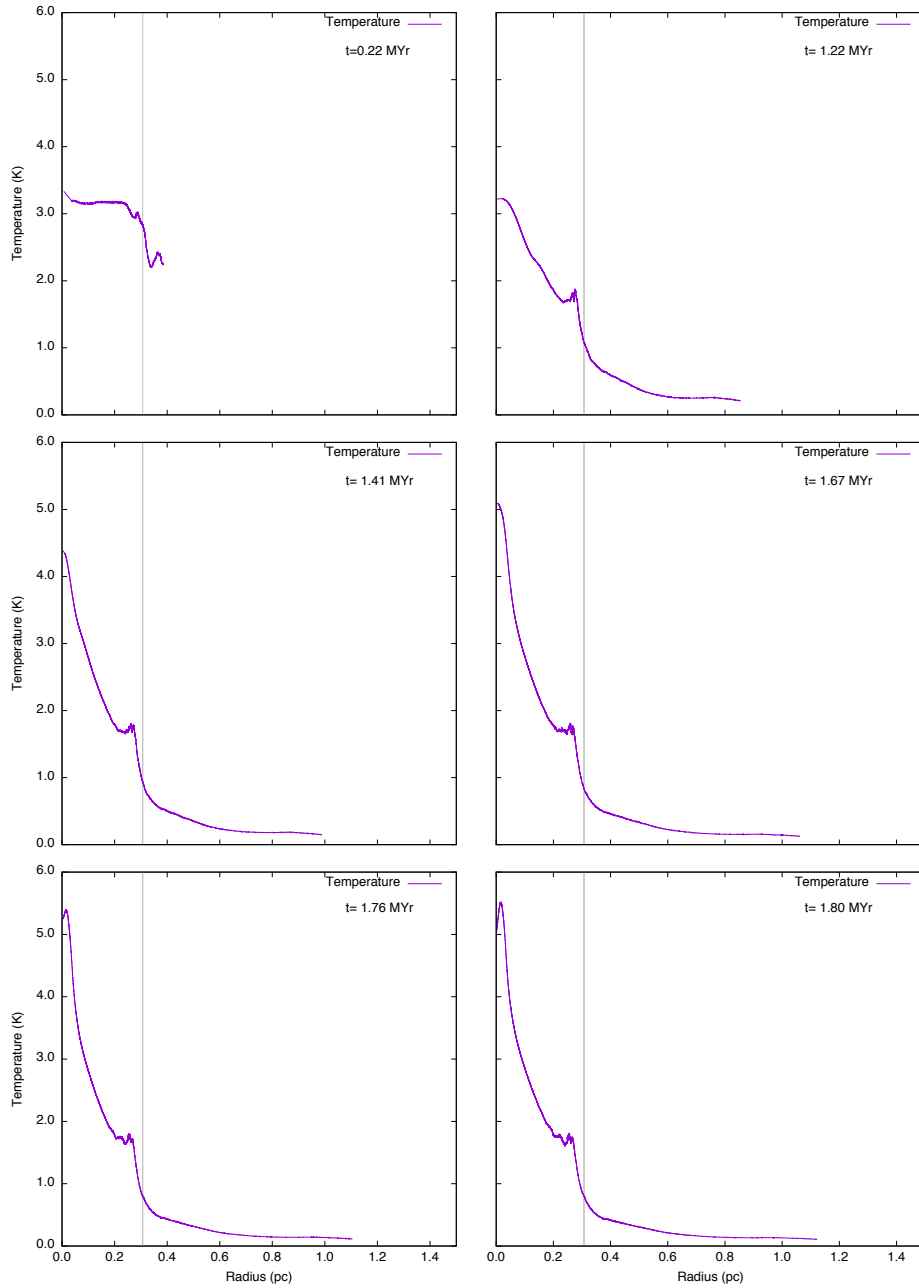
Figure 6.21: Model D: the evolution of the mean temperature distribution with radius r in Cloud Type 4. The grey vertical line shows the initial radius of the cloud.
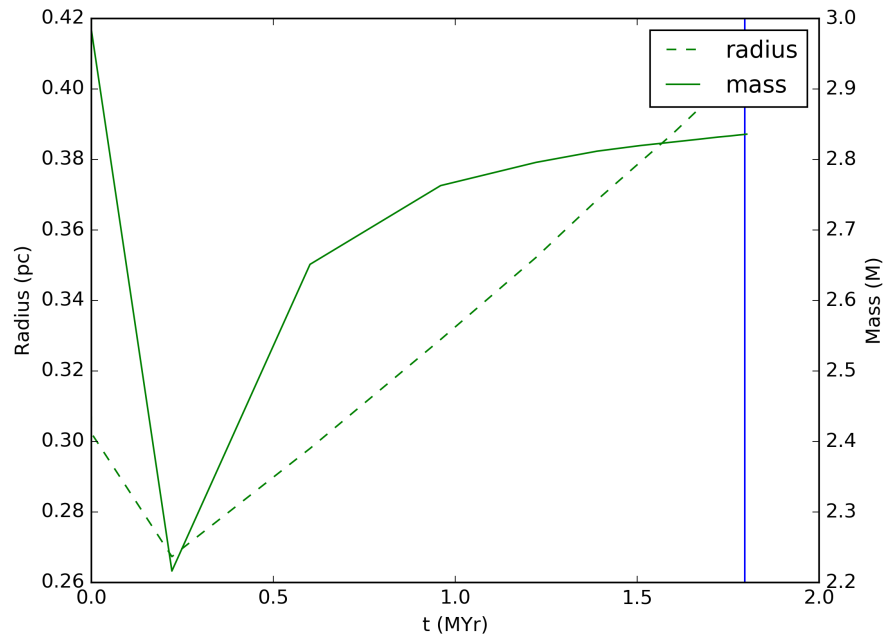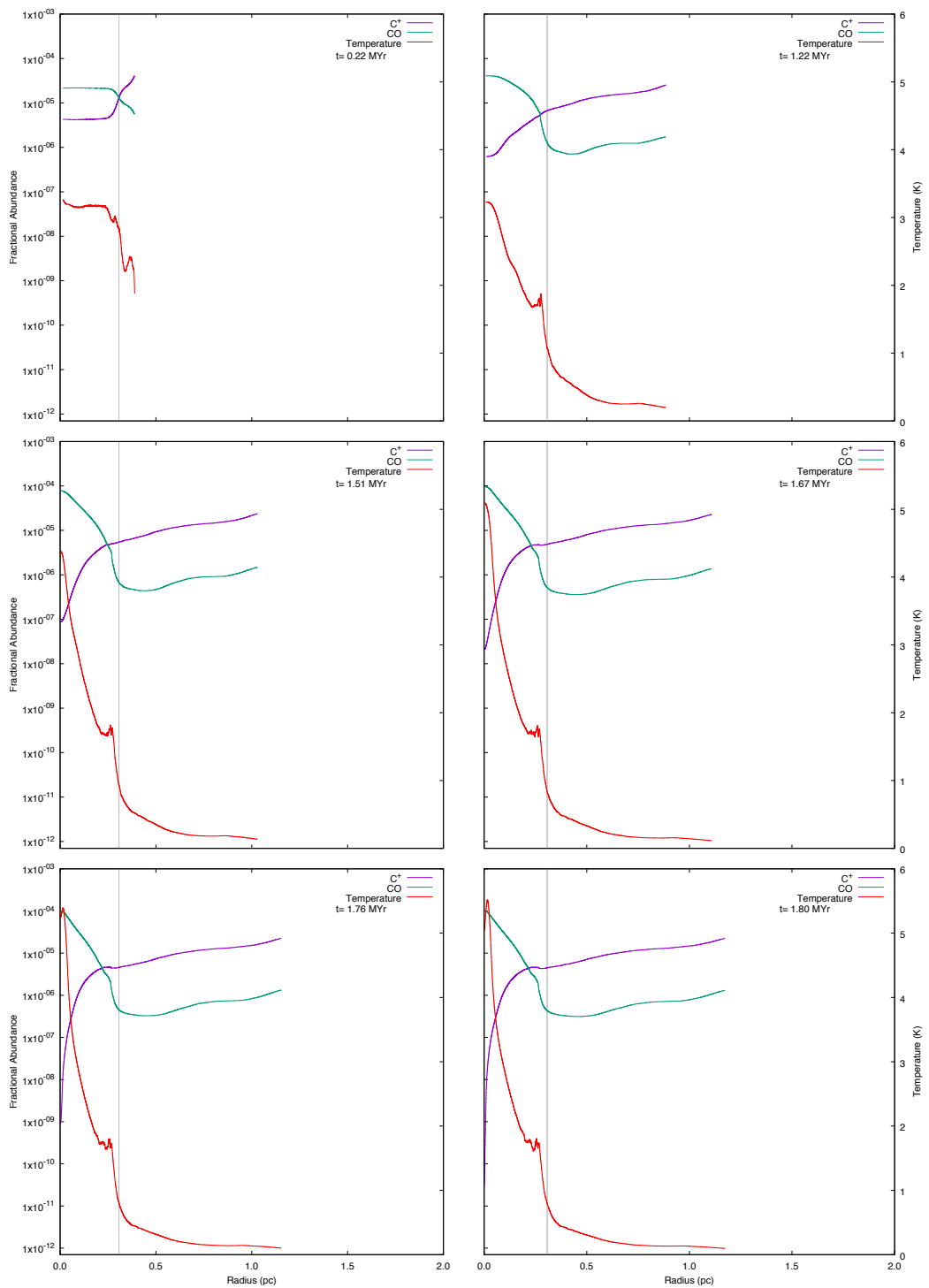
Figure 6.22: Model D: the evolution of the mass and radius of Cloud Type 4.

Figure 6.23: Model D: six snapshots showing the chemical abundances of CO and C^+ for a cloud with an initial density of 500 cm^{-3}, a mass of 3 M$_\odot$ and a radius of 0.31 pc.

6.9 MODEL E: ALL INCLUSIVE

Finally all three categories of micro-physical and chemical feedback - the chemical network, gas-dust thermal exchange and cosmic ray heating as listed in Table 6.1 - are included in the Model E simulations in order to determine how all the processes working together affect the evolution of a molecular cloud. This Model is the closest approximation to the environment that an isolated molecular cloud would experience as the background cosmic ray flux is all-pervasive in space. As before, FUV is inactive.

6.9.1 VARIATION OF MJM WITH n_i

The filled yellow square symbols in Figure 6.1 are the MJMs resulting from the Model E simulations, these decrease from 12 M$_\odot$ at an initial particle density of $n_i = 50$ cm^{-3} to 2 M$_\odot$ at an initial particle density of $n_i = 5000$ cm^{-3}. The relationship of the MJM with n_i for Model E may be described by a power law of the form

$$\mathrm{M}_{MJM} = 32.5 \, n_i^{-0.30} \mathrm{M}_\odot. \qquad (6.10)$$

6.9.2 EVOLUTION OF CLOUD TYPE 4

These results for the MJM lie between those found for the Model C and Model D simulations; they are very close to, but slightly lower than, those found in the Model C simulations and are above the Model D results. The closeness of the Model C and Model E results may be explained because the only difference between the two models is the gas-dust interaction which is activated in the Model E simulations. The energy transfer rate is proportional to the difference in temperature between the gas and the dust particles, that is $\propto (T_{gas} - T_{dust})$ and is only important in high density regions as noted in Section 3.3.5.

In Figures 6.24 and 6.25 six snapshots are presented of the evolution of radial velocity and density with time and of the evolution of the temperature of the cloud with radius and time respectively. The temperature evolution is very similar to that found for Model C which may be found in Figure 6.17. In both cases the temperature of the bulk of the central region falls to a low value of a few Kelvin after the first time step of 0.21 Myr. The outer layer, at a radius of about 0.4 pc and greater, already shows signs of heating. During the rest of the evolution the radius of the central core stays sensibly constant as does its temperature but close to the boundary with the core the outer layer continues to get hotter. The temperature of the layer then falls with
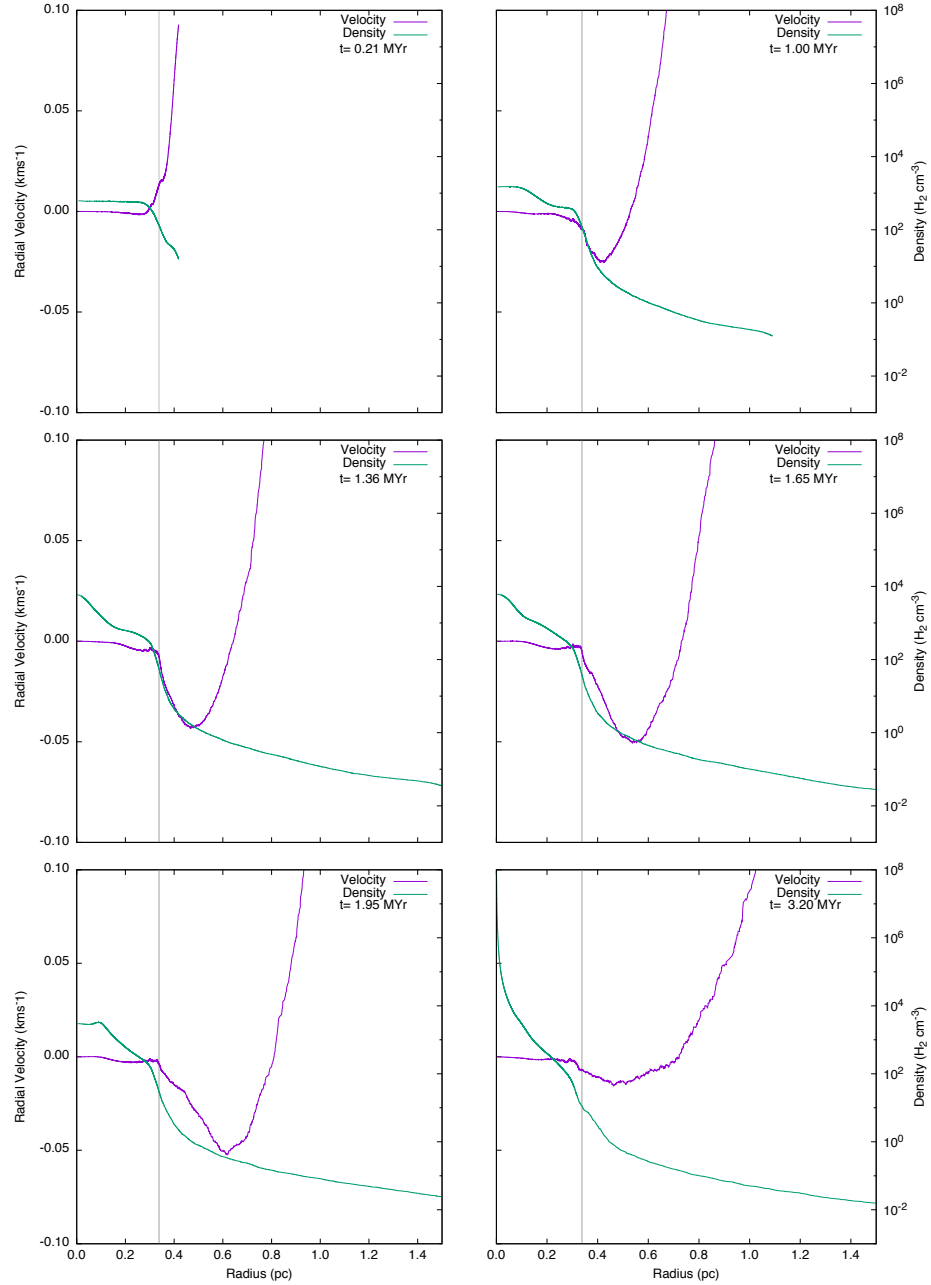
Figure 6.24: Model E: the evolution of the mean density and mean radial velocity distribution with radius r in a Cloud Type 4. The velocity scale is expanded in order to show the collapsing high density core in more detail. The grey vertical line shows the initial radius of the cloud.
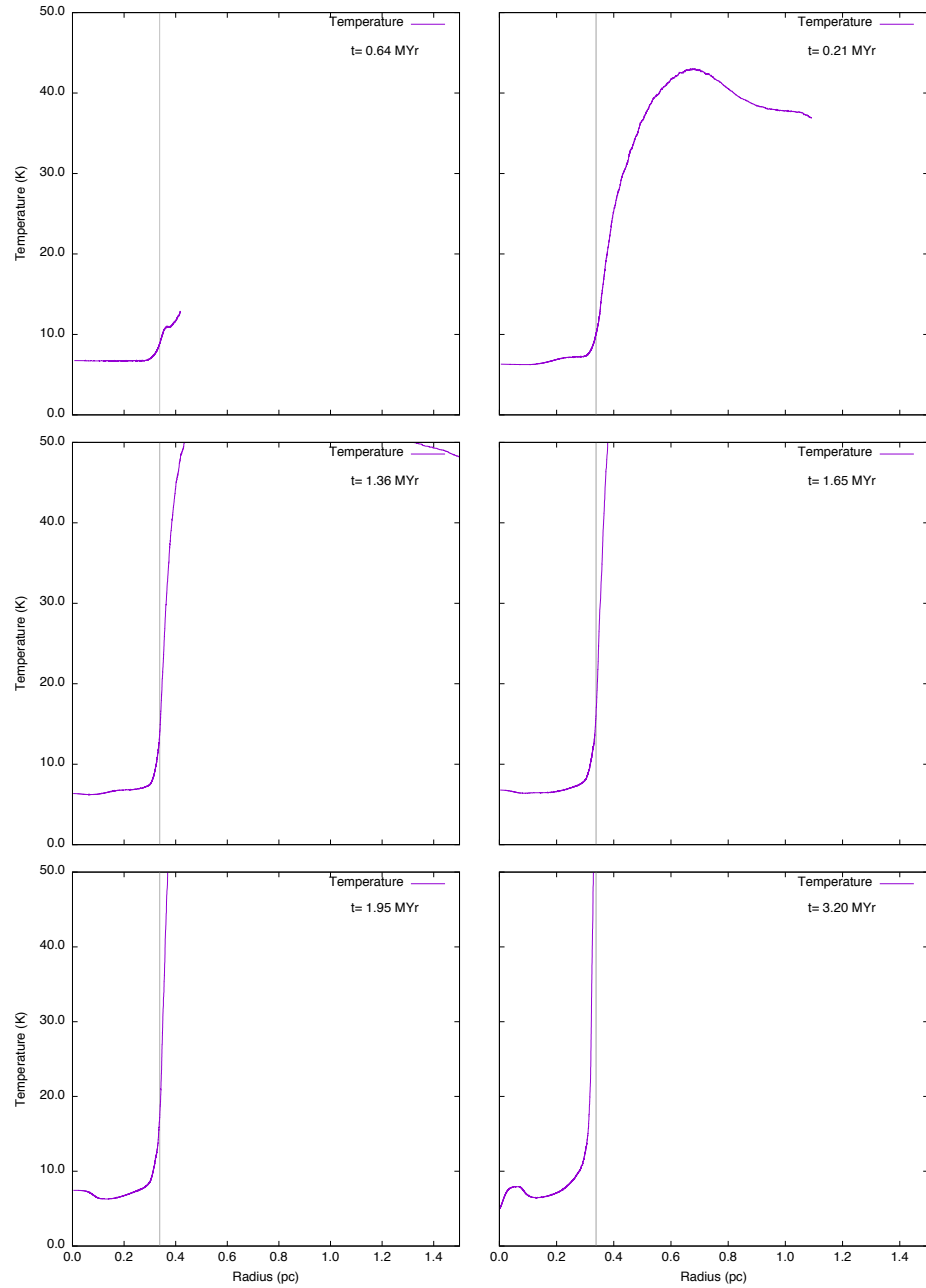
Figure 6.25: Model E: the evolution of the mean temperature distribution with radius r in a Cloud Type 4. The grey vertical line shows the initial radius of the cloud.
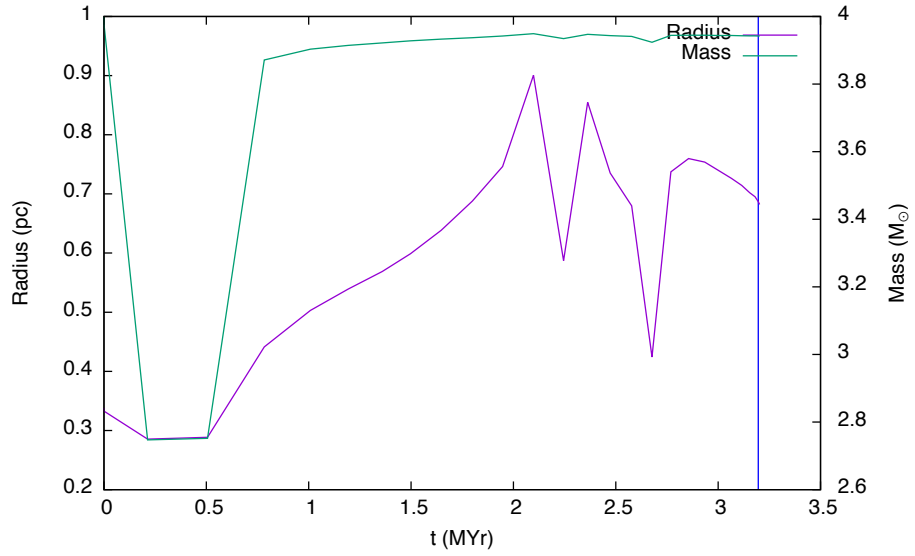
Figure 6.26: Model E: the evolution of the mass and radius of Cloud Type 4.

increasing radius. After 3.2 Myr at a radius of 0.5 pc, close to the core, the Model E gas cloud reaches a maximum of about 240K which exceeds the 180K reached in Model C at its collapsing point which was reached slightly more quickly at 2.63 Myr. At the very central point of the cloud in the Model C simulations, the density is high and a spike of slightly warmer particles ($\sim$ 20 K) may be observed. In the Model E simulations the spike in temperature has been replaced by a slight dip, where the gas-dust interaction may have cooled the dense gas.

Away from the central point, in the major dense core region where the gas temperature ($\sim$ 6.6K) is lower than the dust temperature ($\sim$10K), the effect of the gas-dust interaction is to heat the gas by only a few Kelvin, since the temperature difference between the gas and dust is small. Further away from the core the particle density falls (at radii >0.5pc the density is $n < 10^2$ cm^{-3}) and in this region the gas temperature ($T_{gas} > 50$K) but because of the low particle density the probability of cooling the gas to a great extent by gas-dust interaction is not high. This is the case for both the Model C and Model E simulations in a Cloud Type 4 where the gas temperatures T_{gas} are between 50 - 182K and 50 - 240K respectively.

Thus a limited cooling effect by gas-dust interaction in the very central region and in the major outer envelope of the molecular clouds in Model E is to be expected. This, coupled with a very weak heating effect in the major part of the core of a cloud due to cosmic ray interactions, would imply that the MJMs derived from the Model E simulations would be slightly lower than those in Model C. This is confirmed in Figure 6.1.

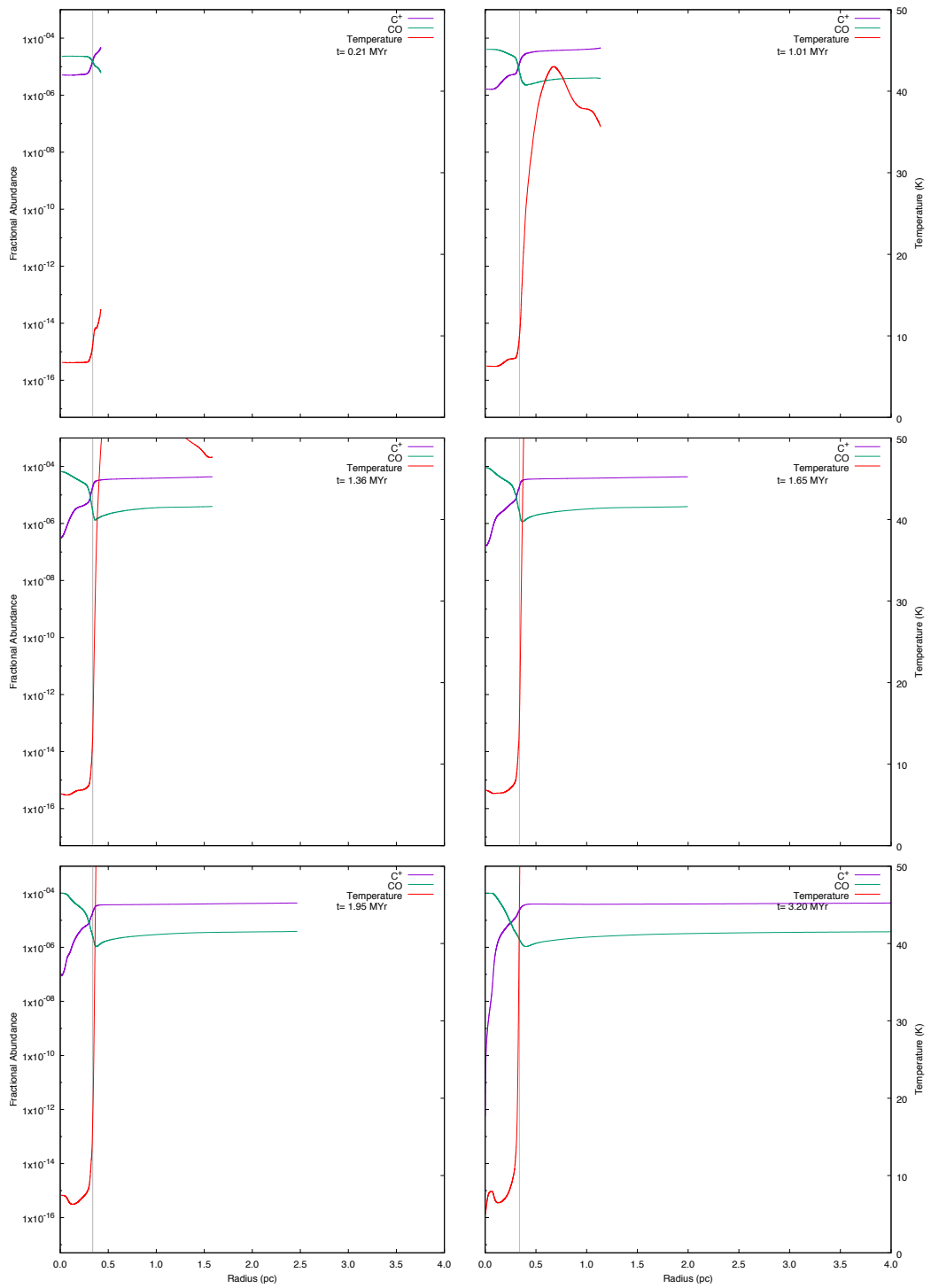Figure 6.26 shows the evolution of the mass of the cloud and its radius. Again this

112

Figure 6.27: Model E: six snapshots showing the chemical abundances of CO and C^+ for a cloud with an initial density of 500 cm^{-3}, a mass of 4 M$_\odot$ and a radius of 0.34 pc.

evolution is very similar to that found for Model C with the exception that the cloud radius oscillates two and a half times compared to the one and a half times seen in Model C. As the low density outer layer can have little direct influence over events near the centre, a delay in the particles near the core reaching the critical density to form the seed of a protostar may be taken as giving the outer layer a longer time for oscillation than that seen for Model C.

The changes in the fractional abundancies of the chemical species C^+ and CO follow a similar pattern to those seen in Models B, F, C and D although, again, the absolute values are slightly different as may be seen Figure 6.27. The distinct changes of gradient in the curves of the fractional abundances at the original cloud radius (0.34 pc) as seen previously remain throughout the cloud's evolution. As in the other Models the fractional abundance of C^+ decreases in the region close to the centre of the cloud with each time step and increases outwards until the original radius is reached. At radii greater than the original radius the abundance returns to near the original value, the temperature rising as discussed above. The development of CO species is almost a mirror image, the fractional abundance increases at the centre with each time step, in each case falling to a value about an order of magnitude lower (reaching $\sim 10^{-6}$) at the original radius, then increases slightly to a radius ~ 1 pc. The fractional abundances of both species then remain at constant values independent of radius for the rest of the evolution.

6.9.3   General Evolutionary Features in Model E Simulations

The detailed evolution of physical properties derived from simulations of Cloud types 1, 2, 5 and 7 under Model E conditions may be found in Appendix A, Figures A.45 to A.56. There are no large qualitative differences between the plots but some smaller scale ones. In all the radius decreases at the start of the simulation, for the Cloud Types 1, 2 and 5 the radius then increases again, for the Cloud type 7 the radius continues to decrease until the seed is rapidly formed at 0.64 Myr. The oscillation in the radius noted above for the Cloud Type 4 may also be seen in the lower density clouds both before and after the maximum radius is reached. The Type 1 cloud ($n_i = 50$ cm^{-3}) shows a series of inflections in the value of the radius as the curve follows a decreasing trend from a maximum to the formation of a protostar seed at 8.27 Myr. In the Type 2 cloud the inflections form a peak before the seed is formed at 5.55 Myr. In contrast the higher density Type 5 and Type 7 clouds show no oscillation.

The variation of temperature with time follows the same general pattern for all the cloud types, although it should be noted that the maximum temperature reached by

the outer layers is inversely proportional to the initial density, the Type 1 cloud reaches a maximum of about 345K at 8.27 Myr and the Type 7 cloud reaches a maximum of 38K at 0.65 Myr. In all cases the temperature shows a slight reduction at the origin, as noted above for the Cloud Type 4, showing the conditions for effective cooling by the gas-dust thermal interchange mechanism exist for all the initial densities. As is the case with the clouds subjected to the other Models, initially higher density clouds develop a protostar seed in less time due to the higher initial self-gravitational attraction of the gas in the cloud.

The variations of particle velocity and cloud mass with time also follow a similar pattern, but there is much greater variation in the velocities with radius in the Type 1 cloud with low initial density as in the other higher density clouds.

The power law describing the relation of time to dense core formation as a function of initial density is of the form

$$t_{col} = 54.23 \, n_i^{-0.48} Myr. \tag{6.11}$$

6.10 Normalised core mass

It may be seen from the previous sections that the different models of simulation conditions have a significant effect on the evolution of the clouds. Not only are the initial masses different but the masses of the clouds at the termination of the evolution, specifically the masses of the cores of the clouds at the point of formation of the protostar seed, are different. These values of the final 'core mass' may be taken as indicators of how efficient the potential star formation process is for the particular combination of initial conditions, micro-physical and chemical processes which were selected.

However as the MJMs for the clouds under investigation can vary by more than 3 orders of magnitude (from < 1 M$_\odot$ to $> 10^3$ M$_\odot$) the absolute value of the core mass may not of itself be a good indicator of the star-forming efficiency of the process and a ratio of final core mass to initial cloud mass may be more informative.

The initial mass of the cloud is taken as the MJM for that particular simulation Model and Cloud Type. The final core mass is taken as the absolute value of the mass of the high density core where the particle density $n > 10^7$ cm^{-3}. This mass is calculated by summing the number of particles lying between the density-radius curve and the density axis assuming that the particle distribution is spherically symmetrical at the final time step. The efficiency of the core formation process is then defined as
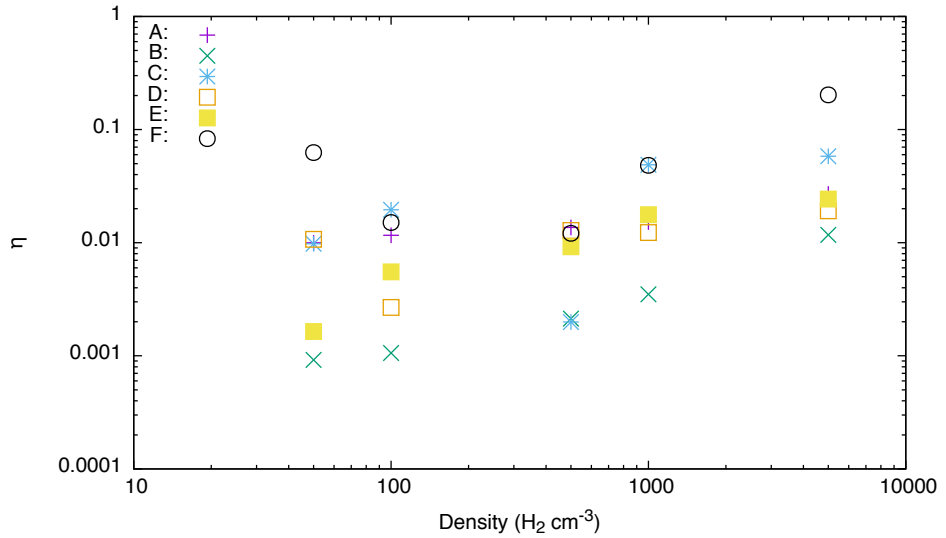
Figure 6.28: Normalised core mass, η, $\left({M_{\text{core}}}/{M_{\text{MJM}}}\right)$, against initial density for Models A-F.

the normalised core mass,

$$\eta = \frac{M_{\text{core}}}{M_{\text{MJM}}}, \tag{6.12}$$

where M_{core} is the core mass and M_{MJM} is the MJM for that cloud.

It should be noted that the core mass is not the same as the cloud mass at the final time step, the latter includes all the particles lying within the radius at which the particles' velocity vector changes from positive to negative.

Figure 6.28 presents the variation of η against initial density for all six simulation models. It may be seen that the dependence of η on the initial density varies for the different simulation models; it does not follow the same pattern of variation as the MJM does with n_i. These differences may be described as follows:

- The normalised core mass η for Model A of the isothermal simulations, shown by the purple crosses in the Figure, is not very sensitive to the initial density as there is no thermal evolution involved, the temperature remaining constant during the evolution of the cloud.

- In Model B, η is very low when the initial density of a cloud is low, due to the dominant heating effect, which results in a high mass loss rate by evaporation. It increases with initial density due to the gas-dust cooling rate gradually dominating over the cosmic ray heating rate as the density increases. Therefore the chances of star formation are increased in a cloud with higher initial density.

116

- η in the Model F simulations follows a non-monotonic change with the initial density. At the lowest initial density of 50 cm^{-3}, the cooling rate is lower relative to that in the clouds with higher initial density; the cloud takes the longest time, 19.28 Myrs, for the central density to reach the threshold value ($n \geq 10^7$ cm^{-3}) for the formation of a protostar seed. Therefore the cores are able to accumulate relatively more gas and show a high η value. When n_i increases, the cooling rate increases with the result that the core collapsing time decreases to 10.94 and 2.18 Myrs at $n_i = 100$ and 500 cm^{-3} respectively. With these shorter times fewer particles can be collected by the core, therefore leading to a lowest η of around 1.3% at $n_i = 500$ cm^{-3}. At higher densities, such as $n_i = 1000$ and $n_i = 5000$ cm^{-3}, the collapsing time does not change much, being 2.20 and 1.41 Myrs, but the higher cooling rate in the clouds of higher initial density enhances the initially stronger gravitational acceleration toward the centre. This means that more particles are attracted into the condensed core being formed. The highest η value of 20% may be seen for the cloud of the highest initial density of $n_i = 5000$ cm^{-3}.

- In Model C simulations, a qualitatively similar non-monotonic dependence of η with n_i is seen as with Model F. This is to be expected as the only difference is that the cosmic ray heating effect is superposed, therefore η has lower values than those for Model F at most densities, except at $n_i = 100$ cm^{-3} but even this is only about 0.5 % higher than that for Model F.

- Qualitatively following the dependence of η with n_i in the Model F simulations as well, η in Model D is lower than that in Model F at most of the initial densities except in the intermediate density of $n_i = 500$ cm^{-3} where it is similar.

- Model E includes all the physical and chemical feedback and it may be seen that η is lower than that for Model F at all densities and increases monotonically with the initial density of a cloud; it can be considered as the result of the combination of the different dependences of η with n_i for Models C, D and F. At lower initial densities, cosmic ray heating dominates the cooling gas-dust interaction which causes a low η value at $n_i = 50$ cm^{-3}. With n_i increasing, the gas-dust and chemical cooling play a more and more important role in helping the gas move towards the centre, therefore yielding an increasing η value.

As shown in Figures 6.1 and 6.28, although Model F has the lowest MJMs, it shows the highest values of η at almost all densities, whilst Model B has the highest MJMs in most cases, it has the lowest η ranging between 0.07 and 1% at all density

points. These are much lower values than those seen in Model F because of the lack of the chemical cooling mechanism. If the maximum and minimum η values for each model are compared, it is possible to get an indication of the potential star formation efficiency of the different models. Starting with Model F, it can be seen from Figure 6.28, that this model has the highest η values at each of the five initial densities from all the six models, with values lying between 1.5 and 20%. When cosmic ray heating is added to Model F, η values in Model C are lowered to between 0.07 and 6%, that is 3 to 20 times lower than those found with Model F. When the gas-dust interaction is combined with Model F, the value of η lies between 0.3 and 2%, which is 5 to 10 times lower than in Model F. When all the physical and chemical mechanisms are included in Model E, η lies between 0.16 and 2.5%, which is still 8 to 10 times lower than in Model F.

If the η values for Model E are compared with those for Model A, it is interesting to find that at lower densities the difference is significant, η is about 10 times lower in Model E than in A. With increasing initial densities the difference is significantly reduced to almost zero at the highest initial density. When none of the mechanisms are included, the Model A simulations give a very stable value of η lying between 1 and 2% over different initial densities.

It is worth mentioning that η values estimated in this work as an indication of the efficiency of potential star formation in a cloud may not be directly comparable to the generally accepted star formation efficiency in the usual astrophysical environment because all of the molecular clouds in this investigation are in an initially critical state considering their tendency to collapse. Other estimates of the efficiency of star formation consider molecular clouds in many other states. As a consequence a higher than normal star formation efficiency is estimated. This is accepted as an artefact since the major concern of this thesis is to explore the role of the basic micro-physical processes and chemical feedback in the evolution of molecular clouds by comparing the calculated MJMs from different simulation models. By doing so it is possible to investigate the importance of these processes in theoretical modelling of the evolution of molecular clouds.

6.11 Conclusions

It is considered it would be useful to summarise the results of the work described in this chapter in order to give a basis for considering the results of the work investigating the effects of different FUV fluxes reported next in Chapter 7.

Firstly, a power law of the form $M_{MJM} = a\,n_i^b$ can describe the dependency of the MJMs with the initial density of the cloud for the different Models used, where a and b depend on the Model.

Secondly, the simulation results presented so far clearly show that the MJM of a molecular cloud is significantly influenced by micro-physical and chemical feedback processes and that the MJM is a sensitive indicator of the degree of influence of these processes. It is clear that they all play roles in the dynamic evolution of molecular clouds which, depending on the set of conditions at the start of the process, can lead to the possibility of star formation within them.

Among the three categories of mechanisms studied, chemical feedback plays a dominant role, significantly reducing the values of the MJM found for the isothermal Model A. The cosmic ray-heating and gas-dust interaction both play a subordinate role in deciding the size of the MJMs. This may be deduced from the consideration that the MJM in Groups C, E, and D are on average 6.22, 4.82 and 0.98 M$_\odot$ higher respectively than in the Group F simulations. That is, a smaller cloud is needed to collapse if only the chemical feedback is active. The results also show that MJMs from Group E lie between Group C and Group D simulations, that is the gas-dust thermal interchange and the cosmic ray heating processes are less significant in their influence on the MJM.

As a summary, the values of the MJMs obtained from each of the conditions in all the Models considered are given in Table 6.2. For completeness the time to collapse for each condition are also included as well as the crossing time calculated using the speed of sound in the initial cloud and the free fall time.

The free fall time is included as it is a very useful estimate of the time required for many astrophysical processes which are mainly dependent on gravitational attraction. In the case of a uniform spherical distribution of mass it may be shown to be given by

$$t_{ff} = \left(\frac{3\pi}{32G\rho} \right)^2 \tag{6.13}$$

where t_{ff} is the free fall time, G is the gravitational constant and ρ is the initial density of the body.

For the cases under investigation in this thesis because the gravitationally influenced free fall time is only dependent on the initial density, it is a good metric for comparison with the actual values of times to collapse obtained by simulation to obtain another indication of the importance of the additional effects incorporated in each of the Models.

All the clouds take longer then t_{ff} to collapse. The most notable increase is in the cases of the very low density models where it takes ~ 4 times longer to collapse than the free fall time predicts, for most other Models the difference is 1.5 times slower at the most. In two cases of high density clouds (Model D, 5000 cm^{-3}) being 4 times

slower and Model F being 2.8 times slower the difference is more pronounced. In these two cases the MJM is less than $1M_\odot$ and the Models have chemical processes active heating the clouds thus inhibiting collapse. In addition the calculation limits to determine the collapsing point are reduced below values of MJM < 2 to $0.1M_\odot$ to be better able to discriminate between collapse and not collapse. Above MJMs of $2M_\odot$ the discrimination is set to $1M_\odot$.

The MJM values for Models A-F shown in Table 6.2 show the point at which the cloud is barely able to collapse due to its own self-gravity. Effects which oppose the collapse of a cloud under its own self-gravity will have most influence on the time to collapse on a cloud which is on the cusp on collapsing or not collapsing. As other influences are in play which inhibit collapse it is to be expected that the time until collapse for such a cloud will be longer than a simple calculation based on gravity alone would predict. Even in Model A, the isothermal case, other effects are occurring such as the interactions between particles falling towards the centre and other particles escaping from the cloud. The collapsing time line of best fit for the different Models combared to t_{ff} can be easily seen in figure 6.29.
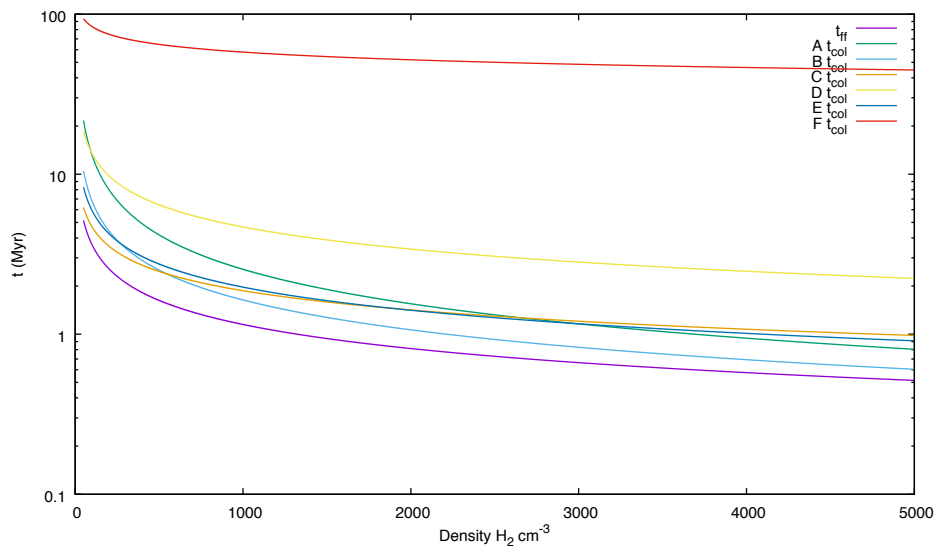
Figure 6.29: The time to collapse as a function of initial density of a molecular for the different Models and $t_f f$. The collapse times are the lines of best fit based on the MJMs found.

Considering each mechanism individually and in isolation, their contributions to a cloud's evolution may be summarised as follows:

- The most effective cooling is by molecular line emission

- Cosmic ray radiation not only warms the dense inner regions of a cloud but also,

Model	Density	Radius	MJM	t_{collapse}	t_c	t_{ff}
	cm^{-3}	pc	M$_\odot$	Myr	Myr	Myr
	50	3.27	362.00	20.42	5.25	5.15
	100	2.42	292.00	14.28	3.88	3.64
A	500	1.15	158.00	3.13	1.85	1.63
	1000	0.82	112.00	2.48	1.31	1.15
	5000	0.37	51.00	0.77	0.59	0.51
	50	5.83	2050.00	10.49	9.36	5.15
	100	3.39	807.00	6.97	5.44	3.64
B	500	0.99	99.00	2.60	1.58	1.63
	1000	0.59	42.00	1.56	0.94	1.15
	5000	0.20	8.00	0.55	0.32	0.51
	50	1.13	15.00	6.21	1.81	5.15
	100	0.76	9.00	4.94	1.21	3.64
C	500	0.36	5.00	2.63	0.58	1.63
	1000	0.29	5.00	1.71	0.46	1.15
	5000	0.14	3.00	0.98	0.23	0.51
	50	0.66	3.00	18.57	1.06	5.15
	100	0.46	2.00	12.84	0.74	3.64
D	500	0.31	3.00	1.80	0.49	1.63
	1000	0.21	2.00	1.44	0.34	1.15
	5000	0.09	0.80	2.19	0.15	0.51
	50	1.05	12.00	8.29	1.69	5.15
	100	0.73	8.00	5.56	1.17	3.64
	200	0.53	6.00	3.70	0.84	2.57
E	500	0.34	4.00	3.20	0.54	1.63
	1000	0.27	4.00	1.86	0.43	1.15
	2000	0.19	3.00	1.15	0.31	0.81
	5000	0.14	3.00	0.52	0.23	0.51
	10000	0.10	2.00	0.37	0.16	0.36
	50	0.56	1.80	19.31	0.90	5.15
	100	0.40	1.30	10.95	0.64	3.64
F	500	0.24	1.50	2.18	0.39	1.63
	1000	0.15	0.70	2.20	0.24	1.15
	5000	0.08	0.60	1.42	0.13	0.51

Table 6.2: This summary Table lists all the Models used in the simulations in this Chapter 6. For each Model the different initial cloud densities (cm^{-3}) used in the simulations are given together with the initial cloud radius (pc), the MJM (M$_\odot$), the time to collapse (t_{collapse}), the sound crossing time (t_c) and the free-fall time (t_{ff}).

in the absence of cooling mechanisms also warms the outer layers effectively, reaching 450K in the conditions simulated

- Gas-dust thermal exchange is most effective at particle densities greater than 500 cm^{-3}.

The calculation of the normalised core mass further demonstrates that the 'efficiency' of the potential star formation is enhanced by chemical feedback as seen in Model F. However, when all the mechanisms are included, as is the case for Model E, the overall 'efficiency' for clouds of low initial density is lower than that for the isothermal Model A and is similar to that for Model A for clouds with a high initial density. It should be noted that the calculated absolute value of the normalised core mass may not be a fair comparison with the concept of star formation efficiency, derived from observations or from theoretical modelling of molecular clouds in normal astrophysical environments, because of the biased initial conditions for the molecular clouds used in these simulations - the clouds being sized so it was known that they would collapse.

Chapter 7

The Effect of FUV Radiation on the Evolution of Molecular Clouds

7.1 Introduction

The level of FUV flux at an arbitrary point in space is a function of the number of OB stars in the vicinity, the intensity of each of them and their separation from the arbitrary point. In turn the FUV flux acting on a molecular cloud can affect the probability of star formation in the cloud. As stated in Section 1.4, FUV radiation is considered to affect the evolution of molecular clouds through two mechanisms. The first mechanism is seen to induce the propagation of density (shock) waves through the cloud originating from the heated outer layers. The shock waves can then cause local clumps of higher density material to form which act as kernels for mass accretion. The other possible mechanism is that the FUV radiation feedback heats material in the cloud's surface layer causing mass loss by photo-evaporation. This mass loss reduces the cloud's net gravitational energy and therefore reduces its tendency to collapse. To identify the relative importance of each of these two mechanisms further investigation by numerical simulation based on a comprehensive model of the micro-physics and

chemical network present in the cloud is necessary in order to identify which effect is dominant under which physical conditions of both the FUV radiation field and of the molecular clouds. In order to obtain such a deeper understanding of this process a series of simulations were designed to identify the significance that different levels of incident FUV may have on the evolution of molecular clouds, over a range of initial particle densities, up to the point of the formation of a seed, a protostar precursor. The results of these simulations are reported and discussed in this chapter.

Nelson and Langer (1997) reported on the evolution of spherical, oblate and prolate molecular clouds subjected to the background level of FUV (G_0=1) using an early version of the CLOUD code. Further work using a version of the CLOUD code with more extensive modelling of the chemical networks, the basis of that used for this thesis, was reported by Nelson and Langer (1999) on the evolution of isolated Bok globules; the globules being isolated the calculations were performed using the background level of FUV only.

Weingartner and Draine (2001) reported on modelling of grain charging and gas heating in interstellar dust using two, fixed, values for radiation fields in the FUV frequency range and the estimate for the cosmic ray energy density and the average interstellar radiation field. FUV photons (6 eV $< h < 13.6$ eV, that is a wavelength range from 207.0 to 91.2 nm) disassociate molecular gas beyond just the H II region creating a PDR. The Habing unit represents the average FUV intensity in the interstellar radiation field for photons within this energy range and is represented by G_0. Many computational models are parameterised by using using G_0, as a ratio of the FUV flux (Gorti and Hollenbach, 2002; Nelson and Langer, 1997).

They also show that dust grain and photoelectric heating is an important physical process in H II and warm ionised medium, the grains absorb radiation which then heat the gas via the photoelectric effect. These gas heating effects can also be seen in cold neutral medium which is similar to the medium used in these studies.

Observational data using the band emission from polycyclic aromatic hydrocarbon (PAH) molecules to study the impact of the FUV radiation from young massive stars on the surrounding molecular material implies that star formation is ongoing and not halted by intense radiation (Rathborne et al., 2001). These results suggest that running the simulations with higher levels of FUV flux may be useful in aligning observational and numerical data.

High levels of radiation have been reported as the reason for the morphology of bright rimmed clouds, often found near the edge of H II regions, using a radiation-driven implosion model. Motoyama et al. (2013) investigated by observation and numerical analysis the interplay between FUV and magnetic fields on the structure of such clouds.

Other published works show that the study of the processes driving star formation is an active field of investigation. Analytical studies leading to shock solutions with some one dimensional simulations have been reported by Kitsionas and Whitworth (2002). Abel and Ferland (2006) reported on analytical studies yielding an equation of state for a single H II region adjacent to a single PDR region. This study took into account both turbulent and magnetic pressure in the cloud. Work to improve chemical modelling has been reported by Andree-Labsch et al. (2013) in which 3-dimensional PDR regions are modelled for detailed chemical analysis, the chemical abundances depending on optical depth from the surface and with the FUV flux dependent on the inverse square of the distance from the source star, but no dynamic movement is simulated. Motoyama et al. (2015) reported on a 2-dimensional grid-based hydrochemical hybrid code being developed; currently this models gas phase reactions and will be extended to include gas dust thermal exchange and will be parallelised for large-scale simulations. This code is designed specifically for PDRs and solves non-equilibrium chemistry and changes of energy due to thermal processes with transfer of the energy of the external UV radiation. Similar to the CLOUD code, it also allows for the self shielding effect on photodissociation of CO and H_2.

The paper already mentioned in Section 1.4 (Gorti and Hollenbach, 2002) is a significant contribution to the understanding of the behaviour of clumps in PDRs. It discusses both analytical and numerical analyses, the latter using one dimensional radial code, of the effects of FUV radiation in these regions and how the rapid heating causes both photo-evaporative mass outflow and also drives shockwaves into clumps creating volumes of high particle density. The paper proposes that for clouds within PDRs subjected to strong FUV fields some may be driven to collapse, that some may be entirely dispersed by photo-evaporation and others may preserve a shielded core with a protective shell that absorbs most of the FUV. The evolution of an individual clump was found to be sensitive to three dimensionless parameters: the ratio of the initial column density of the clump to the column of the warm FUV-heated surface region; the ratio of the sound speed in the heated surface to that in the cold clump material; and the ratio of the rate of increase of the FUV heating flux to the initial sound crossing time. The radius of the clump during the shock compression was found to be dependent on the ratio of the sound speed in the heated surface to that in the cold clump material. Some simplifications were made in the analyses, for example self-gravity was ignored in the analytical model and the numerical model does not model the chemical and micro-physical processes.

However from the published literature it would appear that the effect of the strength of the FUV radiation on the dynamical evolution of molecular cloud and its effect on

the spectrum of star formation within it has not so far been investigated in detail. This is an important issue, because as the range of the FUV radiation flux in different PDRs can run from 1 to 10^6 G_0 (Gorti and Hollenbach, 2002) and the density (n_i) of molecular clouds covers a range of between a few 10s to $10^6 cm^{-3}$, the effect of FUV radiation on the dynamics of the molecular cloud in various regions must be significantly different.

Therefore it was considered that a series of simulations with molecular clouds of different initial densities, exposed to FUV radiation of different energy fluxes would be able to reveal the range of conditions where photo-evaporation is dominant and similarly for shock dominant regions in a two dimensional Flux-initial density phase space. As the intention was to follow the evolution of a molecular cloud being subjected to incident stellar radiation to see if the pre-conditions for star formation could be met, all the chemical and micro-physical processes discussed in Chapter 6 were activated.

The major indicators used to follow the evolution were the effect of different levels of FUV on the MJM for clouds with different initial densities and changes in cloud density and temperature with time and position. The initial mass and the size of the clouds used in the simulations shown in this chapter are the MJMs which have been discussed in Section 5.2. These are the minimum masses for given densities where collapse would still occur. Many simulations using the bisection method discussed in Section 5.2 were performed to determine the MJM. The final results for initial densities of 500 cm^{-3} are shown in detail in this Chapter. The detailed figures for the other densities are given in Appendix B.

The prospects for star formation were examined for each set of conditions by studying the normalised core mass at the termination of the simulation. All the data reported in this chapter and their discussion are original.

7.2 Selected FUV Flux Levels

Four different levels of incident FUV were modelled with flux levels of 1, 2, 50 and 100 times the Habing (1968) unit of background radiation where the Habing unit (G_0) has a value of $1.6 \times 10^{-3} ergs$ $s^{-1} cm^{-2}$. To make subsequent discussion easier these processes are called $1G_0$, $2G_0$, $50G_0$ and $100G_0$. The same fixed value for the cosmic ray flux given in Section 3.3.2 was used for all the simulations. The simulations for an FUV flux level of zero ($G_0 = 0$) have been reported in the previous chapter where it is classified as Model E in Section 6.9. Model E serves as a common factor with which one can compare both the models from Chapter 6 and the sets in this chapter. For this reason the results of Model E simulations are included in the figures where all fluxes

are shown.

To give a more comprehensive picture of the influence of initial particle density on the evolution of the clouds the simulations were performed with an increased range of particle densities than those used in Chapter 6, at the same time the size of some of the intervals between adjacent particle densities was reduced. Thus for each of the four FUV flux levels simulations were performed with initial SPH particle densities of $n_i = 50, 100, 200, 500, 10^3, 2 \times 10^3, 5 \times 10^3$ and 10^4 cm^{-3} to determine the MJM for each flux and for each initial density. To match the convention used in Chapter 6 these are called Cloud Types 1-8 respectively. In all cases the evolution of the cloud was tracked by following the changes in cloud density and temperature with time until the collapsing point was reached. In a manner similar to that reported in Chapter 6 the evolution of the abundances of selected chemical species were tracked as a function of radius.

As mentioned in Section 7.2 above, in order to understand the dynamic evolution of these clouds with critical initial conditions under the effect of FUV radiation field, a detailed analysis of the Cloud Type 4 (with $n_i = 500$cm^{-3}) for each of FUV radiation fluxes is presented. The plots for the results of the numerical analyses for molecular clouds of other initial densities may be found in Appendix FUV chapter B to which reference will be made when necessary.

7.3 OVERALL RESULTS

The results of the variation of MJMs with initial density are presented in Figure 7.1. For completeness and to act as a baseline the results for Model E, as defined in Section 6.2 which has all the micro-physical and chemical processes active but no incident FUV radiation, are also plotted in Figure 7.1.

Two major trends can be observed. Firstly, it can be seen that at all FUV intensity levels the value of the MJMs decrease with increasing initial cloud density following a similar trend to that seen in all the Models studied in Chapter 6. This is because the initial gravitational binding energy per unit mass increases with the initial density of a cloud. Secondly, it is found that the relative importance of the two effects due to the FUV radiation - photo-evaporation and shock propagation - changes when considered over the whole range of initial densities covered by these studies. In comparison with the distribution of MJMs obtained from Model E (zero FUV radiation flux), it can be seen that in the low initial density range of $50 \le n_i \le 500$cm^{-3} the photo-evaporation effect of the FUV radiation is dominant: a cloud with an initial density in this range
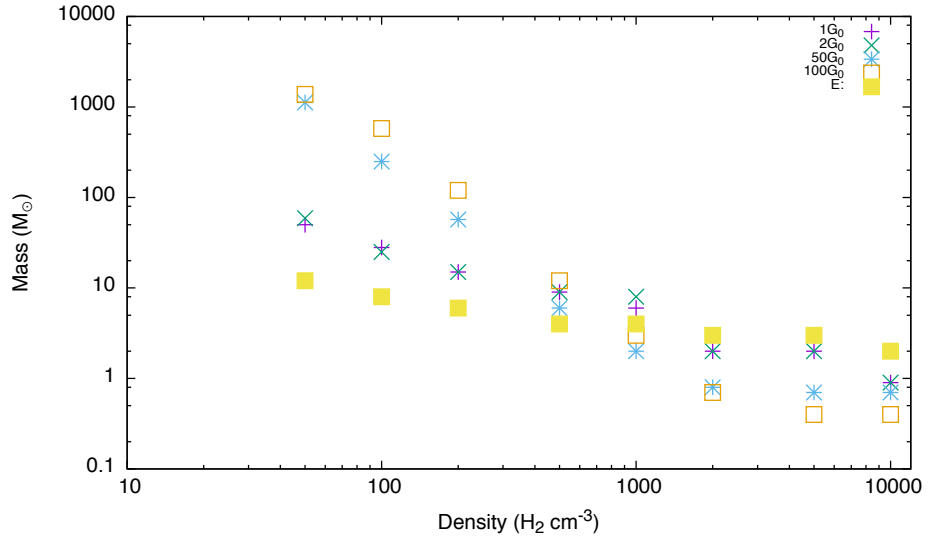
Figure 7.1: The MJM as a function of the initial density of a molecular cloud for different strengths of FUV. Model E MJM is included as a baseline to be able to make comparisons with Figure 6.1.

requires a greater MJM to collapse than that required for zero FUV flux, and the higher the FUV flux, the greater is the MJM. At low initial density, $n_i = 50$ cm^{-3}, stronger radiation of $50G_0$ and $100G_0$, requires 2 orders of magnitude more mass than is the case for the simulation with no FUV radiation. Therefore in this case, as the molecular cloud has to be much larger, the probability of star formation has been reduced by the FUV radiation.

At $n_i = 1000$cm^{-3}, the shock effect from the high flux level of FUV radiation (flux $= 50$ and $100G_0$) starts to become dominant over photo-evaporation, so that the MJMs for the two greatest FUV fluxes are lower than that derived from Model E at the same initial density. This means that for these cloud conditions the FUV radiation enhances the probability of star formation.

At initial densities of $n_i > 1000$cm^{-3}, the shock effect dominates over the photo-evaporation effect over the whole range of FUV radiation fluxes. The MJMs at these initial densities are lower than those obtained from Model E simulations. Therefore, in high density molecular clouds the probability of star formation is increased by FUV radiation at all the energy flux levels: the higher the FUV flux so the lower is the MJM which means that the star formation probability is higher.

The data shown in Figure 7.1 demonstrate that at each FUV flux an initial critical density n_{crit} exists at which the dominance of the two effects caused by the FUV switches from one effect to the other. When the initial density in a cloud is lower than n_{crit}, FUV radiation weakens the cloud's potential to form a star and when $n_i > n_{\mathrm{crit}}$,

FUV radiation enhances its star formation potential.

Due to the twofold effect of the FUV over the range of radiation levels and initial cloud densities modelled, it is understandable that the spread of the sizes of MJMs over the initial density range investigated becomes wider with increasing FUV radiation flux. For example in the case of $G_0 = 1$, the MJMs fall from 80 to 0.9 $M_\odot$ and at $G_0 = 100$ fall from 1500 to 0.4 $M_\odot$, when in both cases the initial density of a cloud increases from 50 to 10^4 cm^{-3}. In general, the gradient of the MJM distribution over the initial density,

$$k = -\frac{d(\log(\text{MJM}))}{d(\log(n_i))}, \tag{7.1}$$

increases with FUV radiation fluxes, with $k_{\max} = 1.71$ at flux of $100G_0$, and $k_{\min} = 0.30$ at zero FUV flux.

In order to understand the dynamic evolution of these clouds with critical initial conditions under the effect of a FUV radiation field, a detailed analysis is presented for the Cloud Type 4 (with $n_i = 500$cm^{-3}) and each of FUV radiation fluxes to get a general view on how FUV radiation affects the evolution of such a cloud. The plots for the simulation results for other molecular clouds can found in Appendix B.

7.4   EVOLUTION OF CLOUDS UNDER FUV FLUX OF $1G_0$

7.4.1   THE MJMs VARIATION OVER n_i

In this series of simulations, the clouds of different initial particle densities referred to above were subjected to an FUV flux of $1G_0$. The MJMs derived from the set of simulations are presented by the purple crosses in Figure 7.1, which follow a power law of

$$M_{MJM} = 847.3\, n_i^{-0.74} \text{M}_\odot \tag{7.2}$$

It is seen from Figure 7.1 that at lower initial density, the MJM is higher than that in zero FUV flux, and the Δ MJM($= \text{MJM}_{1G_0} - \text{MJM}_E$) decreases with the initial density, it increases from 50 $M_\odot$ at $n = 50$ cm^{-3} to 0.9 $M_\odot$ at $n = 10^4$cm^{-3}. The transition point from photo-evaporation dominant to shock dominant occurs at $n_i \geq 2000$cm^{-3}, where the effect of FUV radiation starts enhancing the star formation in a molecular cloud with the specified initial condition, when $n_i < 2000$cm^{-3}, the effect of FUV radiation is opposite.

7.4.2 THE EVOLUTION OF CLOUD TYPE 4

The evolution of the radial distribution of the mean density, mean velocity and mean temperature of the Cloud Type 4 which has an initial mass of 9 $M_\odot$ is displayed in Figures 7.2, 7.3 and 7.4.

The first panels in Figure 7.4 show that photo-electric heating is the dominant factor at the surface as the top layer of the cloud heats from the initial 60K to 115K at t = 0.14 Myr. On the other hand in the central region chemical cooling dominates the thermal evolution as the gas cools from 60K to 20K. The temperature gradient from centre to the outer layers result in a pressure gradient which initiates a shock propagating toward the centre of the cloud. The velocity distribution in the first panel of Figure 7.3 also shows that an inward velocity of around 5 ms^{-2} has been built up at the surface of the cloud.

From the next few panels in Figures 7.4 and 7.3, it is seen that within a radius of 0.1pc the central temperature decreases to about 8K when t = 1.62 Myr, and the inward radial velocity peak moves to the very central point. The central density rises to 10^5cm^{-3} at the same time. This temperature is slightly lower than the 10K normally found at the centre of molecular clouds but the CLOUD code does not model all possible influences on the cloud. The distribution of the raw positions of the simulated SPH particles along the radial direction as shown in Figure 7.5 more intuitively reveals the shock wave propagation process in the first 0.93 Myrs of the evolution the cloud.

At the surface of the cloud it can be seen from Figure 7.2 that during the first 1.55 Myrs the photo-evaporation effect of the FUV radiation blows away much gaseous material; 96% of the initial mass in the warmer outer layer at t = 1.55 Myrs is moving outward. After that time, the radius and the mass start increasing, due to the enhanced central density which pulls back the evaporated gas in the outer layer. The mass of the cloud reaches 7.2 $M_\odot$, i.e., 80% of the initial mass of the cloud. The inward velocity in the outer layer of the cloud is more clearly shown in the last panel of Figure 7.3.

The last panel in Figure 7.3 reveals the final collapsing process driven by the shock induced by the photoelectric heating effect. In the last stage of the evolution at t = 1.98 Myr, the shock wave has propagated to the centre, where the density rises to 10^8cm^{-3}. The velocity profile shows that the warm layer of the cloud reverses its direction of motion from outward to inward as a consequence of the formation of the dense central core, whose strong gravitational force pulls the gas in the outer layer inwards. The highest inward velocity is shown to be around 52 ms^{-1}. Most of the previously evaporated gas is recaptured by the strong gravity of the high density core, so the mass of the cloud rapidly increases to around 8.2 $M_\odot$ at t = 1.98 Myrs, as shown in Figure 7.2. When the central density in a very small high density region is so high,

the shock wave cannot penetrate further and the incoming gas gets reflected, as shown by the positive velocity peak at r = 0.4 pc seen in the last panel of Figure 7.3.

Comparing the evolution of the same Cloud Type 4 in Model E shown in section 6.9 it may be observed that although the MJM is higher than that for Model E, the formation of the high density seed is quicker, taking 3.2 Myrs, due to the FUV radiation induced shock effect in the late stage of the cloud's evolution.

A partial explanation for the shock effect may be given by considering the abundances of the chemical species C^+ and CO. With all the micro-physical and chemical interactions being considered together with the effects of incident FUV on the cloud, the evolution of the fractional abundances of these species show some differences from those presented in Sections 6.5 to 6.9.

The initial fractional abundance for carbon in all forms was set as $n(C_{total}) = 10^{-4}n(H_2)$ and for oxygen as $n(O_{total}) = 2 \times 10^{-4}n(H_2)$ as given in Table 3.2. In a similar manner to the evolution of the species in the previous Chapter it may be seen from Figure 7.6 that the fractional abundance of the C^+ species decreases by 6 orders of magnitude from its starting value with decreasing temperature and increasing density within a radius of ~ 0.2 pc of the centre of the cloud. At radii greater than this value the fractional abundance remains essentially constant close to its initial value throughout the cloud's evolution but that of the CO species decreases strongly with radius. As described above, the temperature of the gas envelope at radii greater than the start value of the cloud increases with time in this simulation. This effect may be partially explained by the reduction in the cooling effect of the CO species with increasing temperature and decreasing density as shown in Figure 3.2. This effect, together with the reduction in the fractional abundance of the CO species by a maximum of about 12 orders of magnitude, will decrease the cooling and increase the temperature of the outer regions of the cloud as energy is still being supplied to it. (This pattern is seen in all the subsequent results with increasing FUV flux levels and so these remarks will not be repeated in the later sections).

The mass finally contained in the high density core is lower than that in the same Cloud Type 4 in Model E, as shown in Figure 7.7. The value of the normalised core mass η is lower at 0.6% than that found in a zero FUV radiation field where $\eta = 0.9\%$. This means that a less massive seed is formed under a background FUV radiation flux of $1G_0$ than that formed with no FUV radiation which may be explained by the photo-evaporation effect of the FUV radiation on the cloud's outer layers. However seed formation is quicker at 1.98 Myrs under the $1G_0$ radiation flux than in Model E which needs 3 Myrs.
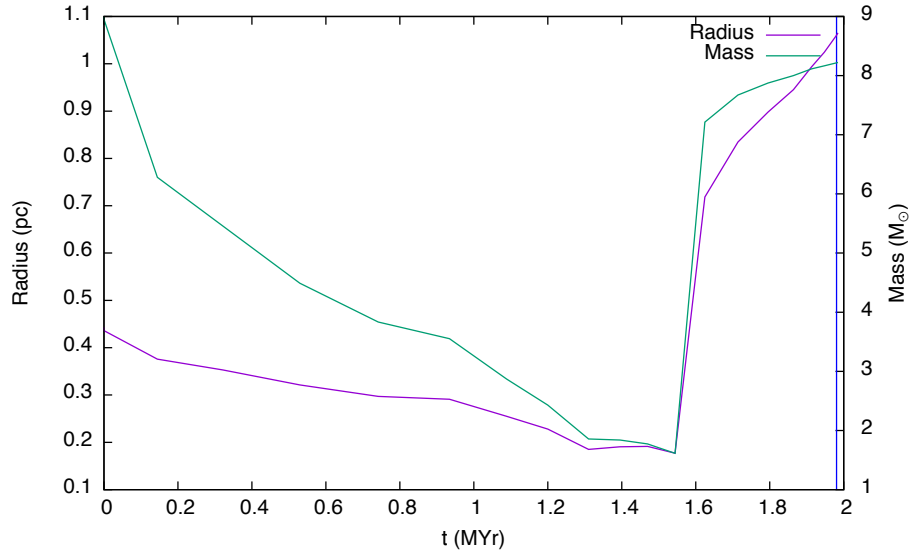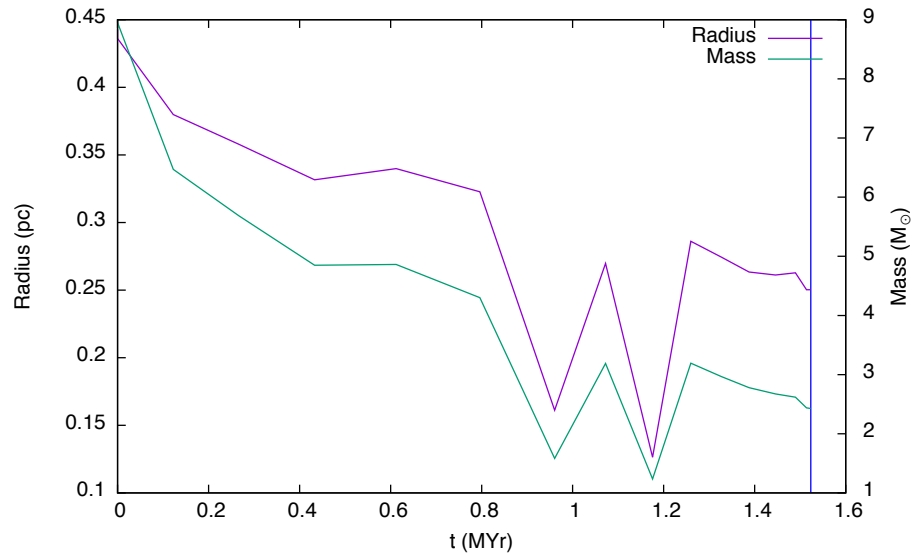
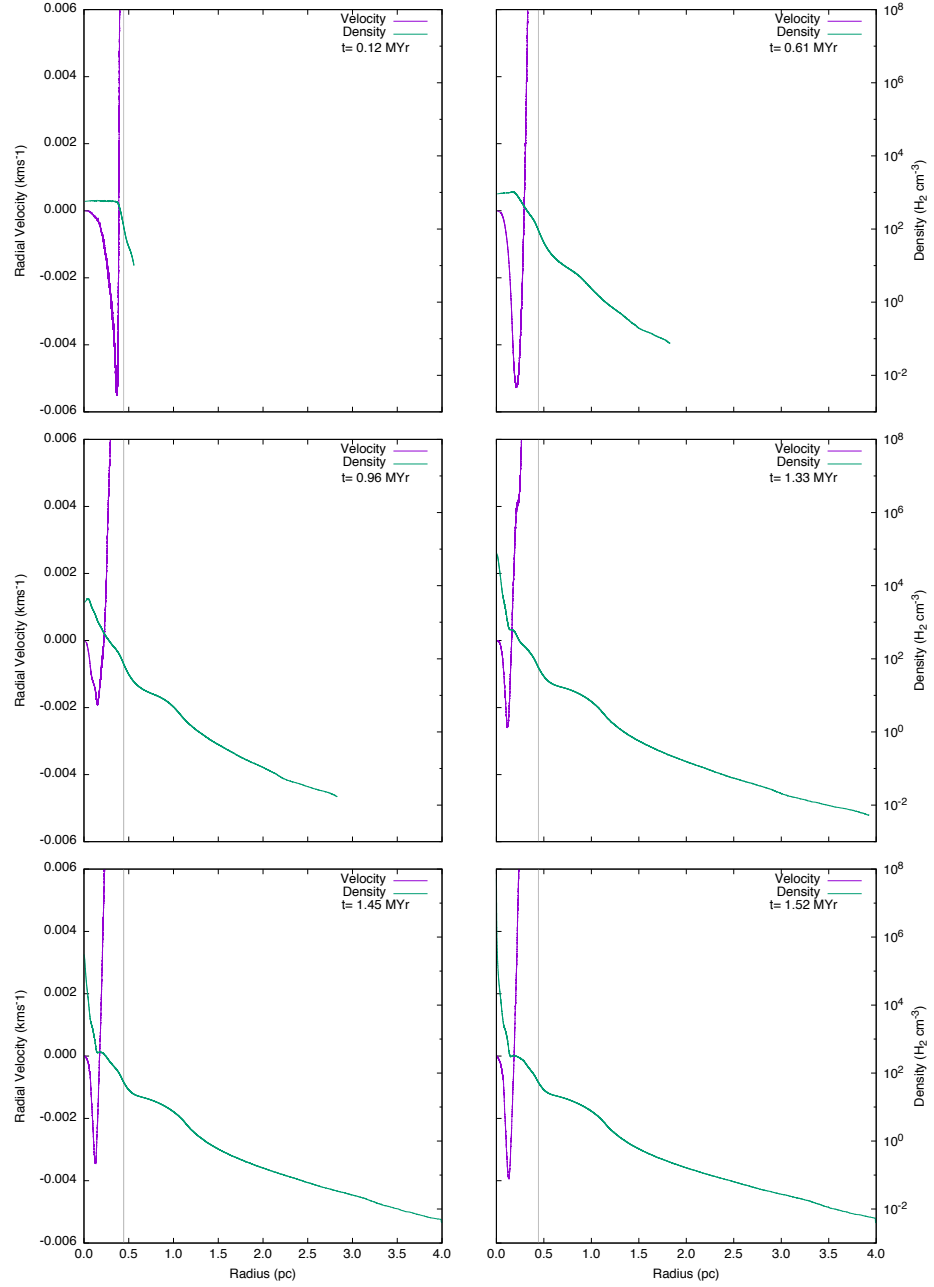Figure 7.2: Set 1G$_0$: The evolution of the mass and radius of Cloud Type 4 ($n_i = 500$ cm^{-3}) with an initial mass of 9 M$_\odot$. The grey vertical line shows the initial radius of the cloud.

7.4.3 THE GENERAL FEATURES

Plots of the evolution of the other molecular clouds of different densities can be found in Appendix B.1, they follow a qualitatively similar path to Cloud Type 4. A two stage evolution of the total cloud mass are clearly seen in almost all of the clouds. Firstly there is an initial cloud mass loss due to the early dominance of the photo-evaporation effect of FUV radiation in the outer layer of a cloud and subsequently there is mass recapture due to the dominance of the shock effect on the inner part of the cloud in the later stages of evolution. The mass recapture rate (M$_{cloud}$/MJM) decreases with increasing initial density of the cloud after the first stage of the process when photo-electric evaporation is dominant, it is 94% at $n_i = 50$cm^{-3} dropping to 37% at $n_i = 10^4$cm^{-3}.

The dominant photoelectric heating effect decreases with the increasing initial density, as described in Equation (3.4). The heating of the outer layers at the initial evolutionary stage triggers a shock wave propagating toward the centre is seen in every cloud by the inward radial velocity built up at the surface. The shock velocity also decreases with the initial density, which is 0.15 kms^{-1}, driven by a temperature difference of 107K at $n_i = 50$cm^{-3}, and 0.16 ms^{-1} driven by a temperature difference of 30K at $n_i = 10^4$cm^{-3}. The inward velocity in the warmer envelope in the later evolutionary stage also decreases with increasing initial density, the maximum v_{inward} is 1.75 kms^{-1} at $n_i = 50$cm^{-3} and almost zero in a cloud of $n_i > 500$cm^{-3}, due to the low efficiency of the photo-evaporation effect in a cloud of high initial density. Wherever the inward

132

velocity peaks the density is very low, so that it would not produce a significant effect on the dynamic behaviour of the cloud core which is finally formed.

However, no matter how much mass is included in a cloud, the formation of the high density seed is definite. When the initial density increases from 50 to 10^4cm^{-3}, the time for the seed formation decreases from 4.66 to 0.24 Myrs, both of which are almost half of the collapsing time for the corresponding molecular clouds under zero FUV radiation (in Model E). This may be attributed to the combination of higher MJMs and the FUV radiation induced shock effect in this set of simulations.

The variation of the normalised core mass (η) as a function of the initial density of the clouds is described in Figure 7.7. It is obvious that η increases with the initial density due to the higher initial gravitational potential which keeps more mass in the seed for the possible future star formation. On the other hand, η is lower in almost all of the cloud types than that in Model E due to the $1G_0$ FUV radiation induced photo-evaporation causing loss of mass.
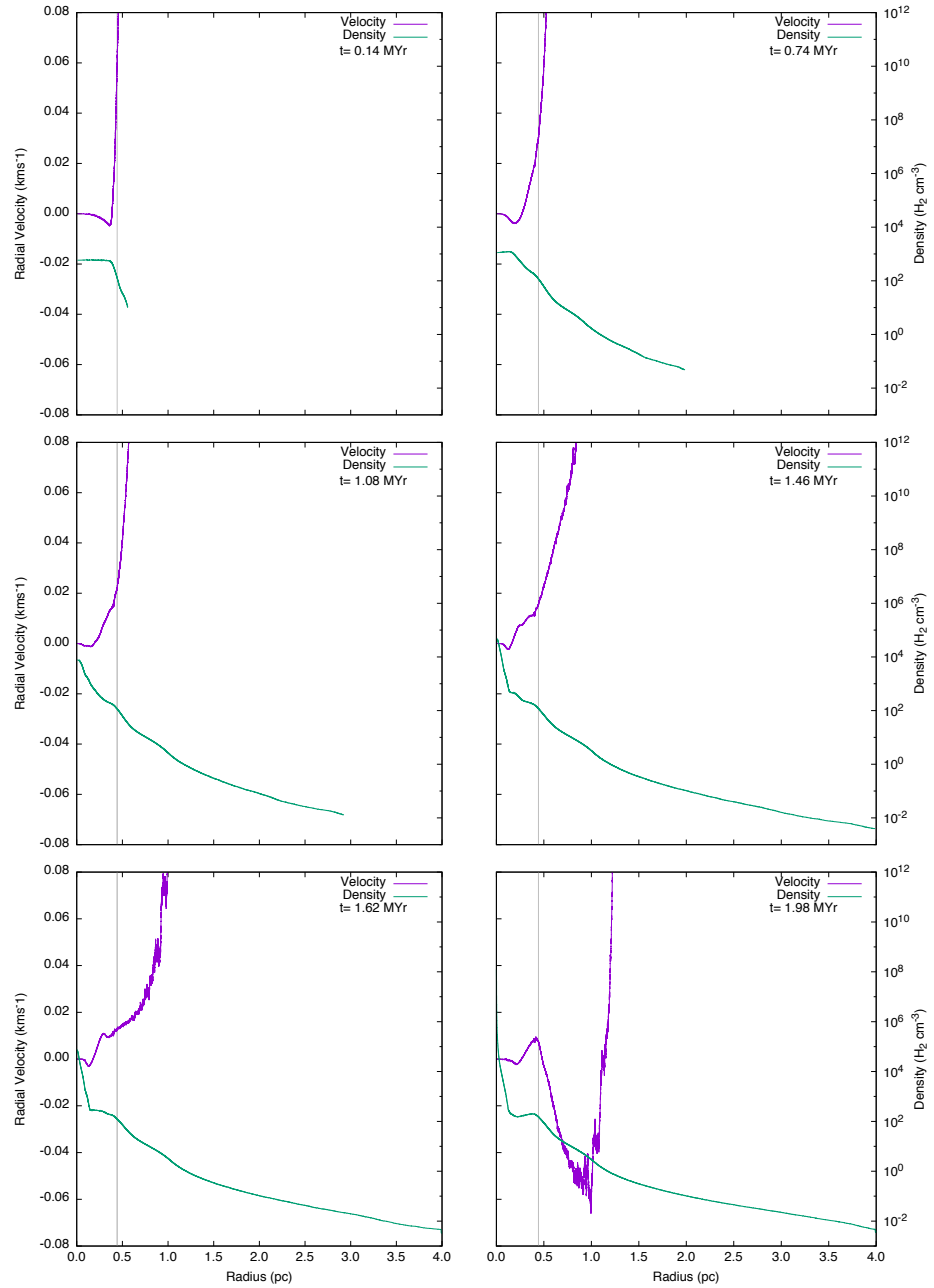
Figure 7.3: Set 1G$_0$: Mean density and mean radial velocity snapshots over radial distance of Cloud Type 4 ($n_i = 500$ cm^{-3}) with an initial mass of 9 M$_\odot$. The grey vertical line shows the initial radius of the cloud.
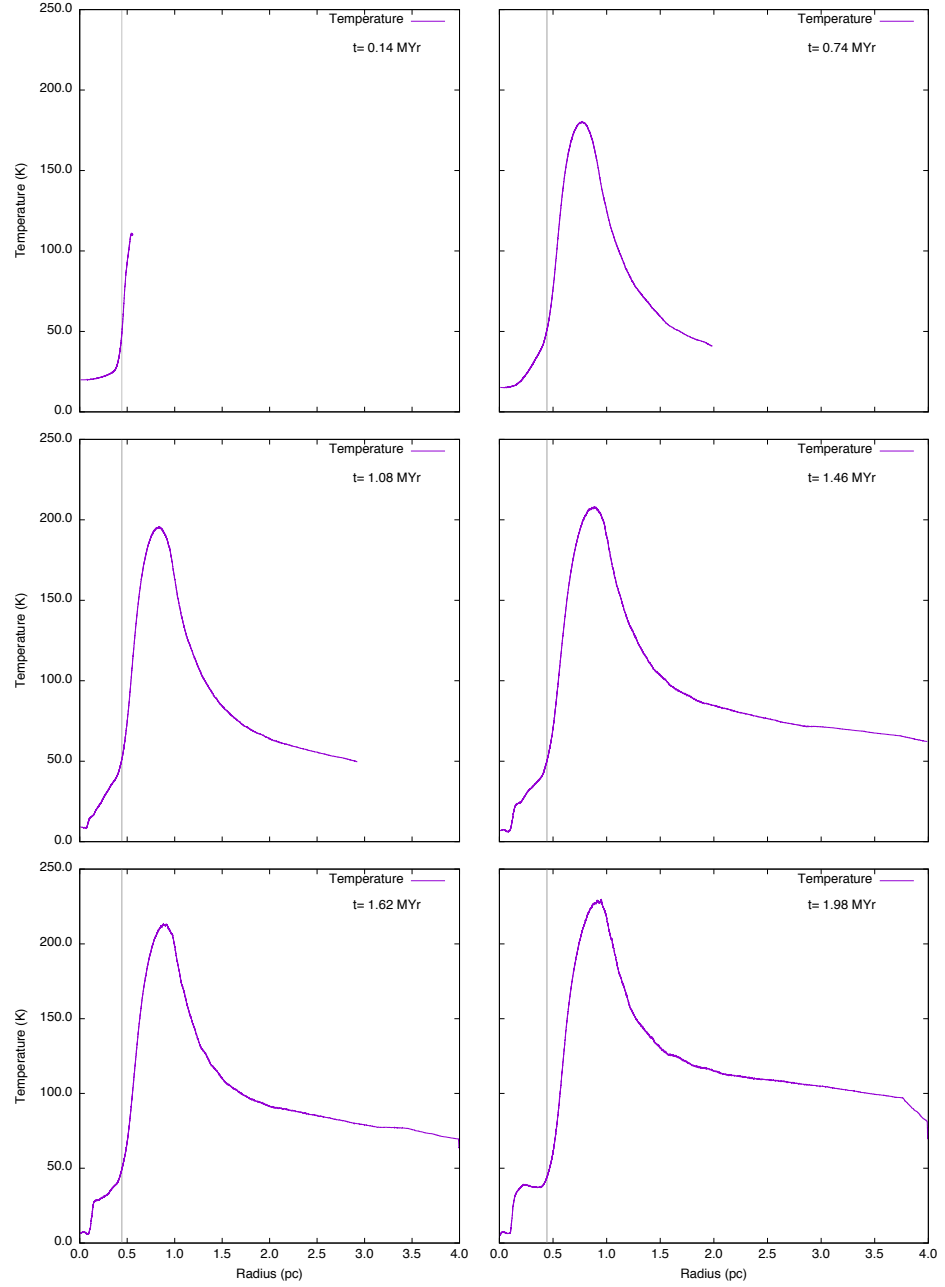
Figure 7.4: Set 1G$_0$: Mean temperature distribution and the radial distance snapshots of Cloud Type 4 ($n_i = 500$ cm^{-3}) with an initial mass of 9 M$_\odot$. The grey vertical line shows the initial radius of the cloud.
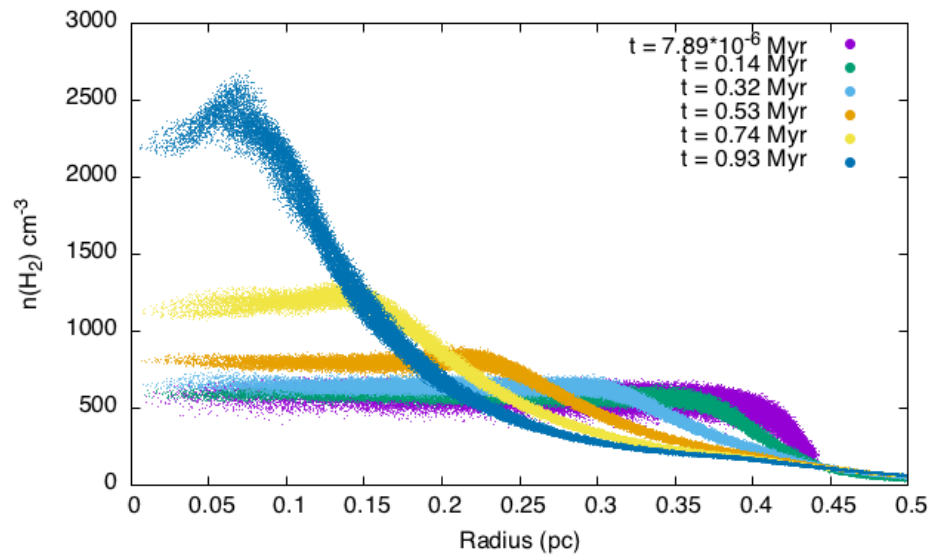
Figure 7.5: Set $1G_0$: Initial density $n_i = 500$ cm^{-3}and mass of 9 M$_\odot$. Evolution of cloud density with radius. Each dot in the plot for each time step represents one SPH particle. Each particle is shown for the first six time steps.
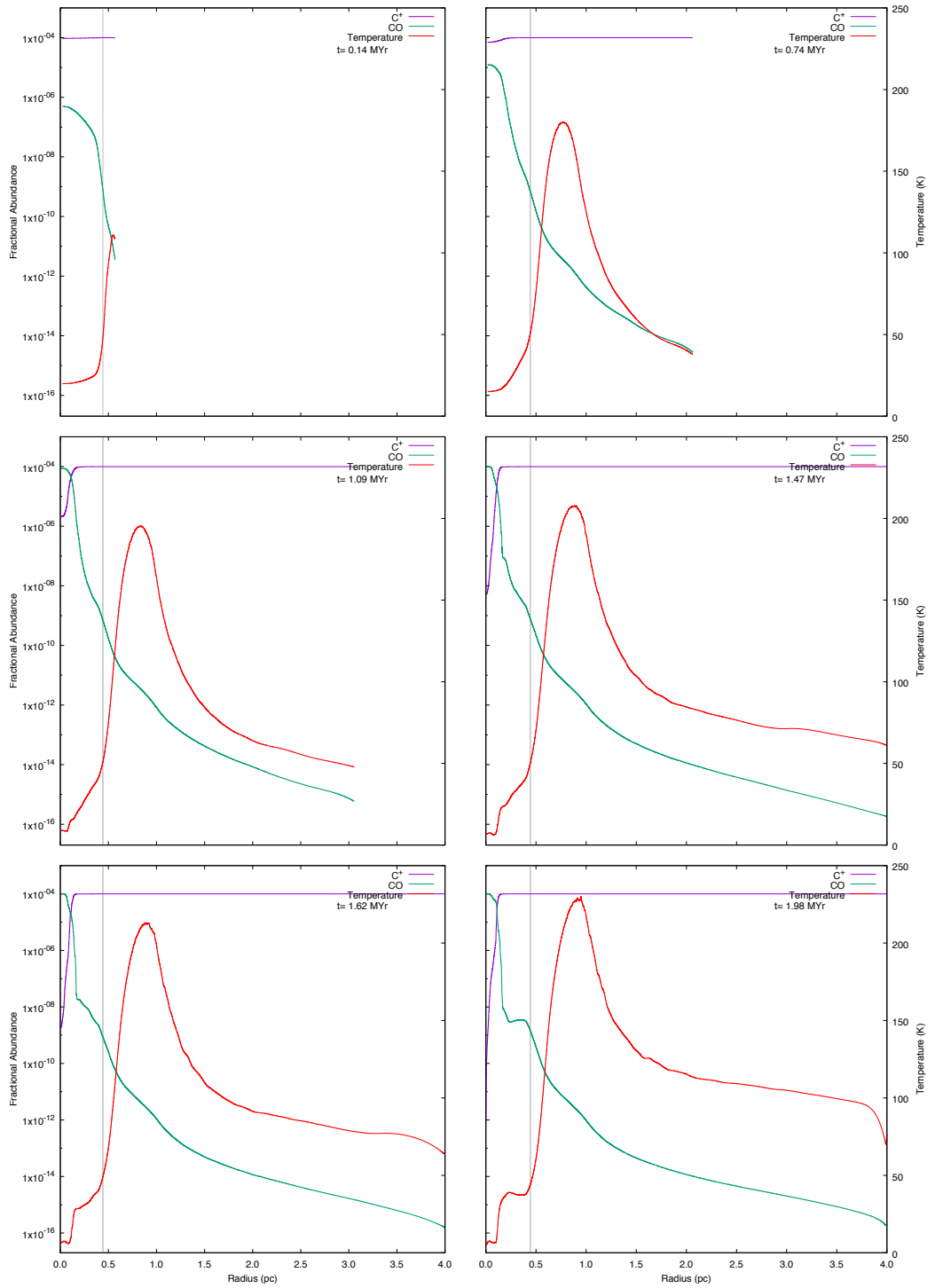
Figure 7.6: FUV radiation = 1 G_0: six snapshots showing the chemical abundances of CO and C^+ for a cloud with an initial density of 500 cm^{-3}, a mass of 9 M$_\odot$ and a radius of 0.44 pc.
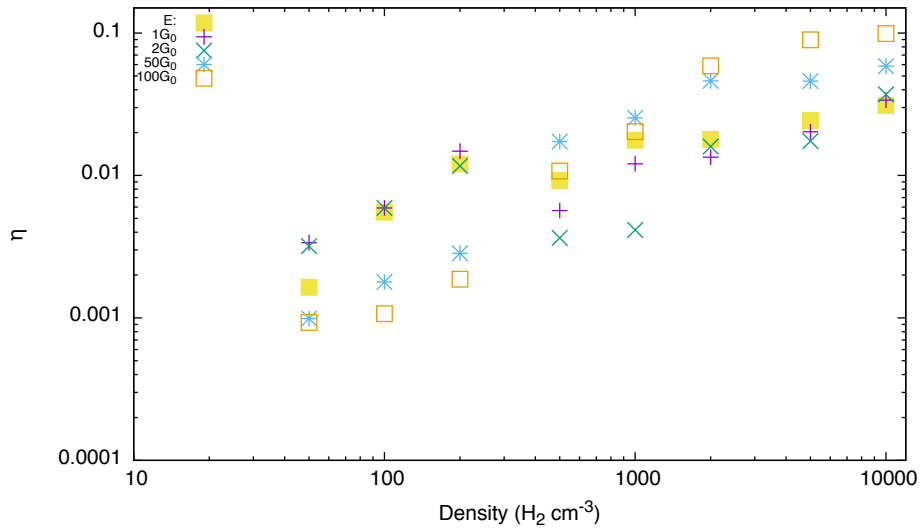
Figure 7.7: The ratio (η) of the mass of the core to the initial cloud mass (MJM) for different strengths of FUV. The criterion for the collapsing point is set at a particle density of $\geq 10^7$ cm^{-3}. Model E is included as a baseline to be able to make comparisons with Figure 6.1.

7.5 Evolution of clouds under FUV Flux of 2G$_0$

7.5.1 The MJMs variation of n_i

When the FUV flux is 2G$_0$, the variation of the MJMs with n_i as shown by the green multiplication symbols for different Cloud Types 1 to 8 are not significantly different from those under 1G$_0$ series of simulation as shown by the purple cross symbols in Figure 7.1.

The variations of MJMs with n_i in this set of simulations can be fitted into a power law of

$$M_{MJM} = 909.7 \, n_i^{-0.75} \text{M}_\odot \tag{7.3}$$

which means that an increase of FUV radiation flux by one Habing unit is not sufficient to change the minimum initial mass of a collapsing cloud significantly. Due to the small difference in the MJMs obtained between the two sets of simulations with G$_0$ = 1 and G$_0$ = 2, the discussion on the evolution of Cloud Type 4 and the general features in the sections 7.5.2 - 7.5.3 will only concentrate on the differences in the evolution of the physical properties. Due to the similar MJMs at each of the eight different initial densities, these differences can be attributed to the increase in FUV radiation flux.

7.5.2 The Evolution of Cloud Type 4

Although the MJM of the Cloud Type 4 is the same as that under 1G$_0$ FUV radiation flux, i.e., 9 M$_\odot$, the differences in the features of its evolution are however not negligible.

It may be seen in Figure 7.8 that after the initial stage of mass loss at $t = 1.18$ Myrs (1.55 Myrs for 1G$_0$) the mass within the cloud then varies with time in an oscillatory pattern, that is the whole cloud changes between expansion and contraction in a quasi-periodic way. The maximum mass capture rate is 33% and the minimum is as low as 13%. It is obvious that the 2G$_0$ FUV radiation flux removes more material than the 1G$_0$ flux. This is different to the situation under 1G$_0$ FUV radiation where the cloud mass keeps a stable value of 80% of its MJM, at the time when the centre high density core forms.

Due to the higher FUV radiation flux, the heating at the very beginning of the evolution in Cloud Type 4 is stronger than that in 1G$_0$, as shown in Figure 7.10 the mean surface temperature rises to 130K within 0.12 Myrs. In comparison in the

$1G_0$ simulation it rises to about 110K within 0.14 Myrs. The greater temperature difference triggers a stronger shock propagating into the centre of the cloud, there is a higher inward velocity of 5.5 ms^{-1} at t = 0.12 Myrs compared to 4.9 ms^{-1} at t = 0.14 Myrs in the $1G_0$ simulation. This stronger shock effect may be seen in the density distributions during the first 0.80 Myrs in Figure 7.11. It shows that the peak density at the shock front reached 800 cm^{-3} at t = 0.43 Myrs in the $2G_0$ simulation, but the same peak density appeared at t = 0.53 Myrs in the $1G_0$ simulation shown in Figure 7.5. Consequently the Cloud Type 4 under $2G_0$ FUV radiation flux collapses in the shorter time of 1.52 Myrs than the 1.98 Myr in the $1G_0$ simulation.

As more material is evaporated by the photoelectric effect than in $1G_0$ simulation, it is not surprising to see a lower η value of 0.35% in Figure 7.7 in this simulation than that seen in the $1G_0$ simulation.

7.5.3 THE GENERAL FEATURES

The obvious two stage evolution of the cloud mass, similar to that seen in the $1G_0$ simulations, is seen in molecular clouds with initial densities of 50 and 100cm^{-3} and the quasi-periodic change of cloud mass with time is seen in higher initial density clouds. The mass capture ratio is lower than that for the clouds in the $1G_0$ simulations by an average of 4% due to the higher FUV radiation flux. It also decreases with the initial density of a cloud.

The maximum surface temperature of a cloud reached during a very short period of initial heating by the photo-electric effect decreases with the initial density. It reaches, for example, 172K at an initial density of 50cm^{-3} and falls to 51K when the initial density of a cloud is 10^4cm^{-3}. The corresponding surface temperatures for the $1G_0$ simulations were 170K and 37K.

Driven by the temperature or pressure gradient between the surface of the cloud and its cool interior, the maximum shock velocity achieved decreases with the initial density of the cloud. This is $0.14\,\mathrm{kms}^{-1}$ at $n_i = 50$cm^{-3} and $0.14\,\mathrm{ms}^{-1}$ with $n_i = 10^4$cm^{-3} which are higher than the values reached in the corresponding clouds in $1G_0$ simulations, 0.15 kms^{-1} and 0.16 ms^{-1} respectively. The high density core formation time is 4.11 and 0.24 Myrs for $n_i = 50$ and 10^4cm^{-3} respectively, which is shorter than 4.6 and 0.25 Myrs in the $1G_0$ simulation.

The much higher inward velocity in the extremely low density and warm envelope would not significantly affect the dynamic evolution of the central region of cloud where a seed could form, therefore it can be neglected.

Finally the mass left in the high density core varies with initial density in a similar way to that in $1G_0$ simulations, as shown in Figure 7.7, the value of the ratio of the

core mass to the corresponding MJM of a cloud is lower than that in 1 G_0 simulations, although the difference is smaller at both low and high initial densities than that in the intermediate initial densities.

Overall it can be concluded that the $2G_0$ FUV radiation flux drives off more material from the surface of a cloud by photo-evaporation, and decreases the 'efficiency' of the potential star formation, but the induced shock effect can accelerate the process of the collapse of a cloud with the densities under study.

Figure 7.8: Set $2G_0$: The evolution of the mass and radius of Cloud Type 4 (n_i = 500 cm^{-3}) with an initial mass of 9 M$_\odot$.

Figure 7.9: Mean density and mean radial velocity snapshots over radial distance of Cloud Type 4 ($n_i = 500$ cm^{-3}) with an initial mass of 9 M$_\odot$ in Set 2G$_0$. The grey vertical line shows the initial radius of the cloud.
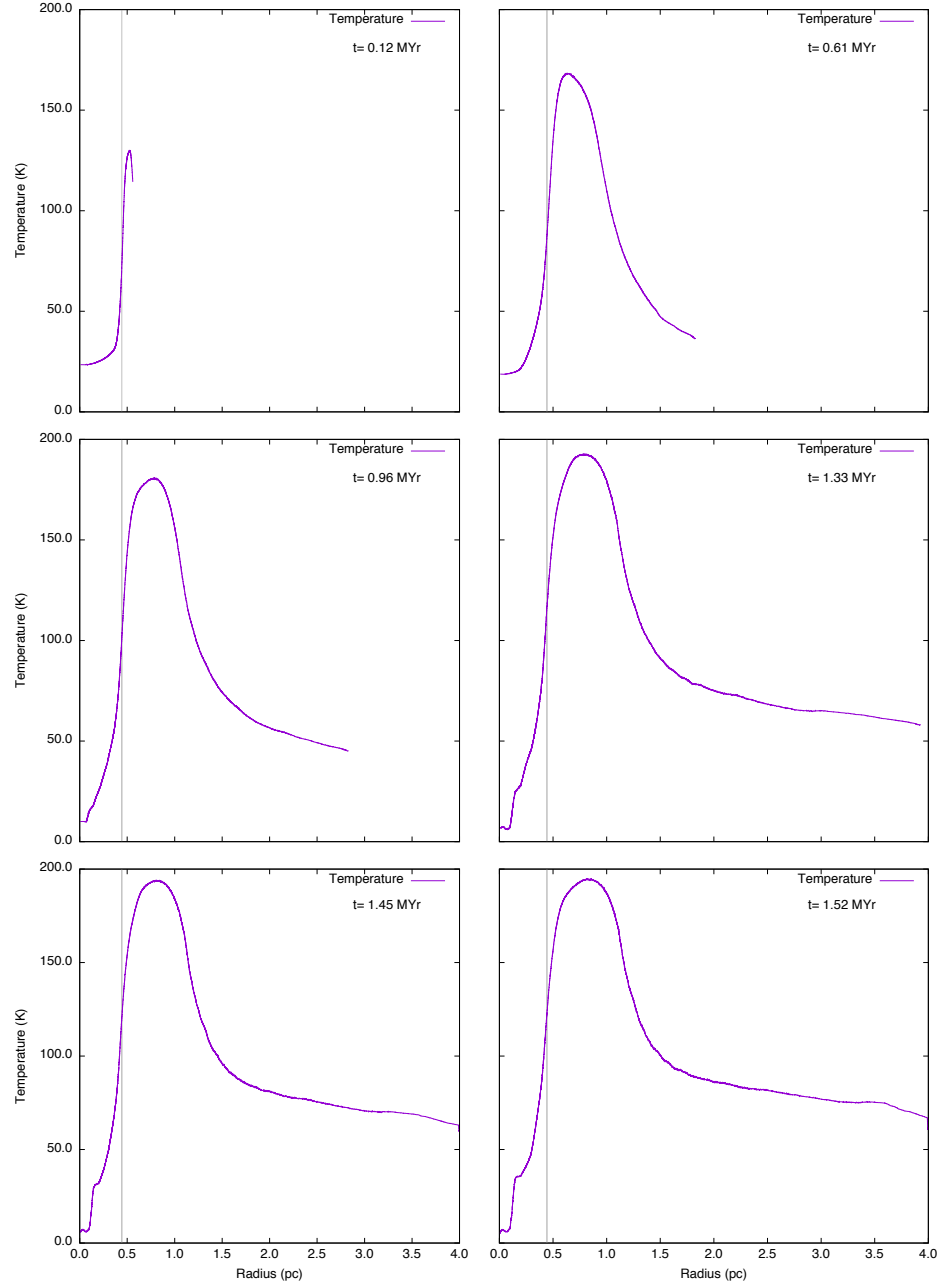
Figure 7.10: Set 2G$_0$: Mean temperature distribution and the radial distance snapshots of Cloud Type 4 ($n_i = 500$ cm^{-3}) with an initial mass of 9 M$_\odot$. The grey vertical line shows the initial radius of the cloud.
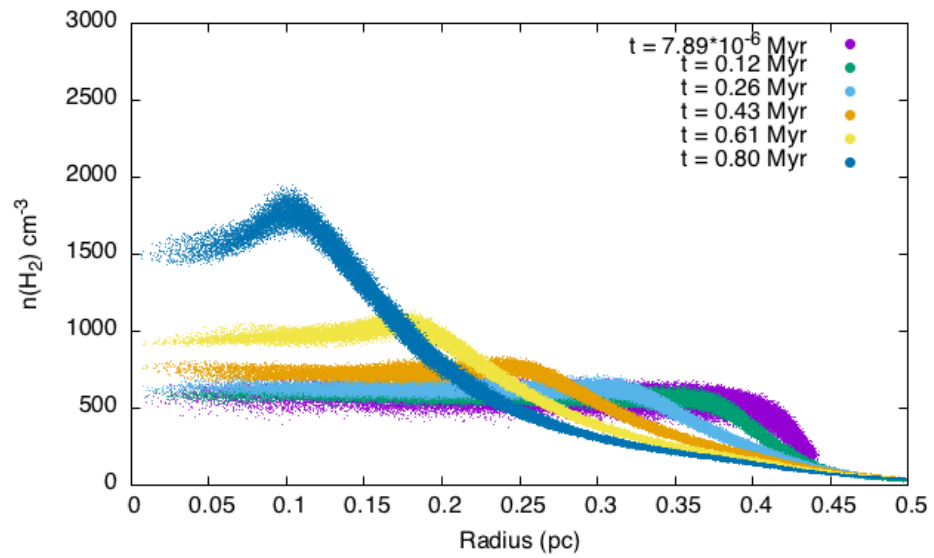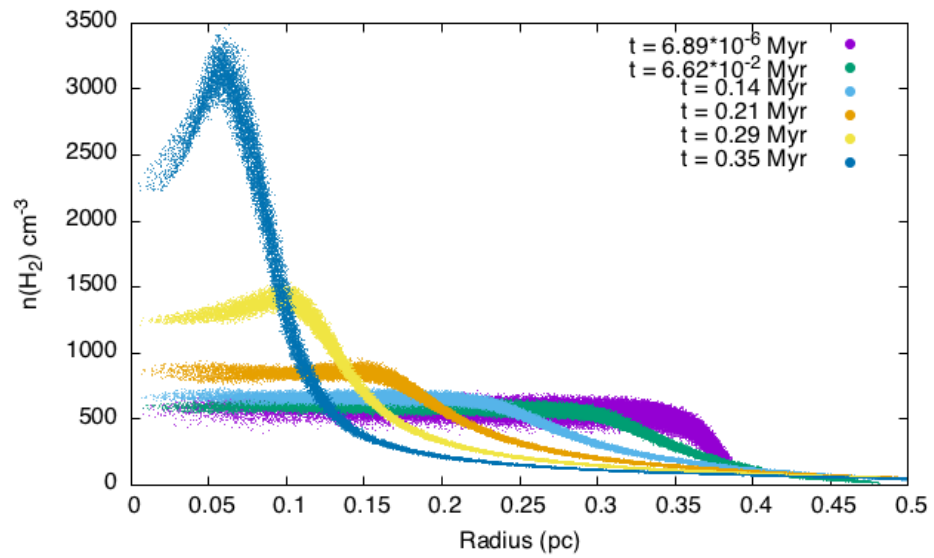
Figure 7.11: Set 2G$_0$: Initial density n$_i$ = 500 cm^{-3}and mass of 9 M$_\odot$. Evolution of cloud density with radius. Each dot in the plot for each time step represents one SPH particle. Each particle is shown for the first six time steps.
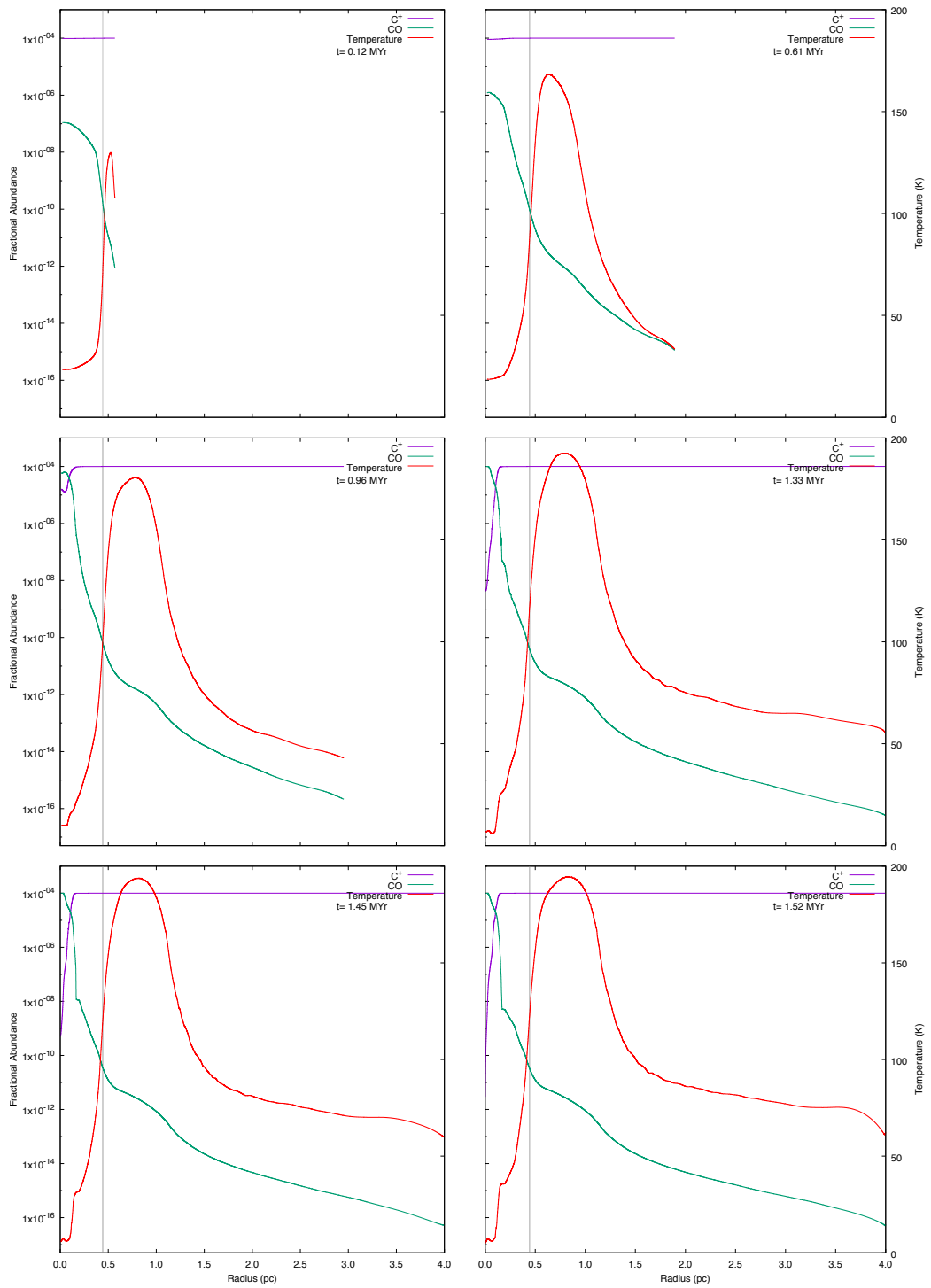
Figure 7.12: FUV radiation $= 2\ \mathrm{G_0}$: six snapshots showing the chemical abundances of CO and $\mathrm{C^+}$ for a cloud with an initial density of 500 cm^{-3}, a mass of $9\ \mathrm{M_\odot}$ and a radius of 0.44 pc.

7.6 EVOLUTION OF CLOUDS UNDER FUV FLUX OF 50G$_0$

7.6.1 THE MJMS VARIATION OF n_i

When the flux is 50G$_0$, the variation of the MJMs with n_i, which are shown with the blue stars in Figure 7.1, covers a much wider range, $1123 \leq$ MJM ≤ 0.7 M$_\odot$ for $50 \leq n_i \leq 10^4$ cm^{-3}, than in the previous two sets of simulations with lower (1G$_0$ and 2G$_0$) FUV fluxes.

The variations of the MJMs with n_i in this set of simulations can be fitted into a power law of

$$M_{MJM} = 1.47 \, n_i^{-1.47} (10^5) \, \text{M}_\odot. \tag{7.4}$$

The gradient of the line $k = 1.47$ is much higher than 0.73 in the previous two sets of simulations, which implies that at low initial densities such as $n_i = 50$ and 100 cm^{-3} the photo-evaporation rate is very high. This means that clouds of these two densities requires much higher initial masses of 1123 and 249 M$_\odot$ to be able to collapse than is the case under low FUV radiation, for example at 2G$_0$ the masses needed are only 59 and 25 M$_\odot$. However when $n_i \geq 500$ cm^{-3} the shock effect induced by the FUV radiation starts taking over from the photo-evaporation effect in determining the evolution of a cloud. The MJM values are 6, 2, 0.8, 0.7 and 0.7 M$_\odot$ for $n_i \geq 500$ cm^{-3}, much lower than that in both 1G$_0$ and 2G$_0$ FUV radiation simulations where they are 9, 8, 2, 2 and 0.9M$_\odot$ respectively in the 2G$_0$ simulations.

Therefore under 50G$_0$ FUV radiation, the photo-evaporation effect of the FUV radiation dominates the evolution of a cloud of $n_i < 500$ cm^{-3}, as a result MJM is higher than that under zero and lower FUV radiation. When $n_i \geq 500$ cm^{-3}, the shock effect dominates the evolution of a cloud, so the MJM is lower than that under zero and the lower values of FUV radiation.

7.6.2 THE EVOLUTION OF CLOUD TYPE 4

From the first panel of Figure 7.15, it is interesting to see that the photo-electric heating heats through the whole cloud quickly in the very short period of time of 0.07 Myrs, with the central temperature being higher than the initial temperature of 60K. However due to the strong attenuation of the FUV radiation while it propagates towards the centre,

the heating effect becomes very much weakened quite quickly resulting in a temperature difference of 70K between the surface and the centre. The resulted pressure gradient helps drive a shock moving to the centre of the cloud, with a peak velocity of about 6 ms^{-1} as shown in the first panel of Figure 7.14 although the density structure has not yet any seen essential change.

At $t = 0.29$ Myrs, the density in the central region increases to around 10^3 cm^{-3}, and molecular cooling starts playing an important role, the temperature in the central region decreases to 60K, as shown in the second panel of Figure 7.15. The increased temperature difference of $190 - 60 = 130$K at 0.29 Myrs drives a stronger shock wave moving toward the centre. In the following panels of Figure 7.15, the temperature difference further increases to $190 - 20 = 170$K at $t = 0.41$ Myrs when the central density rises to 10^4 cm^{-3}. The chemical cooling further decreases the central temperature to less than 10K and the central density finally becomes $> 10^7$ cm^{-3} as shown in the final panel of Figure 7.14. The density distribution by the SPH particles raw data in Figure 7.16 also shows a detailed propagation process of the shock wave into the cloud during the first 0.35 Myrs.

Because the high FUV radiation flux and the low MJM, the evolution of the mass of the cloud monotonically decreases with time as shown in Figure 7.13, while the shock causes the central density to rise to a value of 10^4 cm^{-3} at $t = 0.41$ Myrs. After that, the mass of the cloud is then kept stable without any further loss during the next 0.15 Myrs until the central density is higher than 10^7 cm^{-3} when the high density seed forms at $t = 0.56$ Myrs as shown in Figure 7.14.

From Figure 7.7, it is seen that the at $n_i = 500$cm^{-3}, the ratio of the core mass to MJM is higher than that in both 1 and 2 G$_0$ simulations.

7.6.3 THE GENERAL FEATURES

From the evolution of the temperature profiles in clouds of initial density of 50 and 100 cm^{-3}, as shown in Appendix B.59 and B.63, it is very interesting to find that the FUV radiation flux of 50G$_0$ penetrates the whole molecular cloud very quickly so that the temperature inside the two clouds reaches about 180K in 0.13 and 0.1 Myr respectively. Also the temperature gradient points outward, which results in a thermal pressure gradient inside the clouds against the gravity direction. However as shown in B.58 and B.62 in the Appendix, an inward velocity of 0.2 kms^{-1} and 35 ms^{-1} at the surface of the clouds is seen at the surface of the two clouds at t $= 0.13$ and 0.1 Myr, as the initial gravitational binding of the two clouds is strong enough to overcome the outward thermal pressure force, due to extremely high initial mass of 1123 and 249 M$_\odot$ respectively. Therefore part of the gas is pushed toward the centre at the same time

that a large quantity of gas is evaporated.

In the following evolutionary stages, the inward velocity is not only seen near the centre of the clouds but also in the evaporating outer layers, where the density is very low so these outer layers would not play important role in the evolution of the main part of the clouds. After the central density increases, molecular cooling then plays an important role to bring the central temperature down to a few degrees Kelvin, i.e., a negative thermal difference is created which accelerates the formation of the central high density core as shown in the following panels of B.58 and B.62 in the Appendix. The central density in the in two clouds gradually increases to $> 10^{10}$ cm^{-3} until a high density core forms.

The mass evolution of the two clouds of initial low densities show a two stage evolution path. The evaporating stage stops at $t = 4.7$ and 4.3 Myrs respectively and the mass of the cloud keeps a stable value. The mass in the high density core however is a few times lower (0.1% and 0.2% respectively) than in the same type of cloud under lower FUV radiation as shown in Figure 7.7.

For a cloud of initial density 1000 cm^{-3} the difference starts at the beginning of the evolution. This can be determined by the temperature distribution displayed in B.71 in the Appendix which may be interpreted as being due to the FUV radiation being unable to penetrate into the whole cloud, because the high initial density results in a high optical depth, as it does in the clouds with lower initial densities. Instead a hot surface with temperature of 195K and a cooler central region with a temperature of 49K creates a negative thermal pressure gradient, which points in the same direction as the gravitational force. Therefore it collapses within the shortest time of 0.18 Myrs and has the highest value of the normalised core mass η of 5.9% in this series of simulations, as described in Figure 7.7.

It is clear that when FUV radiation flux increases to 50 times the interstellar background radiation level, it would penetrate and heat the whole cloud to a uniform temperature within very short time if $n_i < 500$ cm^{-3}. A very high MJMs is needed for a cloud to collapse at the given initial temperature of 60K. Also the efficiency of star formation is lower than in the corresponding clouds under lower FUV radiation. When $500 \leq n_i \leq 1000$ cm^{-3} although the FUV radiation can penetrate through the whole cloud, but with its flux attenuated deep inside the cloud creating a negative temperature gradient so enhancing the chances for the cloud to collapse, a much lower MJM is required. When $n_i > 1000$ cm^{-3}, the FUV radiation can only heat the surface layer of the cloud, which creates a very effective negative temperature gradient and therefore greatly help the star formation in the cloud.

In summary the effect of the FUV radiation is photo-evaporation dominant when

$n_i < 500 \text{ cm}^{-3}$ and is shock dominant $n_i > 500 \text{ cm}^{-3}$.
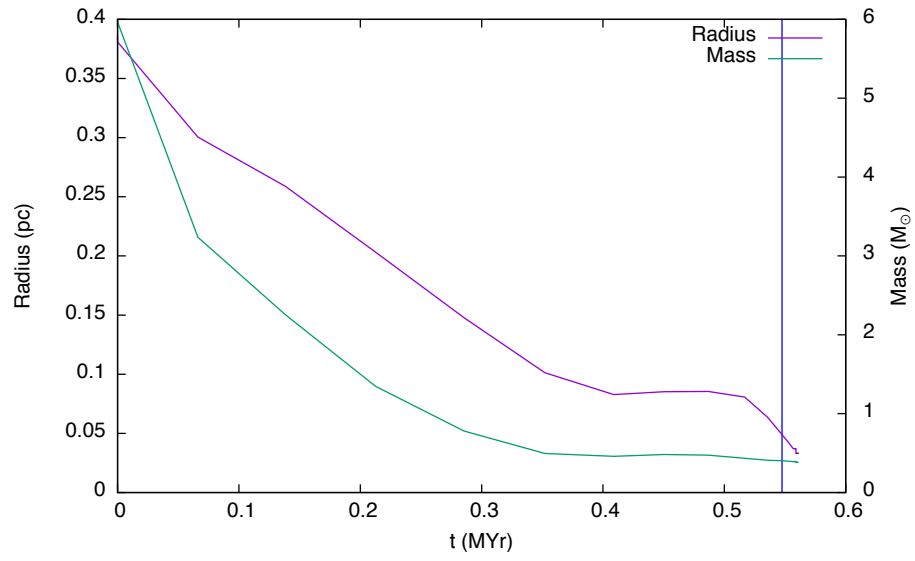
Figure 7.13: Set $50G_0$: The evolution of the mass and radius of Cloud Type 4 $(n_i = 500 \text{ cm}^{-3})$ with an initial mass of 6 $M_\odot$.
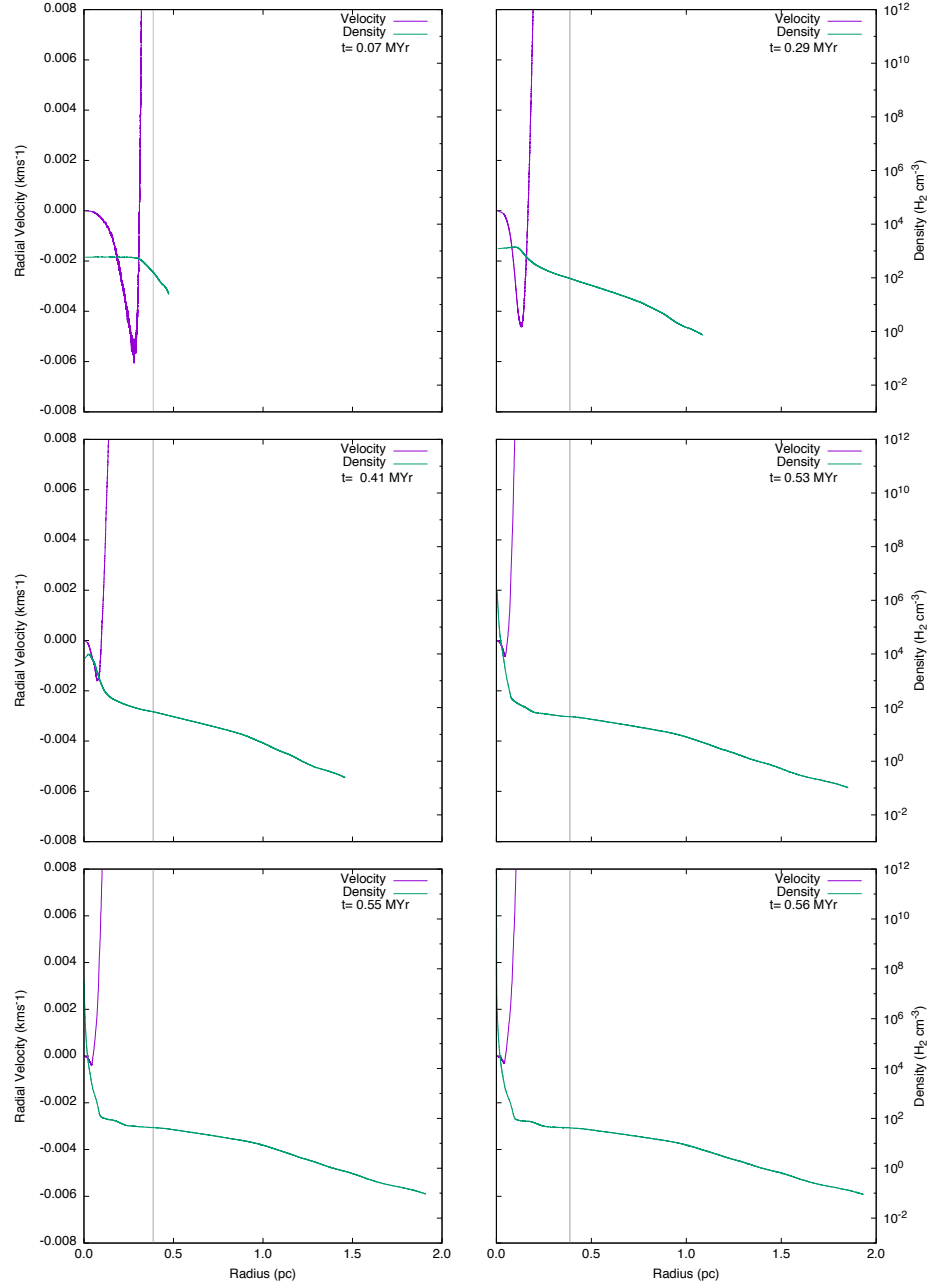
Figure 7.14: Set $50G_0$: Mean density and mean radial velocity snapshots over radial distance of Cloud Type 4 ($n_i = 500$ cm^{-3}) with an initial mass of 6 M$_\odot$. The grey vertical line shows the initial radius of the cloud.
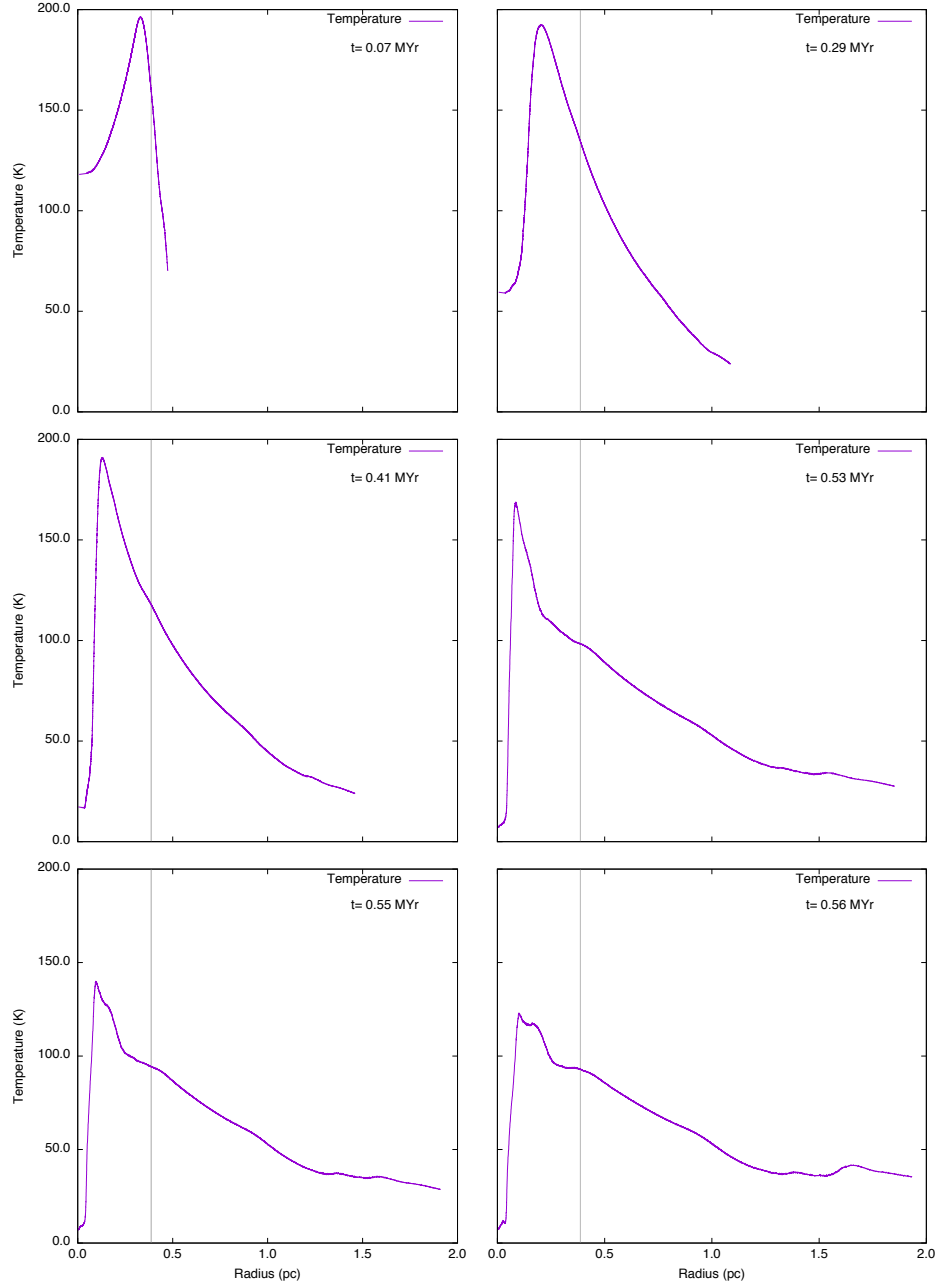
Figure 7.15: Set 50G$_0$: Mean temperature distribution and the radial distance snapshots of Cloud Type 4 ($n_i = 500$ cm^{-3}) with an initial mass of 6 M$_\odot$. The grey vertical line shows the initial radius of the cloud.

Figure 7.16: Set $50G_0$: Initial density $n_i = 500$ cm^{-3} and mass of 6 M$_\odot$. Evolution of cloud density with radius. Each dot in the plot for each time step represents one SPH particle. Each particle is shown for the first six time steps.
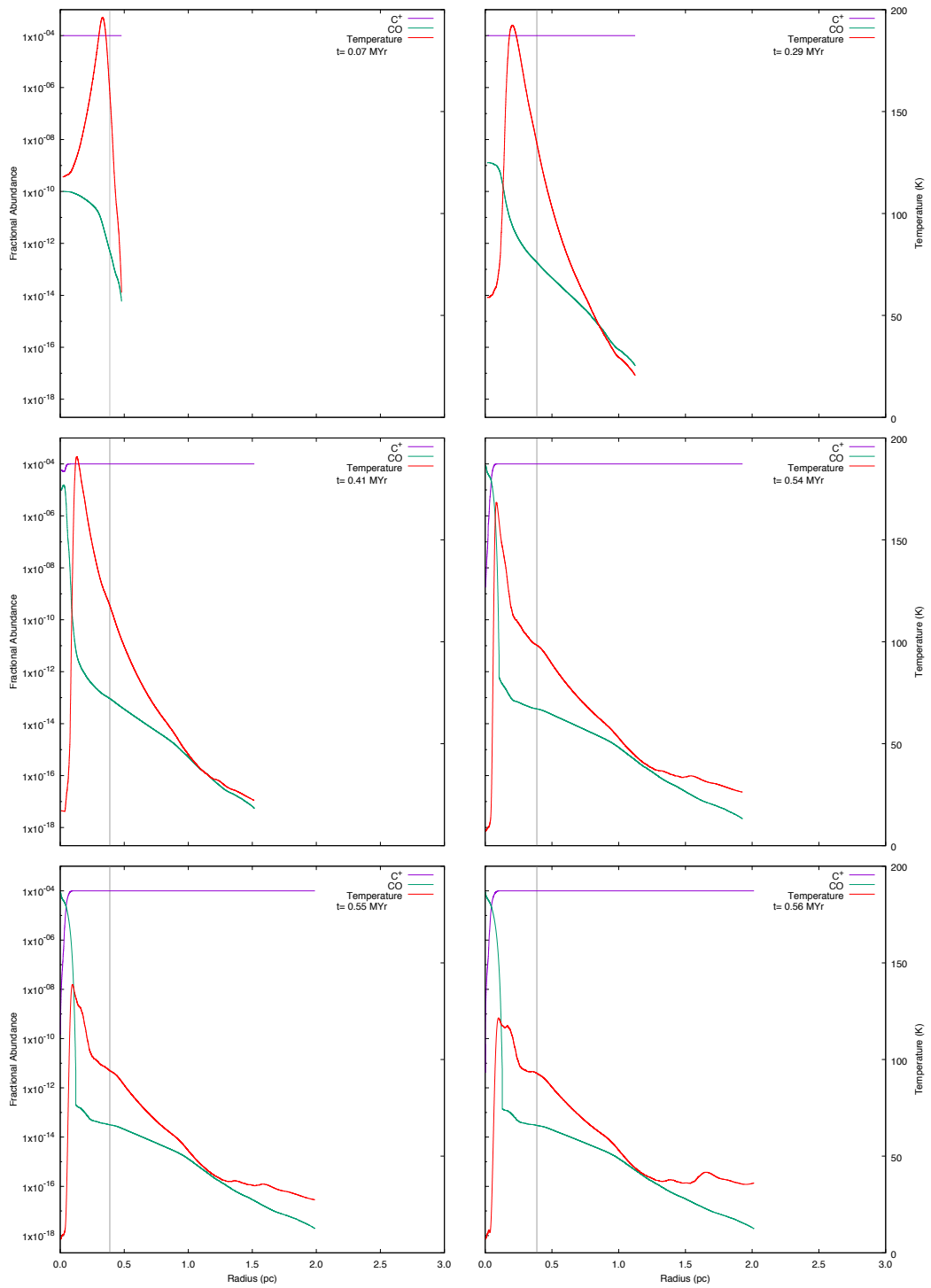
Figure 7.17: FUV radiation = 50 G_0: six snapshots showing the chemical abundances of CO and C^+ for a cloud with an initial density of 500 cm^{-3}, a mass of 6 $M_\odot$ and a radius of 0.39 pc.

7.7 EVOLUTION OF CLOUDS UNDER FUV FLUX OF $100G_0$

In this series of simulations, the FUV flux is twice as strong as that in section 7.6. There are some similarities in the evolution of the physical properties of the clouds to that seen with FUV flux of $50G_0$, so only the differences will be discussed.

7.7.1 THE MJMS VARIATION OF n_i

From Figure 7.1, it is seen that the values of MJMs change from $1367M_\odot$ to $0.4M_\odot$, when n_i varies from 50 to 10^4 cm^{-3}; this is the widest range of MJMs seen among the five series of simulations. The fitted power law can be expressed as

$$M_{MJM} = 8.62 \, n_i^{-1.71}(10^5)M_\odot. \tag{7.5}$$

The gradient of the line of the logarithmic MJM vs n_i has a maximum value of 1.71, which means that the higher the strength of FUV radiation the more dramatic is its effect on the evolution of a cloud. The major effect of FUV radiation at very low initial density is photo-evaporation as the MJM has highest values among all of the four sets of simulations. At a very high density such as 10^4 cm^{-3}, the effect of FUV radiation is shock dominant, so the MJM has the lowest value among the five sets of simulation.

7.7.2 THE EVOLUTION OF CLOUD TYPE 4

The evolution of density, velocity and temperature are shown in Figure 7.18 and 7.19 which are very similar to that of the Cloud Type 4 in the $50G_0$ simulation. The small differences in the quantities are due to the higher FUV radiation to which the cloud is exposed. For example, the maximum temperature reached at the surface is 230K at $t = 0.01$ Myrs which may be compared with 190K reached in the $50G_0$ simulation at a similar time of 0.07 Myrs. Similarly the maximum temperature gradient is 190K obtained at $t = 0.47$ Myrs compared with 180K at $t = 0.41$ Myrs in the $50G_0$ simulation. Therefore the mass evaporation rate is higher than that in the $50G_0$ simulation. As shown in Figure 7.15, 96% of the initial mass of the cloud has been evaporated at $t = 3.33$ Myrs which may be compared with the 93% lost at $t = 0.35$ Myrs in the $50G_0$ simulations.

154

The raw data for the SPH particles shown in Figure 7.21 describes the shock propagation in six snapshots during the first 0.41 Myrs. At $t = 0.41$ Myrs, the central density in the $100G_0$ simulation is 5.93×10^3 cm^{-3} as shown in the 3rd panel of Figure 7.19 but is 10^4 cm^{-3} in the $50G_0$ simulation as shown in Figure 7.14. It seems that the shock propagation into the centre is slower in the $100G_0$ simulation than that in the $50G_0$ simulation, this may be because the Cloud Type 4 has a larger initial radius due to the higher MJM in the $100G_0$ simulation. The collapsing time is 0.57 Myrs, slightly longer than that 0.56 Myrs in the $50G_0$ simulation.

The mass left in the high density core is lower than that in the $50G_0$ simulation, as shown in Figure 7.7 due to the high photo-evaporation rate. The η value is 1% lower than in the simulation of $50G_0$, although it is still higher than that in zero FUV radiation field. The higher MJM and η values seen with the Cloud Type 4 under $100G_0$ than those seen in the zero FUV flux simulations indicate that at $n_i = 500$ cm^{-3} a cloud of $12M_\odot$ at an initial temperature of 60K is at a critical state where photo-evaporation dominancy starts to give way to shock dominancy. This is because when n_i increases to 1000 cm^{-3}, under the same conditions, the MJM is lower and η is higher than in zero FUV field which means the evolution of such a cloud becomes fully shock dominant.

7.7.3 The General Feature of the Evolution of the Clouds

Most of the evolutionary features in the clouds are very similar to those occurring under $50G_0$ radiation. In terms of the evolution of the cloud mass, the only qualitative difference is that the two-stage evolutionary pattern in the mass of cloud only appears in $n_i = 50$ cm^{-3}. For $n_i > 50$ cm^{-3}, the cloud mass evolution is a monotonic function of time before a stable state is reached. Under $50G_0$ simulations, the two-stage pattern appears in clouds with $n_i = 50$ and 100 cm^{-3}. This can be clearly seen by comparing the radial velocity distribution in B.62 and B.90 in the Appendix. No inward velocity in the outer warmer layer is seen at $n_i = 100$ cm^{-3} under $100G_0$, therefore there is no sudden increase of the mass in the cloud after the initial photo-evaporation. This can be understood easily: under the higher FUV radiation of $100G_0$ the evaporation speed of the gas is higher than that in $50G_0$ simulation for the same cloud type of $n_i = 100$ cm^{-3}, in addition the gravity of the core formed later is not strong enough to pull back the evaporated warm mass.

The other difference is that at $n_i > 1000$cm^{-3}, the shock effect of the FUV radiation takes over from the photo-evaporation, even more strongly than that in the same cloud type under $50G_0$ simulation. The η of the high density core formed at the end of the simulation is 10% as shown in Figure 7.7. The core formation efficiency is the
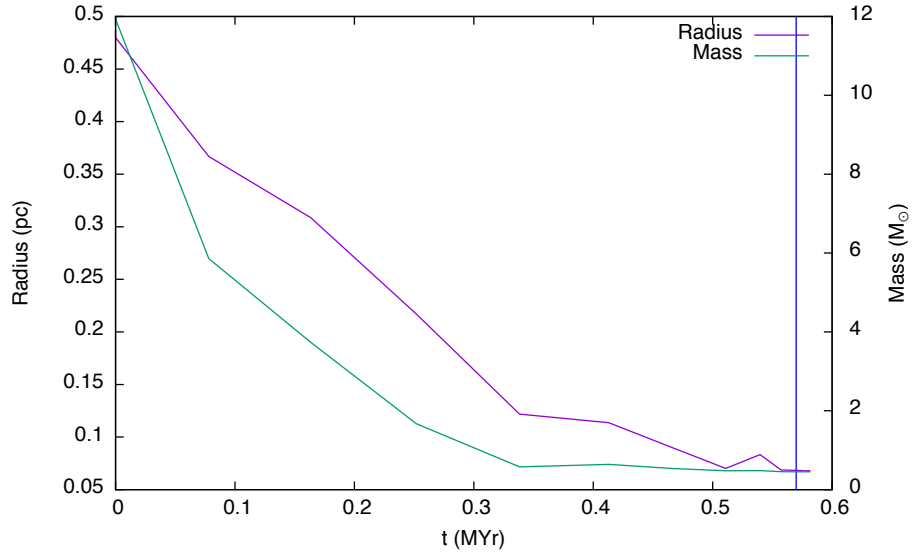
Figure 7.18: Set $100G_0$: The evolution of the mass and radius of Cloud Type 4 ($n_i = 500$ cm^{-3}) with an initial mass of 12 M$_\odot$.

highest seen, not only in the set of simulations under $100G_0$ but also in all of the sets of simulations under different FUV radiation fluxes.

Finally, the photo-evaporation effect of the FUV radiation flux of $100G_0$ dominates the evolution of the low initial density cloud of $n_i < 500$ cm^{-3} and decreases both the probability and the efficiency of star formation with them. The shock effect of the FUV radiation of the same strength dominates the evolution of the high initial density cloud of $n_i > 500$ cm^{-3}, and enhances the probability and efficiency of star formation within it.
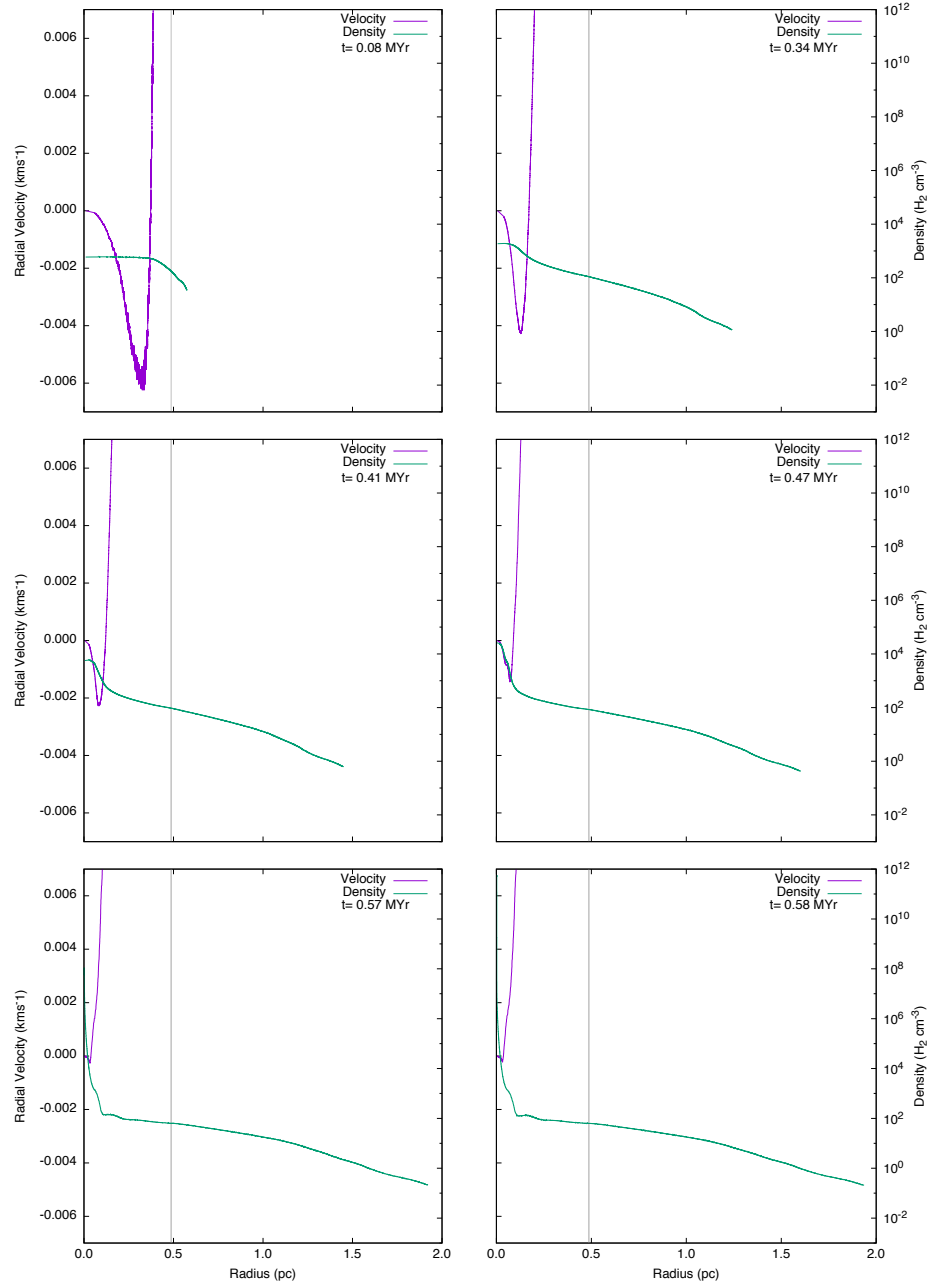
Figure 7.19: Set 100G$_0$: Mean density and mean radial velocity snapshots over radial distance of Cloud Type 4 ($n_i = 500$ cm^{-3}) with an initial mass of 12 M$_\odot$. The grey vertical line shows the initial radius of the cloud.
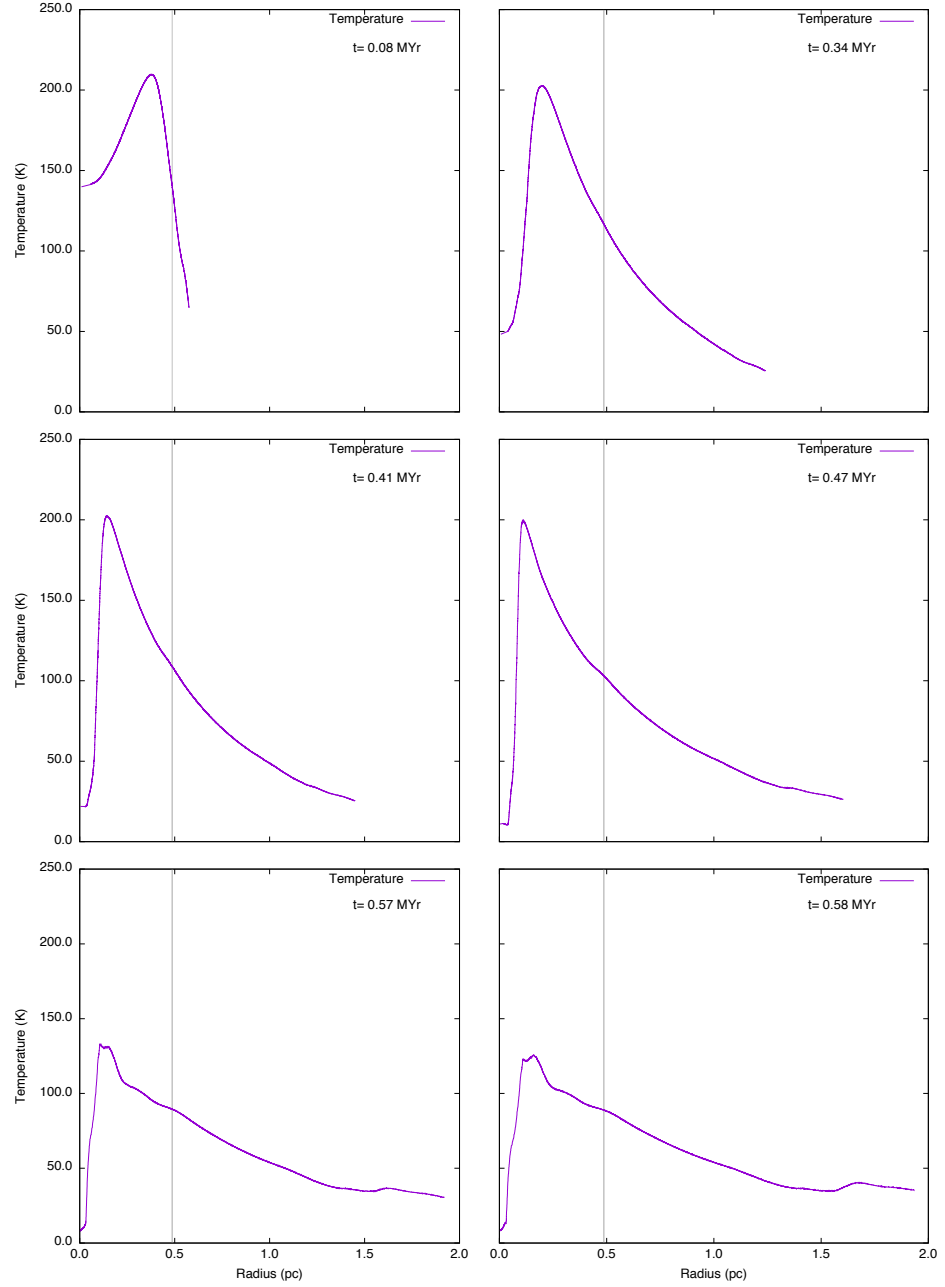
Figure 7.20: Set 100G_0: Mean temperature distribution and the radial distance snapshots of Cloud Type 4 ($n_i = 500$ cm^{-3}) with an initial mass of 12 M$_\odot$. The grey vertical line shows the initial radius of the cloud.
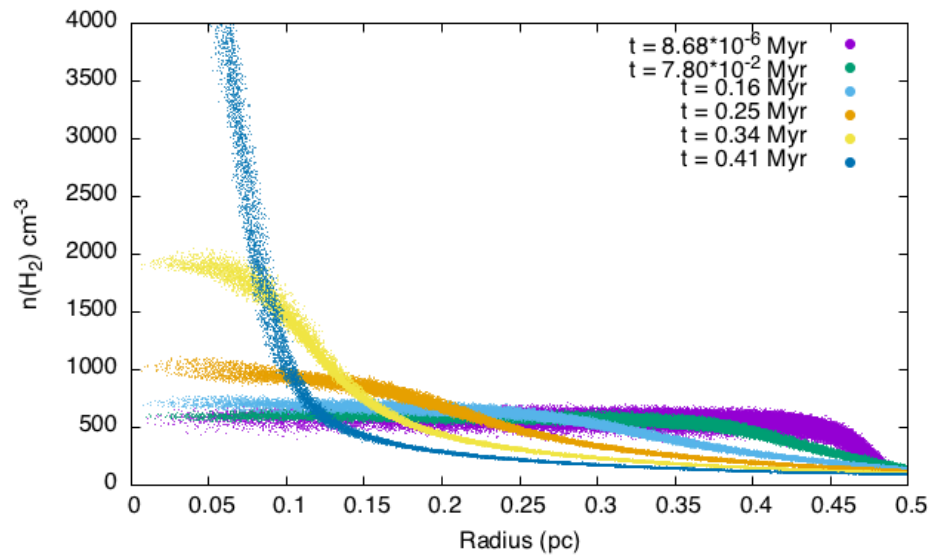
Figure 7.21: Set 100G$_0$: Initial density n$_i$ = 500 cm^{-3}and mass of 12 M$_\odot$. Evolution of cloud density with radius. Each dot in the plot for each time step represents one SPH particle. Each particle is shown for the first six time steps.
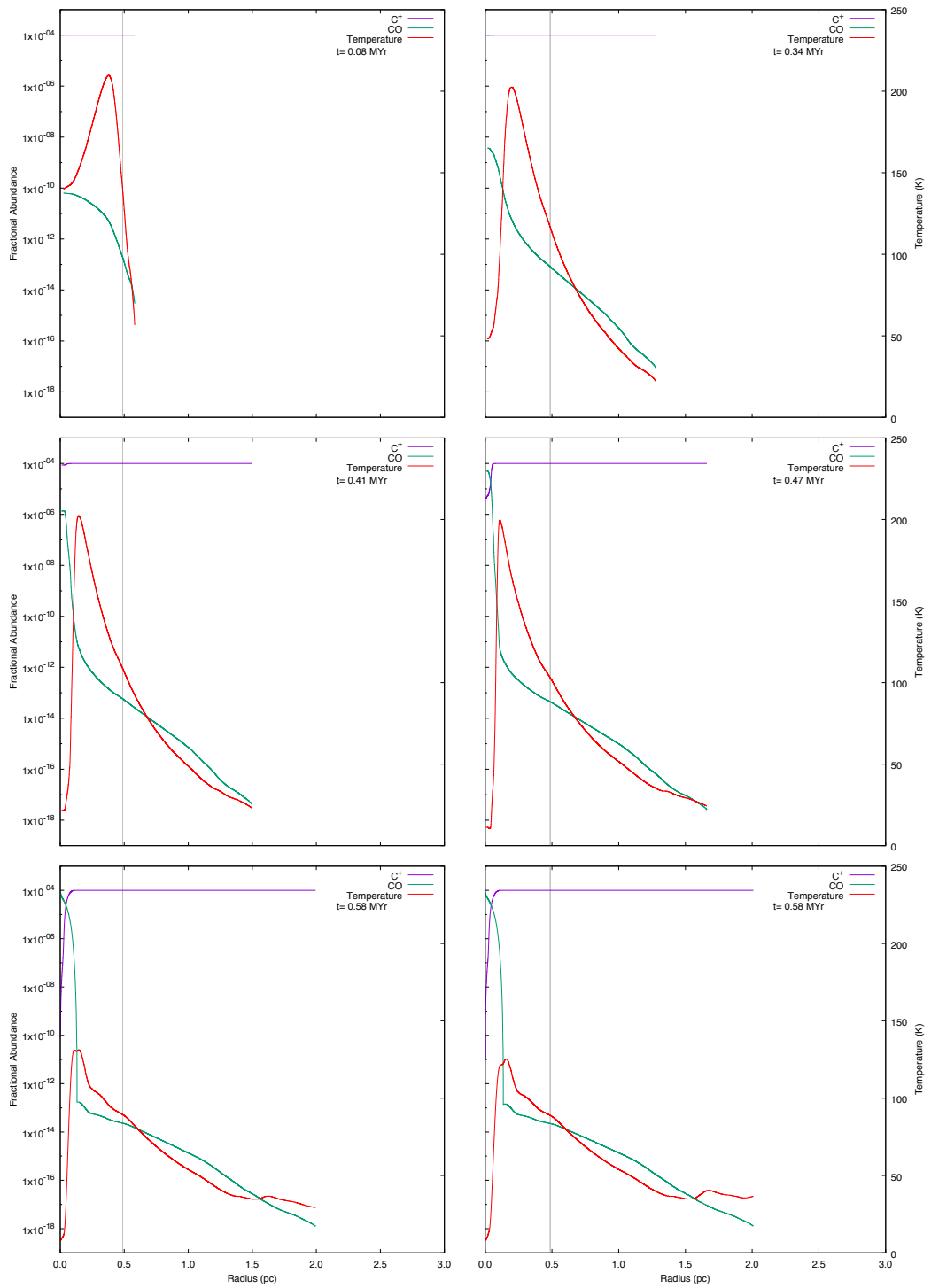
Figure 7.22: FUV radiation = 100 G_0: six snapshots showing the chemical abundances of CO and C^+ for a cloud with an initial density of 500 cm^{-3}, a mass of 12 $M_\odot$ and a radius of 0.49 pc.

7.8 An Overall View

From the above data analysis and discussion, it is clearly seen that the role of FUV radiation on the evolution of molecular clouds and the prospect of star formation within them is closely related to the initial density of the cloud. In order to present a clear picture of this relationship, the variation of the MJMs and normalised core mass η with n_i under different FUV radiation fluxes is replotted showing the differences obtained relative to the corresponding values obtained with zero FUV radiation. These plots are shown in Figures 7.23 and 7.24. Figure 7.23 presents, for each initial density, the difference in MJMs obtained from each set of simulations under four different FUV radiation fluxes relative to the values obtained at zero FUV radiation,

$$\Delta MJM = MJM_{\text{flux}\neq0} - MJM_{\text{Model E}}. \tag{7.6}$$

The relative normalised core mass η under different FUV radiation fluxes to the zero FUV radiation,

$$\Delta\eta = \eta_{\text{flux}\neq0} - \eta_{\text{Model E}}, \tag{7.7}$$

is depicted in Figure 7.24. Although due to the very low mass left in the high density cores in some simulations, especially when it is approaching the resolution of the SPH particles, and the initial randomness unavoidable in the initial particle distribution, the data fluctuates with a small amplitude over some range of the initial density, a clear trend of the variation of $\Delta\eta$ with initial density and FUV radiation flux can be seen.

From the above two Figures, we can classify the role of FUV radiation according to the following range of initial densities:

1. If $n_i < 1000$ cm^{-3}, then ΔMJM > 0 for all of applied FUV radiation fluxes. The role of FUV radiation on the evolution of a cloud is absolutely photo-evaporation dominant, The FUV radiation decreases the probability of star formation in a given giant clumpy cloud which contains a lot of clumps of different masses.

2. If $n_i = 1000$ cm^{-3} and $0 < F_{\text{FUV}} \leq 2$ G$_0$, then ΔMJM > 0, the role of FUV radiation is the same as in 1). However, increasing the FUV radiation flux so that $50 < F_{\text{FUV}} \leq 100$ G$_0$, then ΔMJM< 0, the role of FUV radiation changes to shock dominant, it would increase the probability of star formation in a given giant clumpy cloud. Therefore the role of FUV radiation on the evolution of a

cloud of this density may be defined as transitional.

3. If $n_i > 1000$ cm^{-3}, then ΔMJM < 0 for all of applied FUV radiation fluxes. The role of FUV radiation on the evolution of a cloud of this initial density is absolutely shock dominant. The FUV radiation actually enhances the probability of star formation in a given giant clumpy cloud.

4. For the clouds which are able to collapse only when $n_i \geq 500$ cm^{-3} and $F_{FUV} \geq 50$ G_0, $\Delta\eta > 0$, FUV radiation would also improve the star formation efficiency by increasing the mass left in the seed formed towards the end of the cloud's evolution. When $n_i \geq 10^4$ cm^{-3} all $\Delta\eta$ are positive for all fluxes.

7.9 CONCLUSIONS

The effect of FUV radiation on the evolution of a molecular cloud in the two parameter space [$50 \leq n_i \leq 10^4$ cm^{-3}, $0 \leq F_{FUV} \leq 100$ G_0] has been well illustrated by the variation of the Modified Jeans Mass (MJM) with n_i and F_{FUV}, through intensive sets of numerical simulations. By comparing the MJMs derived from simulations with non-zero FUV radiation with those derived under zero FUV radiation, it is found that the role of FUV radiation on the prospect of star formation in a given molecular cloud can classified into three major phases by the initial density of a cloud, i.e., absolutely photo-evaporation dominant, transitional and absolutely shock dominant

When the initial density is lower than 500 cm^{-3}, the photo-evaporation of the FUV radiation is absolutely dominant in the evolution of a cloud, over the whole flux range investigated the FUV radiation increases the MJMs by one to three orders of magnitude compared to those obtained under zero FUV radiation. FUV radiation diminishes the chance of star formation in a cloud with the given initial temperature and density in the range investigated.

When the initial density is 1000 cm^{-3}, the role of FUV radiation in the evolution of a cloud is transitional with the change of the strength of FUV radiation. When $F_{FUV} \leq 2G_0$, the photo-evaporation effect of the FUV radiation is dominant, so the MJMs were found to be higher than those under zero FUV radiation. When F_{FUV} increases to ≥ 50 G_0 or higher, the shock effect of the FUV radiation becomes dominant, so the calculated MJMs become lower than those under zero FUV radiation. Therefore the role of FUV radiation is to reduce the chance of star formation under the low radiation flux, but enhance the chance of star formation under the high radiation flux.

When the initial density increases to $n_i > 1000$ cm^{-3}, the MJMs found from the simulations under the whole range of FUV radiation fluxes investigated are lower than those found under a zero FUV radiation field. It is obvious that the effect of the FUV radiation is shock dominant in the evolution of such a cloud and that it enhances the chance of star formation within the cloud.

It is also found that the FUV radiation of flux ≥ 50 G$_0$ can also improve the star formation efficiency in molecular clouds of initial density $n_i \geq 500$ cm^{-3} by up to 10%, depending on the strength of the radiation.

To give an overview of the results for all the values of the MJMs obtained at each selected value of FUV flux Table 7.1 has been prepared. For completeness, apart from the MJM, initial cloud radius and time to collapse for each value of FUV flux being given, the crossing time has been calculated using the speed of sound in the initial cloud and the free fall time.

The time to collapse of the clouds studied in this set of results vary considerably as a result of the complex interactions described above - in some cases the t_{collapse} is less than the t_{ff} given by Equation (6.13) for the same density. However except for three cases (FUV = 1G$_0$, cloud density 200 cm^{-3}; FUV = 2G$_0$, cloud density 2000 cm^{-3} and FUV = 50G$_0$ and cloud density 100 cm^{-3} where the ratio of $t_{\mathrm{collapse}}/t_{ff}$ is 3.55, 3.86 and 2.82 respectively the collapse and free fall times are quite similar with the collapse time being generally slightly longer than the free fall time.

The propagation of the shock wave induced by the action of the FUV initially on the outer layers of the cloud has been tracked in the numerical analyses. Qualitatively the propagation speed and magnitude of the shock wave, due to different strengths of FUV, 1G$_0$, 2G$_0$, 50G$_0$ and 100G$_0$, acting on a cloud of initial density of 500 cm^{-3} can be seen in Figures 7.5, 7.11, 7.16 and 7.21 respectively. A faint density wave can be seen to be moving slowly for 1G$_0$ and 2G$_0$ where the first 5 outputs allow more time to pass, 0.93 and 0.8 Myr respectively, a big density peak is not observed whereas 50G$_0$ and 100G$_0$ produce both a greater peak and take less real time, in these cases 0.35 and 0.42 Myr. These figures give a qualitative understanding of how the shocks caused by the FUV have a more noticeable effect on the initiation of collapse for the higher FUV levels on higher density clouds.

A 'recapture' phase may also be seen in the evolution of some clouds. This occurs when v_r is negative, that is the particles have a velocity vector directed towards the cloud's origin; it is present for the lower density clouds and low FUV flux but does not become a feature with clouds of higher initial density at greater FUV flux. In the latter case, however, the mass of the clump stays essentially constant, as can be seen in Figure 7.18. The recapture phase happens to all the clouds at low density before

(a) Low Density region   (b) High Density region
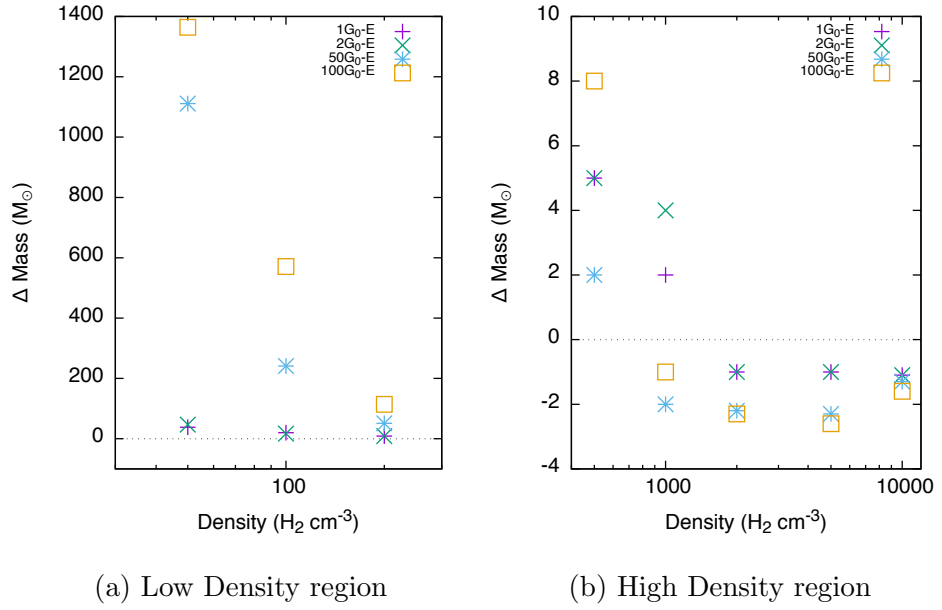
Figure 7.23: The difference in MJM for different FUV levels G_0 and Model E as a function of initial cloud densities. The left panel is for the low densities and the right panel is for the high densities. The zero horizontal line is shown in both which is to show the difference to the baseline of Model E.
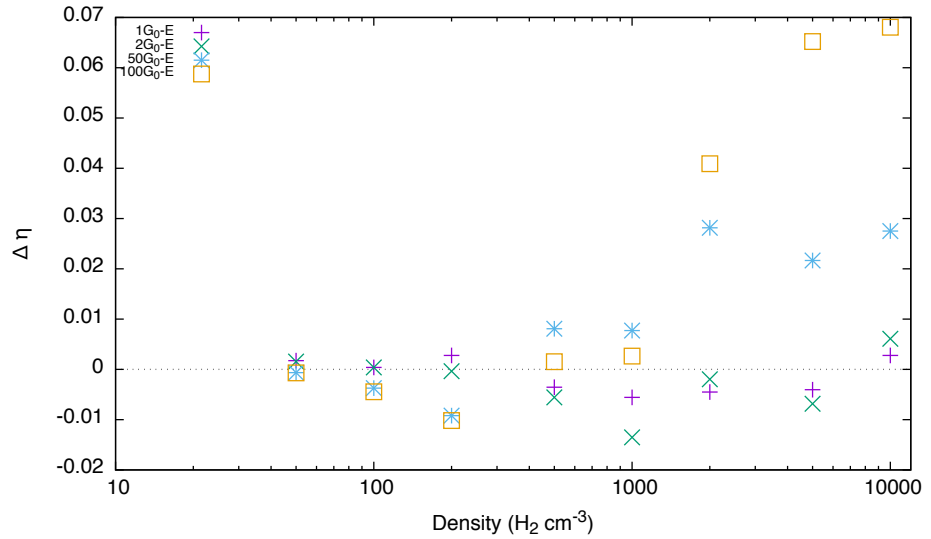
Figure 7.24: The difference between $\eta = \left(M_{core}/M_{MJM}\right)$ for different FUV levels G_0 and η for FUV $= 0G_0$ as a function of initial cloud densities.

FUV flux	Density	Radius	MJM	t_{collapse}	t_c	t_{ff}
G_0	ncm^{-3}	pc	$M_\odot$	Myr	Myr	Myr
	50	1.69	50.00	4.66	2.72	5.15
	100	1.11	28.00	4.29	1.78	3.64
	200	0.71	15.00	9.13	1.14	2.57
1	500	0.44	9.00	1.99	0.71	1.63
	1000	0.31	6.00	1.17	0.49	1.15
	2000	0.17	2.00	2.81	0.27	0.81
	5000	0.13	2.00	0.38	0.20	0.51
	10000	0.08	0.90	0.27	0.12	0.36
	50	1.79	59.00	4.12	2.87	5.15
	100	1.06	25.00	3.03	1.70	3.64
	200	0.71	15.00	2.88	1.14	2.57
2	500	0.44	9.00	1.52	0.71	1.63
	1000	0.34	8.00	0.90	0.54	1.15
	2000	0.17	2.00	3.12	0.27	0.81
	5000	0.13	2.00	0.40	0.20	0.51
	10000	0.08	0.90	0.27	0.12	0.36
	50	4.77	1123.00	6.15	7.66	5.15
	100	2.3	249.00	10.28	3.68	3.64
	200	1.11	57.00	1.57	1.78	2.57
50	500	0.39	6.00	0.56	0.62	1.63
	1000	0.21	2.00	0.31	0.34	1.15
	2000	0.13	0.80	0.29	0.20	0.81
	5000	0.09	0.09	0.23	0.14	0.51
	10000	0.07	0.70	0.21	0.11	0.36
	50	5.10	1376.00	6.83	8.18	5.15
	100	3.03	579.00	3.55	4.86	3.64
	200	1.43	120.00	1.75	2.30	2.57
100	500	0.49	12.00	0.58	0.78	1.63
	1000	0.24	3.00	0.28	0.39	1.15
	2000	0.12	0.70	0.17	0.19	0.81
	5000	0.07	0.40	0.12	0.12	0.51
	10000	0.06	0.40	0.12	0.09	0.36

Table 7.1: This summary Table lists all Flux levels used in the simulations in this Chapter 7. For each Flux (G_0) the different initial cloud densities (cm^{-3}) used in the simulations are given together with the initial cloud radius (pc), the MJM ($M_\odot$), the time to collapse (t_{collapse}), the sound crossing time (t_c) and the free-fall time (t_{ff}).

a protostar seed is formed. For higher densities and FUV this does not occur, the protostar seed forms before such a recapture phase is noticed even though much of the material has a positive radial velocity. This is partly due to the speed with which these higher density regions form compared to the time needed for the less dense clouds. It is clear from Figure 7.1 that the MJM is lower as the density increases. Because the protostar seed forms so quickly at higher initial densities, the CLOUD code time steps become too small so that it is not possible to see if such a recapture phase would happen at a later time or if most of the material would just evaporate away from the cloud.

CHAPTER 8

CONCLUSIONS

It is known that microphysical and chemical processes occurring within a molecular cloud affect the evolution of the cloud through changes in heat balance and temperatures within the cloud. It is also known that incident FUV affects this evolution as some or all of its energy may be deposited into the cloud similarly affecting the heat balance. As shown in Section 1.6 computer models have been written to simulate these processes in order to gain a better understanding of the influence of these effects during the evolution of a cloud and to identify the possible outcomes such as whether the cloud forms a 'seed' of a protostar or fragments to form multiple cores. An alternative outcome is that the cloud may simply dissipate.

However little consideration has been given to understanding the significance that each of these microphysical and chemical processes taken individually may have on the evolution of a molecular cloud. It was felt that a deeper understanding of the processes involved in star formation would be gained if the magnitude of the effects of each these processes could be identified at each stage of the evolution.

This study was therefore undertaken with two aims in view. On the one hand it was hoped to identify and compare the significance of a selection of different physical and chemical processes acting singly and together on the evolution of molecular clouds and, on the other, to show how the dynamic evolution of the clouds depends on the initial physical conditions and the external radiation fields.

In order to do this a simplified model of a spherical cloud was adopted to reduce complications due to anisotropies. To ensure that a cloud with the given set of active

167

processes does collapse, one of the aims of this study being to follow the dynamic changes in the clouds, simulations were made to identify the minimum mass a cloud must have in order to collapse. This was to ensure that the subsequent simulations did achieve collapse and the evolution could be followed.

The minimum mass that a cloud requires to collapse was based on the well known concept of the Jeans Mass of a idealised cloud. The effect of including thermal inputs and chemical pathways will be to produce a variation in the minimum initial cloud mass required for collapse from that predicted by Jeans' model. This changed mass is called in this thesis the Modified Jeans Mass (MJM) and has been shown to be a sensitive indicator of the significance of the various processes; variations of 3 orders of magnitude have been seen in the MJM depending on the combination of processes which are active in any particular simulation.

The starting conditions are intentionally simplified, for example momentum is conserved but the particles are considered stationary at the start as the aim is to understand the processes and their interactions and not to model the complete evolution of a star. A sphere is populated with pseudo-randomly positioned particles to avoid the Poisson noise which would be seen in the results if a regular array were to be used as a start point as well as the local areas of high particle density given by a purely random distribution which could give rise to premature cloud collapse. The sphere is assumed to be isolated in that the thermal and hydrodynamic effects of the surrounding ISM are ignored although it is presumed to be sited in the PDR so EUV radiation plays no role. The initial temperature was set at 60K throughout the sphere to represent a warm medium, the opacity not being sufficient to allow low temperature volumes to develop.

The simulated clouds were modelled using 100,000 SPH mass-particles. This number is a compromise between achieving the maximum resolution during the simulation and the length of computing time needed using the equipment available. The effect of changing the number of particles in the simulation was discussed in Section 4.6 in the context of the time convergence of the simulations. Simulations were run using 20,000, 50,000, 100,000 and 150,000 SPH particles using the same initial cloud mass, that is the mass per SPH particle was reduced with the higher particle count. It was found that the shape of the curves were similar but the collapsing times varied slightly being 3.15, 3.2, 3.48 and 3.45 Myr respectively as shown in Figure 4.4. An increase by a factor 5 in the number of particles, from 20,000 to 100,000, resulted in the collapsing time increasing by 10%. A further increase from 100,000 to 150,000 particles reduced the collapsing time by 0.03 Myr, a change of 0.007% for a 50% increase in the number of particles.

In the cases studied here which are based on simple spherical spheres with the interest being on the overall trends in the clouds' evolution, the need for high resolution is not present. In cases where the morphology is complex, in modelling filamentary structures for example, there is a strong case for using more particles to increase the resolution. Such modelling of the morphology is limited in the current work, so there is less of a need for using a greater number of particles at higher masses. Of the 65 cases listed in Tables 6.2 and 7.1 58 showed MJMs of 250 $M_\odot$ or less, 2 lie between 251 and 500 $M_\odot$. Only 5 cases, which may benefit from a higher resolution, had MJMs lying between 501 and 2050 $M_\odot$. For the purposes of this thesis it has been judged that the errors incurred in using a fixed number of 100,000 particles is acceptable.

Another consideration is the time required for each simulation. Cloud masses varied from 0.4 $M_\odot$ to 2050 $M_\odot$. If a base case of 10 $M_\odot$ with 100,000 particles were taken with a mass/particle of 0.0001, then a 2000 $M_\odot$ cloud would require 20 million particles and the calculation time would increase by a factor of 200 - a run with 100,000 particles takes some 20 hours, 20 million would need 23 weeks which is not feasible.

It is felt that the use of a constant 100,000 mass-particles for these simulations is a good compromise between resolution and time required to execute each simulation.

Another limit on the accuracy of the modelling is the treatment of the particles being emitted from the outer surface of the sphere as the cloud warms up. There are two issues, one concerned with the model and the other is computational. The model assumes the sphere is located in a PDR, but CLOUD does not model the effect of the surrounding ISM and the particle interchange between it and the outer surfaces of the cloud. The model assumes a vacuum around the cloud and this vacuum would permit a somewhat higher loss of material from the cloud's surface as the surface warms, as initially there would be little material returning. The cloud will enlarge slightly more rapidly than it would if there were a counter pressure. This would last until the first particles are emitted - but then the ones on the new outside surface would also preferentially be 'lost'. The minor small amount of particles that leave hit the boundary are small in number and would hardly affect the dynamics of the main body. Generally less then 1% of the particles are within 10% of the bounding box.

As soon as the more central regions of the cloud start to collapse due to the mutual gravitational attraction between the particles much of the material is pulled back towards the centre as can be seen in the density-radius plots so the actual loss of material is not significant for the core development, the greatest mass loss occurring in the high incident FUV intensity situations. The computing limitation is that if a particle reaches the limits of the bounding box of the computing space the particle is deemed to remain there and take no further part in the calculations.

Processes modelled were photo-electric and cosmic ray ionisation heating, gas-dust thermal exchange, and molecular emission line cooling, both individually and in combination. The resulting variations of the calculated MJM for each Model were compared to those predicted for an isothermal cloud. In a second stage the effects of different levels of FUV radiation on the evolution of clouds were modelled.

The two groups of results, the Models of the micro-physical and chemical processes and the effect of incident FUV are now considered.

Firstly, the results for different Models of photo-electric and cosmic ray ionisation heating, gas-dust thermal exchange, and molecular emission line cooling both single and in combination as described in Table 6.1 enable the following general conclusions to be drawn:

- The most effective cooling mechanism is molecular line emission; it is the process which has the greatest effect on the MJM

- Cosmic ray radiation not only heats the denser central volumes of a cloud but also warms the outer layers of the cloud significantly which may seen when no other mechanisms mask the effect

- Gas-dust thermal exchange is most effective at particle densities greater than 500 cm^{-3}.

In these simulations the dust temperature (T_d) was determined by the energy evolution equations rather than by setting a minimum temperature in order to be better able to observe influence of the individual processes on the evolution of the cloud. This allowed the exploration of temperature balancing with the evolution of the energy equations. In section 3.3.5 it was stated that the model used in this study incorporates the calculation of dust temperature using a formula suggested by Hollenbach et al. (1991). It is common to set the minimum dust temperature to 10K in such simulations (Nelson and Langer, 1997) so as a check Model B, which had the coldest core, was re-run with a minimum $T_d = 10$K. The results are shown in Figures 8.1 and 8.2. The differences to the original plots are minor: the general shape of the density and temperature plots remain the same, except that in the final time step the high temperature fluctuations are reduced and the minimum core temperature is 10K, the MJM shifted up slightly from 99 M$_\odot$ to 110 M$_\odot$ and the collapse time increased from 2.33 Myr to 2.80 Myr. It can be concluded that the general behaviour of the cloud did not change and the general qualitative results presented in this thesis are not affected.

Secondly, the effect of the level of FUV radiation on the evolution of a molecular cloud in the two parameter space ($50 \leq n_i \leq 104$ cm^{-3}, $0 \leq$ FUV ≤ 100 G$_0$) has been

clearly demonstrated by the variation of the Modified Jeans Mass. The role of FUV radiation on the prospect of star formation depends on the initial particle density:

- For densities less than 500 cm^{-3}, photo-evaporation is dominant, the FUV increases the MJMs by one to three orders of magnitude compared to those obtained at zero FUV and diminishes the chance of star formation

- For a density of 1000 cm^{-3}, the role of FUV radiation is transitional, low levels reduce the chance of star formation but higher levels increase it. When FUV $\leq$ 2G0, the photo-evaporation effect is dominant, the MJMs were found to be higher than those with zero FUV. When FUV is $\geq$ 50 G$_0$ the shock effect becomes dominant and the MJMs became lower than those under zero FUV flux

- For densities greater than 1000 cm^{-3}, the MJMs are lower than those found with zero FUV. The effect of the FUV radiation is shock dominant and enhances the chance of star formation

- As density increases the time for collapse for all MJMs decreases, but this is most noticeable in the data sets for high FUV intensities.
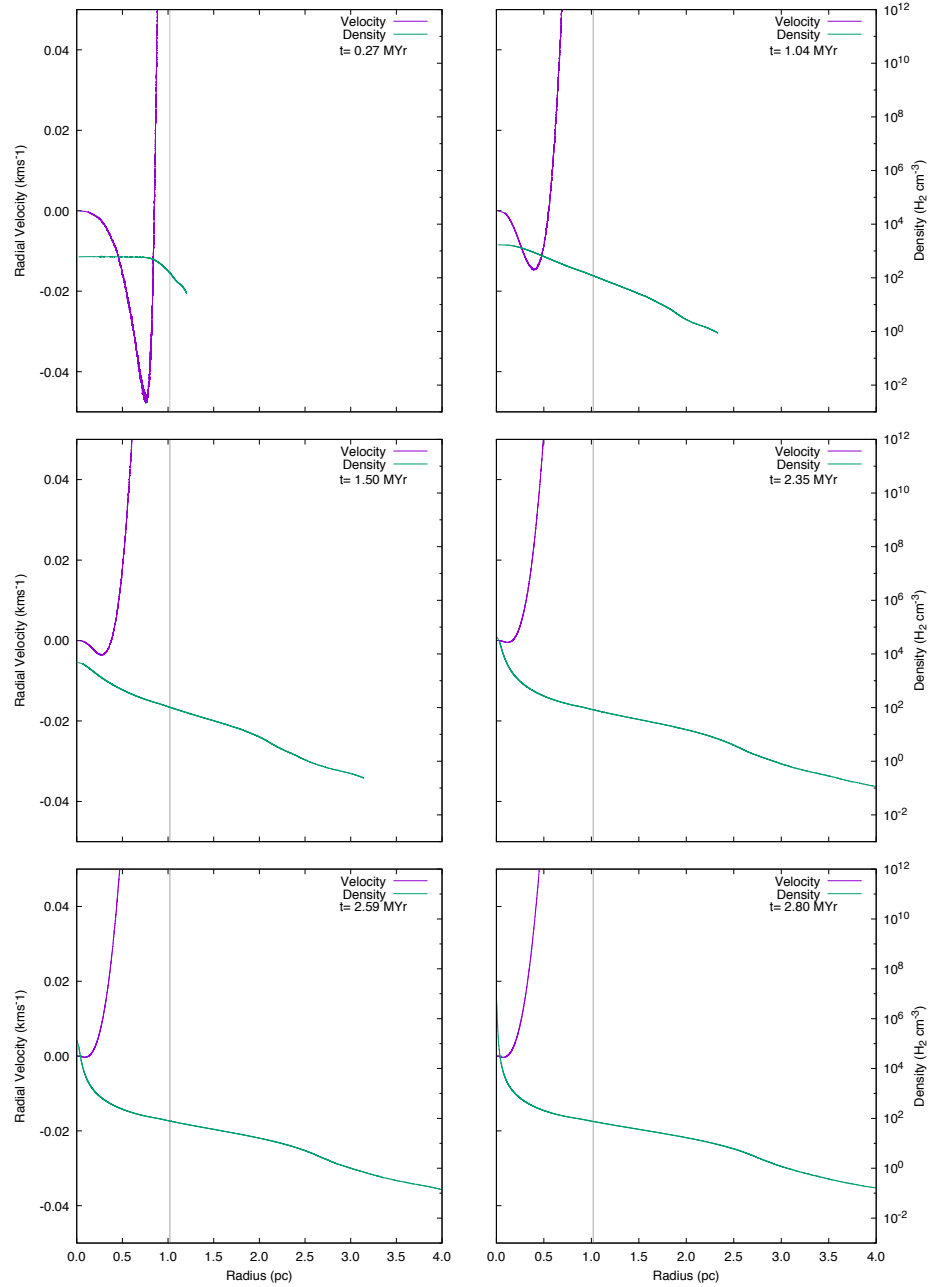
Figure 8.1: Model B: six snapshots showing radial velocity (purple line) and density (green line) for a cloud with an initial density of 500 cm^3, a mass of 110 M$_\odot$ and a radius of 1.02 pc.
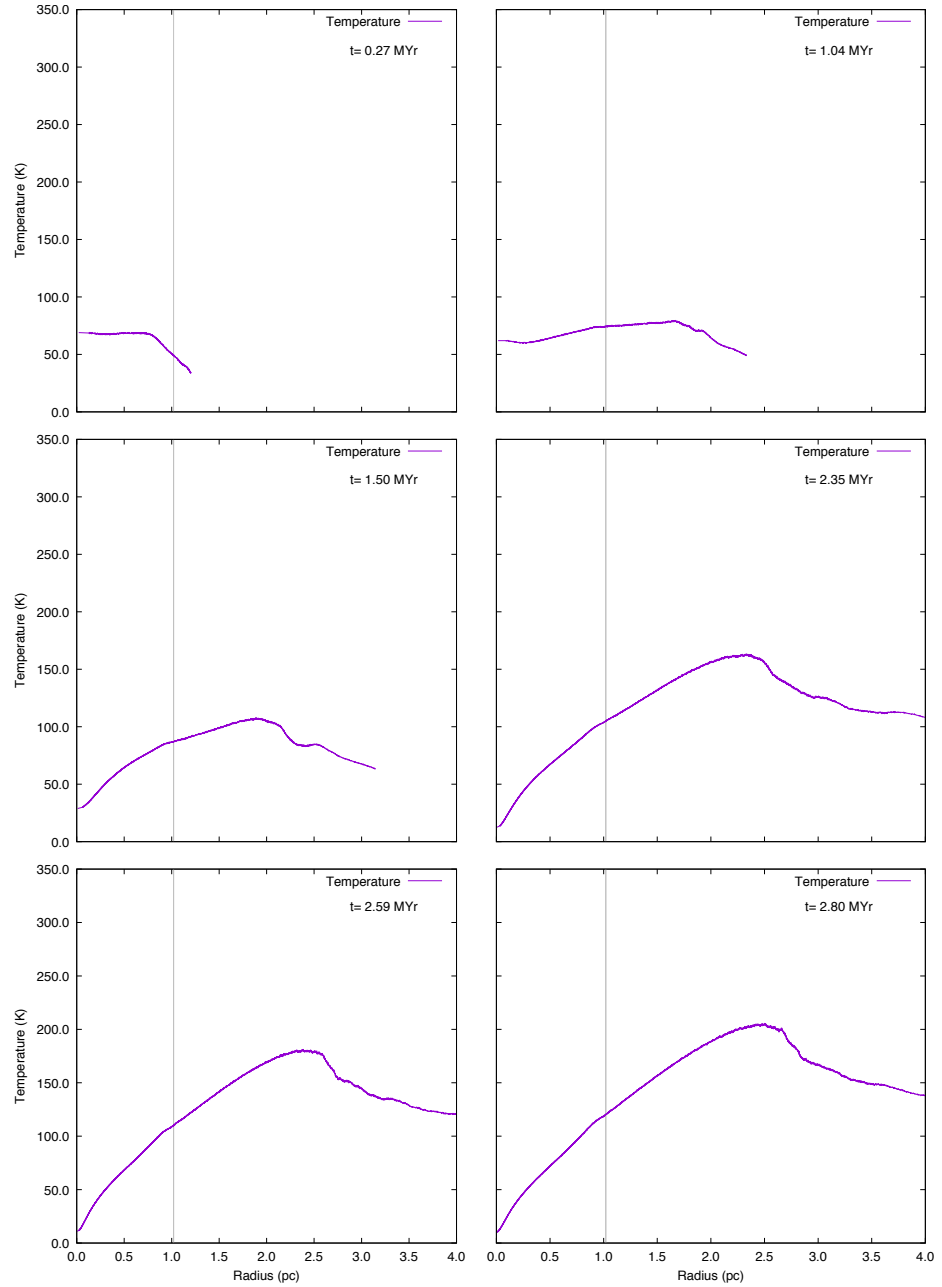
Figure 8.2: Model B: the evolution of the mean temperature distribution with the radial distance in a Cloud Type 4. The grey vertical line shows the initial radius of the cloud.

CHAPTER 9

FURTHER WORK

9.1 SUGGESTED AREAS OF FURTHER WORK

The ultimate aim of that part of astro-physics concerned with star formation is to understand and explain the processes involved starting from the creation of molecular clouds to the evolution of planetary systems. The work reported here represents a small step in this intellectual journey and whilst working on the issues many thoughts, ideas and concepts were considered which could have extended the scope of the work.

One such avenue was investigated but was deemed to be computationally too expensive at the time. This was to study how the mass of a protostar seed, where the seed is defined as any SPH particle of density $> 10^7 \text{cm}^{-3}$ near the origin of the cloud and the seed mass is the sum of the masses of the individual particles, varies with the FUV strength. This was to see where how quickly it would form the biggest seed and at what FUV strength it would no longer form a seed. One of these examples can be seen in Figure 9.1 but some of the other test runs can be seen in the Appendix C. Only seeds that have formed are plotted and the cases where the incident FUV was $> 6.9\text{G}_0$ the cloud evaporated without forming a seed.

Other concepts covered a range of topics from making the initial cloud conditions appear closer to the structures identified by observation, including extra species in the chemical models to changing the computing environment to reduce the computer time
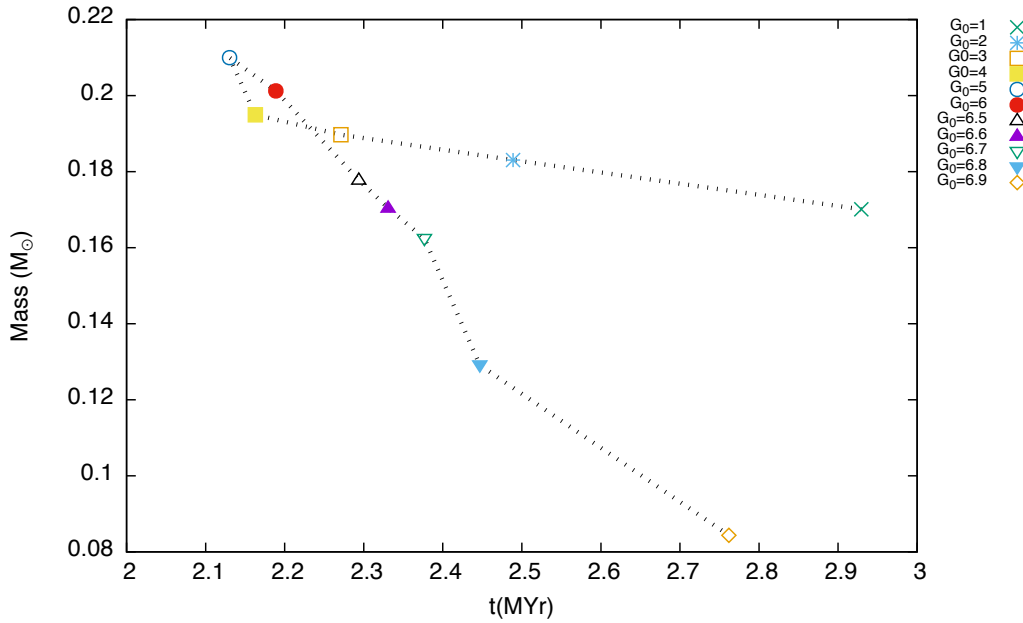
Figure 9.1: The initial condition of the cloud is $35M_\odot$, $n_i = 100$ cm^{-3} with different strengths of FUV. The protostar seed mass is shown as a function of time to the formation of the seed.

needed for each simulation. The effort that would be needed to develop and test the code necessary and to run the simulations it would exceed the time allowance for this study. For example, adding additional features to the SPH code would be sufficiently complex to be the subject of a thesis in its own right.

Nevertheless this chapter lists and discuss some of the concepts and ideas which have been considered in order to improve and extend the studies and illuminate more of the processes which occur in dark molecular clouds. These ideas and concepts have been divided into different categories for easier overview: Initial conditions; SPH additions; alternate problems.

9.2 INITIAL CONDITIONS

The starting conditions used in the thesis are quite idealised - a spherical cloud made up of particles quasi-randomly positioned within it - to make tracking the cloud's evolution and the analysis of the results easier as the results are essentially symmetrical. With this part of the work now completed more complex structures could be considered to replicate more closely those seen by observation.

9.2.1 Clumps and filament structures

A first order improvement would be to model a 'clumpy', rather than an homogenous, cloud with volumes of higher and lower particle density. Another possibility would be to model a more filamentary structure as found in nature. Both these setups include their own added problems of trying to make them close enough to real observable clouds and to not cause random noise and still keep glass like properties for all of the high and low density regions. Expected effects which would be apparent from such models is that the self-gravity within the cloud will not be symmetrical and that temperatures and heat flows will vary in ways which are not symmetrical (Williams et al., 2000; Bigiel et al., 2010; Canning et al., 2014).

9.2.2 Initial turbulence

Observation shows that gas clouds can be turbulent the motion being driven by energy inputs from nearby stars. Setting the initial conditions to either create turbulence in a cloud or to represent a cloud that was already turbulent would be another step in making the model represent actual physical conditions more closely. Monaghan (2002); Ercolano and Gritschneder (2010) have described and discussed code to simulate turbulent conditions. Adding code for the treatment of turbulence would be a significant addition to the SPH code and, as such, could therefore be included under the next heading. However, from a physical point of view it is considered that treating the cloud as turbulent at the start of the simulation should be considered as a change to the initial conditions of the simulation.

For this thesis the cloud has been represented at the start of the simulation as a static array of particles which then begin to move as a result of the mutual gravitational attraction between them. Including turbulence in the model would mean that the particles are given initial velocities at the start of the simulation and these velocities are then subject to the effects included in the SPH code. These effects include the term describing viscosity which will tend to dampen the turbulence. One constraint on the initial conditions is that the net velocity has to be zero to avoid the cloud drifting out of the simulation space. A turbulent cloud may have angular momentum as a result of the particles motion and this would have to be conserved in the simulation.

Turbulence implies that some proportion of the particles will be moving against the mutual gravitational attraction between them and this will therefore affect shock propagation and evaporation rates. In turn it can be anticipated the minimum cloud mass for collapse will be affected as well as the time needed for collapse. As these values are known for a given FUV flux and initial particle densities a judgement would

possible on the effect of different levels of turbulence on these parameters.

9.3   Additional simulation properties and improvements

In this section a number of suggestions are made to permit the simulation to approach more closely the actual point of collapse of a cloud, additions to increase the number of processes being tracked and some considerations on hardware and software aspects of increasing computer efficiency.

9.3.1   Ray tracing of point source(s)

As discussed in Chapter 3 an alternative method of calculating the absorption and scattering of incident FUV is to use the ray tracing technique whereby the density of the SPH particles is interpolated onto the chosen ray paths extending from the cloud surface to the particle positions. In principle this would be more accurate than the approach used and should be considered if higher accuracy is required. Ray tracing would also be very effective for simulating the effects of point sources radiating FUV into the simulation area making it possible to model the effects of one or more nearby OB stars. It would also allow for radiation sources to be formed within the simulation area and the effects of their radiation to be followed. The use of ray tracing would allow more adaptive situations to occur if one want to have more larger dynamic clouds simulated (Altay et al., 2011).

Although ray tracing would use considerably more computational resources if a single (or a few processors) were used, because each ray can be treated separately the process is suitable for parallel processing. See section 9.5 below.

9.3.2   Sink particles and particle subdivision

In the work reported here the critical density for collapse has been set at 10 particles having a number density of $10^7 \, \text{cm}^{-3}$ as, due to the adaptive nature of the calculation, the fewer the number of particles the more likely it is that the code will use larger increments for the time steps between the calculations. This means that in practice the computation is halted otherwise the elapsed computational time would become too long.

To avoid this issue and allow the simulation to run further and so to identify clearly if the high density peaks would become protostars a possible work-round is the adoption of the concept of 'sink particles' (Bate et al., 1995) .

A 'sink particle' replaces a given number of closely packed particles, by a single particle, thus reducing the local particle density and allowing the computation to continue (Hubber et al., 2013). An alternative method is to subdivide high density particles and run the simulation on these in a subsidiary time frame until the next iteration is reached for the remaining particles (Kitsionas and Whitworth, 2002; Vacondio et al., 2016). This approach can save memory and CPU time then a standard simulation since it would only be simulating a fraction of the total matter that forms stars and this fraction would be tracked in the smaller time steps. If the main interest is following the star formation process, this can be done by tracking the sub-set of particles which is therefore time efficient. If the evolution of the rest of the molecular cloud is of interest the compute time would be longer since the extra sub-time steps have to be computed.

Either of these methods would permit the computation to continue to the point where the actual point of collapse of the cloud could be identified

9.3.3 MAGNETIC FIELDS

Molecular clouds contain moving ionised species which in turn will produce electric and magnetic fields. Modelling magnetic fields and properties in SPH has historically been difficult but more recently solutions have been developed. The addition of the effects of magnetic fields on particle behaviour is believed to be one of the most important factors for clouds being able to counter gravitational collapse so effectively and thus make star formation so inefficient. Adding the ability to model the electro-magnetic effects would give a fuller view of how magnetic forces, chemistry, heating and cooling interact and counter the effects of self-gravity in the cloud.(Price and Monaghan, 2003, 2004; Tricco and Price, 2012; Hopkins and Raives, 2016)

9.4 VARYING THE EXTERNAL CLOUD ENVIRONMENT

The conceptual arrangement of the molecular cloud and nearby radiation sources used in this work assumes that the cloud being studied is surrounded by interclump material within the photodissociation region and this arrangement stays constant during the simulation.

It would be interesting to model changes in this set up during the evolution of the molecular cloud. For example it could show how hard it is to form a core if, after a given time, extreme ultra-violet (EUV) radiation generates HII regions and starts irradiating the partially evolved cloud. A variant could be that the HII region moves in from the side of the bounding box so the dissociation front touches the evolving cloud and EUV from an OB star reaches the cloud under study.

9.5 Computing Considerations

With the growth of multi-cored processors and the availability of dedicated graphics processor units (GPU) the possibility arises for accelerating the simulations by using a code base capable of running concurrent tasks. Specifically particle movements and ray tracing would be very efficient if one used a GPU farm to solve such problems as they have an architecture dedicated for concurrent tasks

If it were decided to extend the simulations using some or all of the ideas suggested above then it would seem that this would be a good opportunity to switch to a more modern code base capable of running tasks concurrently in order to reduce the compute time. At present each simulation can now take some 20 hours for each run and adding complexity will slow the calculations further.

9.6 The Way Forward

If it were possible to add code to represent all these extra properties and conditions to make a very comprehensive SPH code capable of simulating the evolution of protostars from gas and dust clouds to the point of ignition the overriding problem is always the computational cost in terms of hardware requirements and time for execution. In particular there is the requirement to keep the particle count high to improve resolution which directly affects compute time. A further consideration is the storage capacity needed to hold the quantity of data necessary to describe the physical properties.

In addition there will be issues of demonstrating the code's accuracy to mimic real physical processes and not to cause high error divergence over time. It is quite feasible, although time-consuming, to test all the individuals systems separately but integrating them and proving that the results are still physically true is a non-trivial problem. With this in mind a step-by-step approach has much to commend it as results emerging from

the changes in the conditions, and any issues arising from the modelling, can be more easily analysed.

Some avenues of further research are a more direct continuation of the work presented in this thesis than some of the others. As a first step it is considered that deeper understanding of the effects of changed initial conditions such as clumpy and filamentary structures would be useful in the understanding of the evolution of molecular clouds. Some additional computing techniques such as sink particles and ray tracing may be of assistance in this area. It would also be interesting to make small test environments for the other factors mentioned and then to examine the effects they may have on the previous results and so determine if these topics could be viable areas for further research.

The following two papers based on the work presented in the thesis are being submitted to MNRAS:

1. Evolution of molecular cloud: I. The effect of micro-physical processes and chemical cooling, Philip Cox, Jingqi Miao, Glenn White and Richard Nelson, MNRAS.

2. Evolution of molecular cloud: II. The effect of the intensity of FUV radiation, Philip Cox, Jingqi Miao, Glenn White and Richard Nelson, MNRAS.

Bibliography

N P Abel and G J Ferland. Determining the H+ Region / PDR Equation of State in Star-forming Regions. *The Astrophysical Journal*, 647(1):367–373, August 2006.

G Altay, R A C Croft, and I Pelupessy. SPHRAY: A Smoothed Particle Hydrodynamics Ray Tracer for Radiative Transfer. *Astrophysics Source Code Library*, page ascl:1103.009, March 2011.

S Andree-Labsch, M Röllig, and V Ossenkopf. 3D Modelling of Clumpy PDRs: the Structure of the ISM in Star Forming Regions. *Protostars and Planets VI*, July 2013.

S Andree-Labsch, V Ossenkopf-Okada, and M Röllig. Modelling clumpy PDRs in 3D - Understanding the Orion Bar stratification. *arXiv*, May 2014.

J Barnes and P Hut. A hierarchical O(N log N) force-calculation algorithm. *Nature (ISSN 0028-0836)*, 324(6096):446–449, December 1986.

M R Bate, I A Bonnell, and N M Price. Modelling Accretion in Protobinary Systems. *arXiv*, October 1995.

M R Bate, T S Tricco, and D J Price. Collapse of a molecular cloud core to stellar densities: stellar-core and outflow formation in radiation magnetohydrodynamic simulations. *Monthly Notices of the Royal Astronomical Society*, 437(1):77–95, January 2014.

M J Berger and P Colella. Local adaptive mesh refinement for shock hydrodynamics. *Journal of Computational Physics (ISSN 0021-9991)*, 82(1):64–84, May 1989.

E A Bergin, W D Langer, and P F Goldsmith. Gas-phase chemistry in dense interstellar clouds including grain surface molecular depletion and desorption. *The Astrophysical Journal*, 441:222, March 1995.

F Bertoldi. The photoevaporation of interstellar clouds. I - Radiation-driven implosion. *The Astrophysical Journal*, 346:735–755, 1989.

F Bigiel, A Leroy, M Seibert, F Walter, L Blitz, D Thilker, and B Madore. Tightly Correlated H I and FUV Emission in the Outskirts of M83. *The Astrophysical Journal Letters*, 720(1):L31–L35, September 2010.

T G Bisbas, R Wünsch, A P Whitworth, D A Hubber, and S Walch. Radiation-driven Implosion and Triggered Star Formation. *arXiv*, 736(2):142, 2011.

T G Bisbas, T J Haworth, M J Barlow, S Viti, T J Harries, T Bell, and J A Yates. TORUS-3DPDR: a self-consistent code treating three-dimensional photoionization and photodissociation regions. *arXiv*, 454(3):2828–2843, 2015.

Bart J Bok and Edith F Reilly. Small Dark Nebulae. 105:255, March 1947.

W B Bonnor. Boyle's Law and gravitational instability. *Monthly Notices of the Royal Astronomical Society*, 116:351, 1956.

R E A Canning, J E Ryon, J S Gallagher, R Kotulla, R W O'Connell, A C Fabian, R M Johnstone, C J Conselice, A Hicks, D Rosario, and R F G Wyse. Filamentary star formation in NGC 1275. *Monthly Notices of the Royal Astronomical Society*, 444(1):336–349, October 2014.

J L Cercos-Pita. AQUAgpusph, a new free 3D SPH solver accelerated with OpenCL. *Computer Physics Communications*, 192:295–312, July 2015.

S Chandrasekhar. The Gravitational Instability of an Infinite Homogeneous Turbulent Medium. *Proceedings of the Royal Society of London Series A*, 210(1100):26–29, 1951.

J P Chieze and G Pineau Des Forets. The fragmentation of molecular clouds. II - Gravitational stability of low-mass molecular cloud cores. *Astronomy and Astrophysics*, 183:98–108, September 1987.

D A Clarke. A Consistent Method of Characteristics for Multidimensional Magneto-hydrodynamics. *Astrophysical Journal v.457*, 457:291–, January 1996.

D A Clarke. On the Reliability of ZEUS-3D. *The Astrophysical Journal Supplement*, 187(1):119–134, March 2010.

R Courant, K Friedrichs, and H Lewy. Über die partiellen Differenzengleichungen der mathematischen Physik. *Mathematische Annalen*, 100(1):32–74, 1928.

A J C Crespo, J M Domínguez, B D Rogers, M Gómez-Gesteira, S Longshaw, R Canelas, R Vacondio, A Barreiro, and O García-Feal. DualSPHysics: Open-source parallel CFD solver based on Smoothed Particle Hydrodynamics (SPH). *Computer Physics Communications*, 187:204–216, February 2015.

G H Darwin. On the Mechanical Conditions of a Swarm of Meteorites, and on Theories of Cosmogony. *Philosophical Transactions of the Royal Society A: Mathematical, Physical and Engineering Sciences*, 180(0):1–69, January 1889.

S Diehl, G Rockefeller, C L Fryer, D Riethmiller, and T S Statler. Generating Optimal Initial Conditions for Smooth Particle Hydrodynamics Simulations. *arXiv*, page 525, November 2012.

R Ebert. Über die Verdichtung von H I-Gebieten. Mit 5 Textabbildungen. *Zeitschrift für Astrophysik*, 37:217, 1955.

B Ercolano and M Gritschneder. Ionisation feedback in star formation simulations: The role of diffuse fields. *arXiv*, (1):401–410, December 2010.

A E Evrard. Beyond N-body: 3D cosmological gas dynamics. *Monthly Notices of the Royal Astronomical Society*, 235(3):911–934, December 1988.

E Falgarone and J L Puget. A model of clumped molecular clouds. I - Hydrostatic structure of dense cores. *Astronomy and Astrophysics (ISSN 0004-6361)*, 142:157–170, January 1985.

C Federrath, S Sur, D R G Schleicher, R Banerjee, and R S Klessen. A New Jeans Resolution Criterion for (M)HD Simulations of Self-gravitating Gas: Application to Magnetic Field Amplification by Gravity-driven Turbulence. *arXiv*, 731(1):62, 2011.

G J Ferland, R L Porter, P A M van Hoof, R J R Williams, N P Abel, M L Lykins, G Shaw, W J Henney, and P C Stancil. The 2013 Release of Cloudy. *Revista Mexicana de Astronomía y Astrofísica Vol. 49*, 49:137–163, April 2013.

J B Foster and A A Goodman. Cloudshine: New Light on Dark Clouds. *The Astrophysical Journal*, 636(2):L105–L108, January 2006.

R A Gingold and J J Monaghan. Smoothed particle hydrodynamics - Theory and application to non-spherical stars. *Royal Astronomical Society*, 181:375, November 1977.

A E Glassgold, D Galli, and M Padovani. Cosmic-ray and X-ray Heating of Interstellar Clouds and Protoplanetary Disks. *arXiv*, page arXiv:1208.0523, August 2012.

P F Goldsmith and W D Langer. Molecular cooling and thermal balance of dense interstellar clouds. *Astrophysical Journal*, 222:881, June 1978.

S Goodwin. Star Formation. *Planets*, (Chapter 5):243–, 2013.

S P Goodwin, A P Whitworth, and D Ward-Thompson. Simulating star formation in molecular cloud cores. I. The influence of low levels of turbulence on fragmentation and multiplicity. *Astronomy and Astrophysics*, 414(2):633–650, February 2004.

U Gorti and D J Hollenbach. Photoevaporation of Clumps in Photodissociation Regions. *The Astrophysical Journal*, 573(1):215–237, 2002.

M Gritschneder, T Naab, A Burkert, S Walch, F Heitsch, and M Wetzstein. iVINE - Ionization in the parallel tree/sph code VINE: first results on the observed age-spread around O-stars. *Monthly Notices of the Royal Astronomical Society*, 393(1): 21–31, February 2009.

H J Habing. The interstellar radiation density between 912 A and 2400 A. *Bulletin of the Astronomical Institutes of the Netherlands*, 19:421, 1968.

T J Haworth, T J Harries, D M Acreman, and T G Bisbas. On the relative importance of different microphysics on the D-type expansion of galactic Hii regions. *Monthly Notices of the Royal Astronomical Society*, 453(3):2278–2290, September 2015.

L Hernquist and N Katz. TREESPH - A unification of SPH with the hierarchical tree method. *Astrophysical Journal Supplement Series (ISSN 0067-0049)*, 70:419–446, June 1989.

D J Hollenbach, T Takahashi, and A G G M Tielens. Low-density photodissociation regions. *The Astrophysical Journal*, 377:192–209, August 1991.

P F Hopkins and M J Raives. Accurate, meshless methods for magnetohydrodynamics. *Monthly Notices of the Royal Astronomical Society*, 455(1):51–88, January 2016.

C Y Hu, T Naab, S Walch, S C O Glover, and P C Clark. Star formation and molecular hydrogen in dwarf galaxies: a non-equilibrium view. *arXiv*, 458(4):3528–3553, 2016.

D A Hubber, C P Batty, A F McLeod, and A P Whitworth. SEREN - a new SPH code for star and planet formation simulations. Algorithms and tests. *Astronomy and Astrophysics*, 529:A27, March 2011.

D A Hubber, S Walch, and A P Whitworth. An improved sink particle algorithm for SPH simulations. *arXiv*, (4):3261–3275, January 2013.

J H Jeans. The Stability of a Spherical Nebula. *Philosophical Transactions of the Royal Society of London. Series A*, 199(312-320):1–53, 1902.

K G Jones. The Search for the Nebulae-I*. *Journal of the British Astronomical Association*, 78:256–267, May 1968.

K G Jones. Messier's Nebulae and Star Clusters. *Messier's Nebulae and Star Clusters*, 1991.

T M Kinnear, J Miao, G J White, and S Goodwin. Evolution of prolate molecular clouds at H II boundaries - I. Formation of fragment-core structures. *arXiv*, 444(2): 1221–1235, 2014.

T M Kinnear, J Miao, G J White, K Sugitani, and S Goodwin. Evolution of prolate molecular clouds at H II boundaries - II. Formation of BRCs of asymmetrical morphology. *arXiv*, 450(1):1017–1031, 2015.

S Kitsionas and A P Whitworth. Smoothed Particle Hydrodynamics with particle splitting, applied to self-gravitating collapse. *Monthly Notices of the Royal Astronomical Society*, 330(1):129–136, February 2002.

R S Klessen and S C O Glover. Physical Processes in the Interstellar Medium. *Star Formation in Galaxy Evolution: Connecting Numerical Models to Reality, Saas-Fee Advanced Course, Volume 43~ISBN 978-3-662-47889-9~Springer-Verlag Berlin Heidelberg, 2016, p~85*, 43(Chapter 2):85–249, 2016.

R S Klessen, Mark R Krumholz, and Fabian Heitsch. Numerical Star-Formation Studies – A Status Report. *arXiv*, pages 258–285, June 2009.

M Köhler, E Habart, H Arab, J Bernard-Salas, H Ayasso, A Abergel, A Zavagno, E Polehampton, M H D van der Wiel, D A Naylor, G Makiwa, K Dassas, C Joblin, P Pilleri, O Berné, A Fuente, M Gerin, J R Goicoechea, and D Teyssier. Physical structure of the photodissociation regions in NGC 7023. Observations of gas and dust emission with Herschel. *arXiv*, 569:A109, 2014.

T Kusune, K Sugitani, J Miao, M Tamura, Y Sato, J Kwon, M Watanabe, S Nishiyama, T Nagayama, and S Sato. Near-IR Imaging Polarimetry toward a Bright-rimmed Cloud: Magnetic Field in SFO 74. *arXiv*, 798(1):60, 2015.

B Lefloch and B Lazareff. Cometary globules. 1: Formation, evolution and morphology. *Astronomy and Astrophysics*, 289:559–578, 1994.

L B Lucy. A numerical approach to the testing of the fission hypothesis. *Astronomical Journal*, 82:1013, December 1977.

C F McKee and Eve C Ostriker. Theory of Star Formation. *Annual Review of Astronomy & Astrophysics*, 45(1):565–687, September 2007.

A F McLeod, J E Dale, A Ginsburg, B Ercolano, M Gritschneder, S Ramsay, and L Testi. The Pillars of Creation revisited with MUSE: gas kinematics and high-mass stellar feedback traced by optical spectroscopy. *Monthly Notices of the Royal Astronomical Society*, 450(1):1057–1076, April 2015.

L Mestel and L Spitzer, Jr. Star formation in magnetic dust clouds. *MNRAS*, 116(5): 503–514, 1956.

J Miao, G J White, R P Nelson, M A Thompson, and L Morgan. Triggered star formation in bright-rimmed clouds: the Eagle nebula revisited. *MNRAS*, 369(1): 143–155, 2006.

J Miao, G J White, M A Thompson, and R P Nelson. An Investigation on the Morphological Evolution of Bright-Rimmed Clouds. *The Astrophysical Journal*, 692(1): 382–401, February 2009.

J J Monaghan. Smoothed particle hydrodynamics. *In: Annual review of astronomy and astrophysics. Vol. 30 (A93-25826 09-90)*, 30(1):543–574, 1992.

J J Monaghan. SPH compressible turbulence. *Monthly Notice of the Royal Astronomical Society*, 335(3):843–852, September 2002.

J J Monaghan and J C Lattanzio. A refined particle method for astrophysical problems. *Astronomy and Astrophysics (ISSN 0004-6361)*, 149:135–143, August 1985.

Kazutaka Motoyama, T Umemoto, H Shang, and T Hasegawa. Effects of Magnetic Field And Far-Ultraviolet Radiation on the Structures of Bright-Rimmed Clouds. *The Astrophysical Journal*, 766(1):50–, March 2013.

Kazutaka Motoyama, Oscar Morata, H Shang, R Krasnopolsky, and T Hasegawa. A Hydrochemical Hybrid Code for Astrophysical Problems. I. Code Verification and Benchmarks for Photon-Dominated Region (PDR). *arXiv*, (1):46, June 2015.

R P Nelson and W D Langer. The Dynamics of Low-Mass Molecular Clouds in External Radiation Fields. *The Astrophysical Journal*, 482(2):796–826, June 1997.

R P Nelson and W D Langer. On the Stability and Evolution of Isolated Bok Globules. *The Astrophysical Journal*, 524(2):923–946, October 1999.

R P Nelson and J C B Papaloizou. Three-dimensional hydrodynamic simulations of collapsing prolate clouds. *Monthly Notices of the Royal Astronomical Society*, 265 (4):905–920, December 1993.

R P Nelson and J C B Papaloizou. Variable smoothing lengths and energy conservation in smoothed particle hydrodynamics. *Monthly Notices of the Royal Astronomical Society*, 270(1):1–20, September 1994.

P Padoan, M Juvela, and V Pelkonen. High-Resolution Mapping of Interstellar Clouds by Near-Infrared Scattering. *The Astrophysical Journal*, 636(2):L101–L104, January 2006.

D J Price. Smoothed Particle Hydrodynamics: Things I wish my mother taught me. *arXiv*, November 2011.

D J Price. Smoothed particle hydrodynamics and magnetohydrodynamics. *Journal of Computational Physics*, 231(3):759–794, February 2012.

D J Price and J J Monaghan. Smoothed Particle Magnetohydrodynamics II. Variational principles and variable smoothing length terms. *arXiv*, (1):139–152, October 2003.

D J Price and J J Monaghan. Smoothed Particle Magnetohydrodynamics - I. Algorithm and tests in one dimension. *Monthly Notices of the Royal Astronomical Society*, 348 (1):123–138, February 2004.

D J Price, J Wurster, C Nixon, T S Tricco, S Toupin, A Pettitt, C Chan, G Laibe, S Glover, C Dobbs, R Nealon, D Liptai, H Worpel, C Bonnerot, G Dipierro, E Ragusa, C Federrath, R Iaconi, T Reichardt, D Forgan, M Hutchison, T Constantino, B Ayliffe, D Mentiplay, K Hirsh, and G Lodato. Phantom: A smoothed particle hydrodynamics and magnetohydrodynamics code for astrophysics. *arXiv*, February 2017.

J M Rathborne, M G Burton, K J Brooks, M Cohen, M C B Ashley, and J W V Storey. Photodissociation regions and star formation in the Carina Nebula. *arXiv*, (1):85–97, November 2001.

D Seifried and S Walch. Modelling the chemistry of star forming filaments - I. H_2 and CO chemistry. *arXiv*, 459(1):L11–L15, 2016.

Y Shimajiri, T Sakai, T Tsukagoshi, Y Kitamura, M Momose, M Saito, T Oshima, K Kohno, and R Kawabe. Extensive [C I] Mapping toward the Orion-A Giant Molecular Cloud. *arXiv*, 774(2):L20, 2013.

F H Shu. Ambipolar diffusion in self-gravitating isothermal layers. *The Astrophysical Journal*, 273:202–213, 1983.

V Springel. The cosmological simulation code GADGET-2. *arXiv*, (4):1105–1134, May 2005.

V Springel, N Yoshida, and S D M White. GADGET: a code for collisionless and gasdynamical cosmological simulations. *New Astronomy*, 6(2):79–117, April 2001.

D J Stock, M G Wolfire, E Peeters, A G G M Tielens, B Vandenbussche, C Boersma, and J Cami. Herschel PACS and SPIRE spectroscopy of the photodissociation regions associated with S 106 and IRAS 23133+6050. *arXiv*, 579:A67, 2015.

J M Stone and M L Norman. ZEUS-2D: A radiation magnetohydrodynamics code for astrophysical flows in two space dimensions. I - The hydrodynamic algorithms and tests. *Astrophysical Journal Supplement Series (ISSN 0067-0049)*, 80:753–790, June 1992.

J M Stone, Thomas A Gardiner, Peter Teuben, John F Hawley, and Jacob B Simon. Athena: A New Code for Astrophysical MHD. *The Astrophysical Journal Supplement Series*, 178(1):137–177, September 2008.

R Teyssier. Cosmological hydrodynamics with adaptive mesh refinement. A new high resolution code called RAMSES. *Astronomy and Astrophysics*, 385(1):337–364, April 2002.

The HDF Group. Hierarchical Data Format, version 5, 1997. URL `http://www.hdfgroup.org/HDF5/`.

A G G M Tielens. *The Physics and Chemistry of the Interstellar Medium*. Cambridge University Press, August 2005.

T S Tricco and D J Price. Constrained Hyperbolic Divergence Cleaning for Smoothed Particle Magnetohydrodynamics. *arXiv*, (2):7214–7236, June 2012.

J Kelly Truelove, Richard I Klein, C F McKee, John H II Holliman, Louis H Howell, and Jeffrey A Greenough. The Jeans Condition: A New Constraint on Spatial Resolution in Simulations of Isothermal Self-gravitational Hydrodynamics. *The Astrophysical Journal*, 489(2):L179–L183, November 1997.

R Vacondio, B D Rogers, P K Stansby, and P Mignosa. Variable resolution for SPH in three dimensions: Towards optimal splitting and coalescing for dynamic adaptivity. *Computer Methods in Applied Mechanics and Engineering*, 300:442–460, March 2016.

J Vainio and I Vilja. Jeans Analysis of Bok globules in $f(R)$ gravity. *arXiv*, 2015.

E F van Dishoeck and J H Black. The photodissociation and chemistry of interstellar CO. *The Astrophysical Journal*, 334:771–802, November 1988.

C F von Weizsäcker. The Evolution of Galaxies and Stars. *The Astrophysical Journal*, 114:165, 1951.

S Walch, A P Whitworth, T G Bisbas, R Wünsch, and D A Hubber. Clumps and triggered star formation in ionized molecular clouds. *Monthly Notices of the Royal Astronomical Society*, 435(2):917–927, October 2013.

S Walch, P Girichidis, T Naab, A Gatto, S C O Glover, R Wünsch, R S Klessen, P C Clark, T Peters, D Derigs, and C Baczynski. The SILCC (SImulating the LifeCycle of molecular Clouds) project - I. Chemical evolution of the supernova-driven ISM. *arXiv*, 454(1):238–268, 2015.

J C Weingartner and B T Draine. Photoelectric Emission from Interstellar Dust: Grain Charging and Gas Heating. *The Astrophysical Journal Supplement*, 134(2):263–281, June 2001.

G J White, R P Nelson, W S Holland, E I Robson, J S Greaves, M J McCaughrean, G L Pilbratt, D S Balser, T Oka, S Sakamoto, T Hasegawa, W H McCutcheon, H E Matthews, C V M Fridlund, N F H Tothill, M Huldtgren, and J R Deane. The Eagle Nebula's fingers - pointers to the earliest stages of star formation? *Astronomy and Astrophysics*, 342:233–256, February 1999.

J P Williams, L Blitz, and C F McKee. The Structure and Evolution of Molecular Clouds: from Clumps to Cores to the IMF. *Protostars and Planets IV (Book - Tucson: University of Arizona Press; eds Mannings*, page 97, May 2000.

Chapter A

Micro-Physical & Chemical Cooling: Mass loss, Radial Velocity, Density and Temperature Profiles
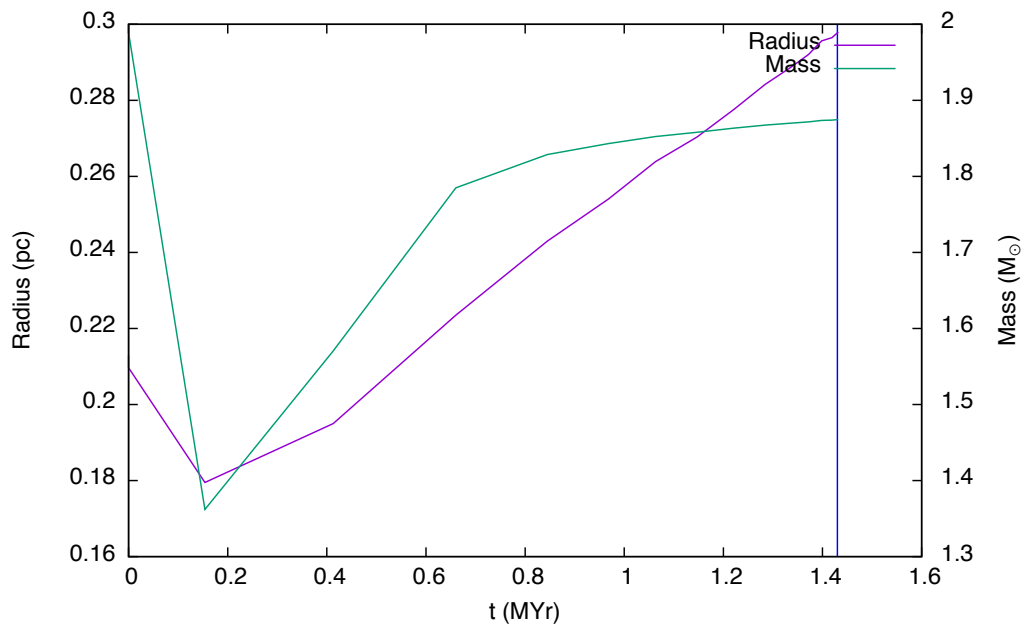

A.1 Model A
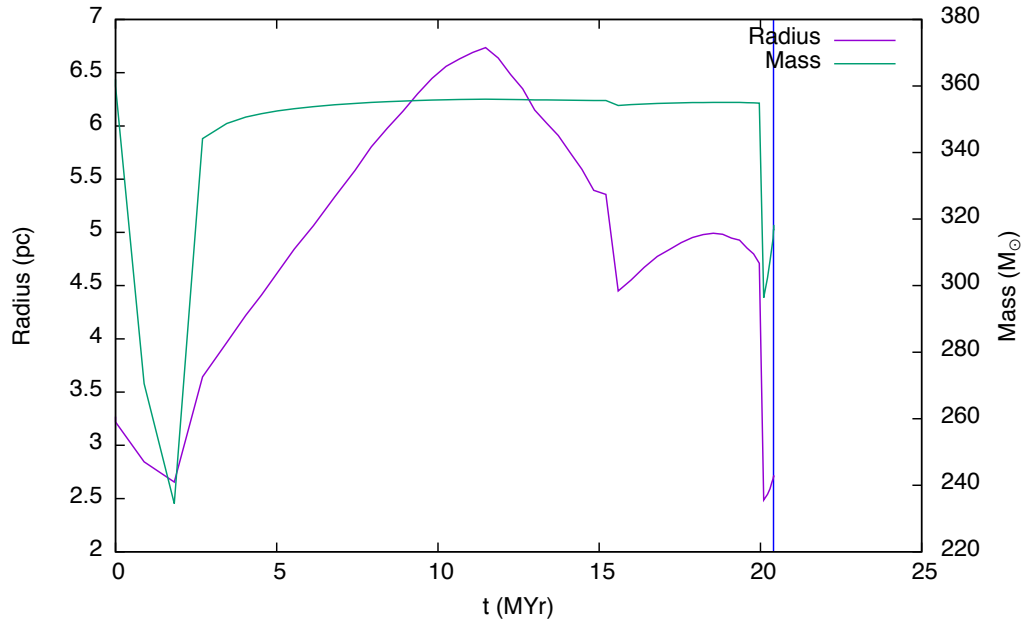
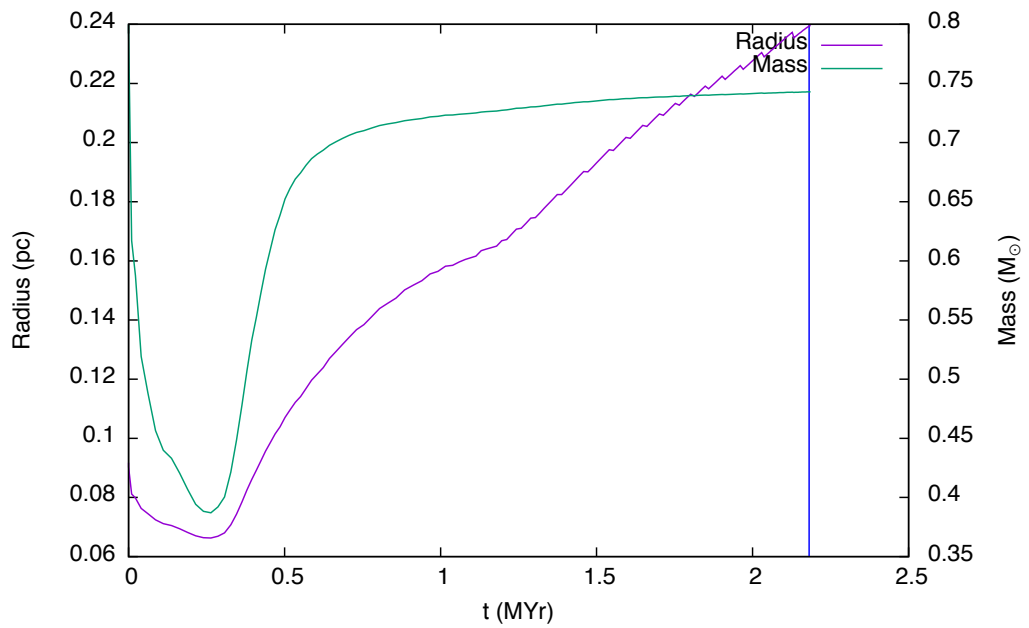Figure A.1: Model A: the time evolution of the cloud with an initial density of 50 cm^{-3}, a mass of 362 M$_\odot$ and a radius of 3.27 pc is shown in this graph. The cloud radius (purple line) is taken to be the zero crossing point of radial velocity and the mass (green line) is taken to be that which lies inside the radius. The blue vertical line denotes the time at which the high density peak first forms. This is the minimum cloud mass which collapses for the selected values of density.
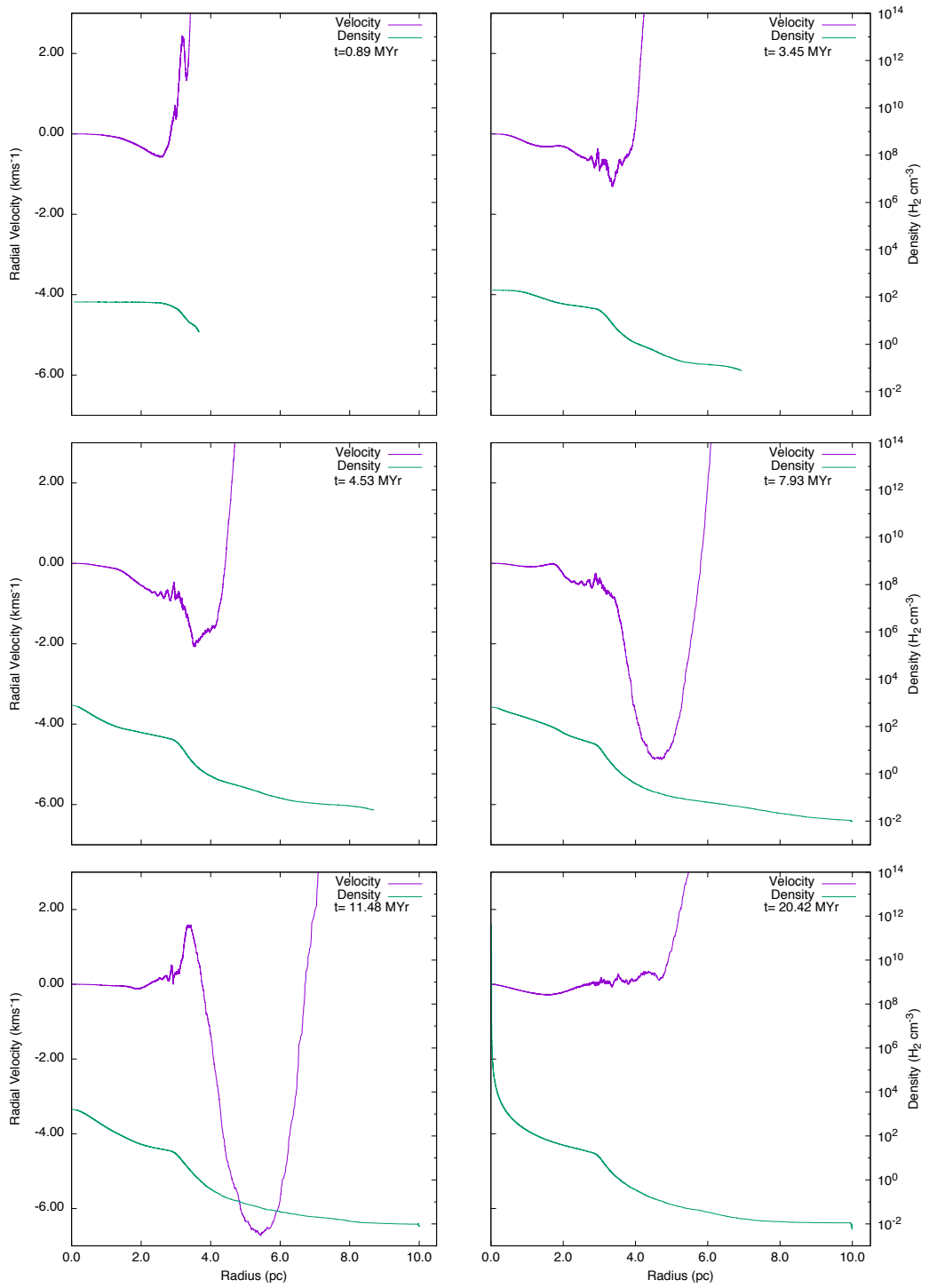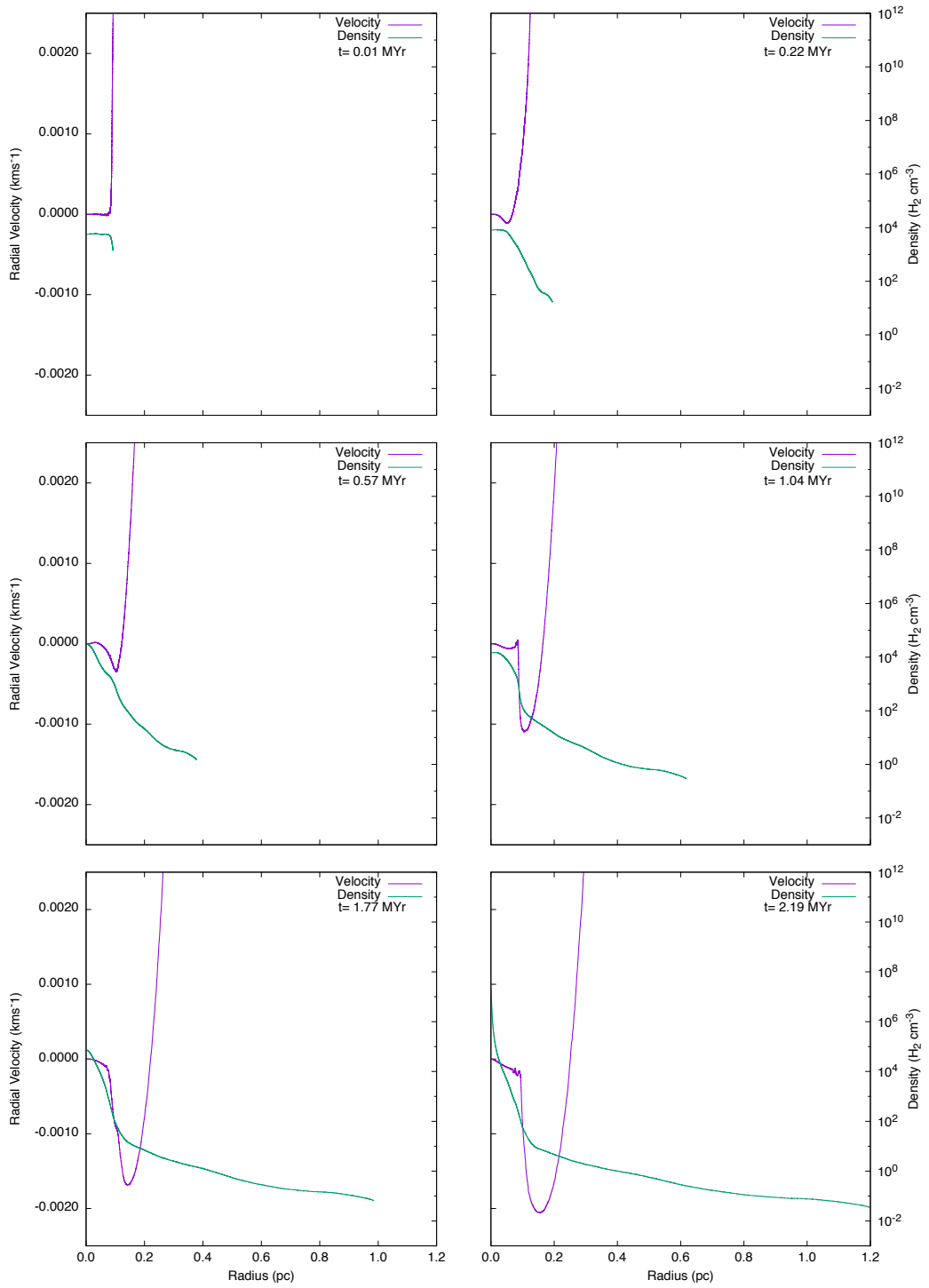
Figure A.2: Model A: six snapshots showing radial velocity (purple line) and density (green line) for a cloud with an initial density of 50 cm^{-3}, a mass of 362 M$_\odot$ and a radius of 3.27 pc.
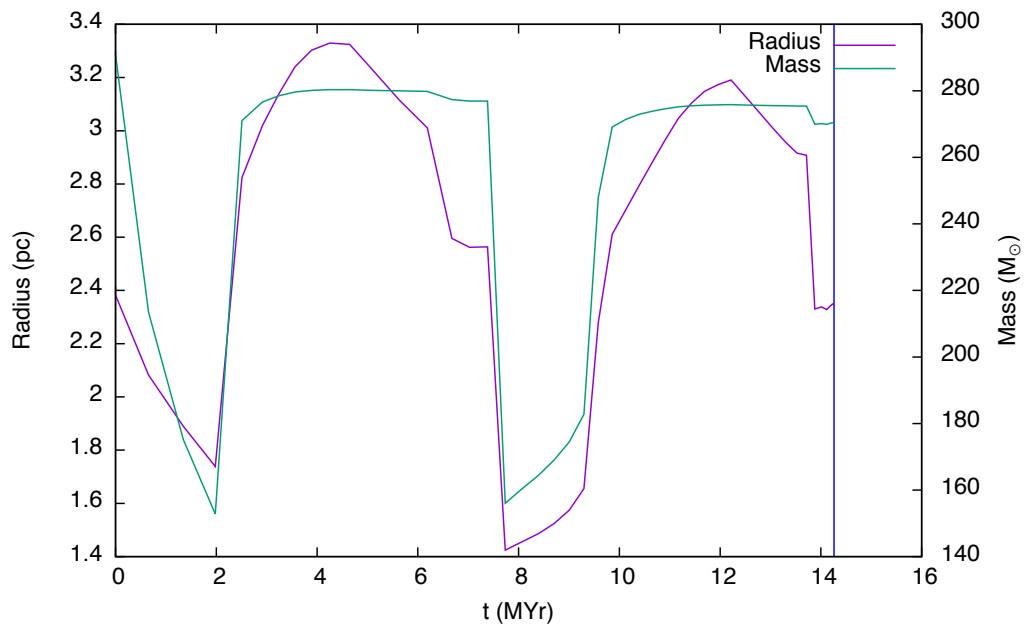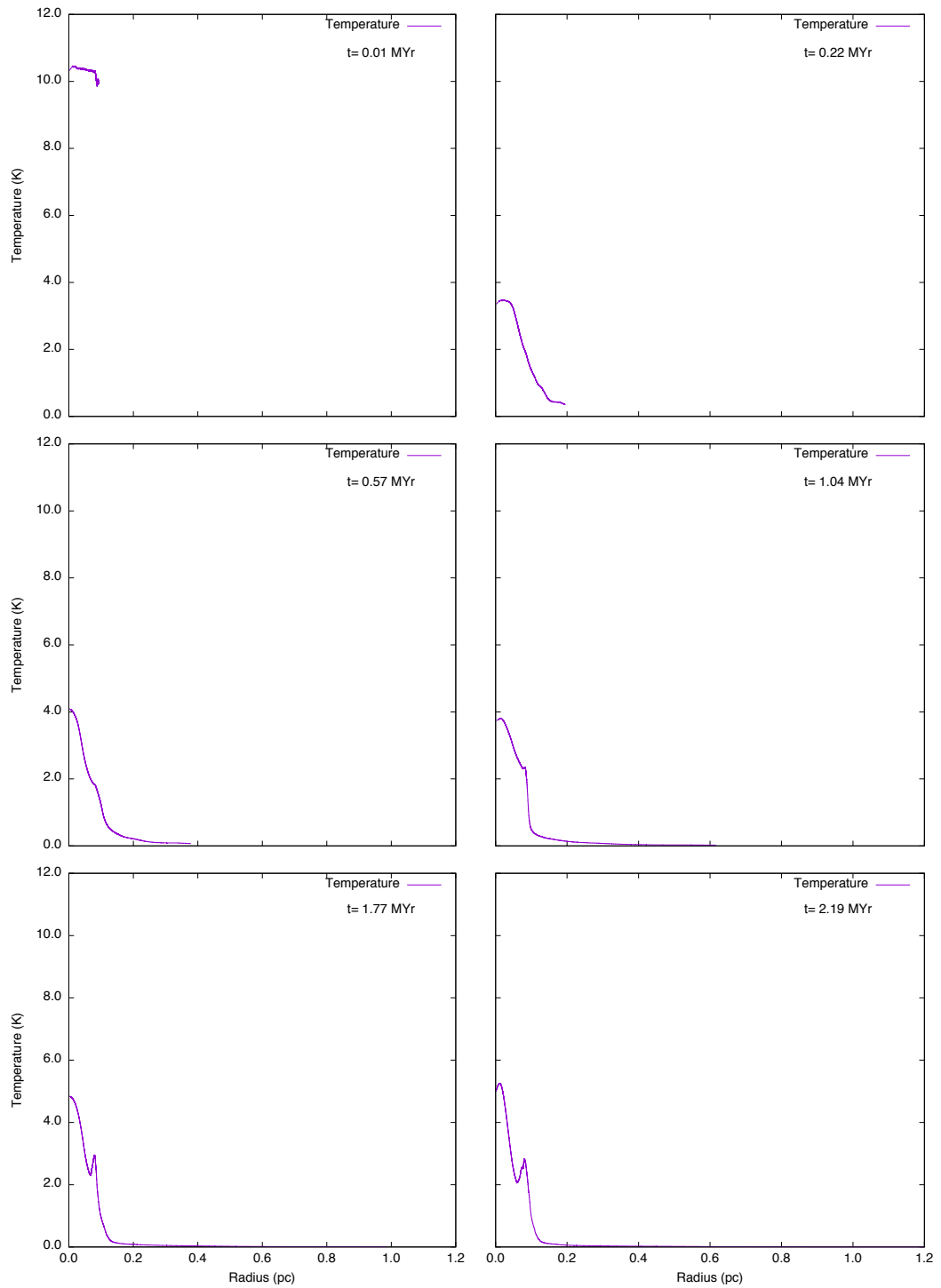
Figure A.3: Model A: the time evolution of the cloud with an initial density of 100 cm^{-3}, a mass of 292 M$_\odot$ and a radius of 2.42 pc is shown in this graph. The cloud radius (purple line) is taken to be the zero crossing point of radial velocity and the mass (green line) is taken to be that which lies inside the radius. The blue vertical line denotes the time at which the high density peak first forms. This is the minimum cloud mass which collapses for the selected values of density.
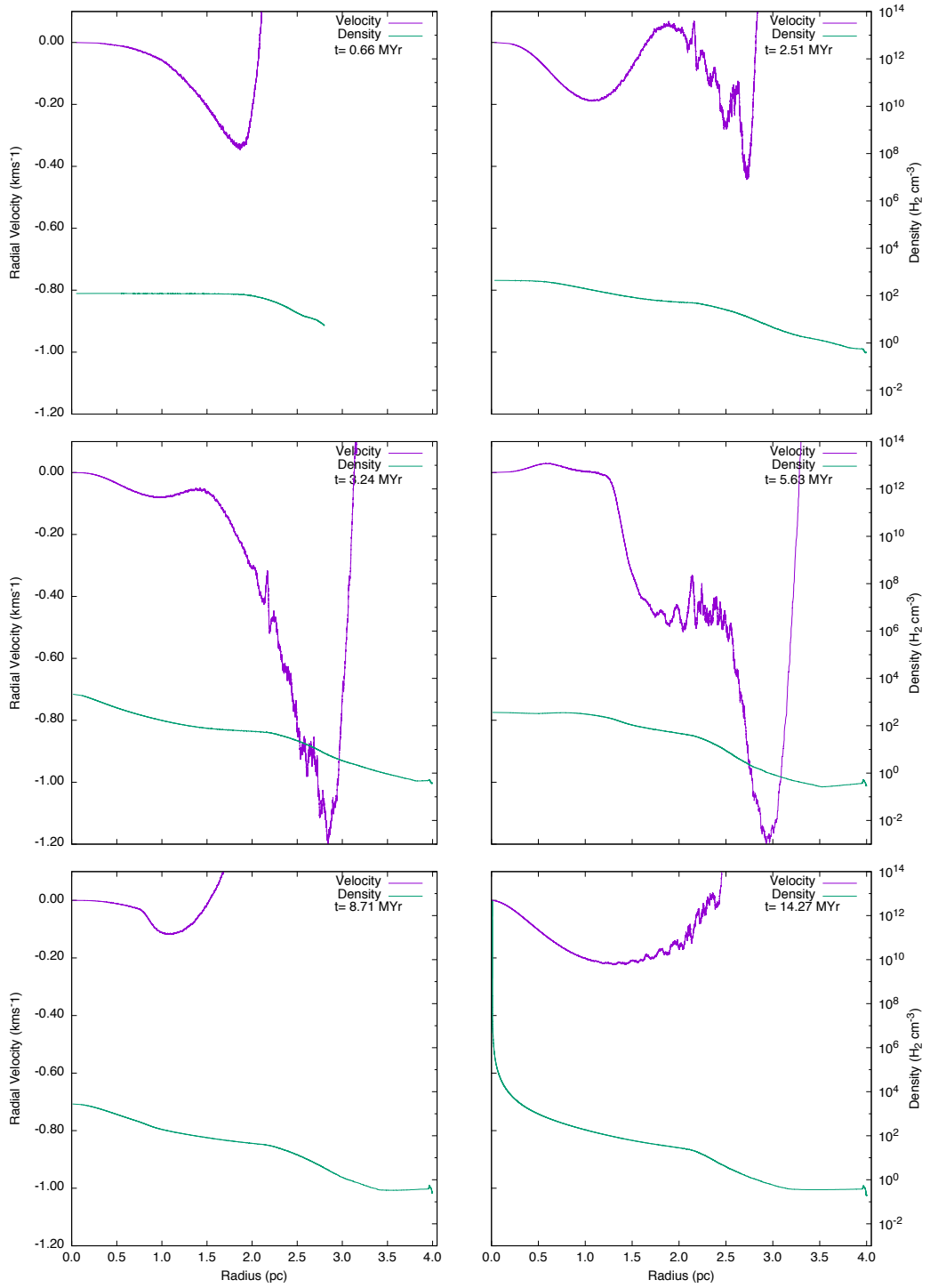
Figure A.4: Model A: six snapshots showing radial velocity (purple line) and density (green line) for a cloud with an initial density of 100 cm^{-3}, a mass of 292 M$_\odot$ and a radius of 2.42 pc.
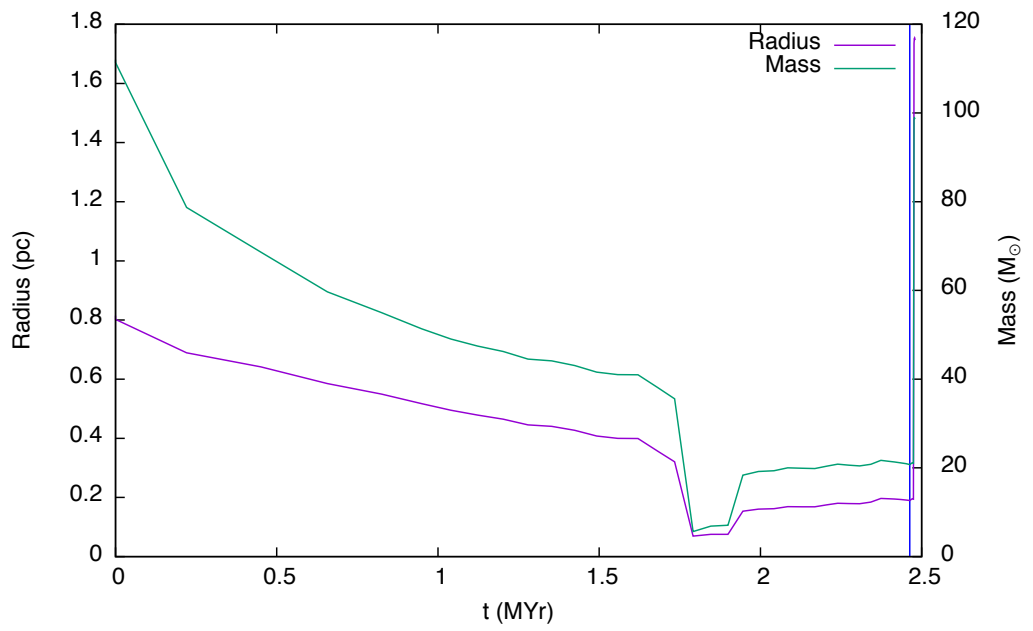
Figure A.5: Model A: the time evolution of the cloud with an initial density of 1000 cm^{-3}, a mass of 112 $M_{\odot}$ and a radius of 0.82 pc is shown in this graph. The cloud radius (purple line) is taken to be the zero crossing point of radial velocity and the mass (green line) is taken to be that which lies inside the radius. The blue vertical line denotes the time at which the high density peak first forms. This is the minimum cloud mass which collapses for the selected values of density.
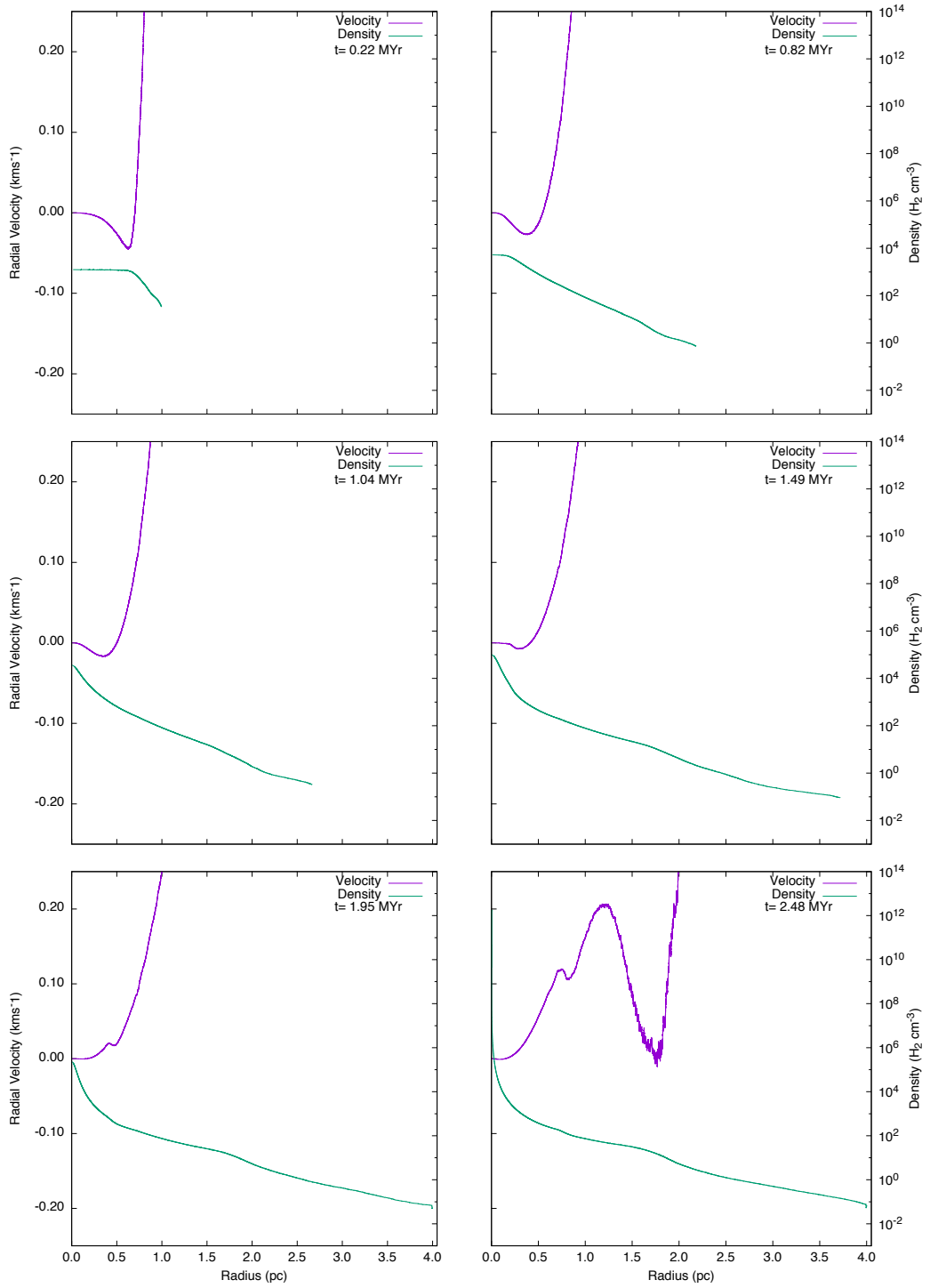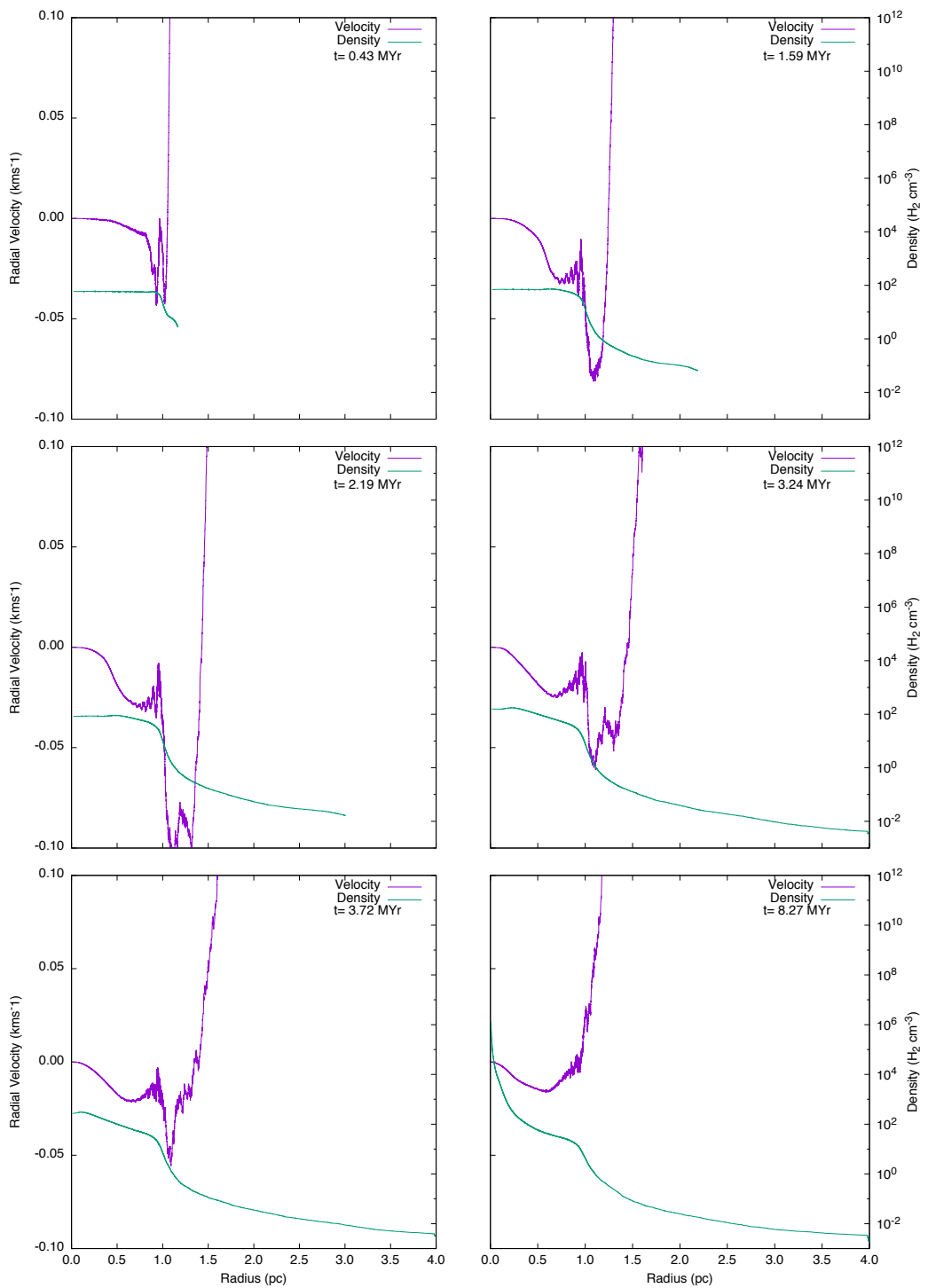
Figure A.6: Model A: six snapshots showing radial velocity (purple line) and density (green line) for a cloud with an initial density of 1000 cm^{-3}, a mass of 112 M$_\odot$ and a radius of 0.82 pc.
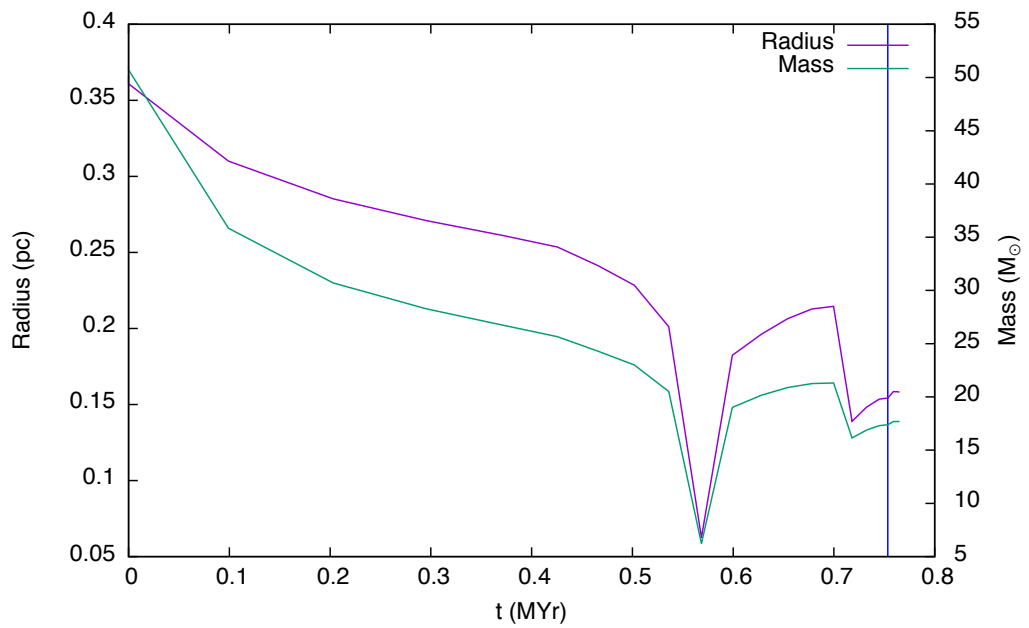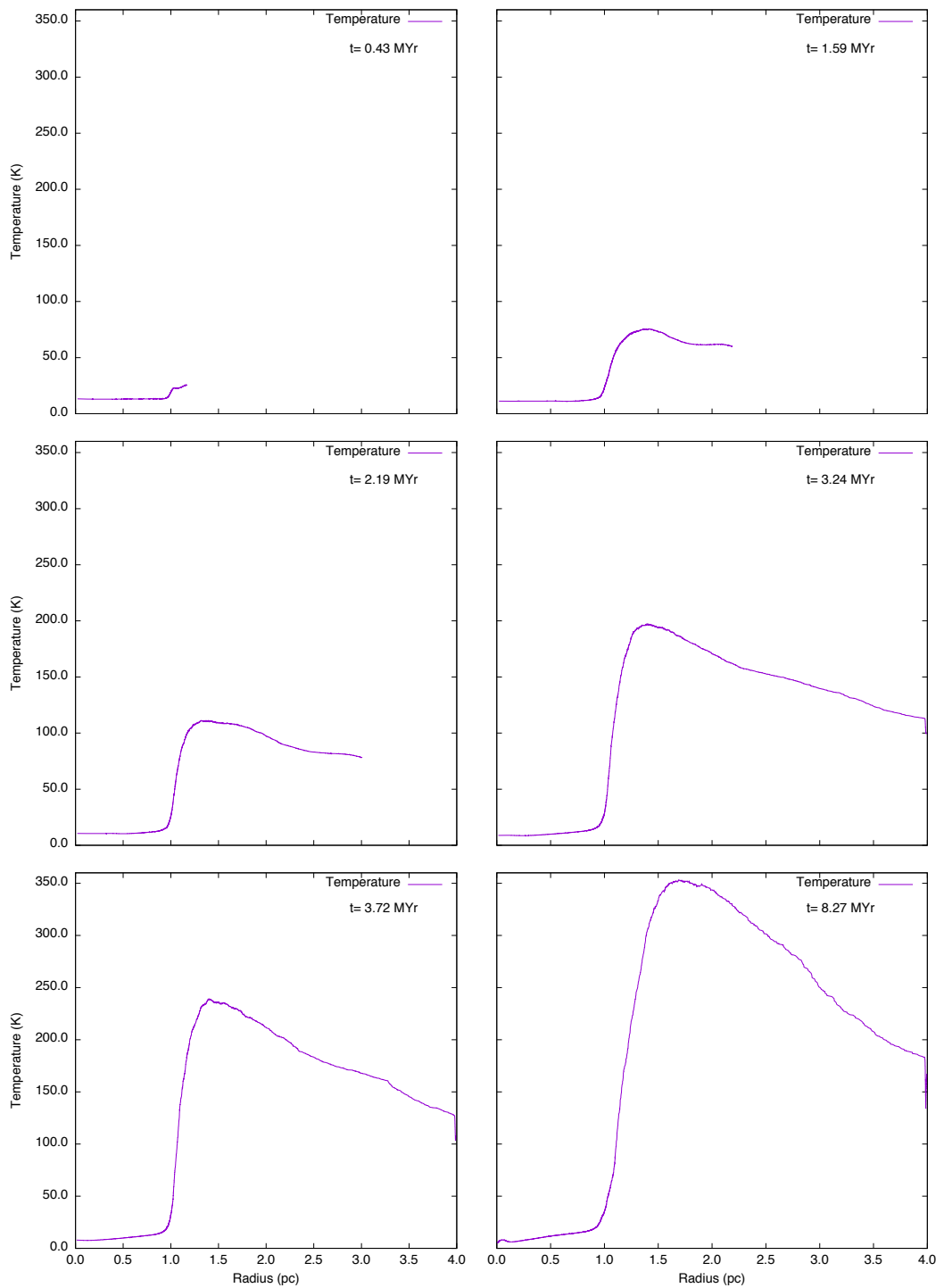
Figure A.7: Model A: the time evolution of the cloud with an initial density of 5000 cm^{-3}, a mass of 51 M$_\odot$ and a radius of 0.37 pc is shown in this graph. The cloud radius (purple line) is taken to be the zero crossing point of radial velocity and the mass (green line) is taken to be that which lies inside the radius. The blue vertical line denotes the time at which the high density peak first forms. This is the minimum cloud mass which collapses for the selected values of density.
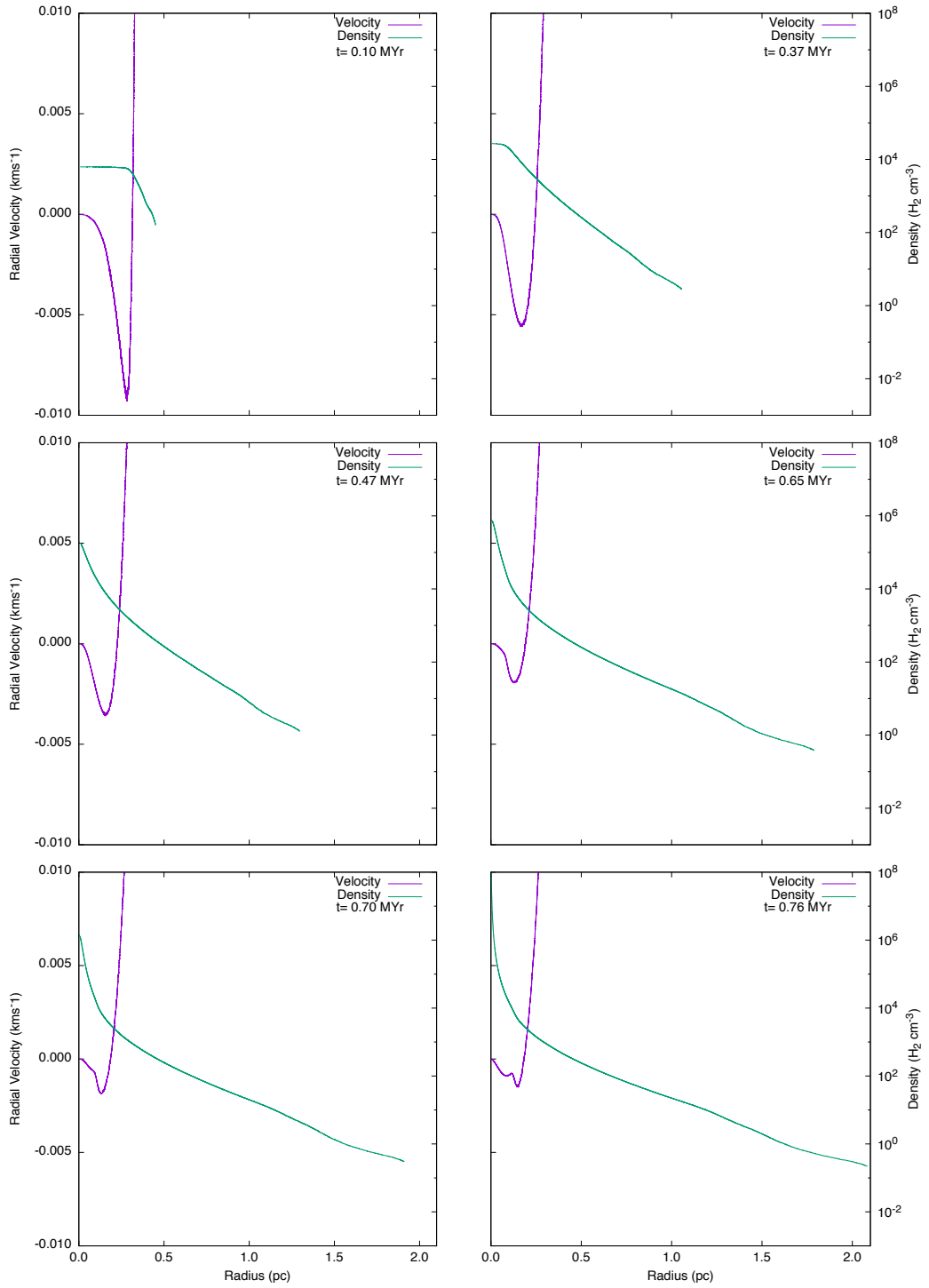
Figure A.8: Model A: six snapshots showing radial velocity (purple line) and density (green line) for a cloud with an initial density of 5000 cm^{-3}, a mass of 51 $M_\odot$ and a radius of 0.37 pc.
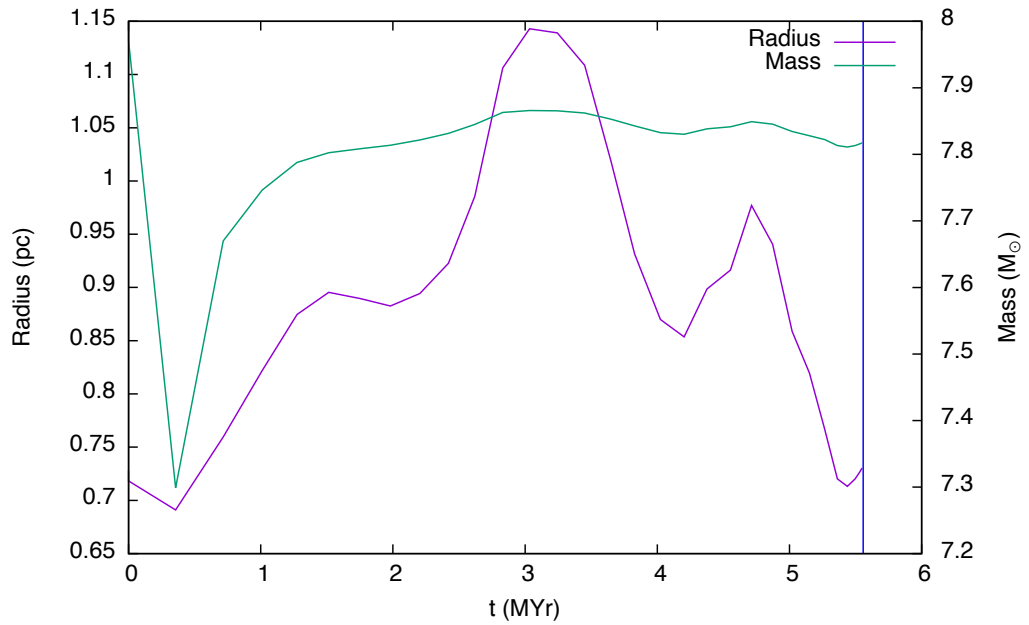
A.2   MODEL B
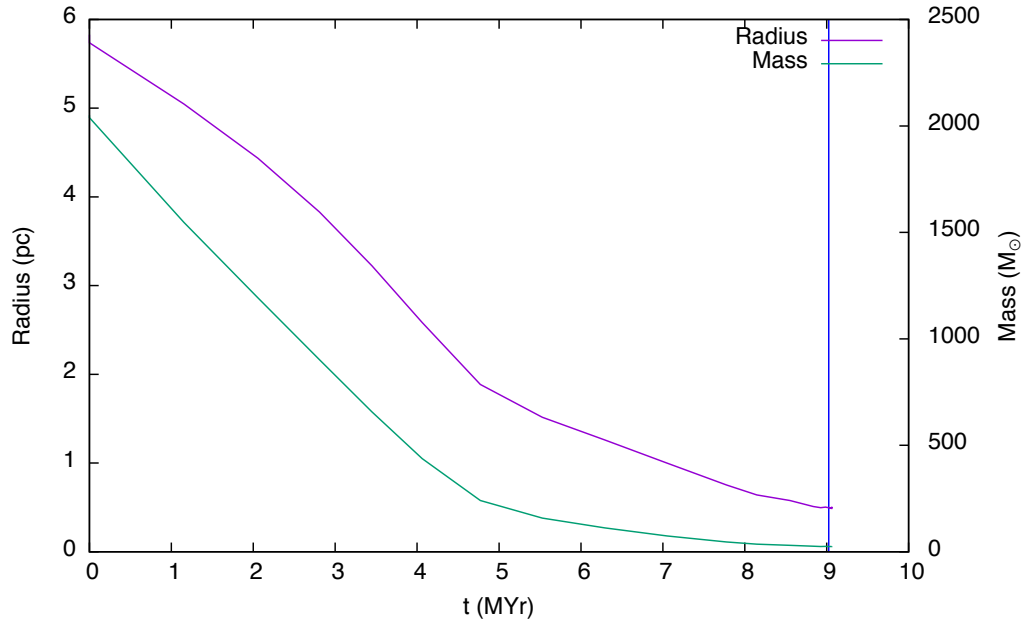
Figure A.9: Model B: the time evolution of the cloud with an initial density of 50 cm^3, a mass of 2050 M$_\odot$ and a radius of 5.83 pc is shown in this graph. The cloud radius (purple line) is taken to be the zero crossing point of radial velocity and the mass (green line) is taken to be that which lies inside the radius. The blue vertical line denotes the time at which the high density peak first forms. This is the minimum cloud mass which collapses for the selected values of density.
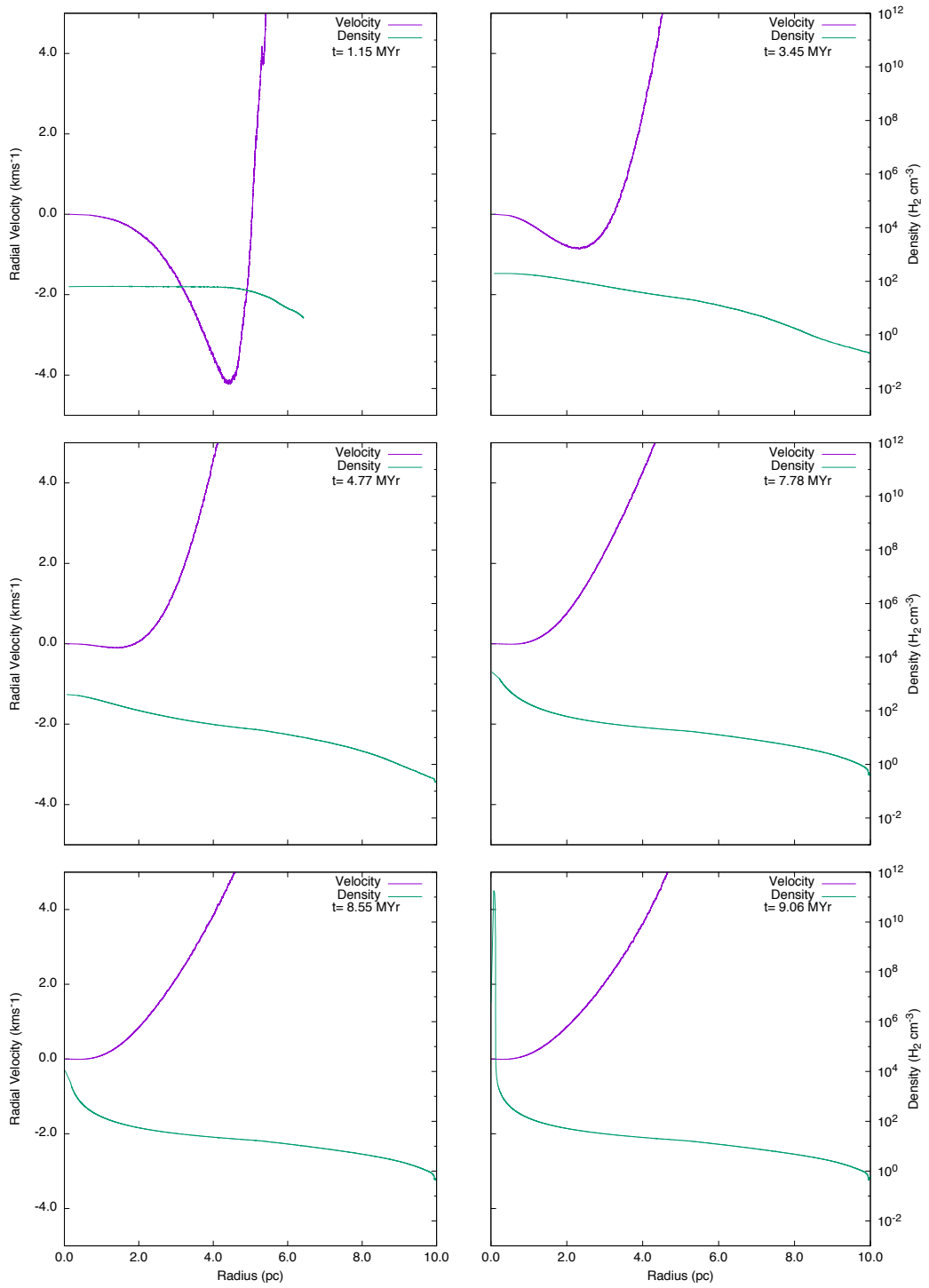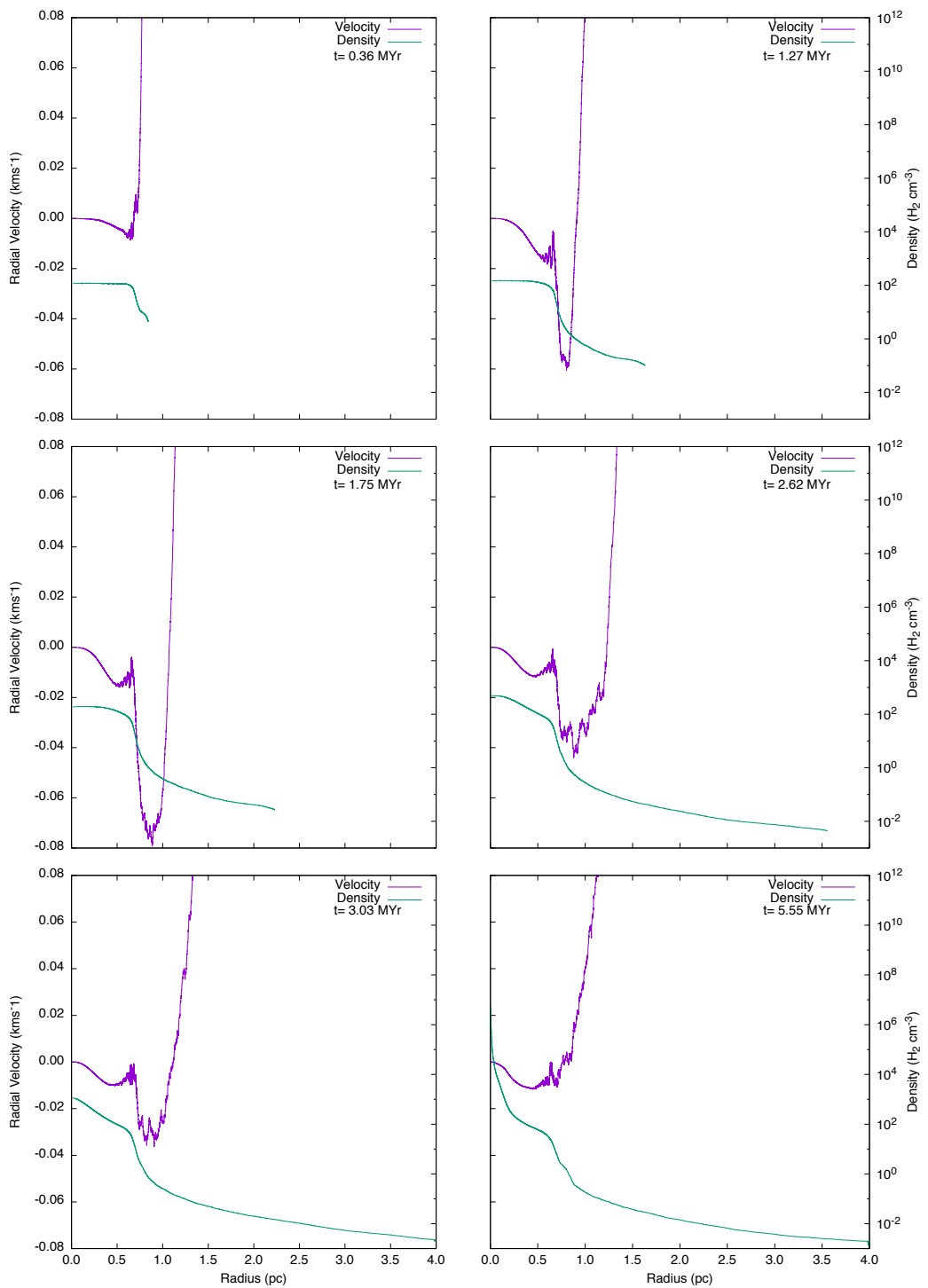
Figure A.10: Model B: six snapshots showing radial velocity (purple line) and density (green line) for a cloud with an initial density of 50 cm^3, a mass of 2050 M$_\odot$ and a radius of 5.83 pc.
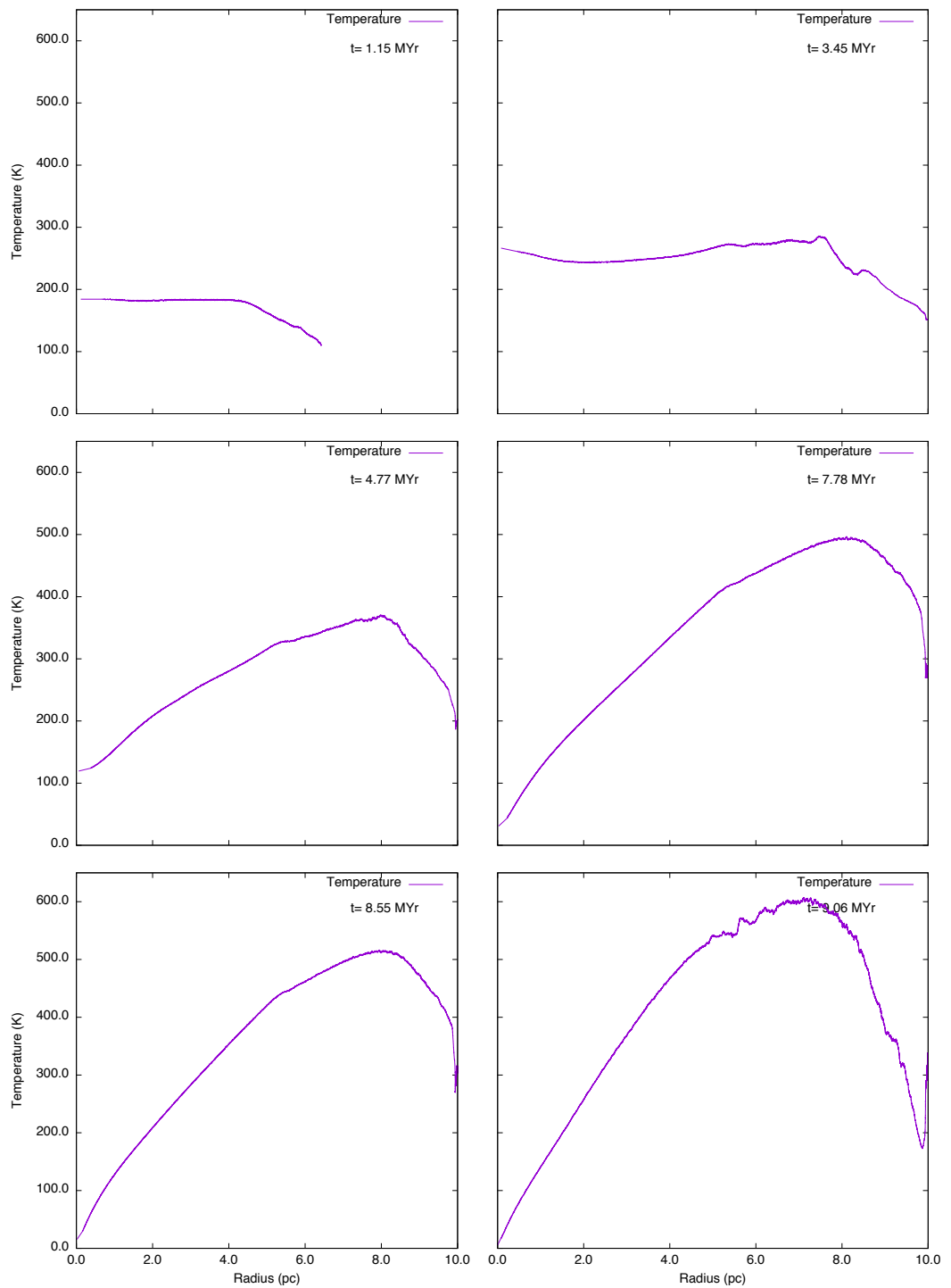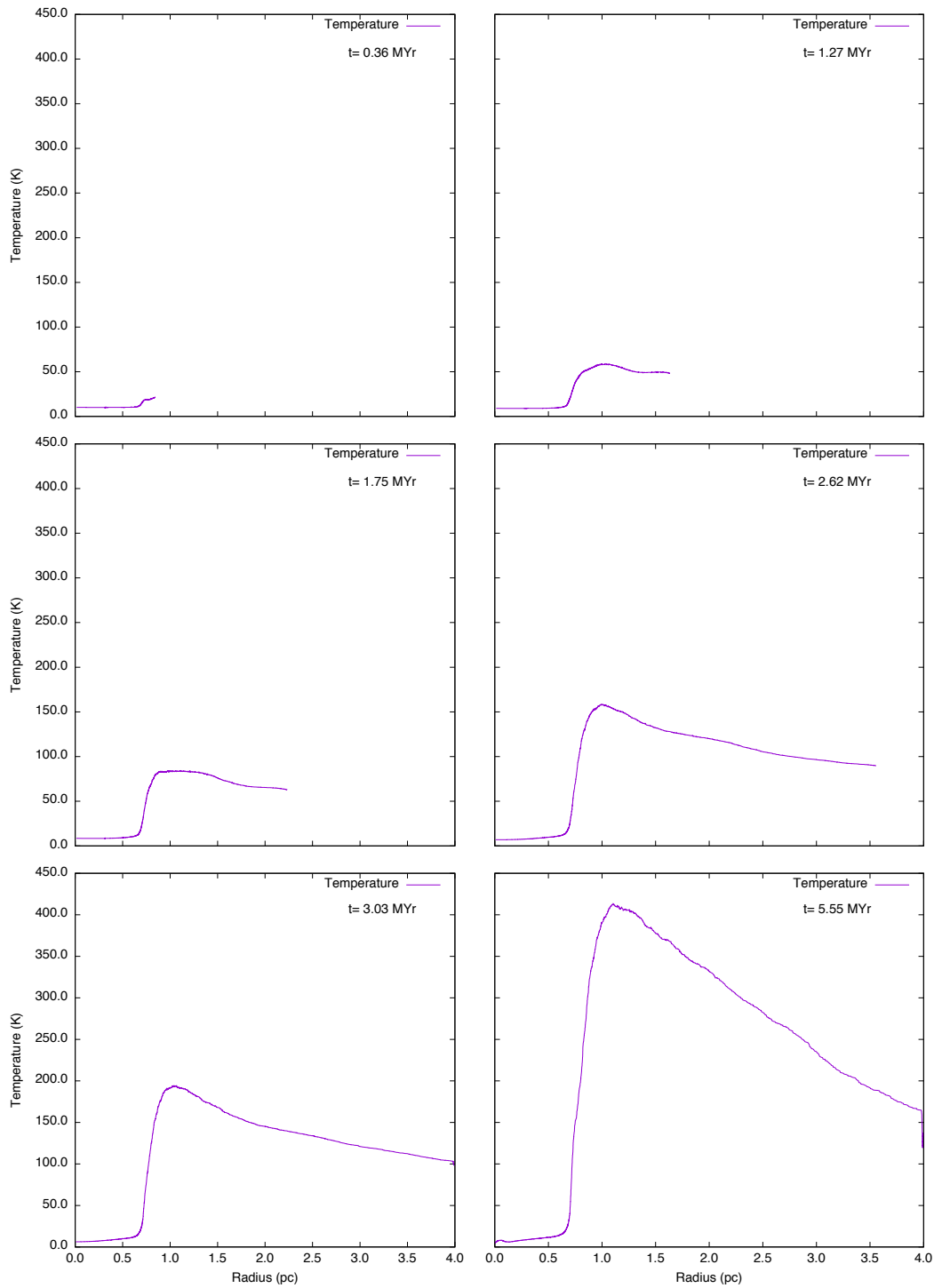
Figure A.11: Model B: six snapshots showing temperature (purple line) for a cloud with an initial density of 50 cm³, a mass of 2050 M$_\odot$ and a radius of 5.83 pc.
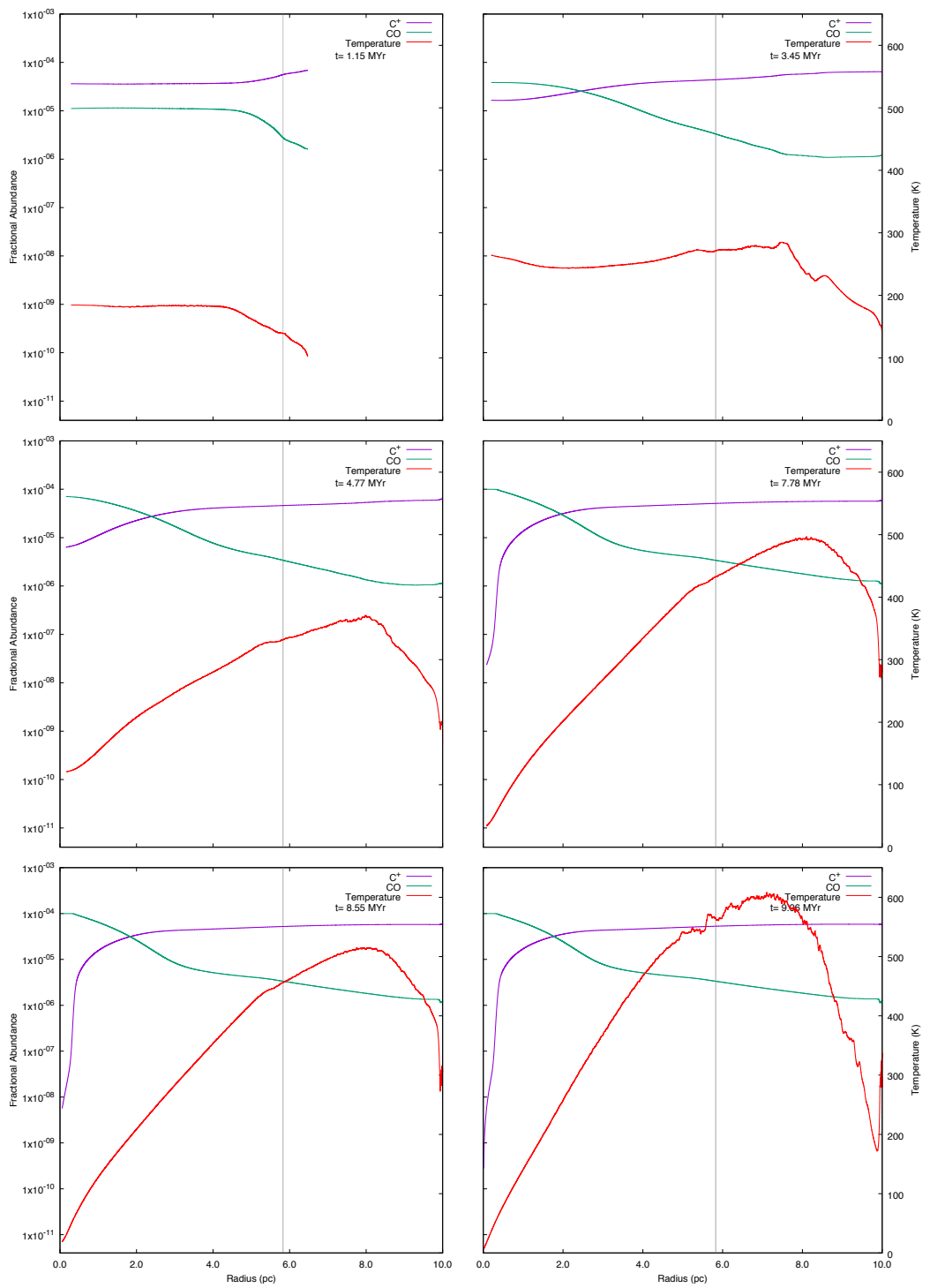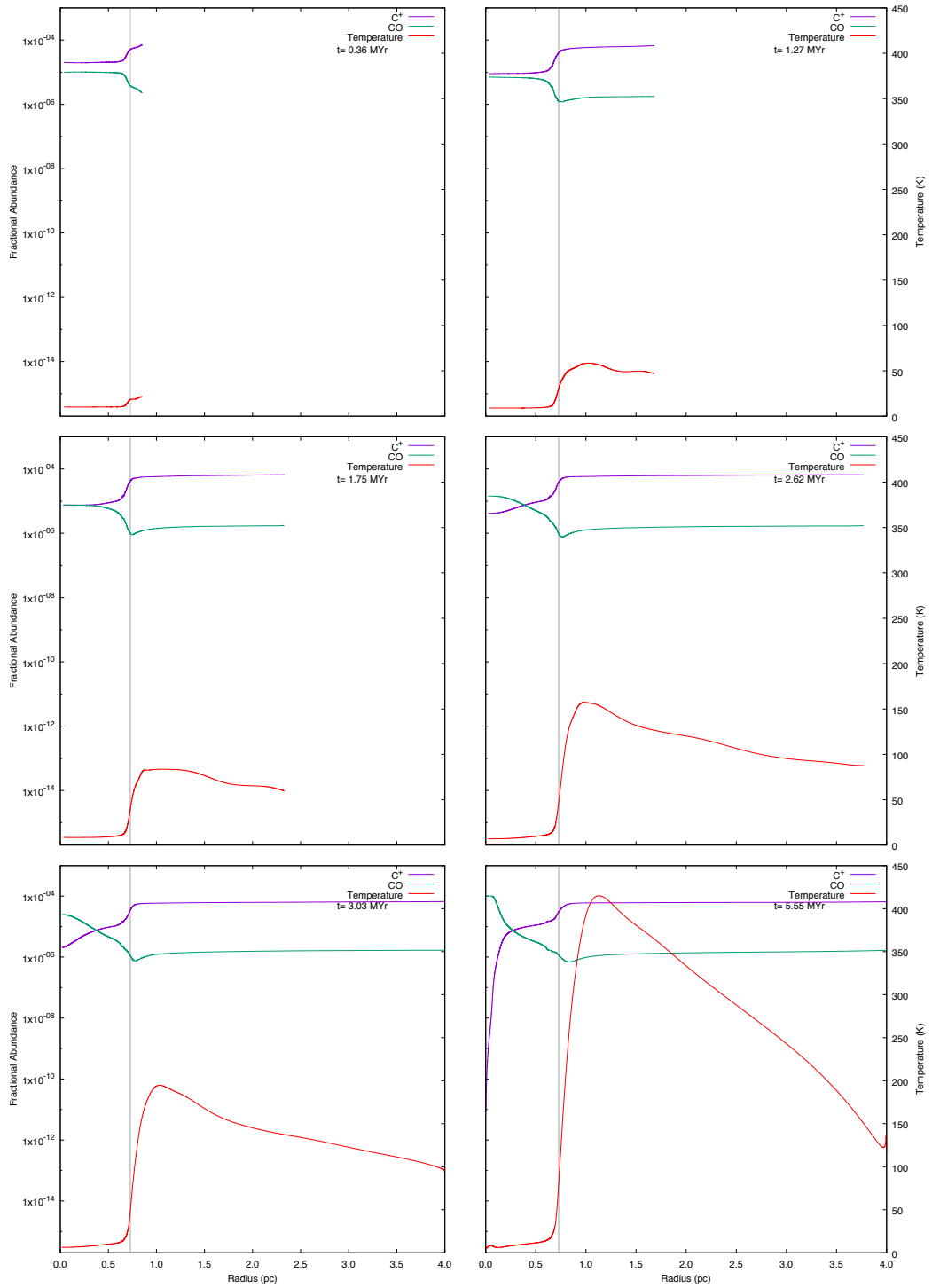
Figure A.12: Model B: six snapshots showing the chemical abundances of CO and C$^+$ for a cloud with an initial density of 50 cm^{-3}, a mass of 2050 M$_\odot$ and a radius of 5.83 pc.
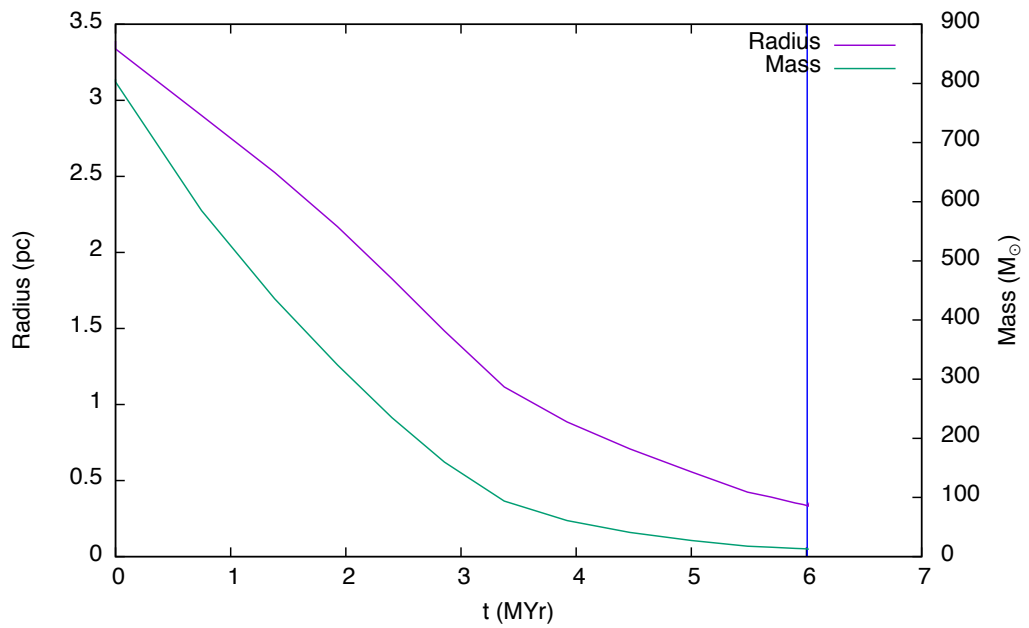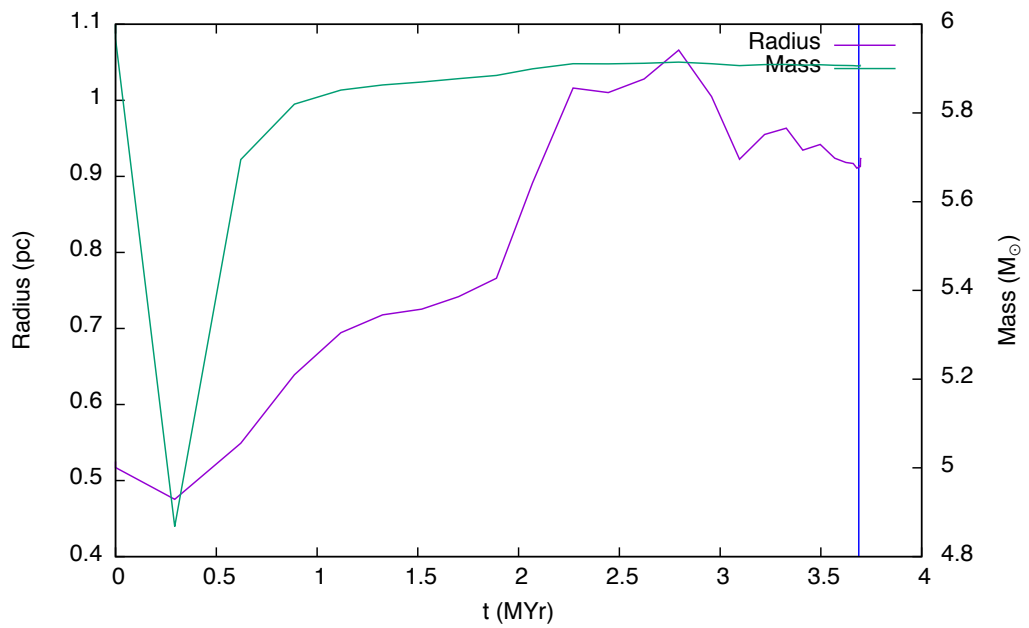
Figure A.13: Model B: the time evolution of the cloud with an initial density of 100 cm^3, a mass of 807 $M_\odot$ and a radius of 3.39 pc is shown in this graph. The cloud radius (purple line) is taken to be the zero crossing point of radial velocity and the mass (green line) is taken to be that which lies inside the radius. The blue vertical line denotes the time at which the high density peak first forms. This is the minimum cloud mass which collapses for the selected values of density.
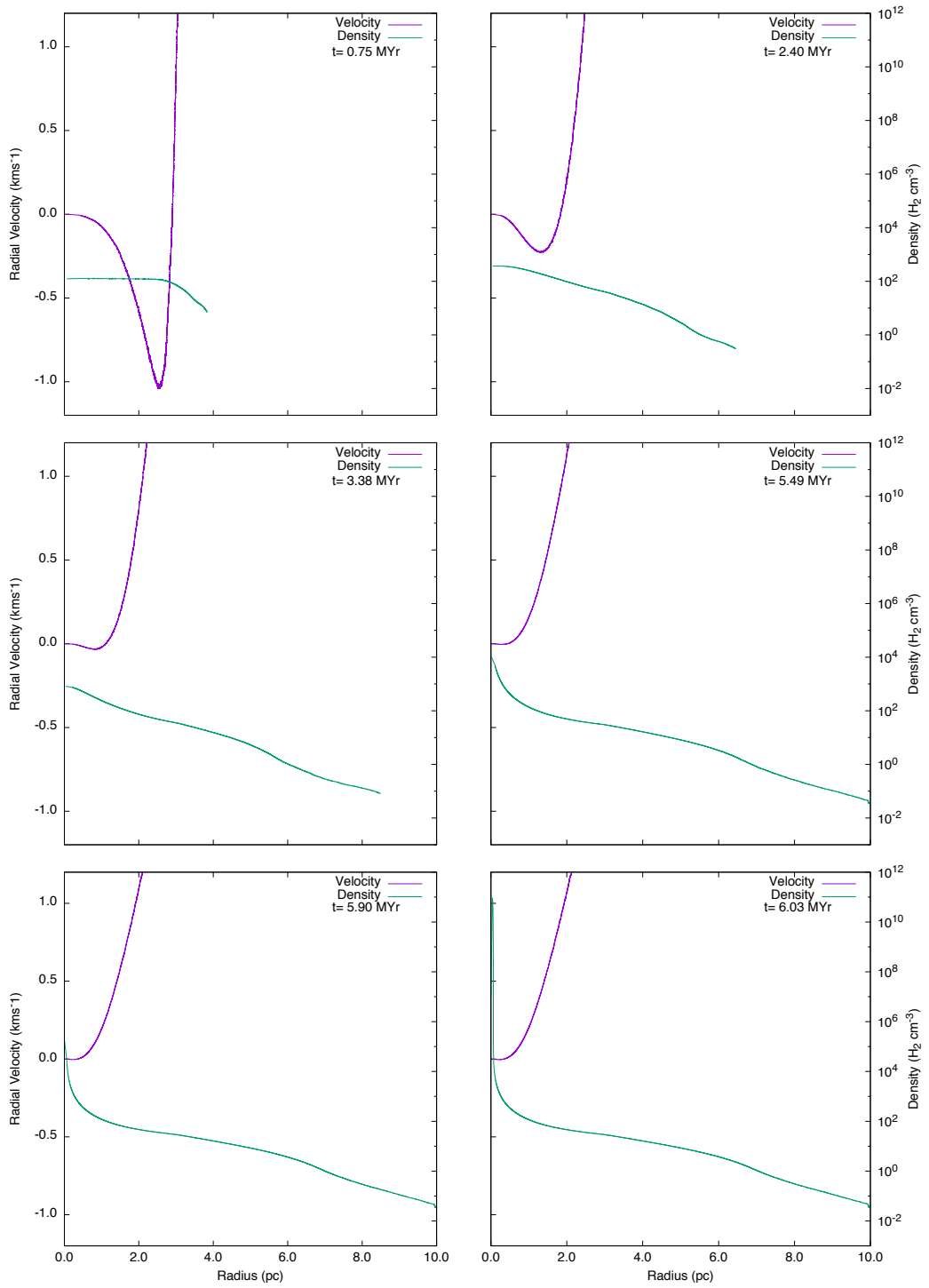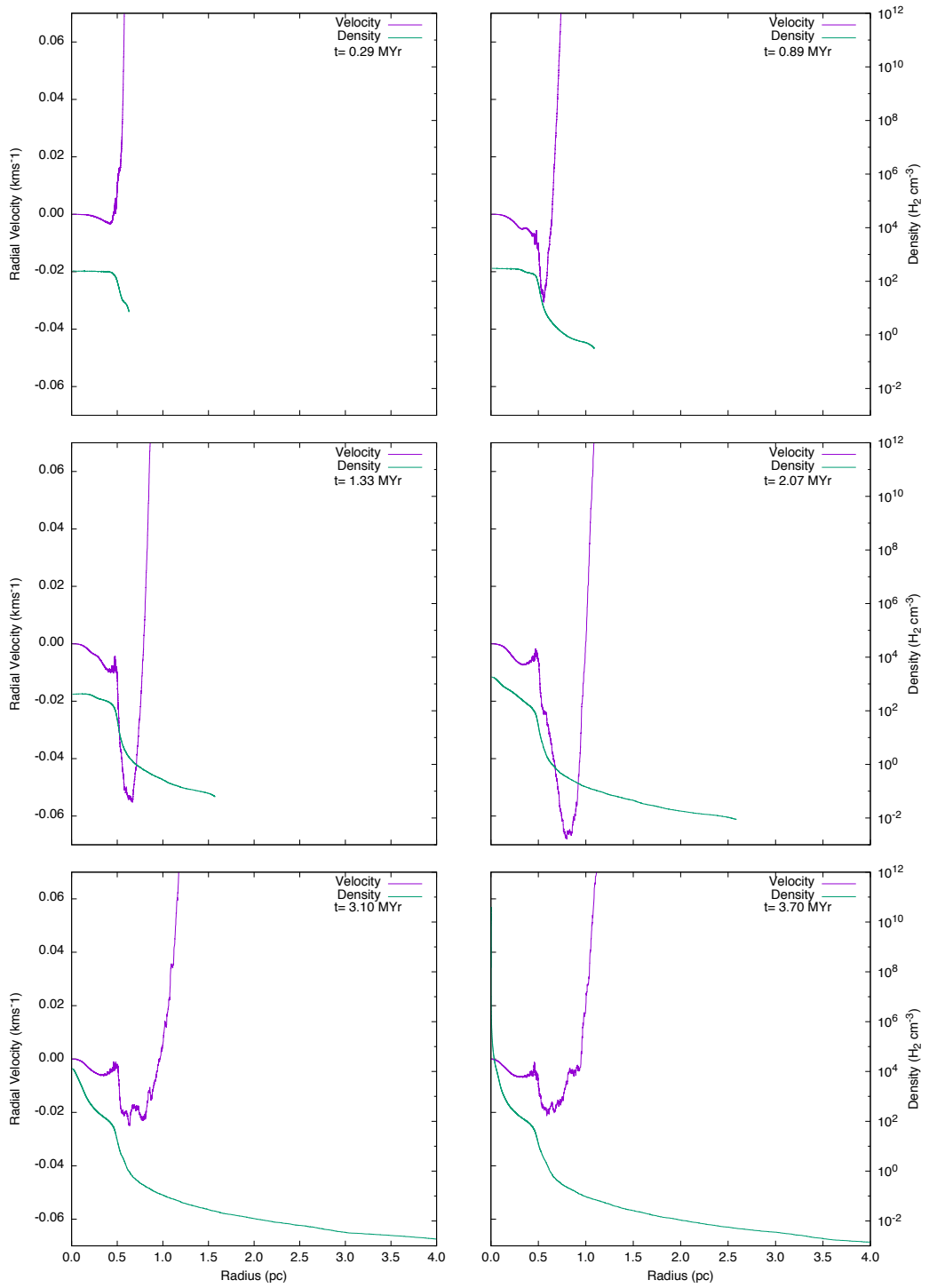
Figure A.14: Model B: six snapshots showing radial velocity (purple line) and density (green line) for a cloud with an initial density of 100 cm^3, a mass of 807 M$_\odot$ and a radius of 3.39 pc.
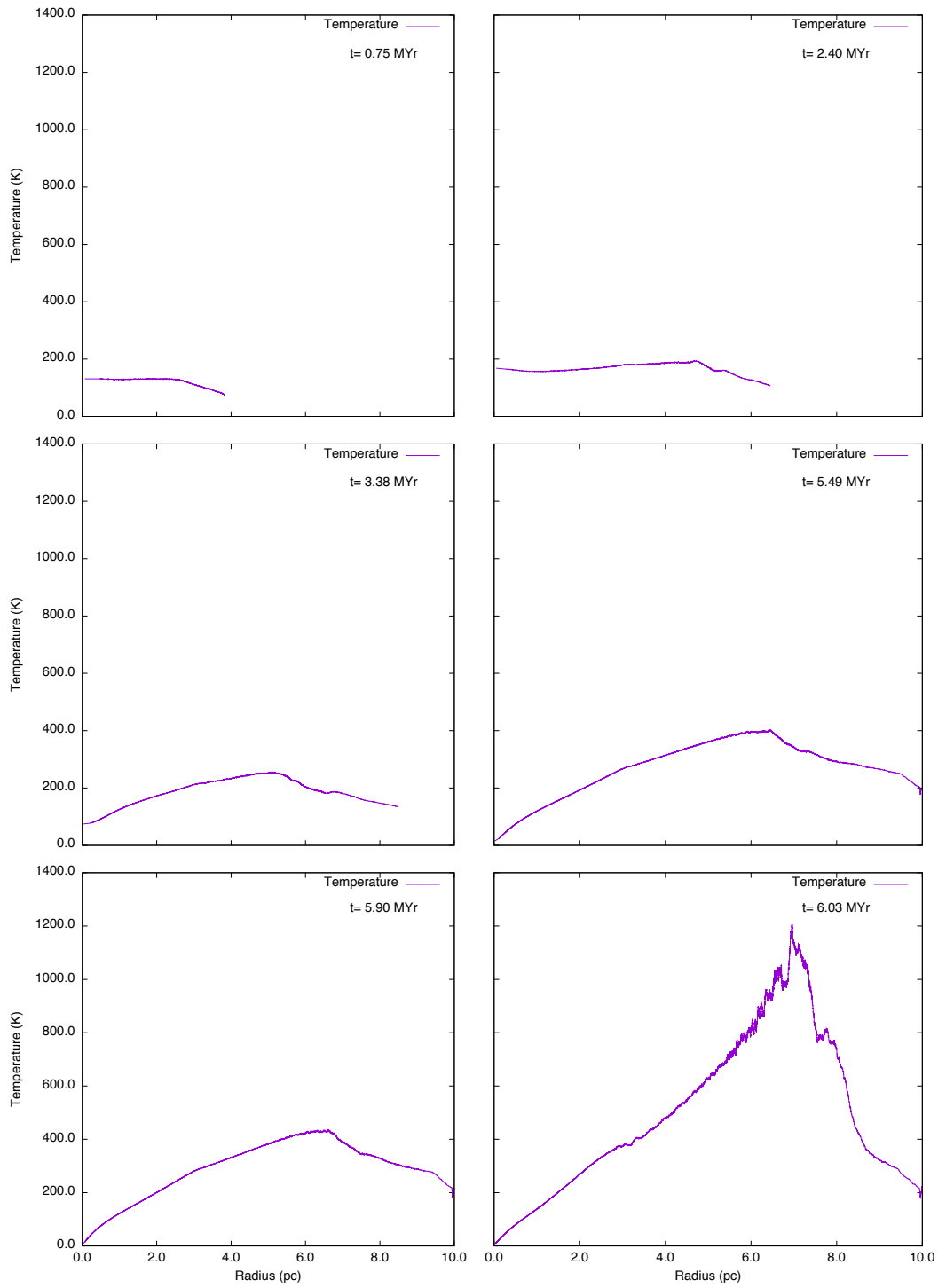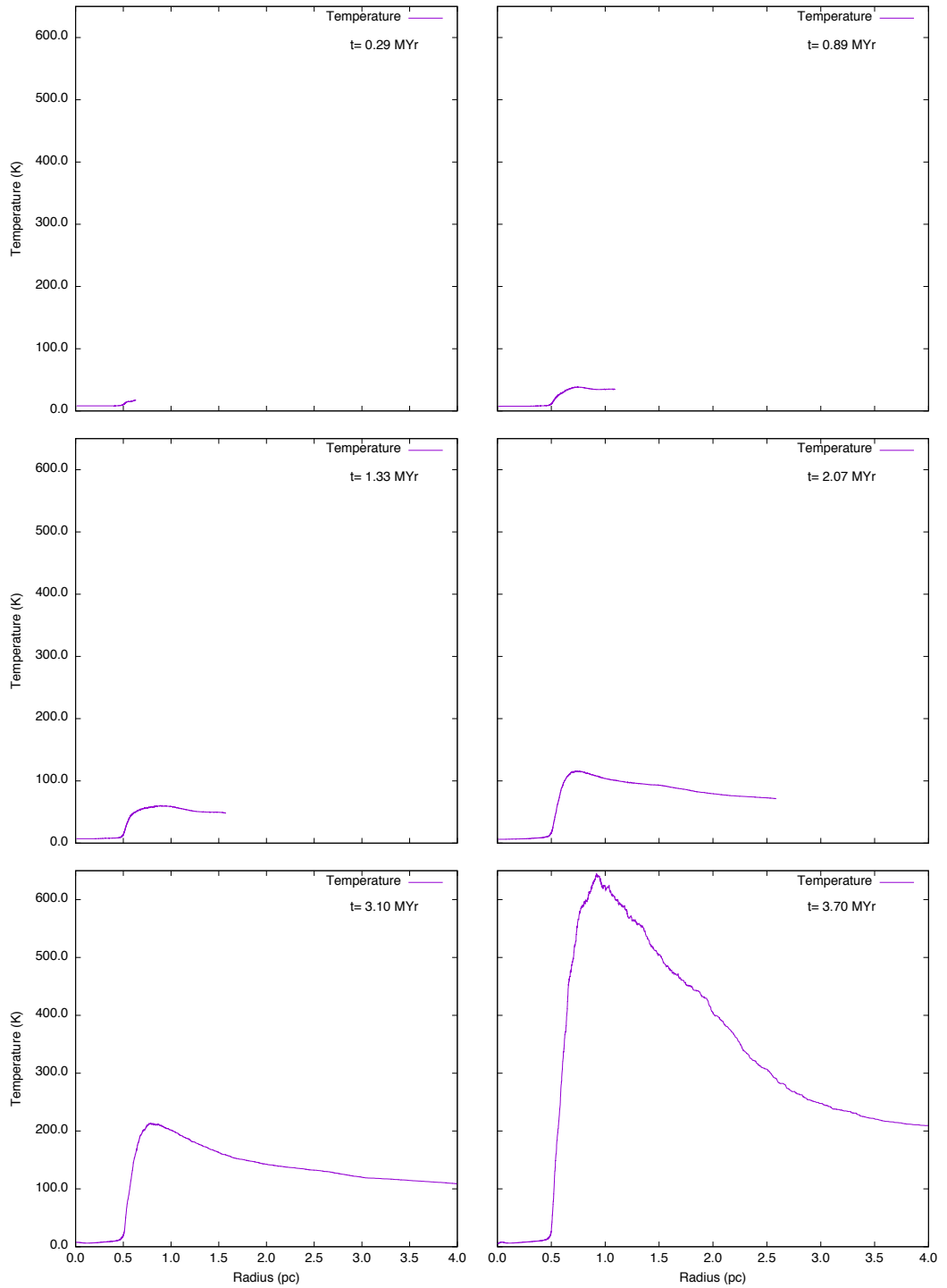
Figure A.15: Model B: six snapshots showing temperature (purple line) for a cloud with an initial density of 100 cm³, a mass of 807 M$_\odot$ and a radius of 3.39 pc.
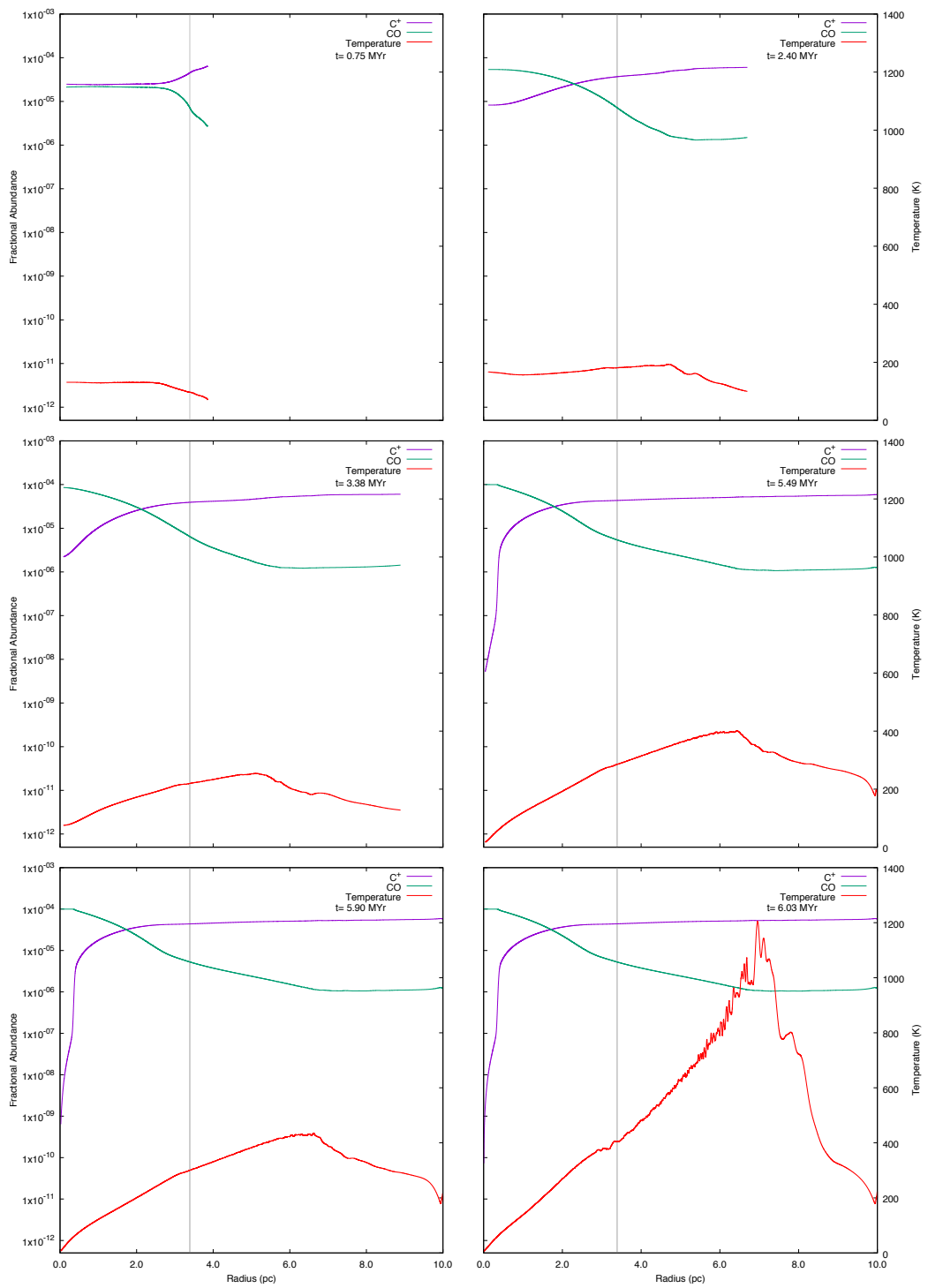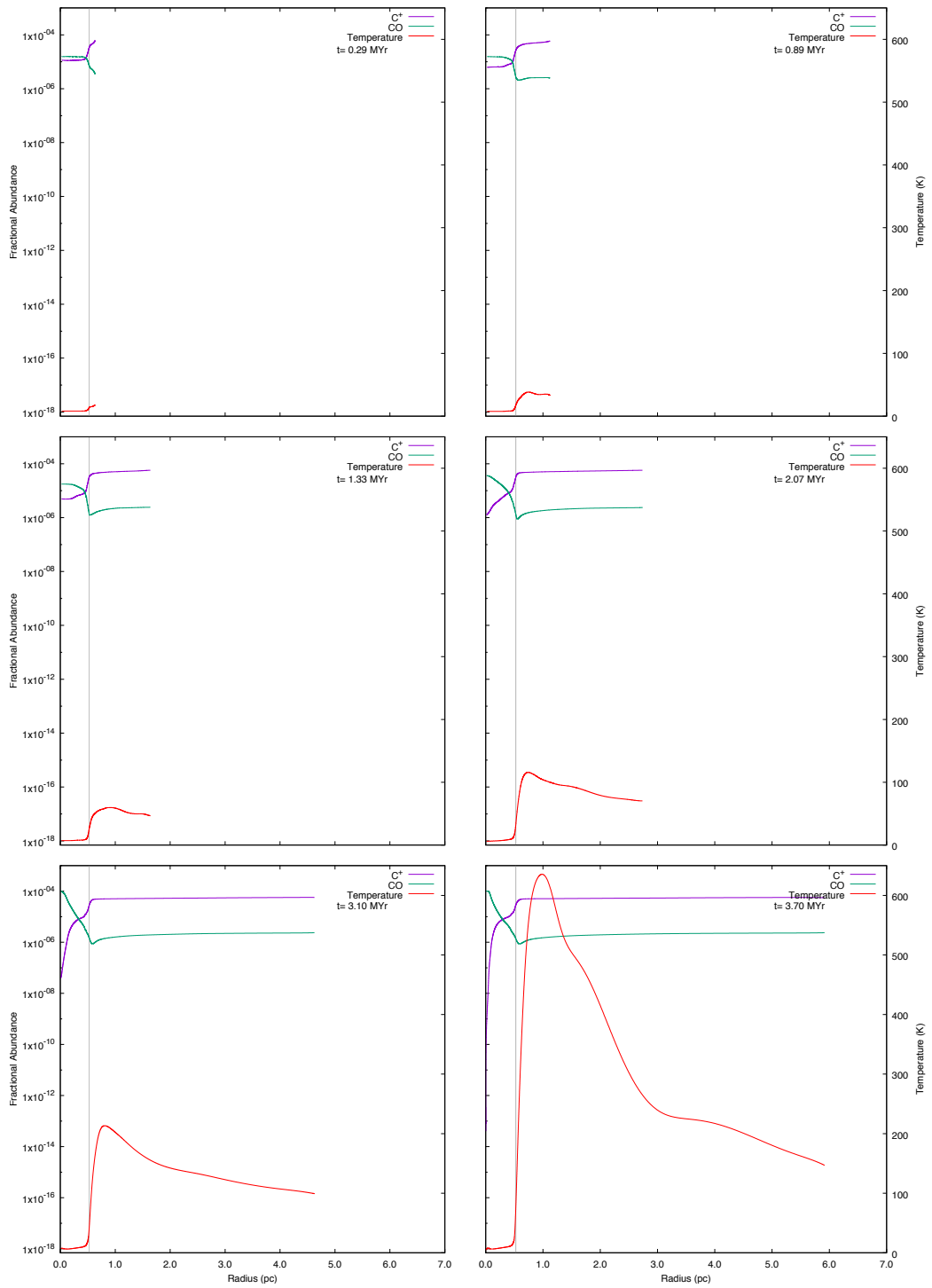
Figure A.16: Model B: six snapshots showing the chemical abundances of CO and C$^+$ for a cloud with an initial density of 100 cm^{-3}, a mass of 807 M$_\odot$ and a radius of 3.39 pc.
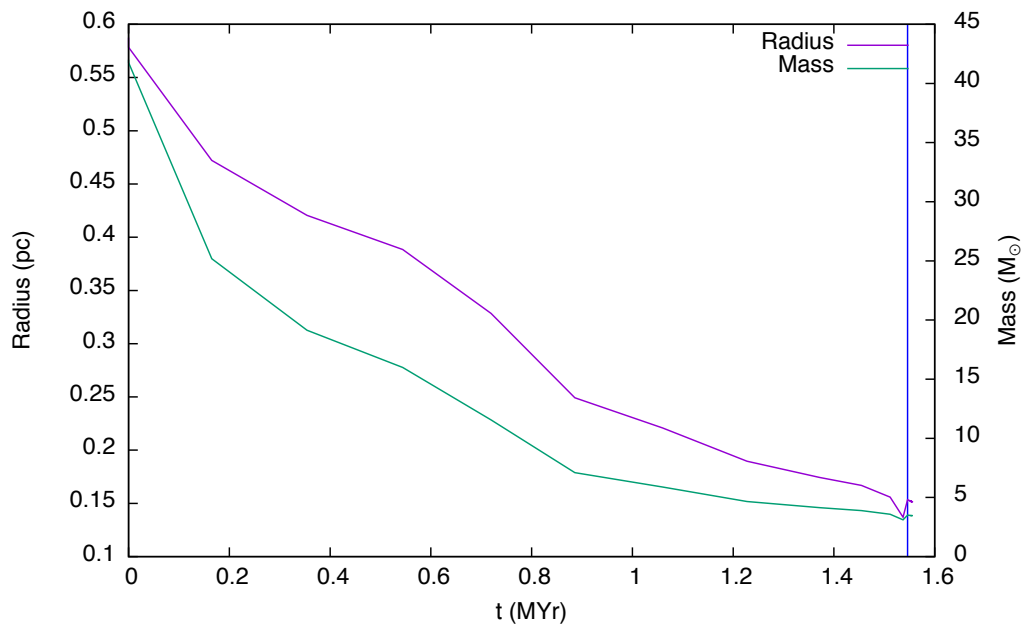
Figure A.17: Model B: the time evolution of the cloud with an initial density of 1000 cm^3, a mass of 42 M$_\odot$ and a radius of 0.59 pc is shown in this graph. The cloud radius (purple line) is taken to be the zero crossing point of radial velocity and the mass (green line) is taken to be that which lies inside the radius. The blue vertical line denotes the time at which the high density peak first forms. This is the minimum cloud mass which collapses for the selected values of density.
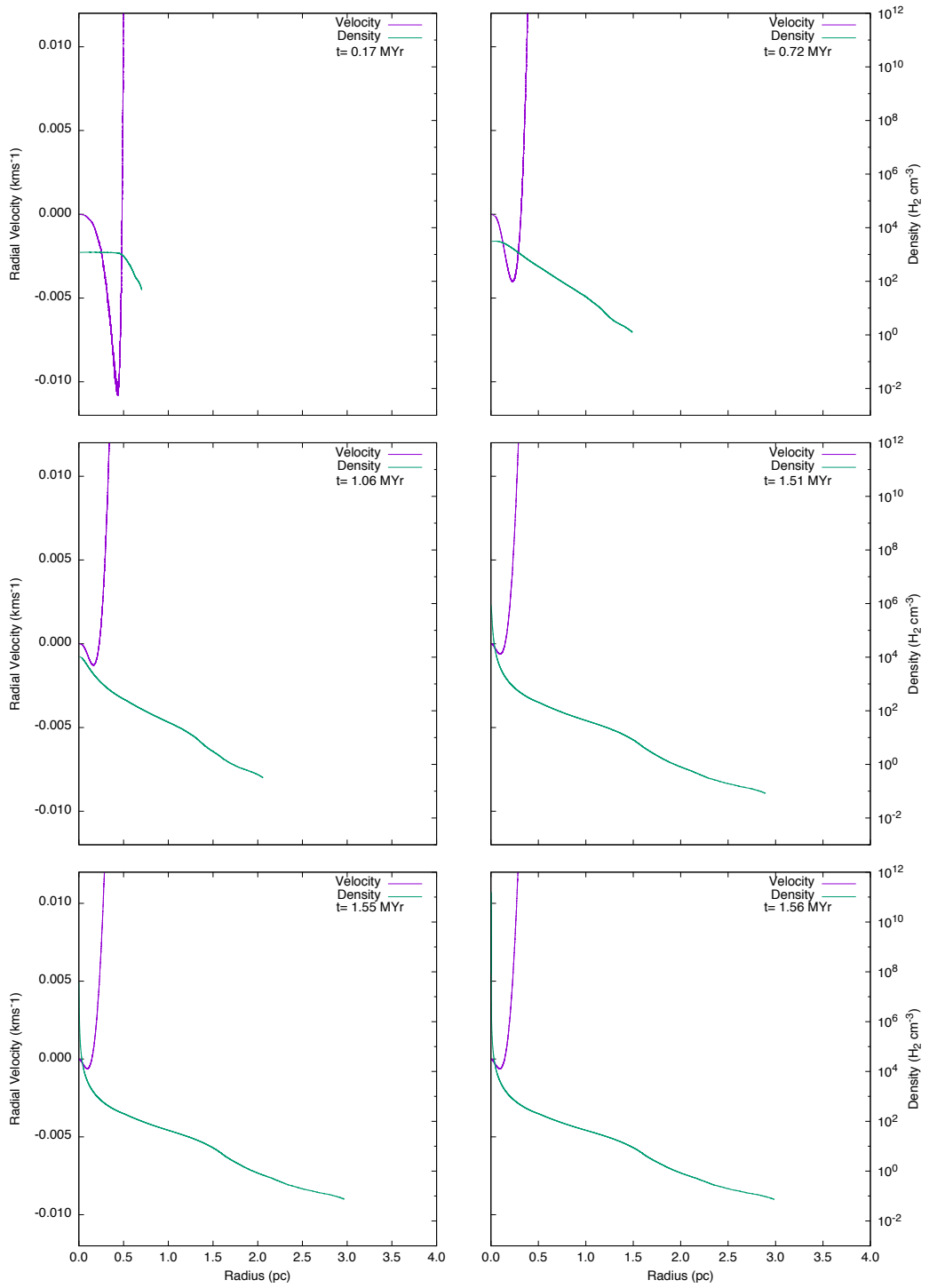
Figure A.18: Model B: six snapshots showing radial velocity (purple line) and density (green line) for a cloud with an initial density of 1000 cm³, a mass of 42 $M_\odot$ and a radius of 0.59 pc.
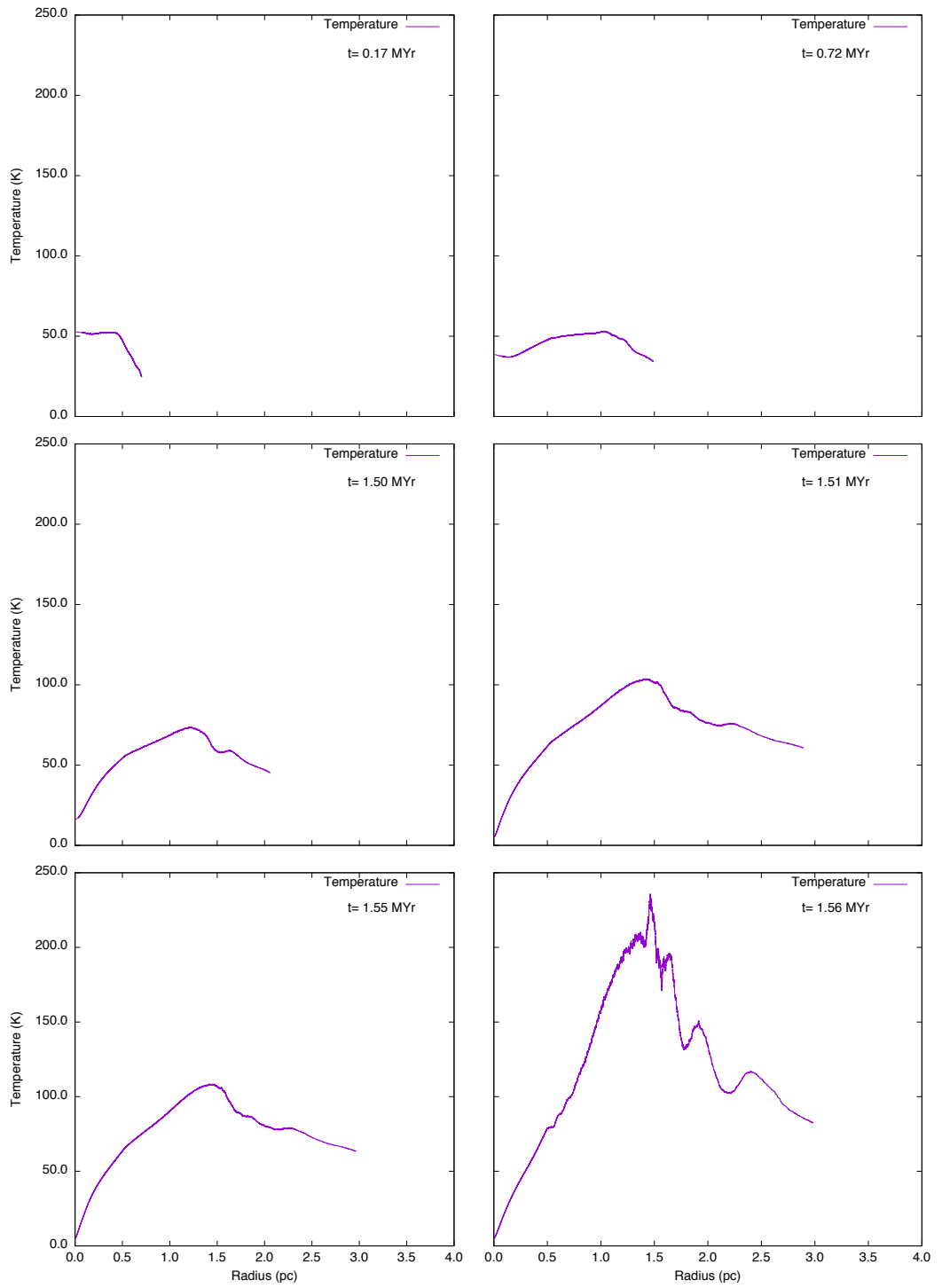
Figure A.19: Model B: six snapshots showing temperature (purple line) for a cloud with an initial density of 1000 cm³, a mass of 42 M$_\odot$ and a radius of 0.59 pc.
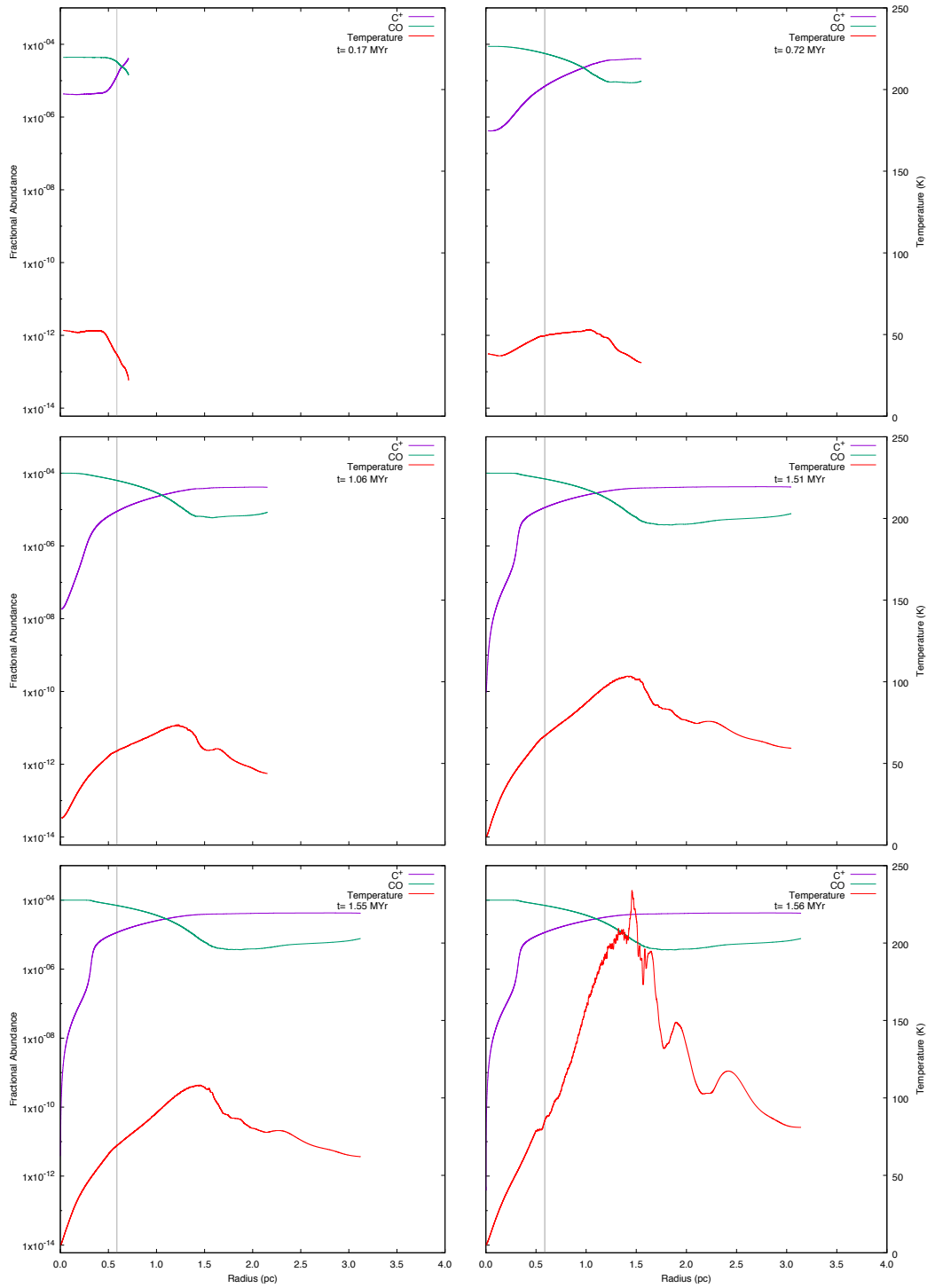
Figure A.20: Model B: six snapshots showing the chemical abundances of CO and C^+ for a cloud with an initial density of 1000 cm^{-3}, a mass of 42 M$_\odot$ and a radius of 0.59 pc.
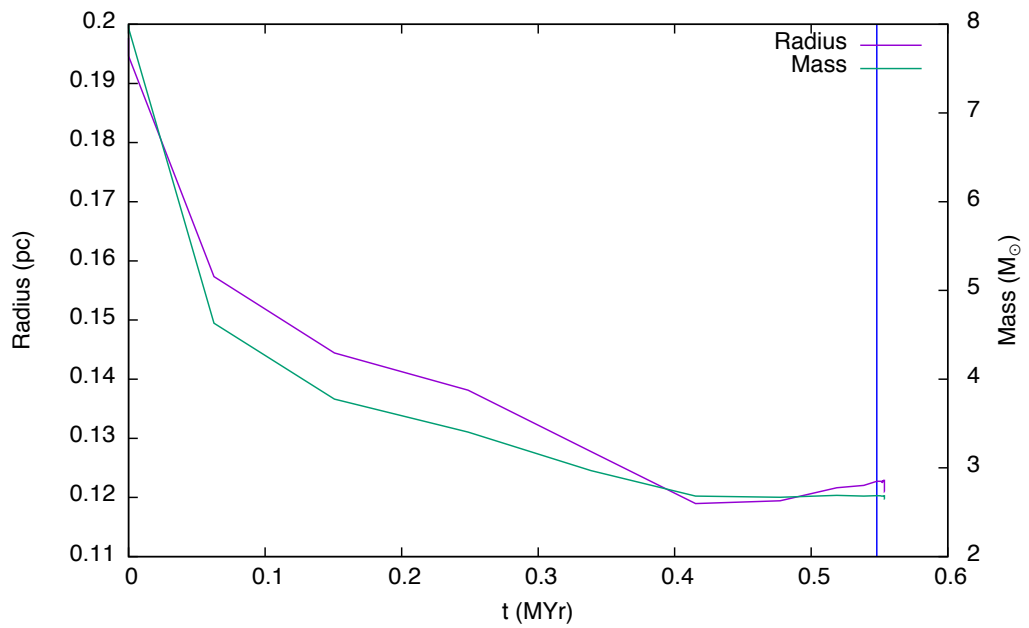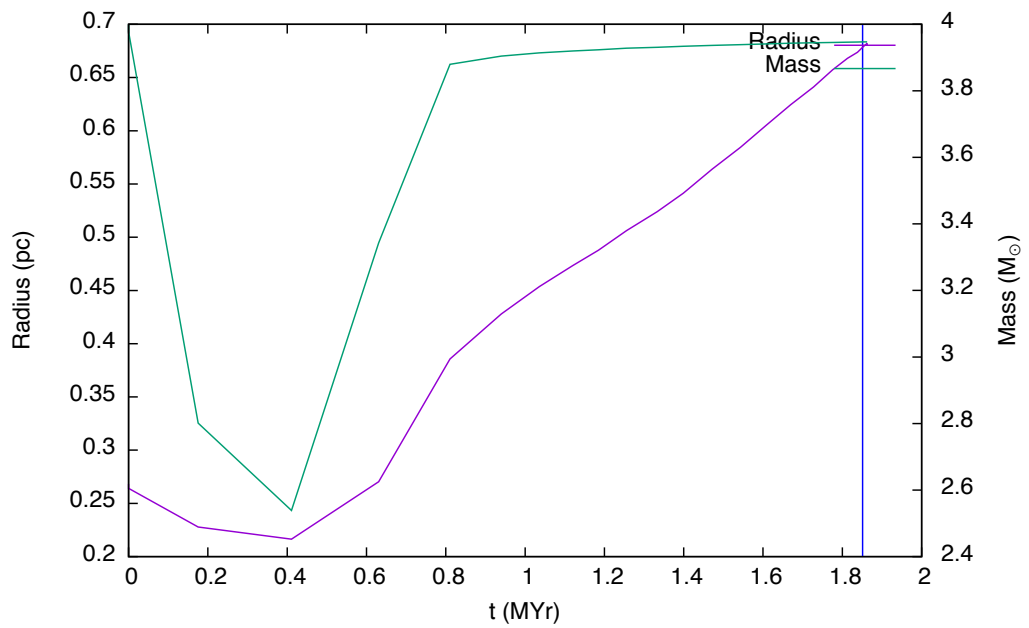
Figure A.21: Model B: the time evolution of the cloud with an initial density of 5000 cm^3, a mass of 8 M$_\odot$ and a radius of 0.20 pc is shown in this graph. The cloud radius (purple line) is taken to be the zero crossing point 0.20of radial velocity and the mass (green line) is taken to be that which lies inside the radius. The blue vertical line denotes the time at which the high density peak first forms. This is the minimum cloud mass which collapses for the selected values of density.
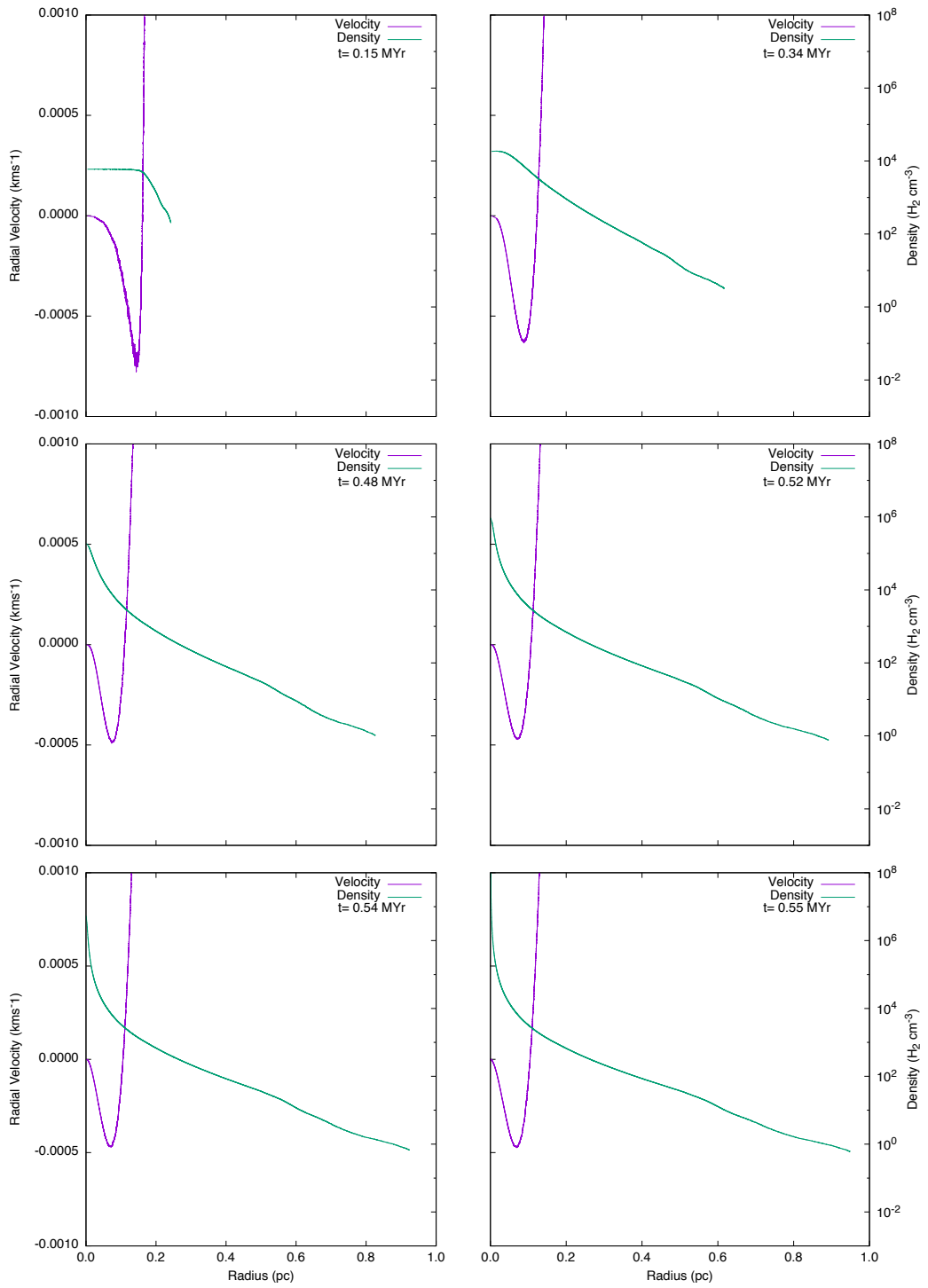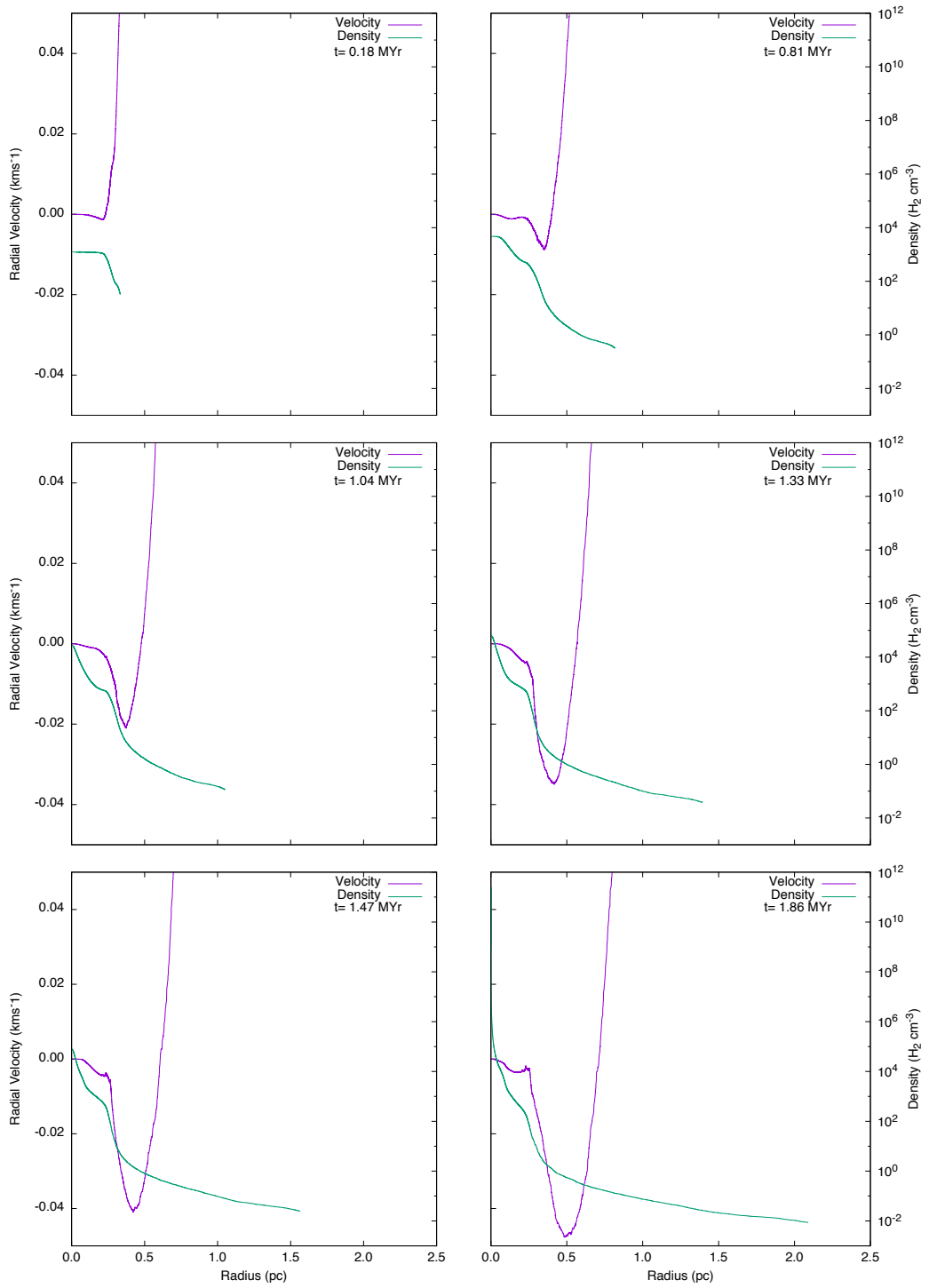
Figure A.22: Model B: six snapshots showing radial velocity (purple line) and density (green line) for a cloud with an initial density of 5000 cm^3, a mass of 8 M$_\odot$ and a radius of 0.20 pc.
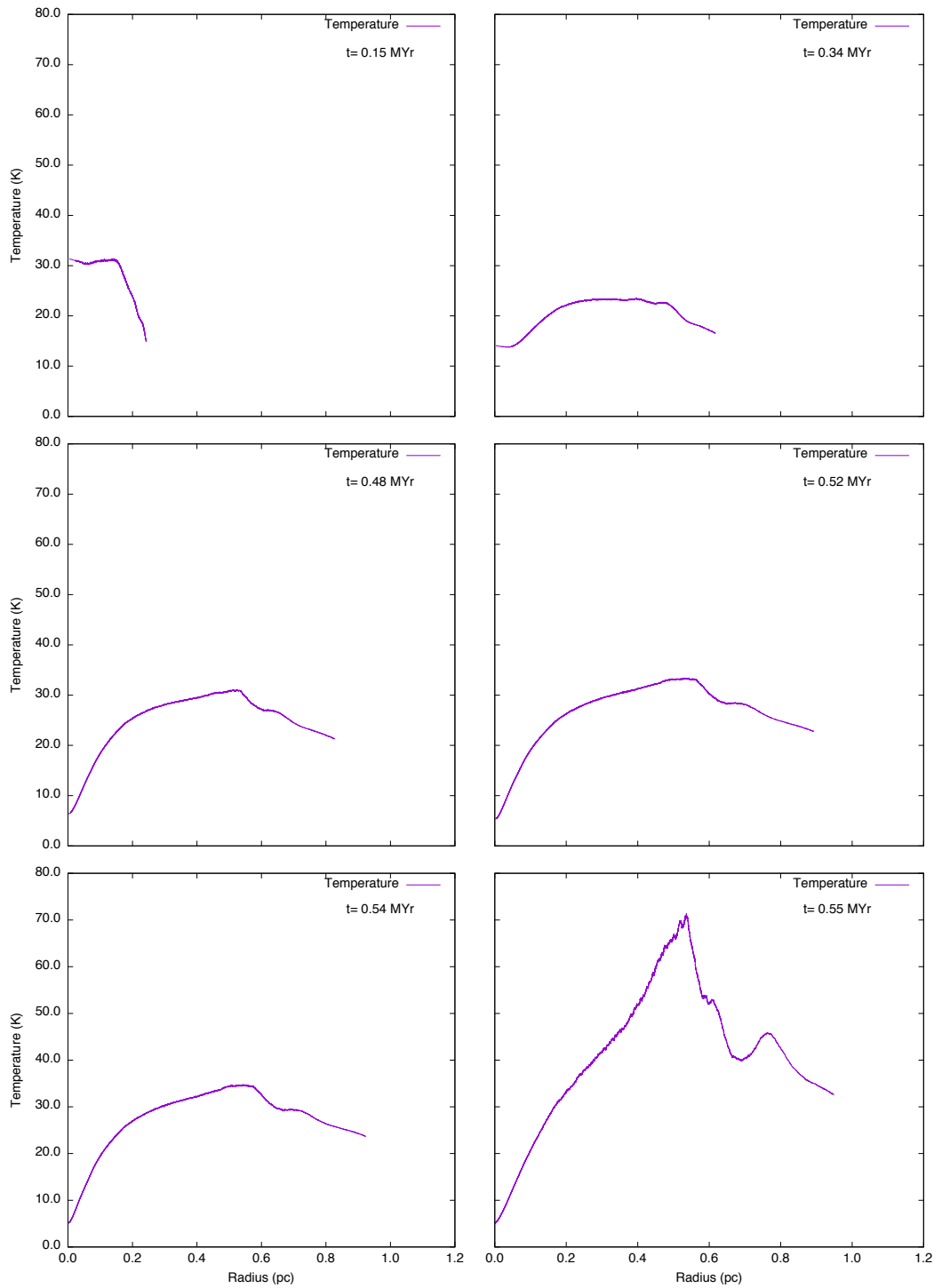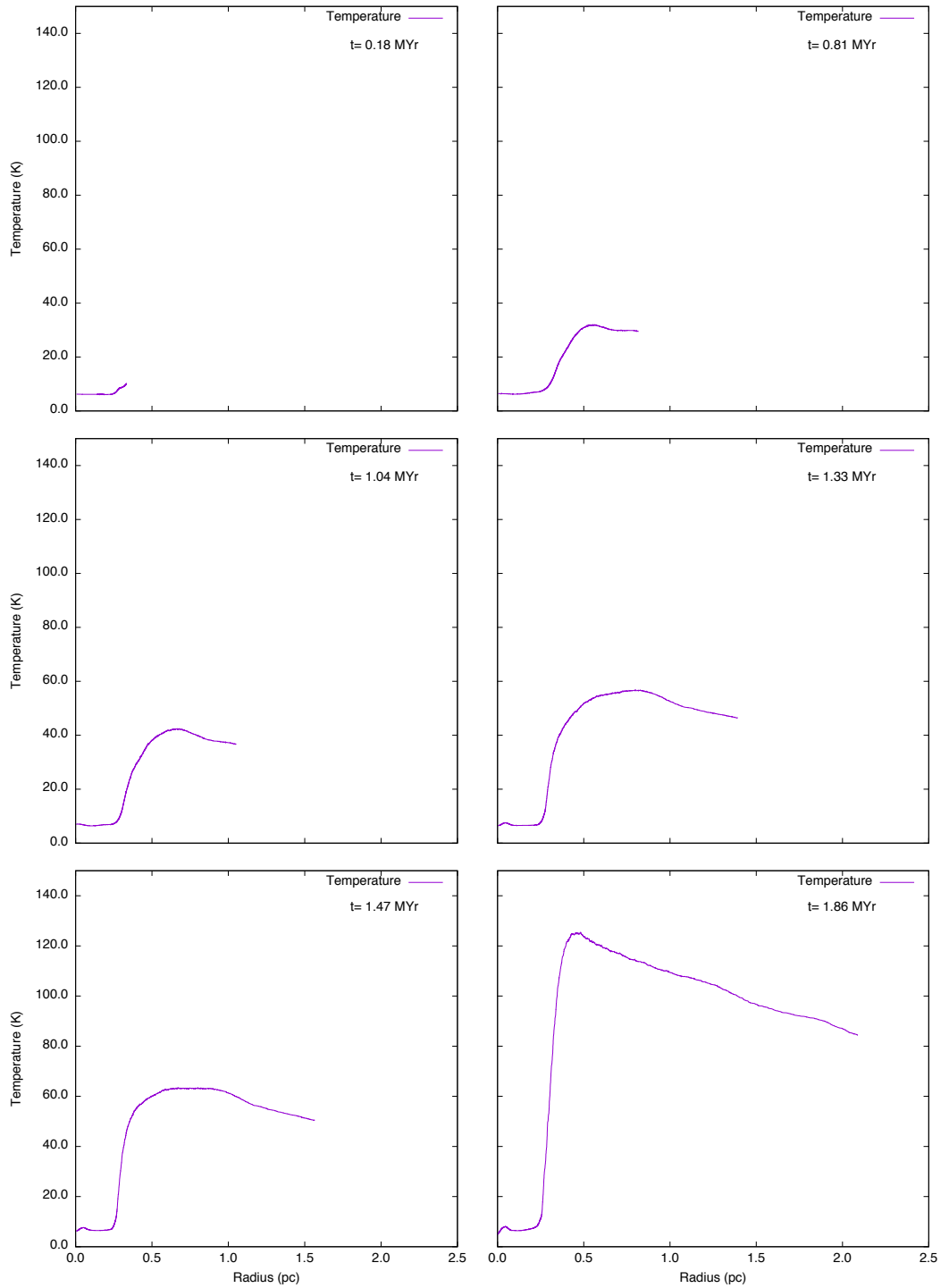
Figure A.23: Model B: six snapshots showing temperature (purple line) for a cloud with an initial density of 5000 cm^3, a mass of 8 M$_\odot$ and a radius of 0.20 pc.
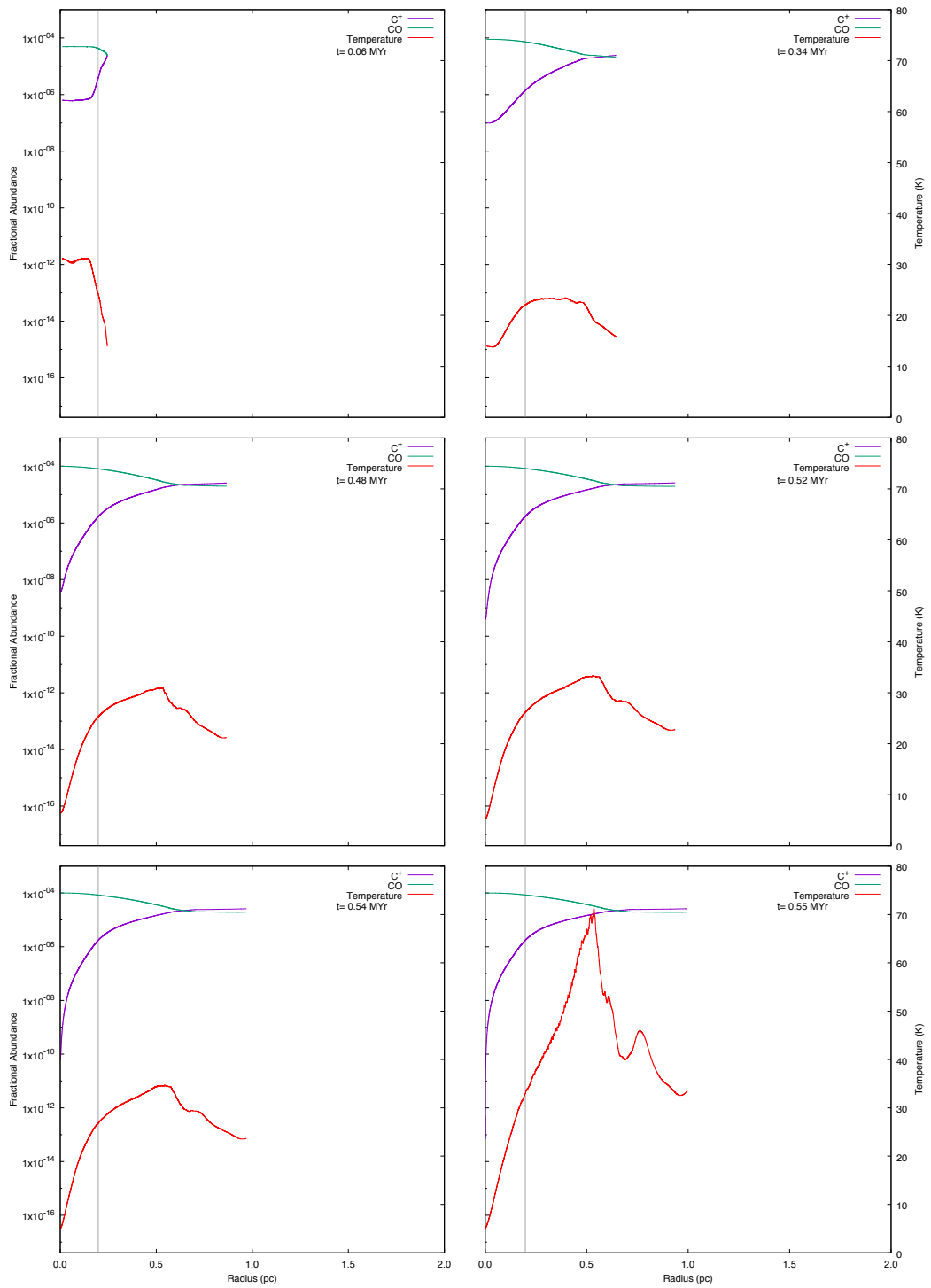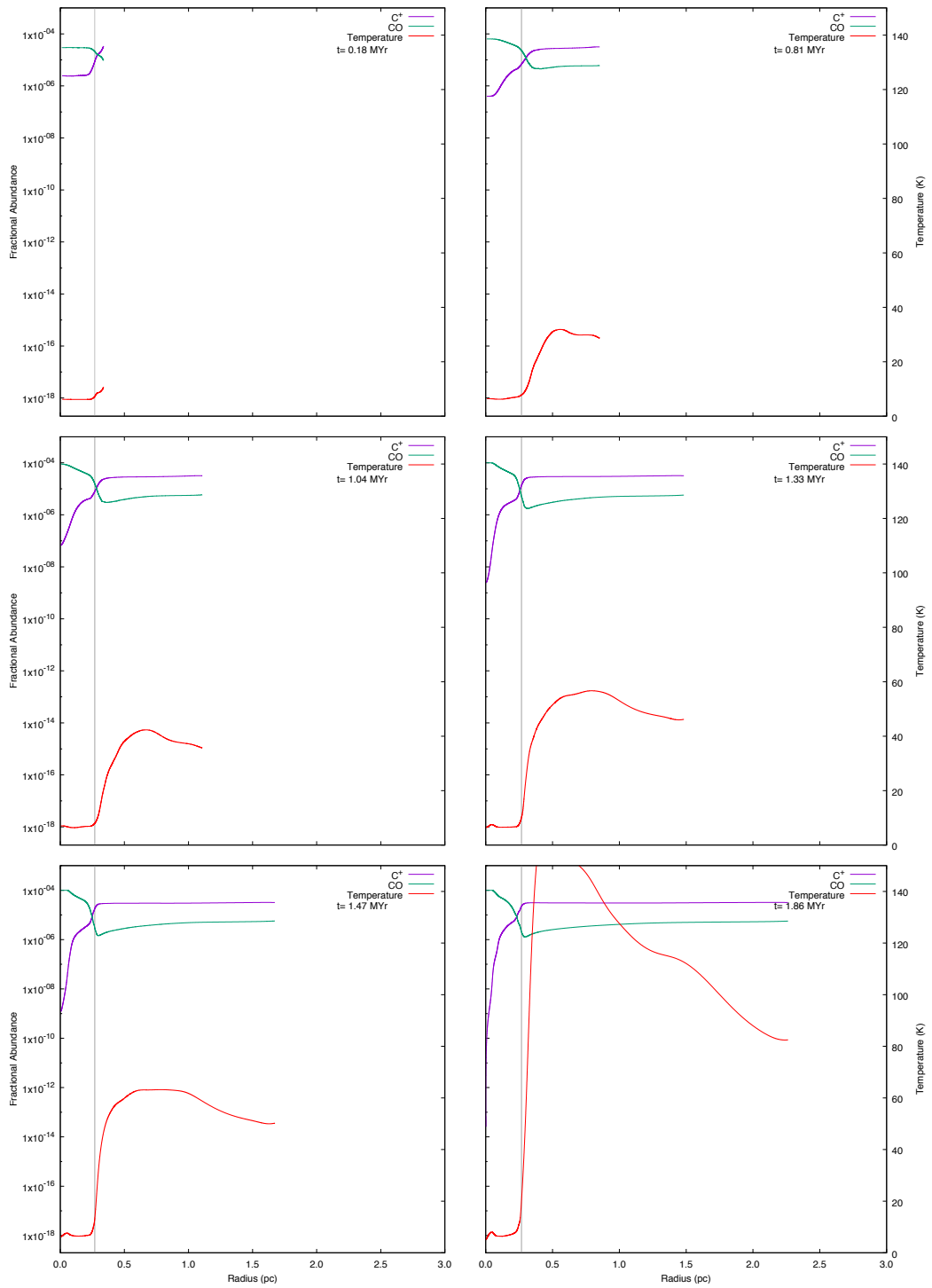
Figure A.24: Model B: six snapshots showing the chemical abundances of CO and C^+ for a cloud with an initial density of 5000 cm^{-3}, a mass of 8 M$_\odot$ and a radius of 0.20 pc.
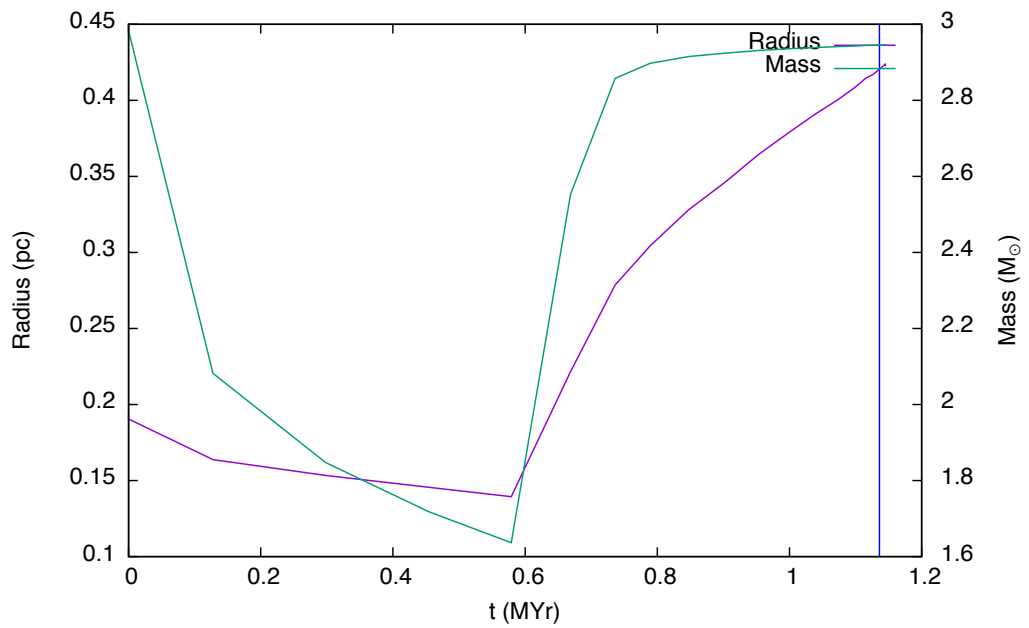
A.3   MODEL C
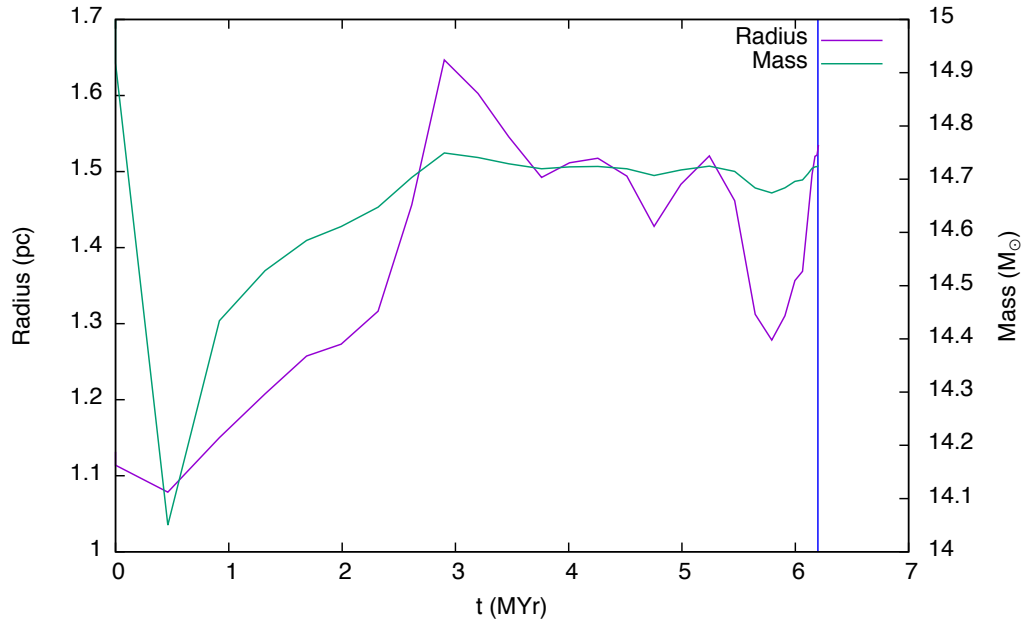
Figure A.25: Model C: the time evolution of the cloud with an initial density of $50 \, \text{cm}^3$, a mass of $15 \, \text{M}_\odot$ and a radius of $1.13 \, \text{pc}$ is shown in this graph. The cloud radius (purple line) is taken to be the zero crossing point of radial velocity and the mass (green line) is taken to be that which lies inside the radius. The blue vertical line denotes the time at which the high density peak first forms. This is the minimum cloud mass which collapses for the selected values of density.
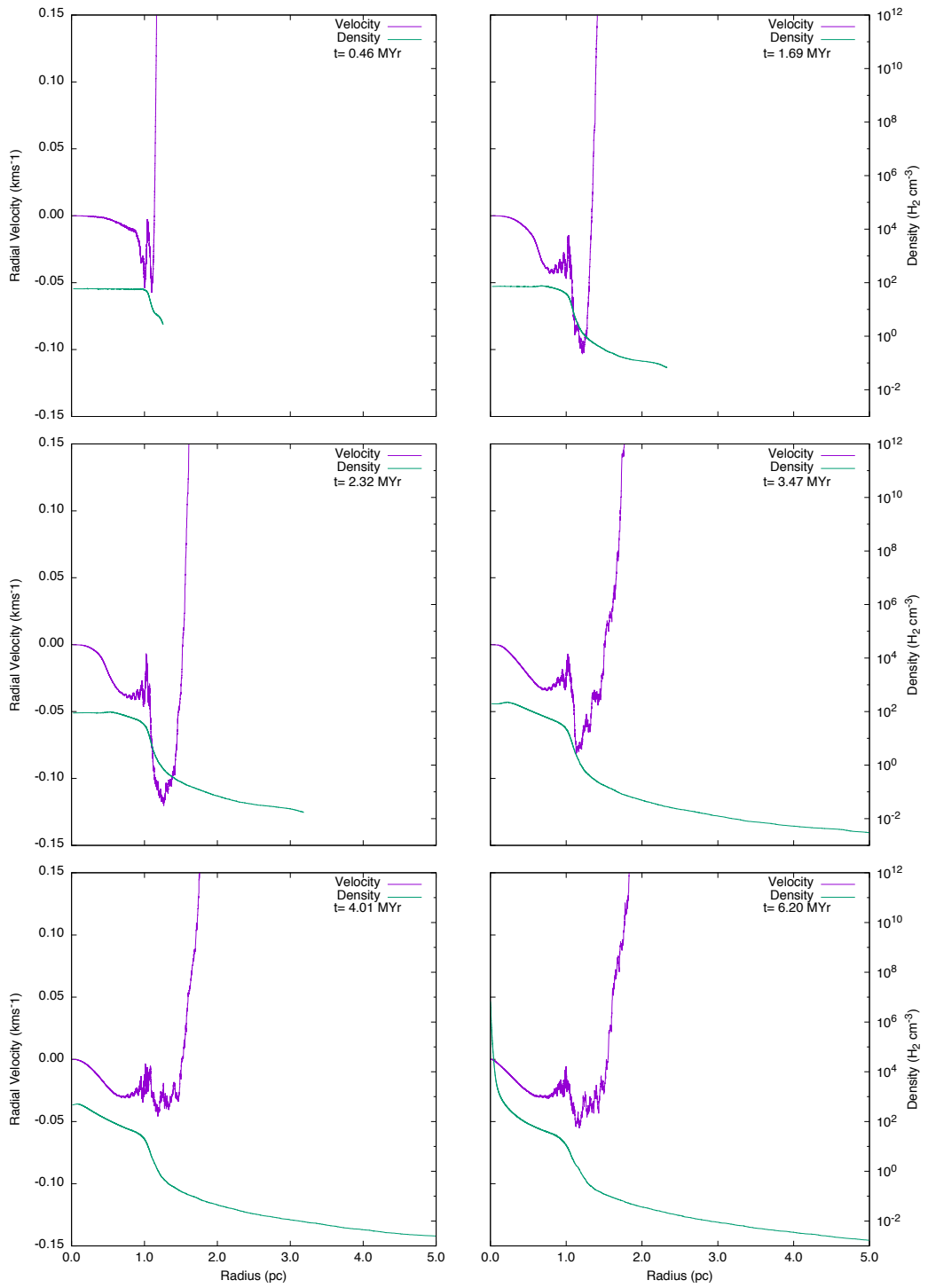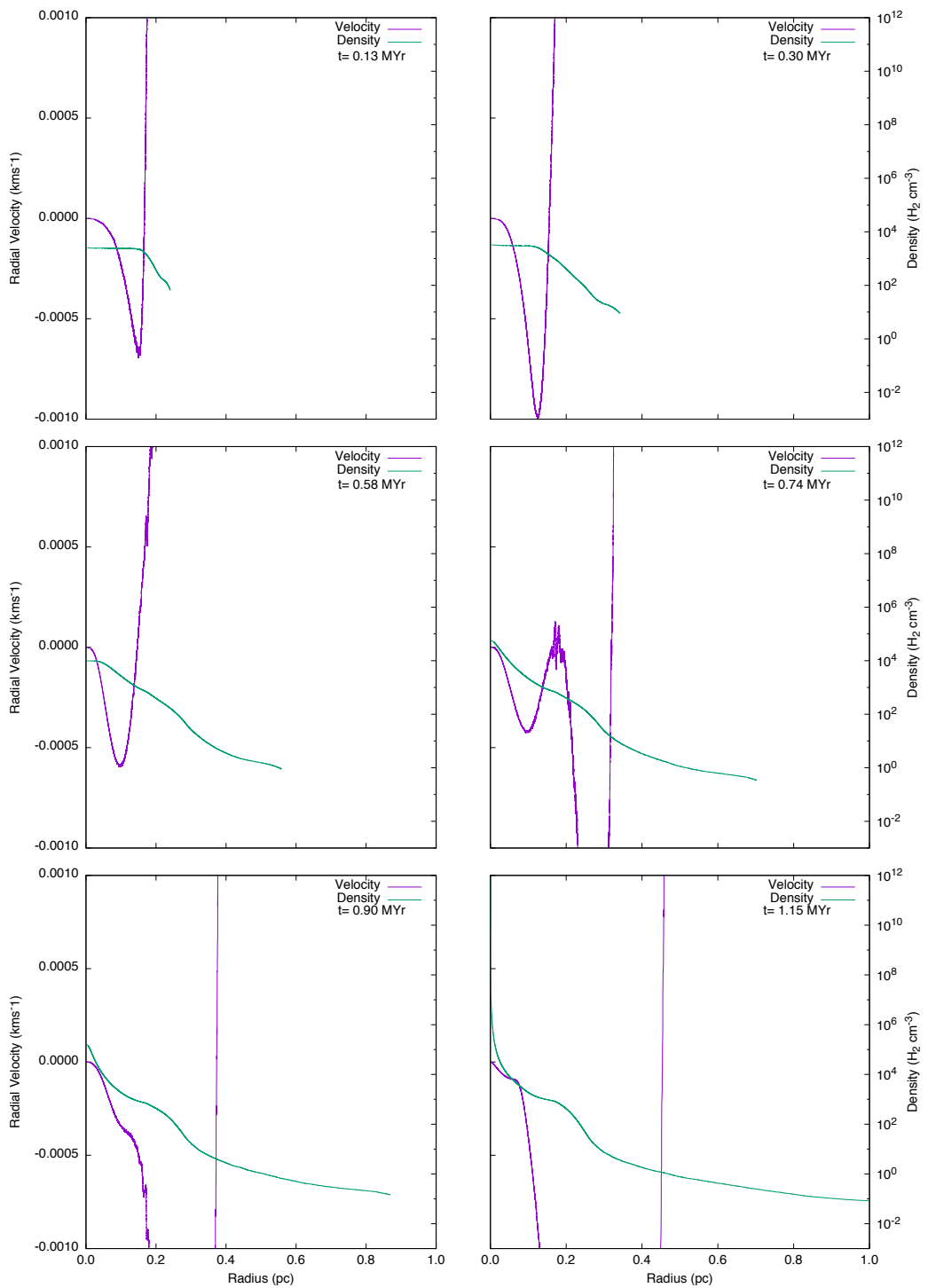
Figure A.26: Model C: six snapshots showing radial velocity (purple line) and density (green line) for a cloud with an initial density of 50 cm^3, a mass of 15 M$_\odot$ and a radius of 1.13 pc.
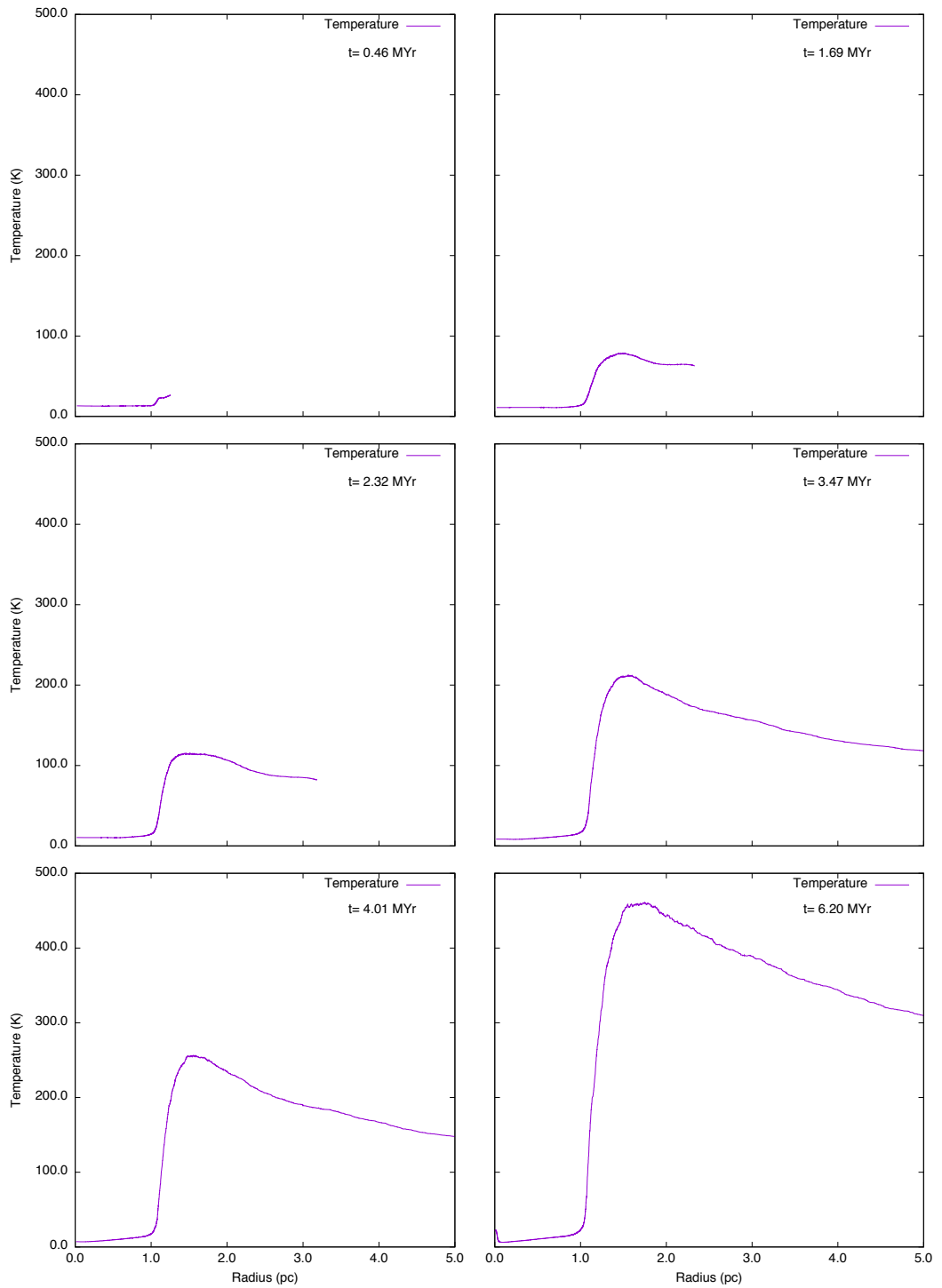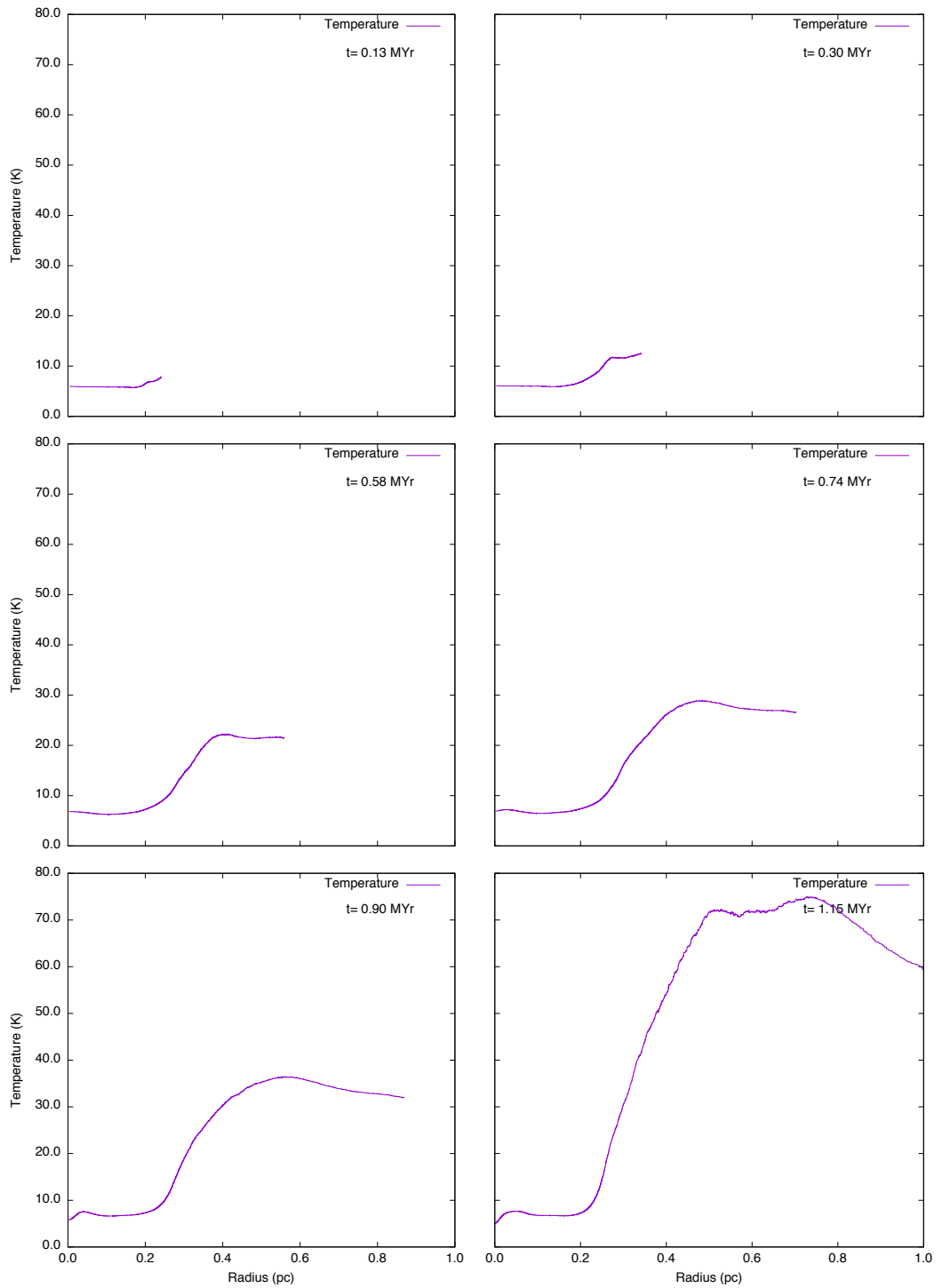
Figure A.27: Model C: six snapshots showing temperature (purple line) for a cloud with an initial density of 50 cm^3, a mass of 15 M$_\odot$ and a radius of 1.13 pc.
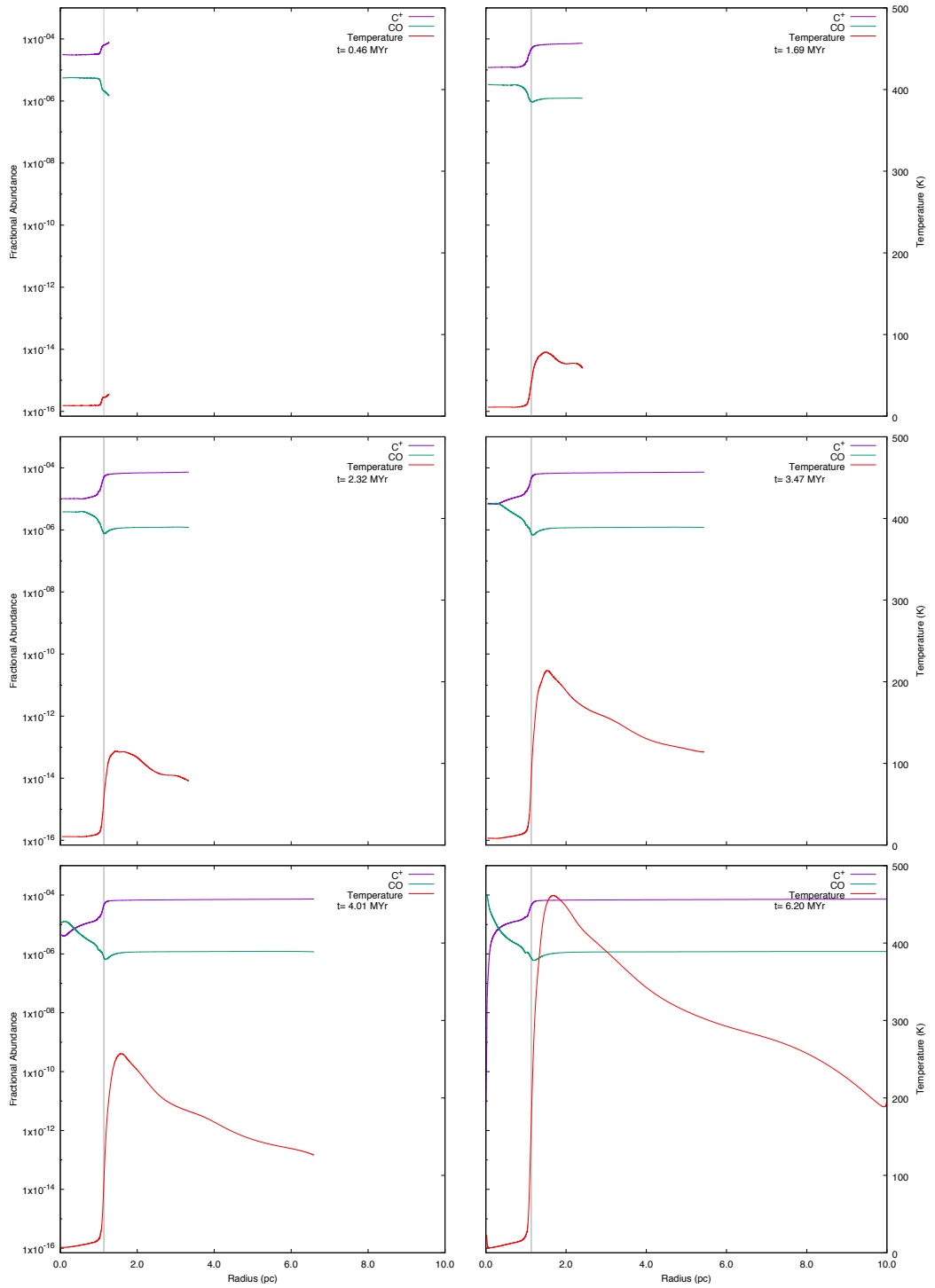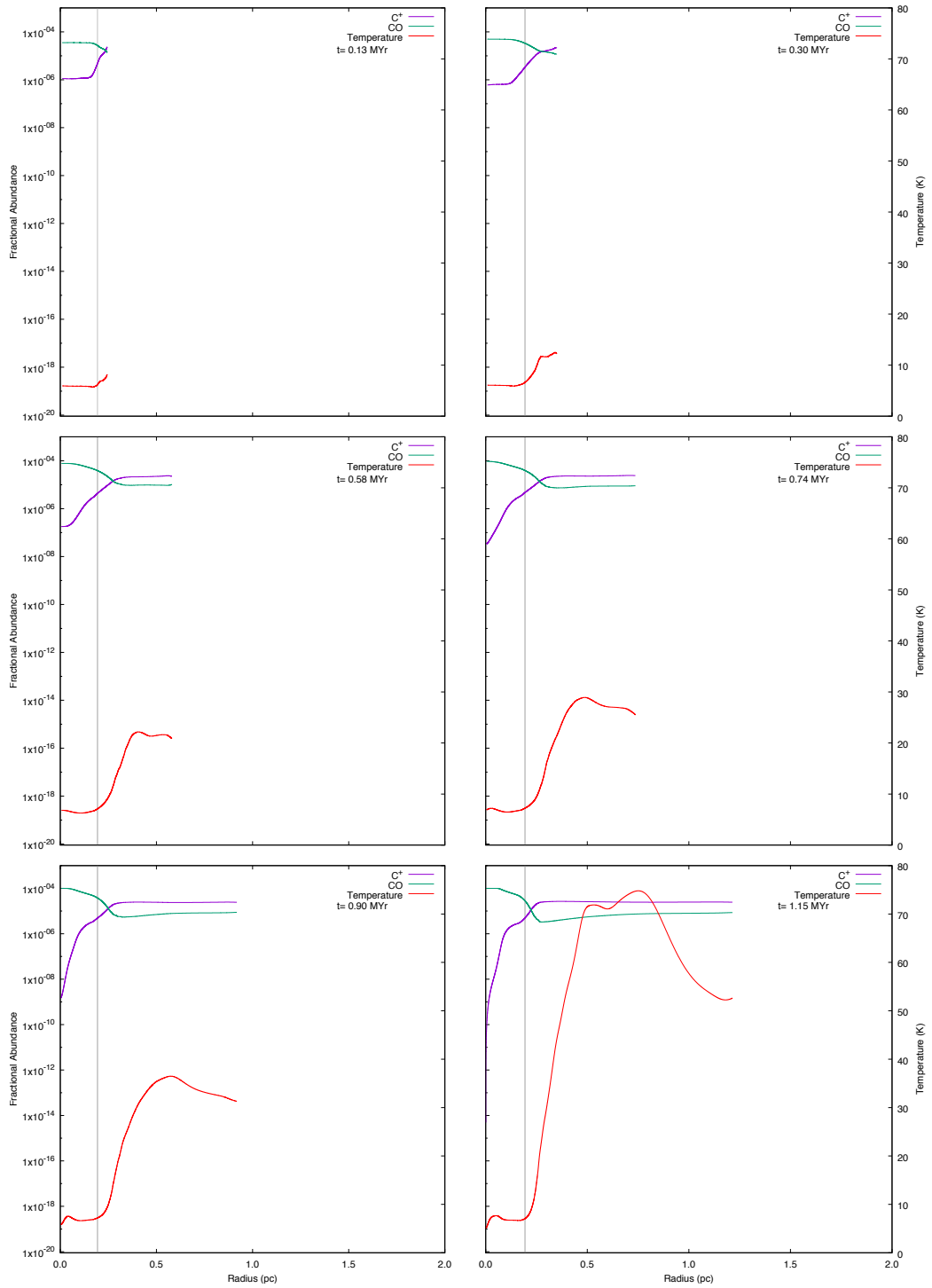
Figure A.28: Model C: six snapshots showing the chemical abundances of CO and C^+ for a cloud with an initial density of 50 cm^{-3}, a mass of 15 M$_\odot$ and a radius of 1.13 pc.
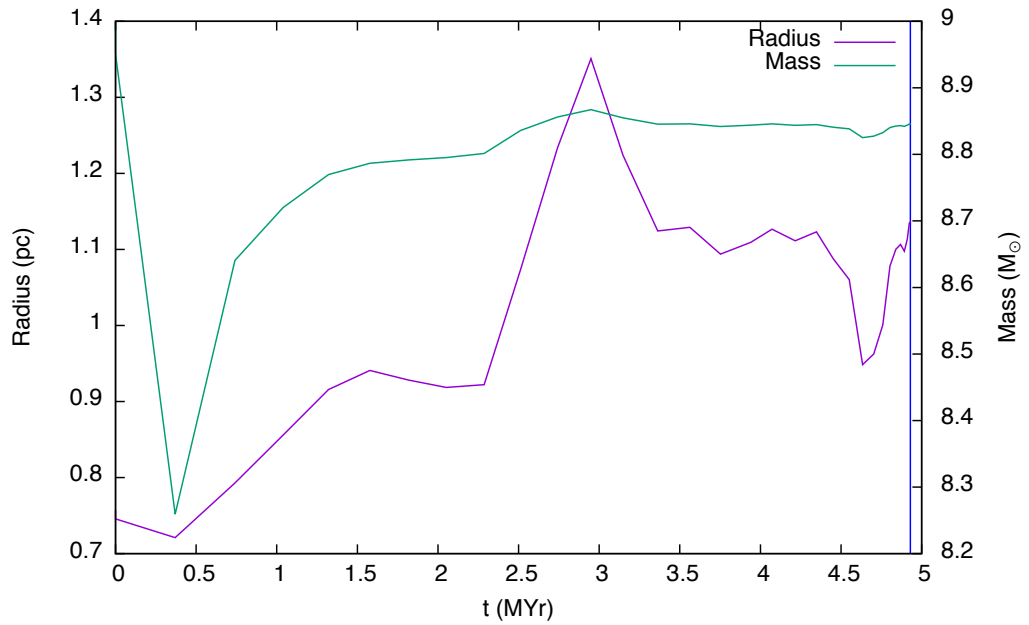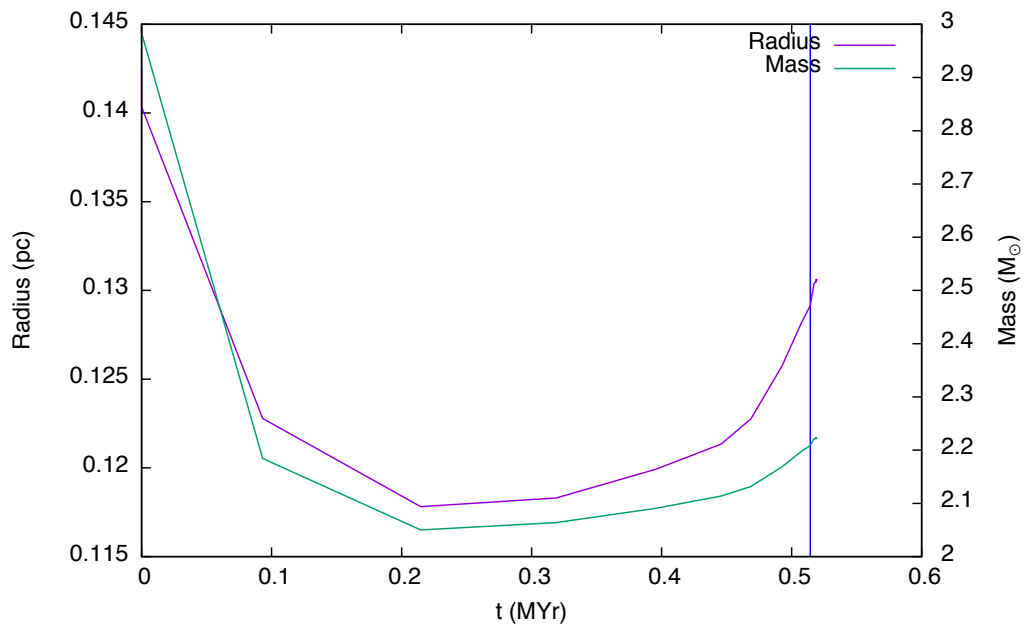
Figure A.29: Model C: the time evolution of the cloud with an initial density of 100 cm^3, a mass of 9 $M_\odot$ and a radius of 0.76 pc is shown in this graph. The cloud radius (purple line) is taken to be the zero crossing point of radial velocity and the mass (green line) is taken to be that which lies inside the radius. The blue vertical line denotes the time at which the high density peak first forms. This is the minimum cloud mass which collapses for the selected values of density.
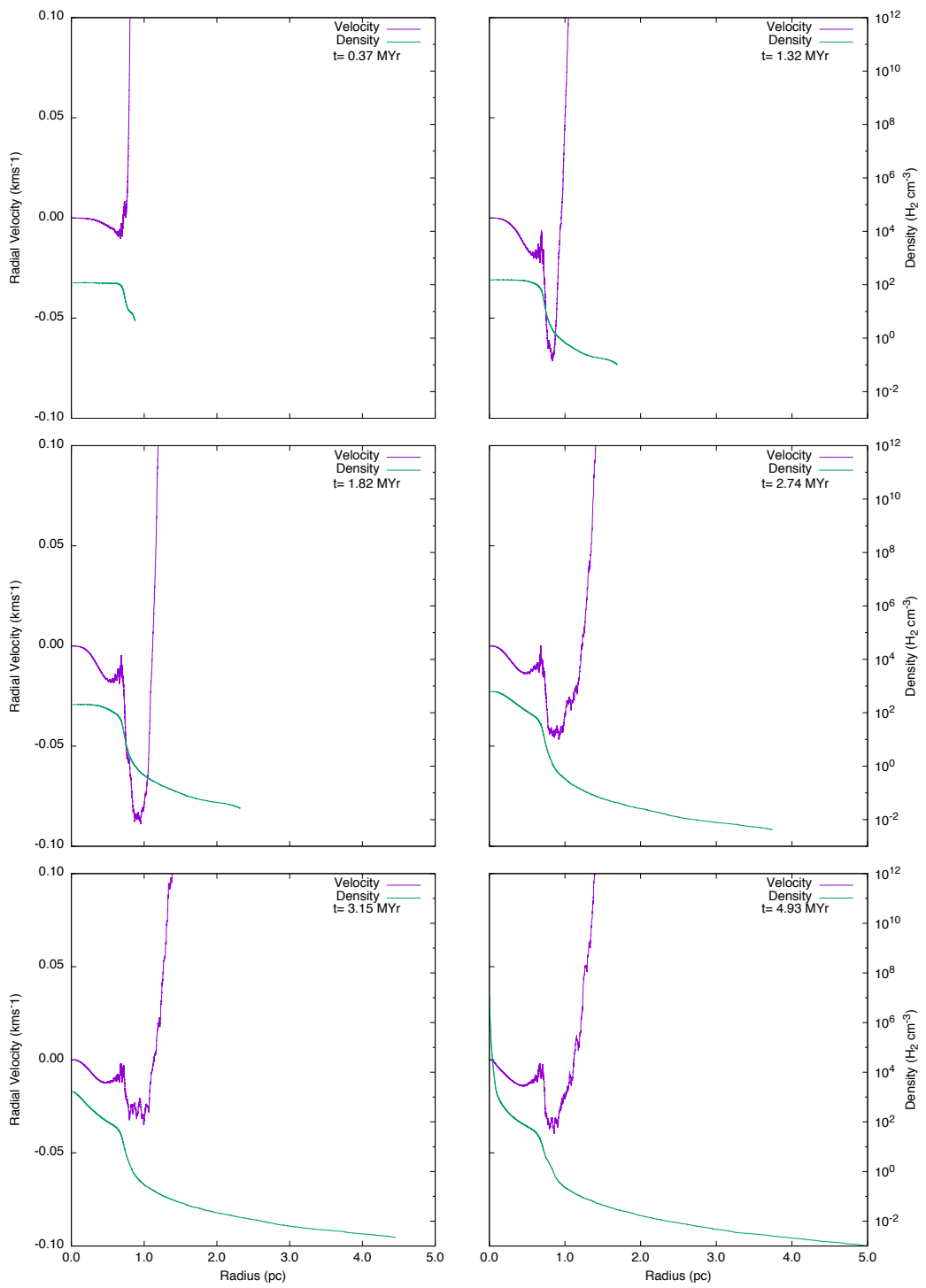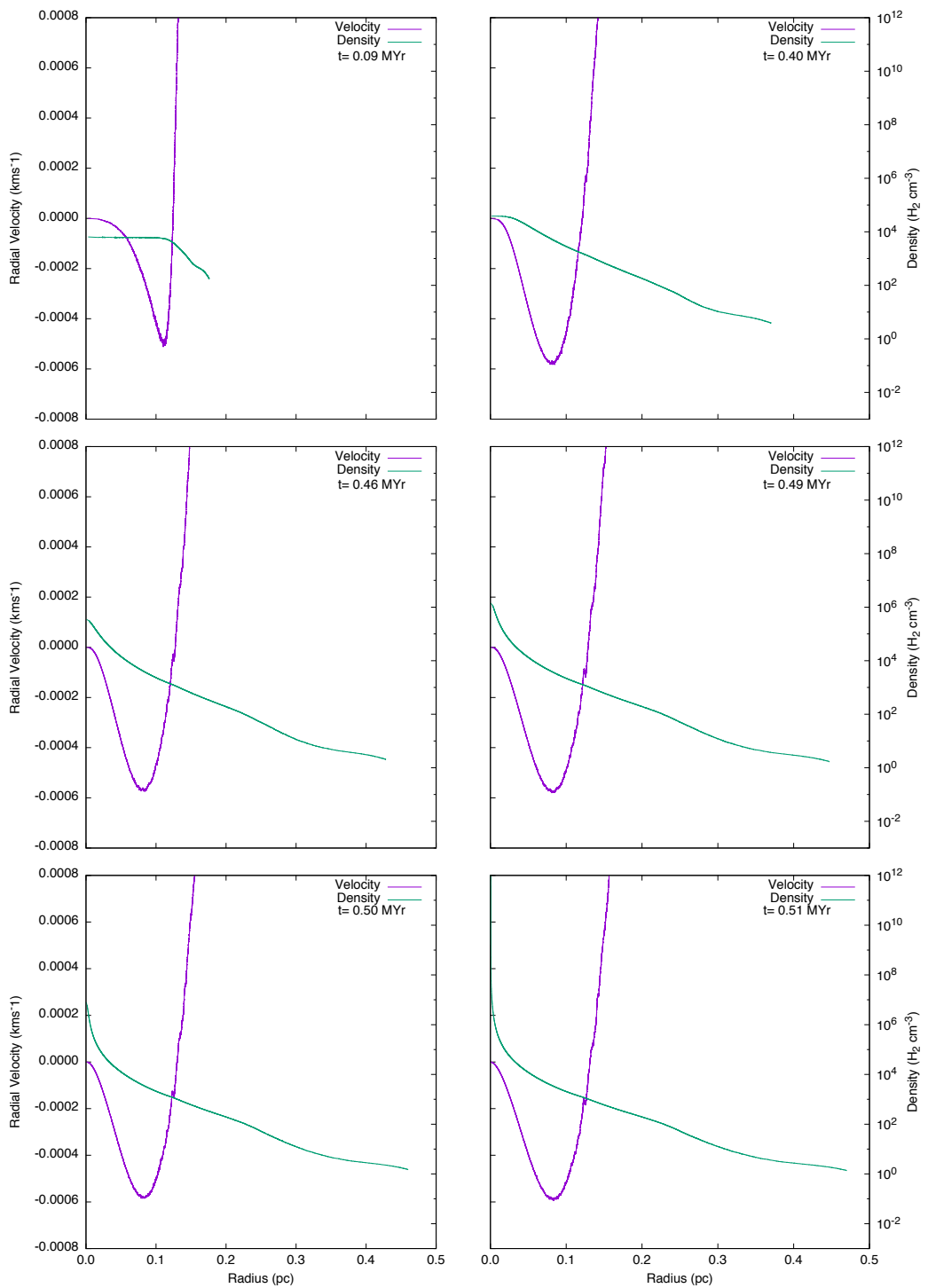
Figure A.30: Model C: six snapshots showing radial velocity (purple line) and density (green line) for a cloud with an initial density of 100 cm^3, a mass of 9 M$_\odot$ and a radius of 0.76 pc.
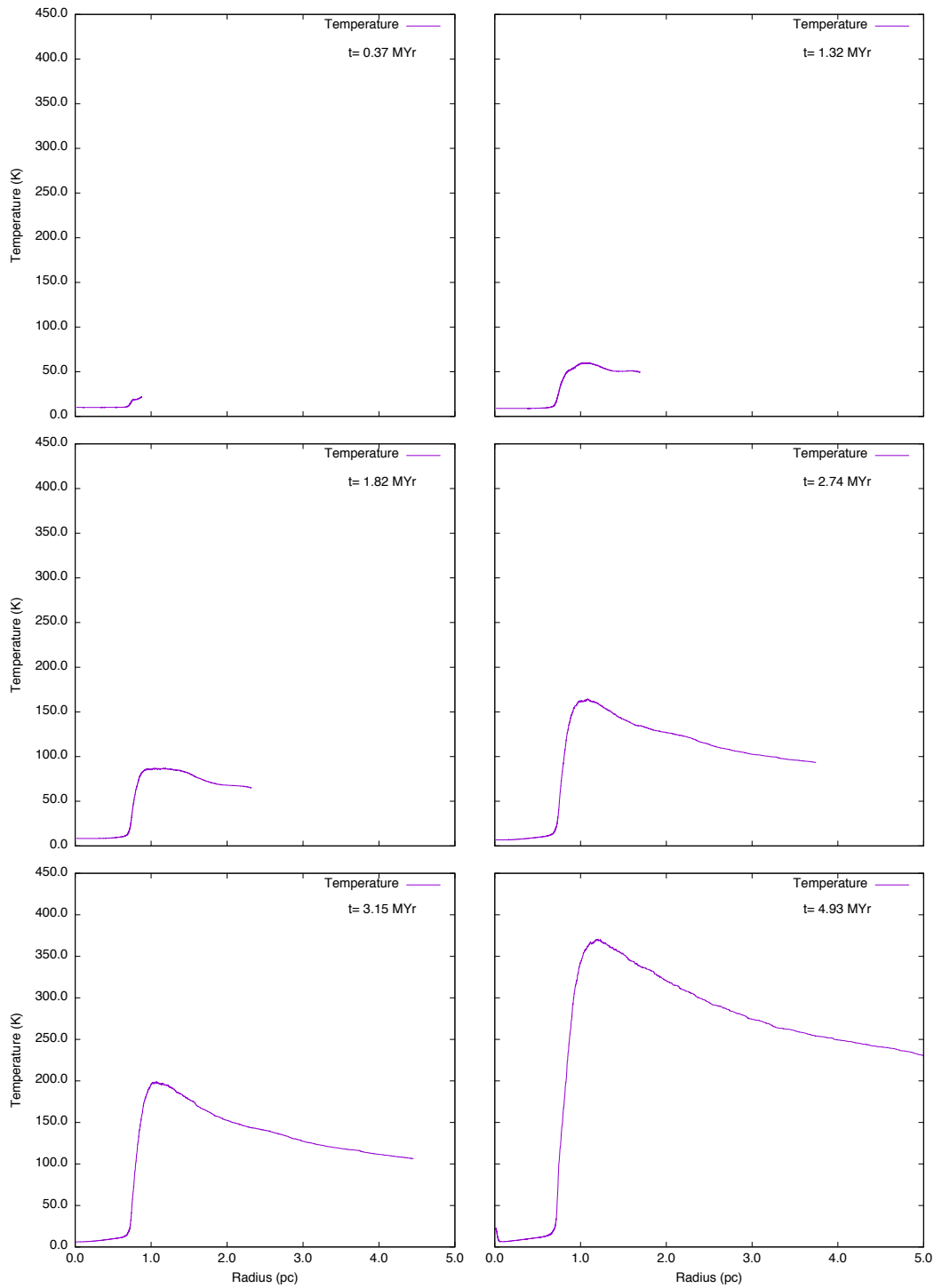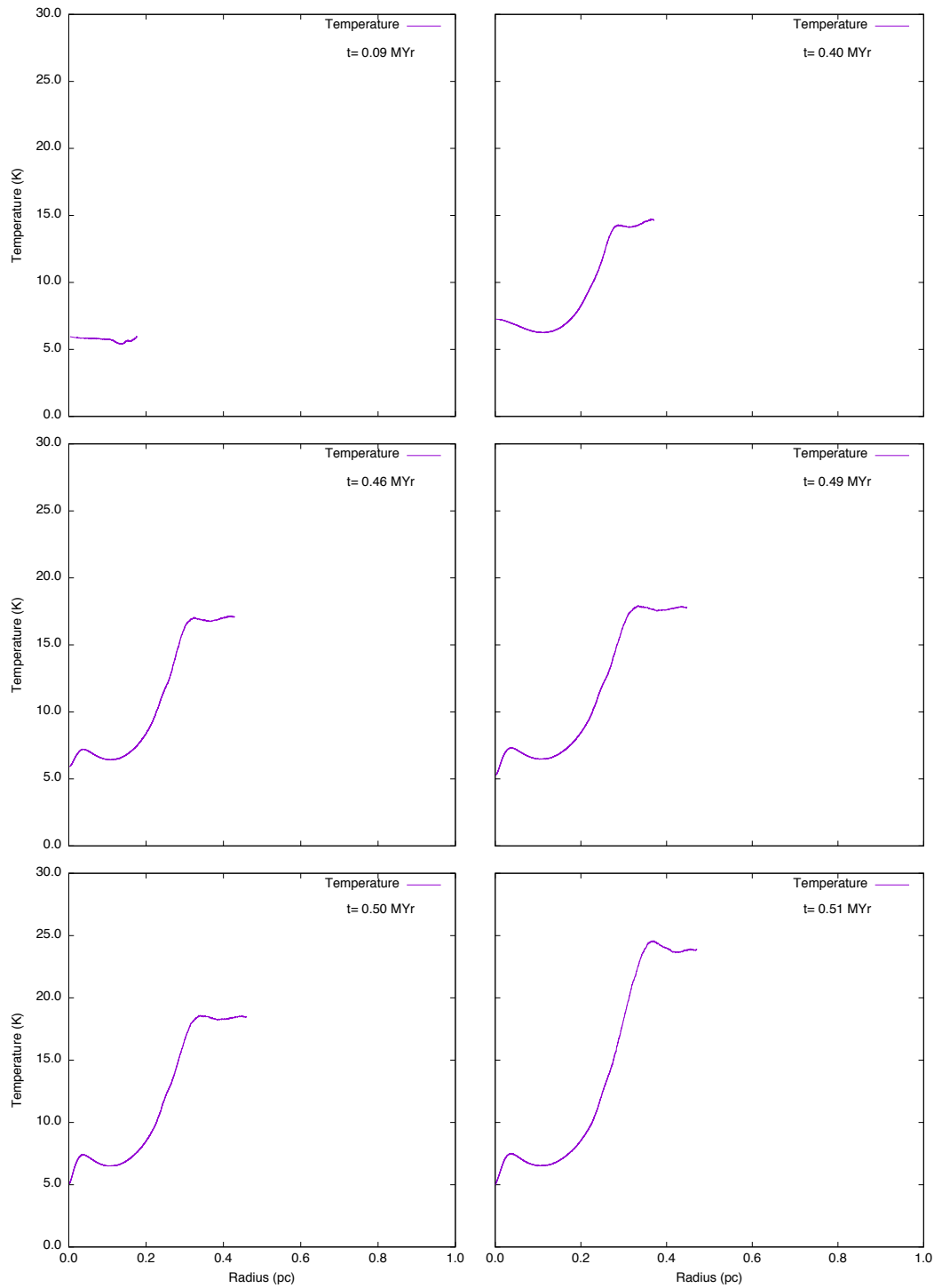
Figure A.31: Model C: six snapshots showing temperature (purple line) for a cloud with an initial density of 100 cm^3, a mass of 9 M$_\odot$ and a radius of 0.76 pc.
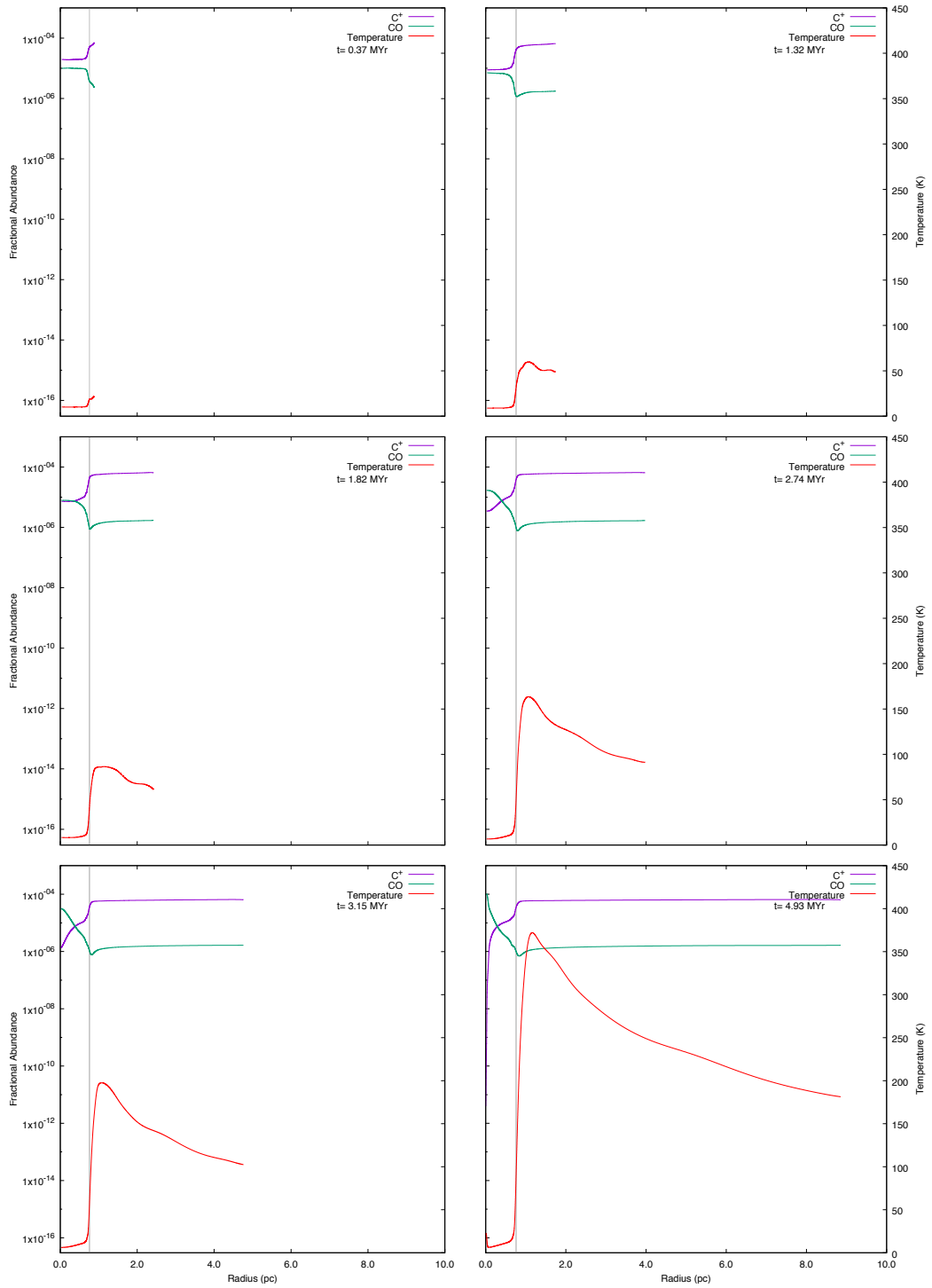
Figure A.32: Model C: six snapshots showing the chemical abundances of CO and C^+ for a cloud with an initial density of 100 cm^{-3}, a mass of 9 M$_\odot$ and a radius of 0.76 pc.
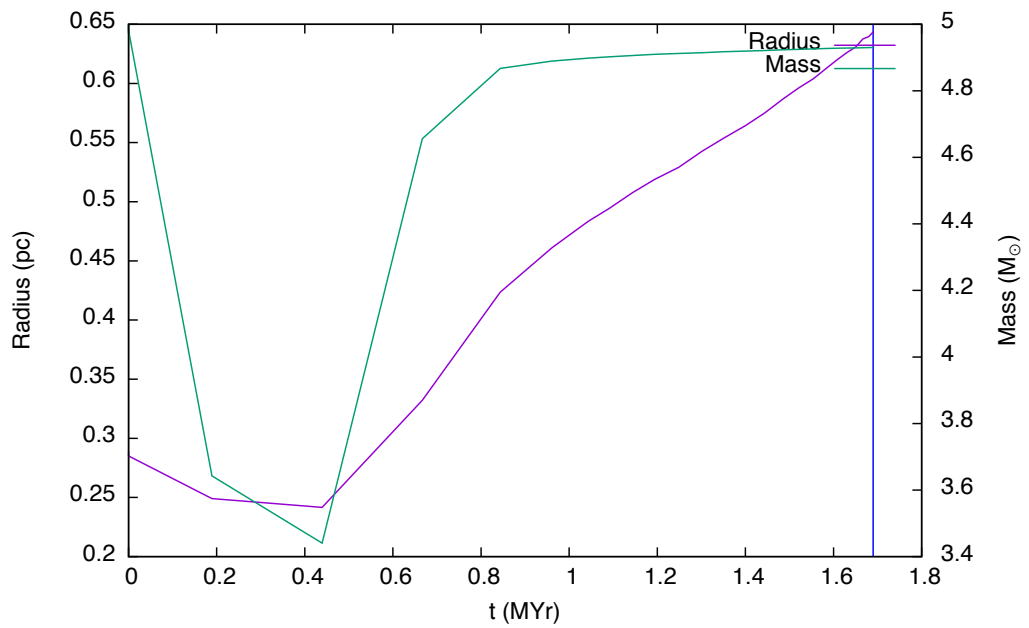
Figure A.33: Model C: the time evolution of the cloud with an initial density of 1000 cm^3, a mass of 4 M$_\odot$ and a radius of 0.27 pc is shown in this graph. The cloud radius (purple line) is taken to be the zero crossing point of radial velocity and the mass (green line) is taken to be that which lies inside the radius. The blue vertical line denotes the time at which the high density peak first forms. This is the minimum cloud mass which collapses for the selected values of density.
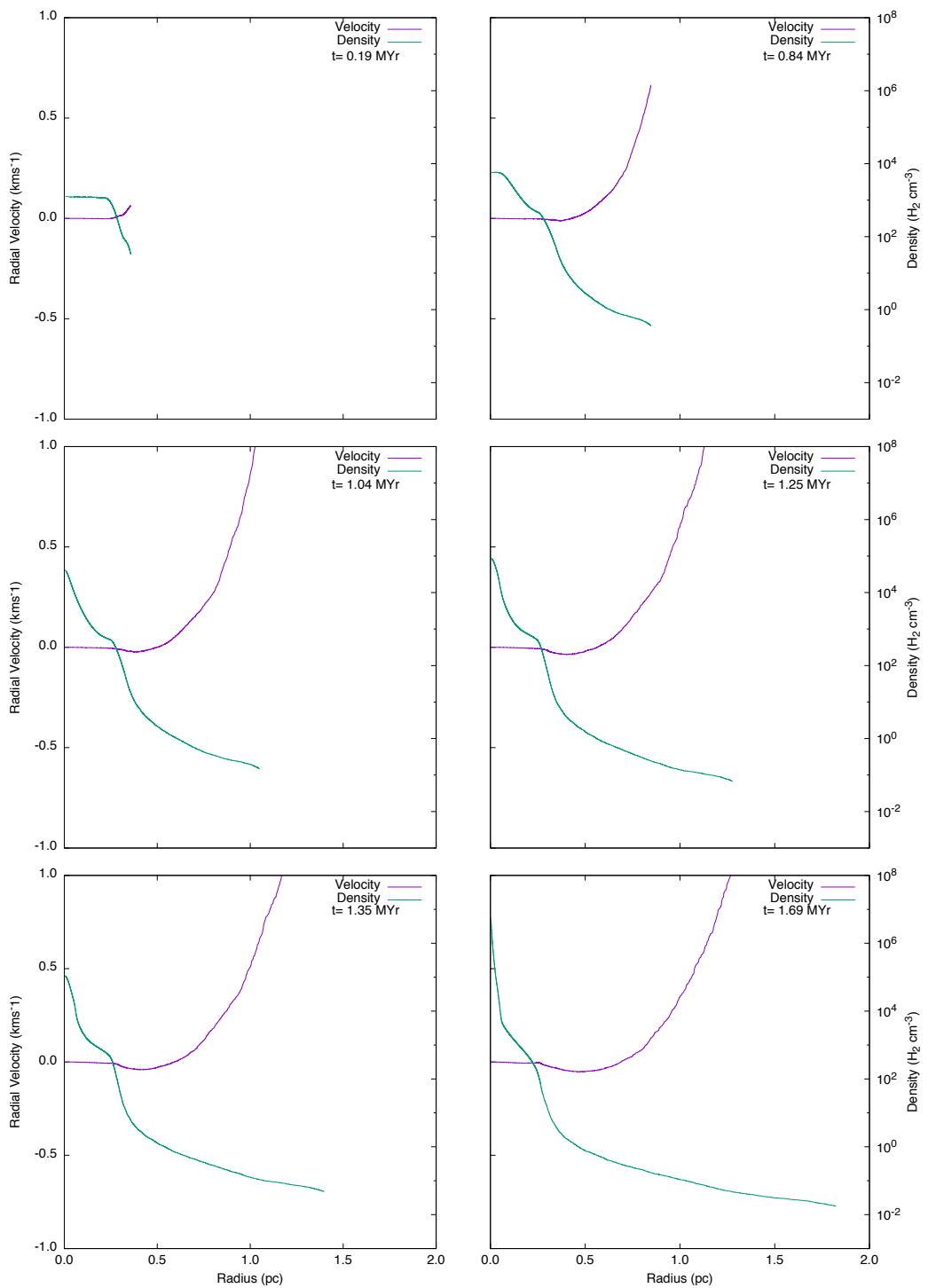
Figure A.34: Model C: six snapshots showing radial velocity (purple line) and density (green line) for a cloud with an initial density of 1000 cm^3, a mass of 4 M$_\odot$ and a radius of 0.27 pc.
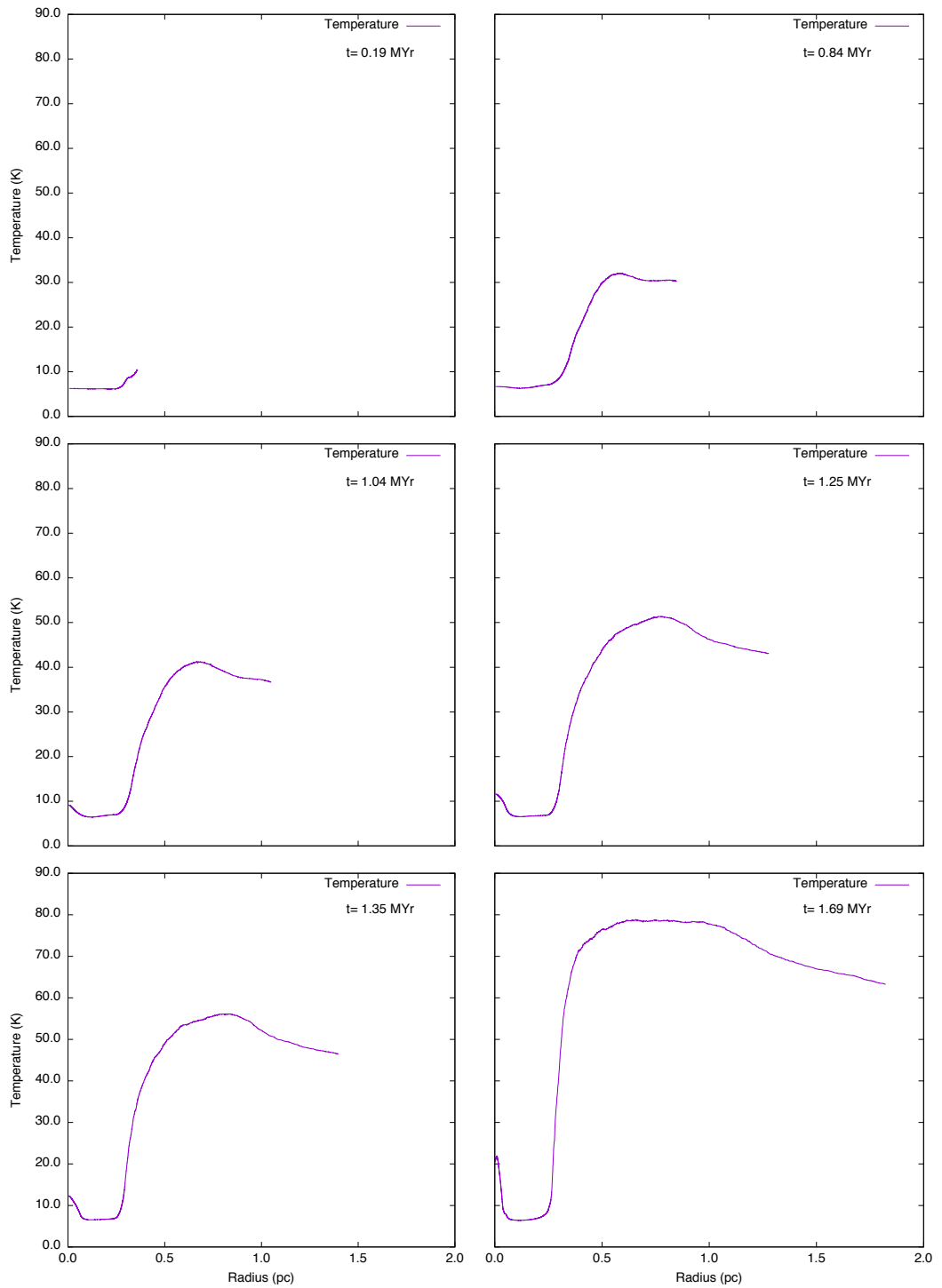
Figure A.35: Model C: six snapshots showing temperature (purple line) for a cloud with an initial density of 1000 cm^3, a mass of 4 M$_\odot$ and a radius of 0.27 pc.
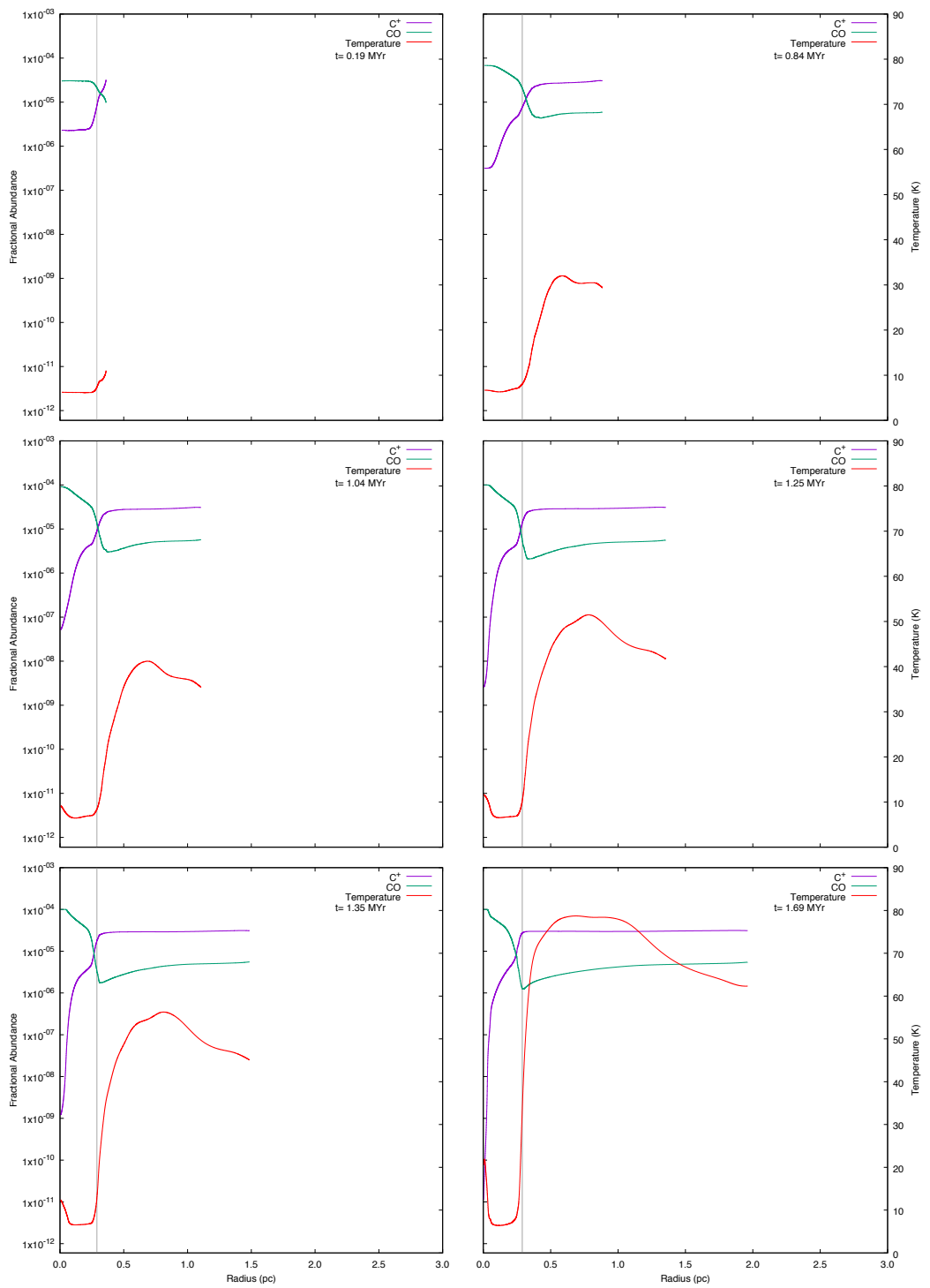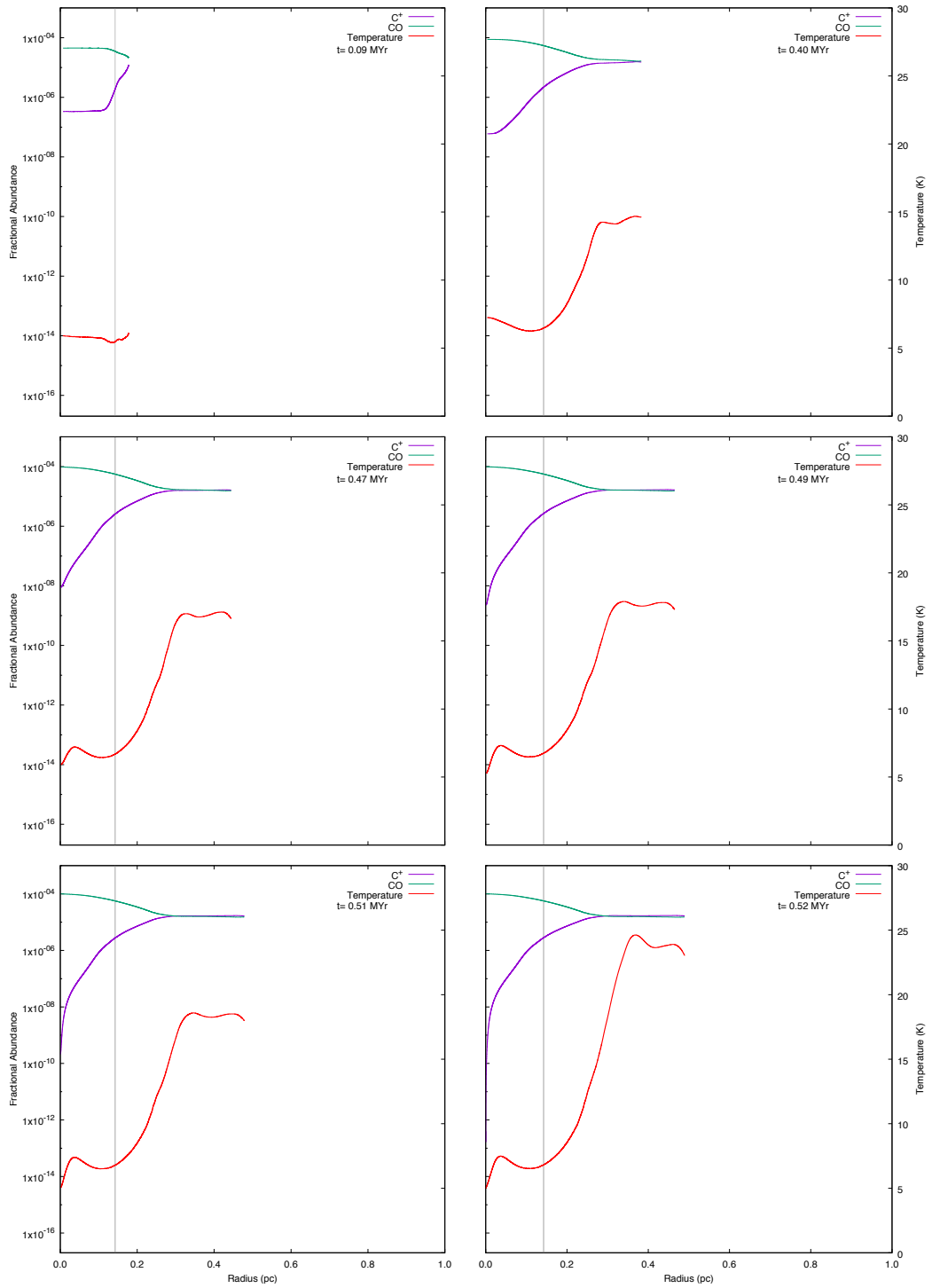
Figure A.36: Model C: six snapshots showing the chemical abundances of CO and C^+ for a cloud with an initial density of 1000 cm^{-3}, a mass of 5 M$_\odot$ and a radius of 0.29 pc.
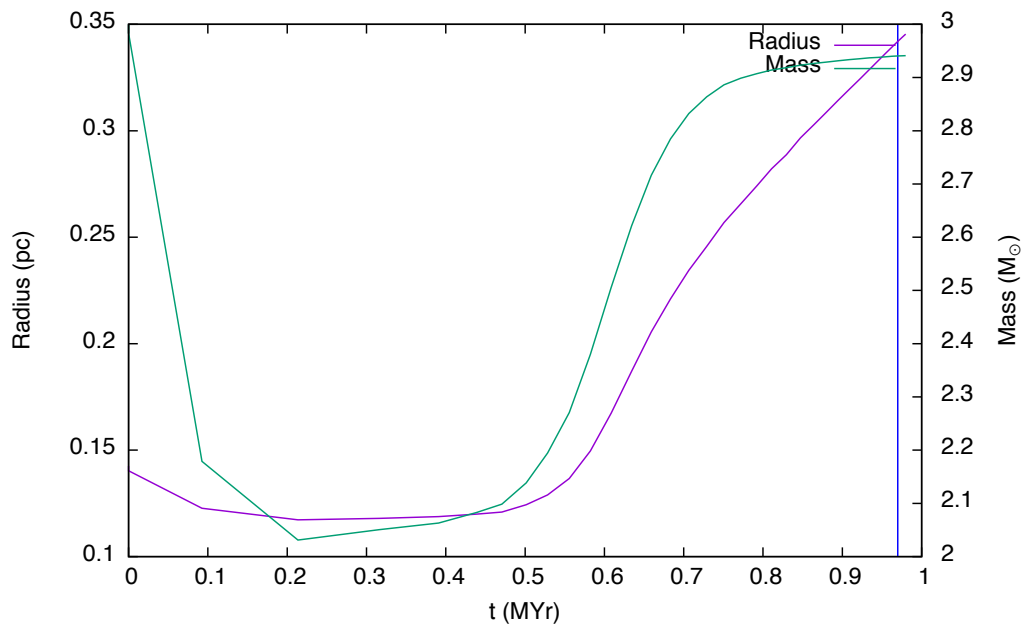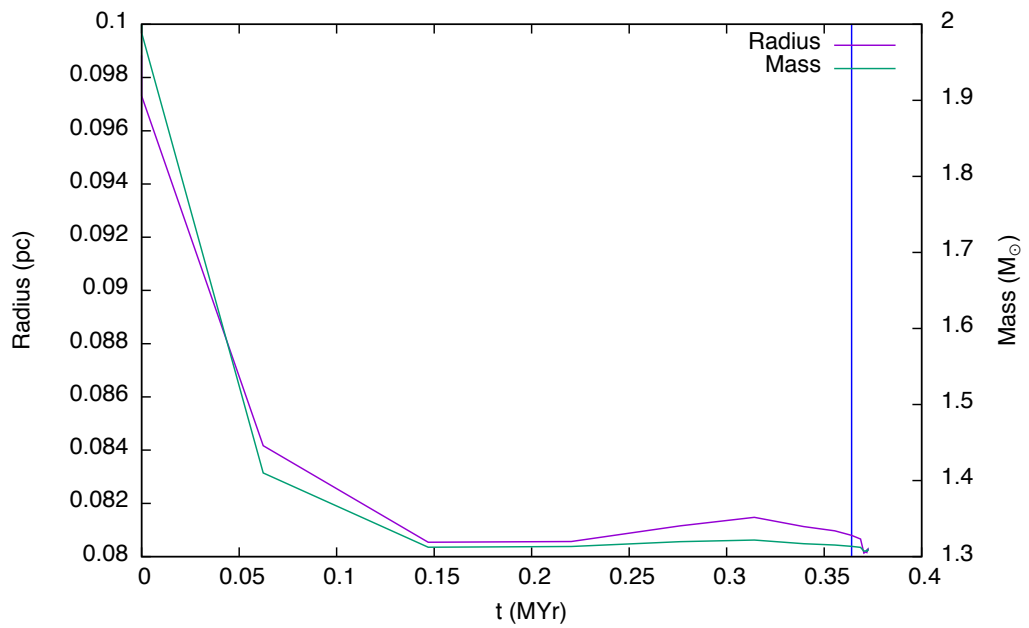
Figure A.37: Model C: the time evolution of the cloud with an initial density of 5000 cm^3, a mass of 3 M$_\odot$ and a radius of 0.14 pc is shown in this graph. The cloud radius (purple line) is taken to be the zero crossing point of radial velocity and the mass (green line) is taken to be that which lies inside the radius. The blue vertical line denotes the time at which the high density peak first forms. This is the minimum cloud mass which collapses for the selected values of density.
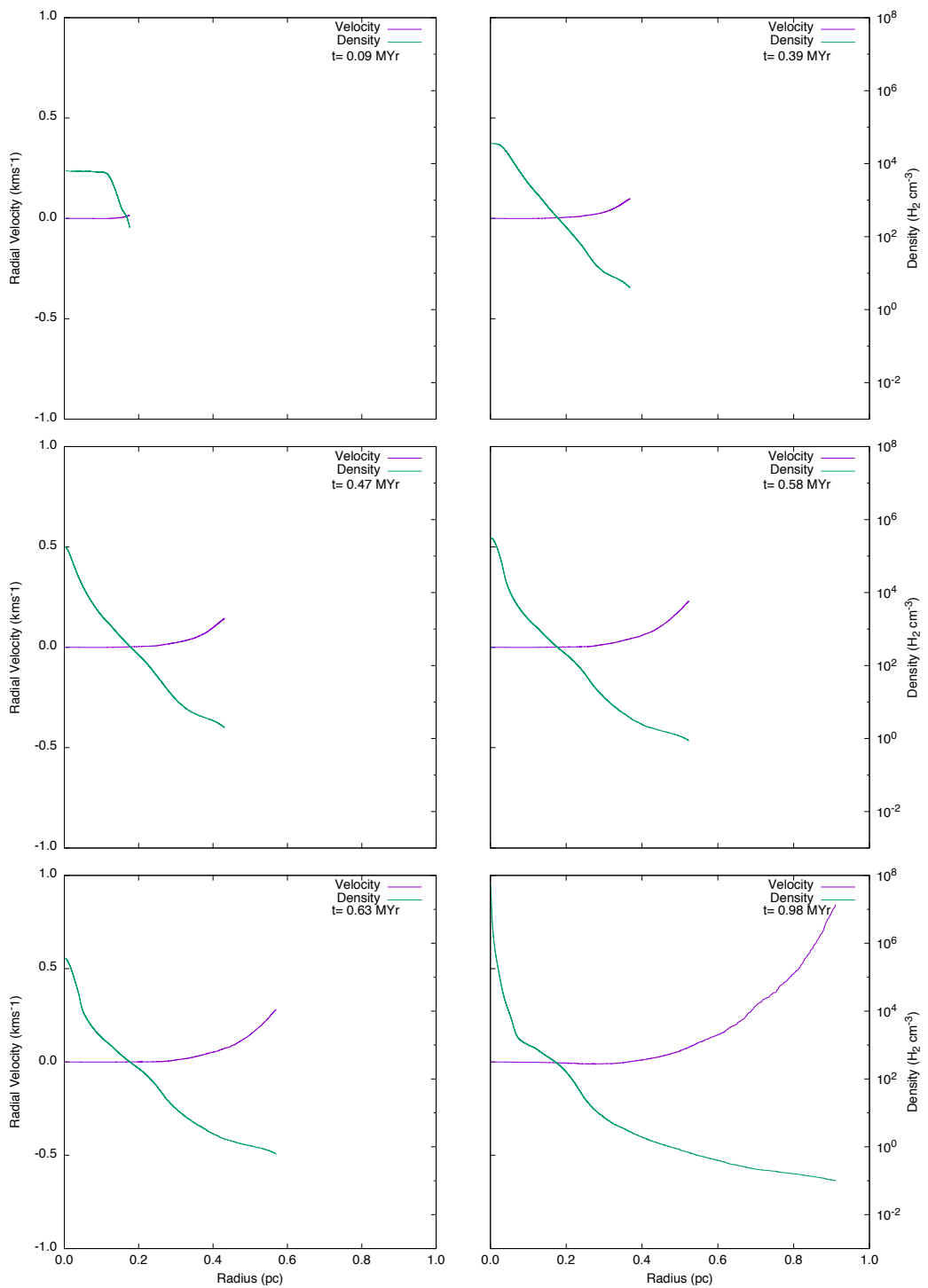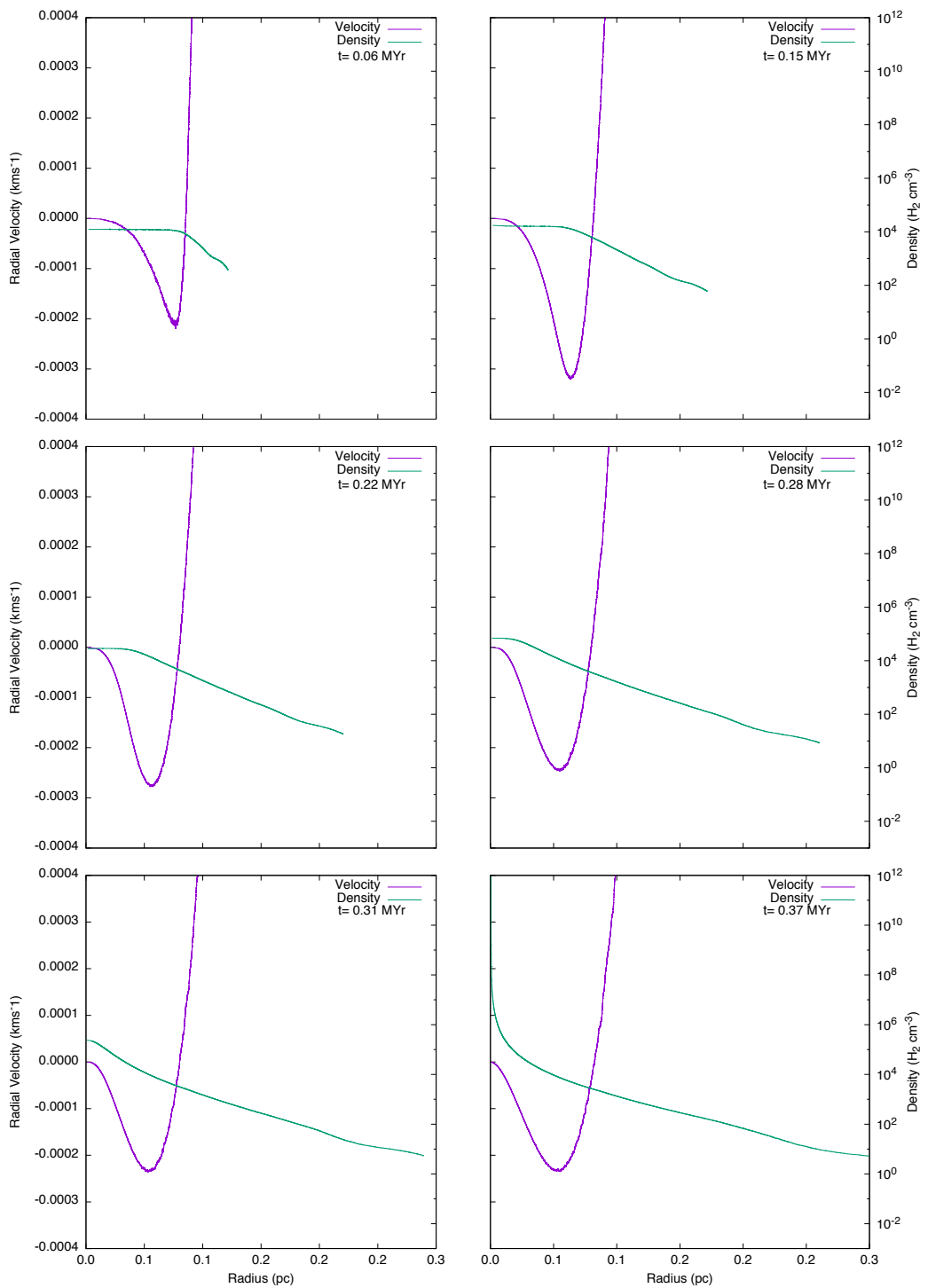
Figure A.38: Model C: six snapshots showing radial velocity (purple line) and density (green line) for a cloud with an initial density of 5000 cm^3, a mass of 3 M$_\odot$ and a radius of 0.14 pc.
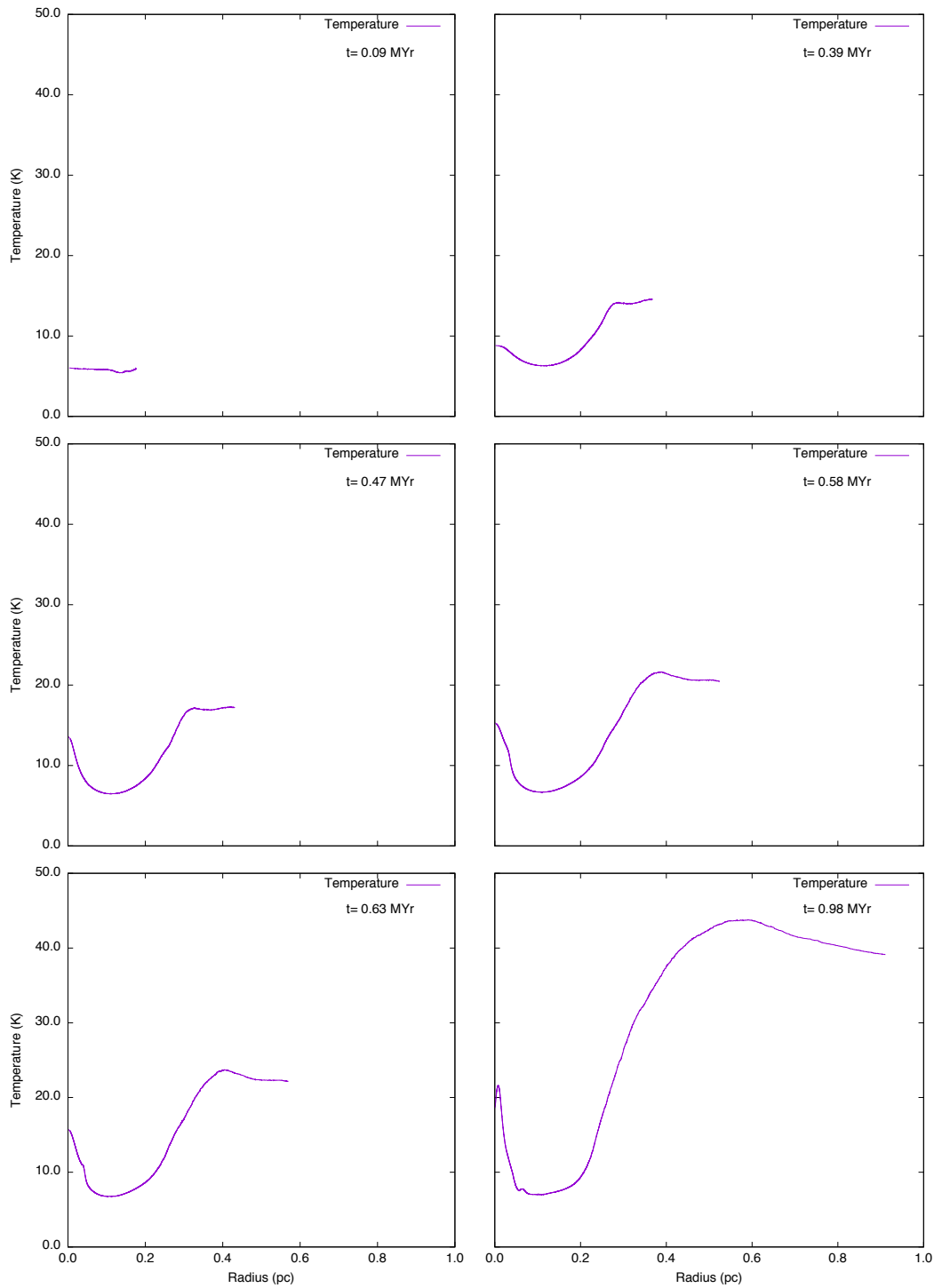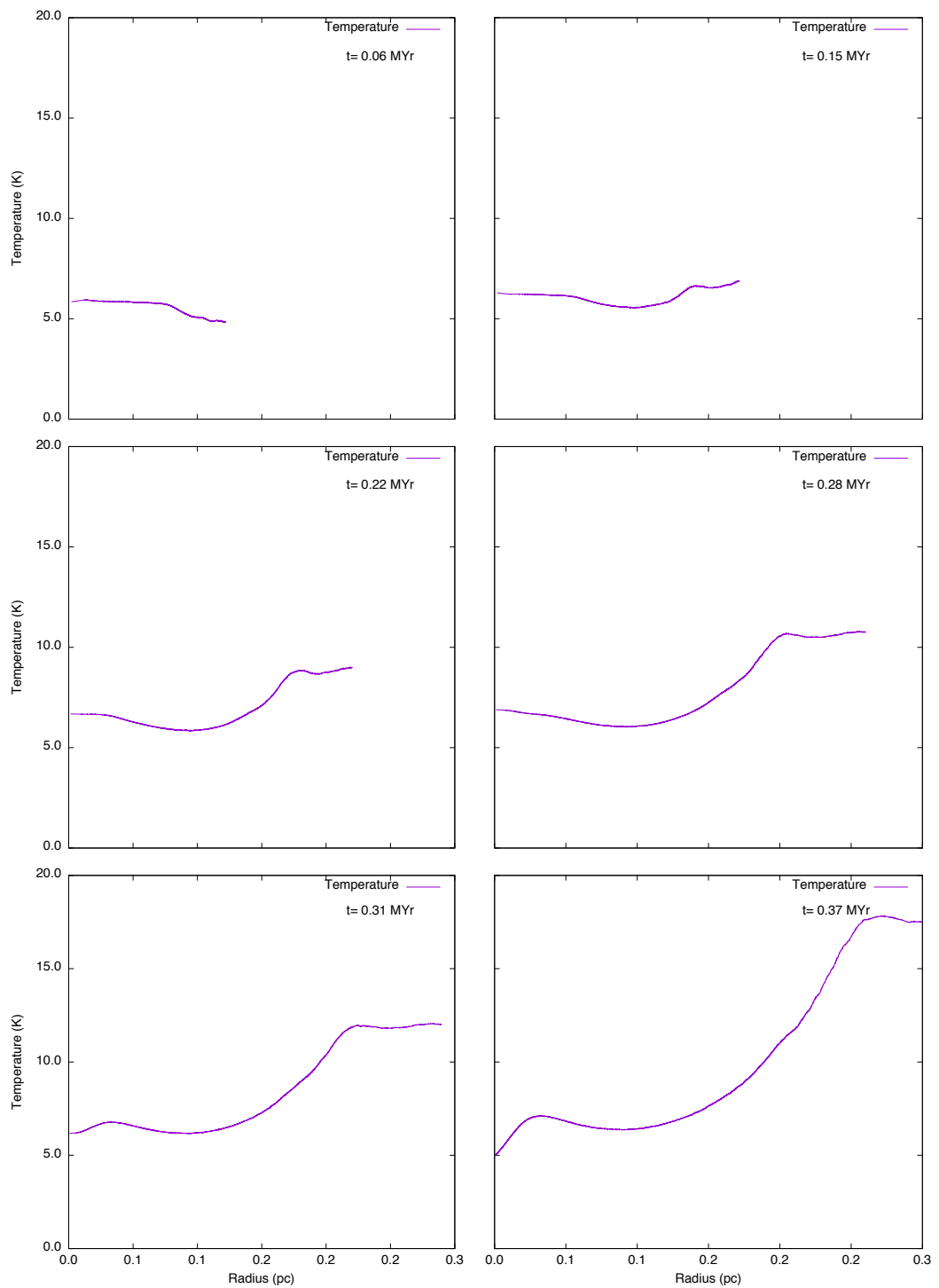
Figure A.39: Model C: six snapshots showing temperature (purple line) for a cloud with an initial density of 5000 cm^3, a mass of 3 M$_\odot$ and a radius of 0.14 pc.
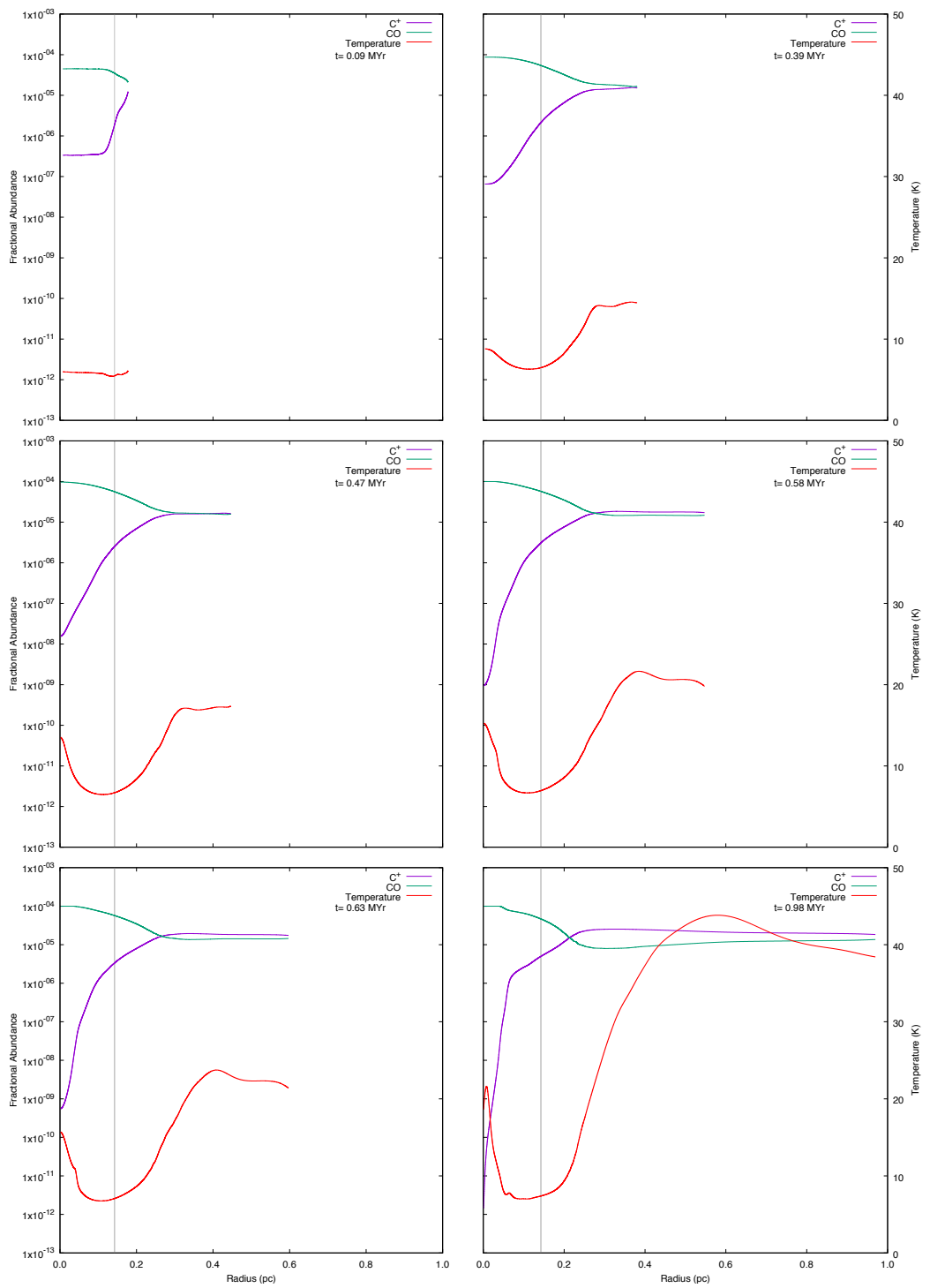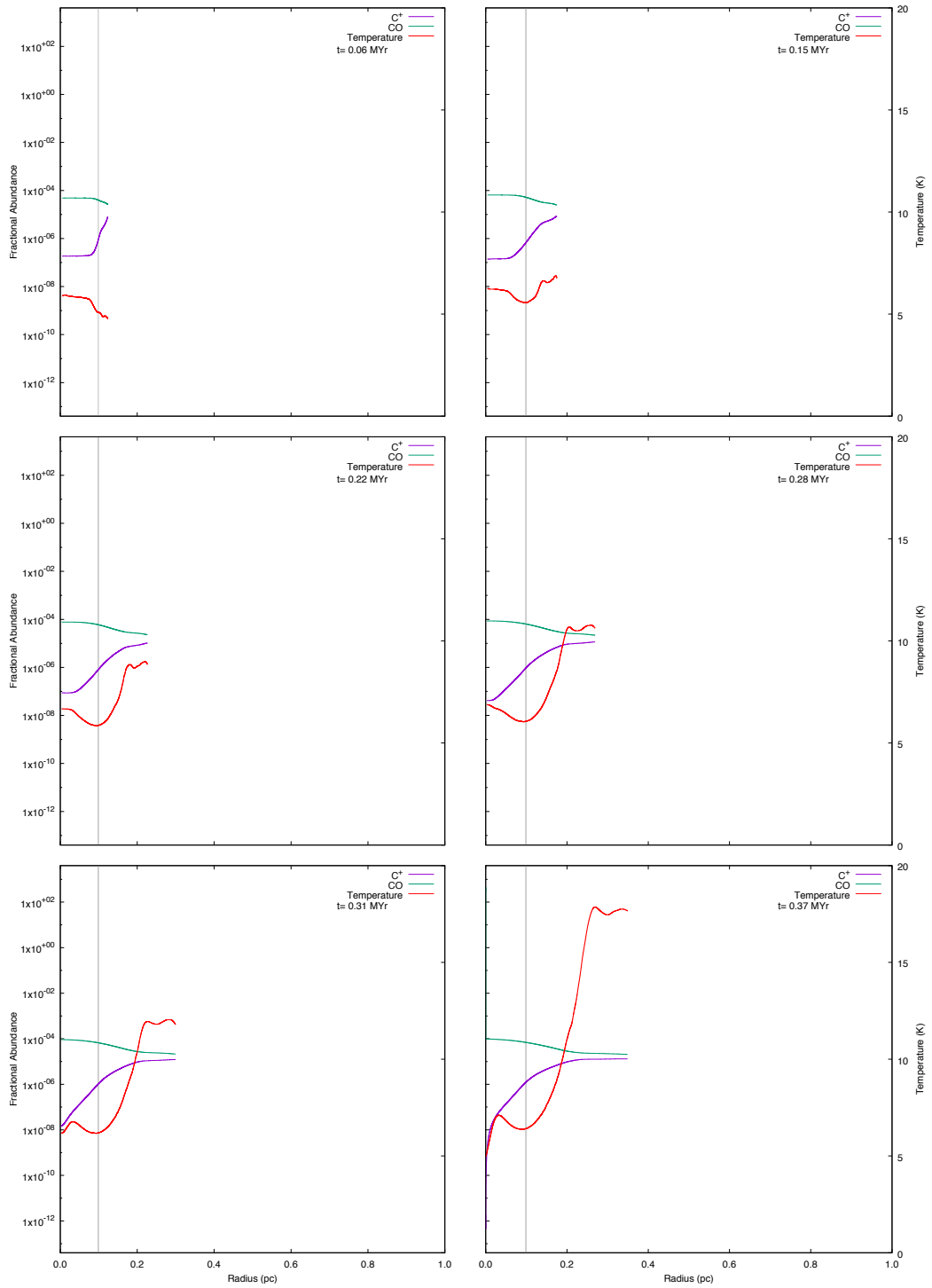
Figure A.40: Model C: six snapshots showing the chemical abundances of CO and C^+ for a cloud with an initial density of 5000 cm^{-3}, a mass of 3 $M_\odot$ and a radius of 0.14 pc.
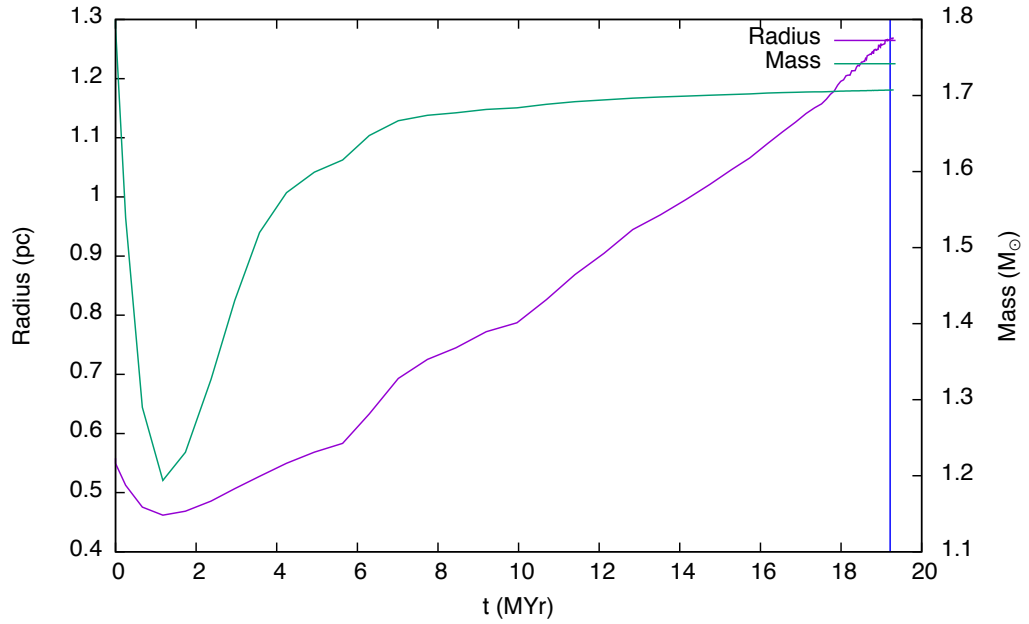
A.4   Model D
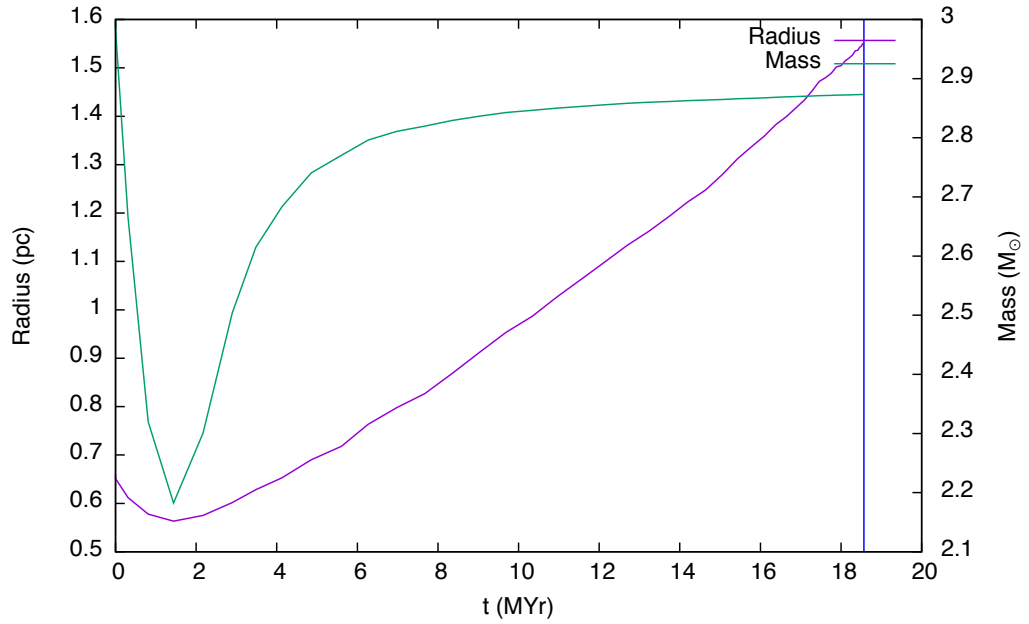
Figure A.41: Model D: the time evolution of the cloud with an initial density of 50 cm^3, a mass of 3 M$_\odot$ and a radius of 0.66 pc is shown in this graph. The cloud radius (purple line) is taken to be the zero crossing point of radial velocity and the mass (green line) is taken to be that which lies inside the radius. The blue vertical line denotes the time at which the high density peak first forms. This is the minimum cloud mass which collapses for the selected values of density.
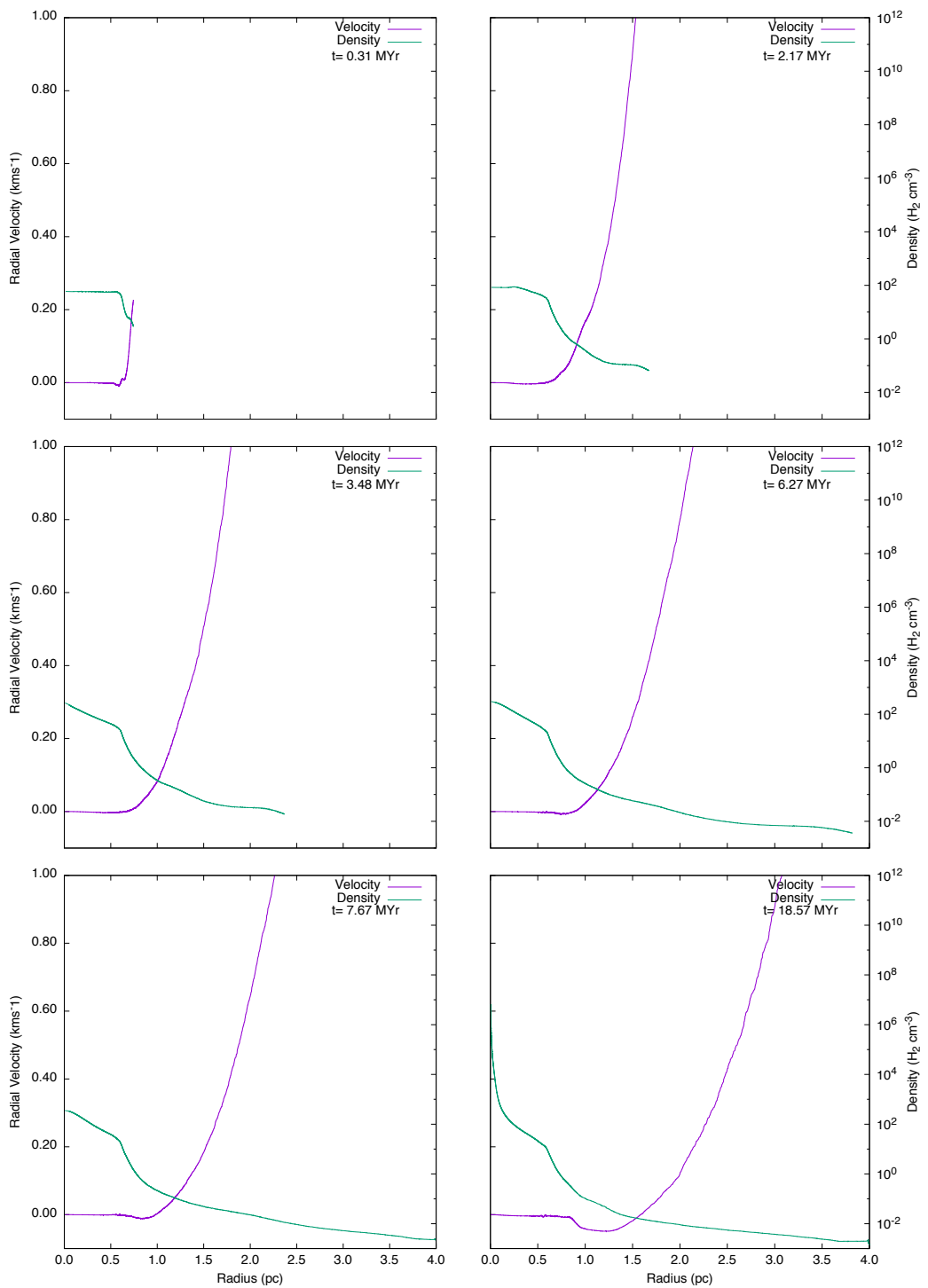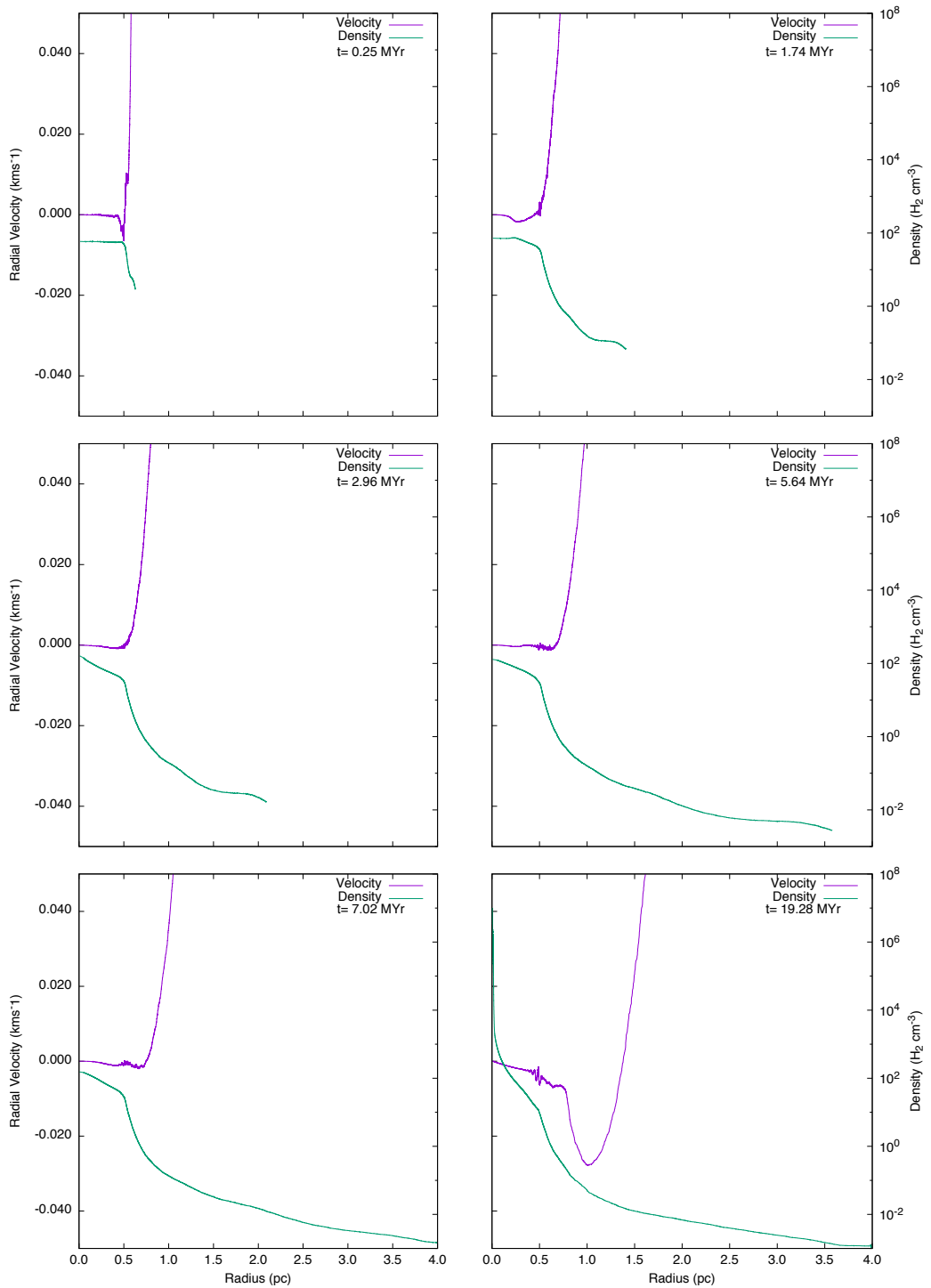
Figure A.42: Model D: six snapshots showing radial velocity (purple line) and density (green line) for a cloud with an initial density of 50 cm³, a mass of 3 M$_\odot$ and a radius of 0.66 pc.
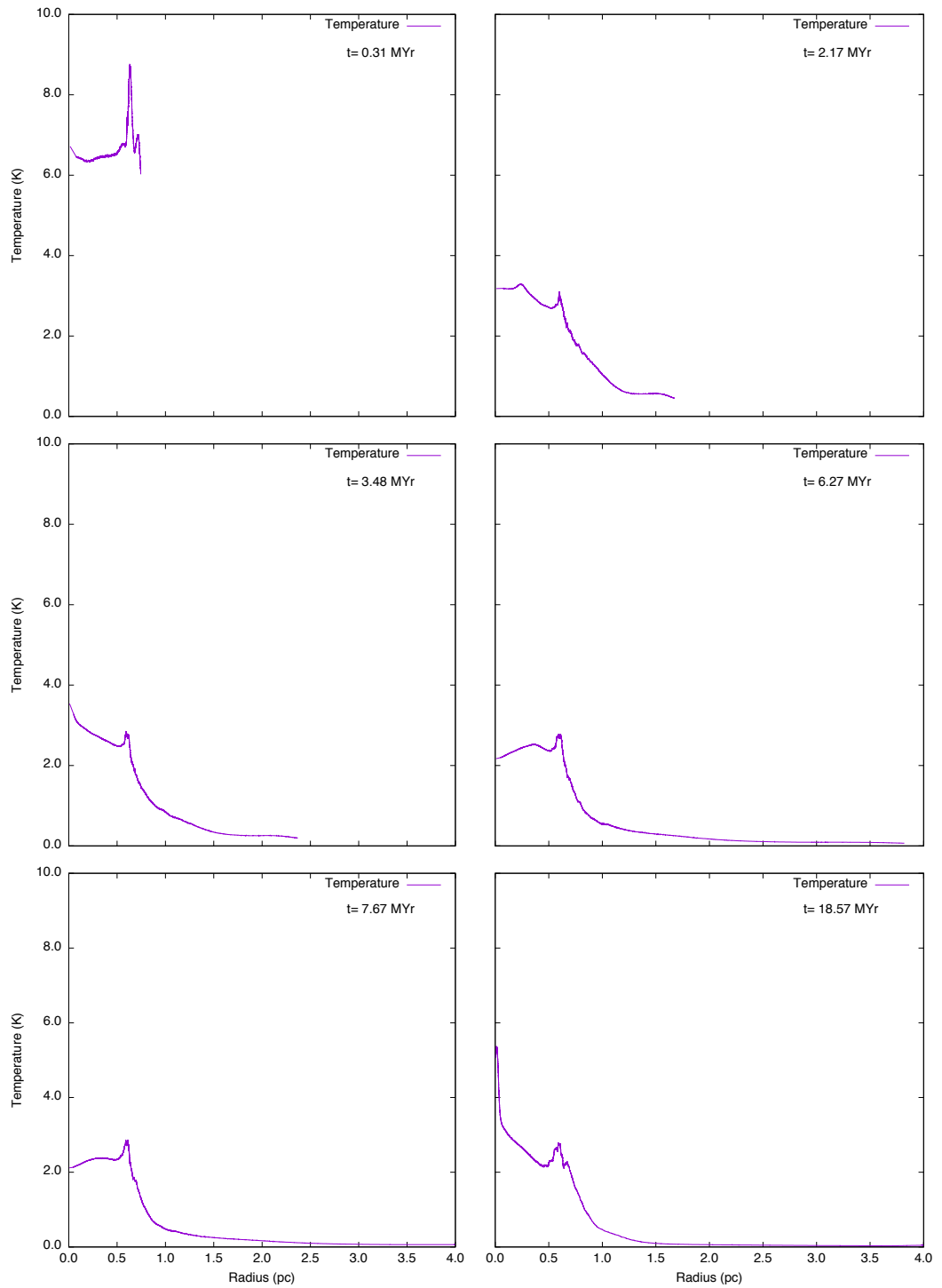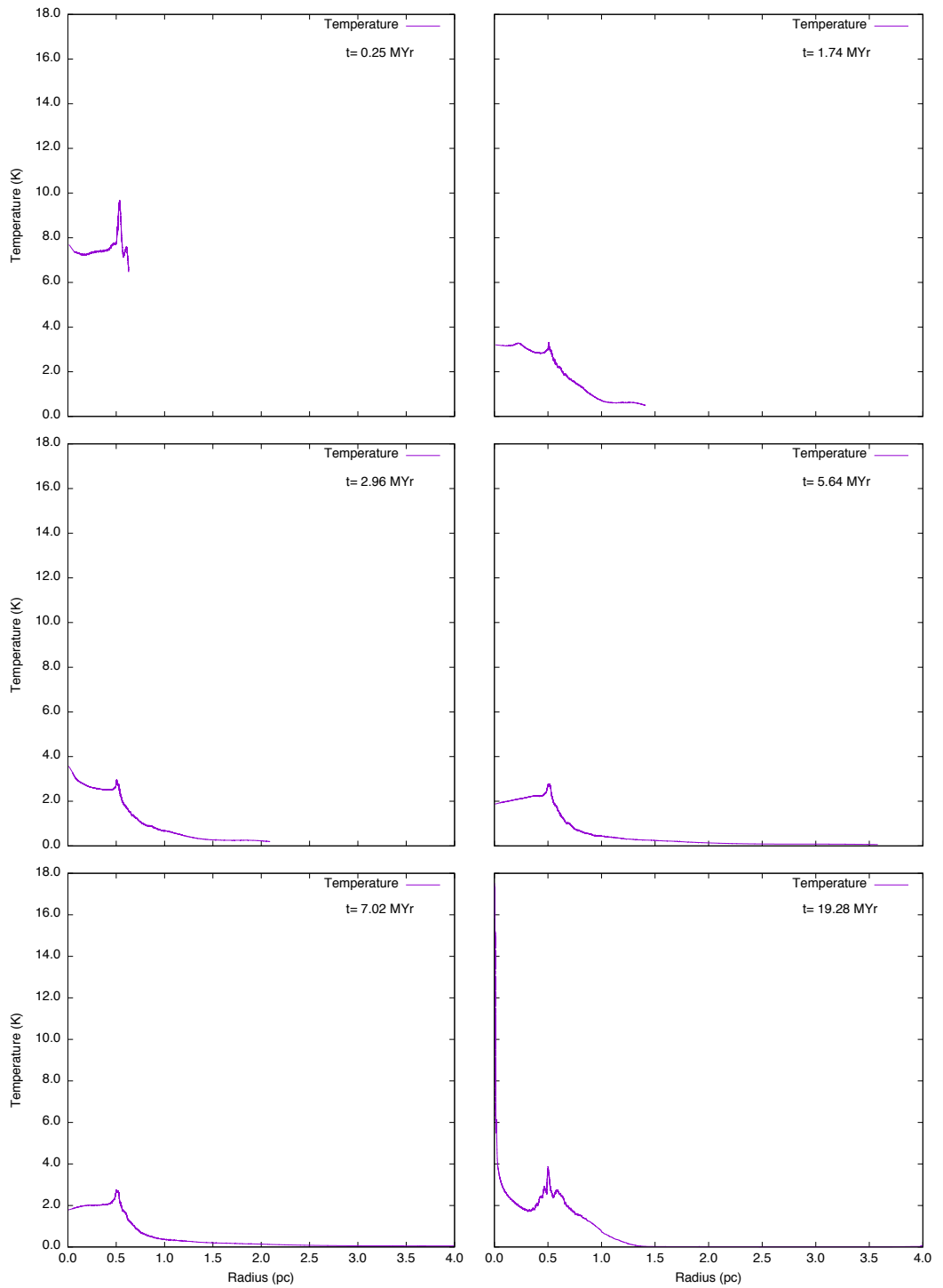
Figure A.43: Model D: six snapshots showing temperature (purple line) for a cloud with an initial density of 50 cm³, a mass of 3 M$_\odot$ and a radius of 0.66 pc.
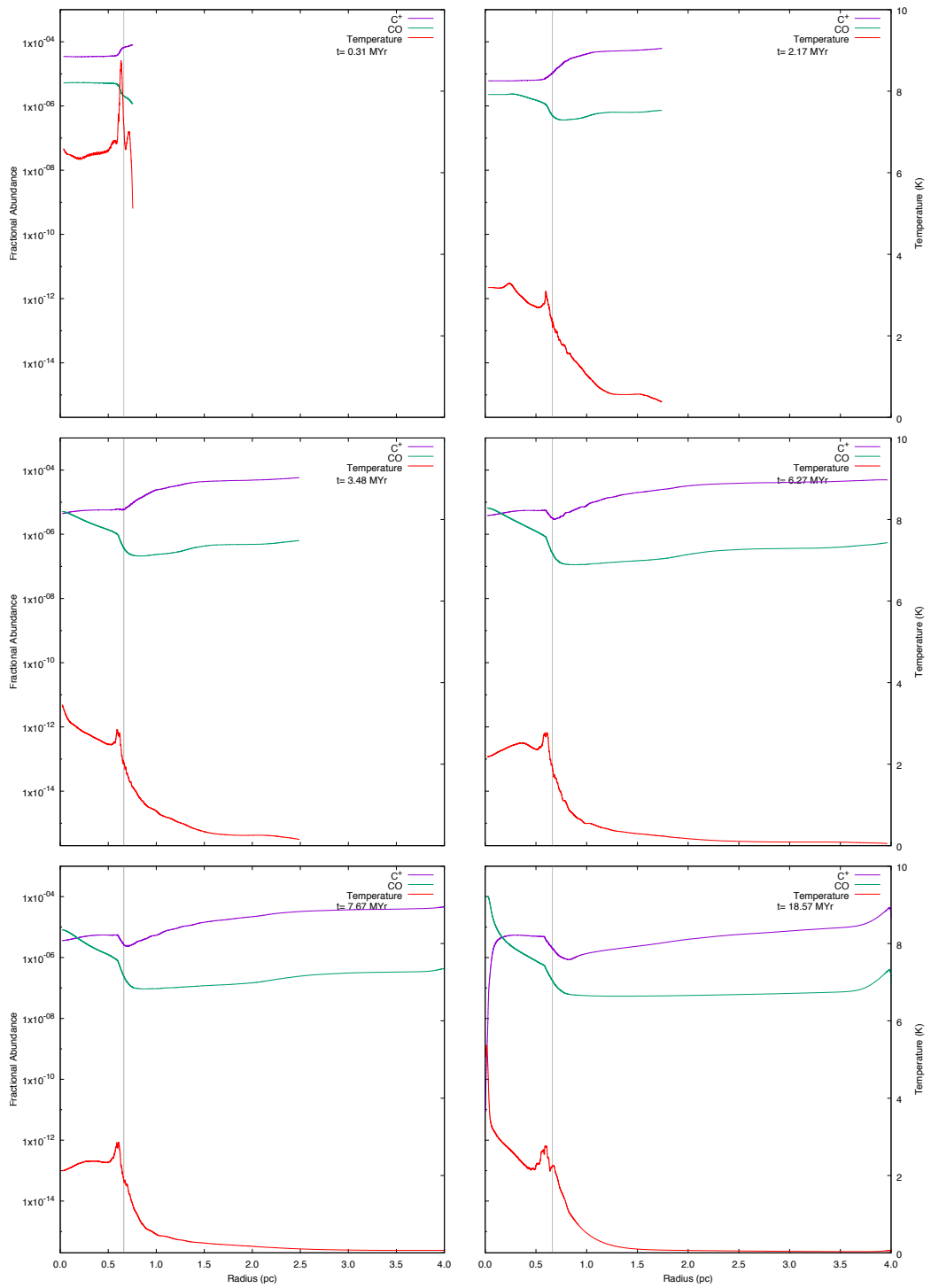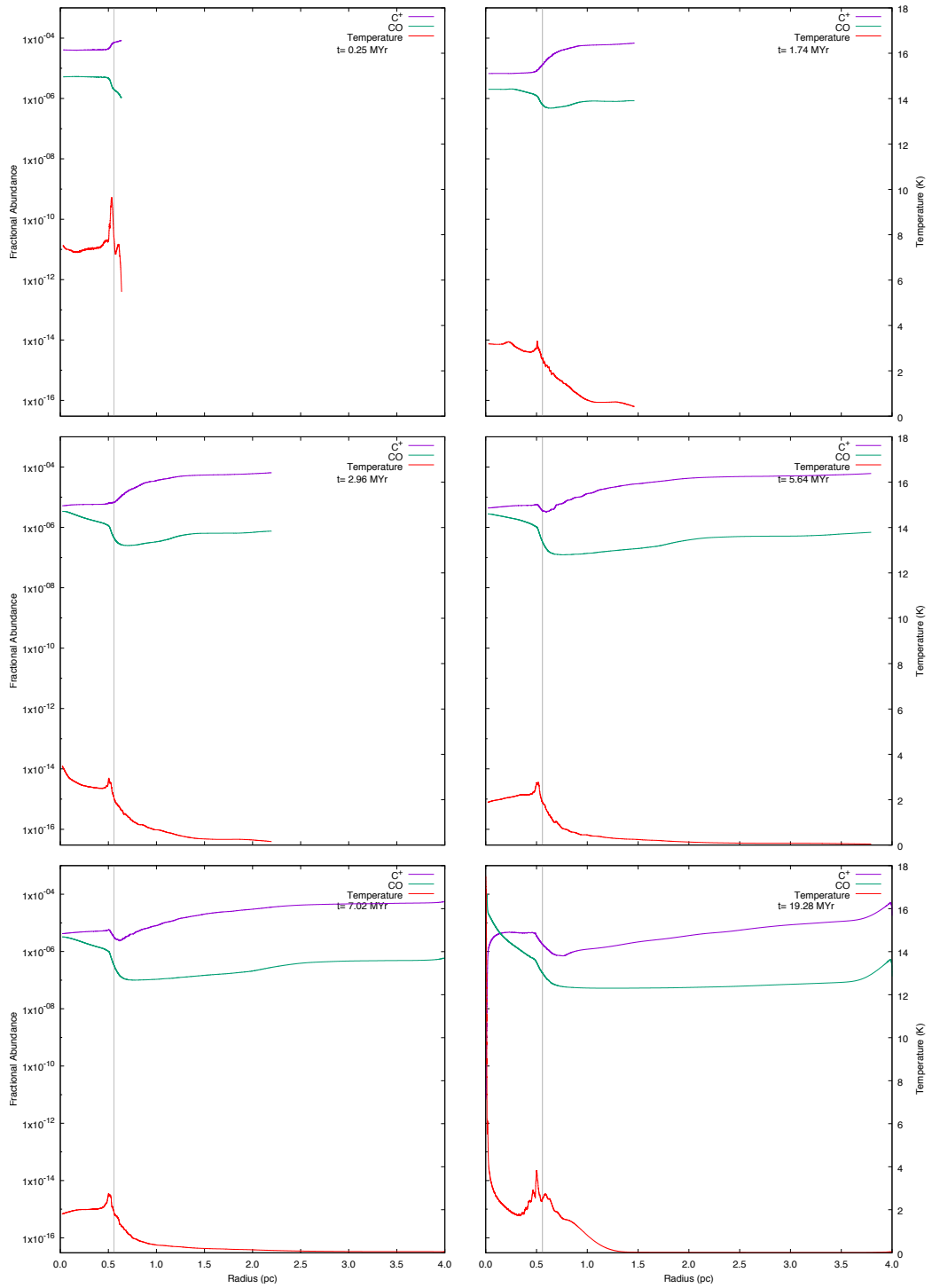
Figure A.44: Model D: six snapshots showing the chemical abundances of CO and C$^+$ for a cloud with an initial density of 50 cm^{-3}, a mass of 3 M$_\odot$ and a radius of 0.66 pc.
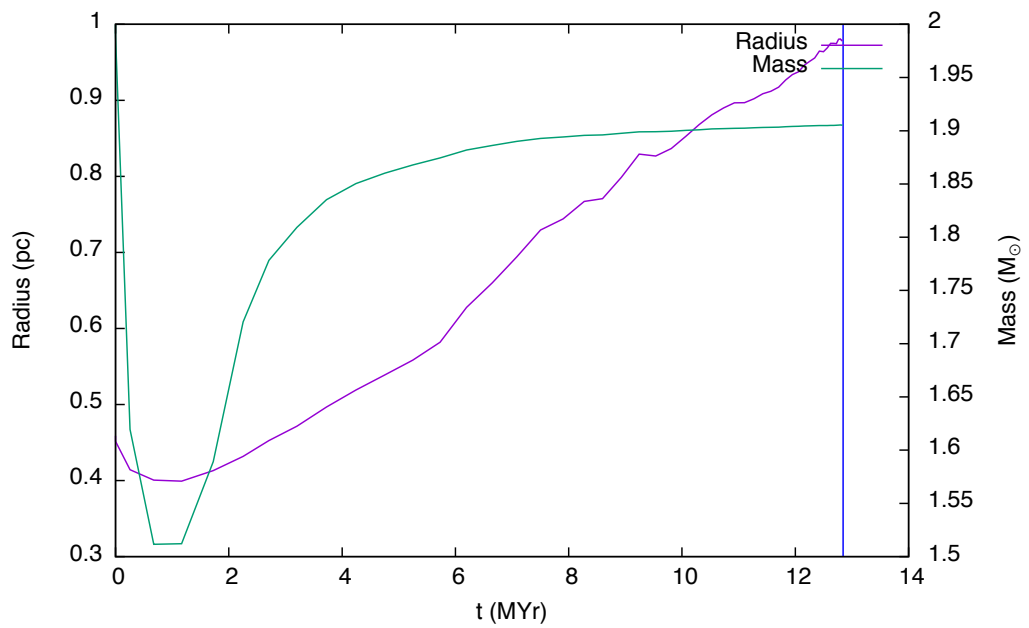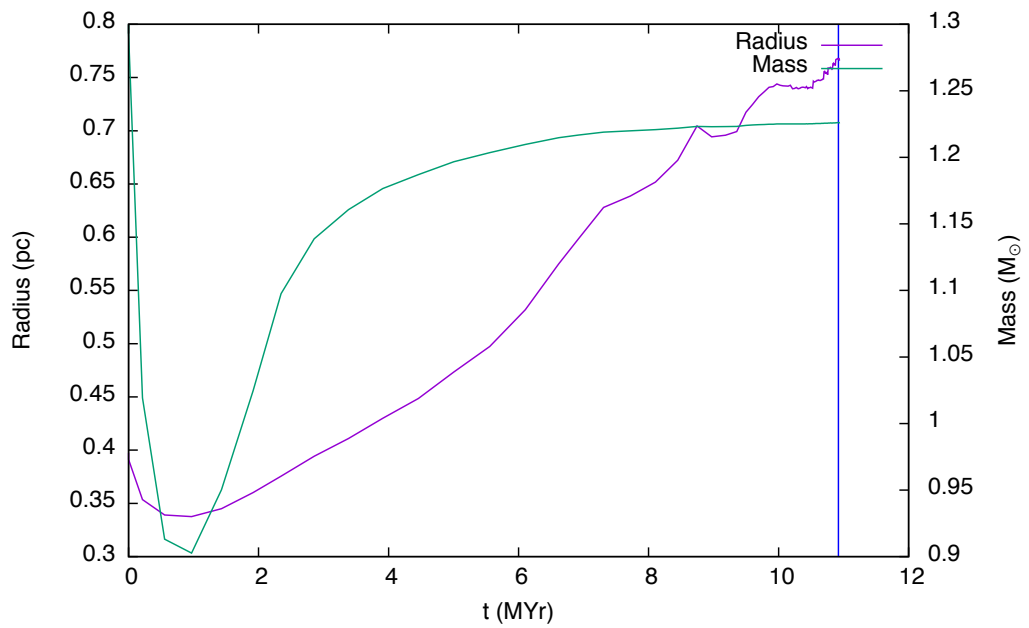
Figure A.45: Model D: the time evolution of the cloud with an initial density of $100 \, \text{cm}^3$, a mass of $2 \, \text{M}_\odot$ and a radius of 0.46 pc is shown in this graph. The cloud radius (purple line) is taken to be the zero crossing point of radial velocity and the mass (green line) is taken to be that which lies inside the radius. The blue vertical line denotes the time at which the high density peak first forms. This is the minimum cloud mass which collapses for the selected values of density.
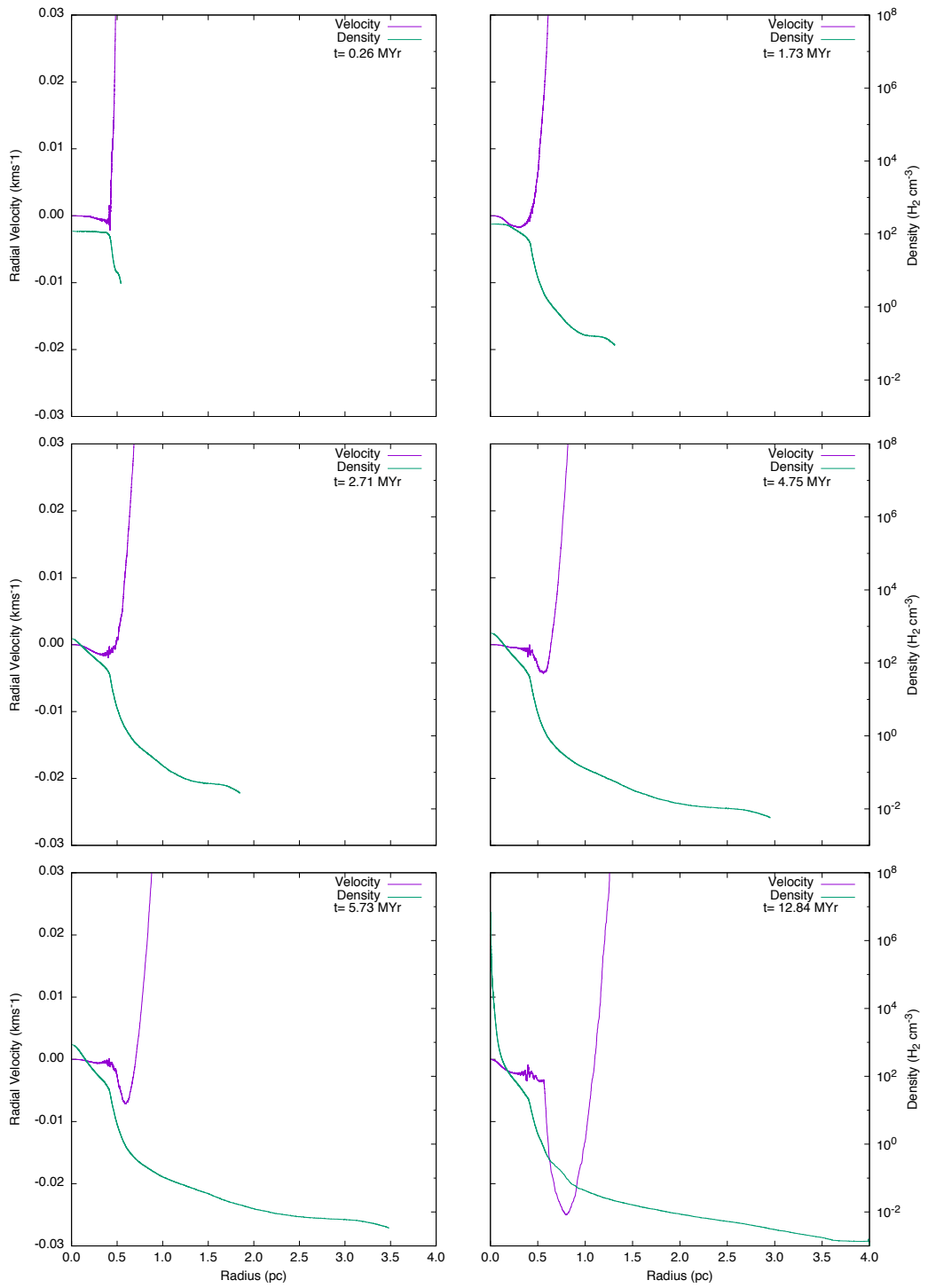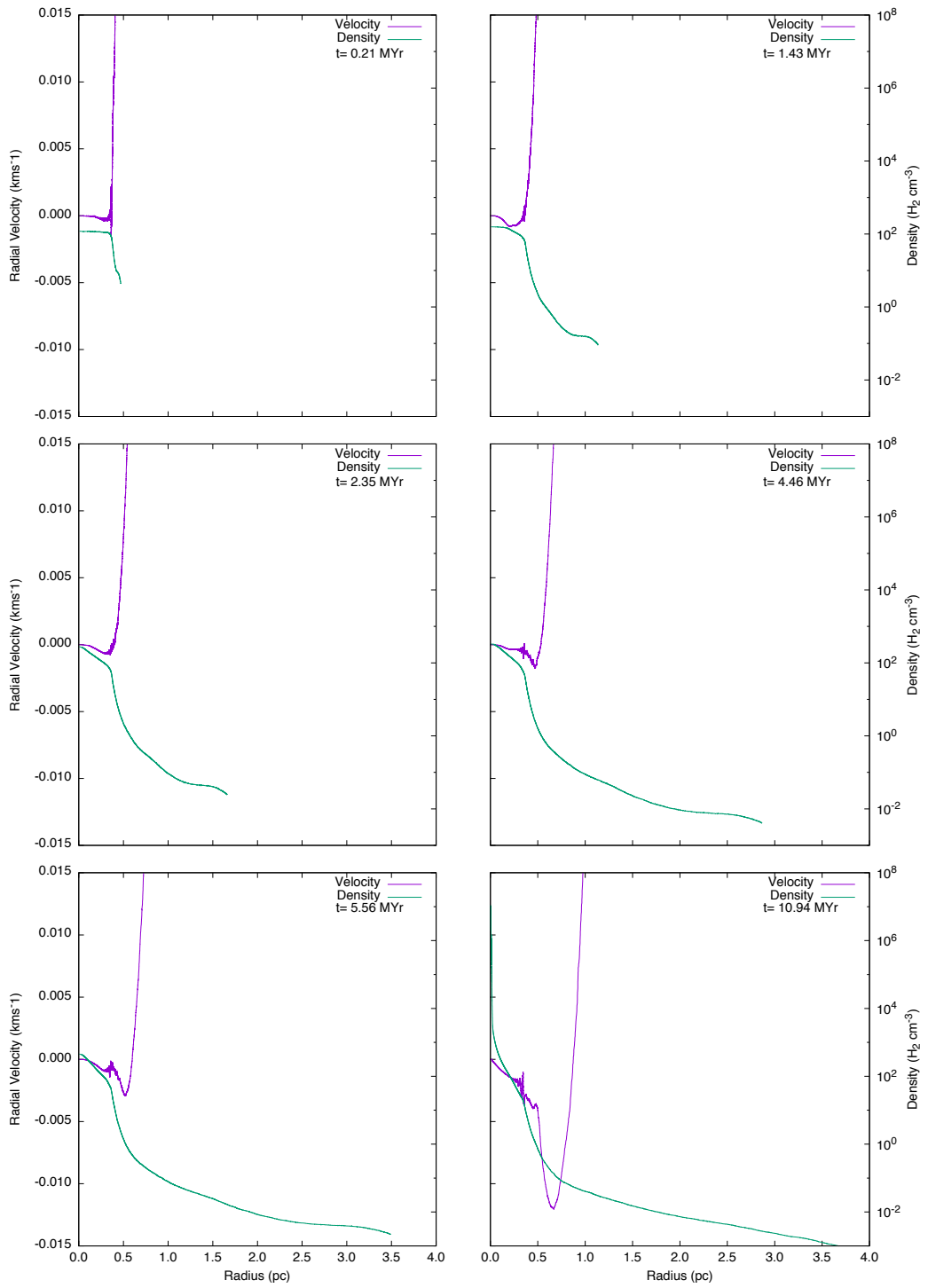
Figure A.46: Model D: six snapshots showing radial velocity (purple line) and density (green line) for a cloud with an initial density of 100 cm^3, a mass of 2 M$_\odot$ and a radius of 0.46 pc.
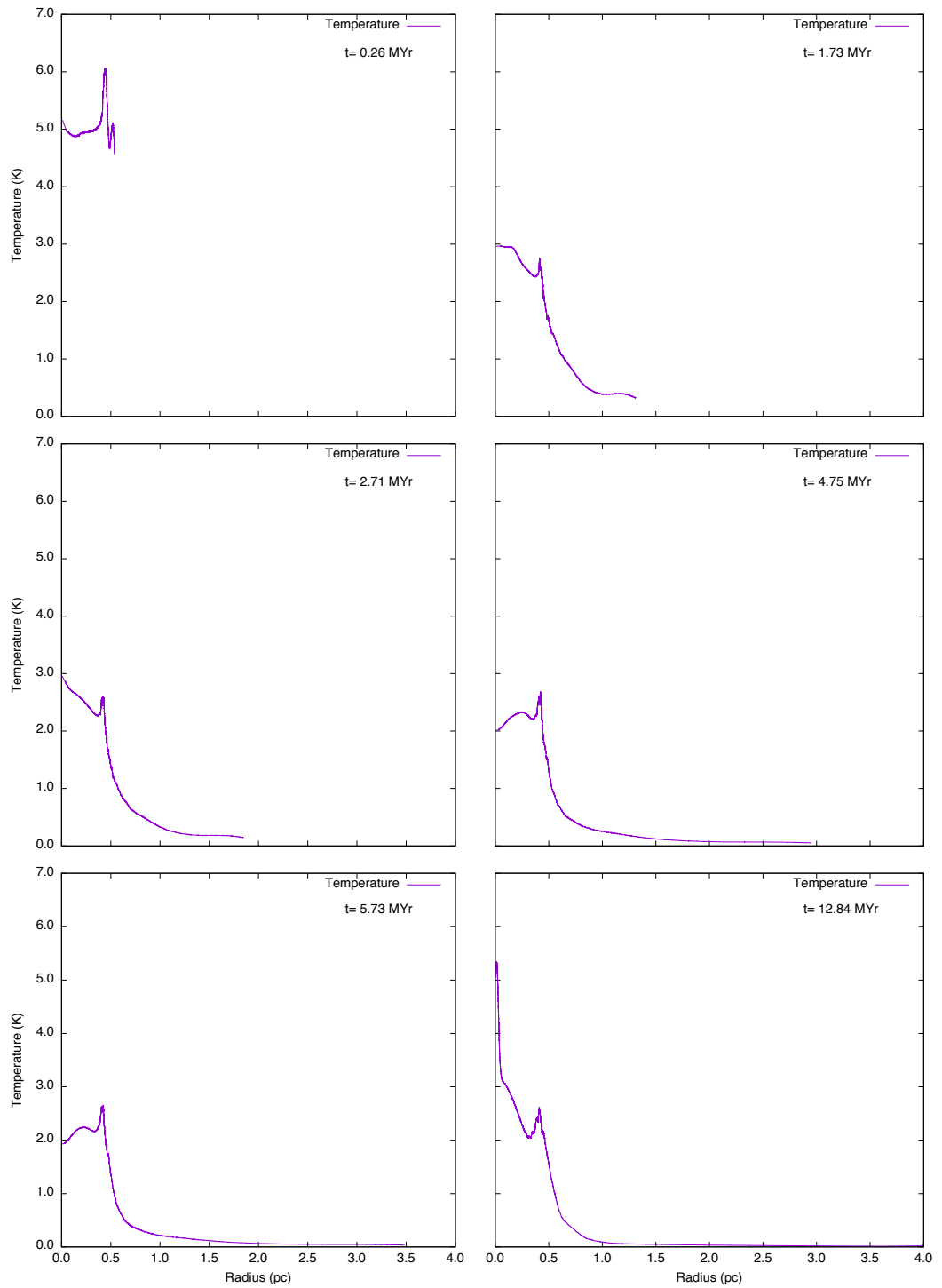
Figure A.47: Model D: six snapshots showing temperature (purple line) for a cloud with an initial density of 100 cm^3, a mass of 2 M$_\odot$ and a radius of 0.46 pc.
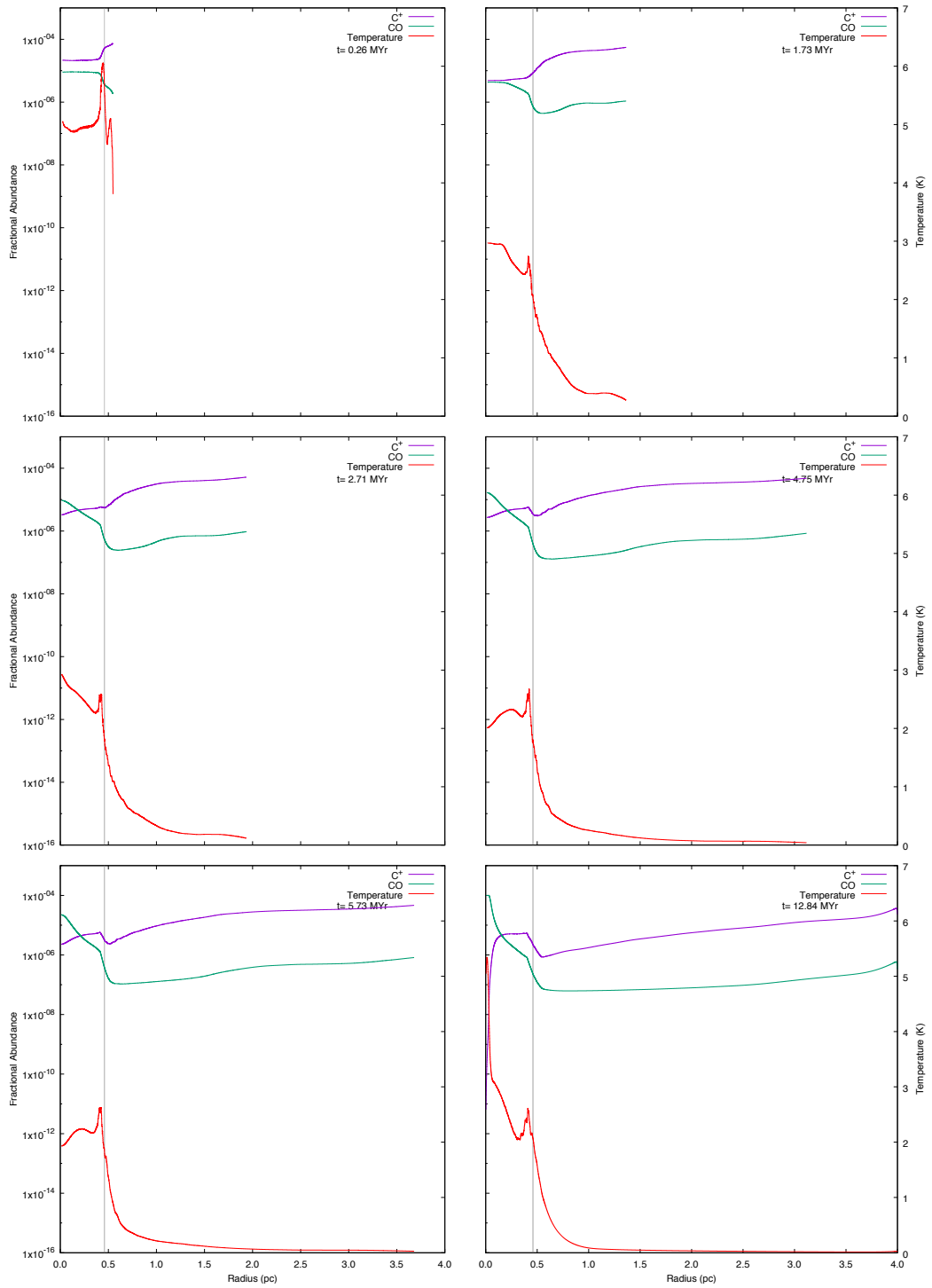
Figure A.48: Model D: six snapshots showing the chemical abundances of CO and C^+ for a cloud with an initial density of 100 cm^{-3}, a mass of 2 M$_\odot$ and a radius of 0.46 pc.

Figure A.49: Model D: the time evolution of the cloud with an initial density of 1000 cm^3, a mass of 2 M$_\odot$ and a radius of 0.21 pc is shown in this graph. The cloud radius (purple line) is taken to be the zero crossing point of radial velocity and the mass (green line) is taken to be that which lies inside the radius. The blue vertical line denotes the time at which the high density peak first forms. This is the minimum cloud mass which collapses for the selected values of density.
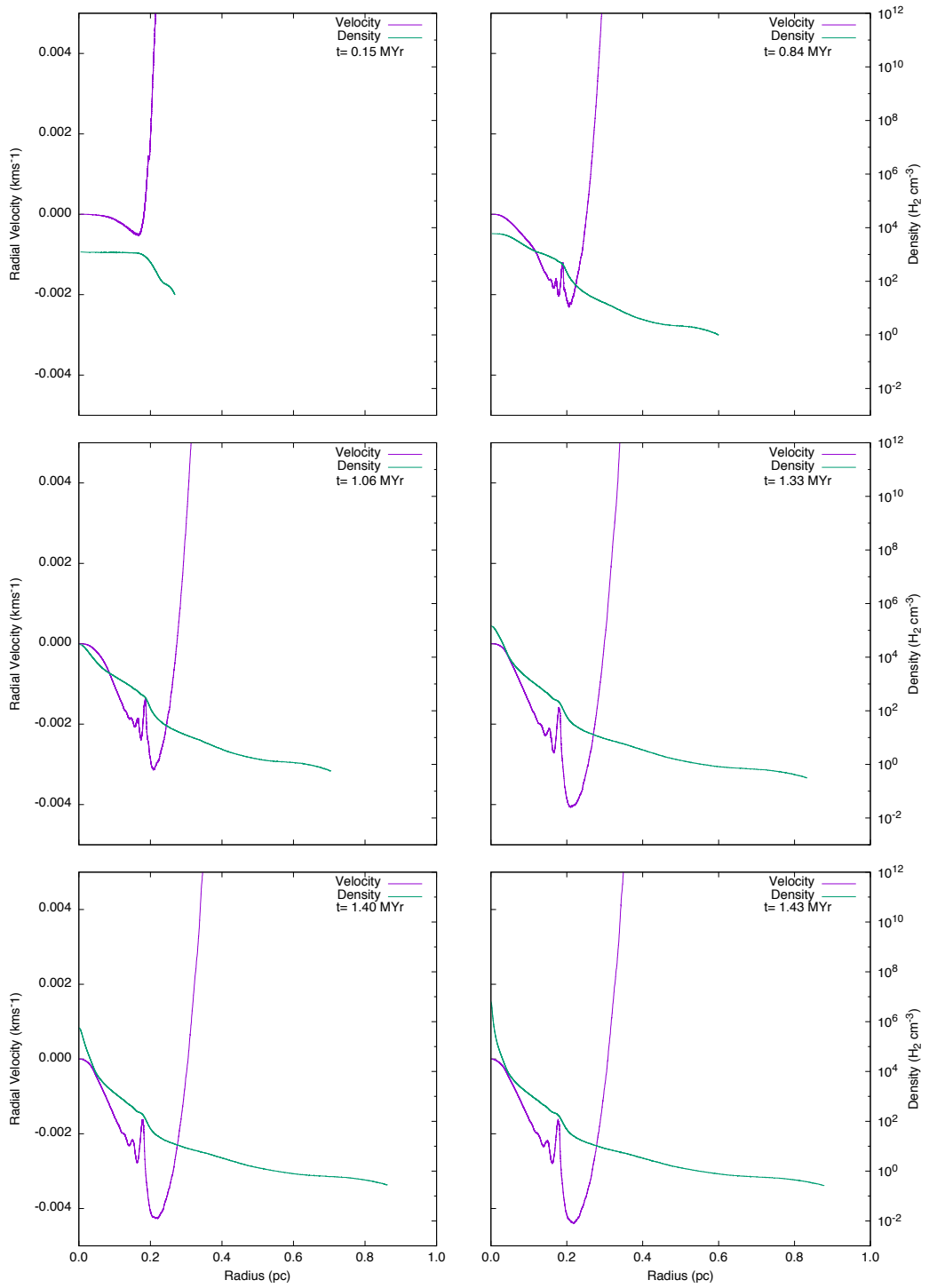
Figure A.50: Model D: six snapshots showing radial velocity (purple line) and density (green line) for a cloud with an initial density of 1000 cm^3, a mass of 2 M$_\odot$ and a radius of 0.21 pc.
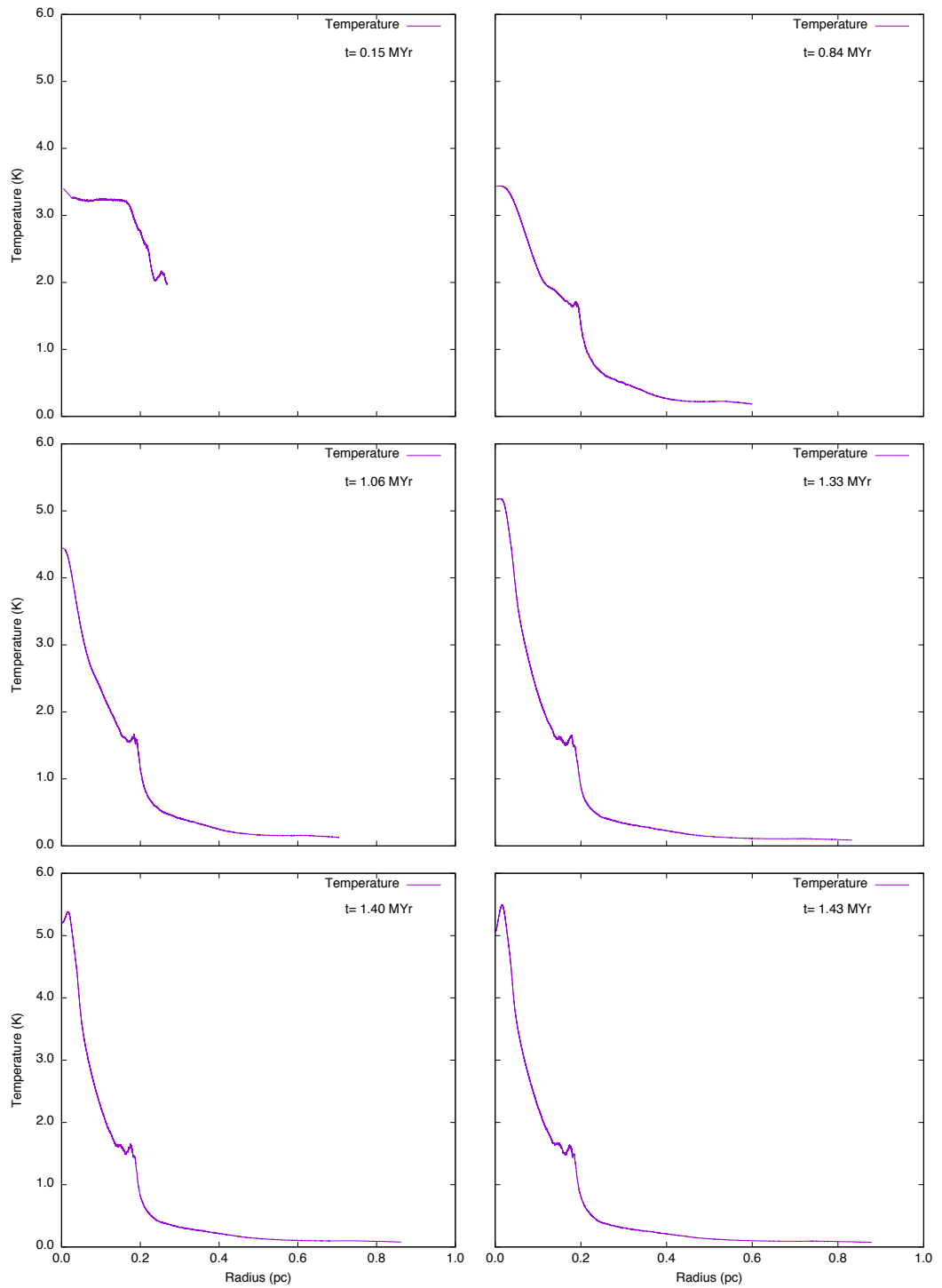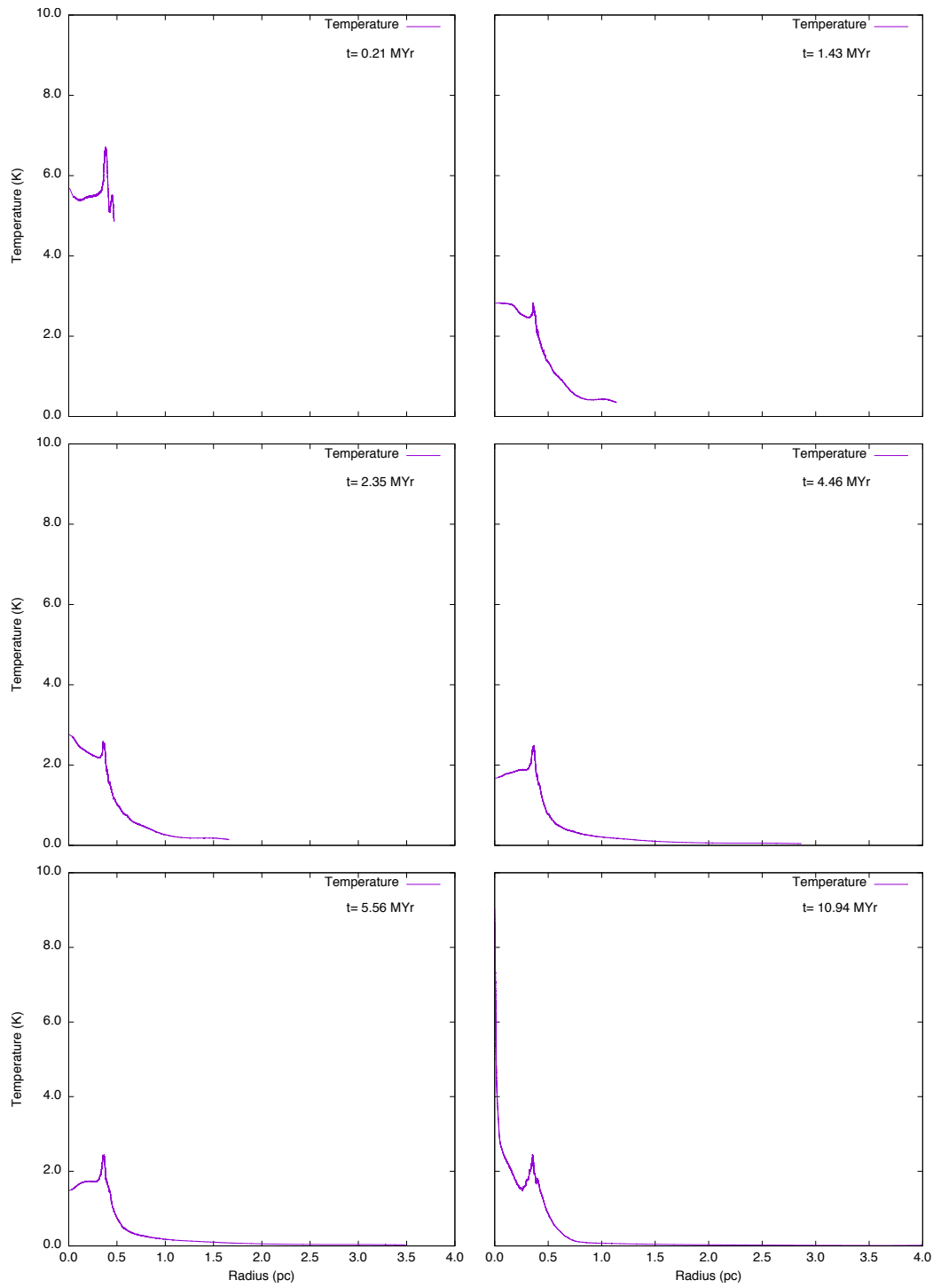
Figure A.51: Model D: six snapshots showing temperature (purple line) for a cloud with an initial density of 1000 cm^3, a mass of 2 M$_\odot$ and a radius of 0.21 pc.
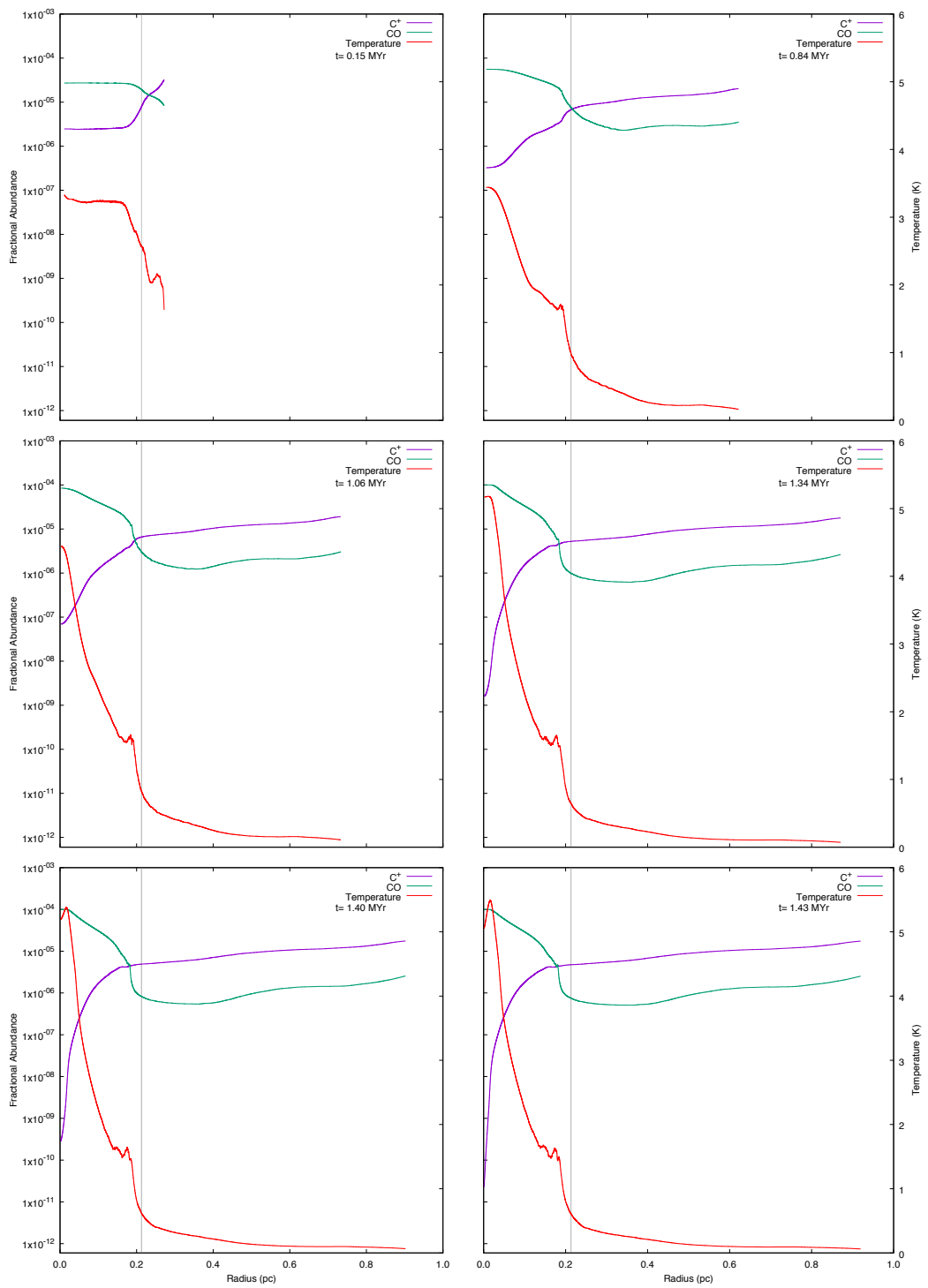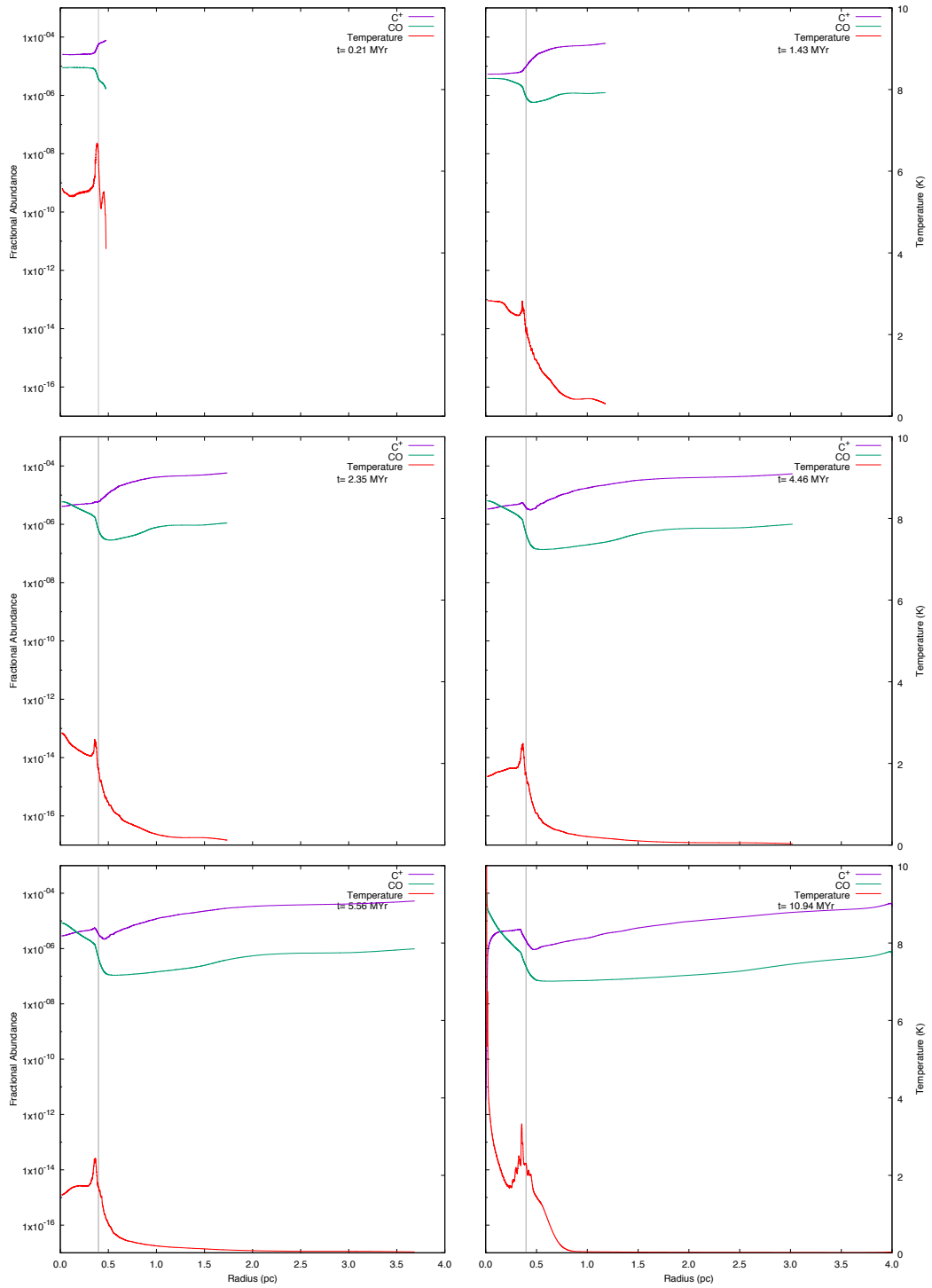
Figure A.52: Model D: six snapshots showing the chemical abundances of CO and C^+ for a cloud with an initial density of 1000 cm^{-3}, a mass of 2 M$_\odot$ and a radius of 0.21 pc.
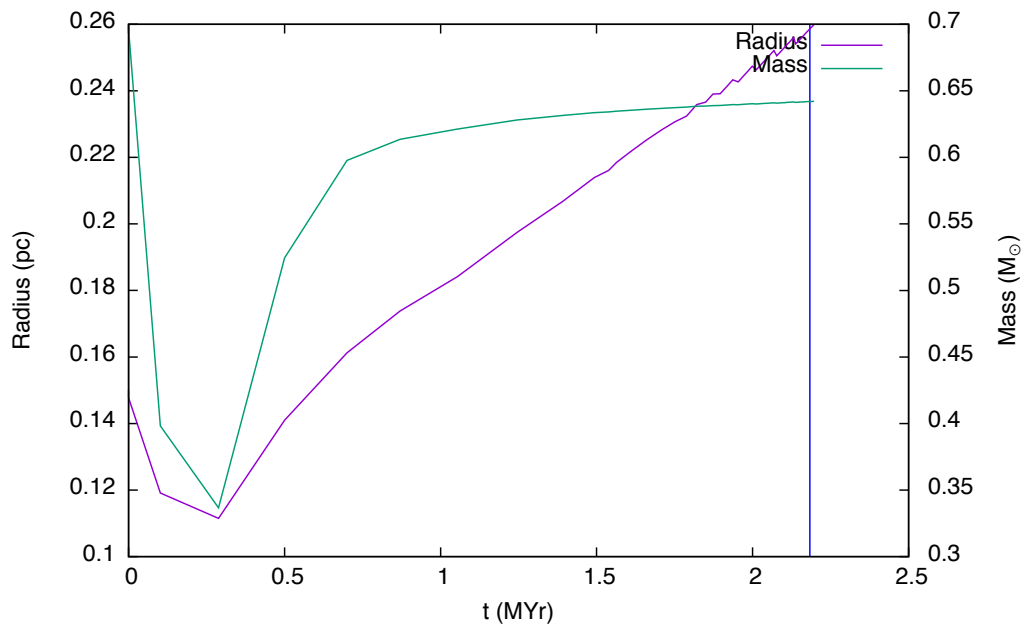
Figure A.53: Model D: the time evolution of the cloud with an initial density of 5000 cm^3, a mass of $0.8_{\odot}$ and a radius of 0.09 pc is shown in this graph. The cloud radius (purple line) is taken to be the zero crossing point of radial velocity and the mass (green line) is taken to be that which lies inside the radius. The blue vertical line denotes the time at which the high density peak first forms. This is the minimum cloud mass which collapses for the selected values of density.
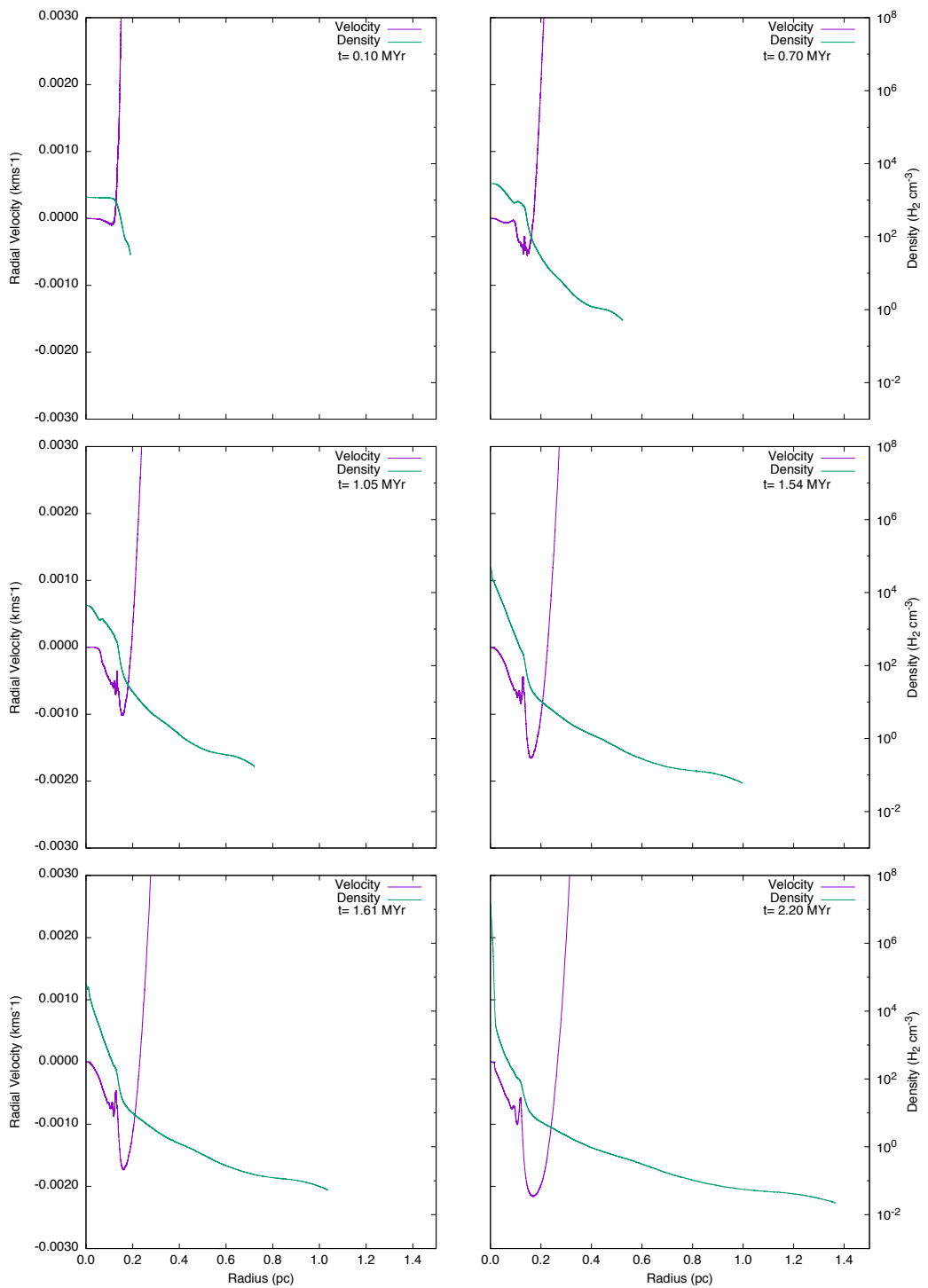
Figure A.54: Model D: six snapshots showing radial velocity (purple line) and density (green line) for a cloud with an initial density of 5000 cm^3, a mass of 0.8$_\odot$ and a radius of 0.09 pc.
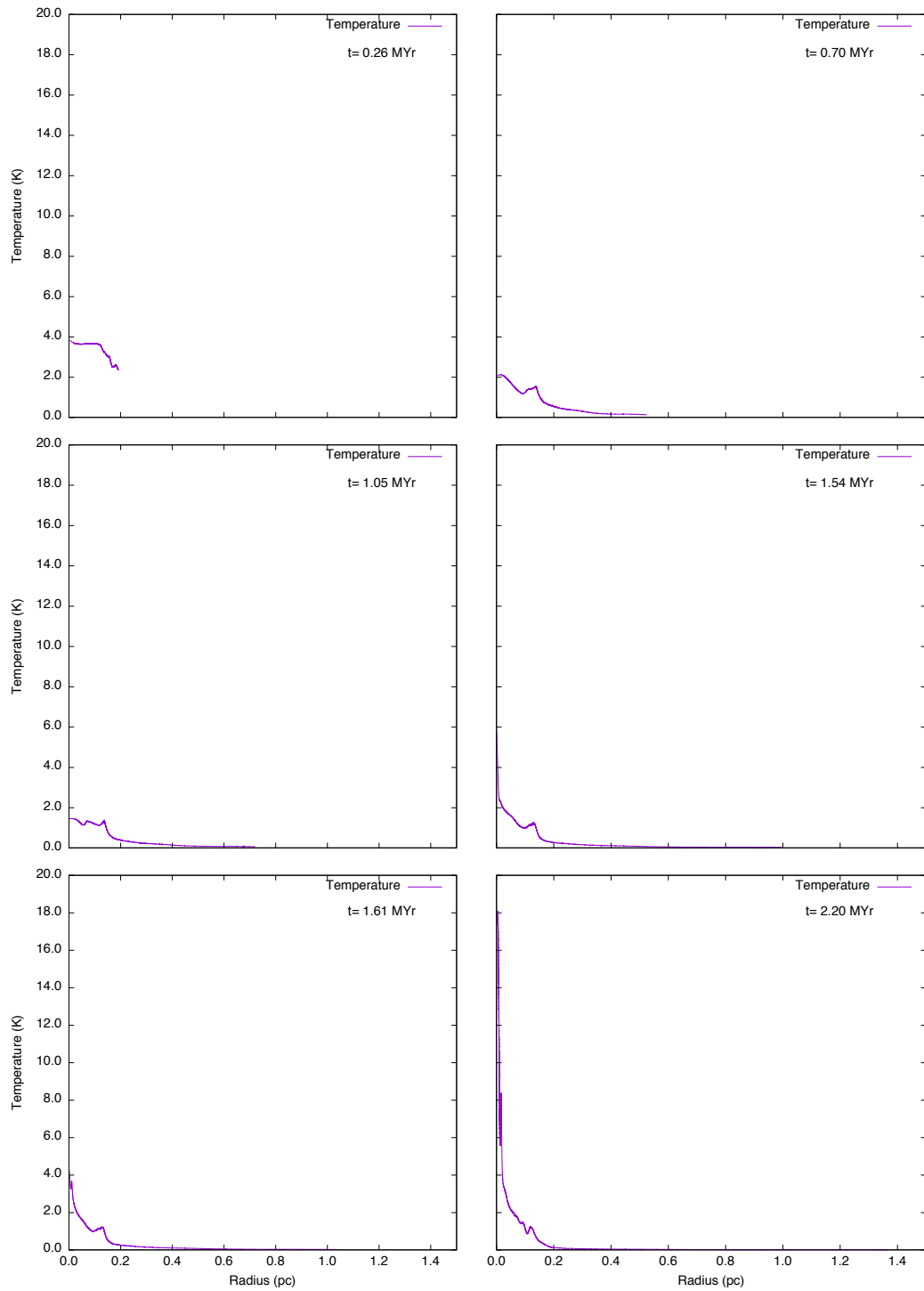
Figure A.55: Model D: six snapshots showing temperature (purple line) for a cloud with an initial density of 5000 cm^3, a mass of 0.8$_\odot$ and a radius of 0.09 pc.
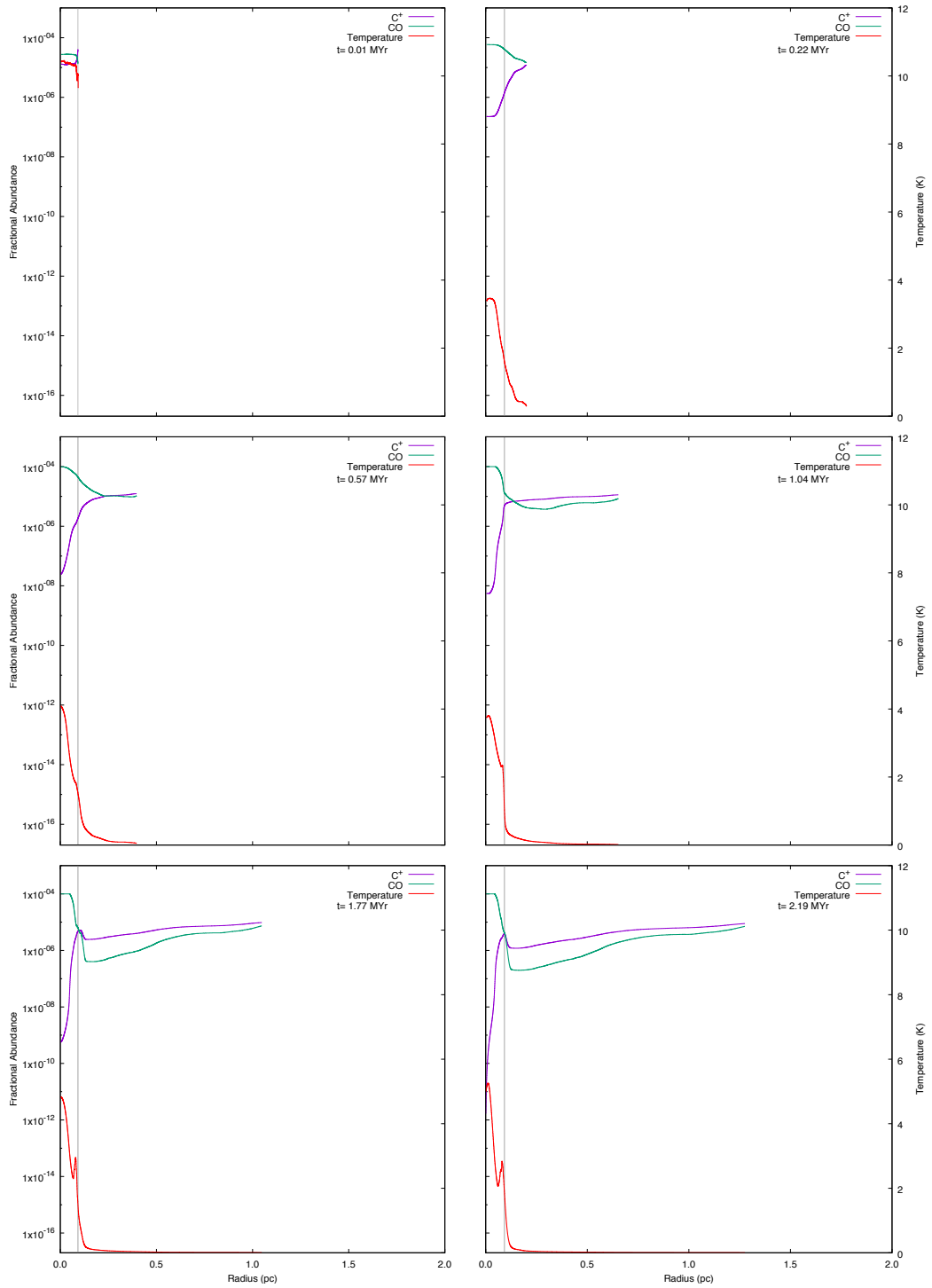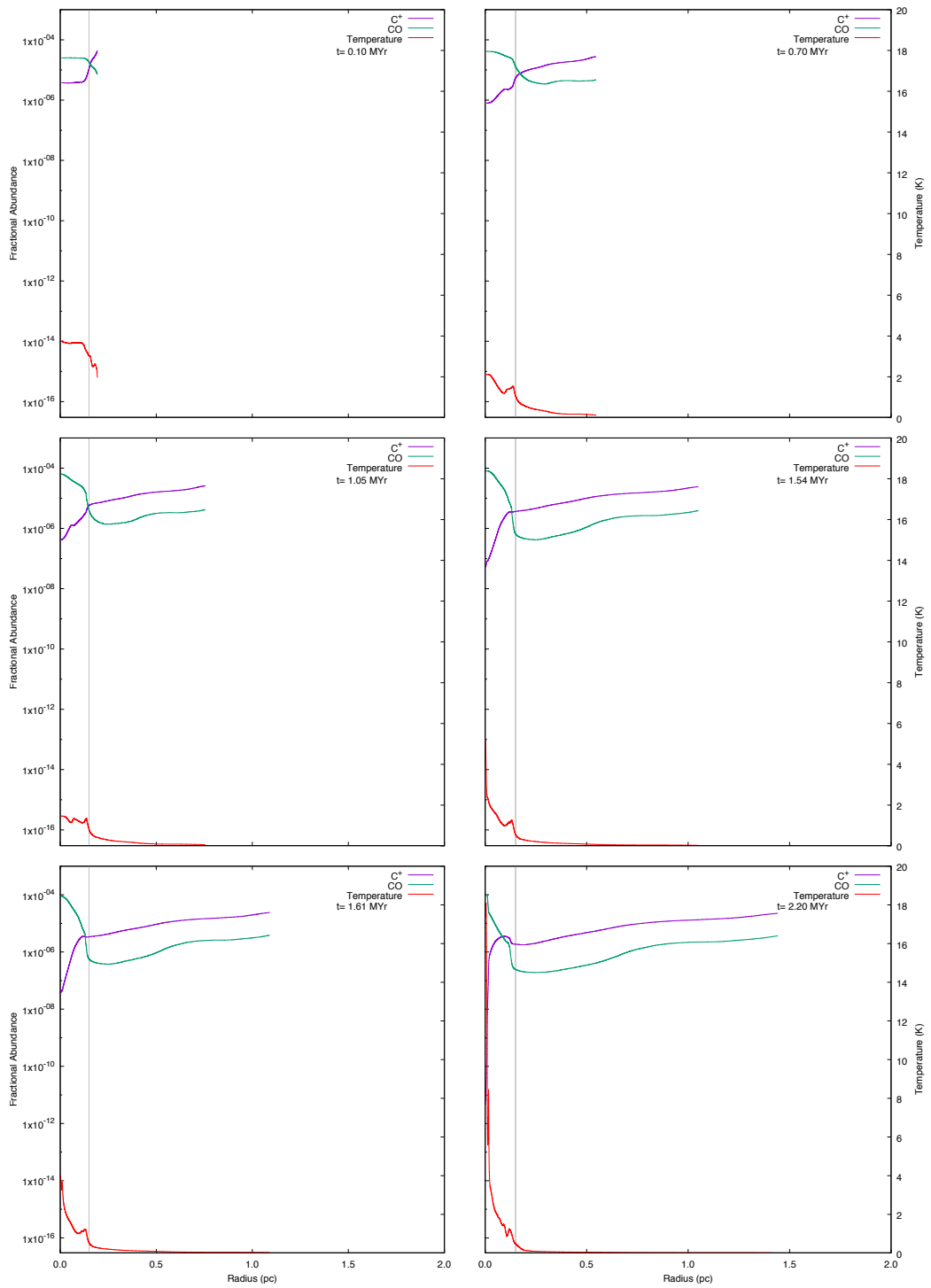
Figure A.56: Model D: six snapshots showing the chemical abundances of CO and C^+ for a cloud with an initial density of 5000 cm^{-3}, a mass of 0.8 M$_\odot$ and a radius of 0.09 pc.
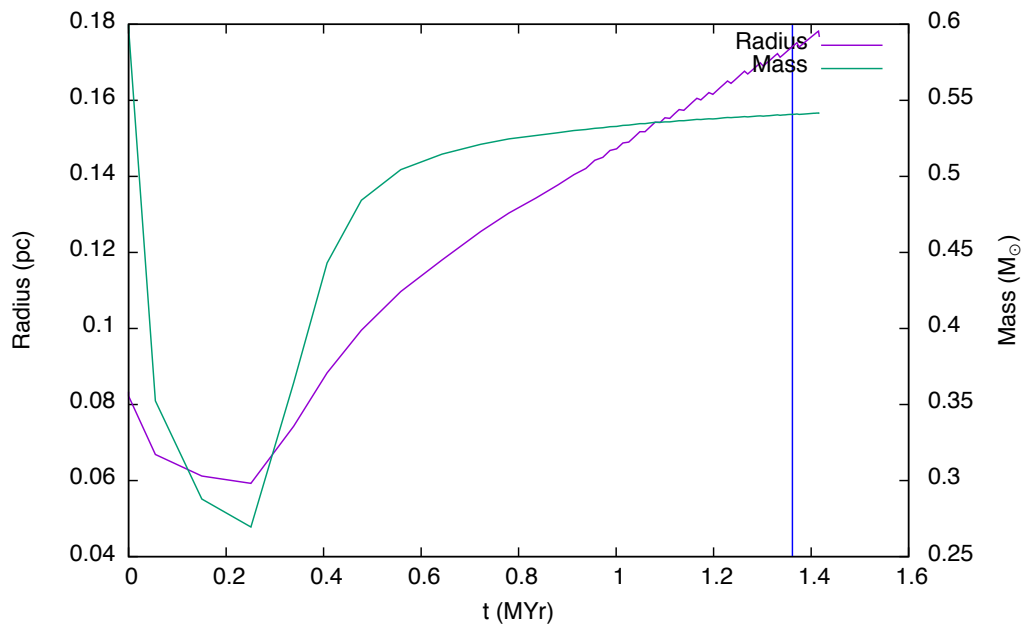
A.5 MODEL E
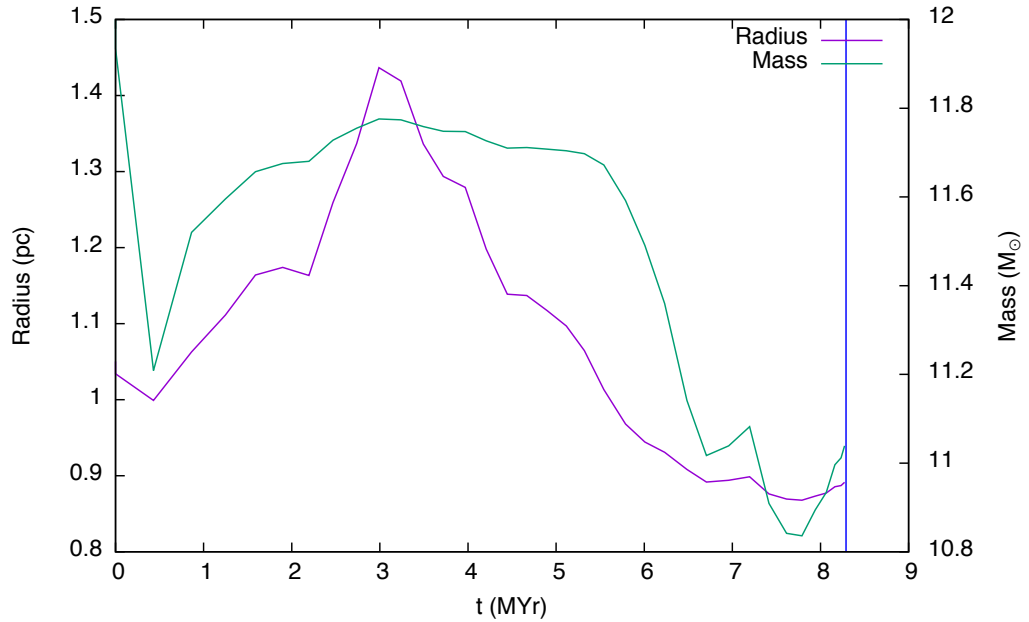
Figure A.57: Model E: the time evolution of a cloud with an initial density of 50 cm^3, a mass of 12 M$_\odot$ and a radius of 1.05 pc is shown in this graph. The cloud radius (purple line) is taken to be the zero crossing point of radial velocity and the mass (green line) is taken to be that which lies inside the radius. The blue vertical line denotes the time at which the high density peak first forms. This is the minimum cloud mass which collapses for the selected values of density.
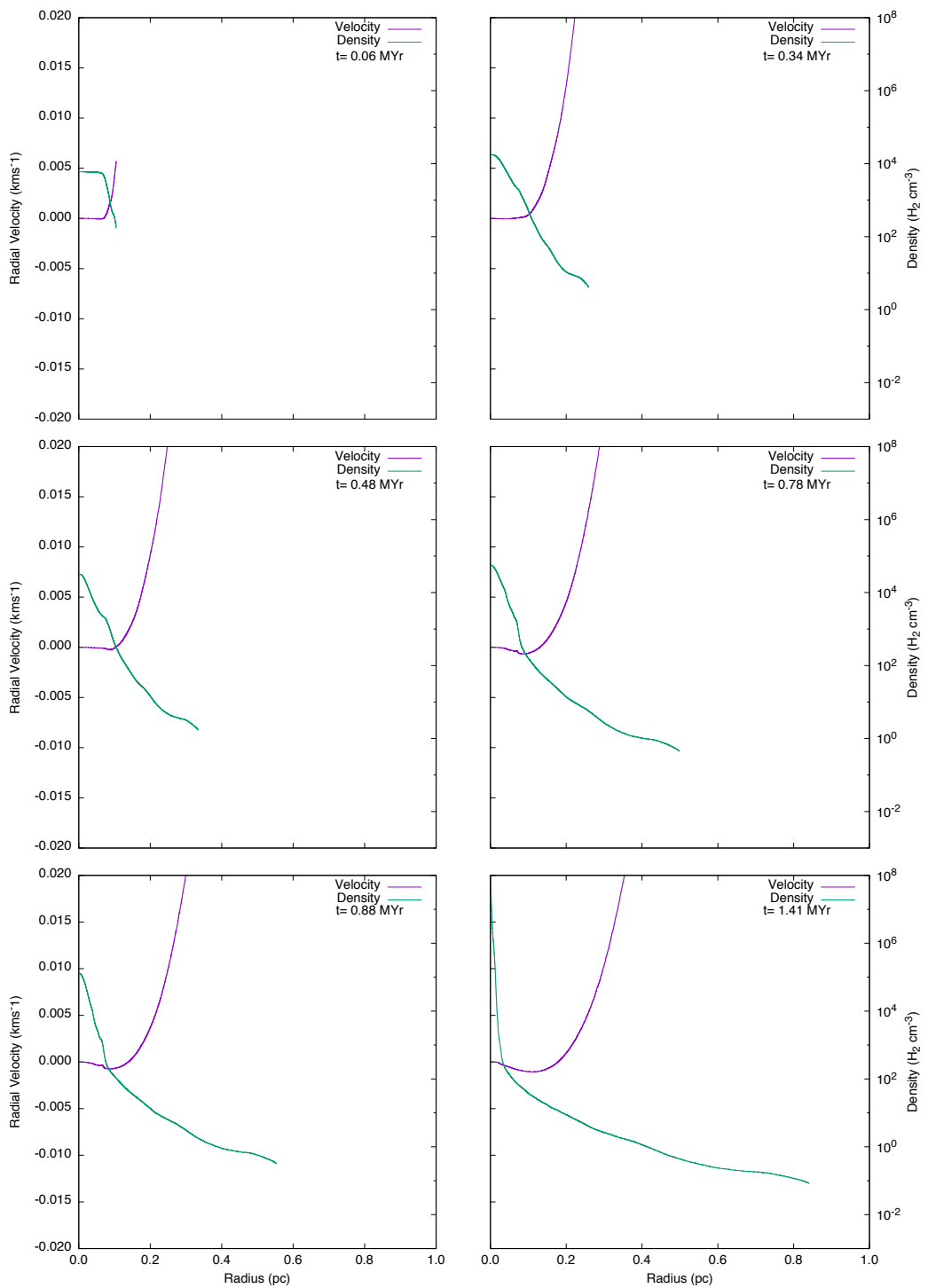
Figure A.58: Model E: six snapshots showing radial velocity (purple line) and density (green line) for a cloud with an initial density of 50 cm³, a mass of 12 M$_\odot$ and a radius of 1.05 pc.
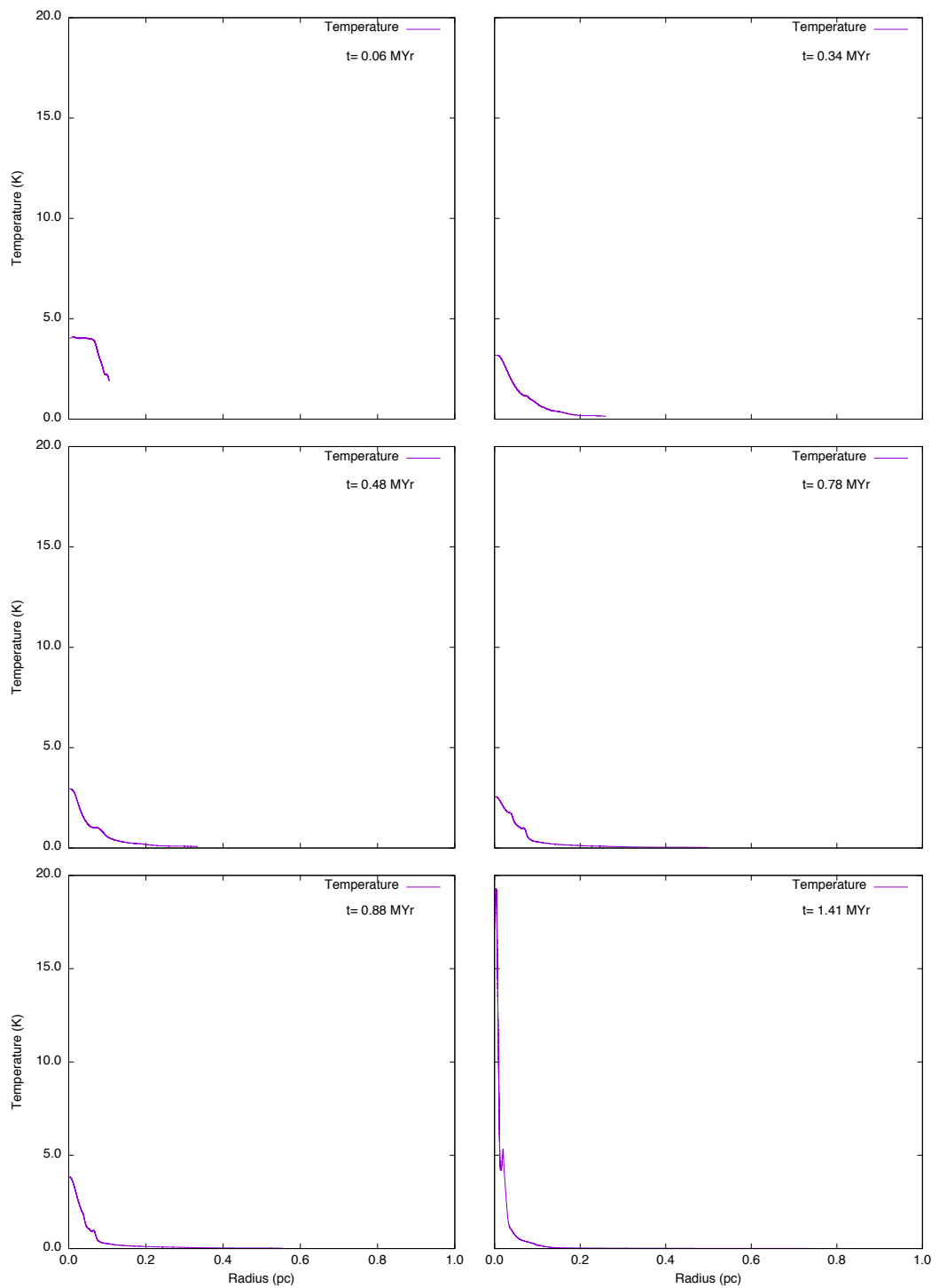
Figure A.59: Model E: six snapshots showing temperature (purple line) for a cloud with an initial density of 50 cm^3, a mass of 12 M$_\odot$ and a radius of 1.05 pc. This is one of the simulations included in set A.
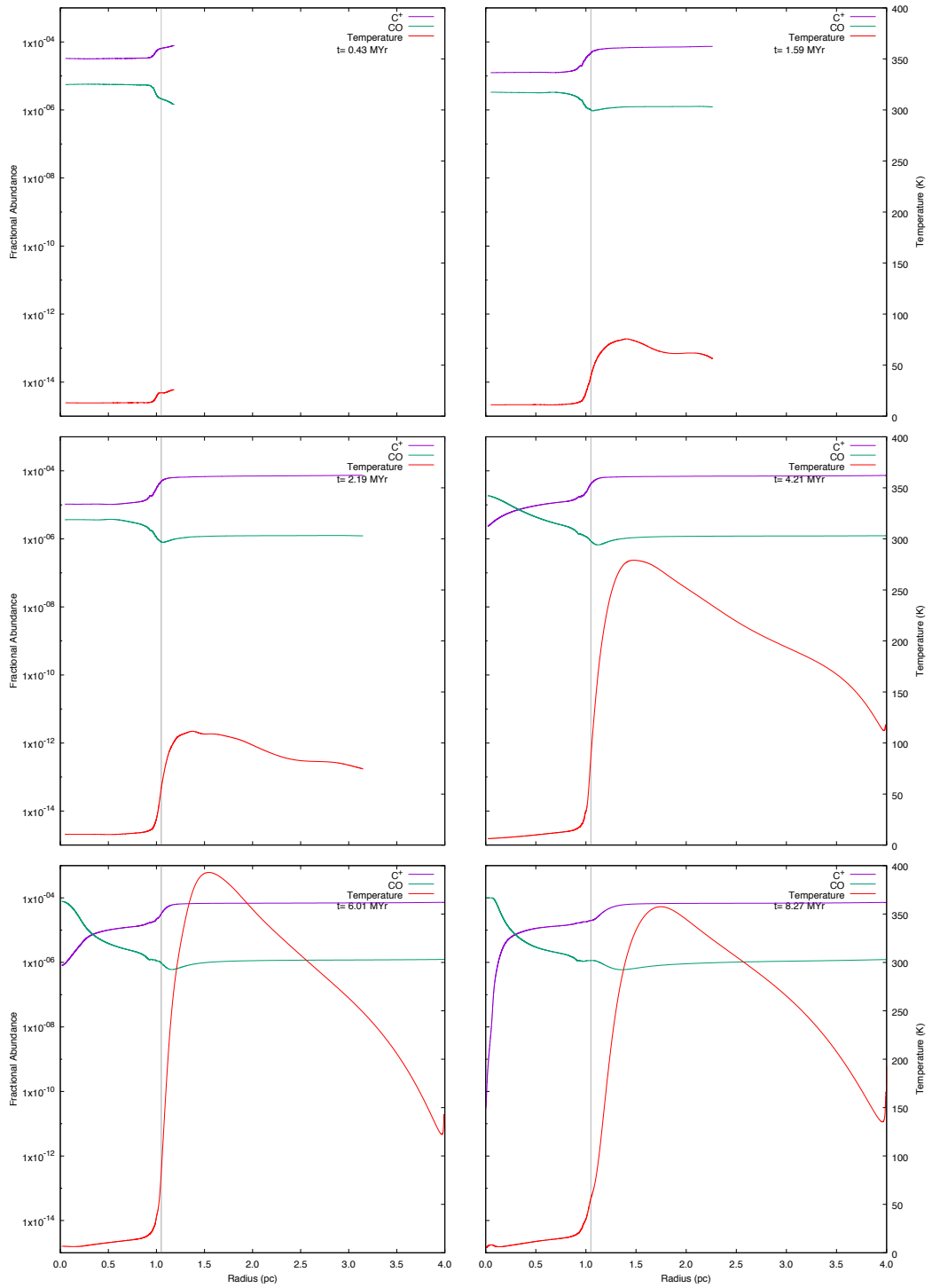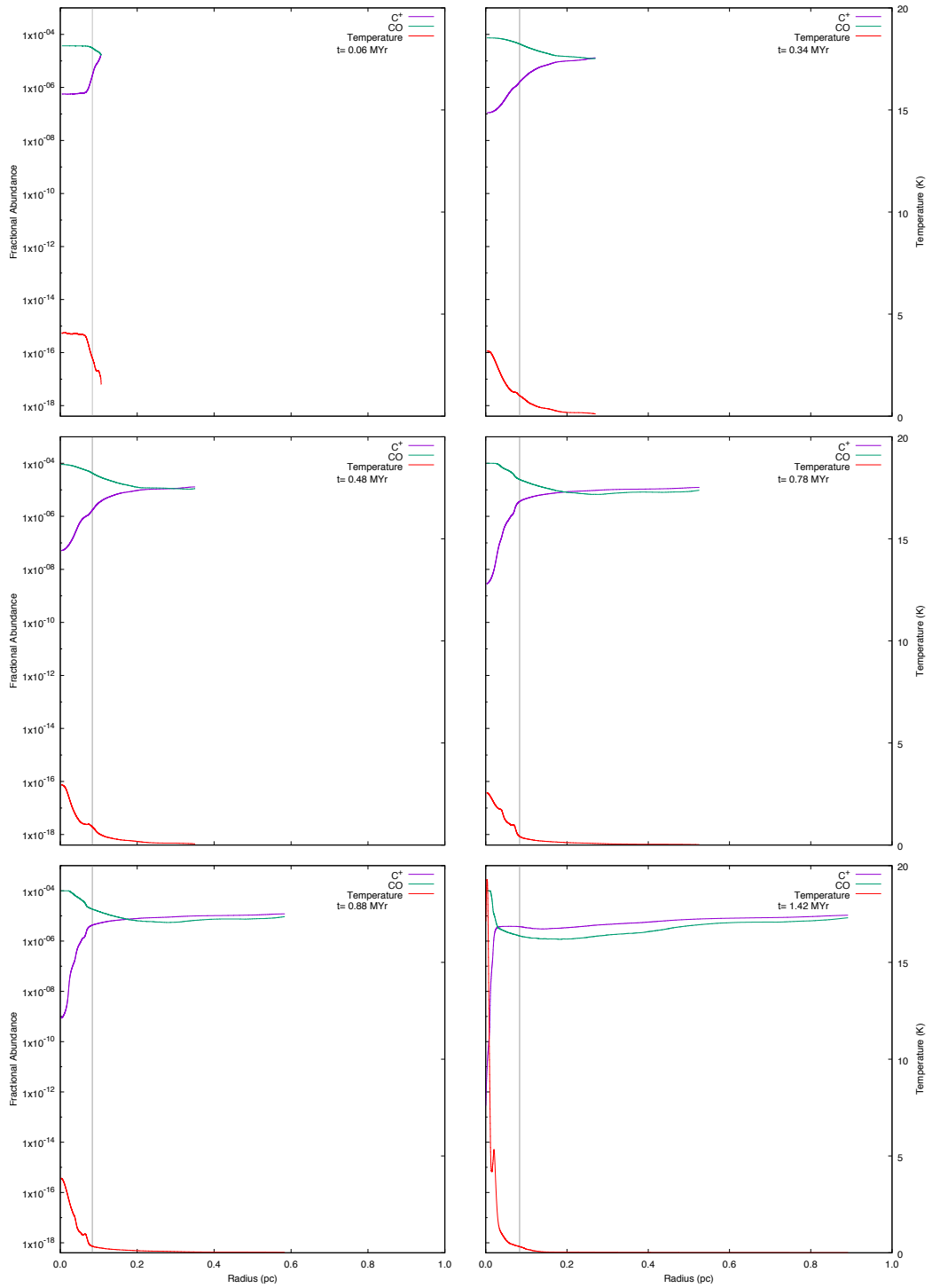
Figure A.60: Model E: six snapshots showing the chemical abundances of CO and C^+ for a cloud with an initial density of 50 cm^{-3}, a mass of 12 M$_\odot$ and a radius of 1.05 pc.

Figure A.61: Model E: the time evolution of a cloud with an initial density of 100 cm^3, a mass of 8 M$_\odot$ and a radius of 0.73 pc is shown in this graph. The cloud radius (purple line) is taken to be the zero crossing point of radial velocity and the mass (green line) is taken to be that which lies inside the radius. The blue vertical line denotes the time at which the high density peak first forms. This is the minimum cloud mass which collapses for the selected values of density.
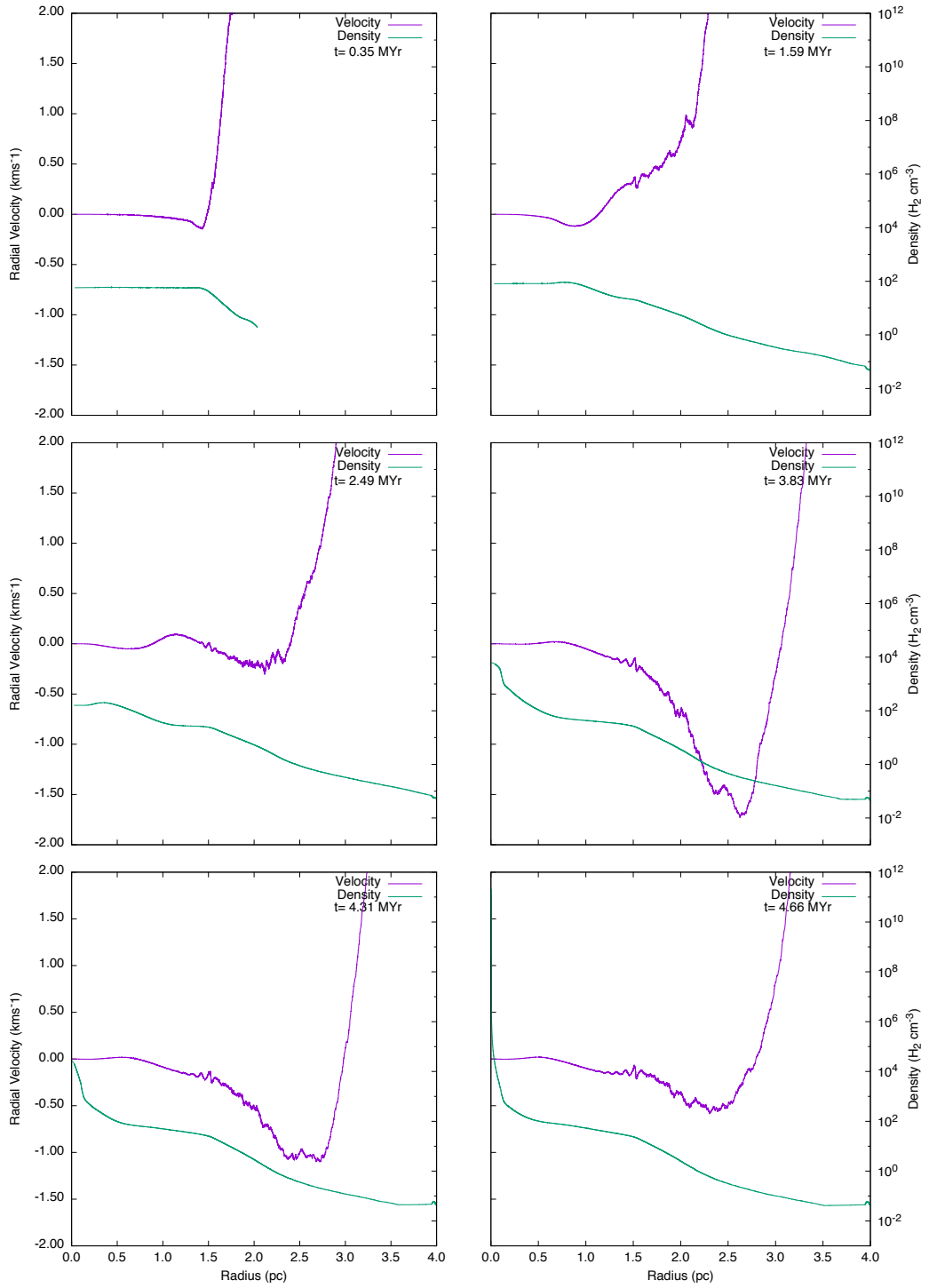
Figure A.62: Model E: six snapshots showing radial velocity (purple line) and density (green line) for a cloud with an initial density of 100 cm³, a mass of 8 M⊙ and a radius of 0.73 pc.

Figure A.63: Model E: six snapshots showing temperature (purple line) for a cloud with an initial density of 100 cm^3, a mass of 8 M$_\odot$ and a radius of 0.73 pc.

Figure A.64: Model E: six snapshots showing the chemical abundances of CO and C^+ for a cloud with an initial density of 100 cm^{-3}, a mass of 8 M$_\odot$ and a radius of 0.73 pc.

Figure A.65: Model E: the time evolution of a cloud with an initial density of 200 cm^3, a mass of 6 M$_\odot$ and a radius of 0.53 pc is shown in this graph. The cloud radius (purple line) is taken to be the zero crossing point of radial velocity and the mass (green line) is taken to be that which lies inside the radius. The blue vertical line denotes the time at which the high density peak first forms. This is the minimum cloud mass which collapses for the selected values of density.

Figure A.66: Model E: six snapshots showing radial velocity (purple line) and density (green line) for a cloud with an initial density of 200 cm³, a mass of 6 M$_\odot$ and a radius of 0.53 pc.
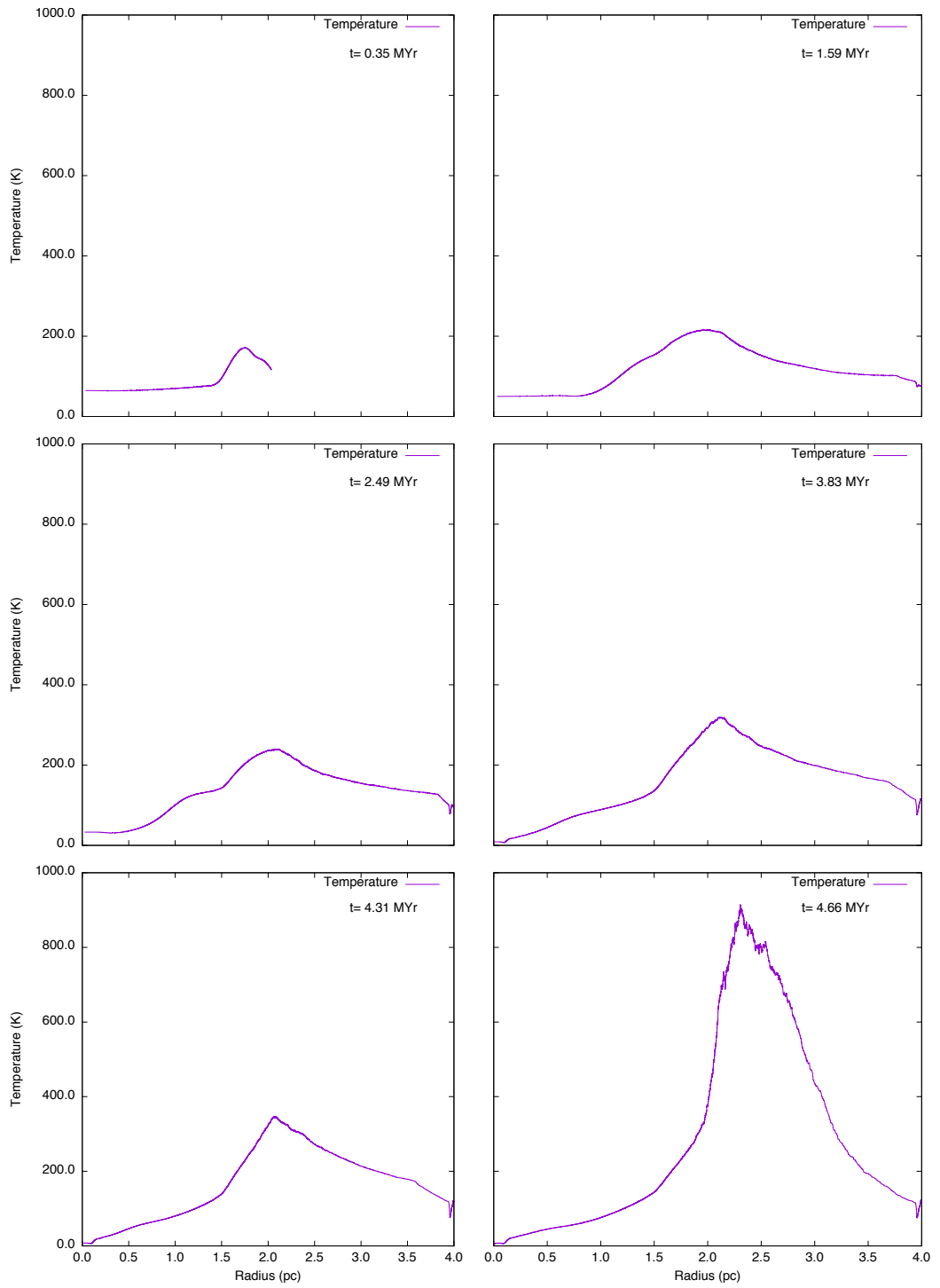
Figure A.67: Model E: six snapshots showing temperature (purple line) for a cloud with an initial density of 200 cm^3, a mass of 6 M$_\odot$ and a radius of 0.73 pc.
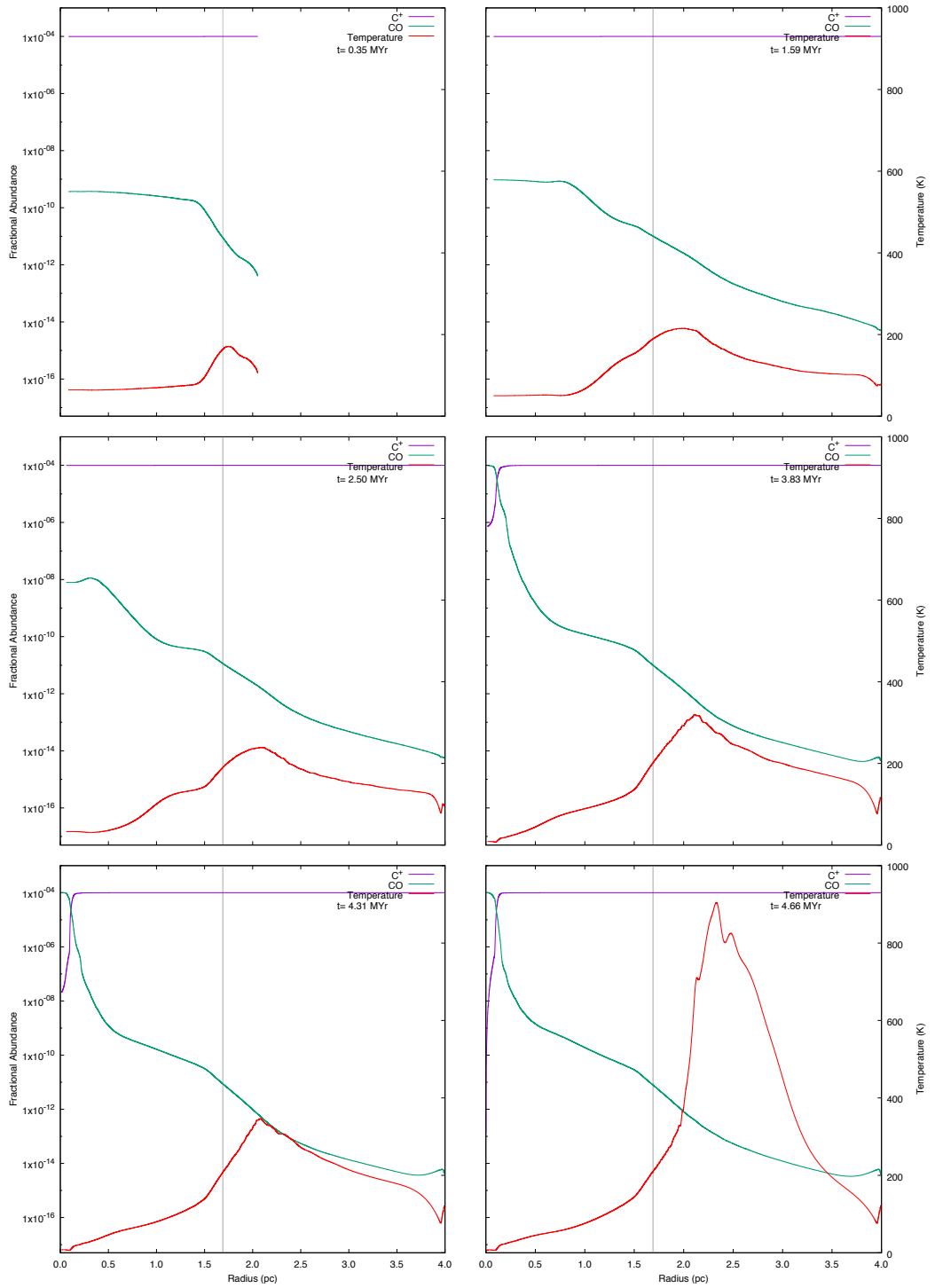
Figure A.68: Model E: six snapshots showing the chemical abundances of CO and C^+ for a cloud with an initial density of 200 cm^{-3}, a mass of 6 M$_\odot$ and a radius of 0.53 pc.
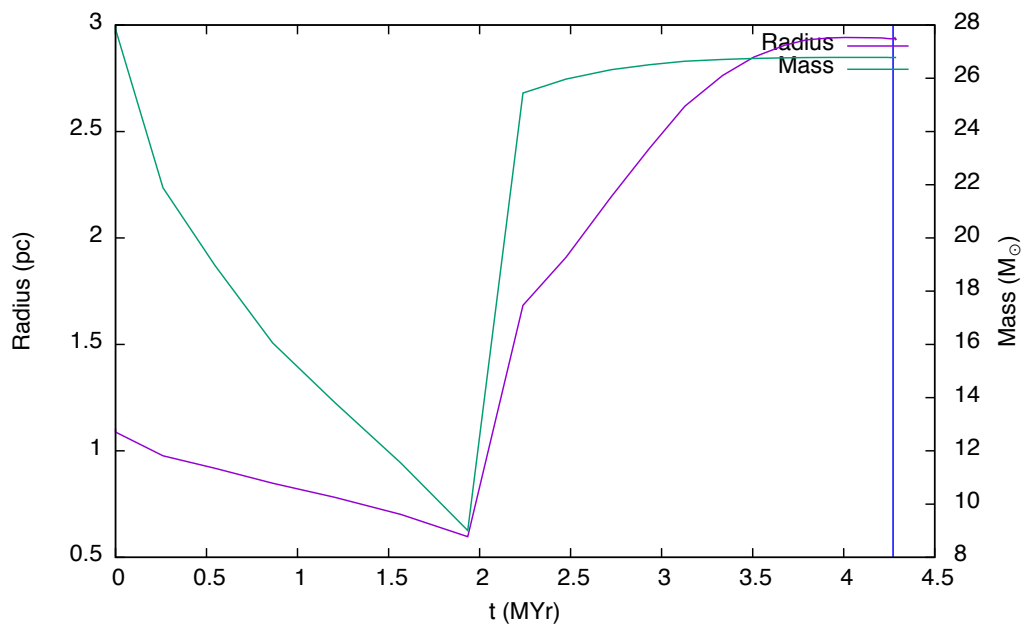
Figure A.69: Model E: the time evolution of a cloud with an initial density of 1000 cm^3, a mass of 4 M$_\odot$ and a radius of 0.27 pc is shown in this graph. The cloud radius (purple line) is taken to be the zero crossing point of radial velocity and the mass (green line) is taken to be that which lies inside the radius. The blue vertical line denotes the time at which the high density peak first forms. This is the minimum cloud mass which collapses for the selected values of density.
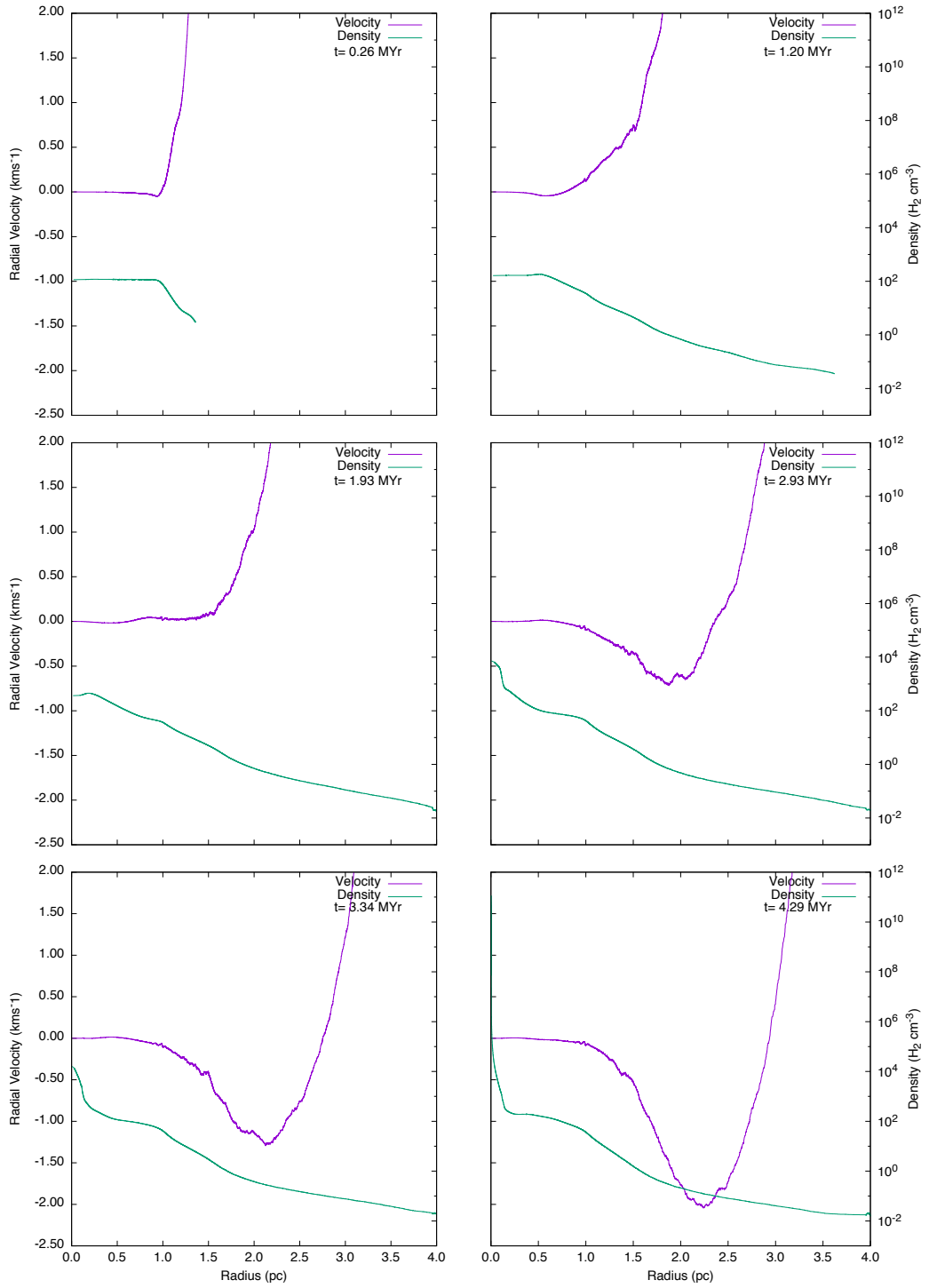
Figure A.70: Model E: six snapshots showing radial velocity (purple line) and density (green line) for a cloud with an initial density of 1000 cm^3, a mass of 4 M$_\odot$ and a radius of 0.27 pc.
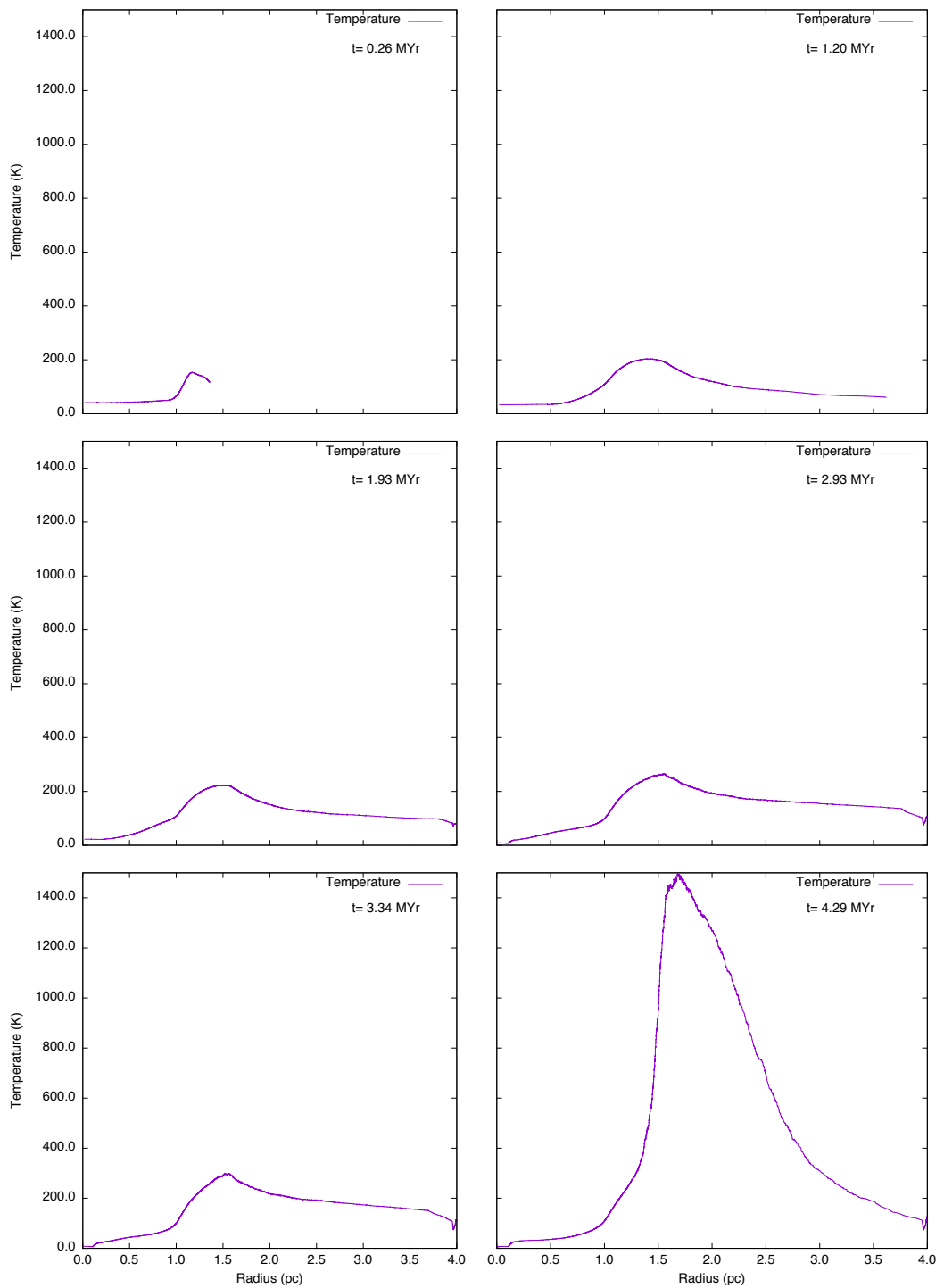
Figure A.71: Model E: six snapshots showing temperature (purple line) for a cloud with an initial density of 1000 cm^3, a mass of 4 M$_\odot$ and a radius of 0.27 pc.
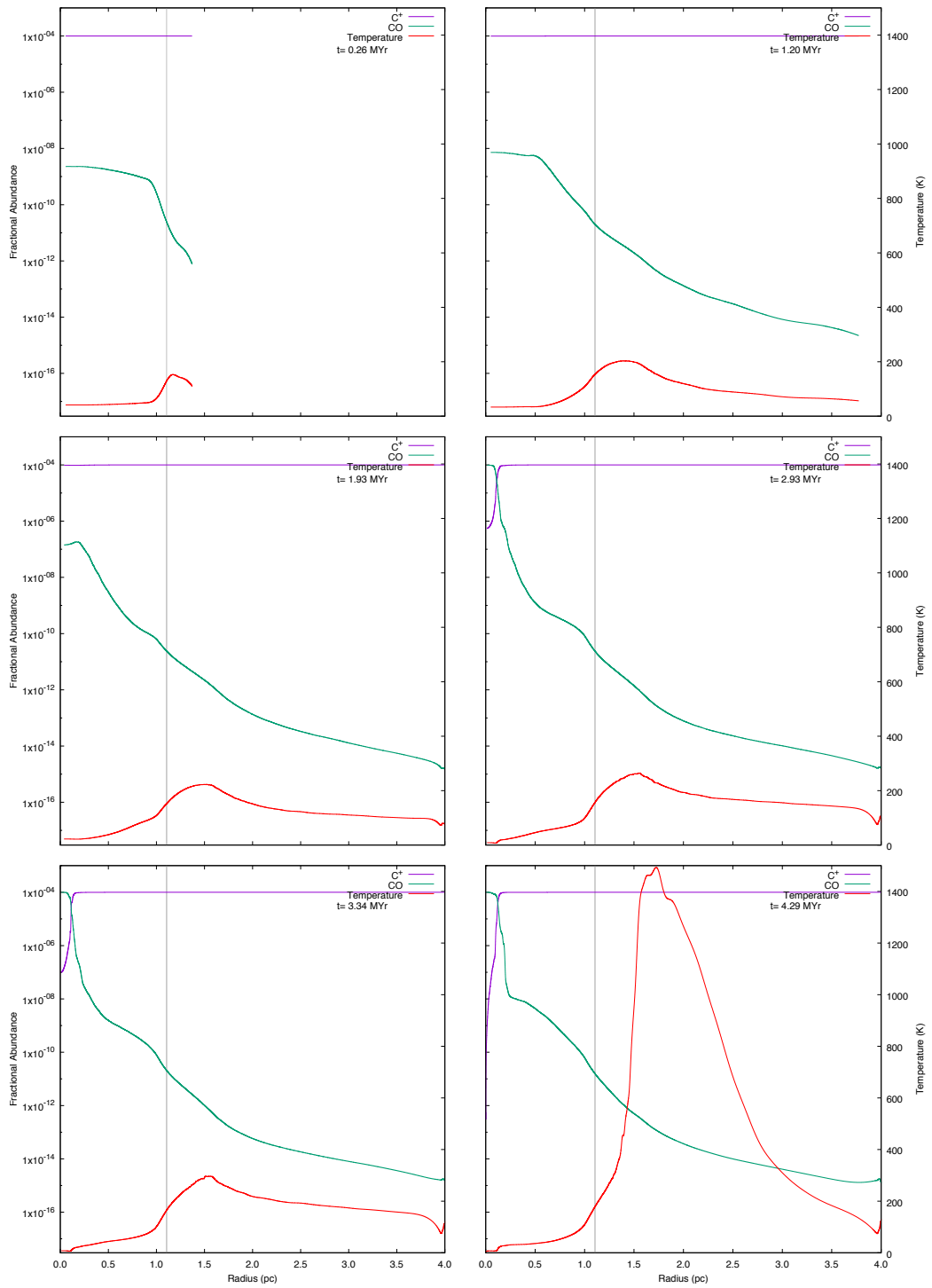
Figure A.72: Model E: six snapshots showing the chemical abundances of CO and C^+ for a cloud with an initial density of 1000 cm^{-3}, a mass of 4 M$_\odot$ and a radius of 0.27 pc.
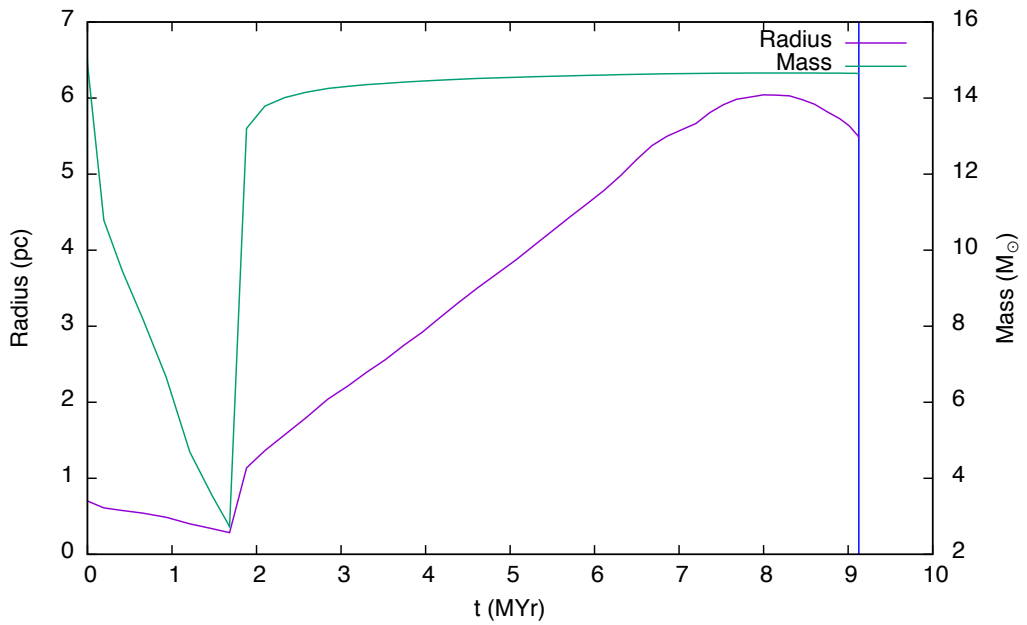
Figure A.73: Model E: the time evolution of a cloud with an initial density of 2000 cm^3, a mass of 3 M$_\odot$ and a radius of 0.19 pc is shown in this graph. The cloud radius (purple line) is taken to be the zero crossing point of radial velocity and the mass (green line) is taken to be that which lies inside the radius. The blue vertical line denotes the time at which the high density peak first forms. This is the minimum cloud mass which collapses for the selected values of density.
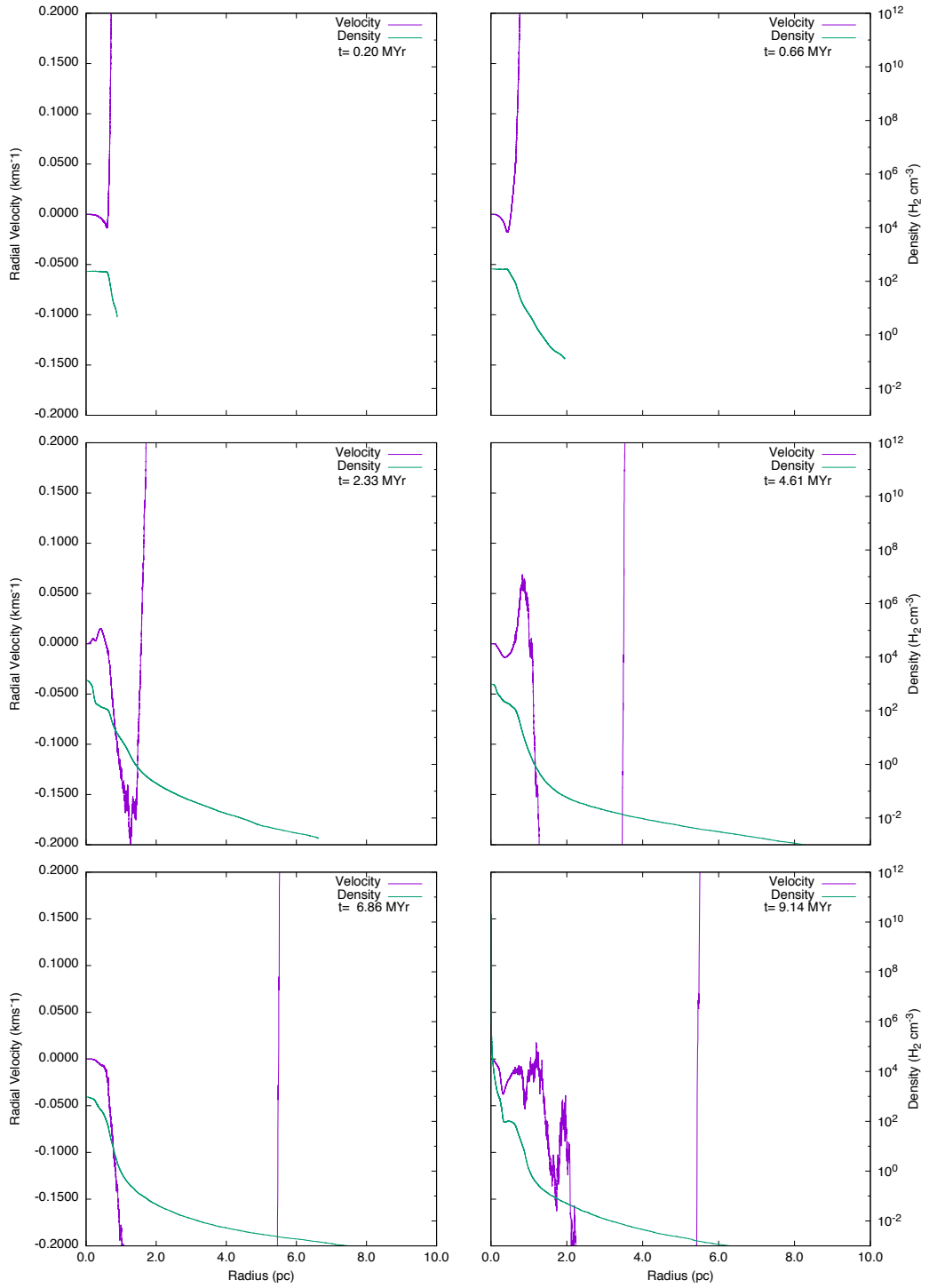
Figure A.74: Model E: six snapshots showing radial velocity (purple line) and density (green line) for a cloud with an initial density of 2000 cm³, a mass of 3 M⊙ and a radius of 0.19 pc.

Figure A.75: Model E: six snapshots showing temperature (purple line) for a cloud with an initial density of 2000 cm^3, a mass of 3 M$_\odot$ and a radius of 0.19 pc.

Figure A.76: Model E: six snapshots showing the chemical abundances of CO and C^+ for a cloud with an initial density of 2000 cm^{-3}, a mass of 3 M$_\odot$ and a radius of 0.19 pc.

Figure A.77: Model E: the time evolution of a cloud with an initial density of 5000 cm^3, a mass of 3 M$_\odot$ and a radius of 0.14 pc is shown in this graph. The cloud radius (purple line) is taken to be the zero crossing point of radial velocity and the mass (green line) is taken to be that which lies inside the radius. The blue vertical line denotes the time at which the high density peak first forms. This is the minimum cloud mass which collapses for the selected values of density.

Figure A.78: Model E: six snapshots showing radial velocity (purple line) and density (green line) for a cloud with an initial density of 5000 cm^3, a mass of 3 M$_\odot$ and a radius of 0.14 pc.
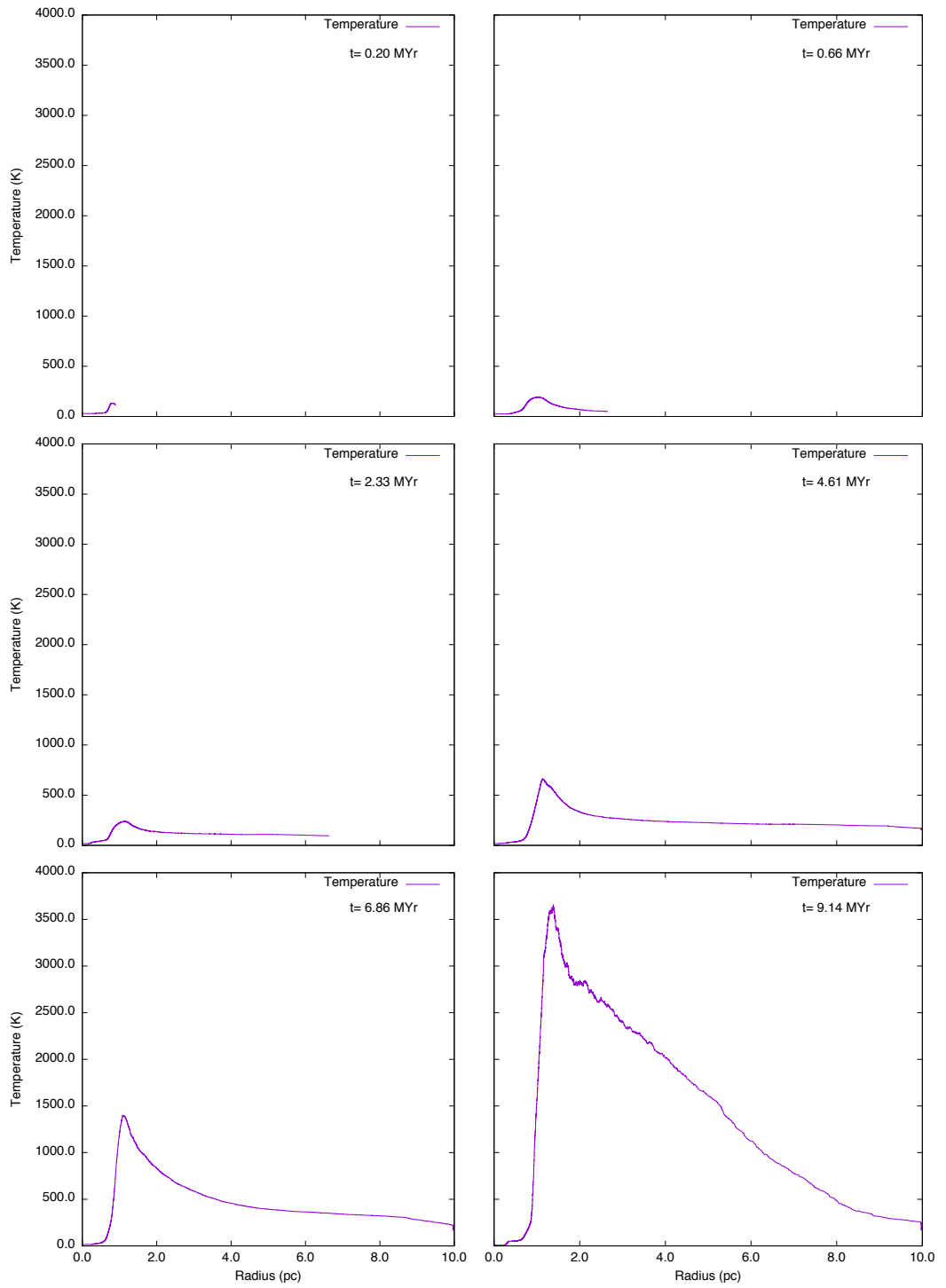
Figure A.79: Model E: six snapshots showing temperature (purple line) for a cloud with an initial density of 5000 cm^3, a mass of 3 M$_\odot$ and a radius of 0.14 pc.
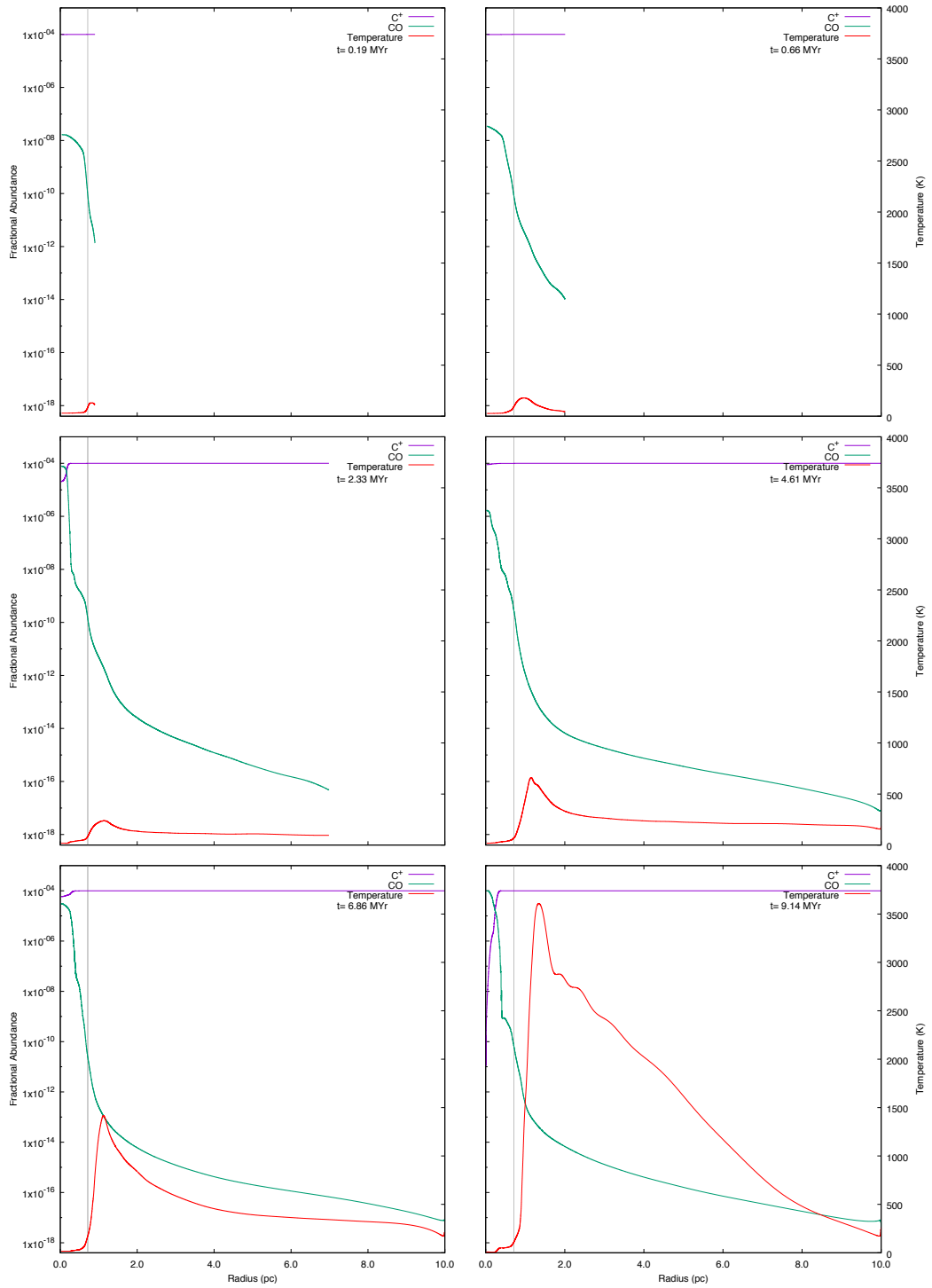
Figure A.80: Model E: six snapshots showing the chemical abundances of CO and C$^+$ for a cloud with an initial density of 5000 cm^{-3}, a mass of 3 M$_\odot$ and a radius of 0.14 pc.
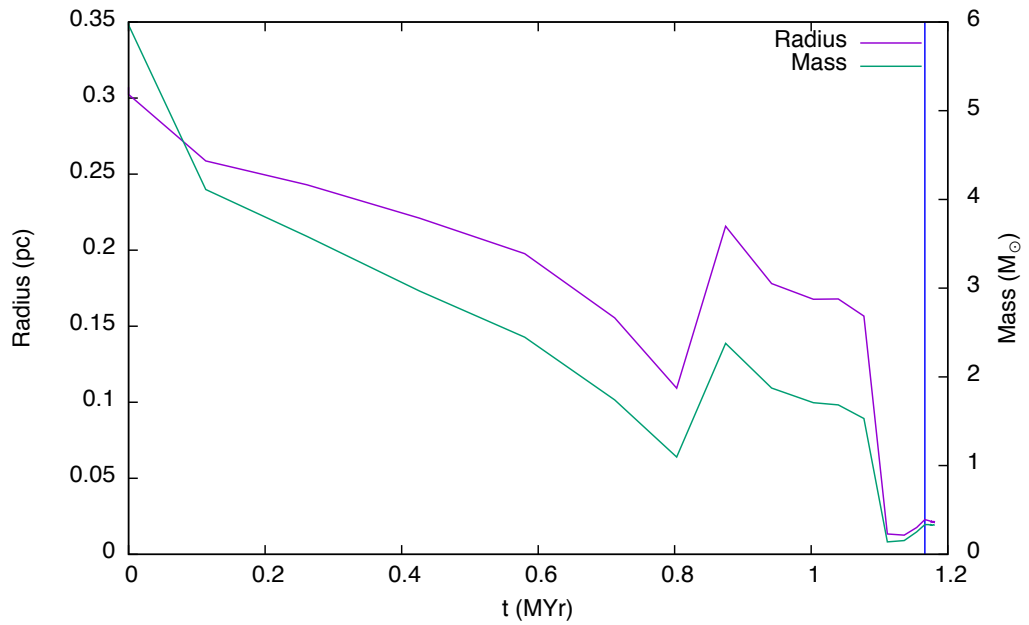
Figure A.81: Model E: the time evolution of a cloud with an initial density of 10000 cm^3, a mass of 2 $M_{\odot}$ and a radius of 0.10 pc is shown in this graph. The cloud radius (purple line) is taken to be the zero crossing point of radial velocity and the mass (green line) is taken to be that which lies inside the radius. The blue vertical line denotes the time at which the high density peak first forms. This is the minimum cloud mass which collapses for the selected values of density.
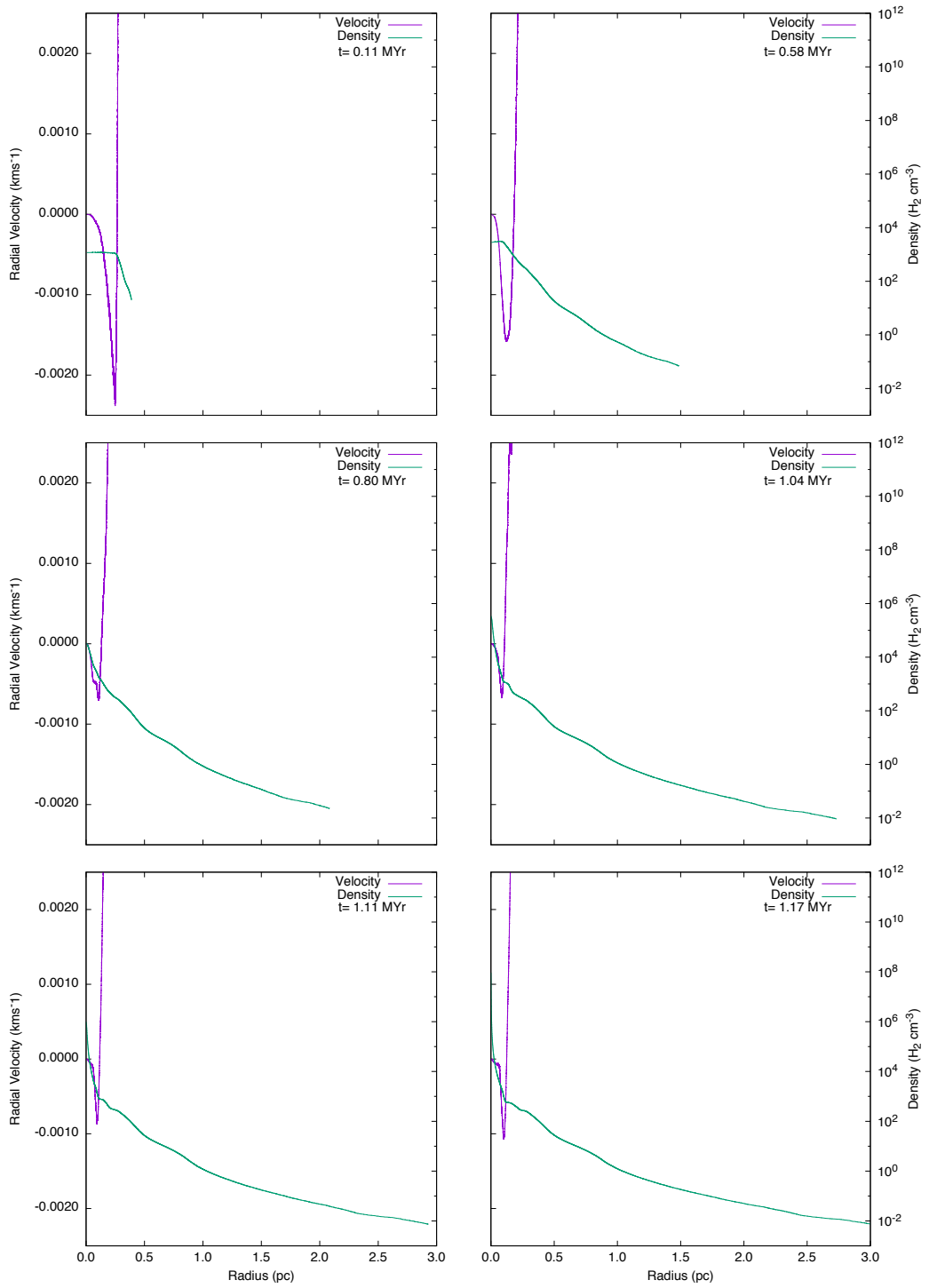
Figure A.82: Model E: six snapshots showing radial velocity (purple line) and density (green line) for a cloud with an initial density of 10000 cm^3, a mass of 2 M$_\odot$ and a radius of 0.10 pc.
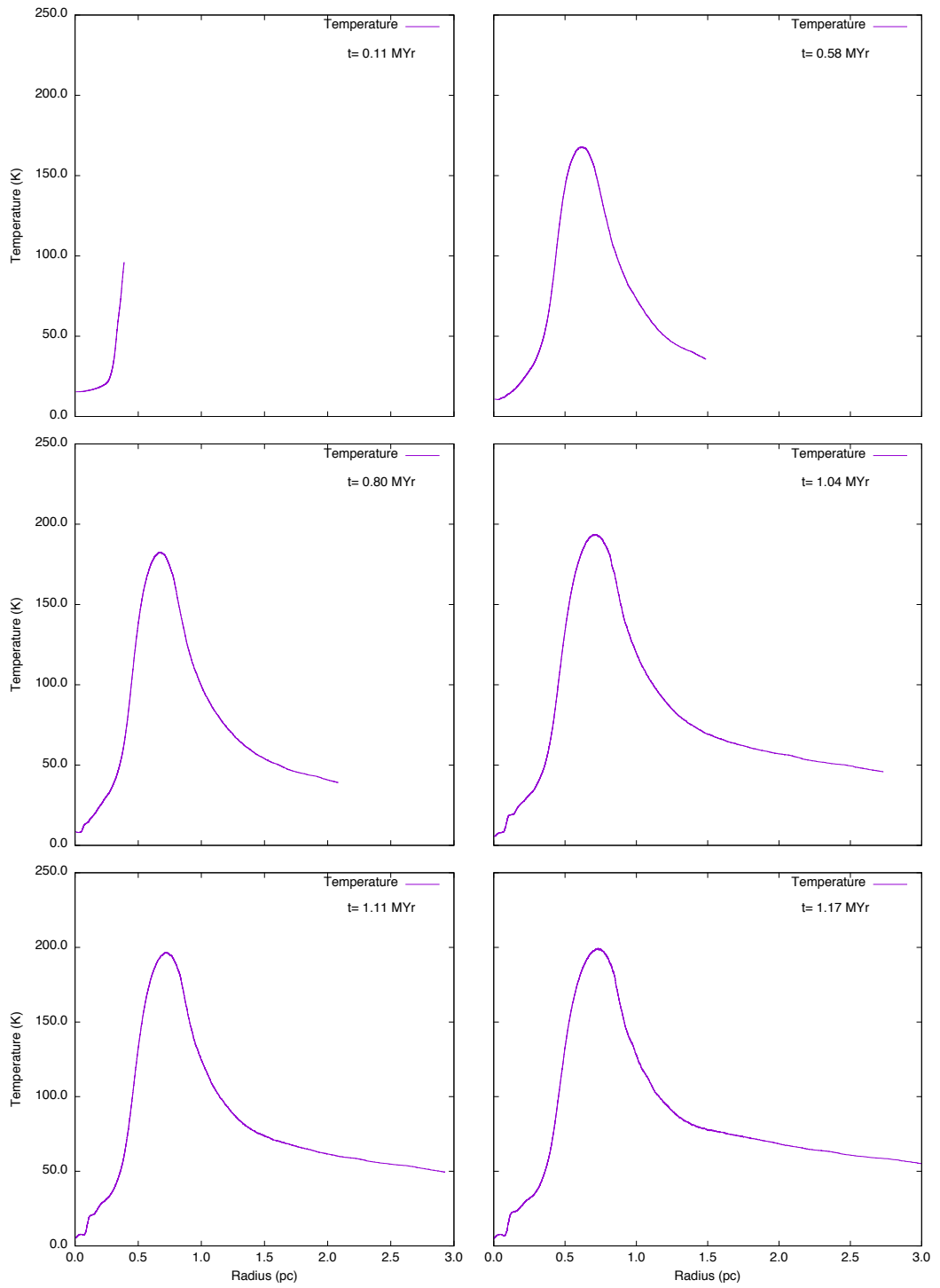
Figure A.83: Model E: six snapshots showing temperature (purple line) for a cloud with an initial density of 10000 cm³, a mass of 2 M$_\odot$ and a radius of 0.10 pc.
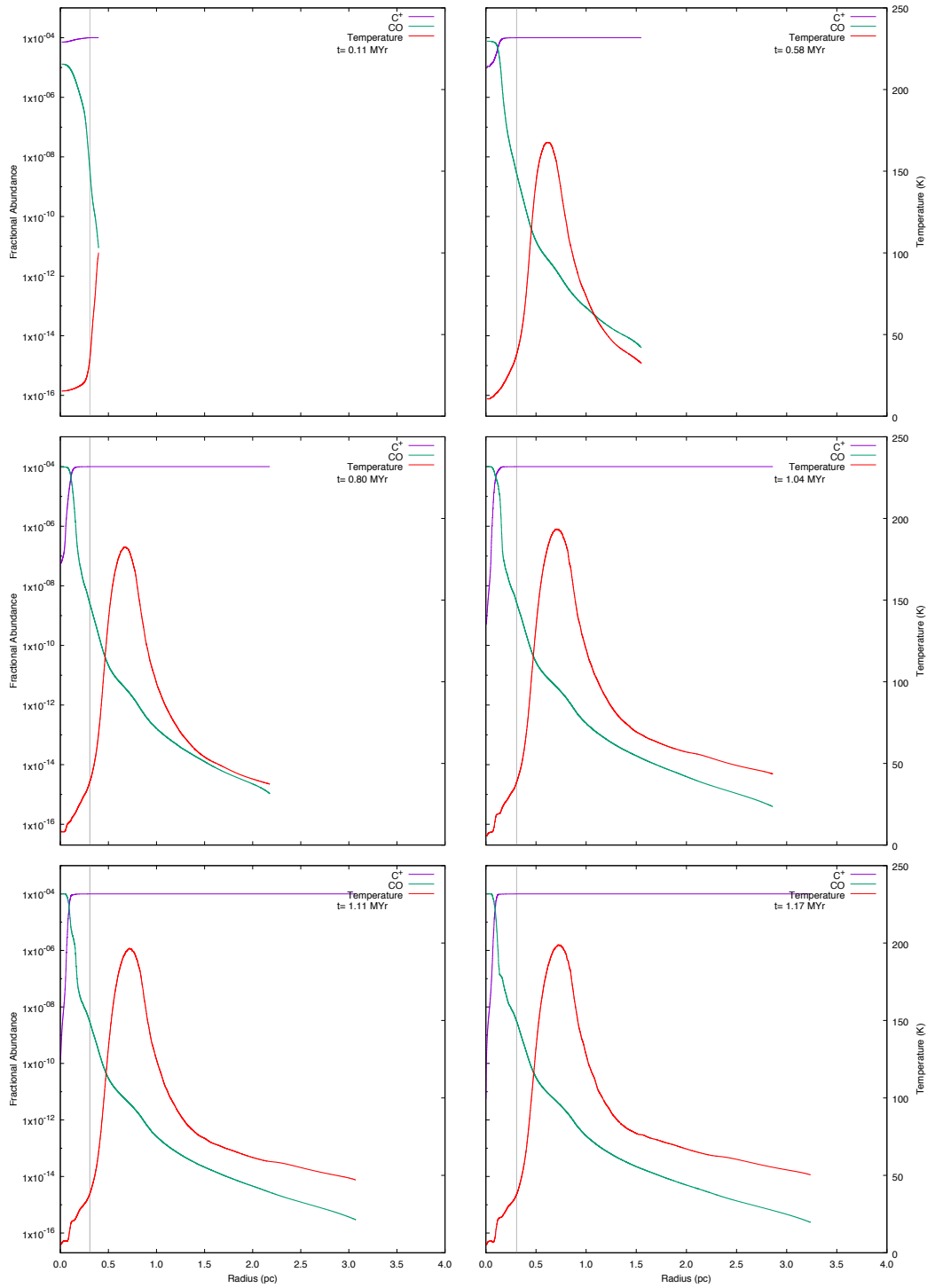
Figure A.84: Model E: six snapshots showing the chemical abundances of CO and C^+ for a cloud with an initial density of 10000 cm^{-3}, a mass of 2 M$_\odot$ and a radius of 0.10 pc.
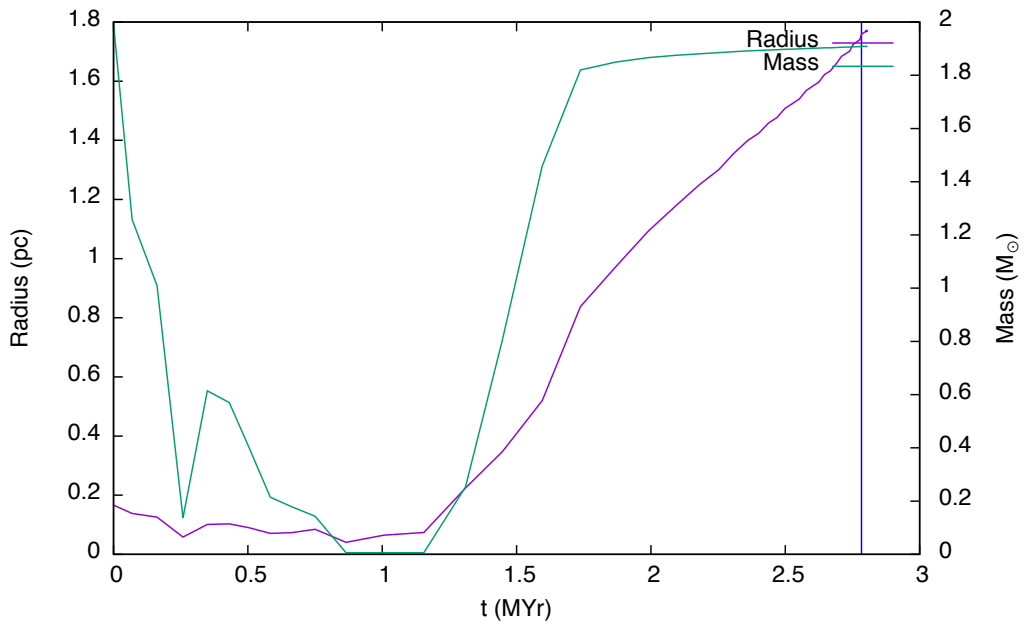
A.6 MODEL F

Figure A.85: Model F: the time evolution of the cloud with an initial density of 50 cm^3, a mass of 1.8 M$_\odot$ and a radius of 0.56 pc is shown in this graph. The cloud radius (purple line) is taken to be the zero crossing point of radial velocity and the mass (green line) is taken to be that which lies inside the radius. The blue vertical line denotes the time at which the high density peak first forms. This is the minimum cloud mass which collapses for the selected values of density.
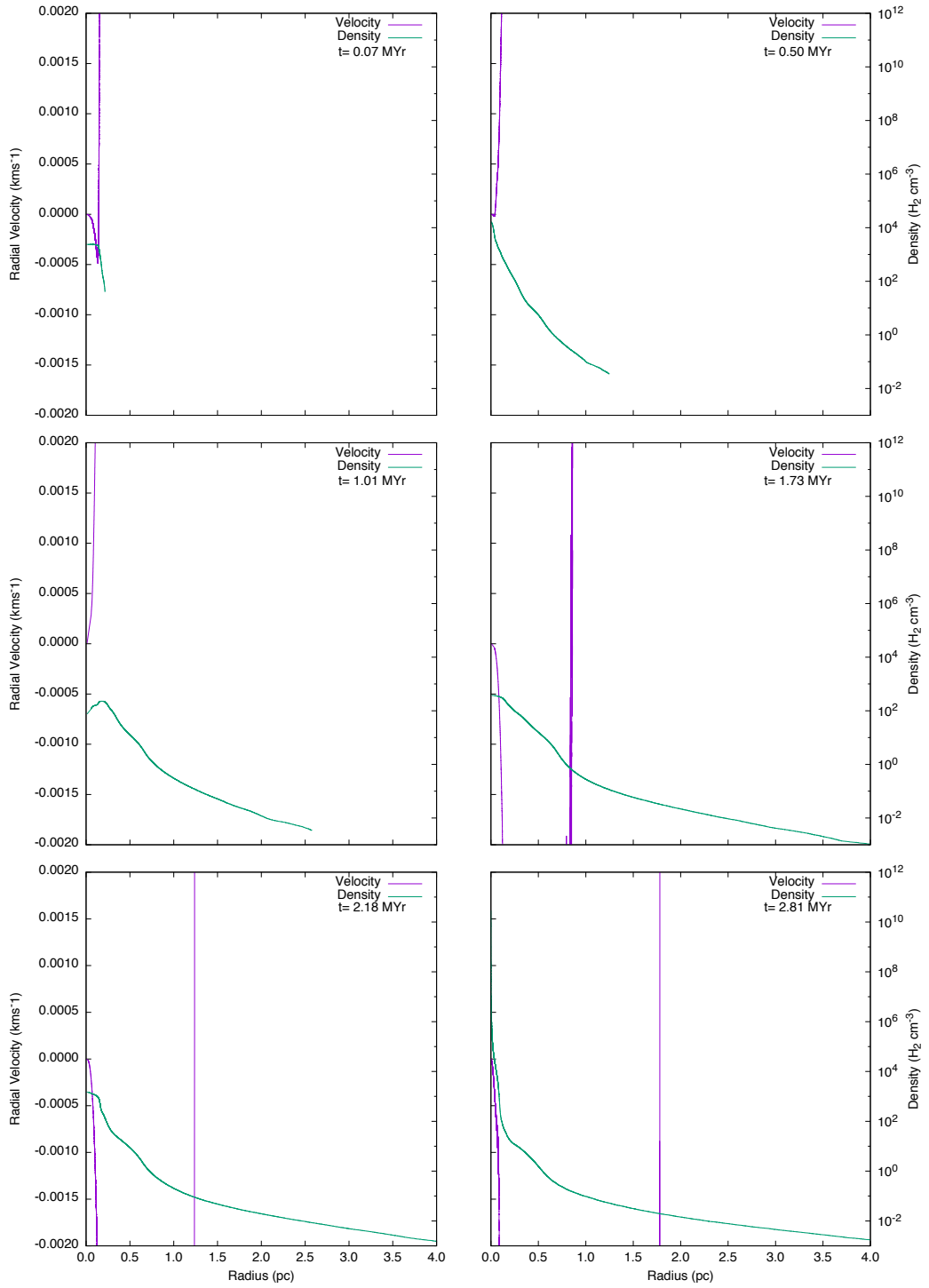
Figure A.86: Model F: six snapshots showing radial velocity (purple line) and density (green line) for a cloud with an initial density of 50 cm^3, a mass of 1.8 M$_\odot$ and a radius of 0.56 pc.
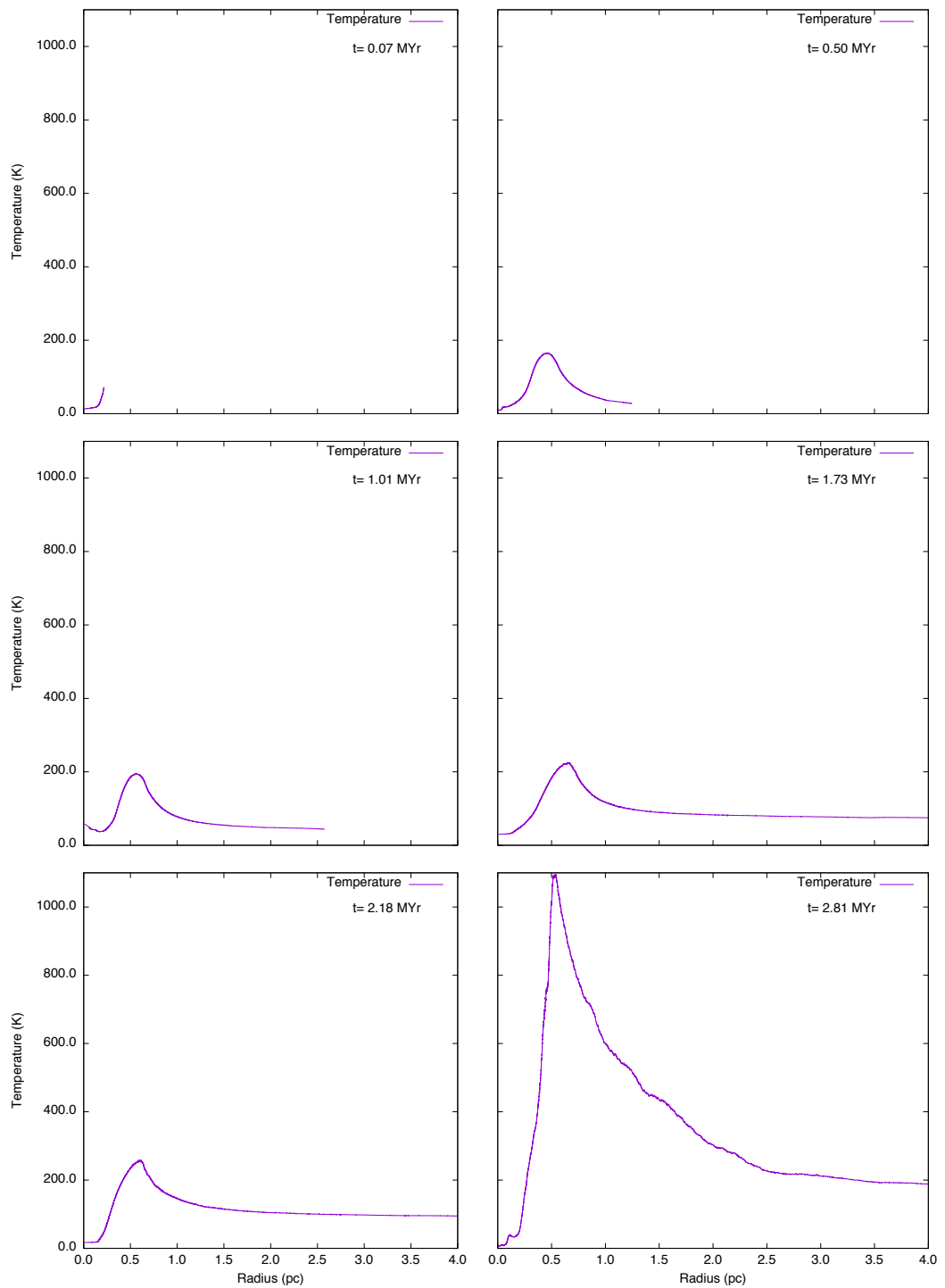
Figure A.87: Model F: six snapshots showing temperature (purple line) for a cloud with an initial density of 50 cm^3, a mass of 1.8 M$_\odot$ and a radius of 0.56 pc.

Figure A.88: Model F: six snapshots showing the chemical abundances of CO and C^+ for a cloud with an initial density of 50 cm^{-3}, a mass of 1.8 M$_\odot$ and a radius of 0.56 pc.

Figure A.89: Model F: the time evolution of the cloud with an initial density of 100 cm^3, a mass of 1.3 $M_\odot$ and a radius of 0.40 pc is shown in this graph. The cloud radius (purple line) is taken to be the zero crossing point of radial velocity and the mass (green line) is taken to be that which lies inside the radius. The blue vertical line denotes the time at which the high density peak first forms. This is the minimum cloud mass which collapses for the selected values of density.

Figure A.90: Model F: six snapshots showing radial velocity (purple line) and density (green line) for a cloud with an initial density of 100 cm³, a mass of 1.3 M_⊙ and a radius of 0.40 pc.

Figure A.91: Model F: six snapshots showing temperature (purple line) for a cloud with an initial density of 100 cm³, a mass of 1.3 M$_\odot$ and a radius of 0.40 pc.
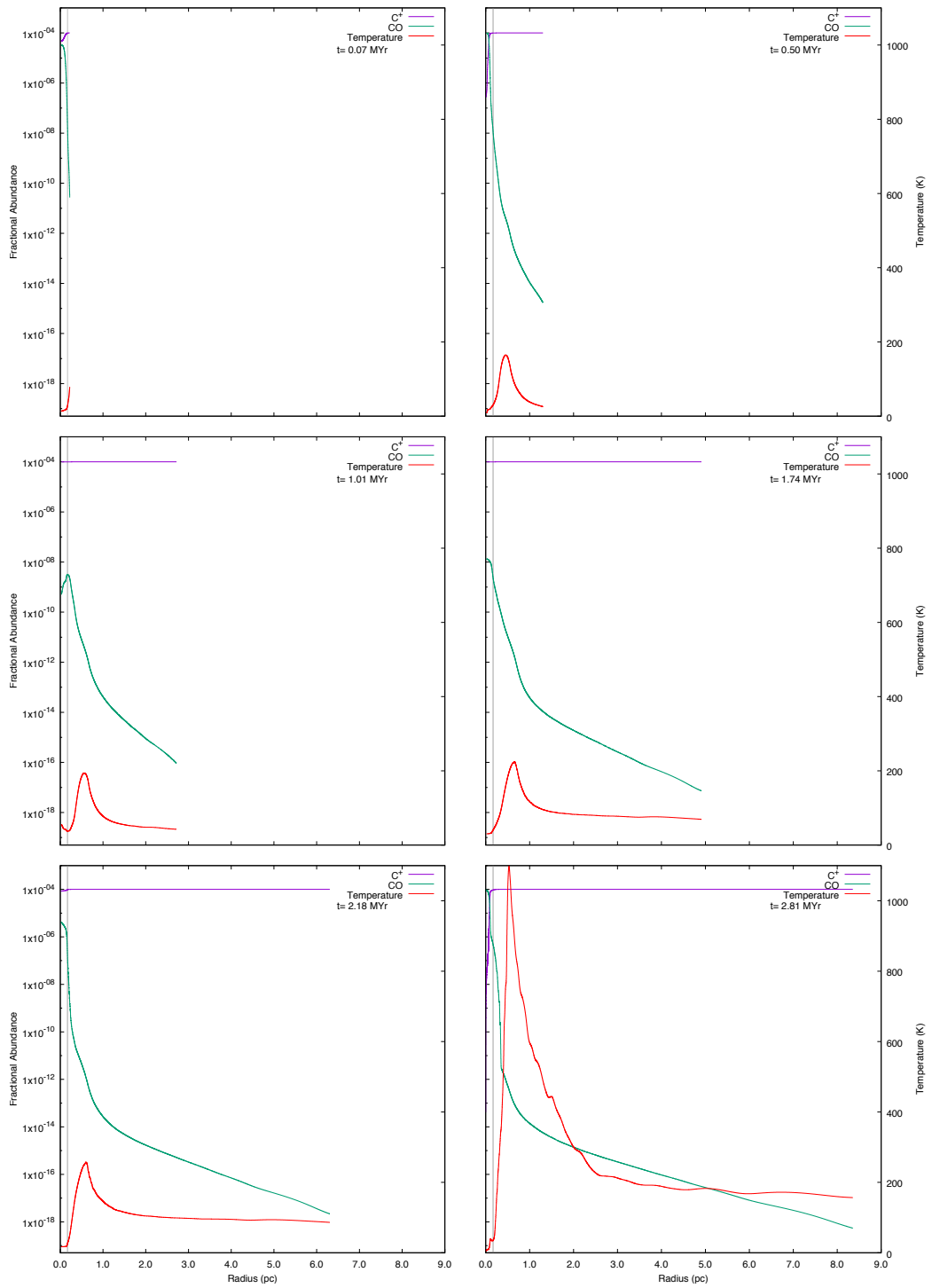
Figure A.92: Model F: six snapshots showing the chemical abundances of CO and C$^+$ for a cloud with an initial density of 100 cm^{-3}, a mass of 1.3 M$_\odot$ and a radius of 0.40 pc.
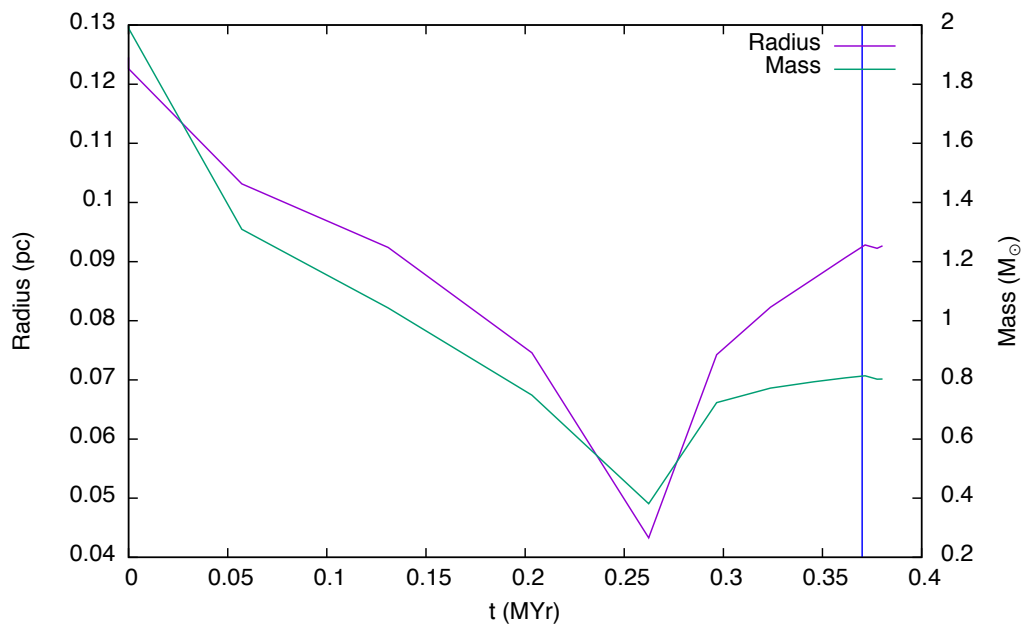
Figure A.93: Model F: the time evolution of the cloud with an initial density of 1000 cm^3, a mass of $0.7_\odot$ and a radius of 0.15 pc is shown in this graph. The cloud radius (purple line) is taken to be the zero crossing point of radial velocity and the mass (green line) is taken to be that which lies inside the radius. The blue vertical line denotes the time at which the high density peak first forms. This is the minimum cloud mass which collapses for the selected values of density.
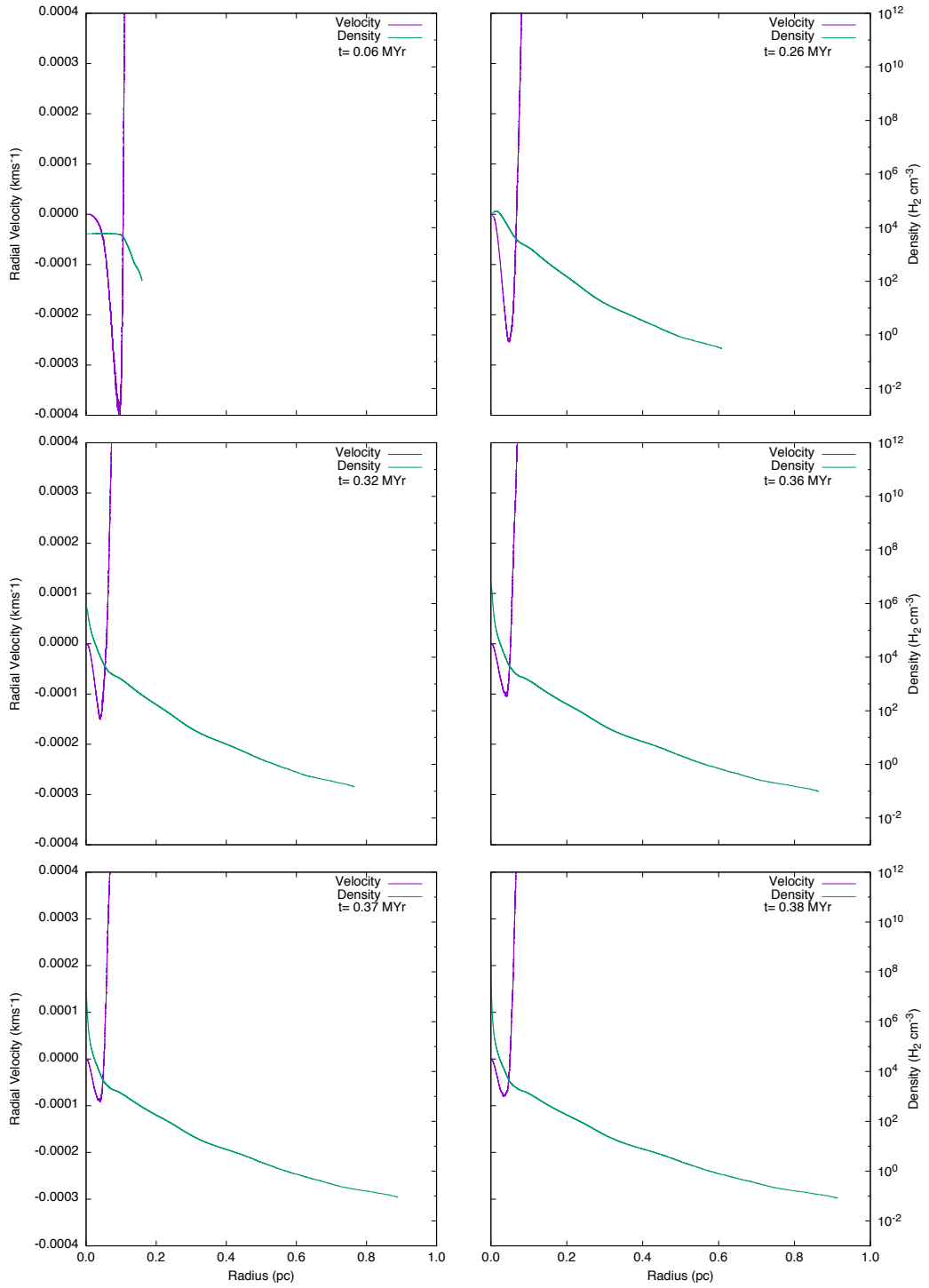
Figure A.94: Model F: six snapshots showing radial velocity (purple line) and density (green line) for a cloud with an initial density of 1000 cm³, a mass of $0.7_{\odot}$ and a radius of 0.15 pc.

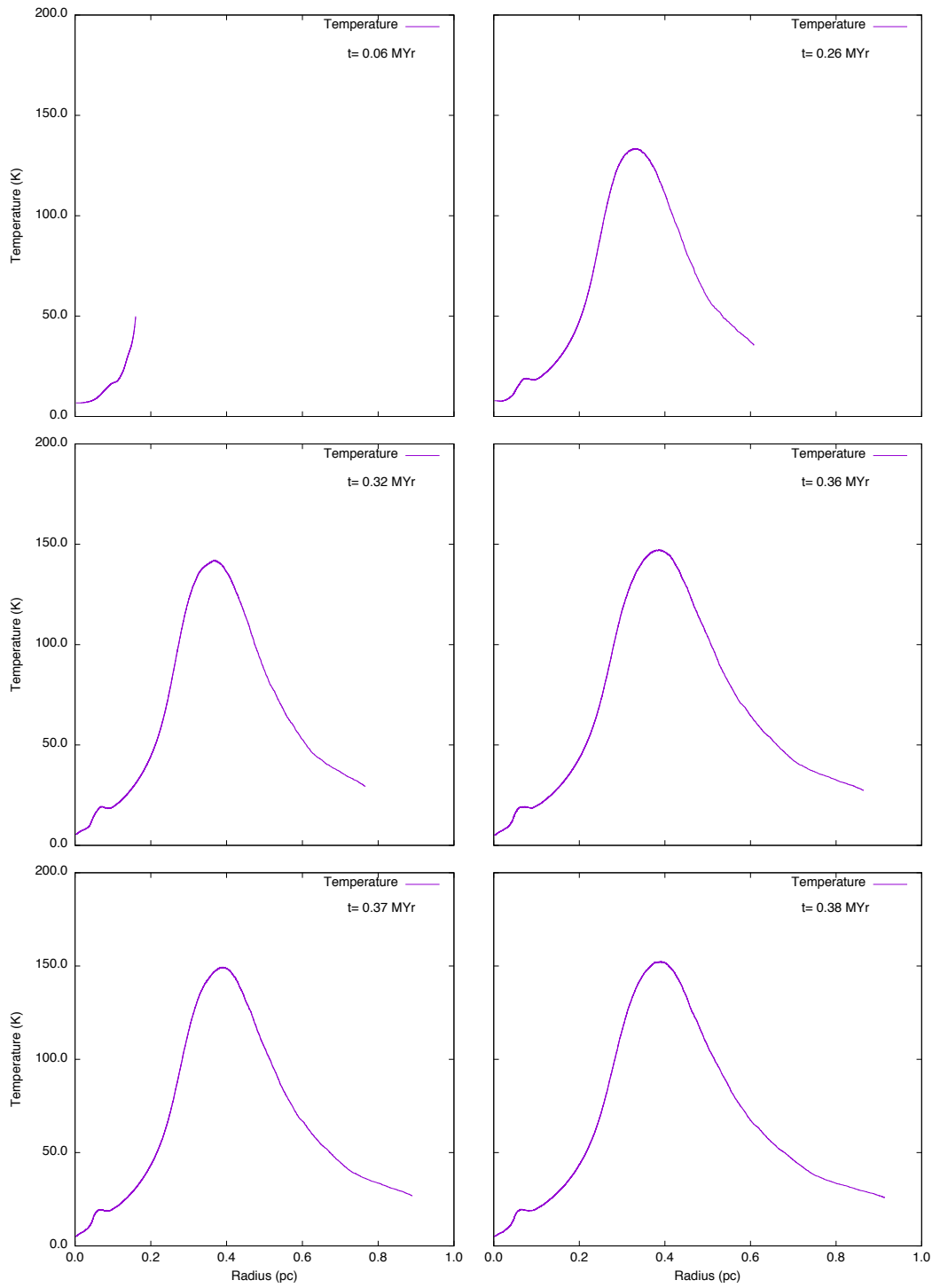Figure A.95: Model F: six snapshots showing temperature (purple line) for a cloud with an initial density of 1000 cm^3, a mass of 0.7$_\odot$ and a radius of 0.15 pc.
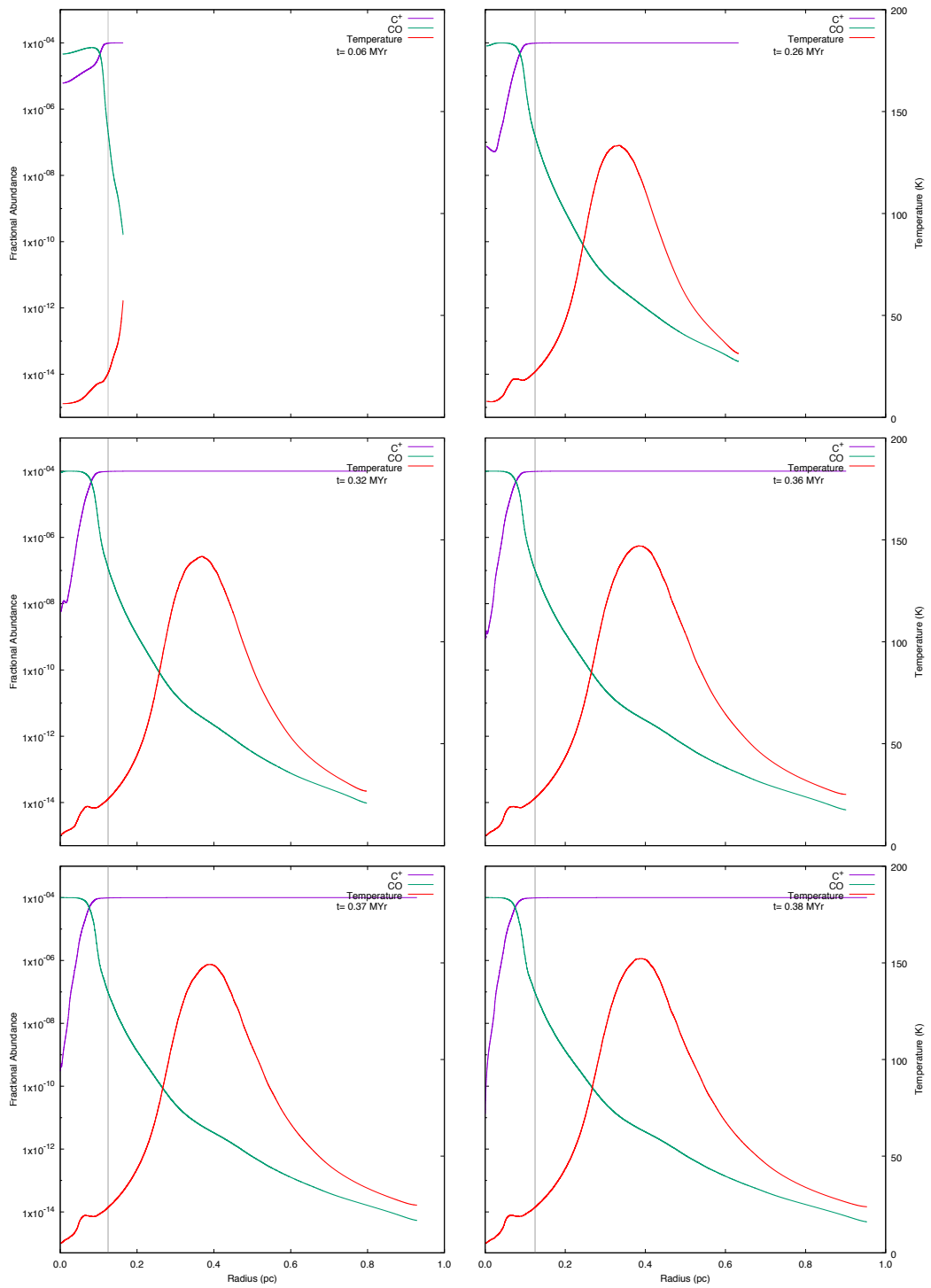
Figure A.96: Model F: six snapshots showing the chemical abundances of CO and C^+ for a cloud with an initial density of 1000 cm^{-3}, a mass of 0.7 M$_\odot$ and a radius of 0.15 pc.
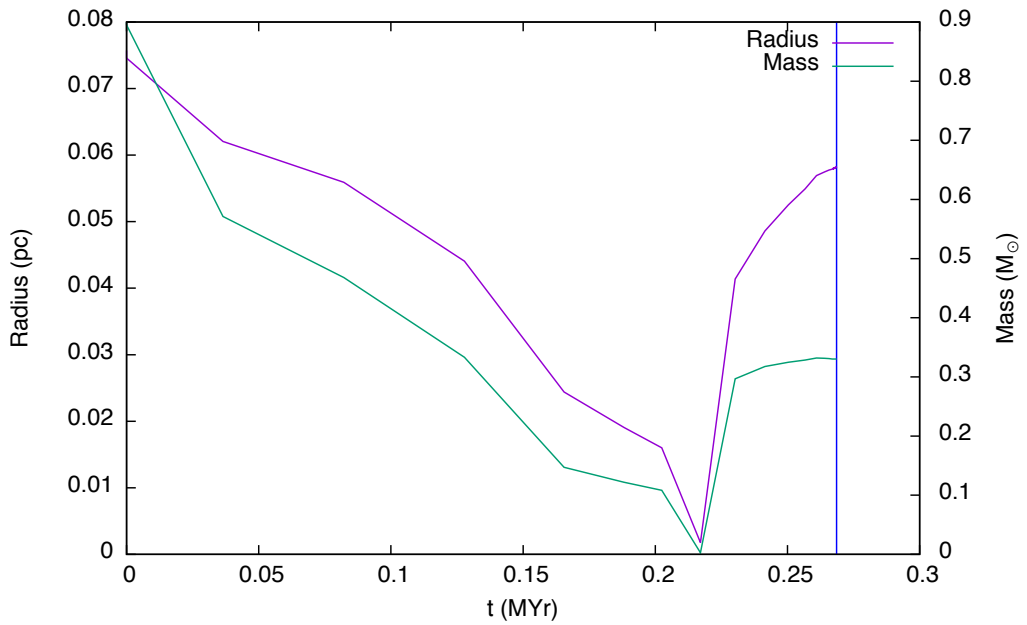
286

Figure A.97: Model F: the time evolution of the cloud with an initial density of 5000 cm^3, a mass of 0.6 M$_\odot$ and a radius of 0.08 pc is shown in this graph. The cloud radius (purple line) is taken to be the zero crossing point of radial velocity and the mass (green line) is taken to be that which lies inside the radius. The blue vertical line denotes the time at which the high density peak first forms. This is the minimum cloud mass which collapses for the selected values of density.
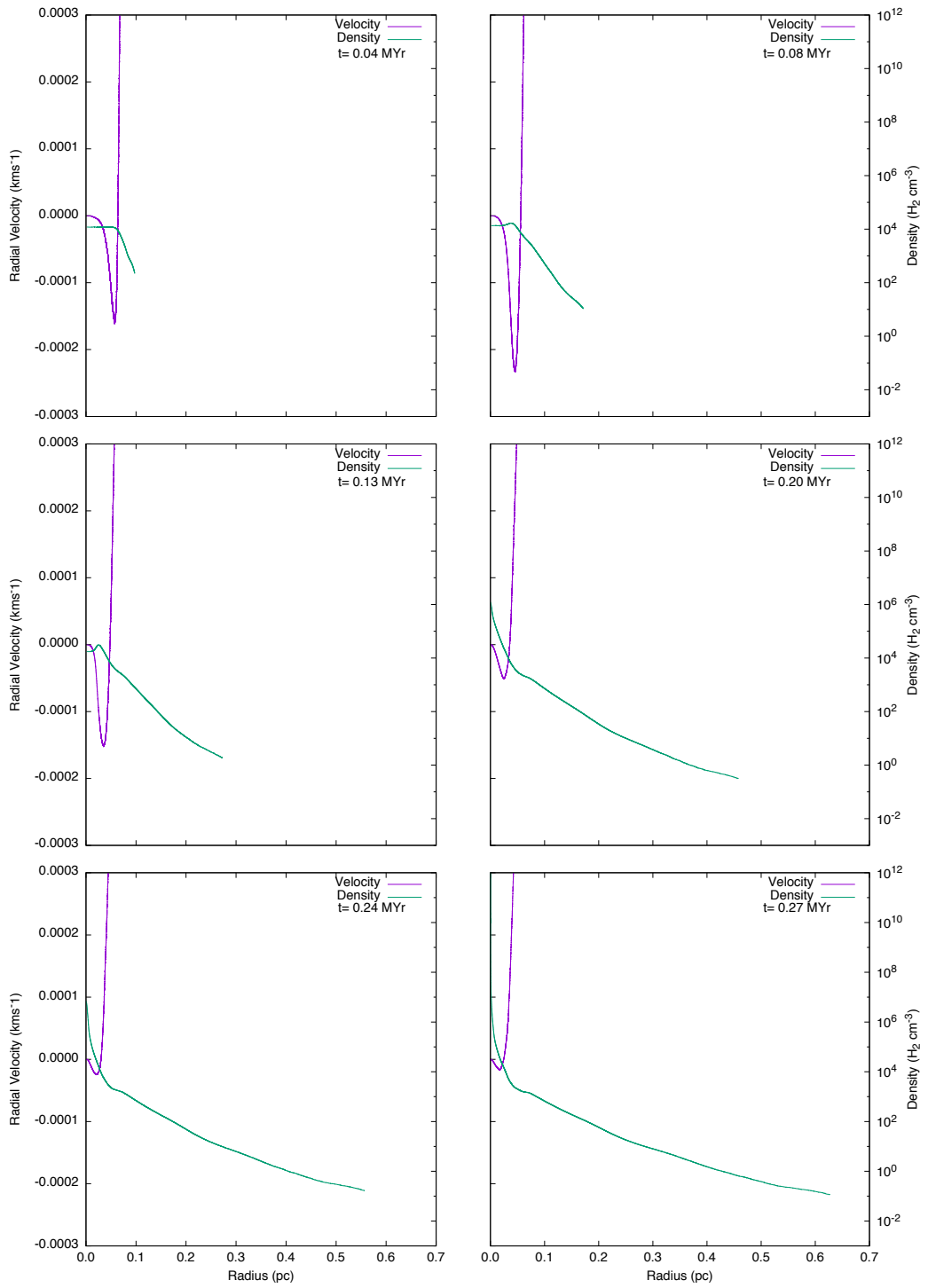
Figure A.98: Model F: six snapshots showing radial velocity (purple line) and density (green line) for a cloud with an initial density of 5000 cm³, a mass of 0.6 $M_\odot$ and a radius of 0.08 pc.
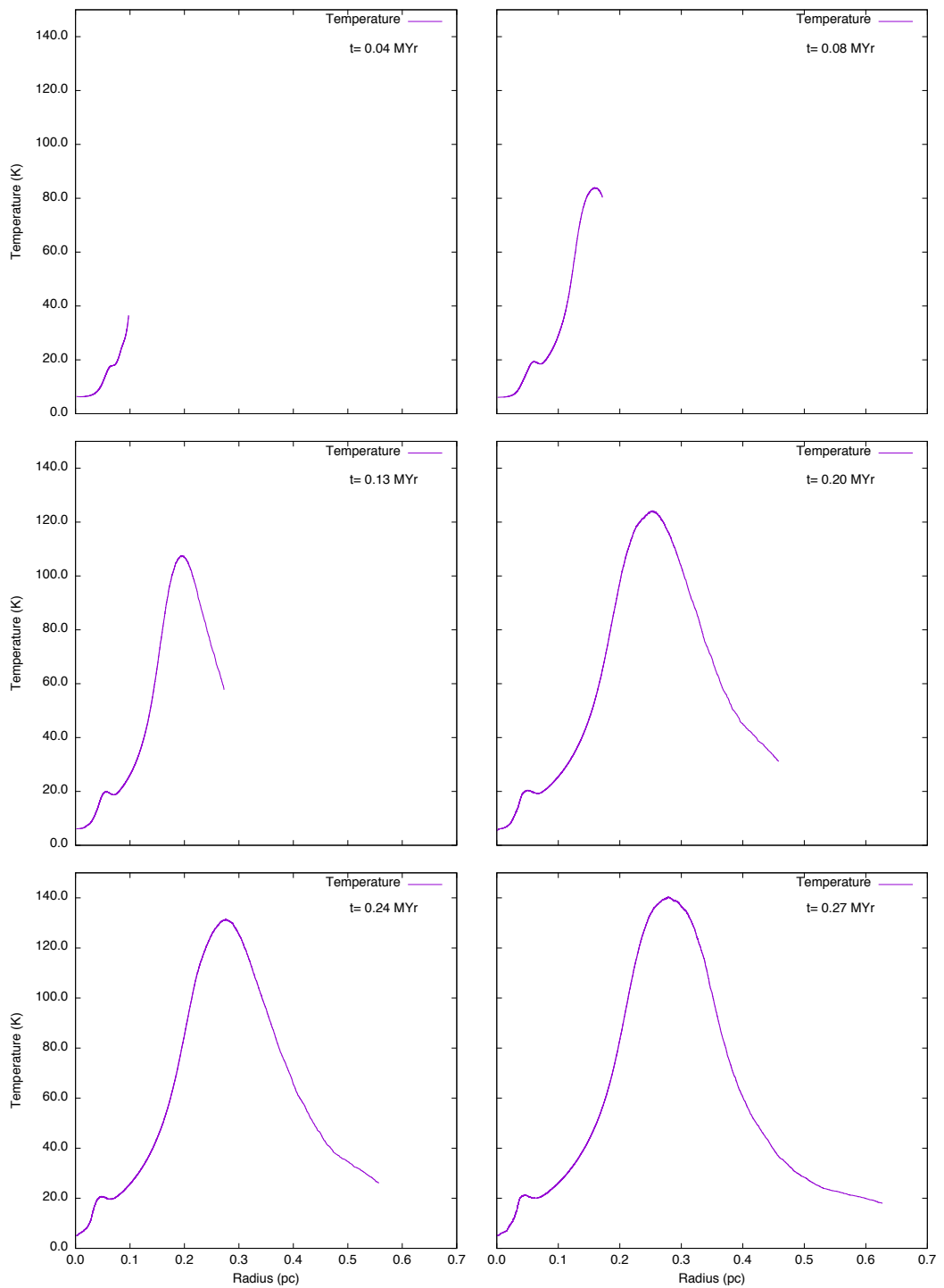
Figure A.99: Model F: six snapshots showing temperature (purple line) for a cloud with an initial density of 5000 cm³, a mass of 0.6 M⊙ and a radius of 0.08 pc.

Figure A.100: Model F: six snapshots showing the chemical abundances of CO and C^+ for a cloud with an initial density of 5000 cm^{-3}, a mass of 0.6 M$_\odot$ and a radius of 0.08 pc.

Chapter B

FUV: mass loss, radial velocity, density and temperature profiles

---
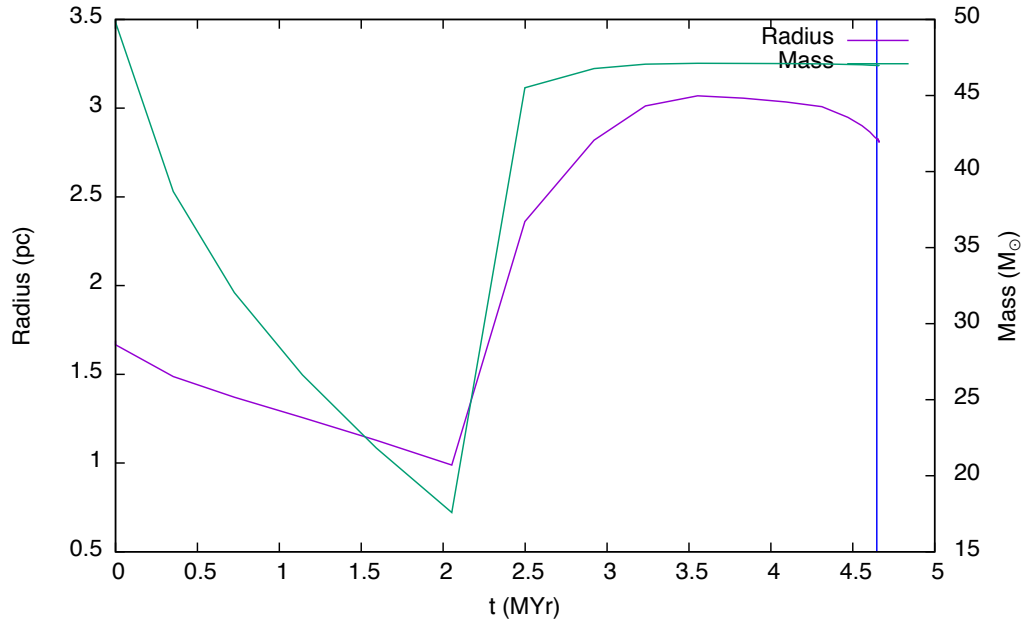
Figure B.1: FUV radiation = 1 G$_0$. The time evolution of a cloud with an initial density of 50 cm^{-3}, a mass of 50 M$_\odot$ and a radius of 1.69 pc is shown in this graph. The cloud radius (purple line) is taken to be the zero crossing point of radial velocity and the mass (green line) is taken to be that which lies inside the radius. The blue vertical line denotes the time at which the high density peak first forms. This is the minimum cloud mass which collapses for the selected values of density and FUV flux.

Figure B.2: FUV radiation = 1 G_0. Six snapshots showing radial velocity (purple line) and density (green line) for a cloud with an initial density of 50 cm^{-3}, a mass of 50 $M_\odot$ and a radius of 1.69 pc.

Figure B.3: FUV radiation $= 1$ G_0. Six snapshots showing temperature (purple line) for a cloud with an initial density of 50 cm^{-3}, a mass of 50 M$_\odot$ and a radius of 1.69 pc.
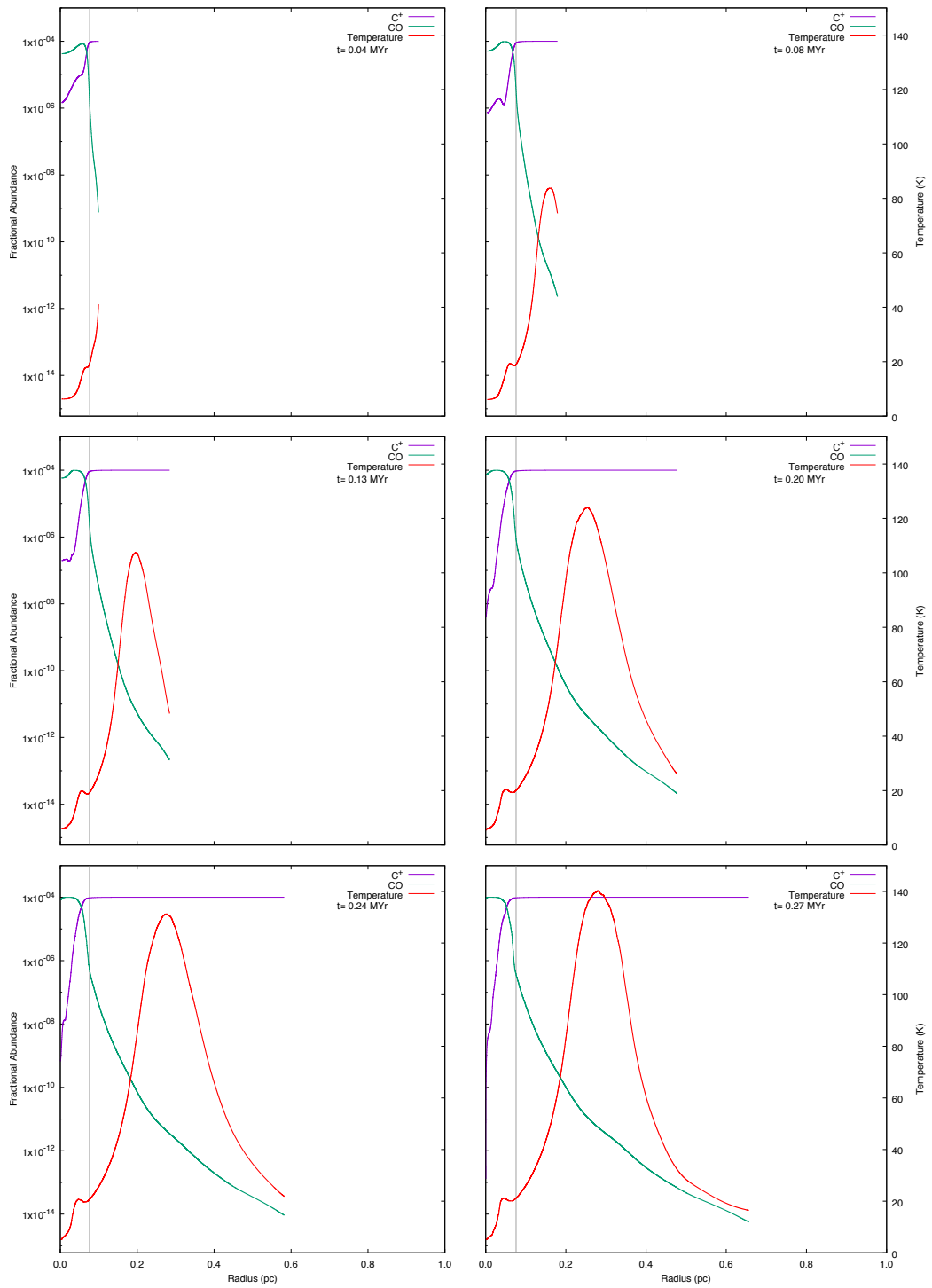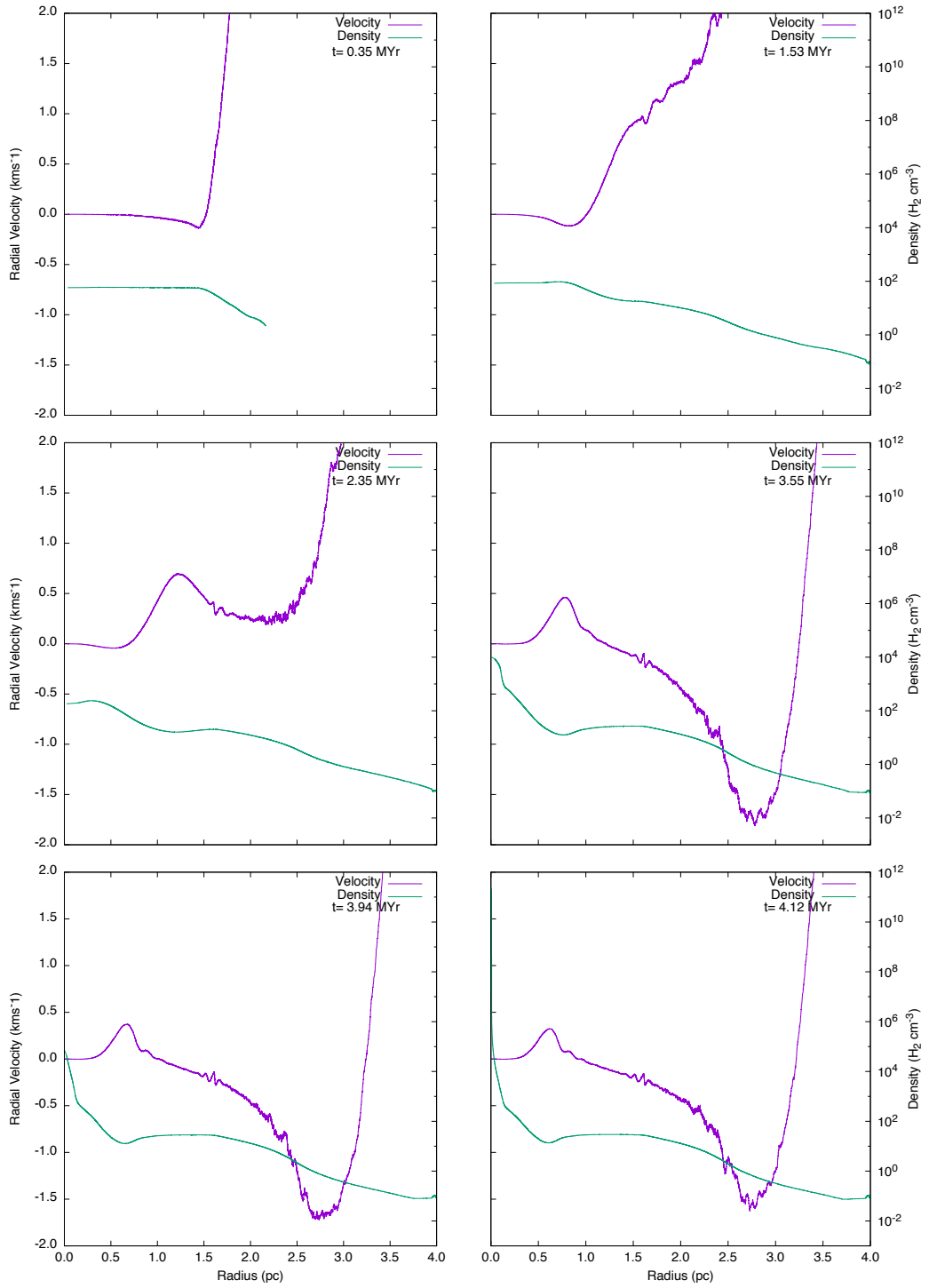
Figure B.4: FUV radiation = 1 G_0: six snapshots showing the chemical abundances of CO and C^+ for a cloud with an initial density of 50 cm^{-3}, a mass of 50 $M_\odot$ and a radius of 1.69 pc.

Figure B.5: FUV radiation $= 1$ G_0. The time evolution of a cloud with an initial density of 100 cm^{-3}, a mass of 28 M$_\odot$ and a radius of 1.11 pc is shown in this graph. The cloud radius (purple line) is taken to be the zero crossing point of radial velocity and the mass (green line) is taken to be that which lies inside the radius. The blue vertical line denotes the time at which the high density peak first forms. This is the minimum cloud mass which collapses for the selected values of density and FUV flux.

Figure B.6: FUV radiation $= 1$ G_0. Six snapshots showing radial velocity (purple line) and density (green line) for a cloud with an initial density of 100 cm^{-3}, a mass of 28 M$_\odot$ and a radius of 1.11 pc.
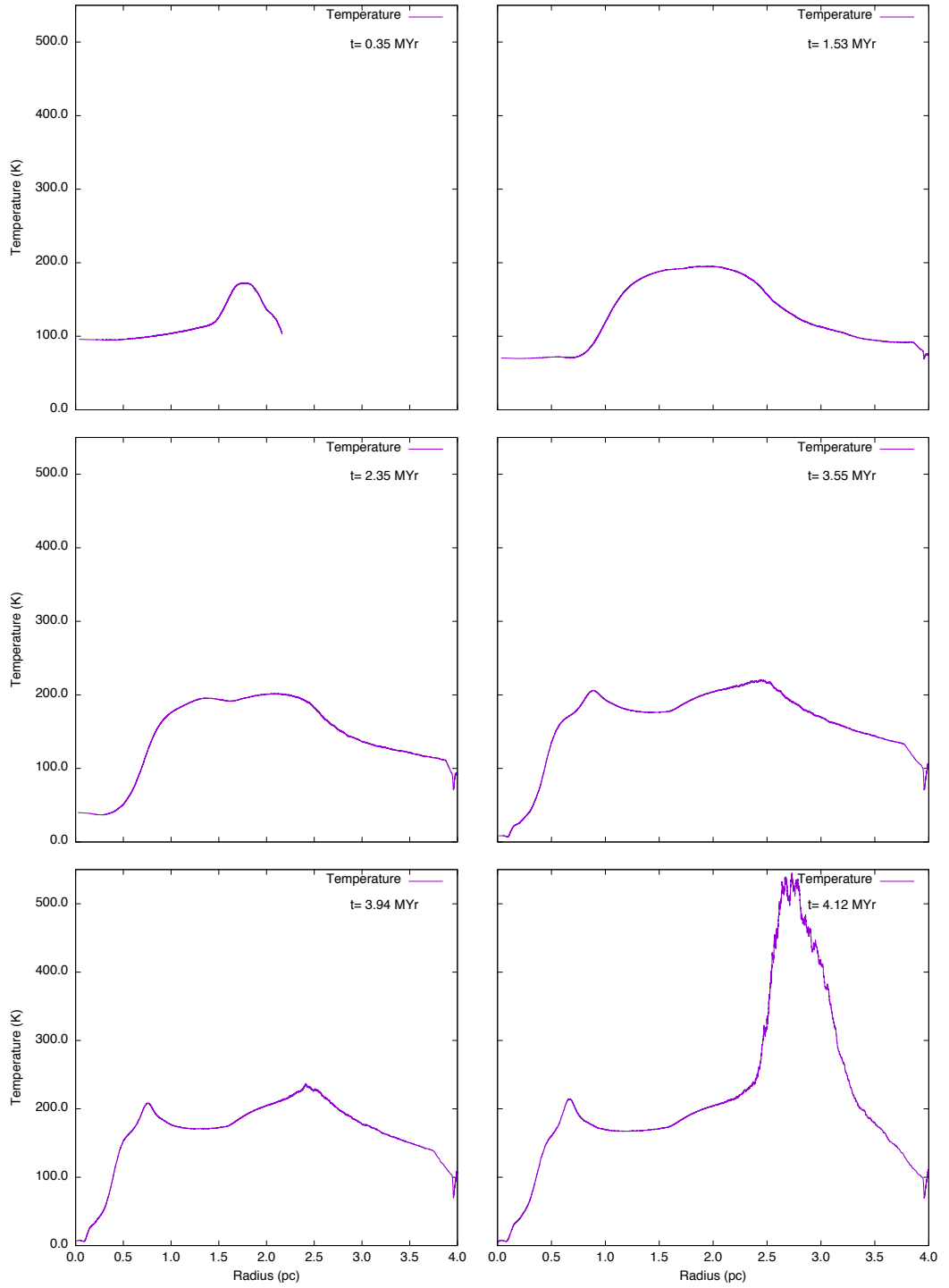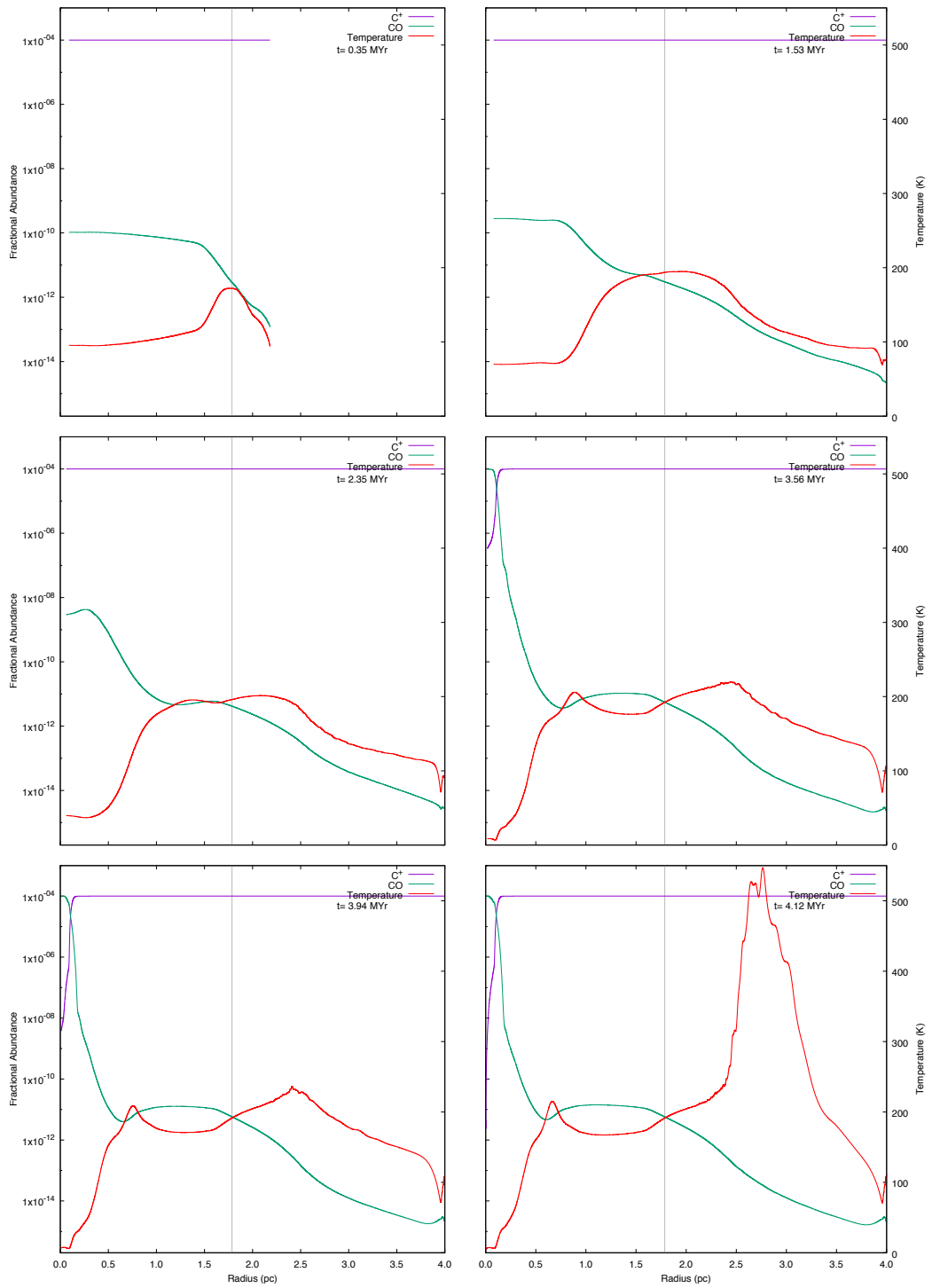
Figure B.7: FUV radiation $= 1 \, G_0$. Six snapshots showing temperature (purple line) for a cloud with an initial density of $100 \, \text{cm}^{-3}$, a mass of $28 \, M_{\odot}$ and a radius of $1.11 \, \text{pc}$.

Figure B.8: FUV radiation = 1 G_0: six snapshots showing the chemical abundances of CO and C^+ for a cloud with an initial density of 100 cm^{-3}, a mass of 28 $M_\odot$ and a radius of 1.11 pc.
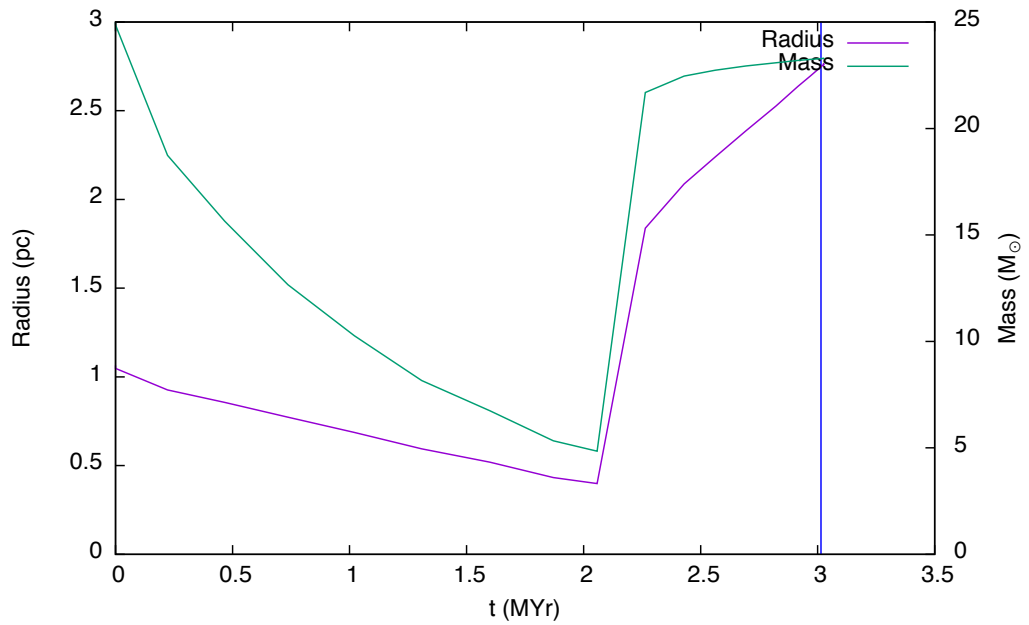
Figure B.9: FUV radiation $= 1$ G_0. The time evolution of a cloud with an initial density of 200 cm^{-3}, a mass of 15 M$_\odot$ and a radius of 0.71 pc is shown in this graph. The cloud radius (purple line) is taken to be the zero crossing point of radial velocity and the mass (green line) is taken to be that which lies inside the radius. The blue vertical line denotes the time at which the high density peak first forms. This is the minimum cloud mass which collapses for the selected values of density and FUV flux.
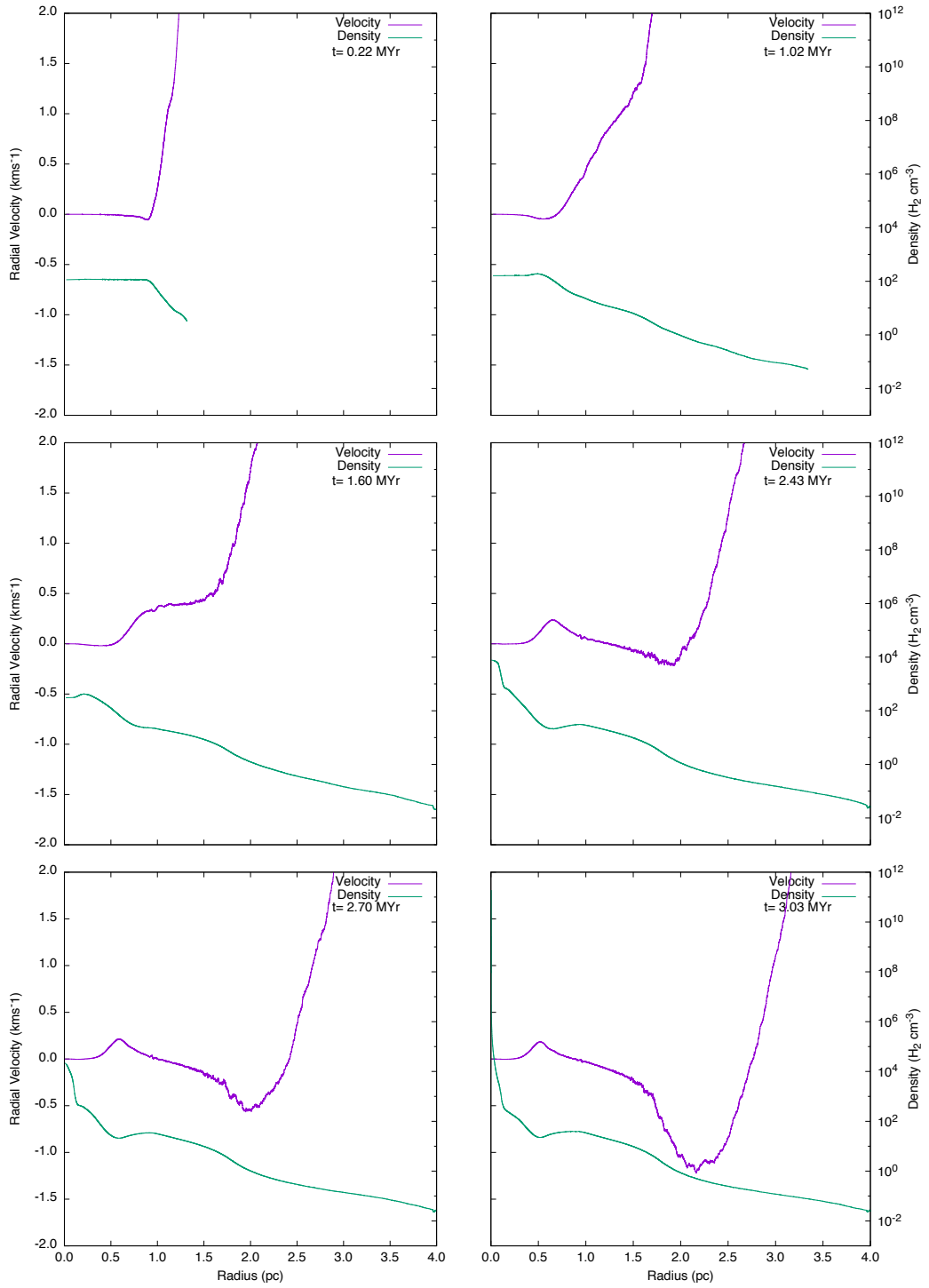
Figure B.10: FUV radiation $= 1\,G_0$. Six snapshots showing radial velocity (purple line) and density (green line) for a cloud with an initial density of 200 cm^{-3}, a mass of 15 M$_\odot$ and a radius of 0.71 pc.
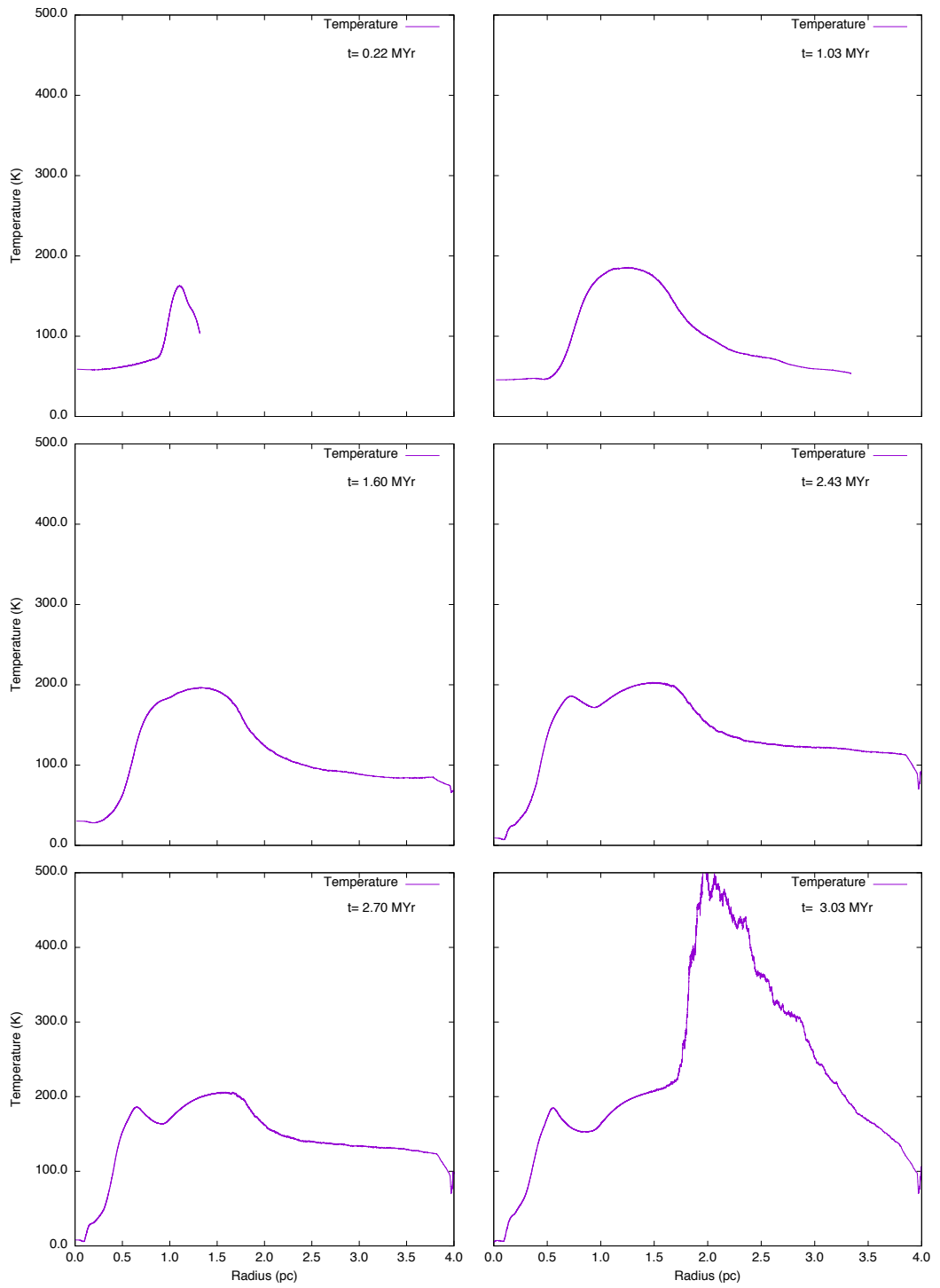
Figure B.11: FUV radiation $= 1$ G_0. Six snapshots showing temperature (purple line) for a cloud with an initial density of 200 cm^{-3}, a mass of 15 M$_\odot$ and a radius of 0.71 pc.
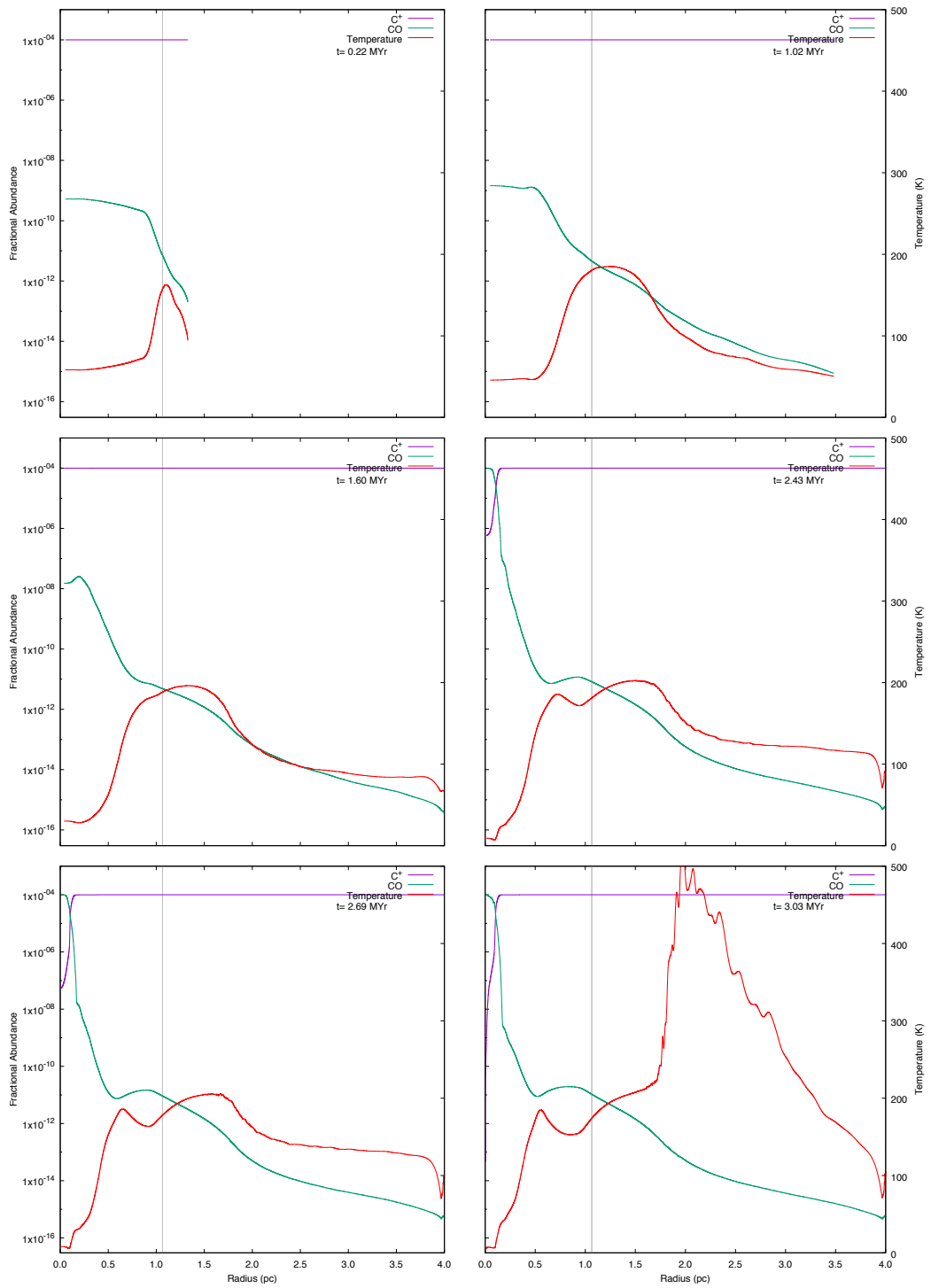
Figure B.12: FUV radiation = 1 G_0: six snapshots showing the chemical abundances of CO and C^+ for a cloud with an initial density of 200 cm^{-3}, a mass of 15 M$_\odot$ and a radius of 0.71 pc.
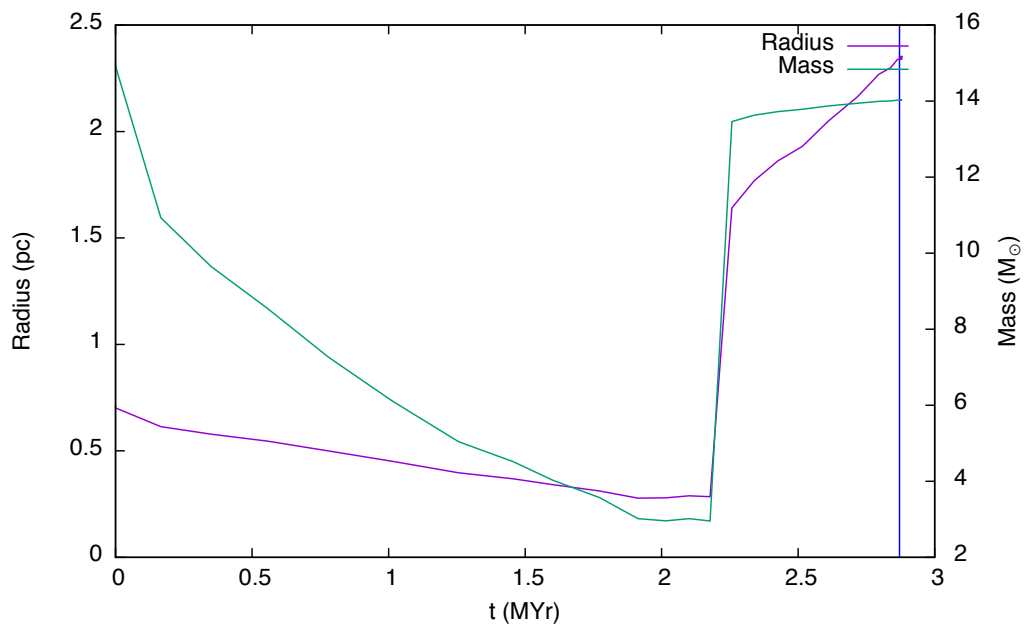
Figure B.13: FUV radiation $= 1$ G_0: the time evolution of a cloud with an initial density of 1000 cm^{-3}, a mass of 6 M$_\odot$ and a radius of 0.31 pc is shown in this graph. The cloud radius (purple line) is taken to be the zero crossing point of radial velocity and the mass (green line) is taken to be that which lies inside the radius. The blue vertical line denotes the time at which the high density peak first forms. This is the minimum cloud mass which collapses for the selected values of density and FUV flux.
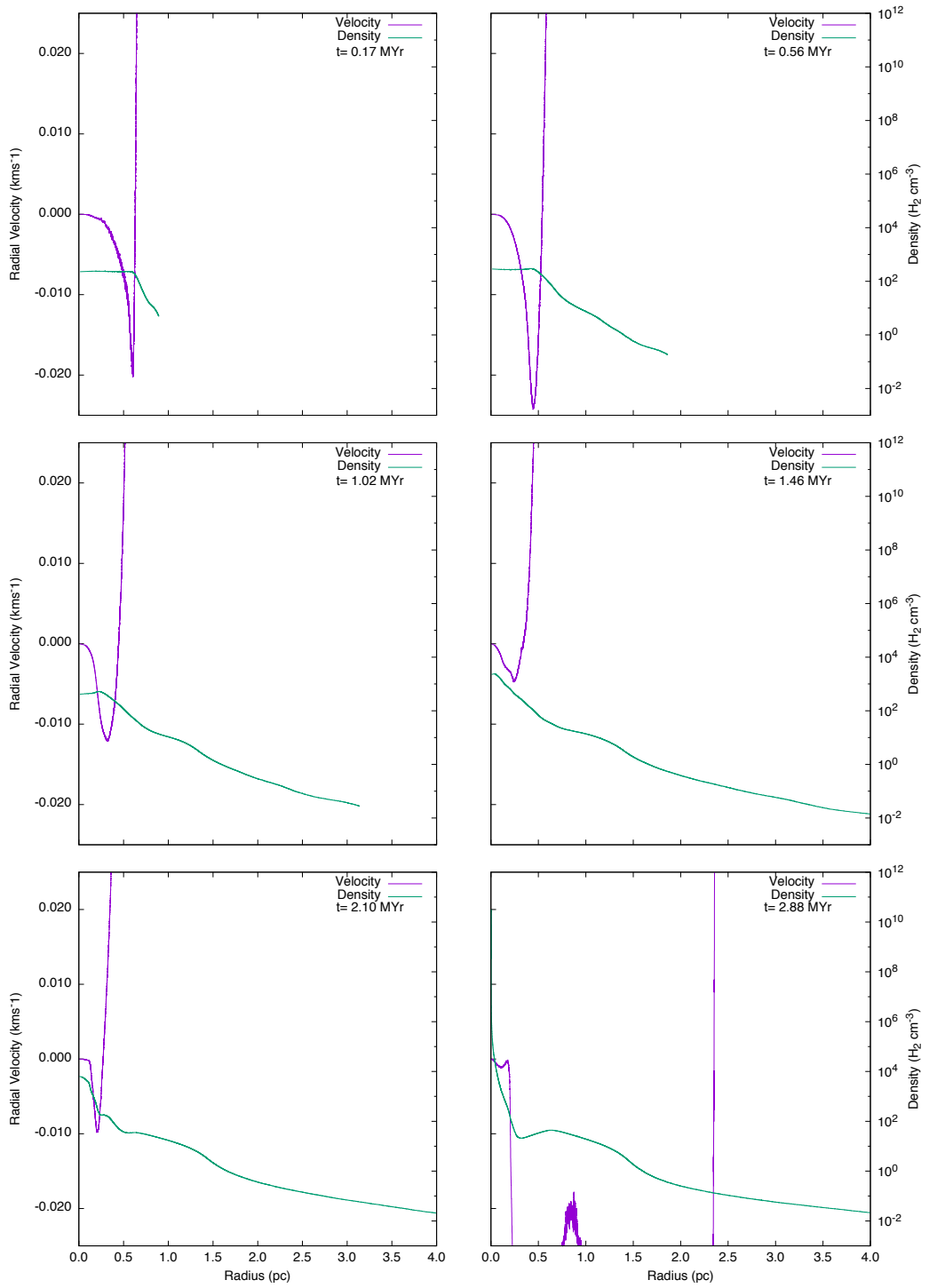
Figure B.14: FUV radiation $= 1\,G_0$. Six snapshots showing radial velocity (purple line) and density (green line) for a cloud with an initial density of 1000 cm^{-3}, a mass of 6 M$_\odot$ and a radius of 0.31 pc.
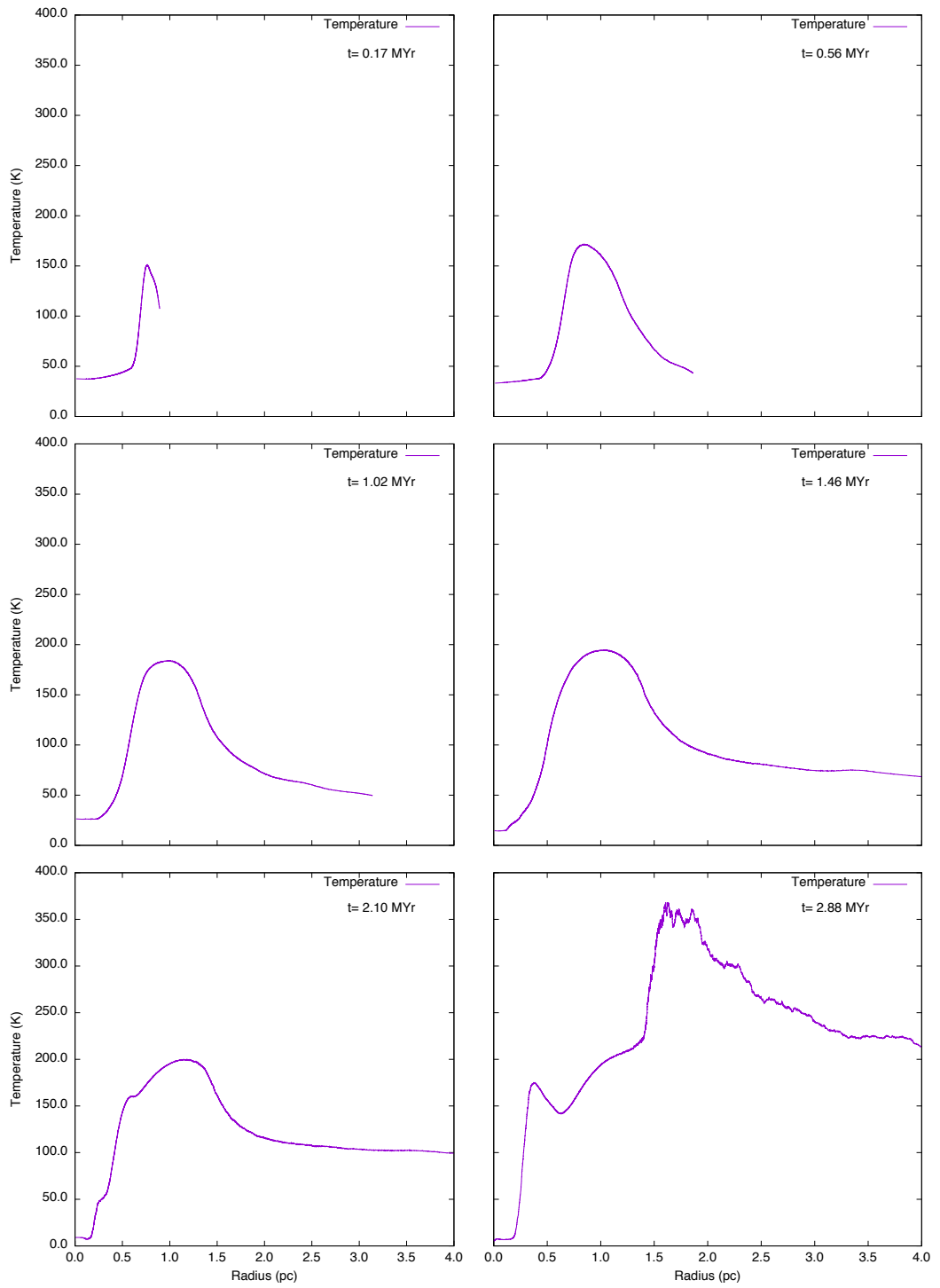
Figure B.15: FUV radiation $= 1$ G_0. Six snapshots showing temperature (purple line) for a cloud with an initial density of 1000 cm^{-3}, a mass of 6 M$_\odot$ and a radius of 0.31 pc.
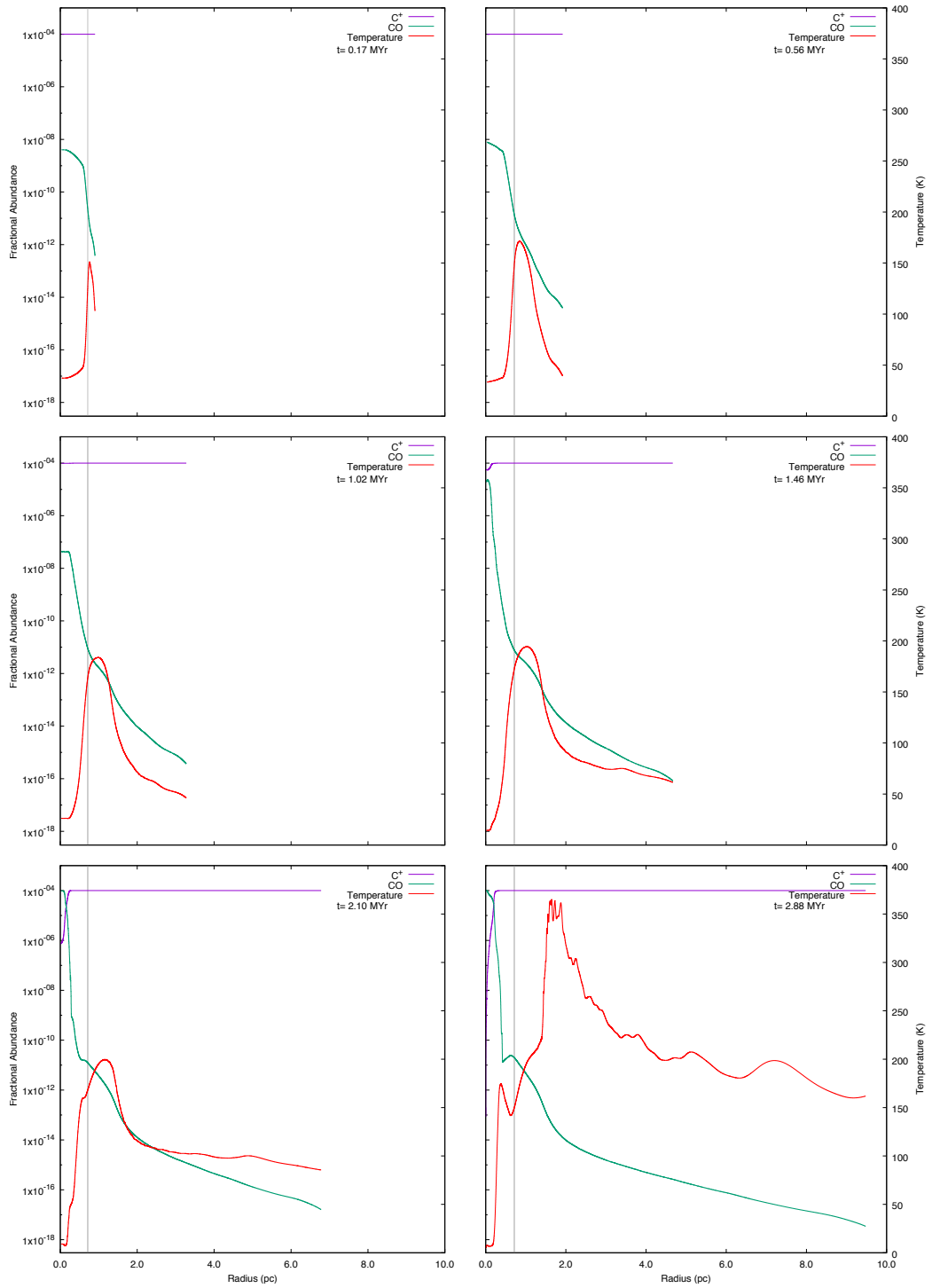
Figure B.16: FUV radiation = 1 G_0: six snapshots showing the chemical abundances of CO and C^+ for a cloud with an initial density of 1000 cm^{-3}, a mass of 6 $M_\odot$ and a radius of 0.31 pc.
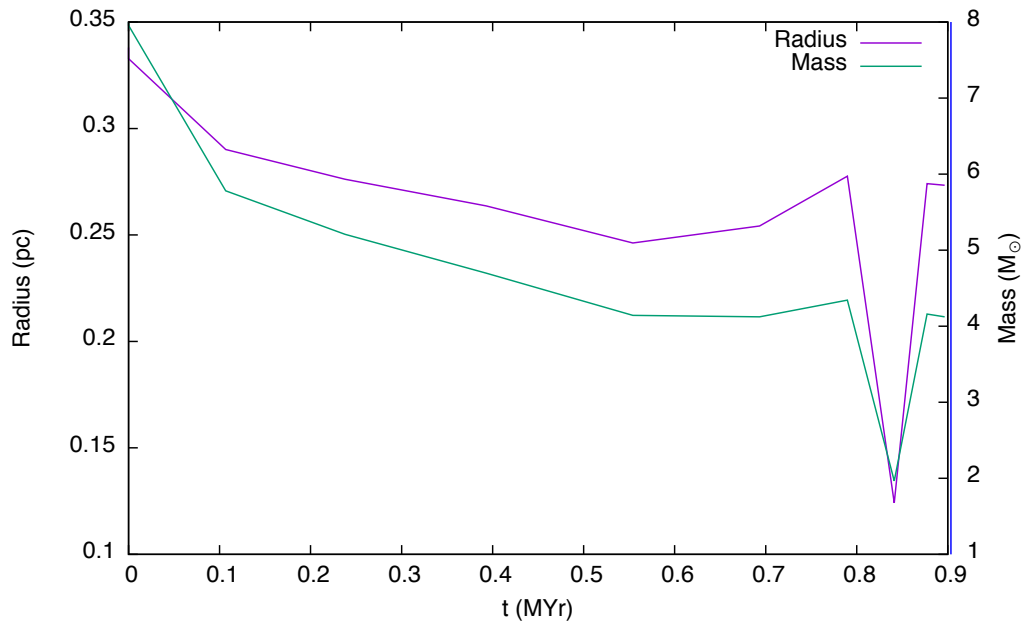
Figure B.17: FUV radiation = 1 G_0: the time evolution of a cloud with an initial density of 2000 cm^{-3}, a mass of 2 M$_\odot$ and a radius of 0.17 pc is shown in this graph. The cloud radius (purple line) is taken to be the zero crossing point of radial velocity and the mass (green line) is taken to be that which lies inside the radius. The blue vertical line denotes the time at which the high density peak first forms. This is the minimum cloud mass which collapses for the selected values of density and FUV flux.
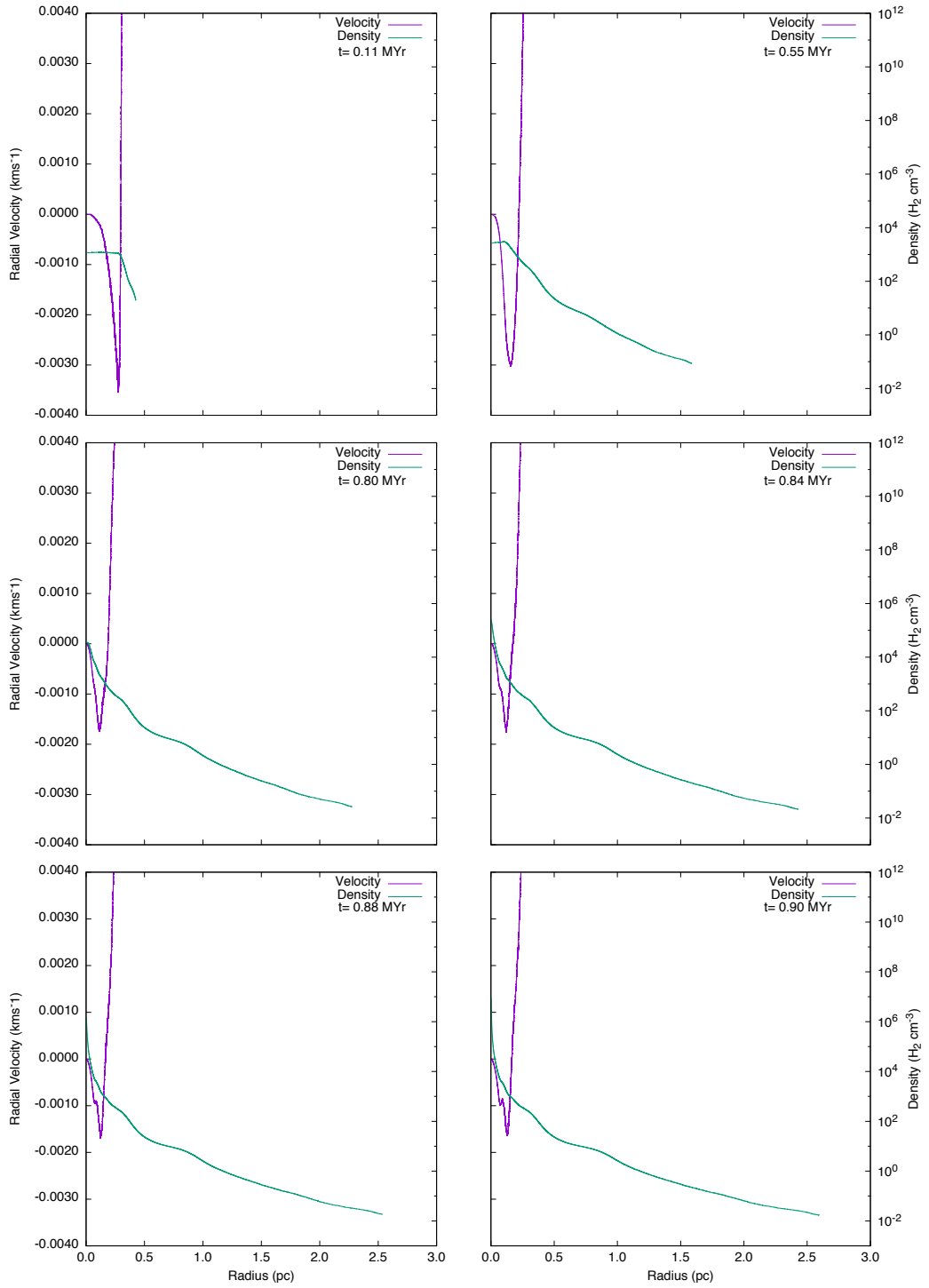
Figure B.18: FUV radiation $= 1\,\mathrm{G_0}$. Six snapshots showing radial velocity (purple line) and density (green line) for a cloud with an initial density of $2000\ \mathrm{cm^{-3}}$, a mass of $2\ \mathrm{M_\odot}$ and a radius of 0.17 pc.

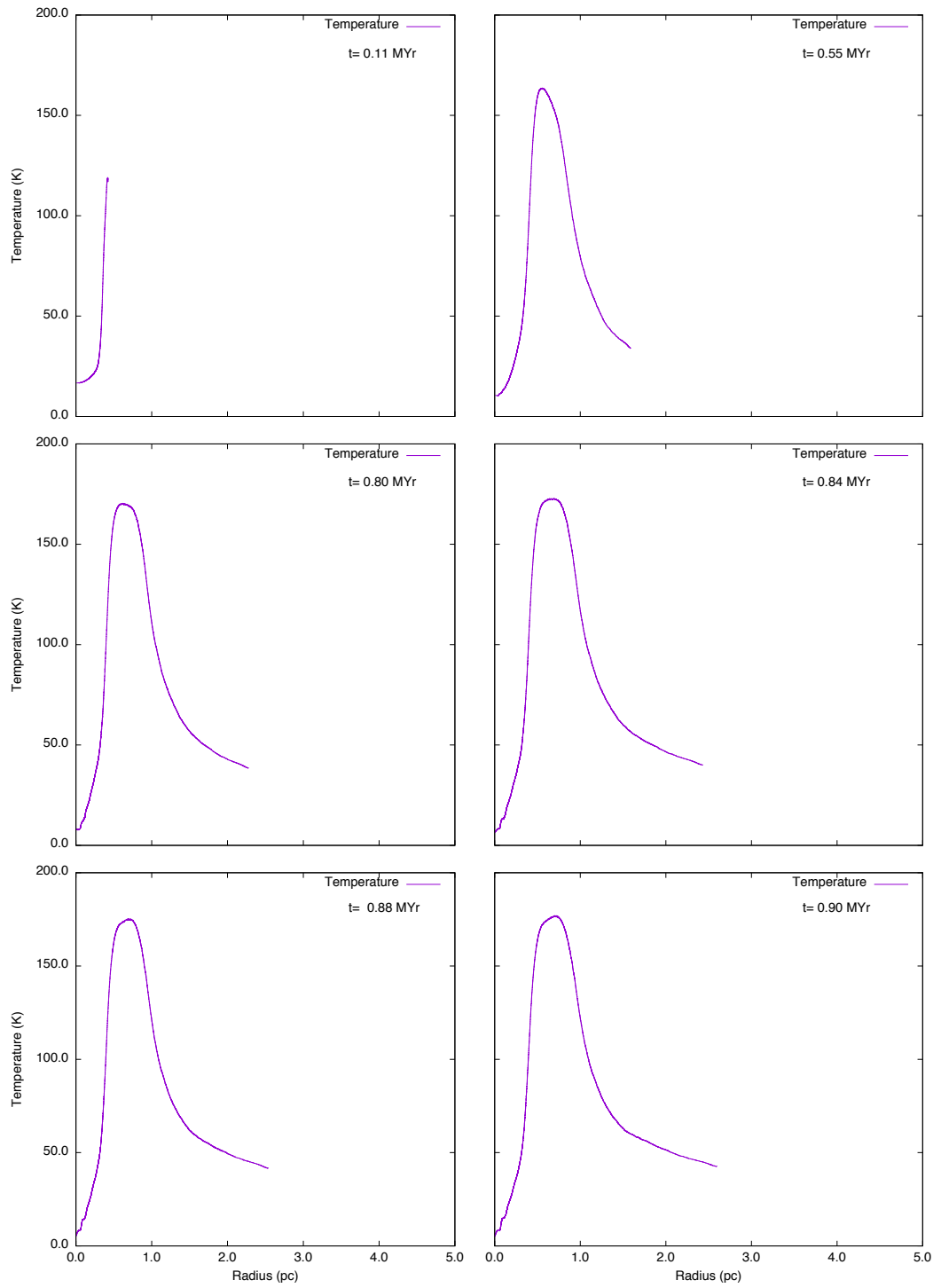Figure B.19: FUV radiation $= 1$ G_0. Six snapshots showing temperature (purple line) for a cloud with an initial density of 2000 cm^{-3}, a mass of 2 $M_\odot$ and a radius of 0.17 pc.
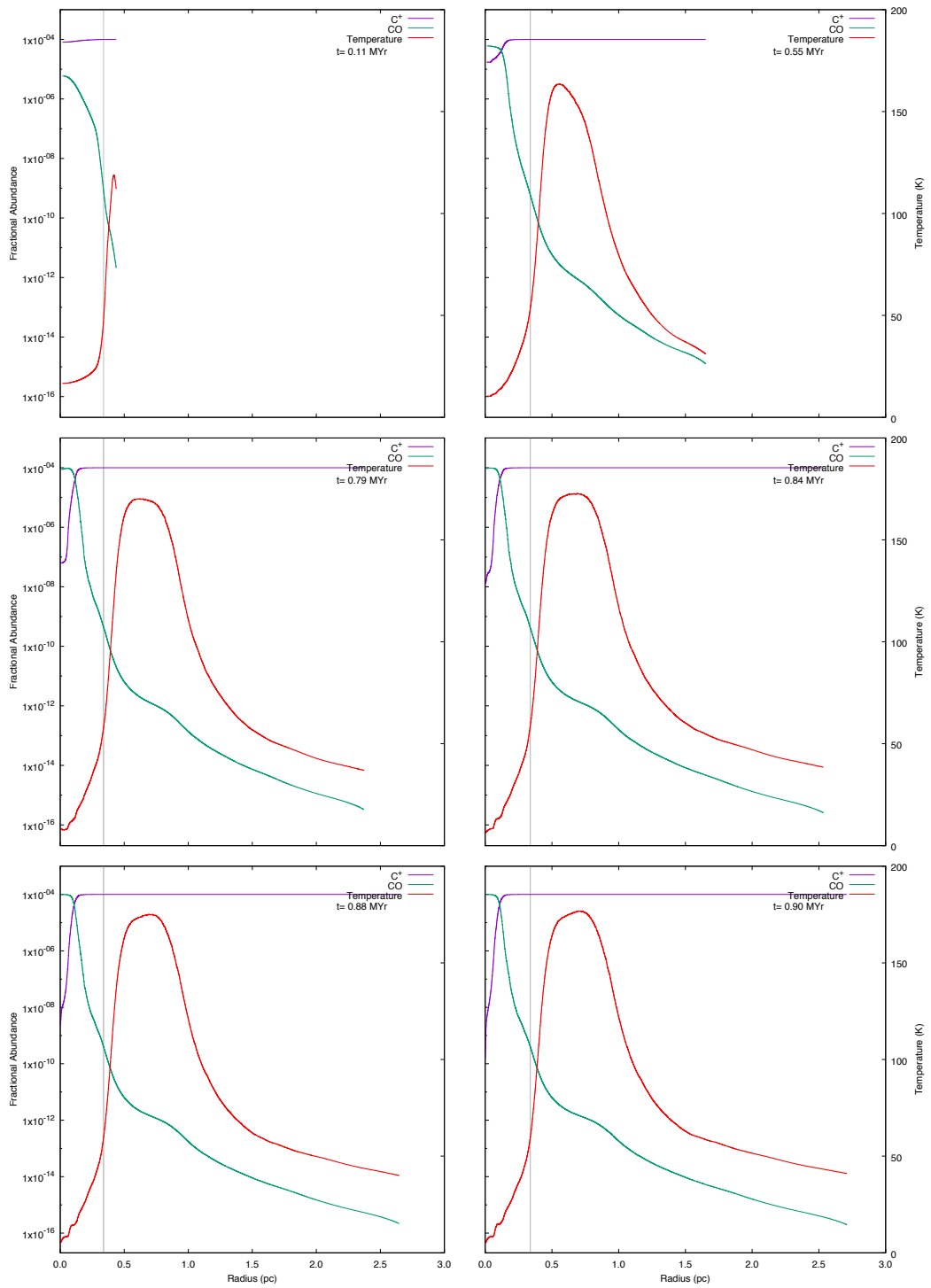
Figure B.20: FUV radiation = 1 G_0: six snapshots showing the chemical abundances of CO and C^+ for a cloud with an initial density of 2000 cm^{-3}, a mass of 2 $M_\odot$ and a radius of 0.17 pc.
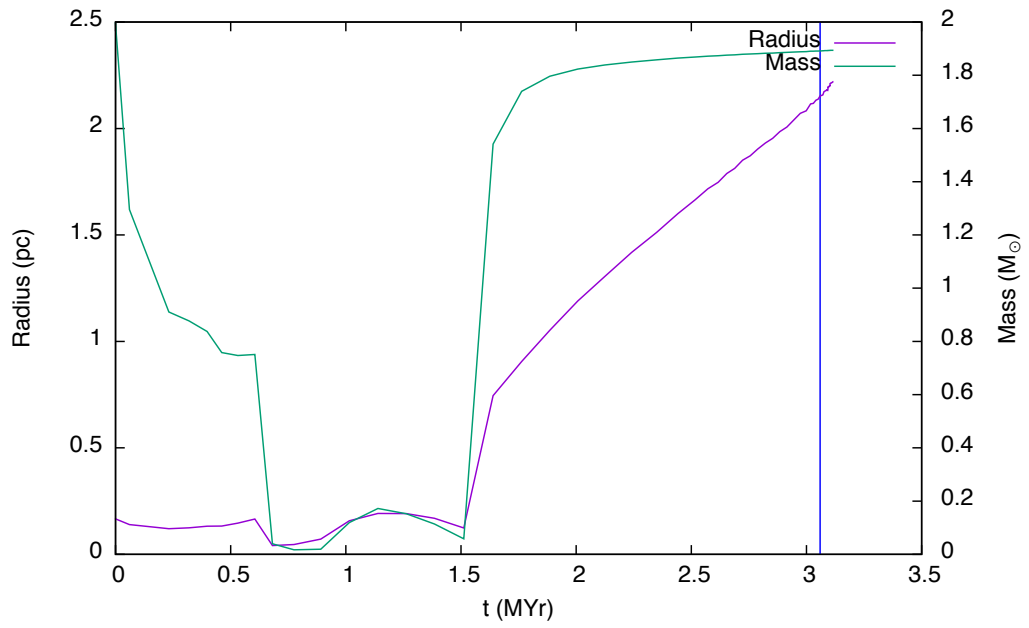
Figure B.21: FUV radiation = 1 G_0: the time evolution of a cloud with an initial density of 5000 cm^{-3}, a mass of 2 M$_\odot$ and a radius of 0.13 pc is shown in this graph. The cloud radius (purple line) is taken to be the zero crossing point of radial velocity and the mass (green line) is taken to be that which lies inside the radius. The blue vertical line denotes the time at which the high density peak first forms. This is the minimum cloud mass which collapses for the selected values of density and FUV flux.

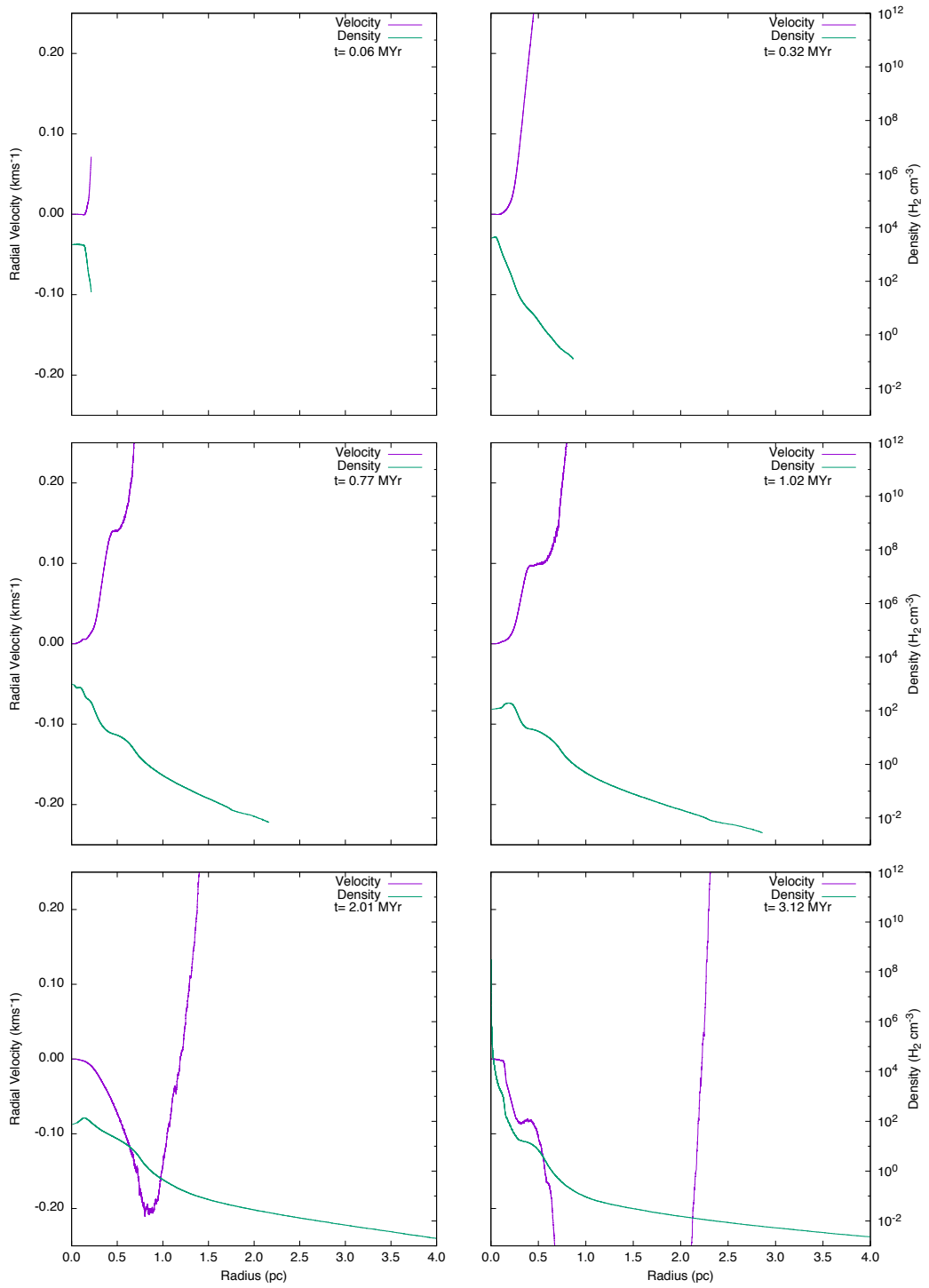Figure B.22: FUV radiation $= 1 \, \mathrm{G}_0$. Six snapshots showing radial velocity (purple line) and density (green line) for a cloud with an initial density of 5000 cm^{-3}, a mass of 2 M$_\odot$ and a radius of 0.13 pc.

Figure B.23: FUV radiation $= 1$ G_0. Six snapshots showing temperature (purple line) for a cloud with an initial density of 5000 cm^{-3}, a mass of 2 M$_\odot$ and a radius of 1.69 pc.

Figure B.24: FUV radiation = 1 G$_0$: six snapshots showing the chemical abundances of CO and C$^+$ for a cloud with an initial density of 5000 cm^{-3}, a mass of 2 M$_\odot$ and a radius of 0.12 pc.

Figure B.25: FUV radiation = 1 G_0: the time evolution of a cloud with an initial density of 10000 cm^{-3}, a mass of 0.9 M$_\odot$ and a radius of 0.08 pc is shown in this graph. The cloud radius (purple line) is taken to be the zero crossing point of radial velocity and the mass (green line) is taken to be that which lies inside the radius. The blue vertical line denotes the time at which the high density peak first forms. This is the minimum cloud mass which collapses for the selected values of density and FUV flux.

Figure B.26: FUV radiation $= 1\,G_0$. Six snapshots showing radial velocity (purple line) and density (green line) for a cloud with an initial density of 10000 cm^{-3}, a mass of 0.9 M$_\odot$ and a radius of 0.08 pc.
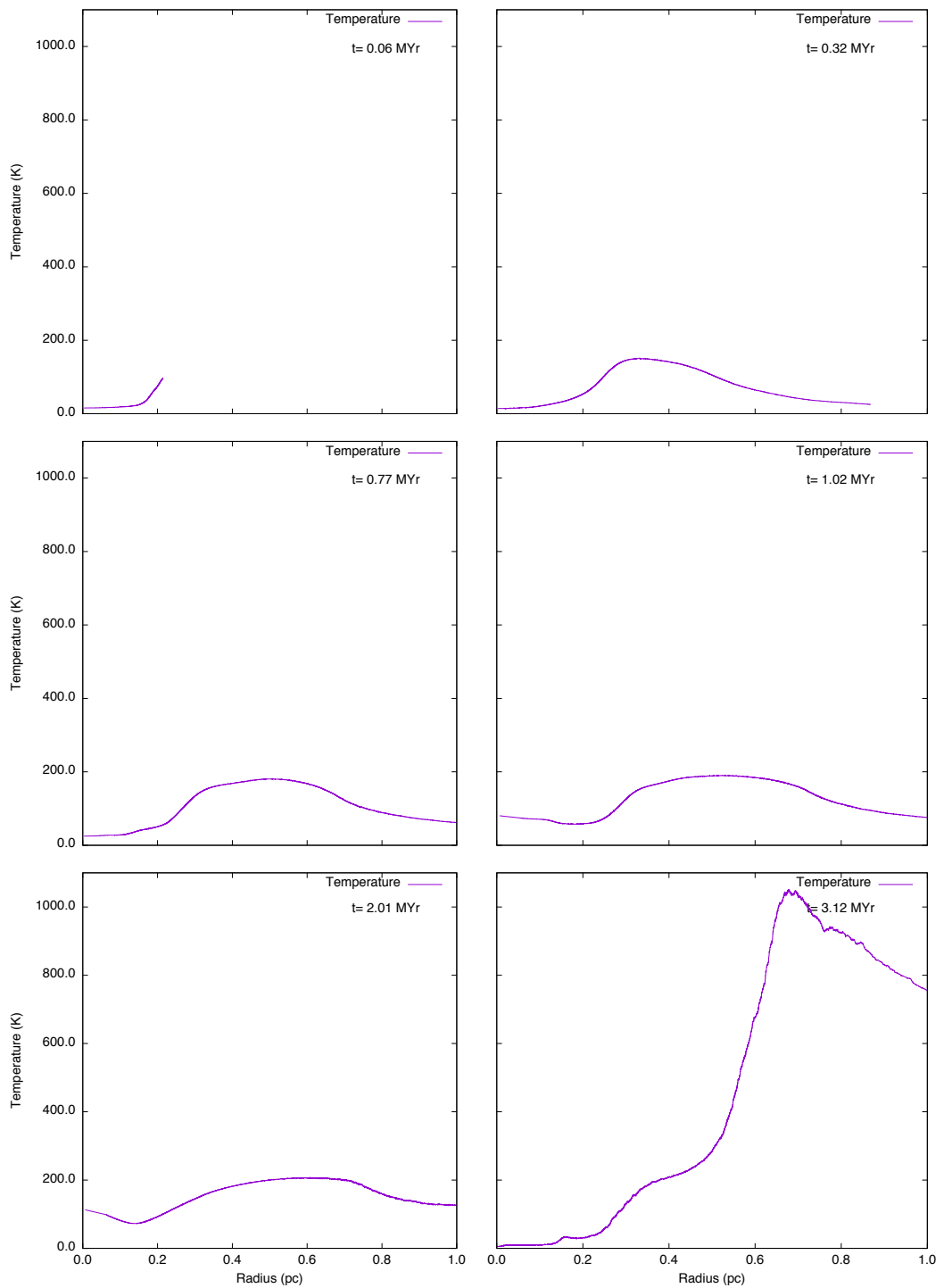
Figure B.27: FUV radiation $= 1$ G$_0$. Six snapshots showing temperature (purple line) for a cloud with an initial density of 10000 cm^{-3}, a mass of 0.9 M$_\odot$ and a radius of 1.69 pc.
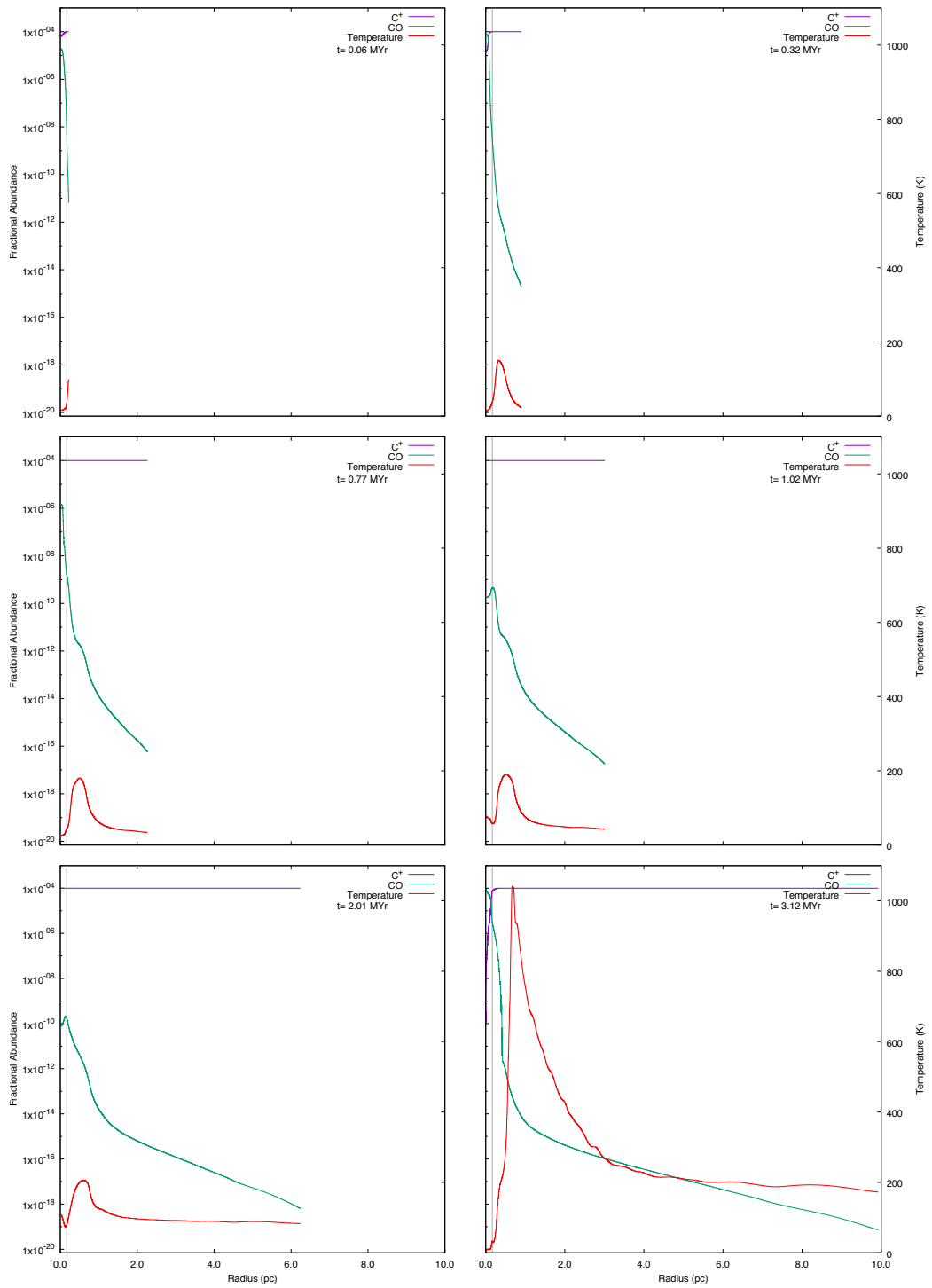
Figure B.28: FUV radiation $= 1$ G_0: six snapshots showing the chemical abundances of CO and C^+ for a cloud with an initial density of 10000 cm^{-3}, a mass of 0.9 M$_\odot$ and a radius of 0.08 pc.
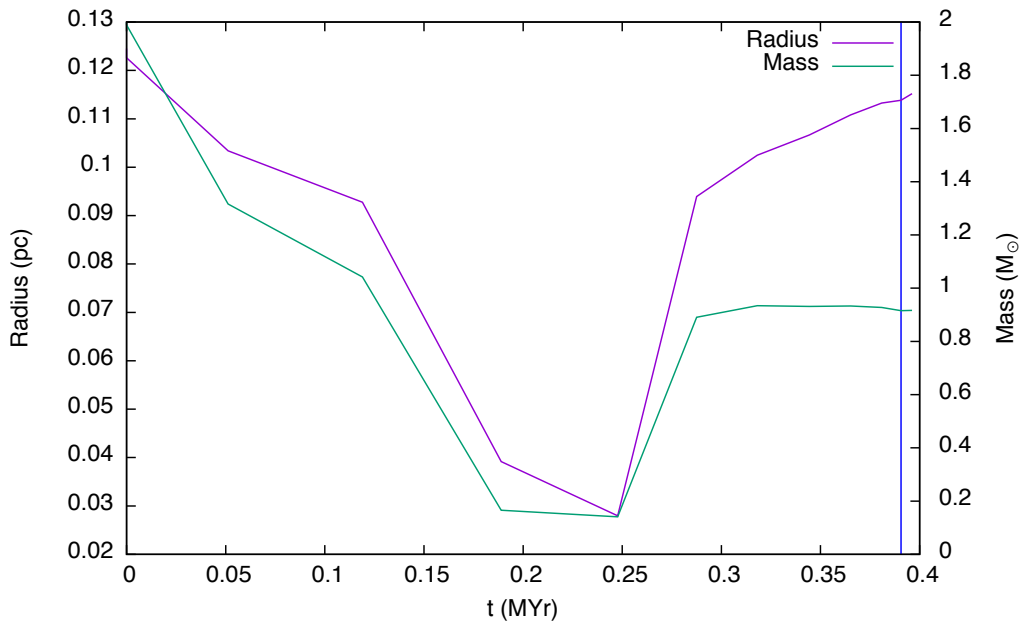
B.2 Set 2G$_0$
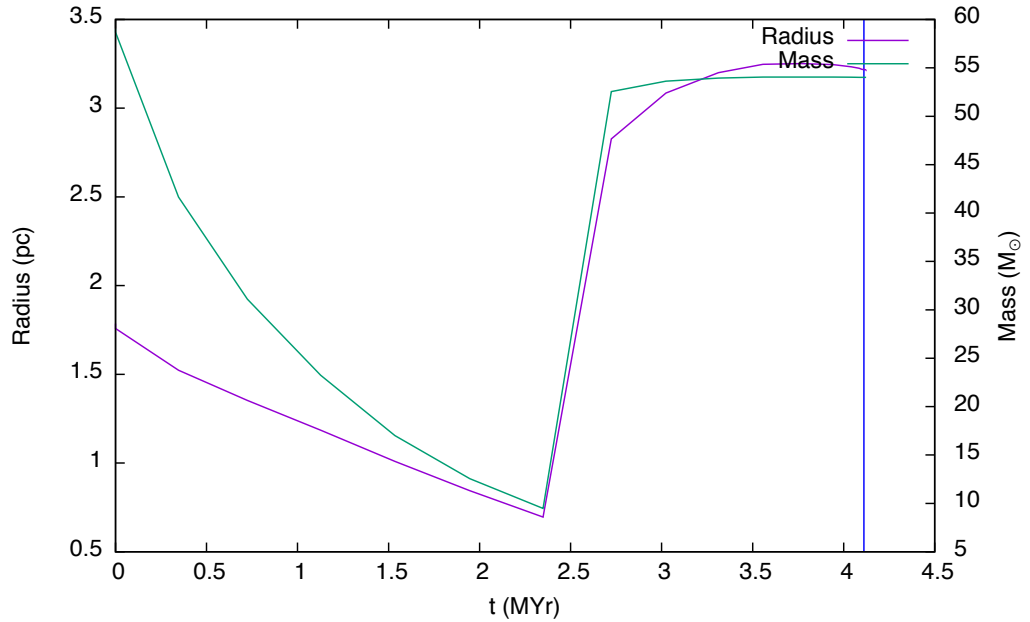
Figure B.29: FUV = 2 G_0. The time evolution of a cloud with an initial density of 50 cm^{-3}, a mass of 59 M$_\odot$ and a radius of 1.79 pc is shown in this graph. The cloud radius (purple line) is taken to be the zero crossing point of radial velocity and the mass (green line) is taken to be that which lies inside the radius. The blue vertical line denotes the time at which the high density peak first forms. This is the minimum cloud mass which collapses for the selected values of density and FUV flux.
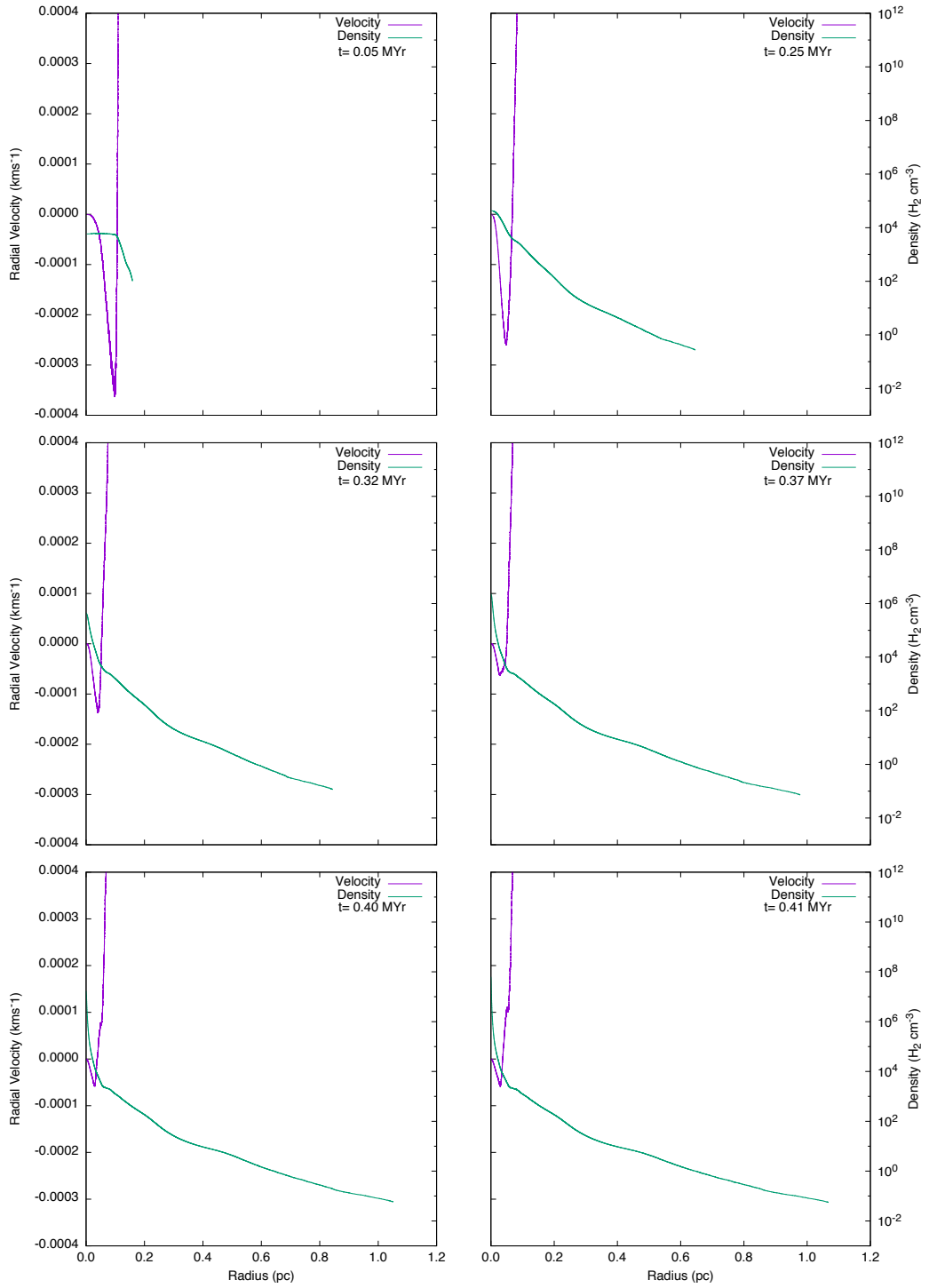
Figure B.30: FUV $= 2$ G_0. Six snapshots showing radial velocity (purple line) and density (green line) for a cloud with an initial density of 50 cm^{-3}, a mass of 59 M$_\odot$ and a radius of 1.79 pc.
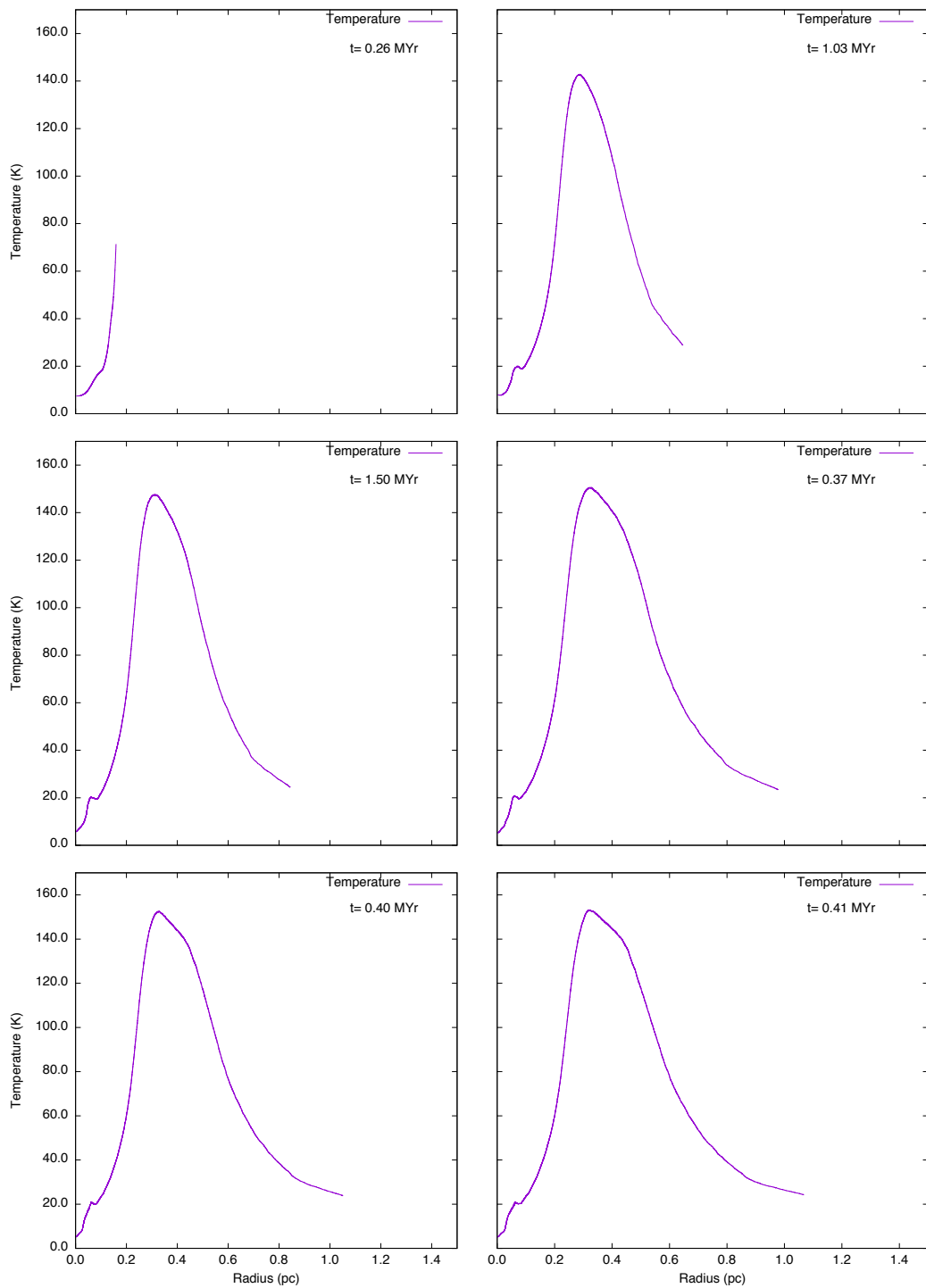
Figure B.31: FUV $= 2 \, G_0$. Six snapshots showing temperature (purple line) for a cloud with an initial density of 50 cm^{-3}, a mass of 59 M$_\odot$ and a radius of 1.79 pc.
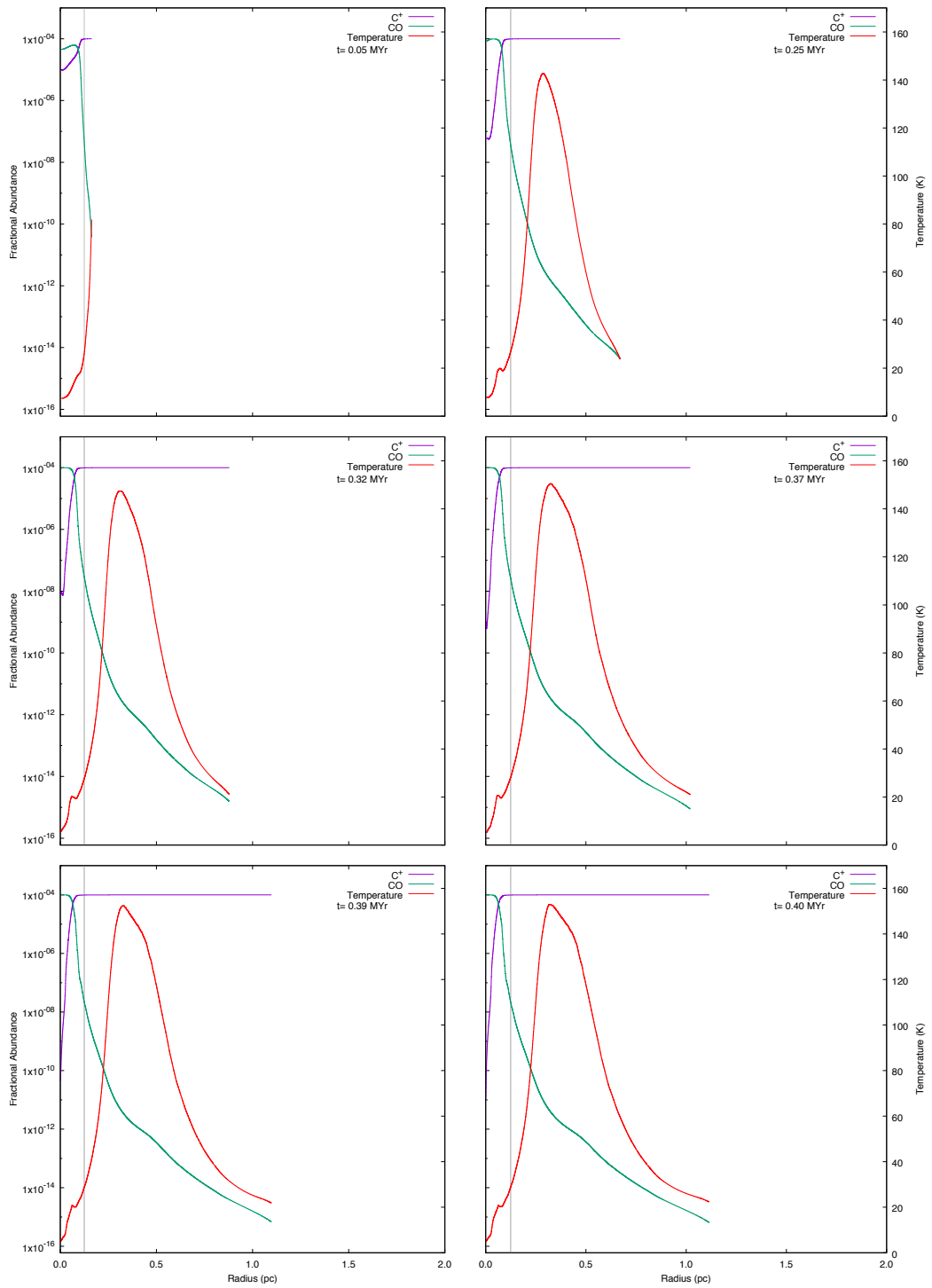
Figure B.32: FUV radiation = 2 G_0: six snapshots showing the chemical abundances of CO and C^+ for a cloud with an initial density of 50 cm^{-3}, a mass of 59 $M_\odot$ and a radius of 1.79 pc.
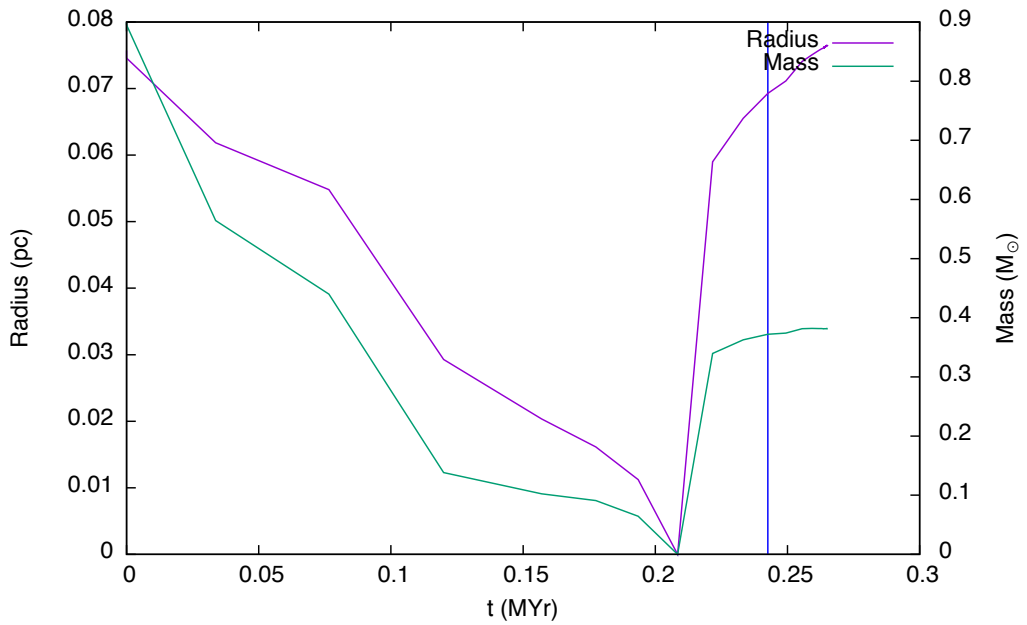
Figure B.33: FUV = 2 G_0. The time evolution of a cloud with an initial density of 100 cm^{-3}, a mass of 25 M$_\odot$ and a radius of 1.06 pc is shown in this graph. The cloud radius (purple line) is taken to be the zero crossing point of radial velocity and the mass (green line) is taken to be that which lies inside the radius. The blue vertical line denotes the time at which the high density peak first forms. This is the minimum cloud mass which collapses for the selected values of density and FUV flux.
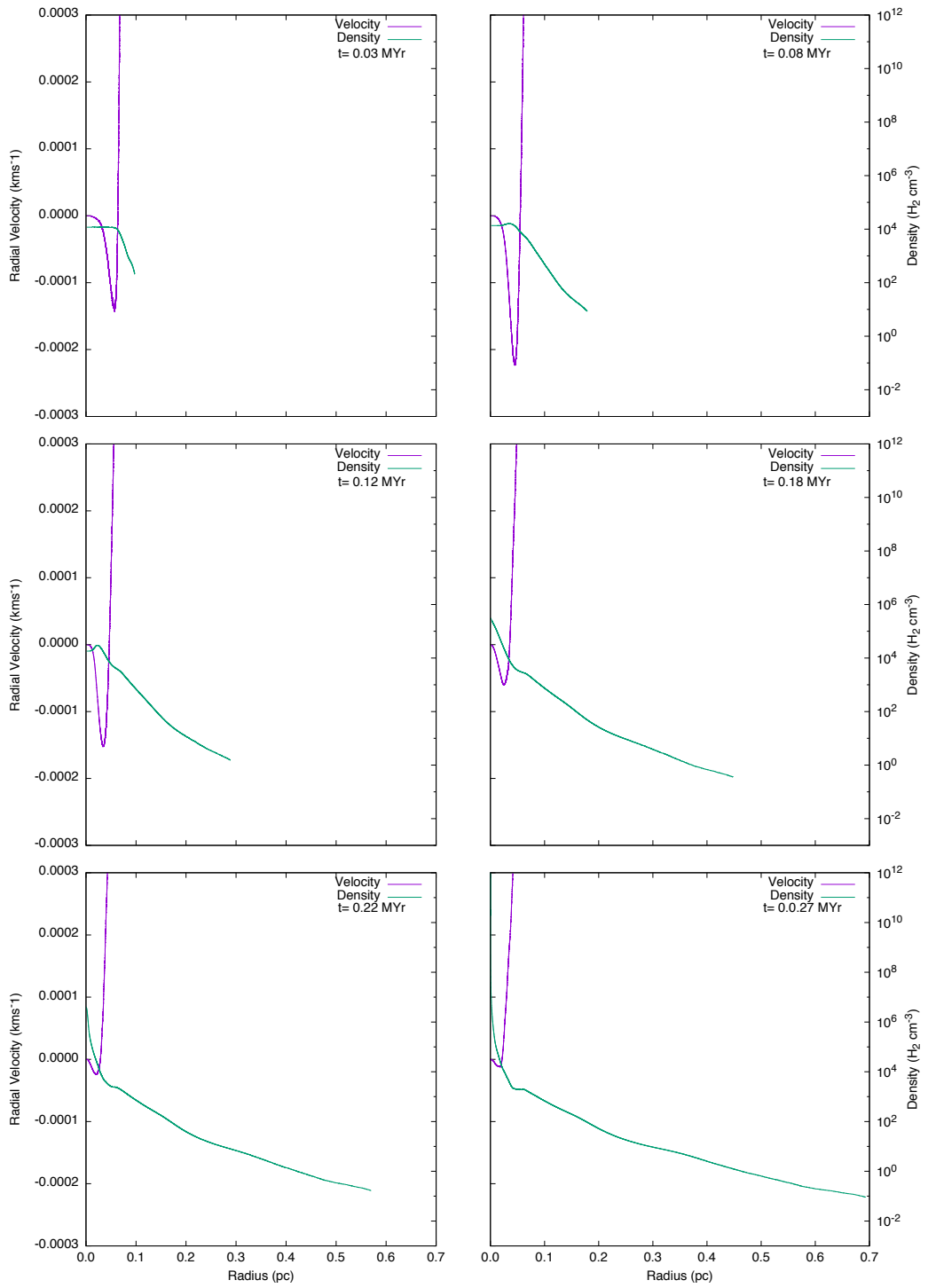
Figure B.34: FUV $= 2\ G_0$. Six snapshots showing radial velocity (purple line) and density (green line) for a cloud with an initial density of 100 cm^{-3}, a mass of 25 M$_\odot$ and a radius of 1.06 pc.
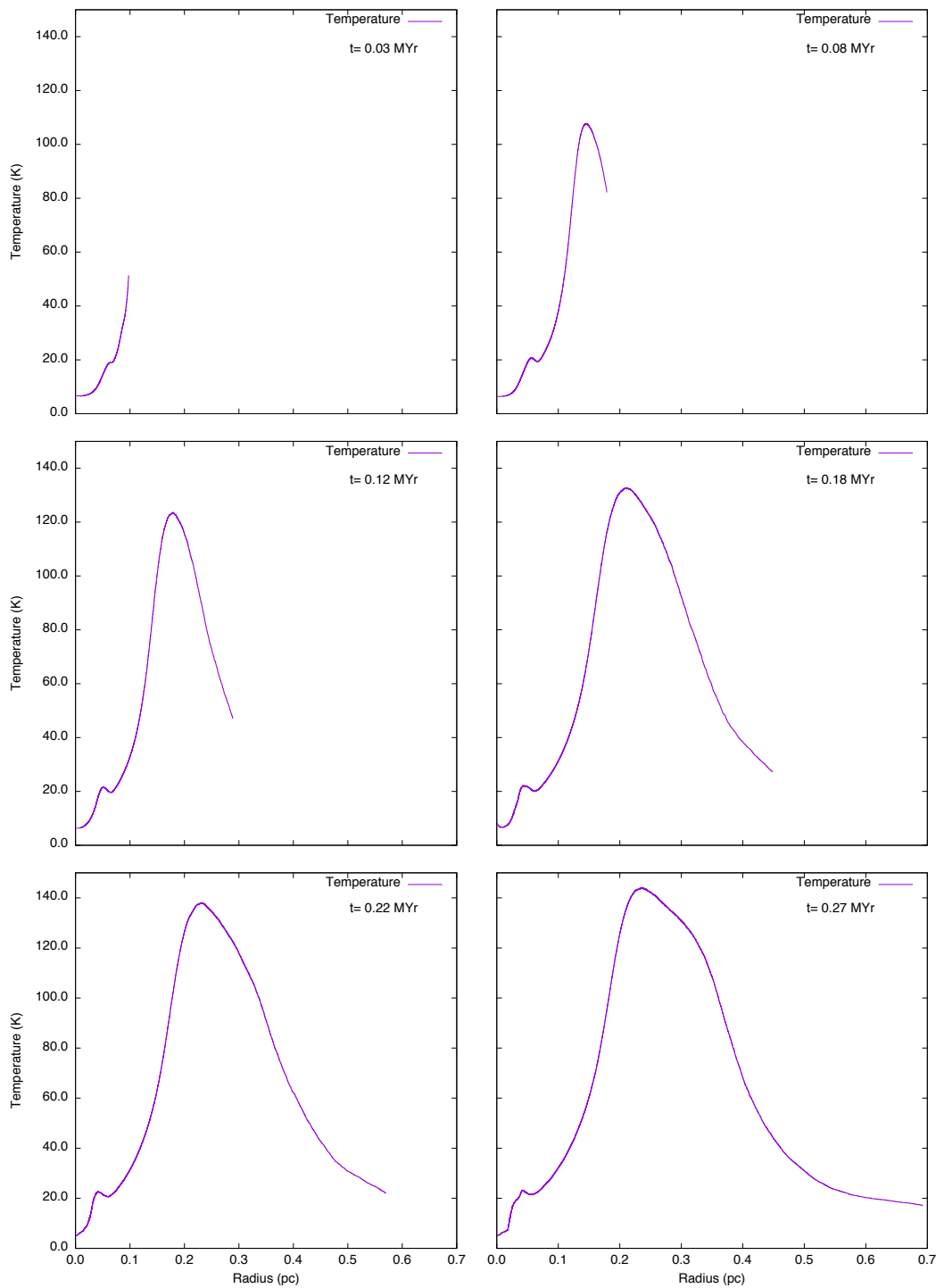
Figure B.35: FUV = 2 G_0. Six snapshots showing temperature (purple line) for a cloud with an initial density of 100 cm^{-3}, a mass of 25 M$_\odot$ and a radius of 1.06 pc.
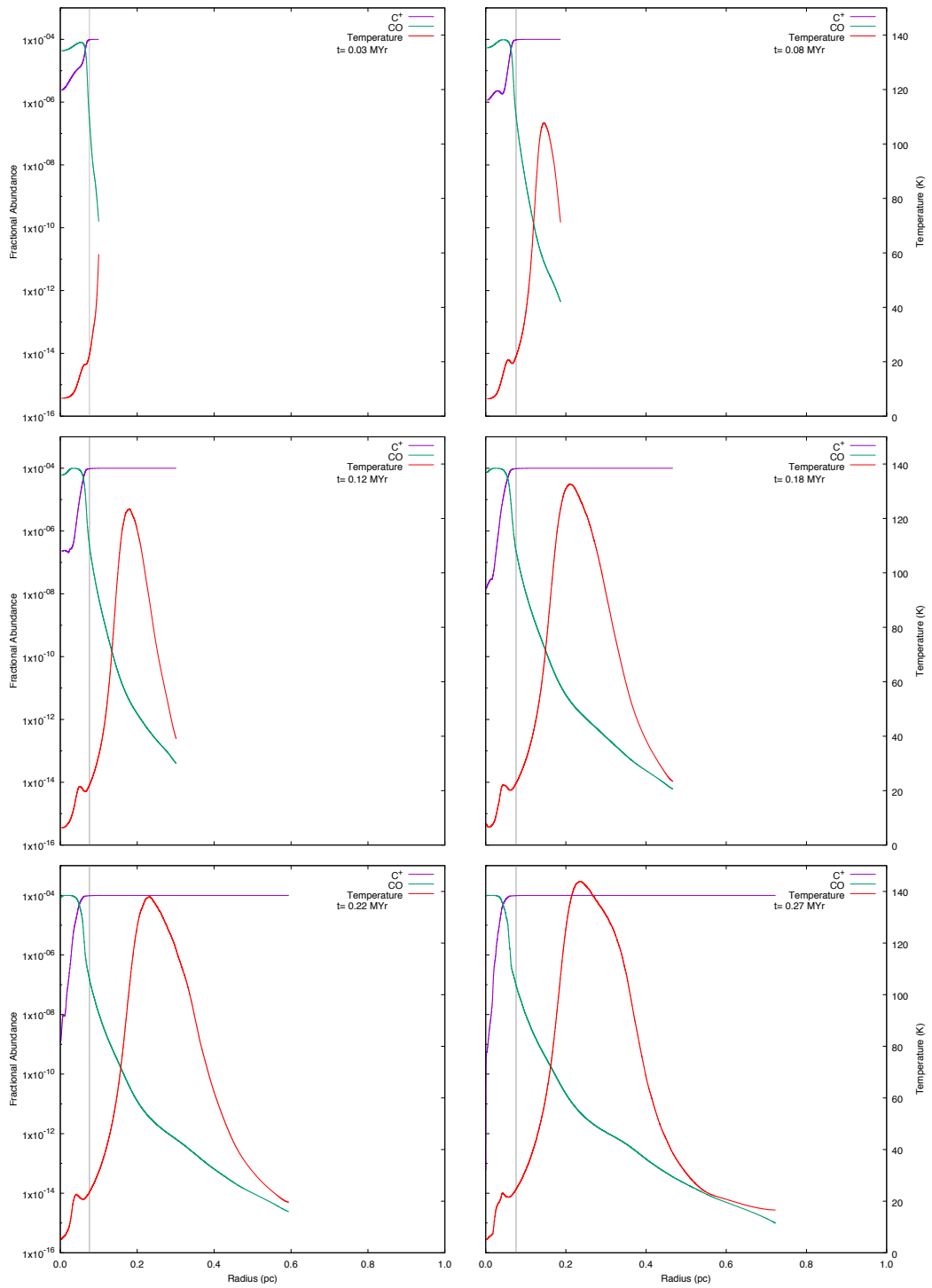
Figure B.36: FUV radiation = 2 G$_0$: six snapshots showing the chemical abundances of CO and C$^+$ for a cloud with an initial density of 100 cm^{-3}, a mass of 25 M$_\odot$ and a radius of 1.06 pc.
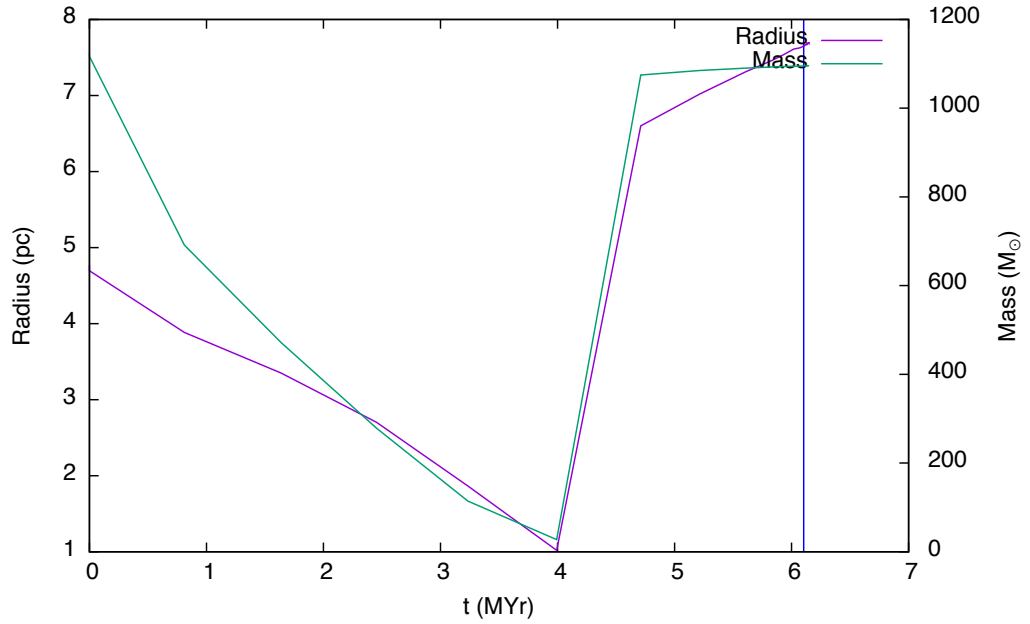
Figure B.37: FUV = 2 G_0. The time evolution of a cloud with an initial density of 200 cm^{-3}, a mass of 15 M$_\odot$ and a radius of 0.71 pc is shown in this graph. The cloud radius (purple line) is taken to be the zero crossing point of radial velocity and the mass (green line) is taken to be that which lies inside the radius. The blue vertical line denotes the time at which the high density peak first forms. This is the minimum cloud mass which collapses for the selected values of density and FUV flux.
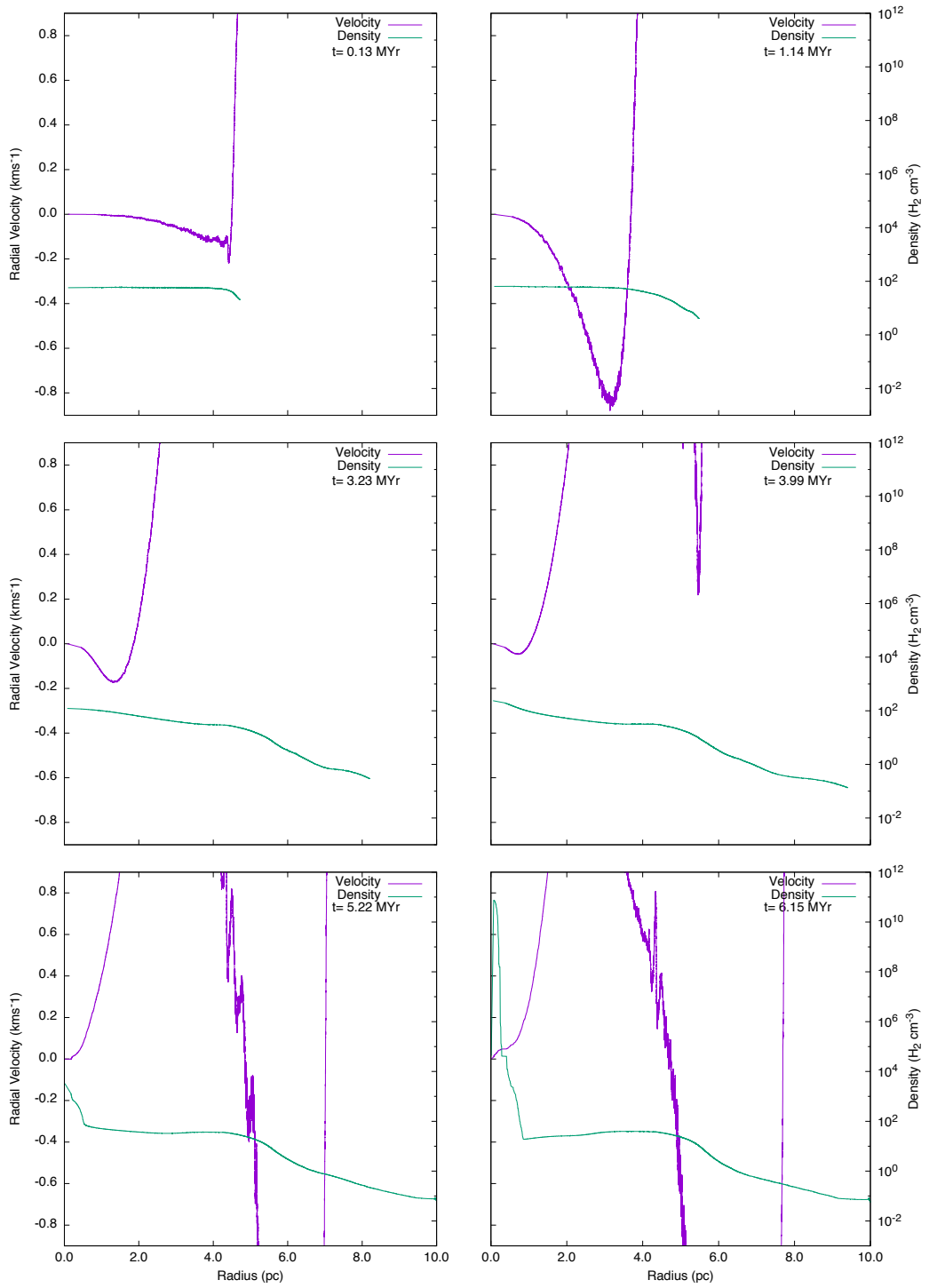
Figure B.38: FUV = 2 G_0. Six snapshots showing radial velocity (purple line) and density (green line) for a cloud with an initial density of 200 cm^{-3}, a mass of 15 M$_\odot$ and a radius of 0.71 pc.

Figure B.39: FUV $= 2\ G_0$. Six snapshots showing temperature (purple line) for a cloud with an initial density of 200 cm^{-3}, a mass of 15 M$_\odot$ and a radius of 0.71 pc.

Figure B.40: FUV radiation = 2 G_0: six snapshots showing the chemical abundances of CO and C^+ for a cloud with an initial density of 200 cm^{-3}, a mass of 15 $M_\odot$ and a radius of 0.71 pc.

Figure B.41: FUV = 2 G_0. The time evolution of a cloud with an initial density of 1000 cm^{-3}, a mass of 8 M$_\odot$ and a radius of 0.34 pc is shown in this graph. The cloud radius (purple line) is taken to be the zero crossing point of radial velocity and the mass (green line) is taken to be that which lies inside the radius. The blue vertical line denotes the time at which the high density peak first forms. This is the minimum cloud mass which collapses for the selected values of density and FUV flux.

Figure B.42: FUV = 2 G_0. Six snapshots showing radial velocity (purple line) and density (green line) for a cloud with an initial density of 1000 cm^{-3}, a mass of 8 M$_\odot$ and a radius of 0.34 pc.
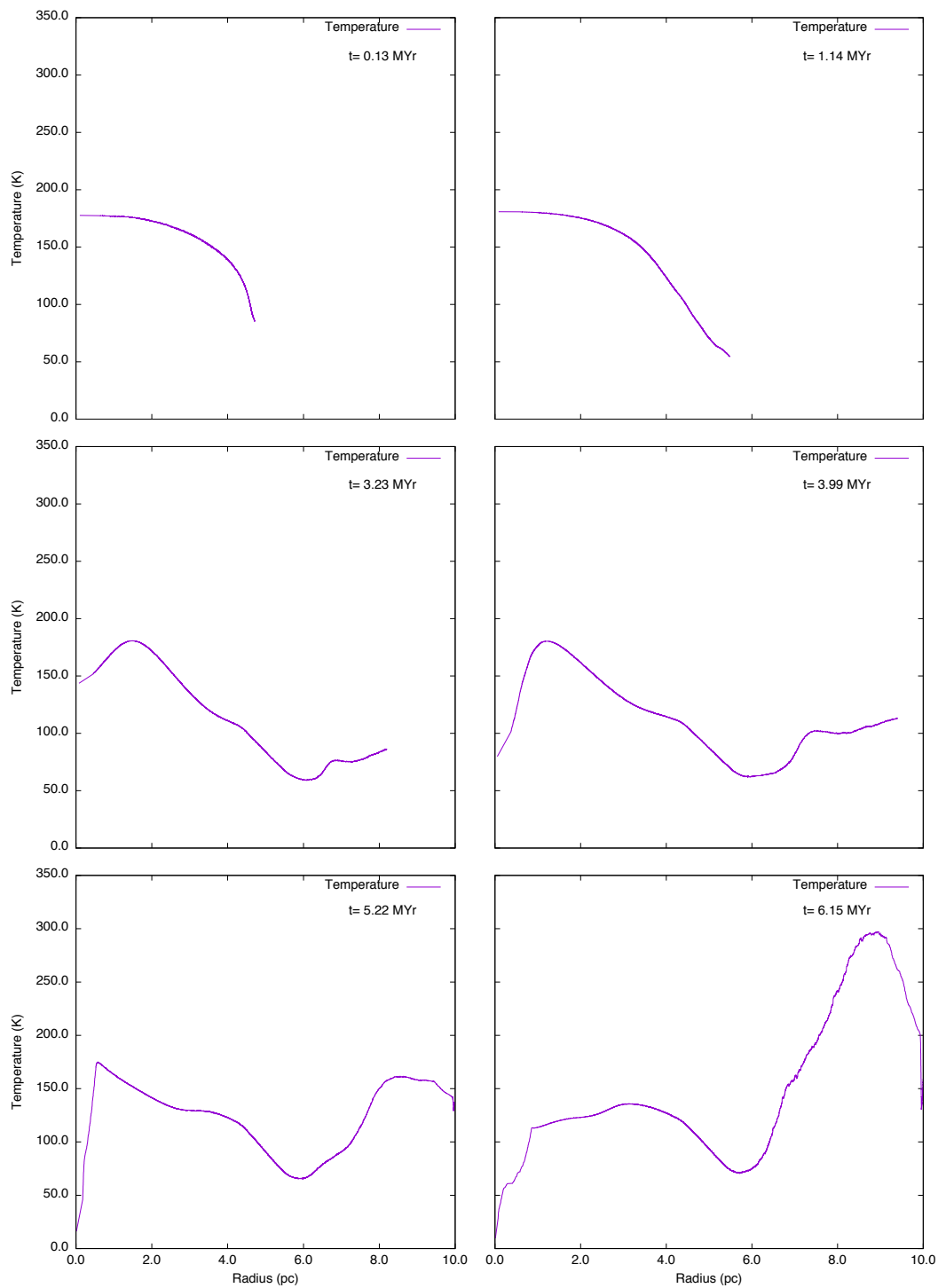
Figure B.43: FUV $= 2$ G_0. Six snapshots showing temperature (purple line) for a cloud with an initial density of 1000 cm^{-3}, a mass of 8 M$_\odot$ and a radius of 0.34 pc.
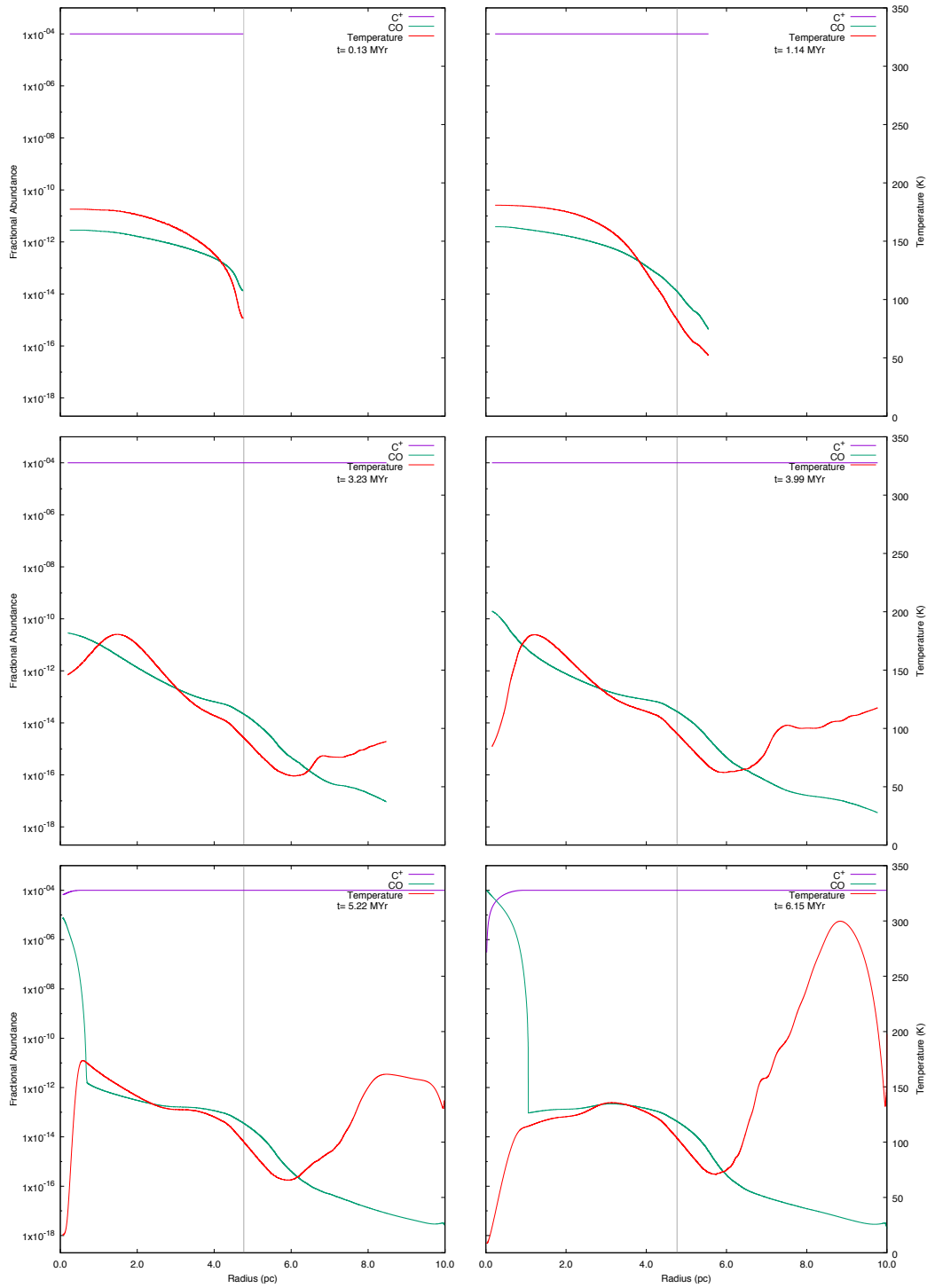
Figure B.44: FUV radiation $= 2$ G_0: six snapshots showing the chemical abundances of CO and C^+ for a cloud with an initial density of 1000 cm^{-3}, a mass of 8 M$_\odot$ and a radius of 0.34 pc.
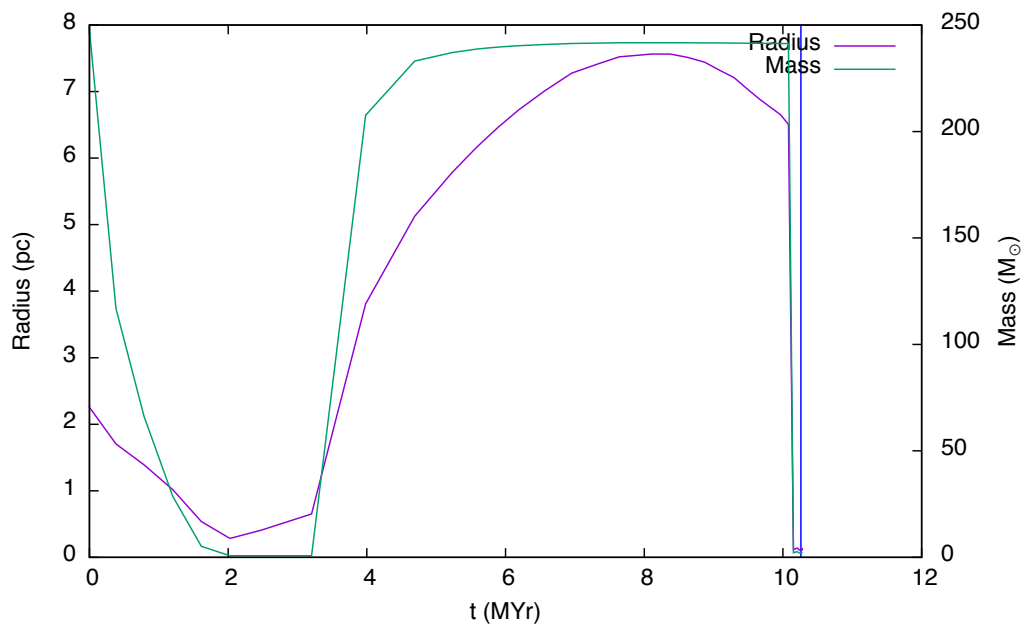
Figure B.45: FUV = 2 G_0. The time evolution of a cloud with an initial density of 2000 cm^{-3}, a mass of 2 M$_\odot$ and a radius of 0.17 pc is shown in this graph. The cloud radius (purple line) is taken to be the zero crossing point of radial velocity and the mass (green line) is taken to be that which lies inside the radius. The blue vertical line denotes the time at which the high density peak first forms. This is the minimum cloud mass which collapses for the selected values of density and FUV flux.
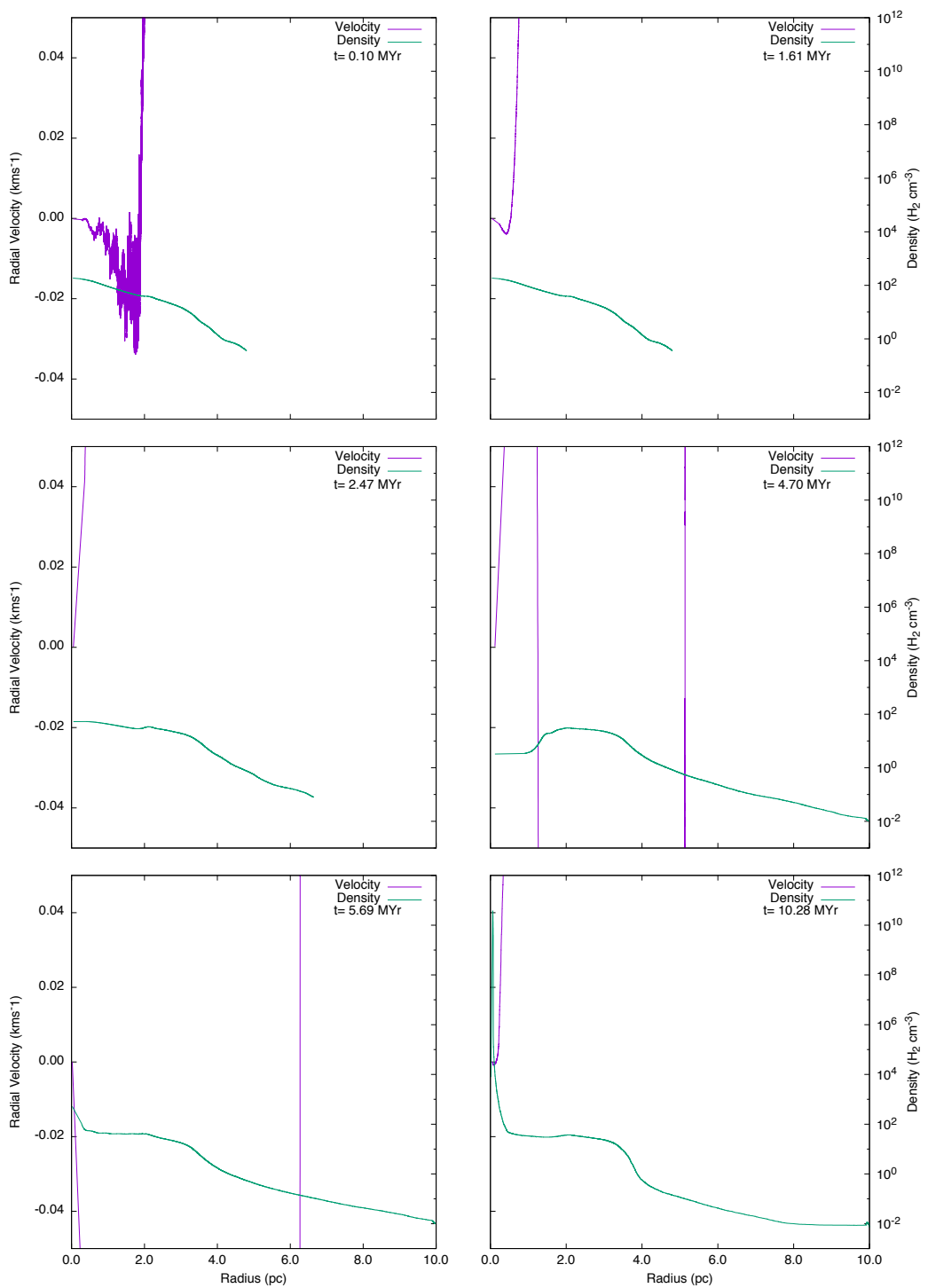
Figure B.46: FUV $= 2$ G_0. Six snapshots showing radial velocity (purple line) and density (green line) for a cloud with an initial density of 2000 cm^{-3}, a mass of 2 M$_\odot$ and a radius of 0.17 pc.
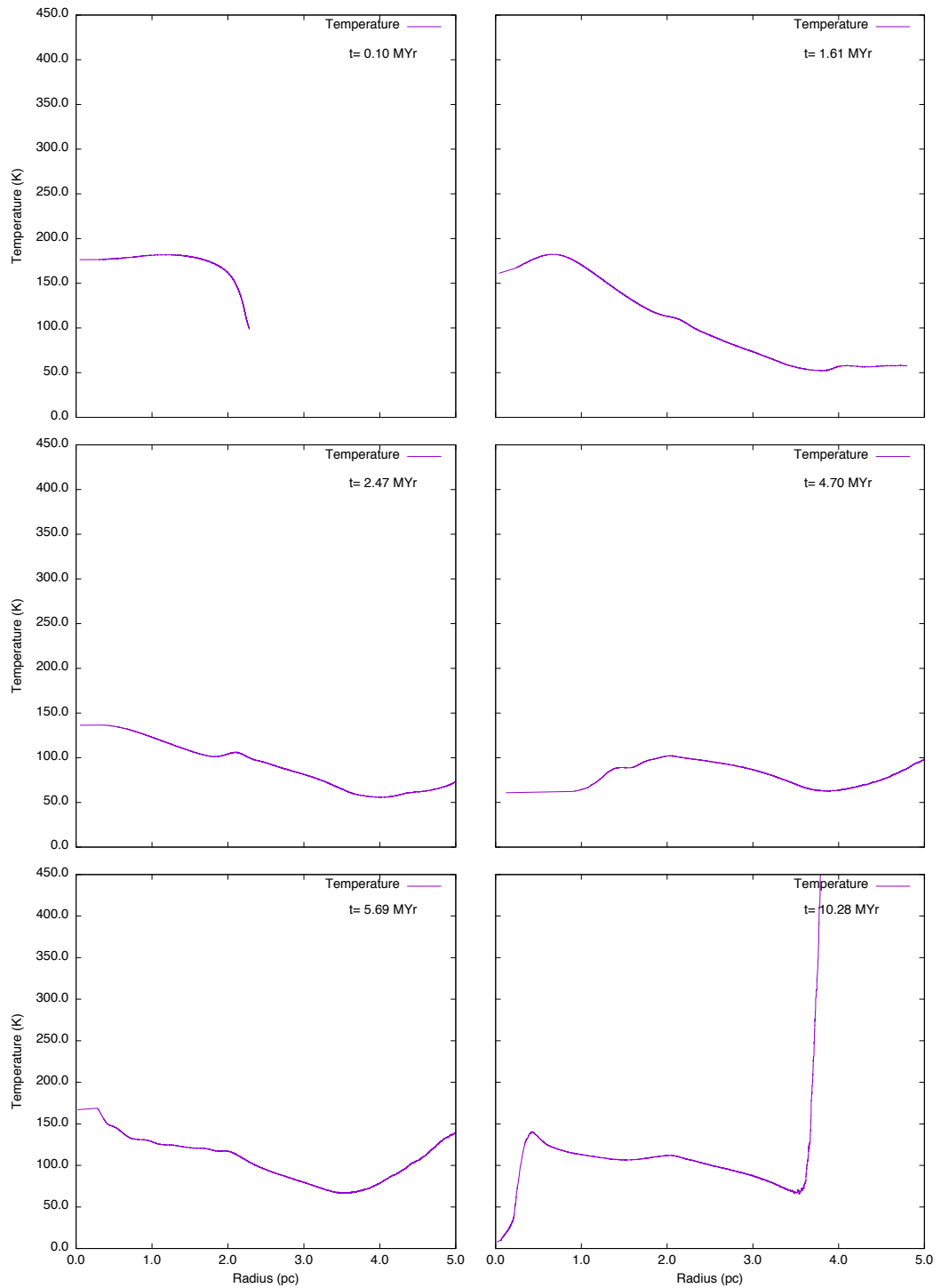
Figure B.47: FUV = 2 G_0. Six snapshots showing temperature (purple line) for a cloud with an initial density of 2000 cm^{-3}, a mass of 2 M$_\odot$ and a radius of 0.17 pc.
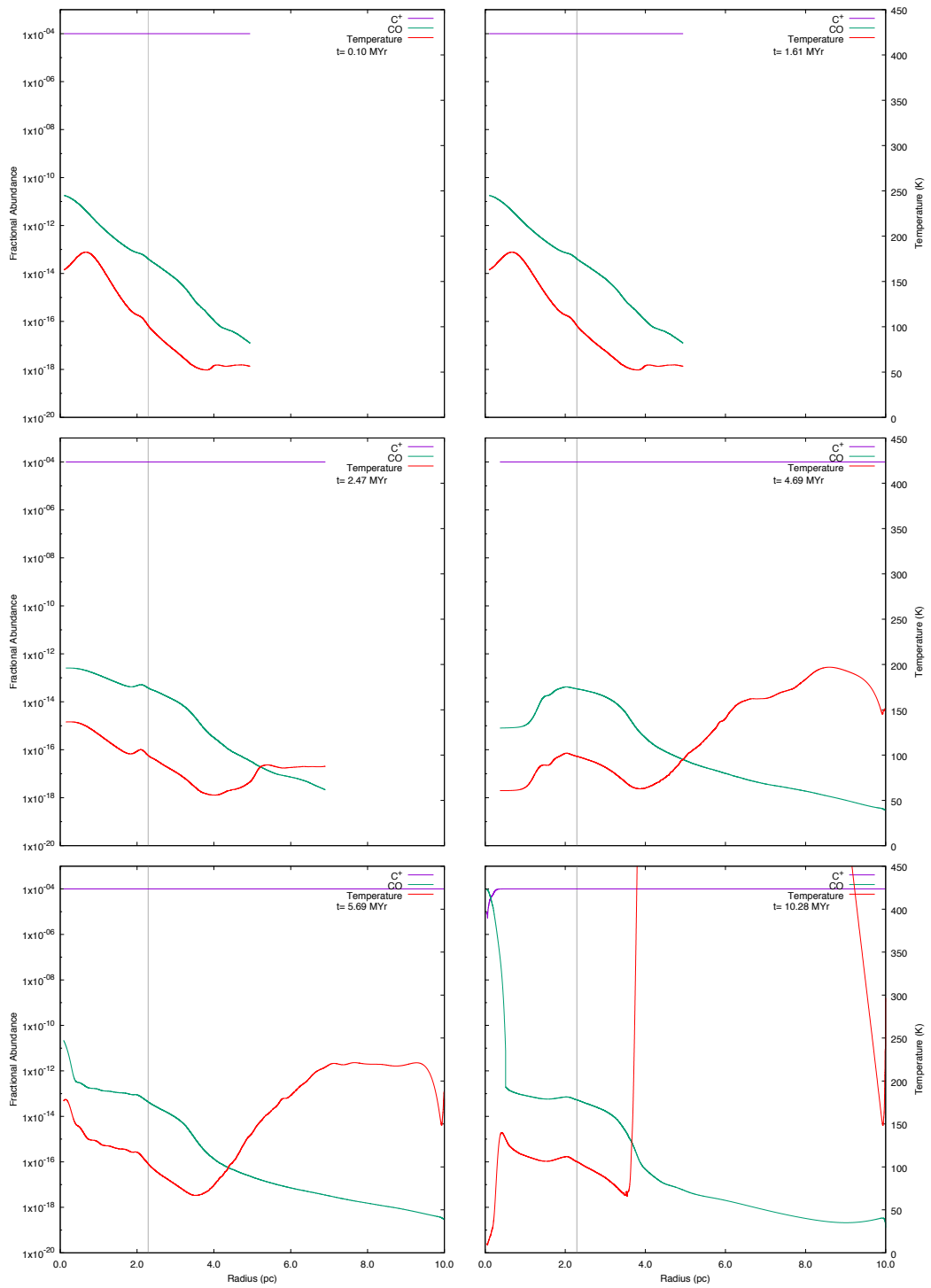
Figure B.48: FUV radiation = 2 G_0: six snapshots showing the chemical abundances of CO and C^+ for a cloud with an initial density of 2000 cm^{-3}, a mass of 2 $M_\odot$ and a radius of 0.17 pc.
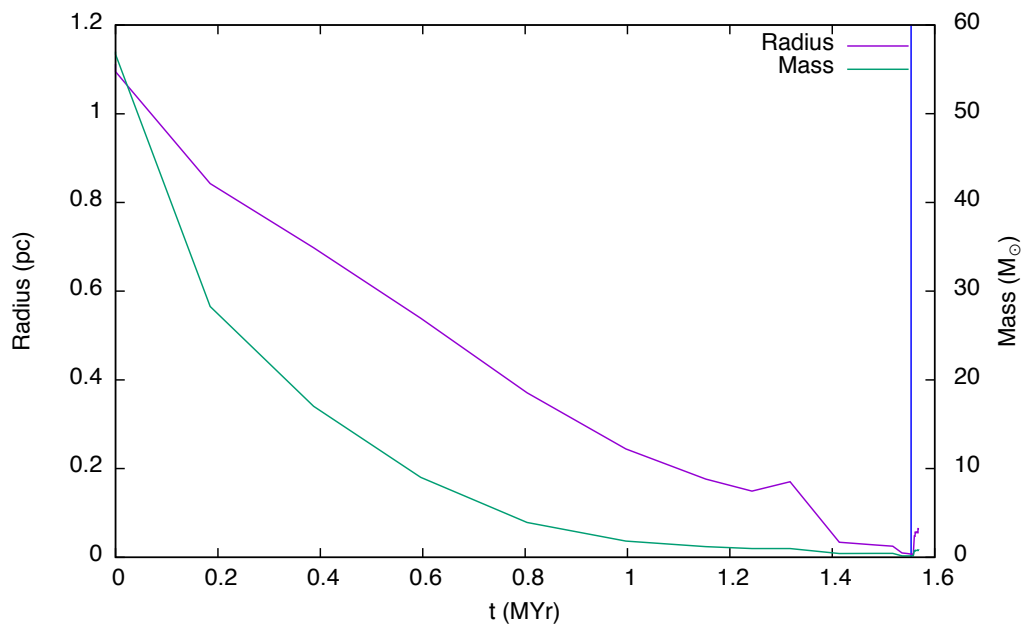
Figure B.49: FUV = 2 G_0. The time evolution of a cloud with an initial density of 5000 cm^{-3}, a mass of 2 M$_\odot$ and a radius of 0.13 pc is shown in this graph. The cloud radius (purple line) is taken to be the zero crossing point of radial velocity and the mass (green line) is taken to be that which lies inside the radius. The blue vertical line denotes the time at which the high density peak first forms. This is the minimum cloud mass which collapses for the selected values of density and FUV flux.
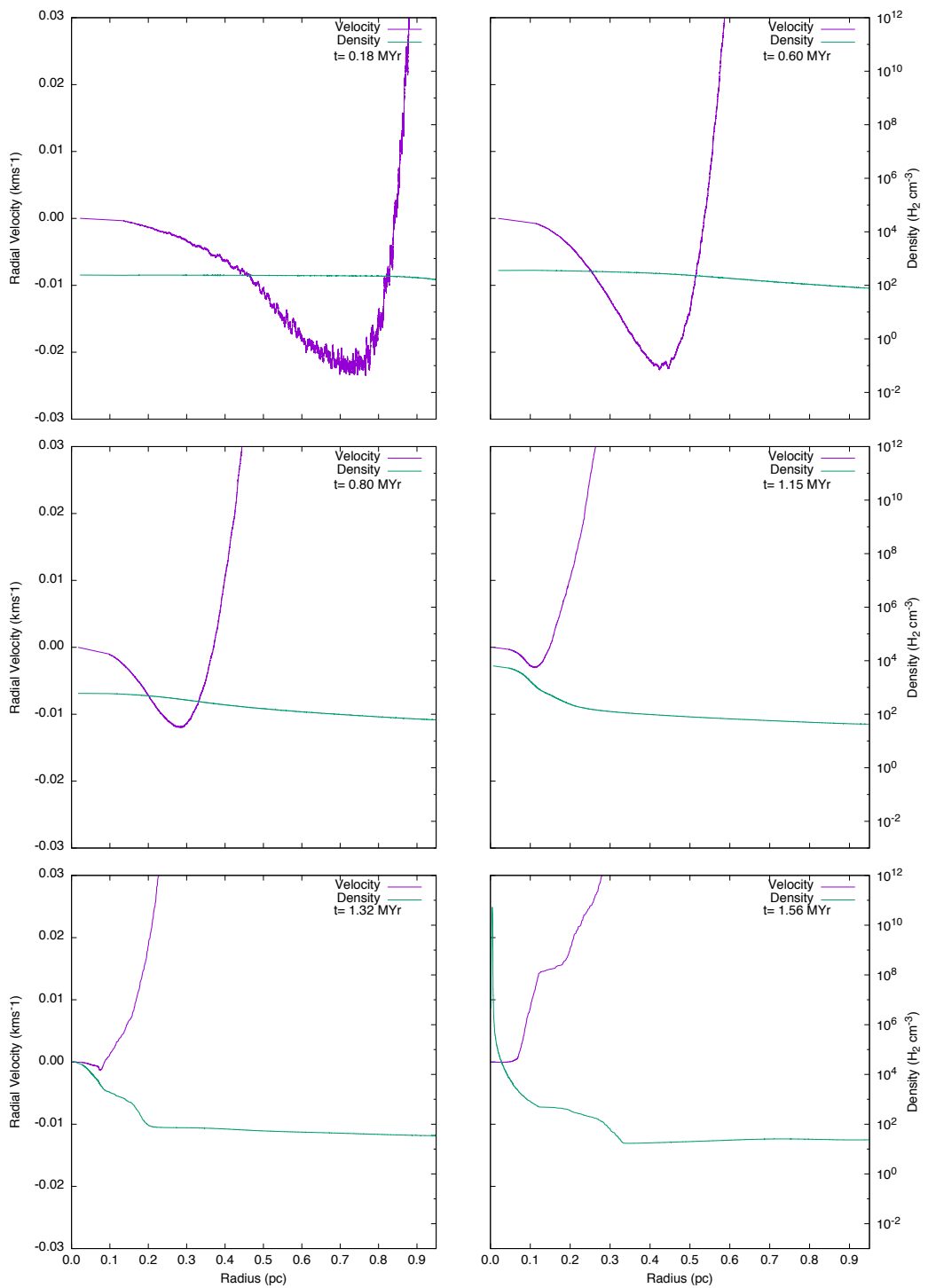
340

Figure B.50: FUV = 2 G_0. Six snapshots showing radial velocity (purple line) and density (green line) for a cloud with an initial density of 5000 cm^{-3}, a mass of 2 M$_\odot$ and a radius of 0.13 pc.
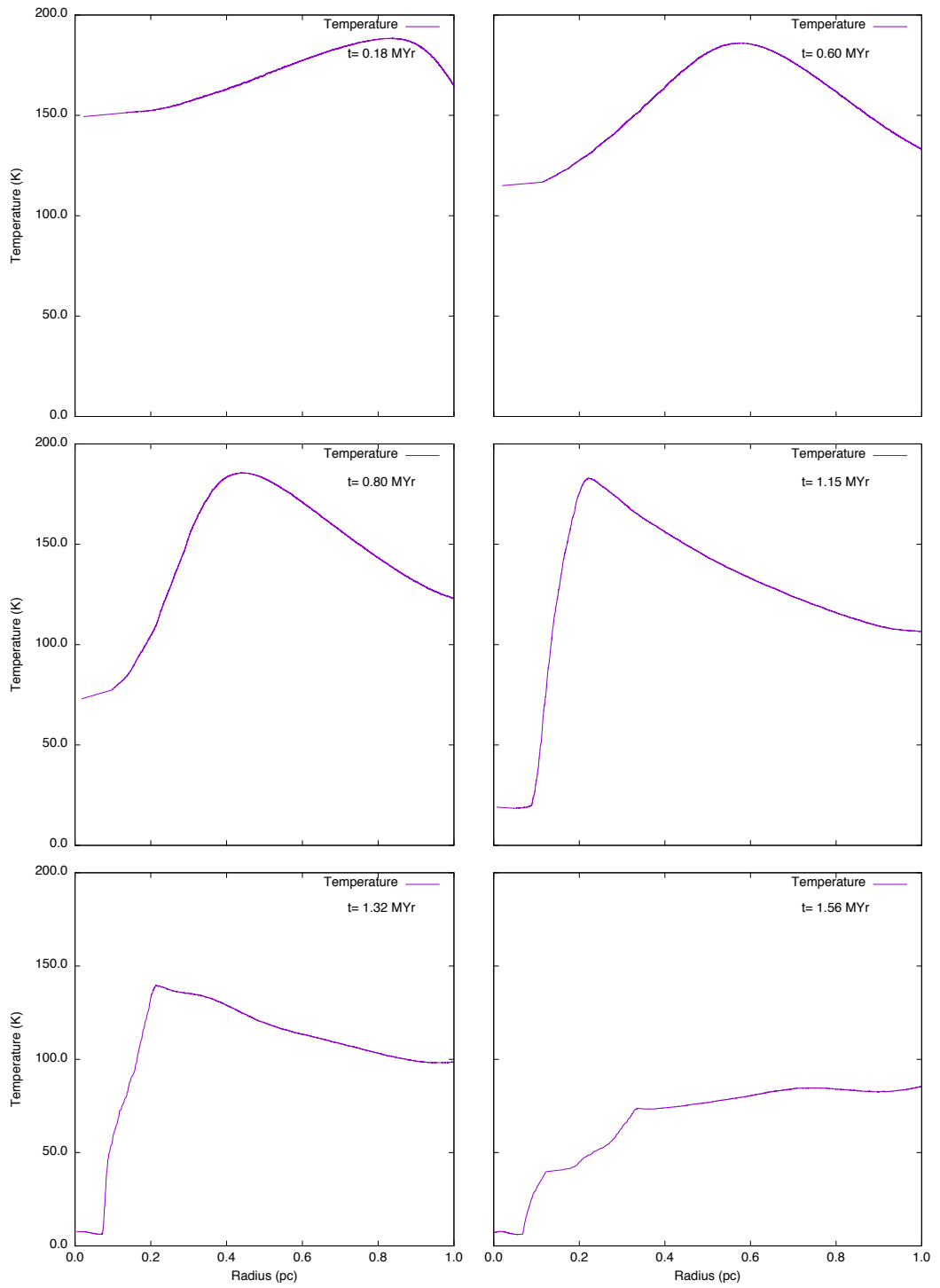
Figure B.51: FUV = 2 G_0. Six snapshots showing temperature (purple line) for a cloud with an initial density of 5000 cm^{-3}, a mass of 2 M$_\odot$ and a radius of 0.13 pc.
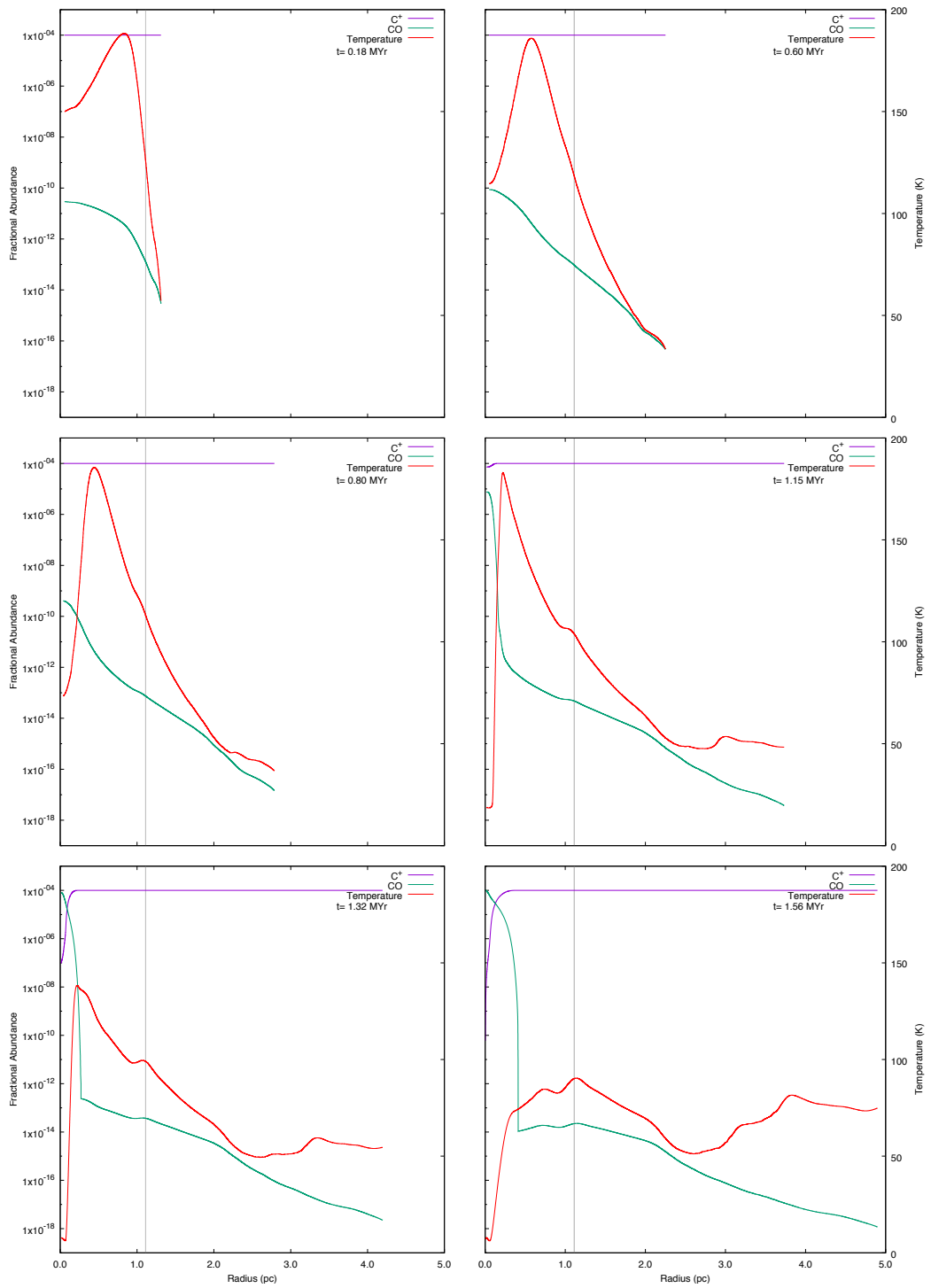
Figure B.52: FUV radiation = 2 G_0: six snapshots showing the chemical abundances of CO and C^+ for a cloud with an initial density of 5000 cm^{-3}, a mass of 2 $M_\odot$ and a radius of 0.12 pc.

Figure B.53: FUV = 2 G_0. The time evolution of a cloud with an initial density of 10000 cm^{-3}, a mass of 0.9 M$_\odot$ and a radius of 0.08 pc is shown in this graph. The cloud radius (purple line) is taken to be the zero crossing point of radial velocity and the mass (green line) is taken to be that which lies inside the radius. The blue vertical line denotes the time at which the high density peak first forms. This is the minimum cloud mass which collapses for the selected values of density and FUV flux.

Figure B.54: FUV = 2 G_0. Six snapshots showing radial velocity (purple line) and density (green line) for a cloud with an initial density of 10000 cm^{-3}, a mass of 0.9 M$_\odot$ and a radius of 0.08 pc.

Figure B.55: FUV $= 2\,G_0$. Six snapshots showing temperature (purple line) for a cloud with an initial density of $10000\ \mathrm{cm}^{-3}$, a mass of $0.9\ \mathrm{M}_\odot$ and a radius of 0.08 pc.

Figure B.56: FUV radiation = 2 G_0: six snapshots showing the chemical abundances of CO and C^+ for a cloud with an initial density of 10000 cm^{-3}, a mass of 0.9 $M_\odot$ and a radius of 0.08 pc.
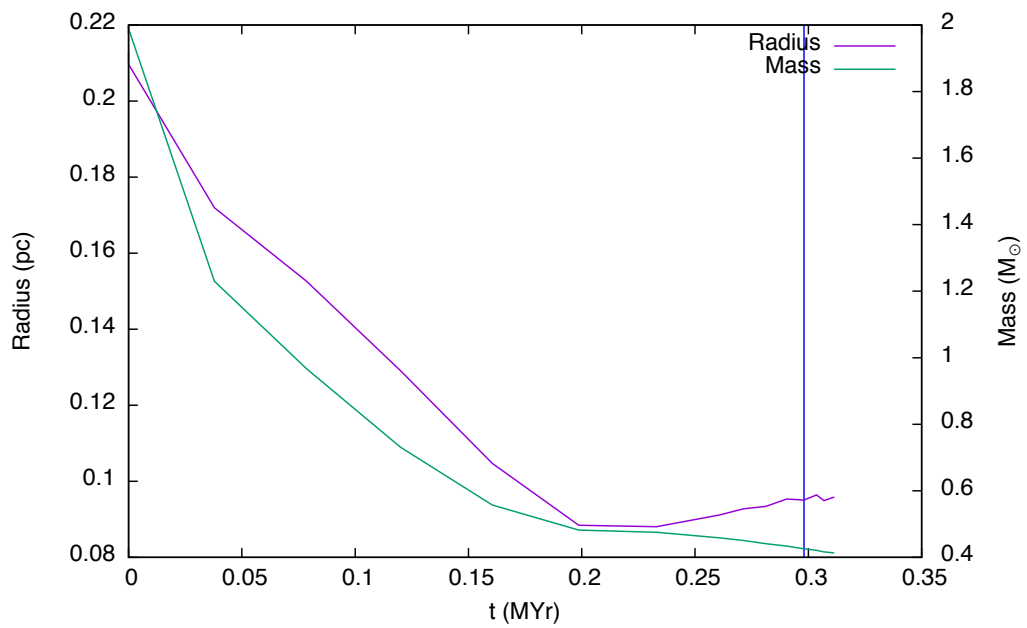
B.3 SET 50G_0

Figure B.57: FUV radiation = 50 G_0. The time evolution of a cloud with an initial density of 50 cm^{-3}, a mass of 1123 M$_\odot$ and a radius of 4.77 pc is shown in this graph. The cloud radius (purple line) is taken to be the zero crossing point of radial velocity and the mass (green line) is taken to be that which lies inside the radius. The blue vertical line denotes the time at which the high density peak first forms. This is the minimum cloud mass which collapses for the selected values of density and FUV flux.

Figure B.58: FUV radiation = 50 G_0. Six snapshots showing radial velocity (purple line) and density (green line) for a cloud with an initial density of 50 cm^{-3}, a mass of 1123 M$_\odot$ and a radius of 4.77 pc.
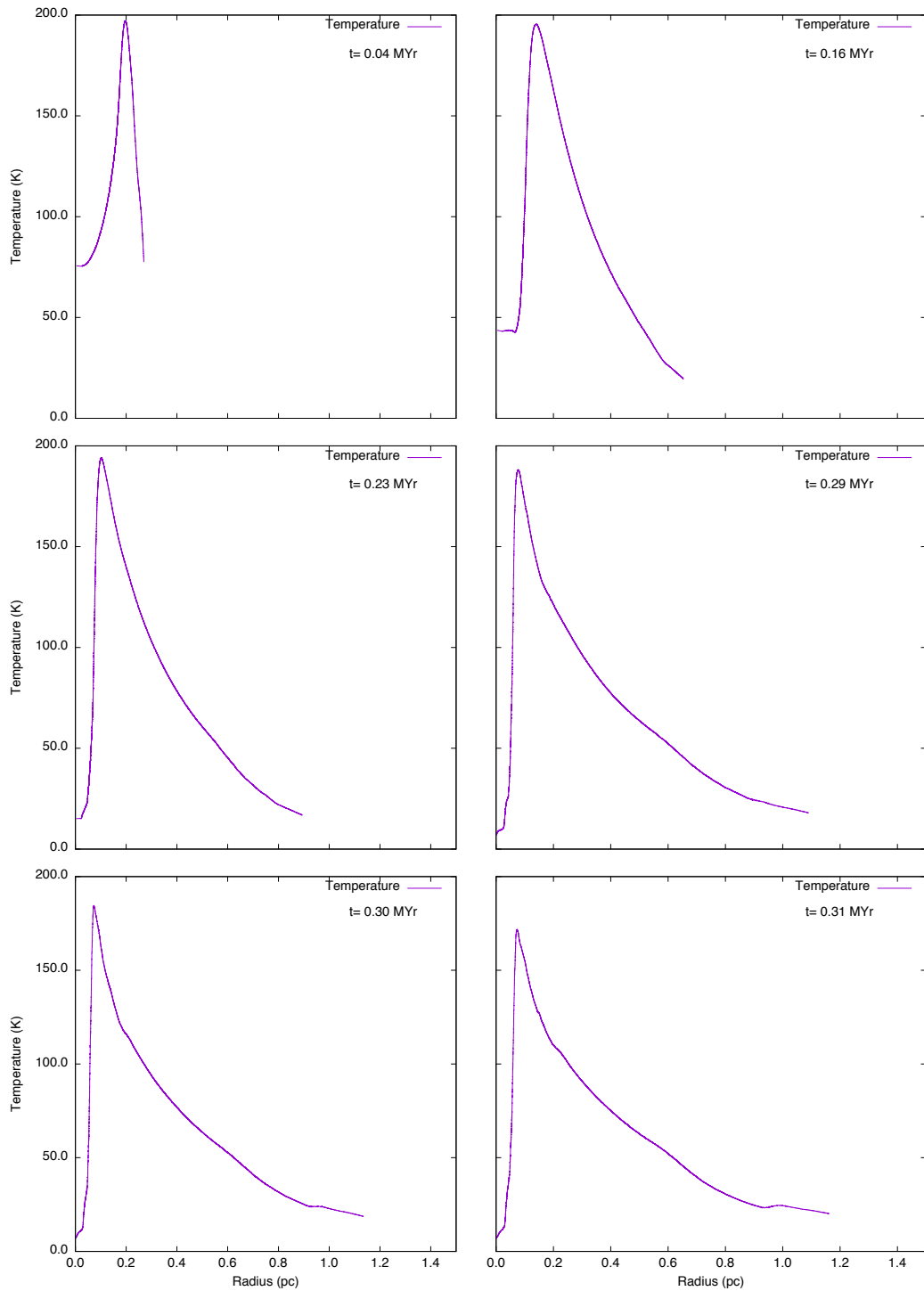
Figure B.59: FUV radiation $= 50\ G_0$. Six snapshots showing temperature (purple line) for a cloud with an initial density of 50 cm^{-3}, a mass of 1123 M$_\odot$ and a radius of 4.77 pc.
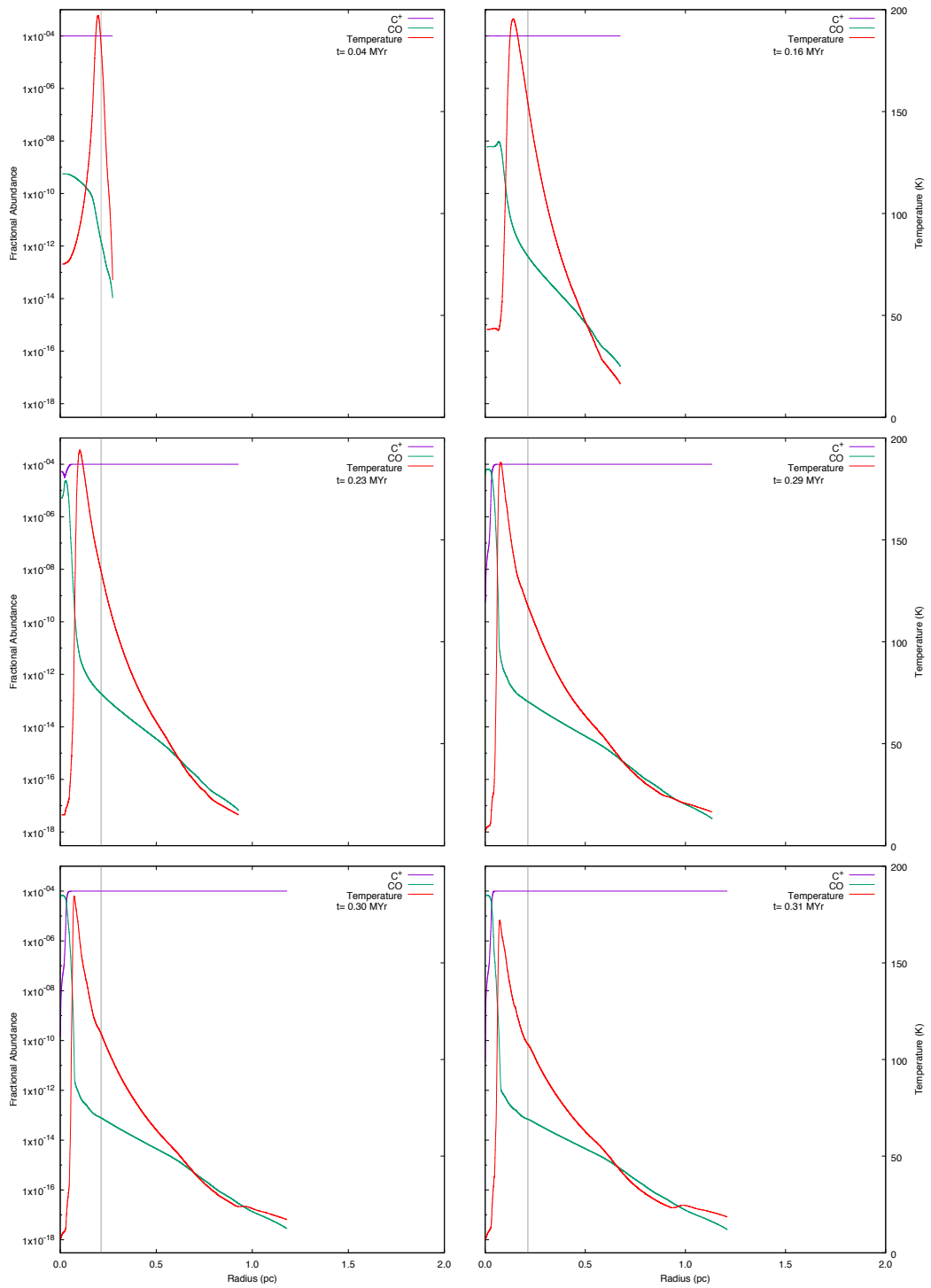
Figure B.60: FUV radiation = 50 G_0: six snapshots showing the chemical abundances of CO and C^+ for a cloud with an initial density of 50 cm^{-3}, a mass of 1123 $M_\odot$ and a radius of 4.77 pc.
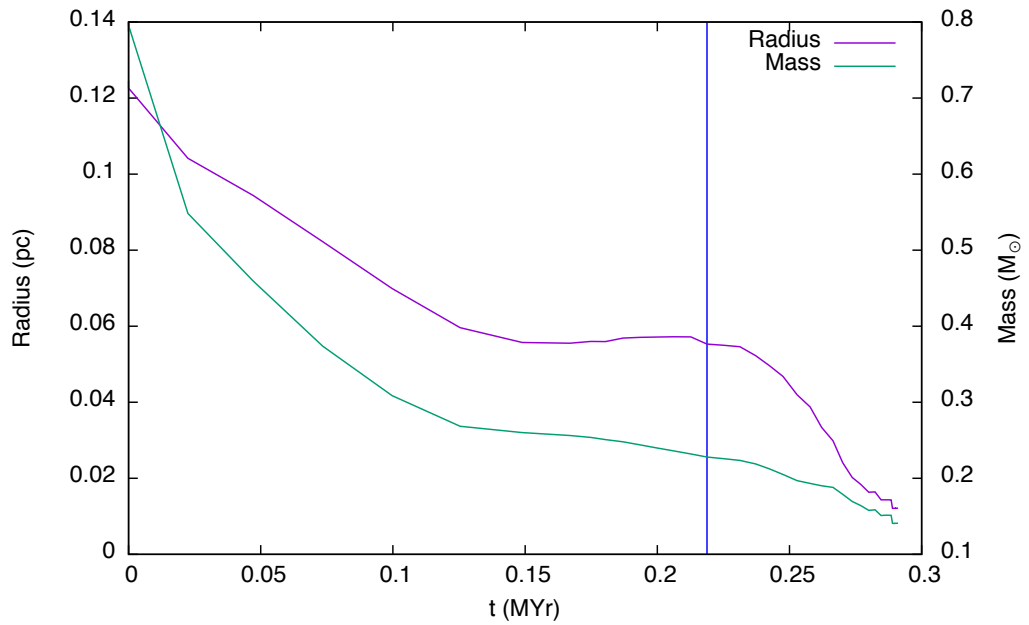
Figure B.61: FUV radiation $= 50\ G_0$. The time evolution of a cloud with an initial density of $100\ \mathrm{cm}^{-3}$, a mass of $249\ \mathrm{M}_\odot$ and a radius of $2.29\ \mathrm{pc}$ is shown in this graph. The cloud radius (purple line) is taken to be the zero crossing point of radial velocity and the mass (green line) is taken to be that which lies inside the radius. The blue vertical line denotes the time at which the high density peak first forms. This is the minimum cloud mass which collapses for the selected values of density and FUV flux.
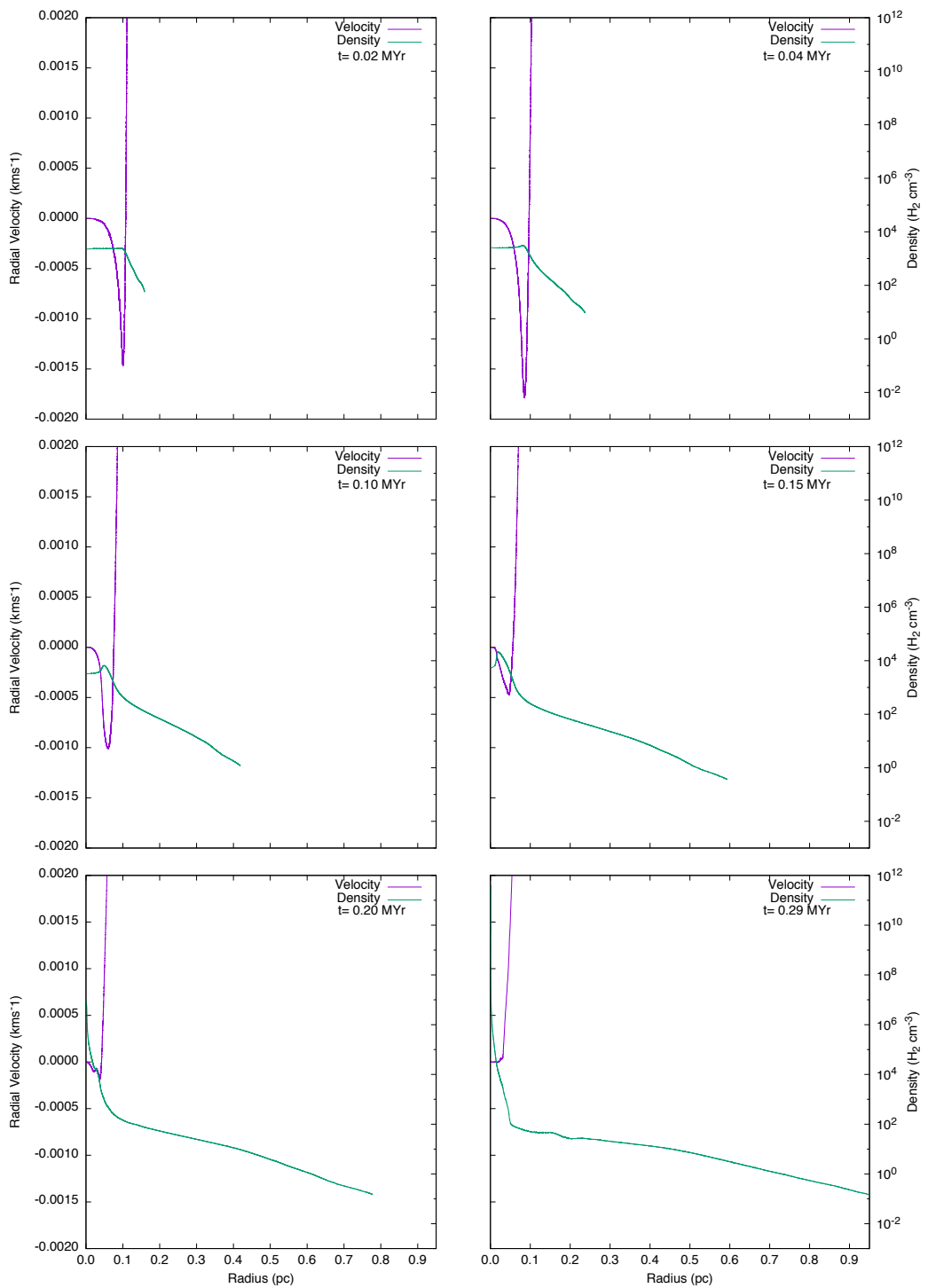
Figure B.62: FUV radiation $= 50$ G_0. Six snapshots showing radial velocity (purple line) and density (green line) for a cloud with an initial density of 100 cm^{-3}, a mass of 249 M$_\odot$ and a radius of 2.29 pc.
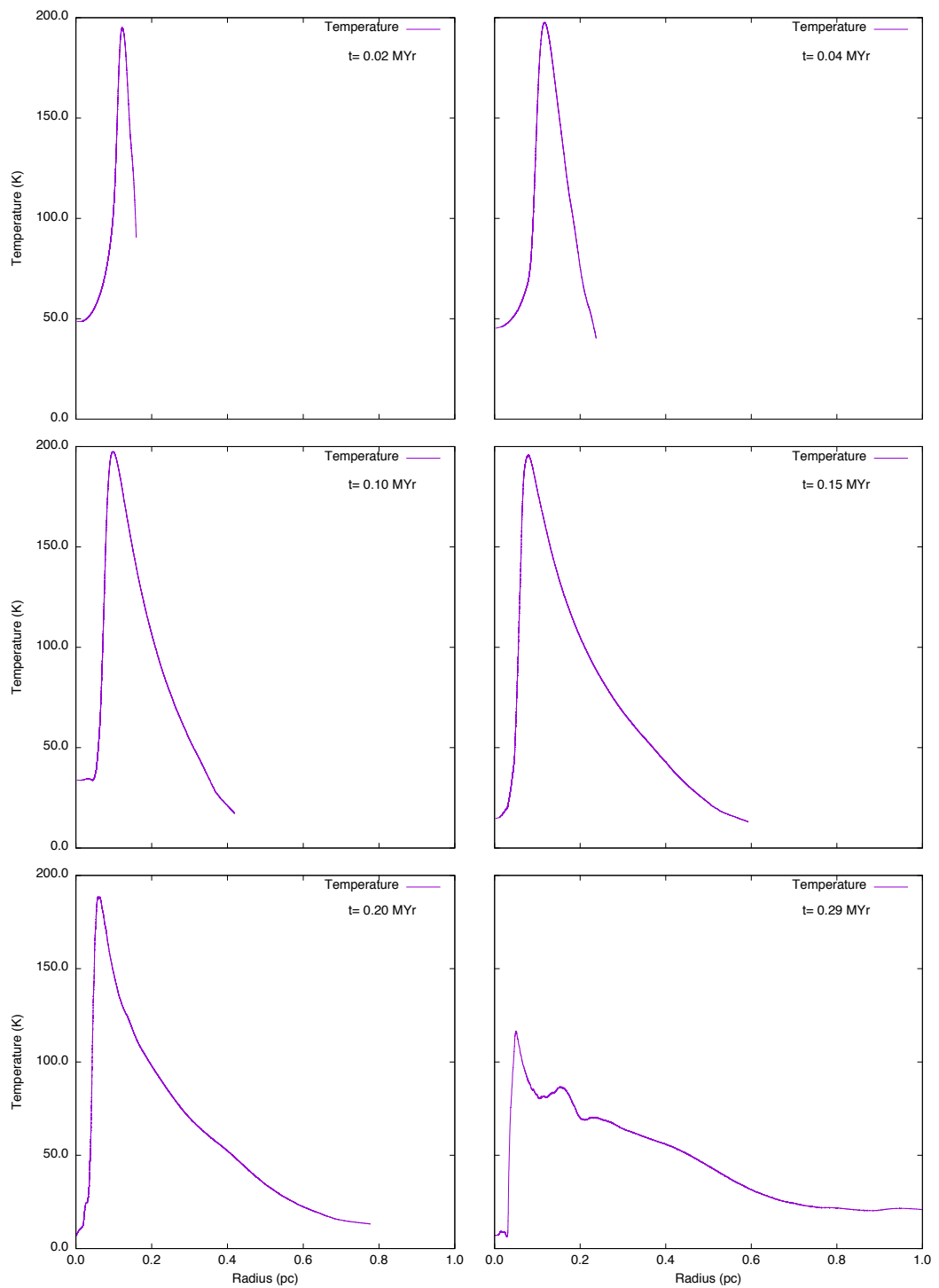
Figure B.63: FUV radiation $= 50\ G_0$. Six snapshots showing temperature (purple line) for a cloud with an initial density of $100\ \mathrm{cm}^{-3}$, a mass of $249\ \mathrm{M}_\odot$ and a radius of 2.29 pc.
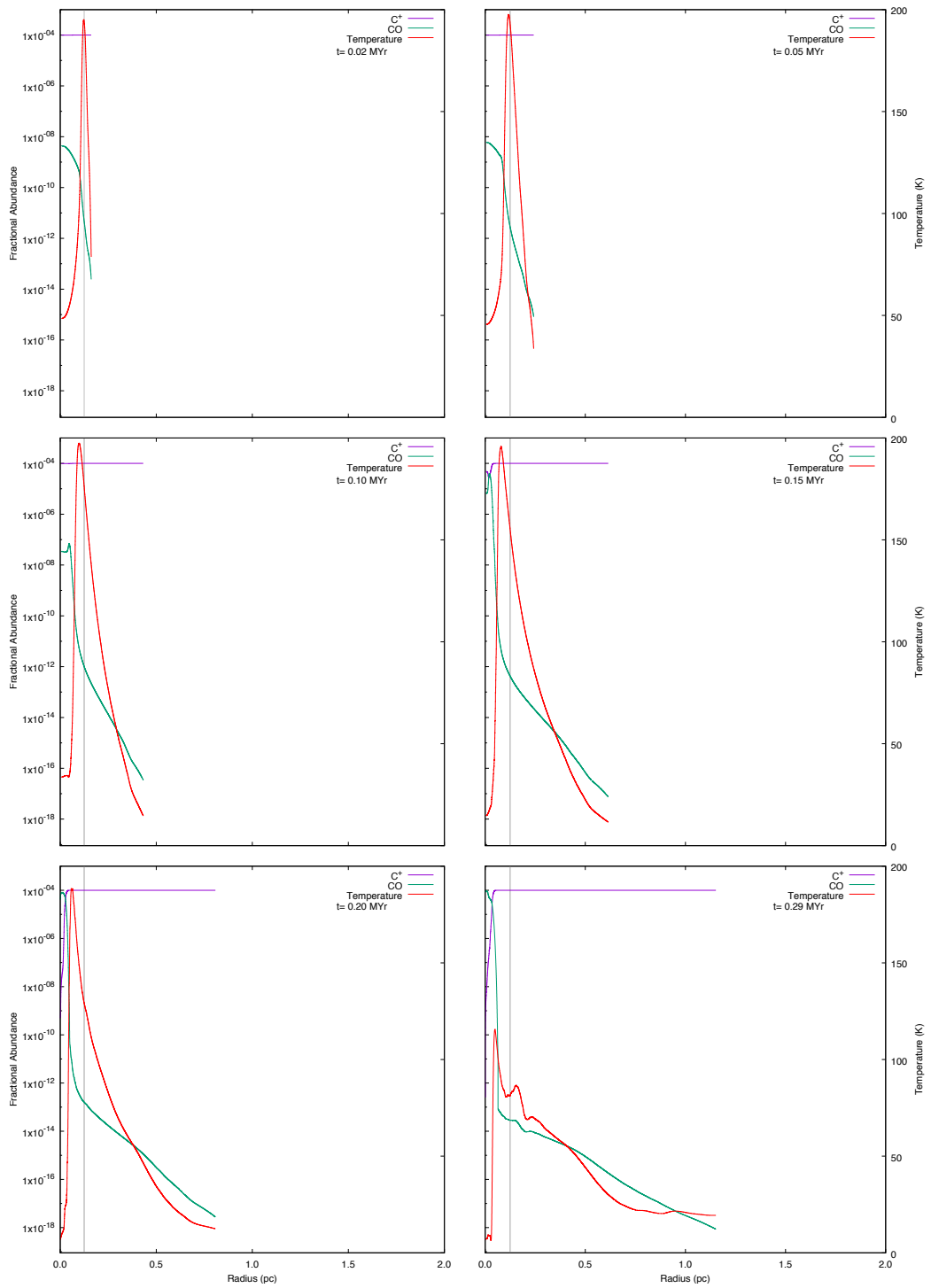
Figure B.64: FUV radiation = 50 G$_0$: six snapshots showing the chemical abundances of CO and C$^+$ for a cloud with an initial density of 100 cm^{-3}, a mass of 249 M$_\odot$ and a radius of 2.29 pc.
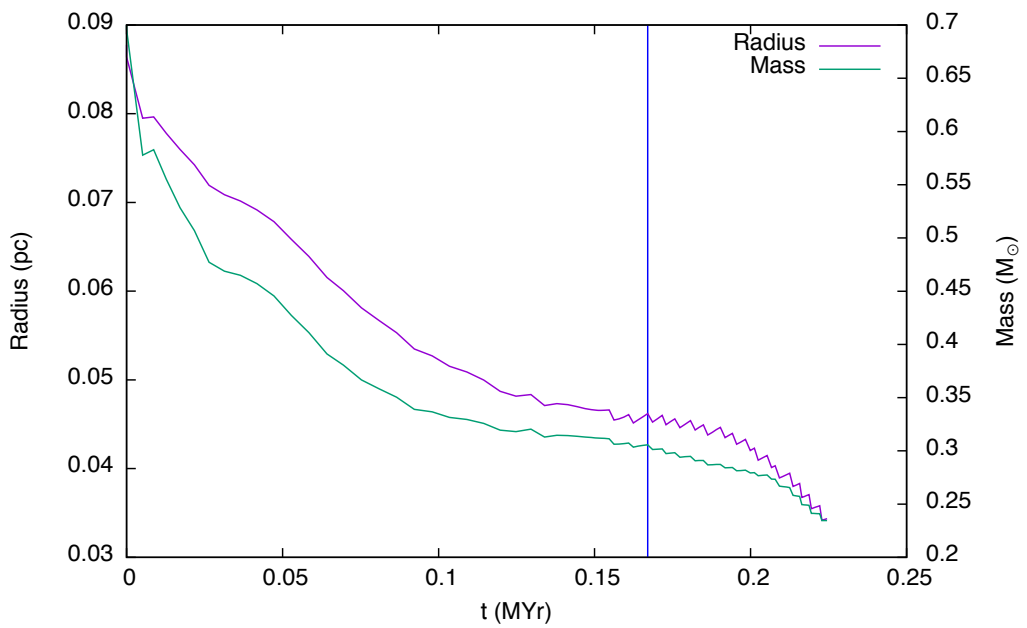
Figure B.65: FUV radiation $= 50\ G_0$. The time evolution of a cloud with an initial density of 200 cm^{-3}, a mass of 57 M$_\odot$ and a radius of 1.11 pc is shown in this graph. The cloud radius (purple line) is taken to be the zero crossing point of radial velocity and the mass (green line) is taken to be that which lies inside the radius. The blue vertical line denotes the time at which the high density peak first forms. This is the minimum cloud mass which collapses for the selected values of density and FUV flux.
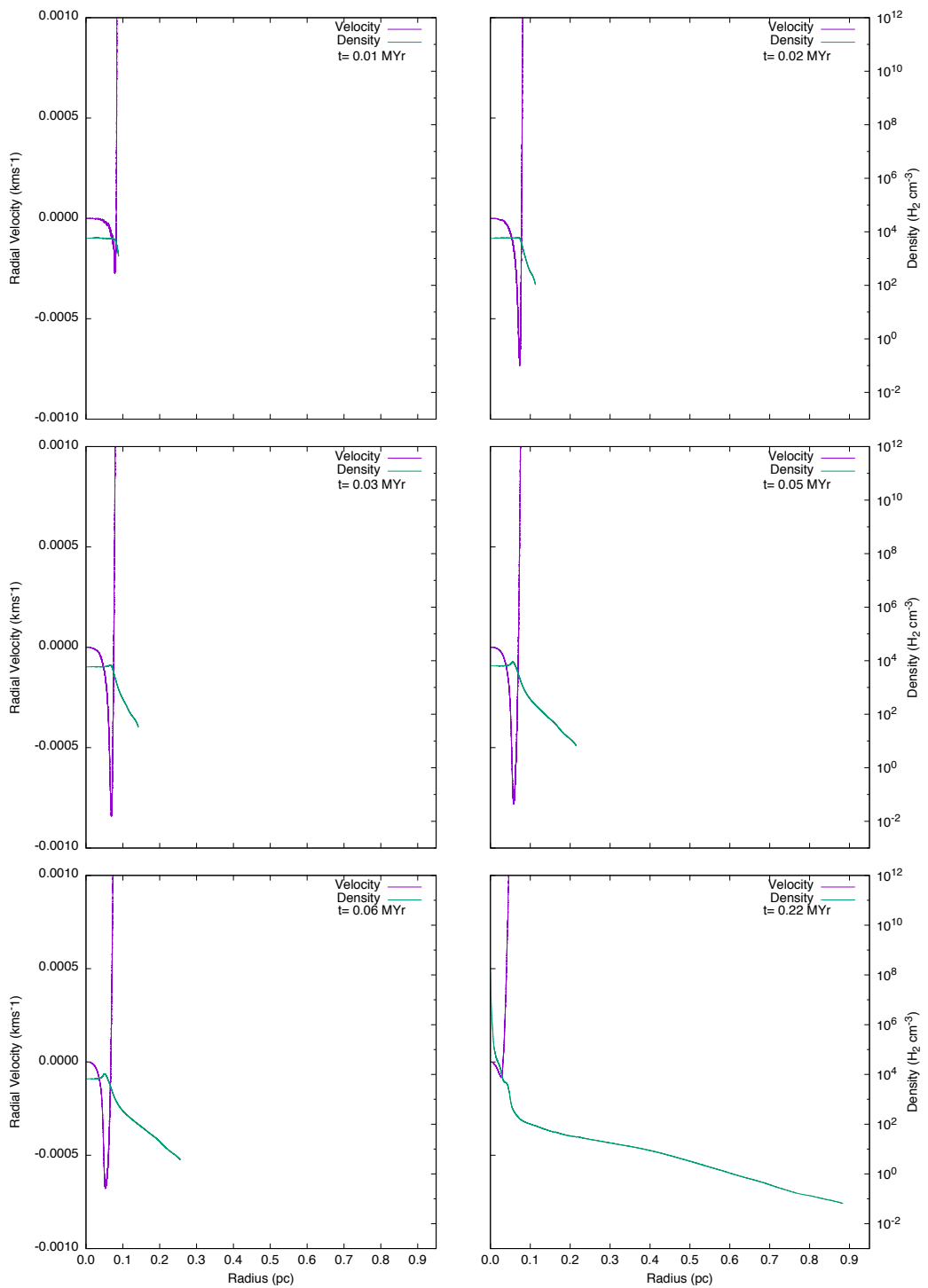
Figure B.66: FUV radiation = 50 G_0. Six snapshots showing radial velocity (purple line) and density (green line) for a cloud with an initial density of 200 cm^{-3}, a mass of 57 M$_\odot$ and a radius of 1.11 pc.
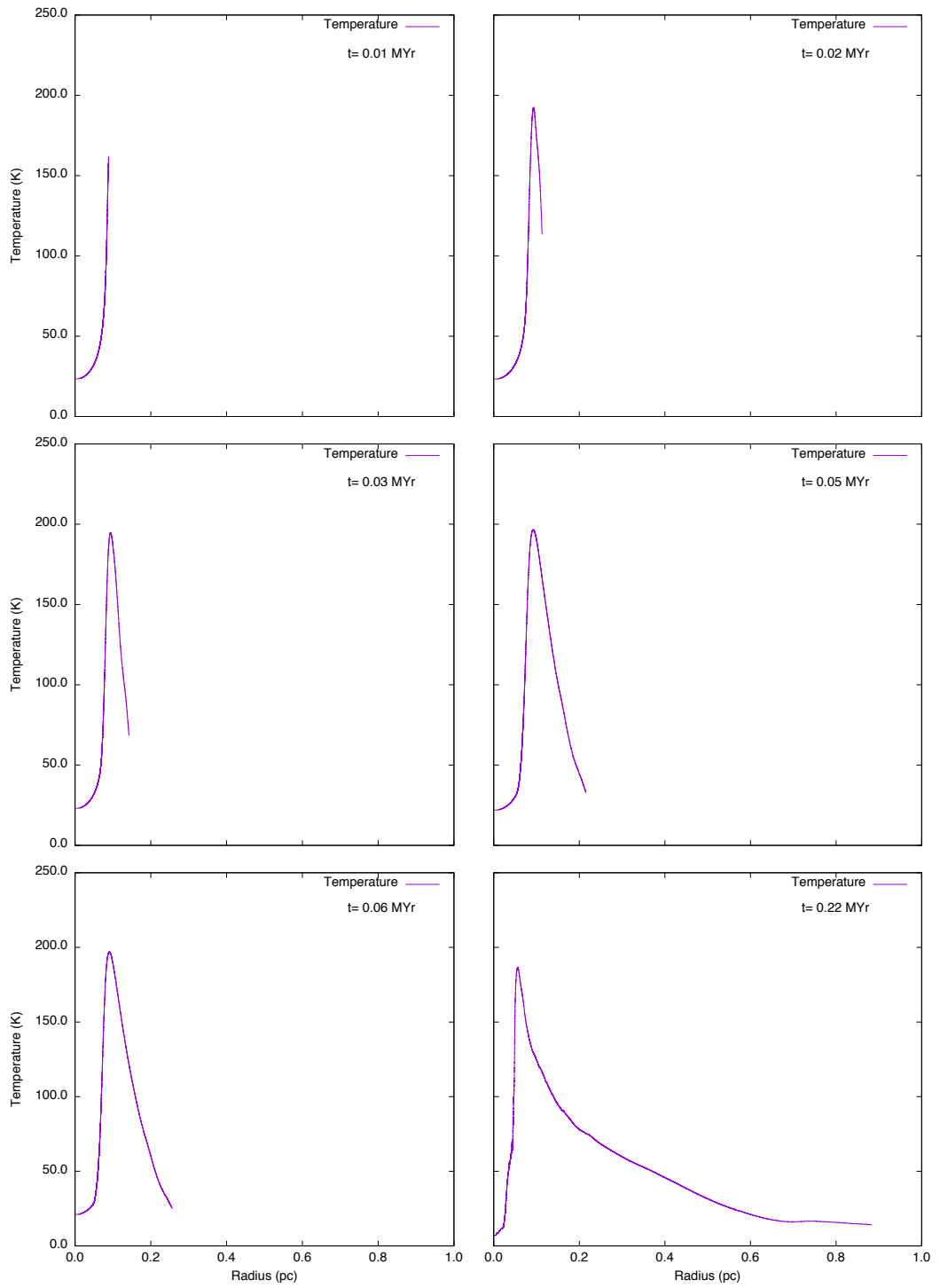
Figure B.67: FUV radiation $= 50 \, G_0$. Six snapshots showing temperature (purple line) for a cloud with an initial density of $200 \ \mathrm{cm}^{-3}$, a mass of $57 \ \mathrm{M}_\odot$ and a radius of 1.11 pc.
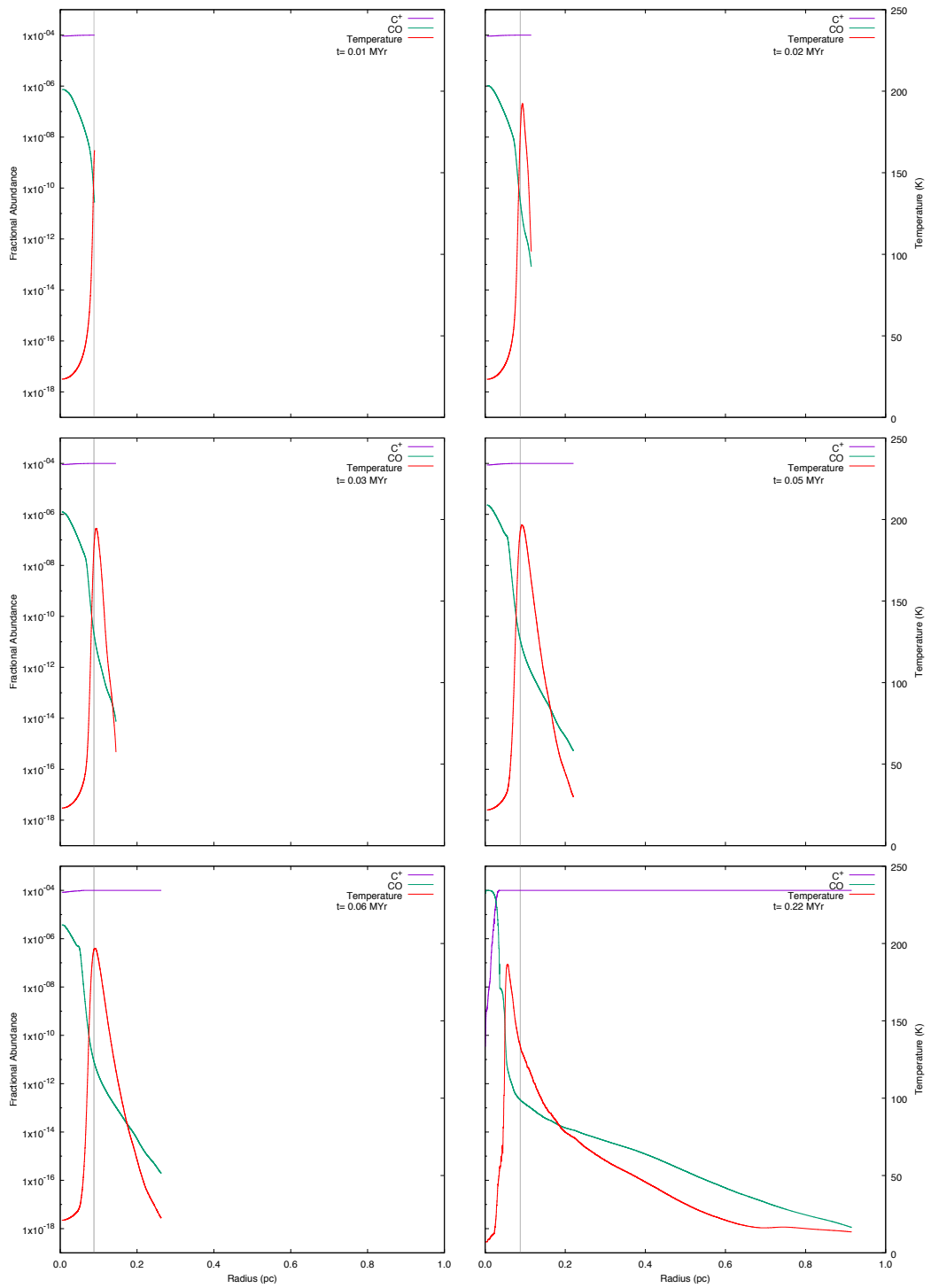
Figure B.68: FUV radiation = 50 G$_0$: six snapshots showing the chemical abundances of CO and C$^+$ for a cloud with an initial density of 200 cm^{-3}, a mass of 57 M$_\odot$ and a radius of 1.11 pc.
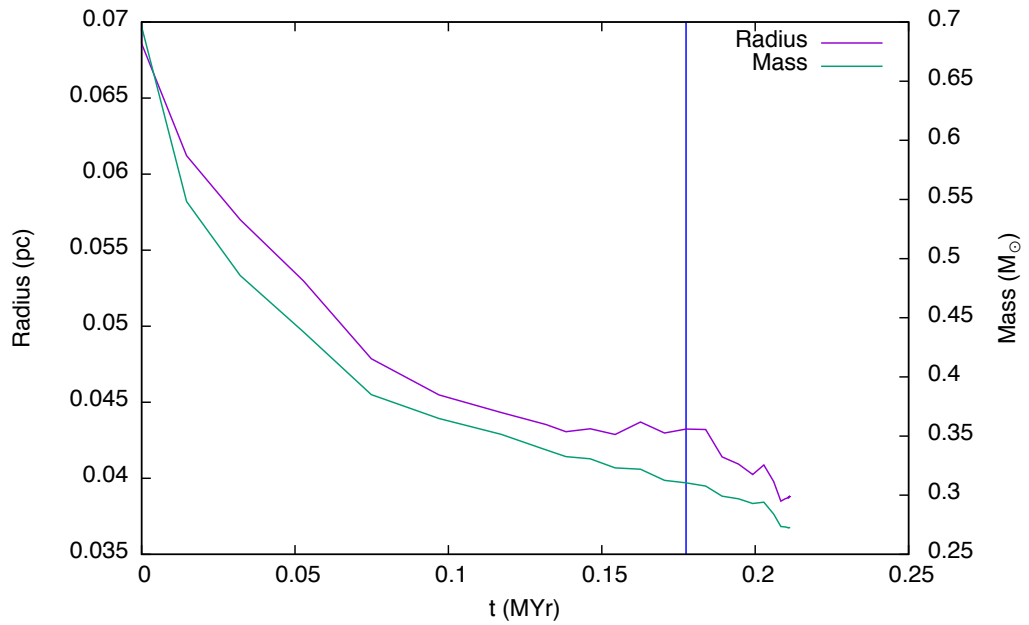
Figure B.69: FUV radiation $= 50$ G_0. The time evolution of a cloud with an initial density of 1000 cm^{-3}, a mass of 2 M$_\odot$ and a radius of 0.21 pc is shown in this graph. The cloud radius (purple line) is taken to be the zero crossing point of radial velocity and the mass (green line) is taken to be that which lies inside the radius. The blue vertical line denotes the time at which the high density peak first forms. This is the minimum cloud mass which collapses for the selected values of density and FUV flux.
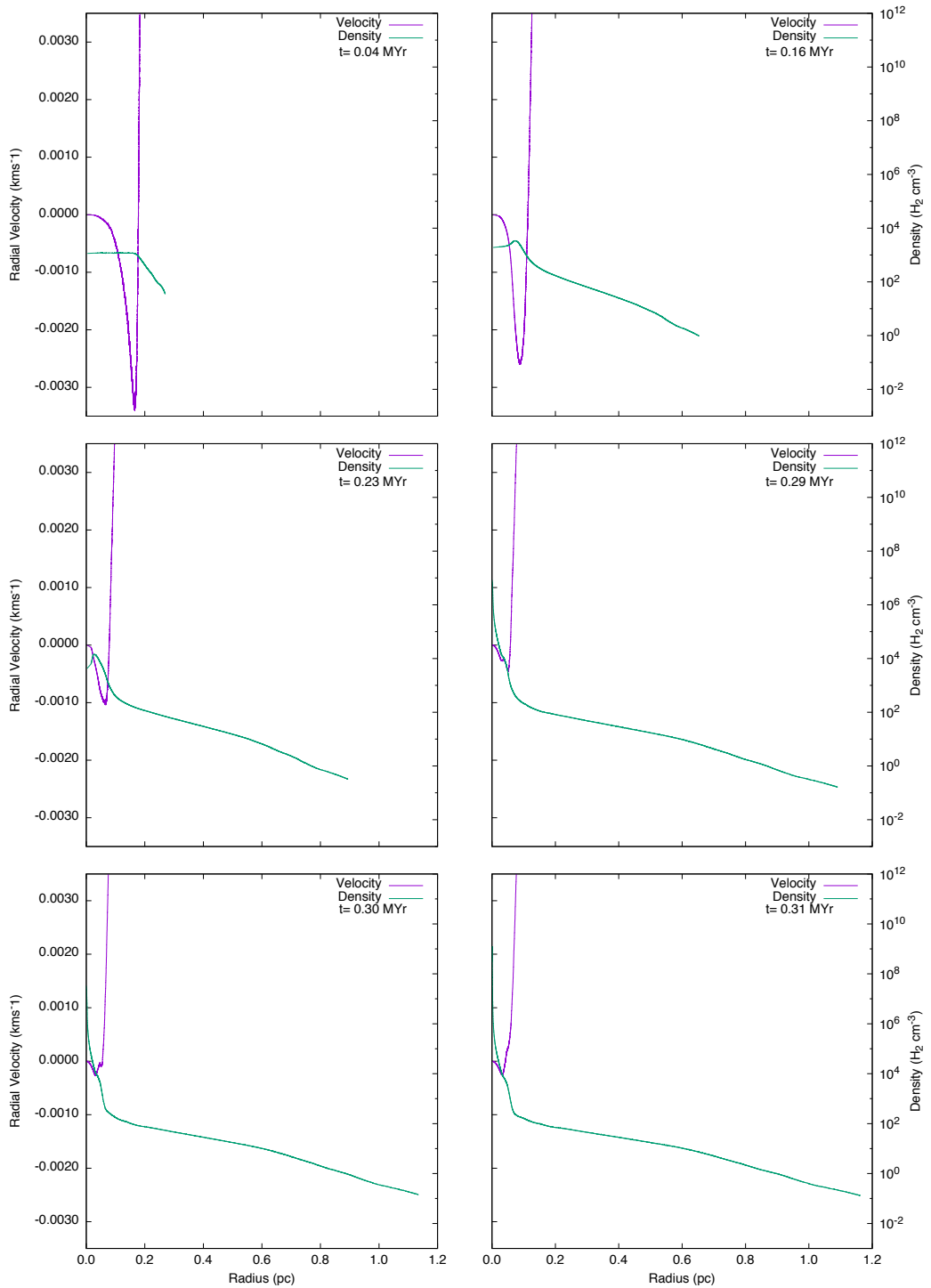
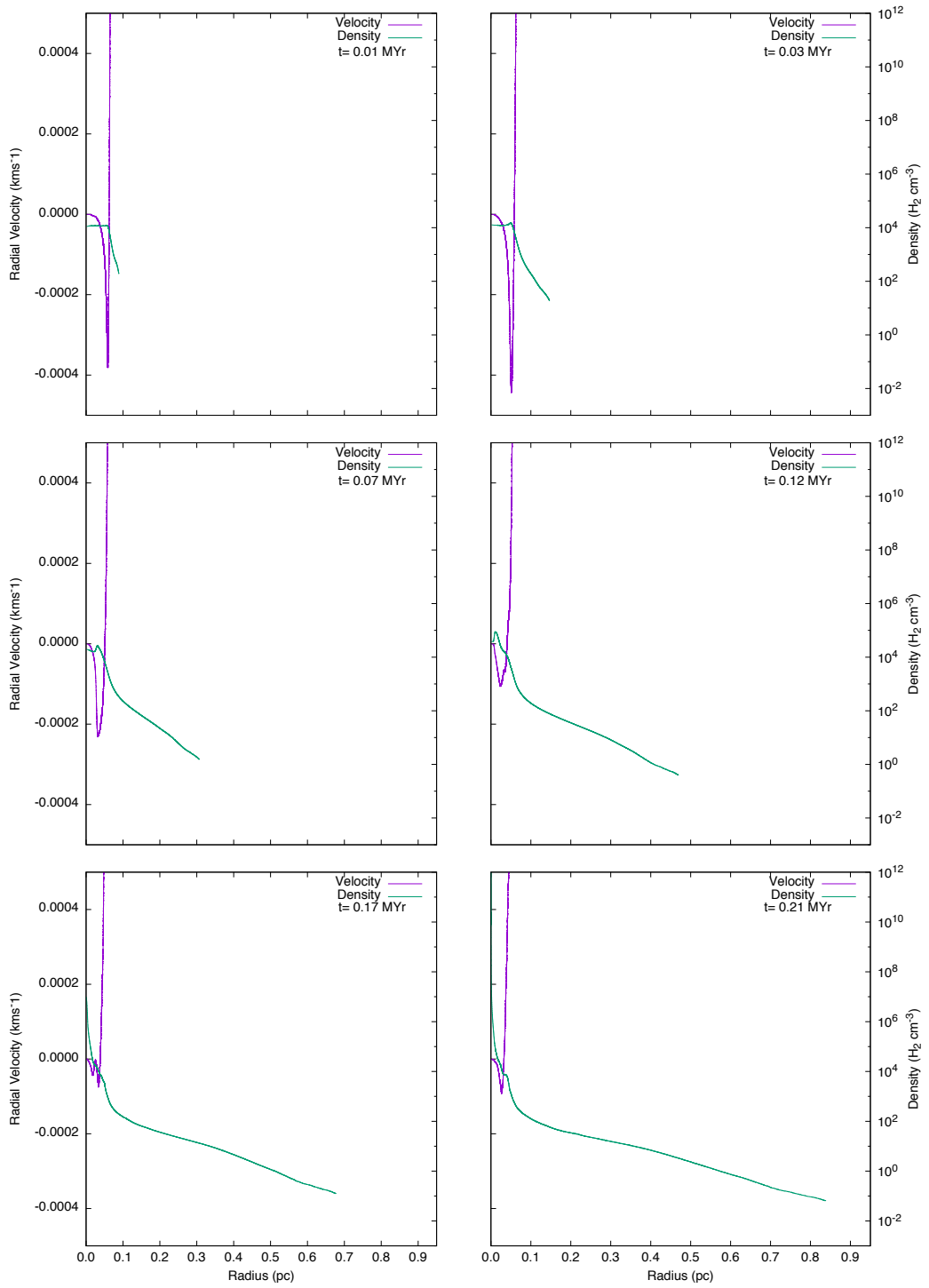Figure B.70: FUV radiation = 50 G_0. Six snapshots showing radial velocity (purple line) and density (green line) for a cloud with an initial density of 1000 cm^{-3}, a mass of 2 M$_\odot$ and a radius of 0.213 pc.

Figure B.71: FUV radiation $= 50\ G_0$. Six snapshots showing temperature (purple line) for a cloud with an initial density of $1000\ \mathrm{cm}^{-3}$, a mass of $2\ \mathrm{M}_\odot$ and a radius of 0.21 pc.

Figure B.72: FUV radiation = 50 G$_0$: six snapshots showing the chemical abundances of CO and C$^+$ for a cloud with an initial density of 1000 cm^{-3}, a mass of 2 M$_\odot$ and a radius of 0.21 pc.

Figure B.73: FUV radiation $= 50$ G_0. The time evolution of a cloud with an initial density of 2000 cm^{-3}, a mass of 0.8 M$_\odot$ and a radius of 0.13 pc is shown in this graph. The cloud radius (purple line) is taken to be the zero crossing point of radial velocity and the mass (green line) is taken to be that which lies inside the radius. The blue vertical line denotes the time at which the high density peak first forms. This is the minimum cloud mass which collapses for the selected values of density and FUV flux.

Figure B.74: FUV radiation = 50 G_0. Six snapshots showing radial velocity (purple line) and density (green line) for a cloud with an initial density of 2000 cm^{-3}, a mass of 0.8 M$_\odot$ and a radius of 0.13 pc.
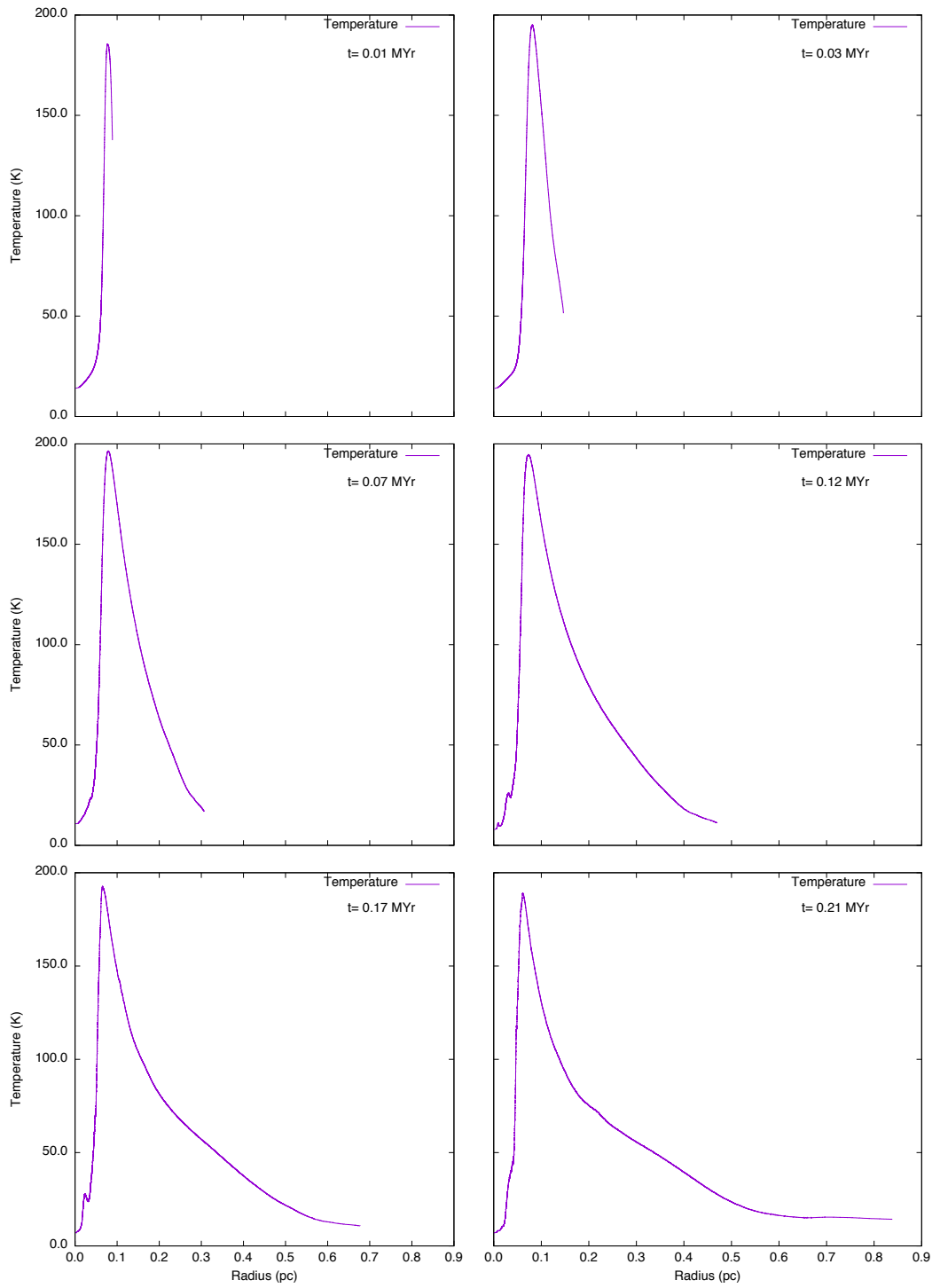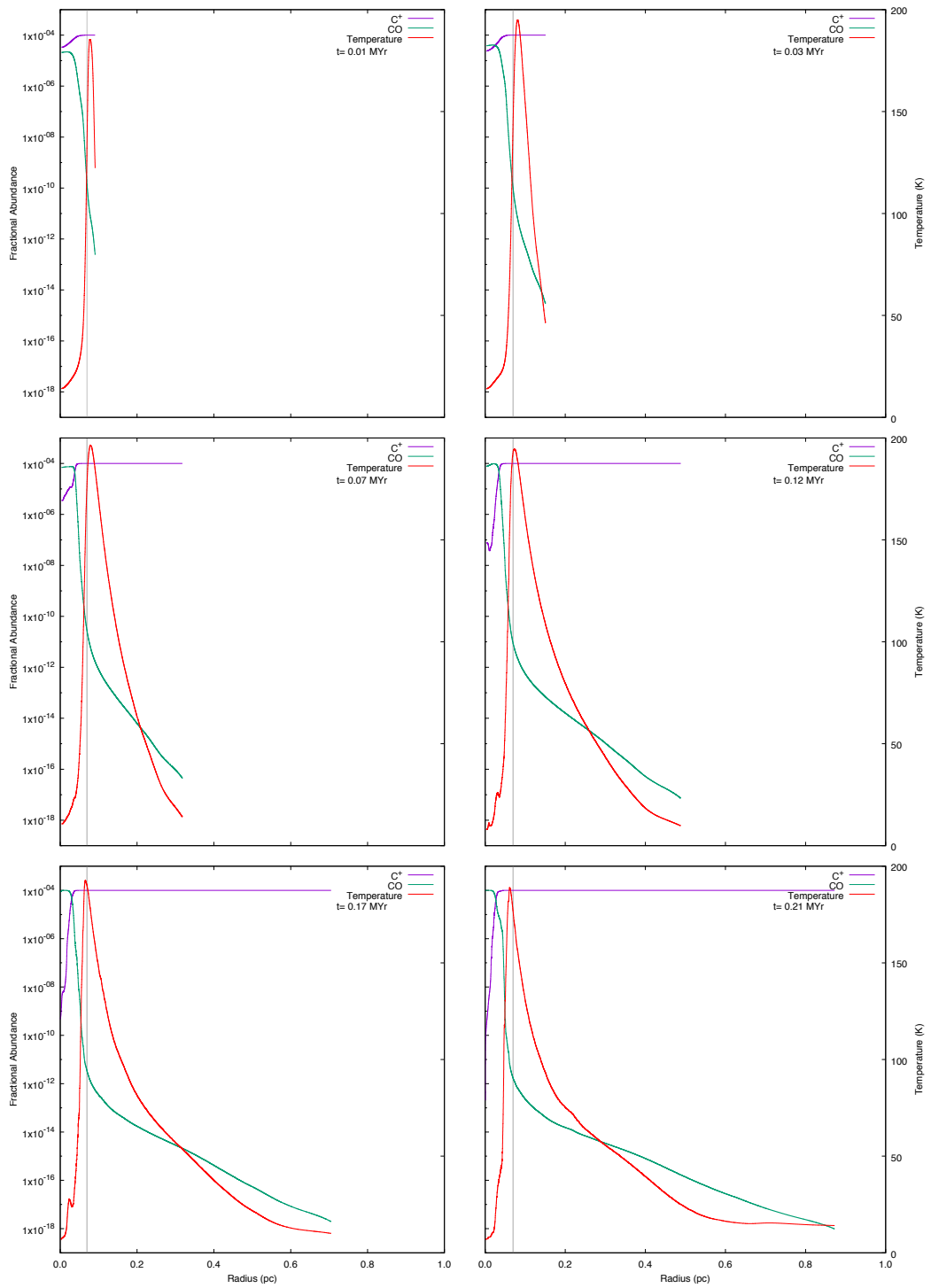
Figure B.75: FUV radiation $= 50 \, G_0$. Six snapshots showing temperature (purple line) for a cloud with an initial density of 2000 cm^{-3}, a mass of 0.8 M$_\odot$ and a radius of 0.13 pc.

Figure B.76: FUV radiation = 50 G_0: six snapshots showing the chemical abundances of CO and C^+ for a cloud with an initial density of 2000 cm^{-3}, a mass of 0.8 $M_\odot$ and a radius of 0.12 pc.
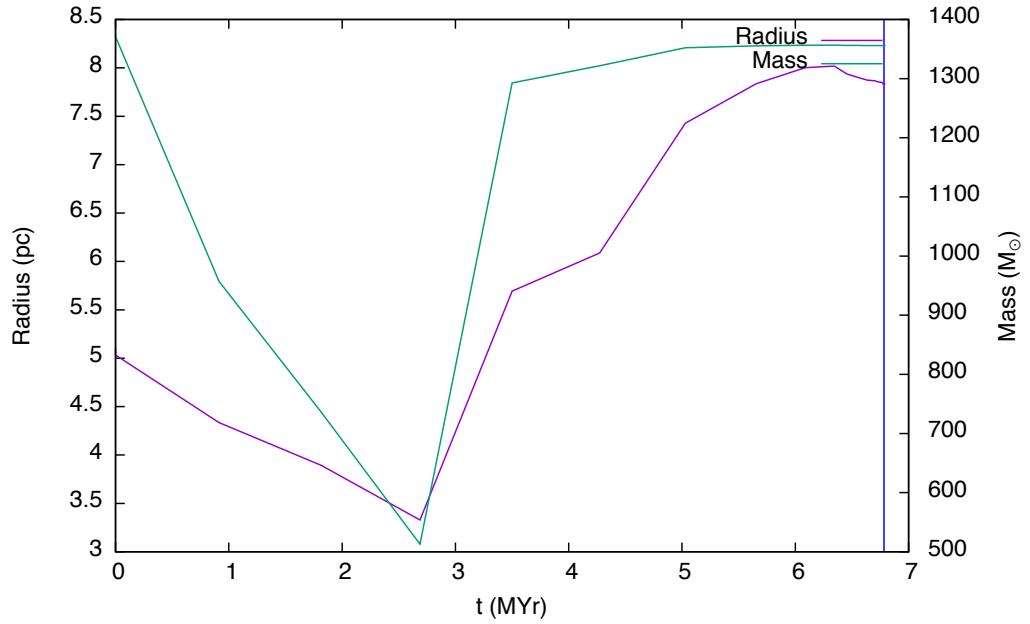
Figure B.77: FUV radiation $= 50\ G_0$. The time evolution of a cloud with an initial density of 5000 cm^{-3}, a mass of 0.08 M$_\odot$ and a radius of 0.09 pc is shown in this graph. The cloud radius (purple line) is taken to be the zero crossing point of radial velocity and the mass (green line) is taken to be that which lies inside the radius. The blue vertical line denotes the time at which the high density peak first forms. This is the minimum cloud mass which collapses for the selected values of density and FUV flux.
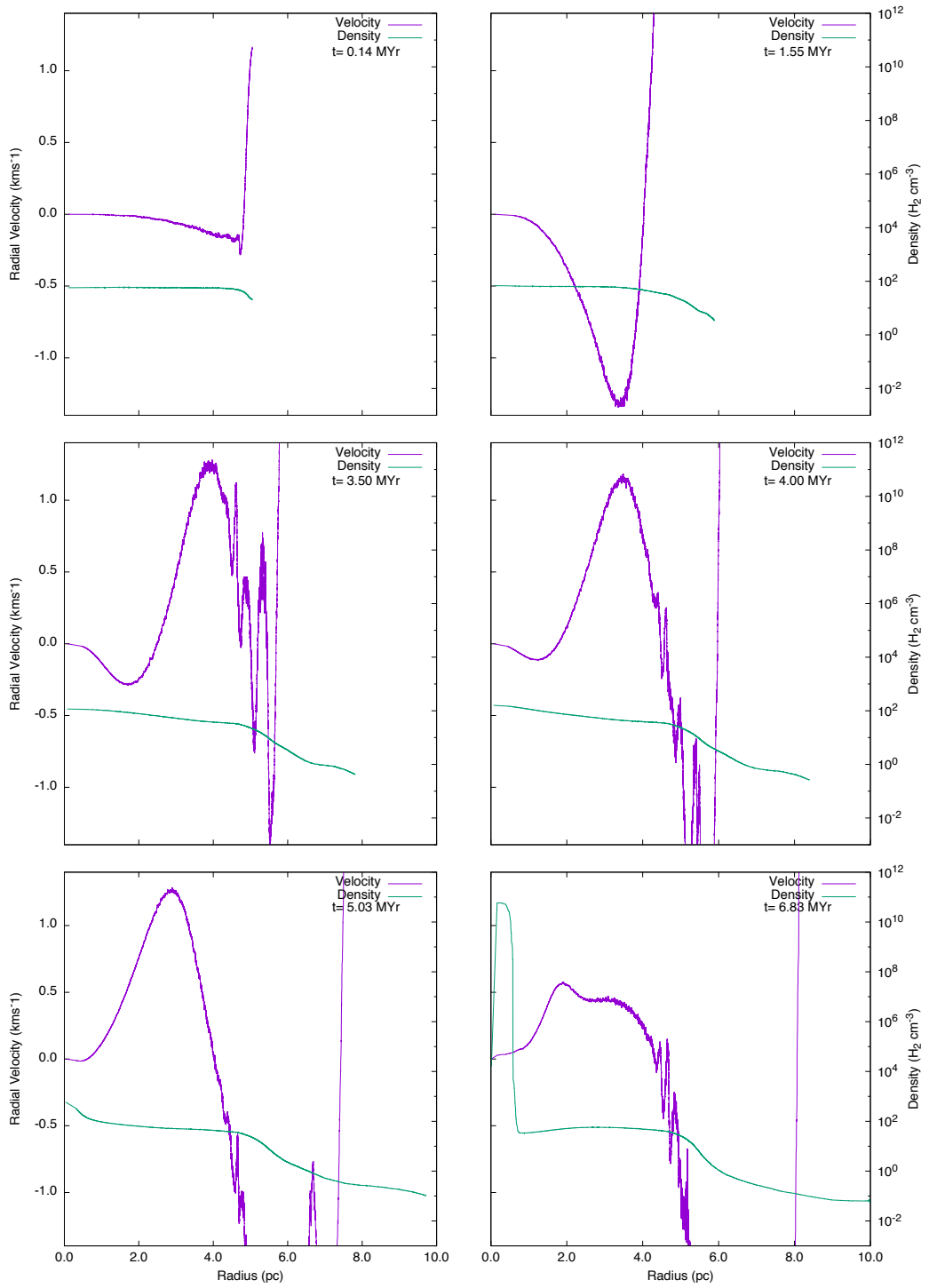
Figure B.78: FUV radiation = 50 G_0. Six snapshots showing radial velocity (purple line) and density (green line) for a cloud with an initial density of 5000 cm^{-3}, a mass of 0.08 M$_\odot$ and a radius of 0.09 pc.
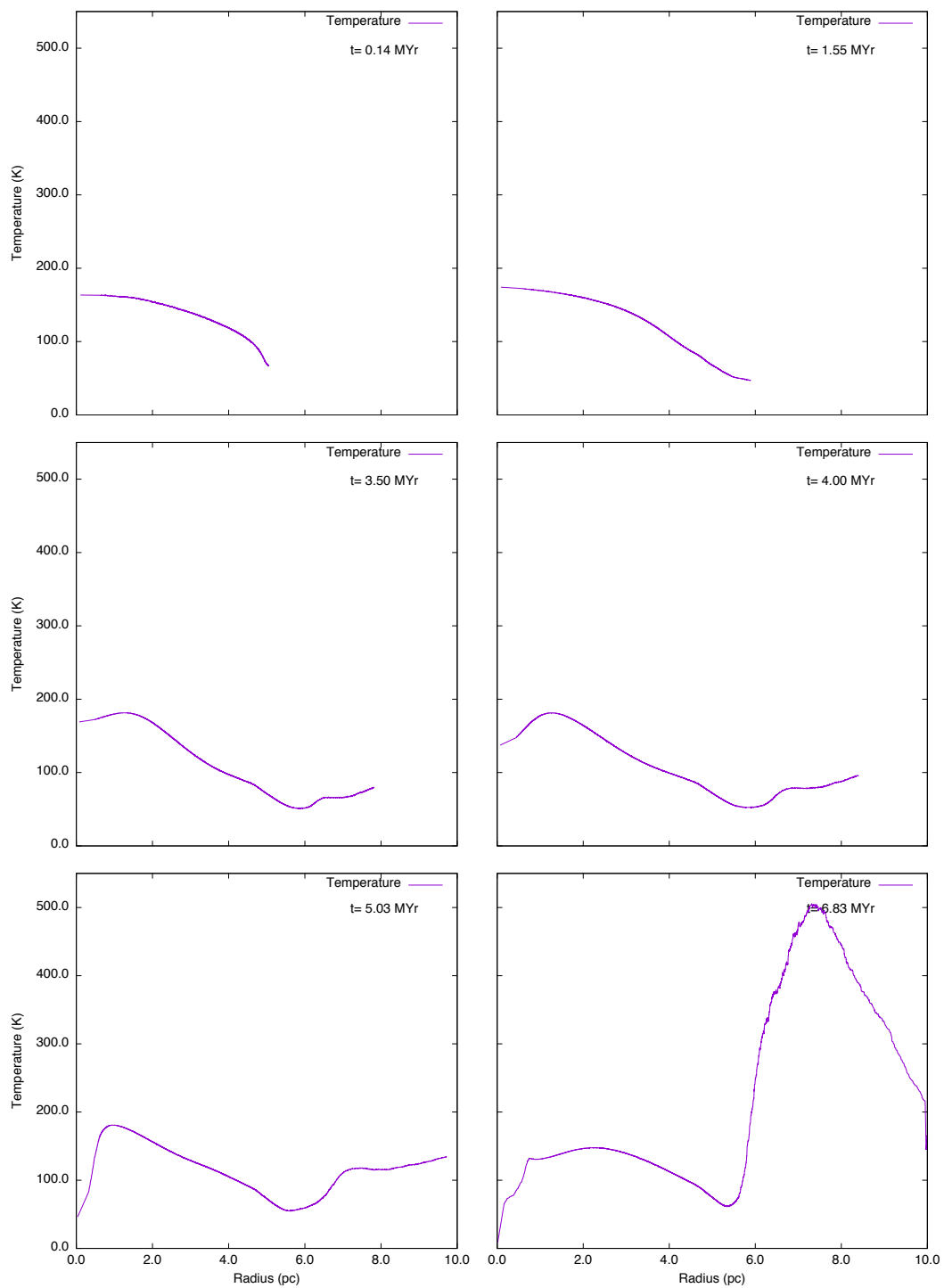
Figure B.79: FUV radiation $= 50\ G_0$. Six snapshots showing temperature (purple line) for a cloud with an initial density of 5000 cm^{-3}, a mass of 0.09 M$_\odot$ and a radius of 0.09 pc.
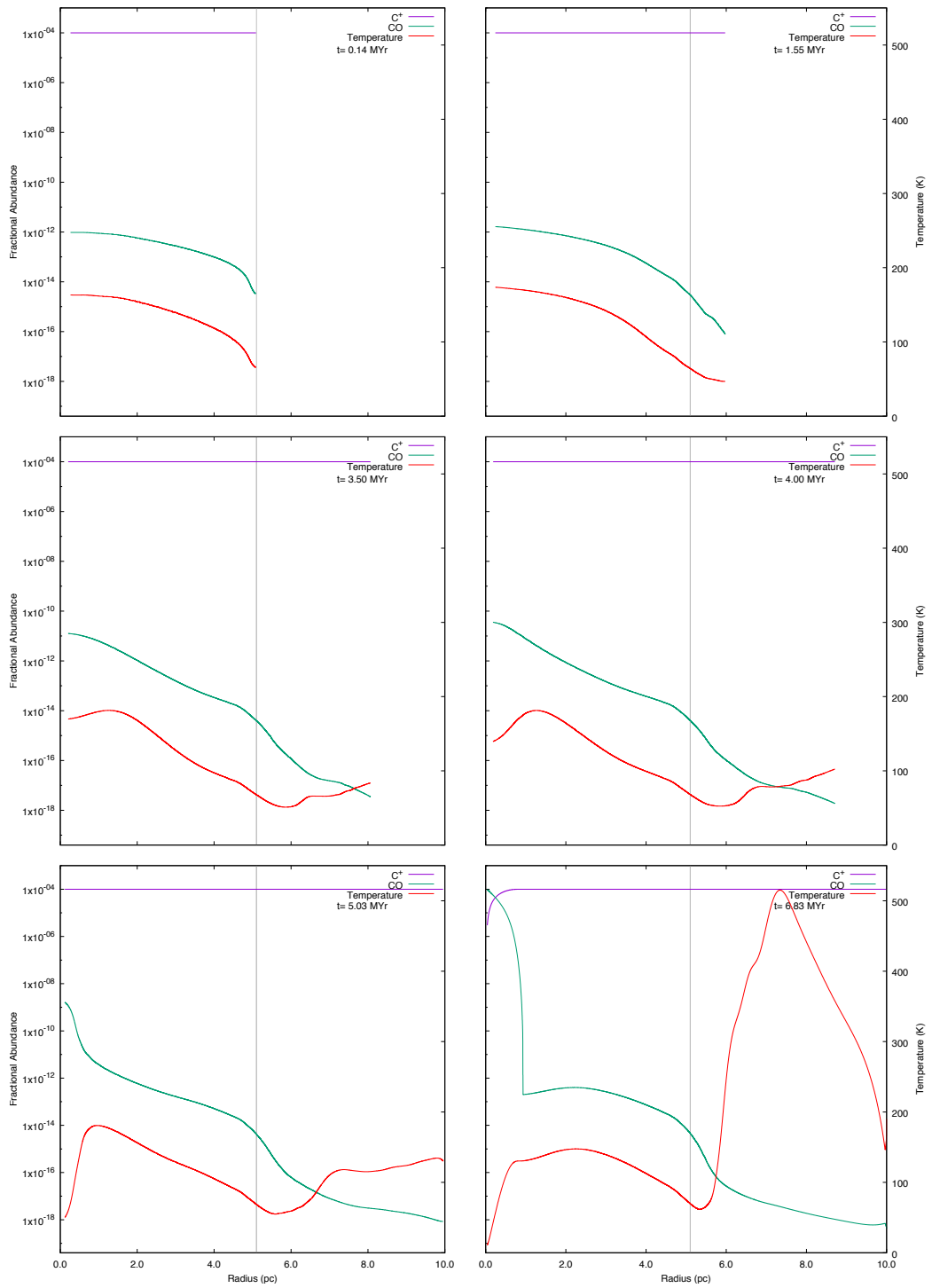
Figure B.80: FUV radiation = 50 G_0: six snapshots showing the chemical abundances of CO and C^+ for a cloud with an initial density of 5000 cm^{-3}, a mass of 0.7 $M_\odot$ and a radius of 0.09 pc.
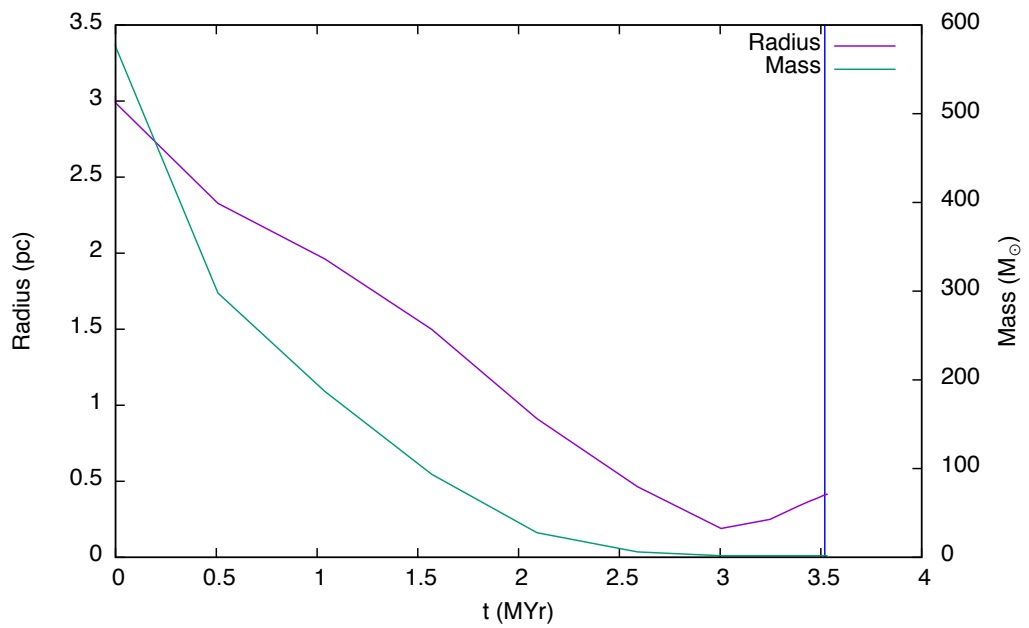
Figure B.81: FUV radiation $= 50\ G_0$. The time evolution of a cloud with an initial density of 10000 cm^{-3}, a mass of 0.7 M$_\odot$ and a radius of 0.07 pc is shown in this graph. The cloud radius (purple line) is taken to be the zero crossing point of radial velocity and the mass (green line) is taken to be that which lies inside the radius. The blue vertical line denotes the time at which the high density peak first forms. This is the minimum cloud mass which collapses for the selected values of density and FUV flux.
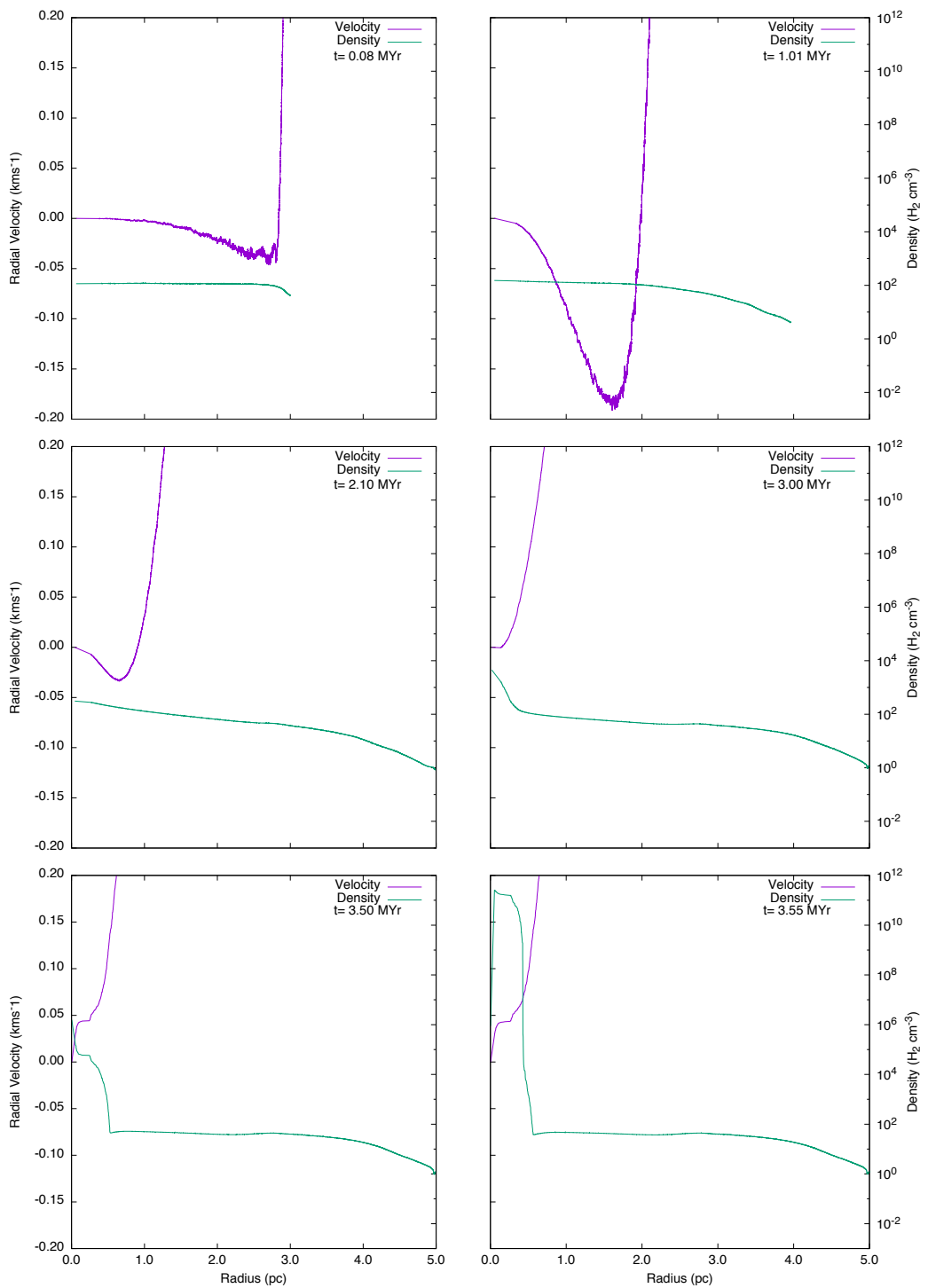
Figure B.82: FUV radiation = 50 G_0. Six snapshots showing radial velocity (purple line) and density (green line) for a cloud with an initial density of 10000 cm^{-3}, a mass of 0.7 M$_\odot$ and a radius of 0.07 pc.
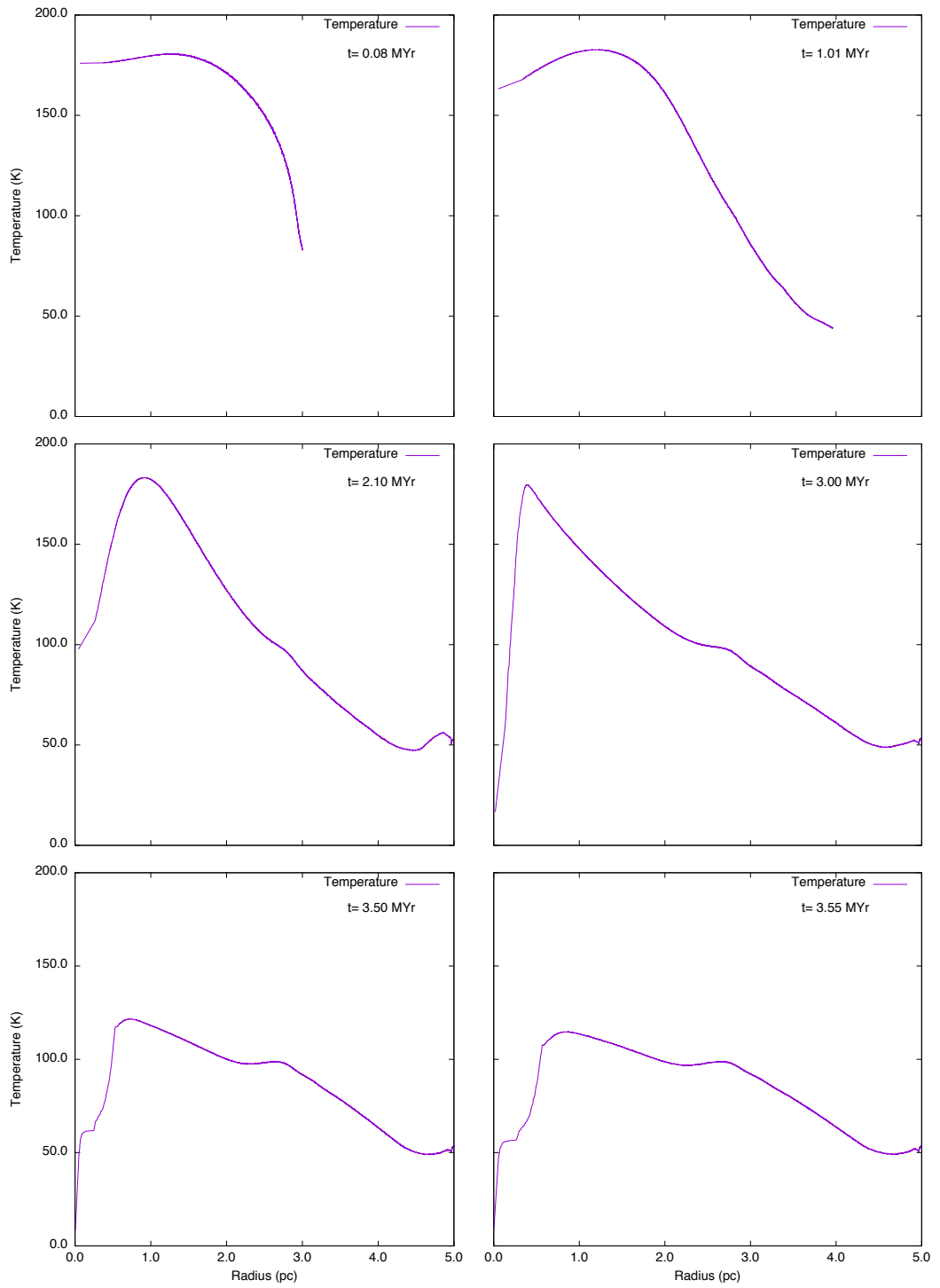
Figure B.83: FUV radiation $= 50\ G_0$. Six snapshots showing temperature (purple line) for a cloud with an initial density of $10000\ \mathrm{cm}^{-3}$, a mass of $0.7\ \mathrm{M}_\odot$ and a radius of 0.07 pc.

Figure B.84: FUV radiation = 50 G_0: six snapshots showing the chemical abundances of CO and C^+ for a cloud with an initial density of 10000 cm^{-3}, a mass of 0.7 $M_\odot$ and a radius of 0.07 pc.

B.4 SET 100G$_0$

Figure B.85: FUV radiation = 100 G_0. The time evolution of a cloud with an initial density of 50 cm^{-3}, a mass of 1376 M$_\odot$ and a radius of 5.1 pc is shown in this graph. The cloud radius (purple line) is taken to be the zero crossing point of radial velocity and the mass (green line) is taken to be that which lies inside the radius. The blue vertical line denotes the time at which the high density peak first forms. This is the minimum cloud mass which collapses for the selected values of density and FUV flux.

Figure B.86: FUV radiation = 100 G_0. Six snapshots showing radial velocity (purple line) and density (green line) for a cloud with an initial density of 50 cm^{-3}, a mass of 1376 M$_\odot$ and a radius of 5.1 pc.

Figure B.87: FUV radiation $= 100\ G_0$. Six snapshots showing temperature (purple line) for a cloud with an initial density of 50 cm^{-3}, a mass of 1376 M$_\odot$ and a radius of 5.1 pc.
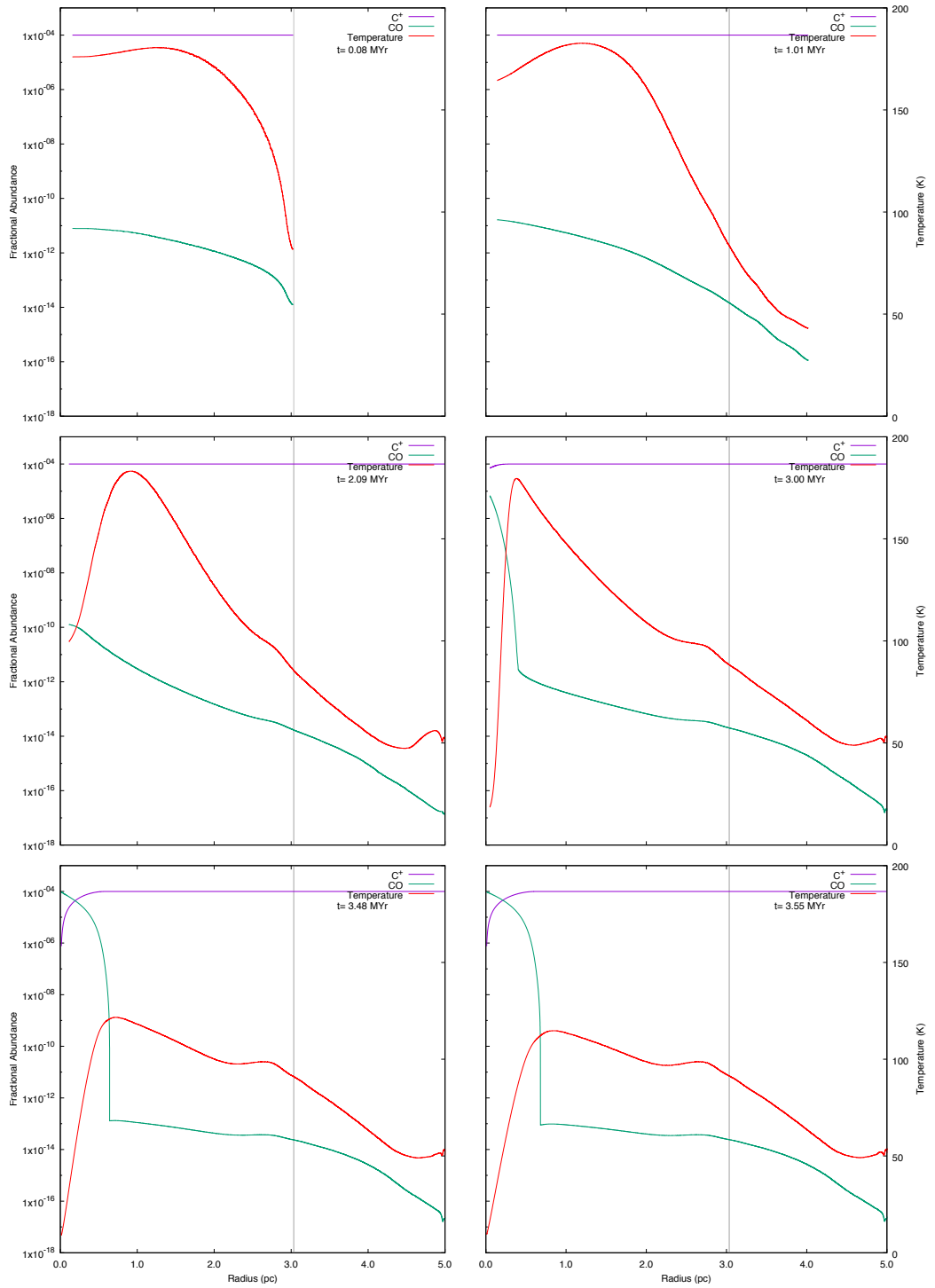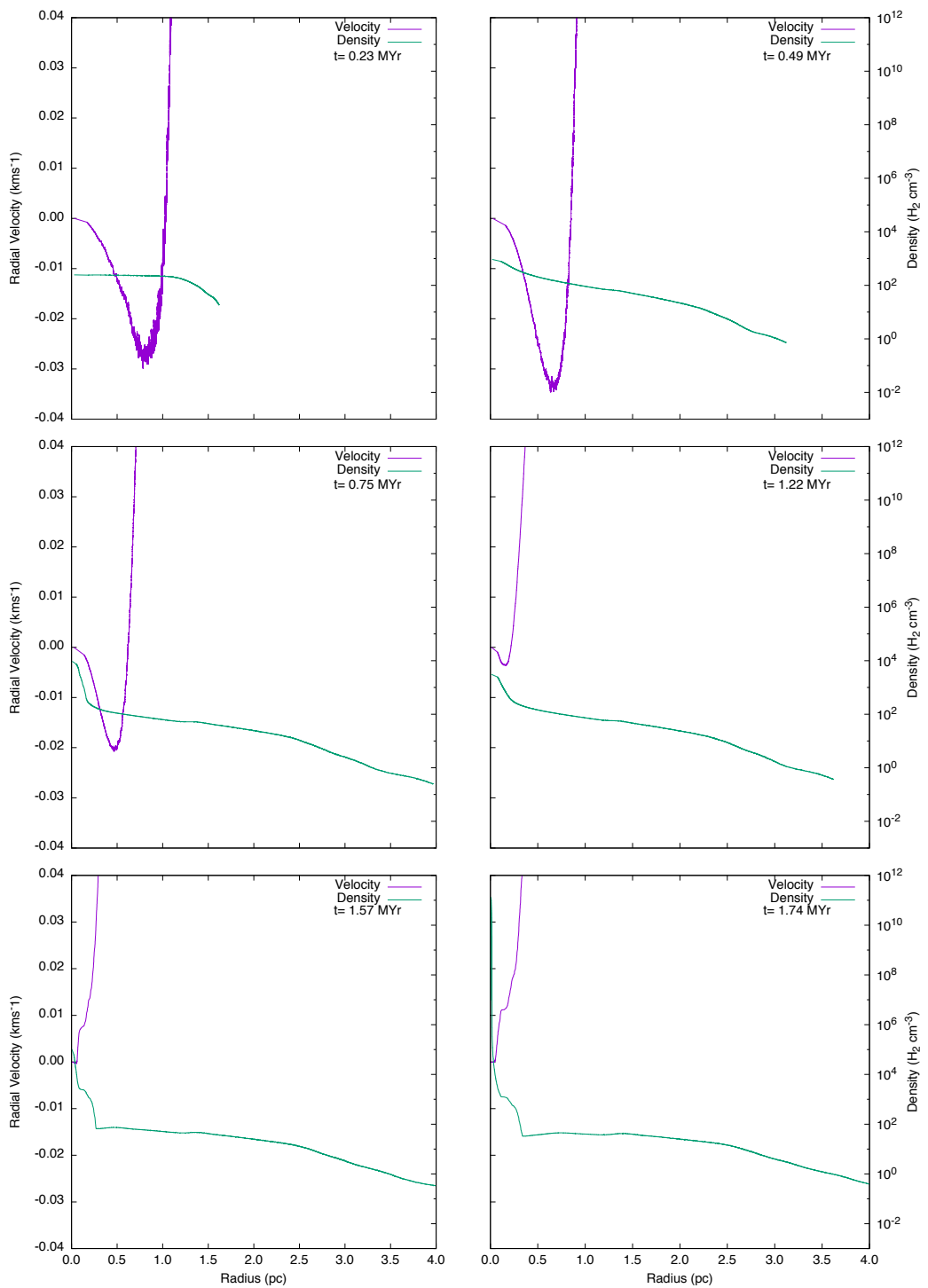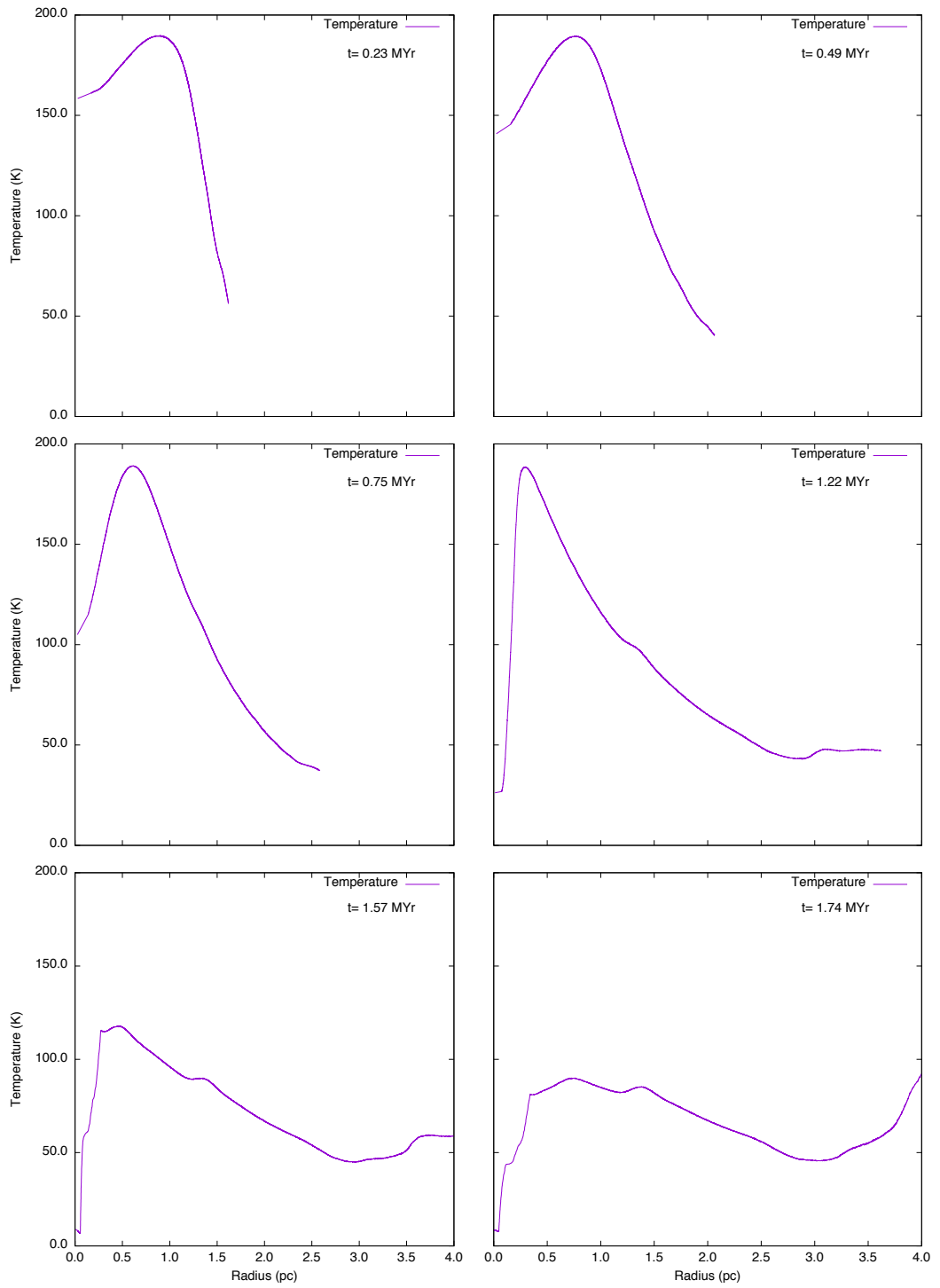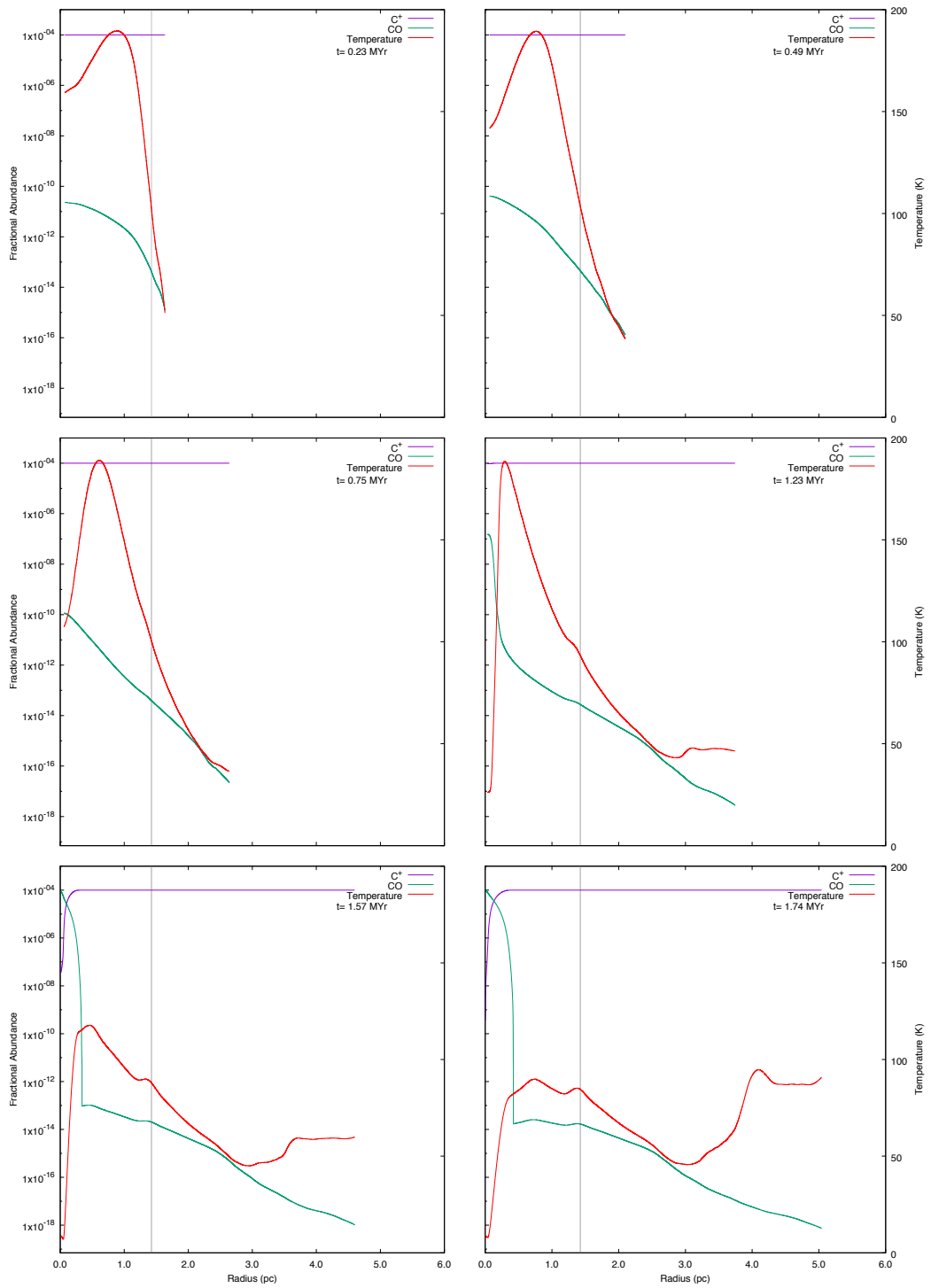
Figure B.88: FUV radiation $= 100$ G$_0$: six snapshots showing the chemical abundances of CO and C$^+$ for a cloud with an initial density of 50 cm^{-3}, a mass of 1376 M$_\odot$ and a radius of 5.10 pc.

Figure B.89: FUV radiation $= 100$ G_0. The time evolution of a cloud with an initial density of 100 cm^{-3}, a mass of 579 M$_\odot$ and a radius of 3.03 pc is shown in this graph. The cloud radius (purple line) is taken to be the zero crossing point of radial velocity and the mass (green line) is taken to be that which lies inside the radius. The blue vertical line denotes the time at which the high density peak first forms. This is the minimum cloud mass which collapses for the selected values of density and FUV flux.

Figure B.90: FUV radiation $= 100~G_0$. Six snapshots showing radial velocity (purple line) and density (green line) for a cloud with an initial density of 100 cm^{-3}, a mass of 579 M$_\odot$ and a radius of 3.03 pc.

Figure B.91: FUV radiation = 100 G_0. Six snapshots showing temperature (purple line) for a cloud with an initial density of 100 cm^{-3}, a mass of 579 M$_\odot$ and a radius of 3.03 pc.

Figure B.92: FUV radiation = 100 G_0: six snapshots showing the chemical abundances of CO and C^+ for a cloud with an initial density of 100 cm^{-3}, a mass of 579 $M_\odot$ and a radius of 3.03 pc.
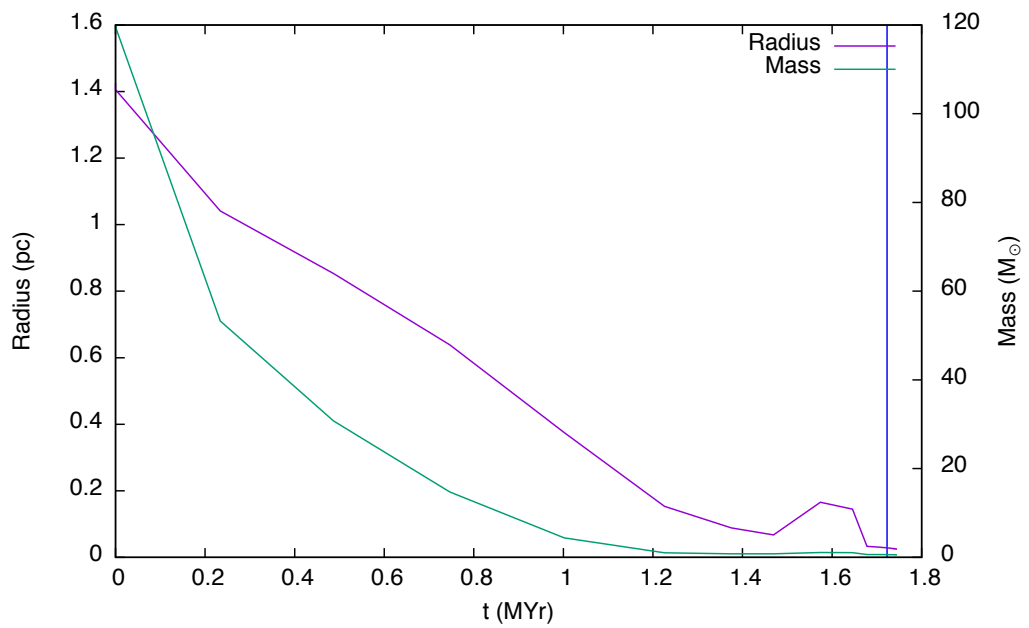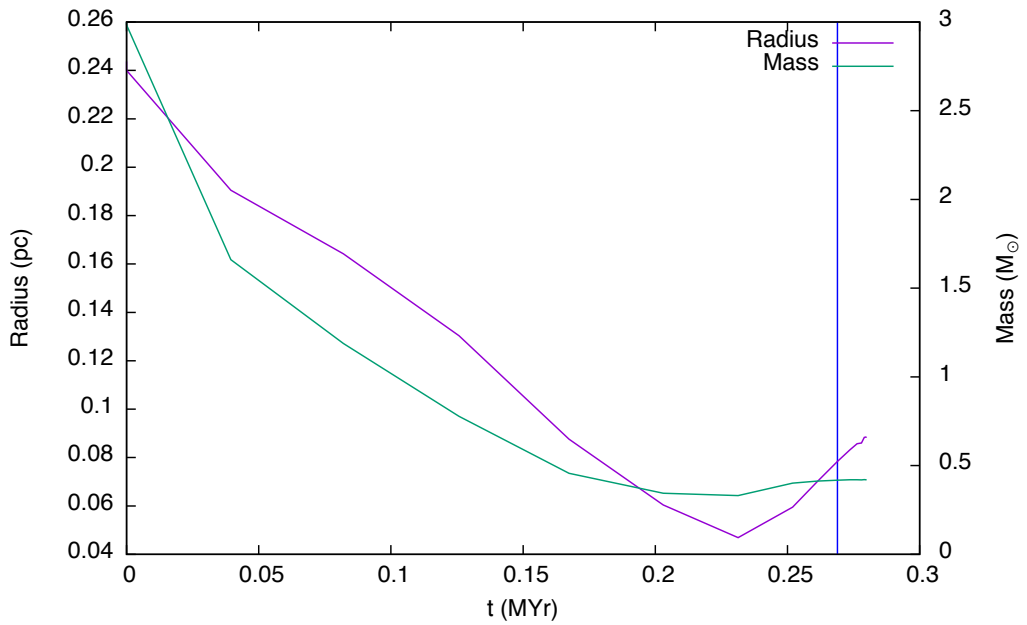
Figure B.93: FUV radiation $= 100$ G_0. The time evolution of a cloud with an initial density of 200 cm^{-3}, a mass of 120 M$_\odot$ and a radius of 1.43 pc is shown in this graph. The cloud radius (purple line) is taken to be the zero crossing point of radial velocity and the mass (green line) is taken to be that which lies inside the radius. The blue vertical line denotes the time at which the high density peak first forms. This is the minimum cloud mass which collapses for the selected values of density and FUV flux.
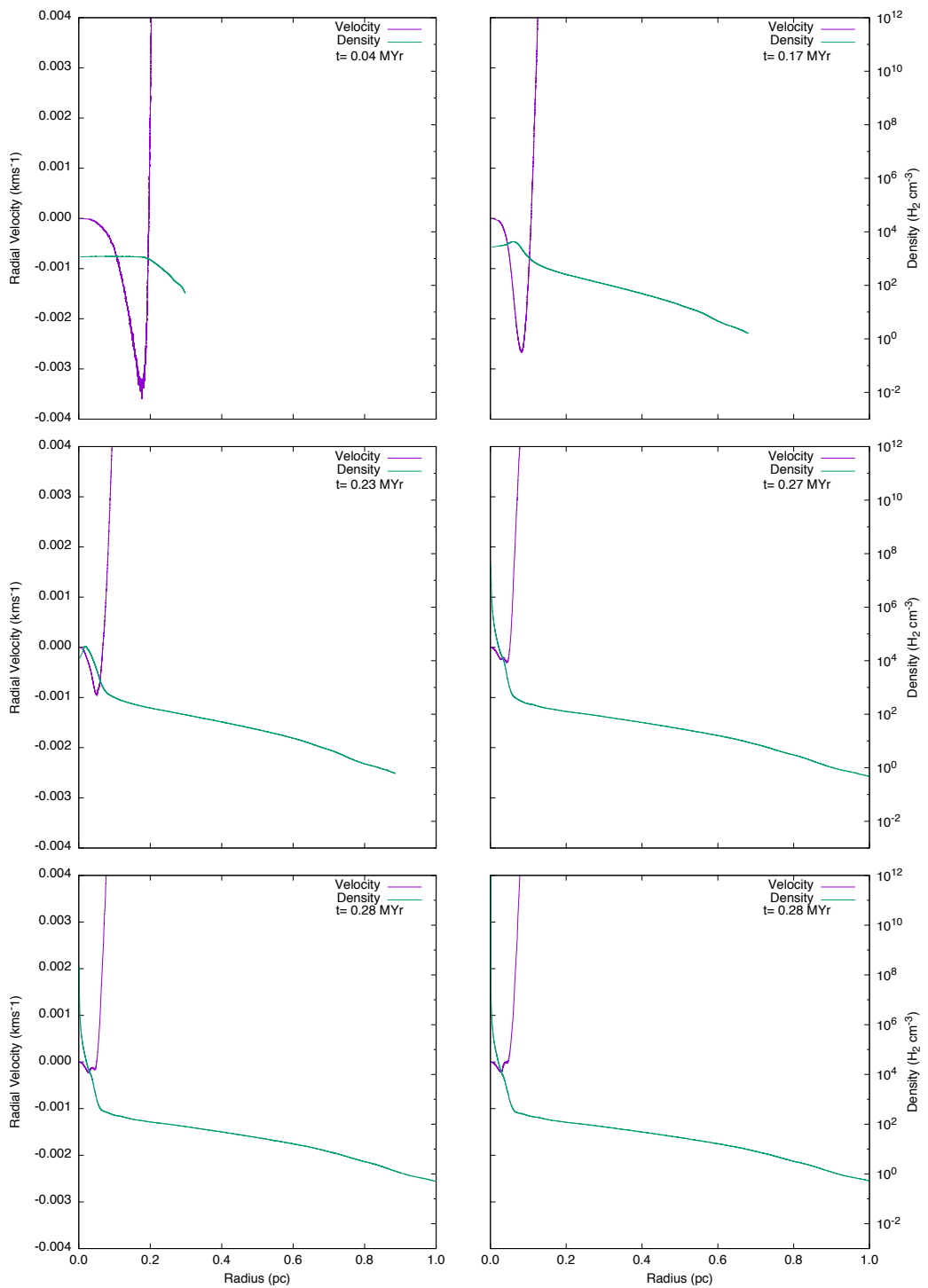
Figure B.94: FUV radiation = 100 G_0. Six snapshots showing radial velocity (purple line) and density (green line) for a cloud with an initial density of 200 cm^{-3}, a mass of 120 M$_\odot$ and a radius of 1.43 pc.
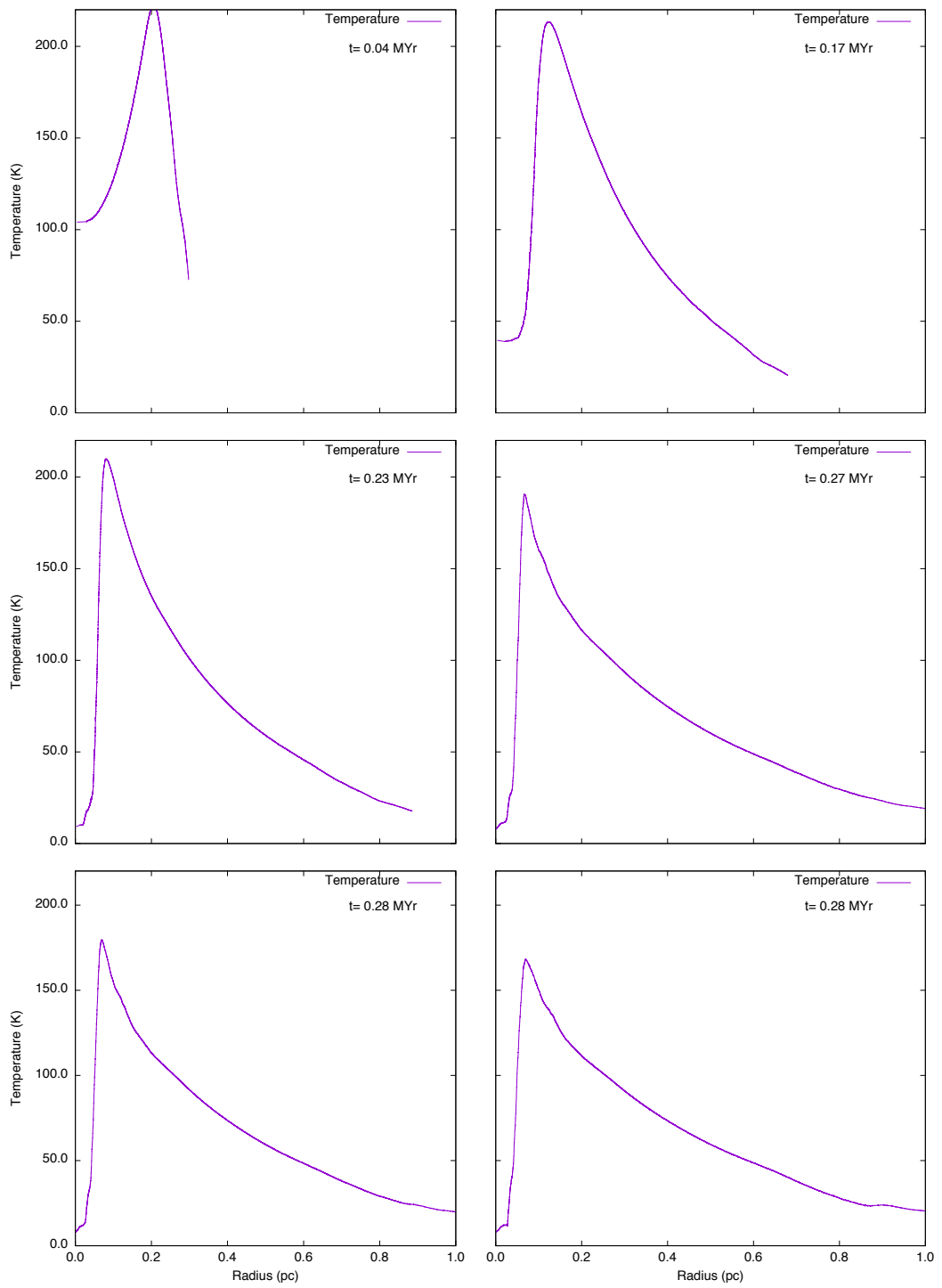
Figure B.95: FUV radiation $= 100\ G_0$. Six snapshots showing temperature (purple line) for a cloud with an initial density of 200 cm^{-3}, a mass of 120 M$_\odot$ and a radius of 1.43 pc.
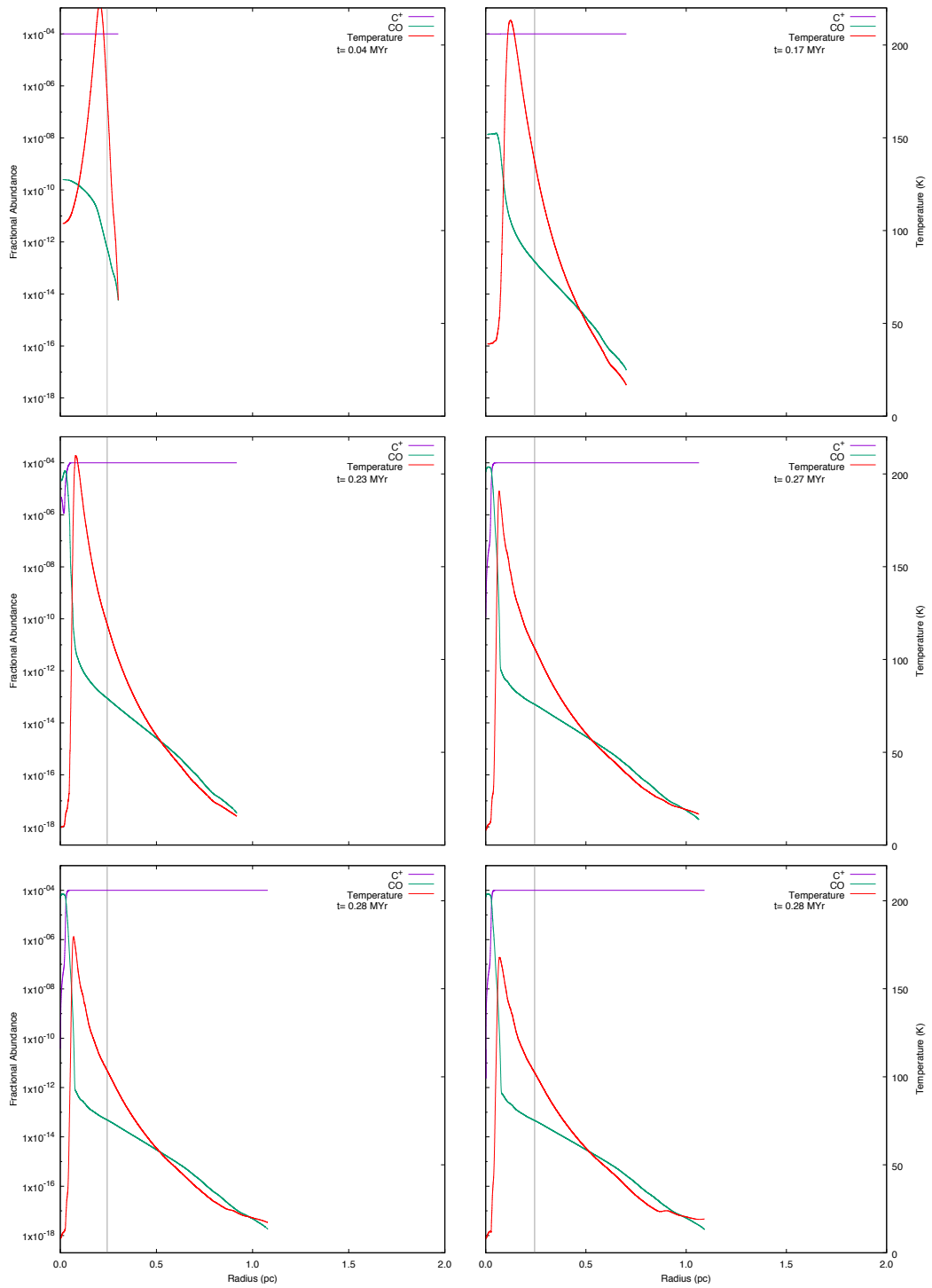
Figure B.96: FUV radiation = 100 G_0: six snapshots showing the chemical abundances of CO and C^+ for a cloud with an initial density of 200 cm^{-3}, a mass of 120 $M_\odot$ and a radius of 1.43 pc.
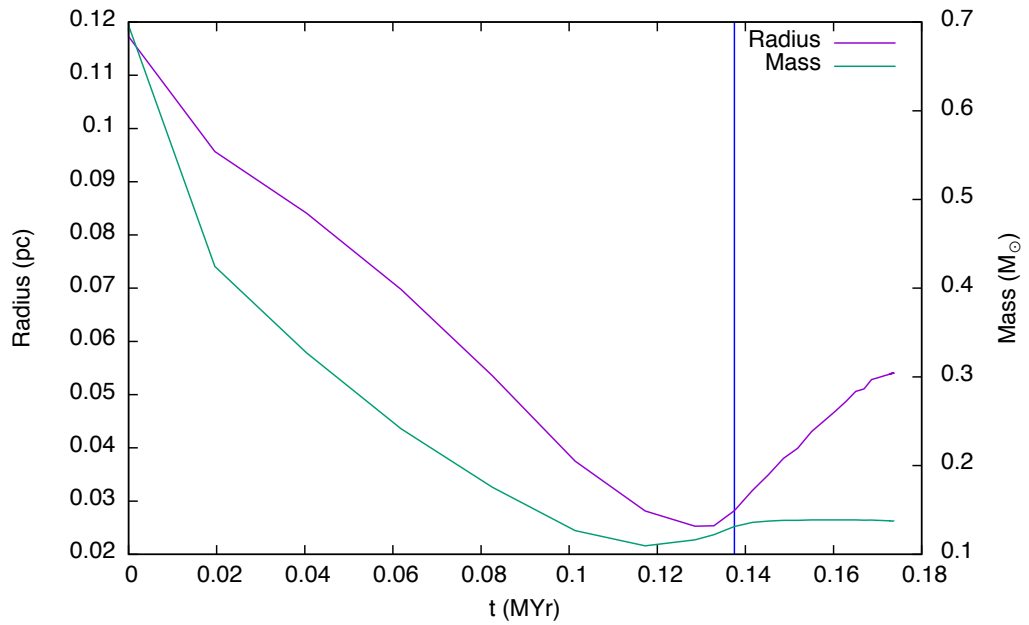
Figure B.97: FUV radiation $= 100$ G_0. The time evolution of a cloud with an initial density of 1000 cm^{-3}, a mass of 3 M$_\odot$ and a radius of 0.24 pc is shown in this graph. The cloud radius (purple line) is taken to be the zero crossing point of radial velocity and the mass (green line) is taken to be that which lies inside the radius. The blue vertical line denotes the time at which the high density peak first forms. This is the minimum cloud mass which collapses for the selected values of density and FUV flux.
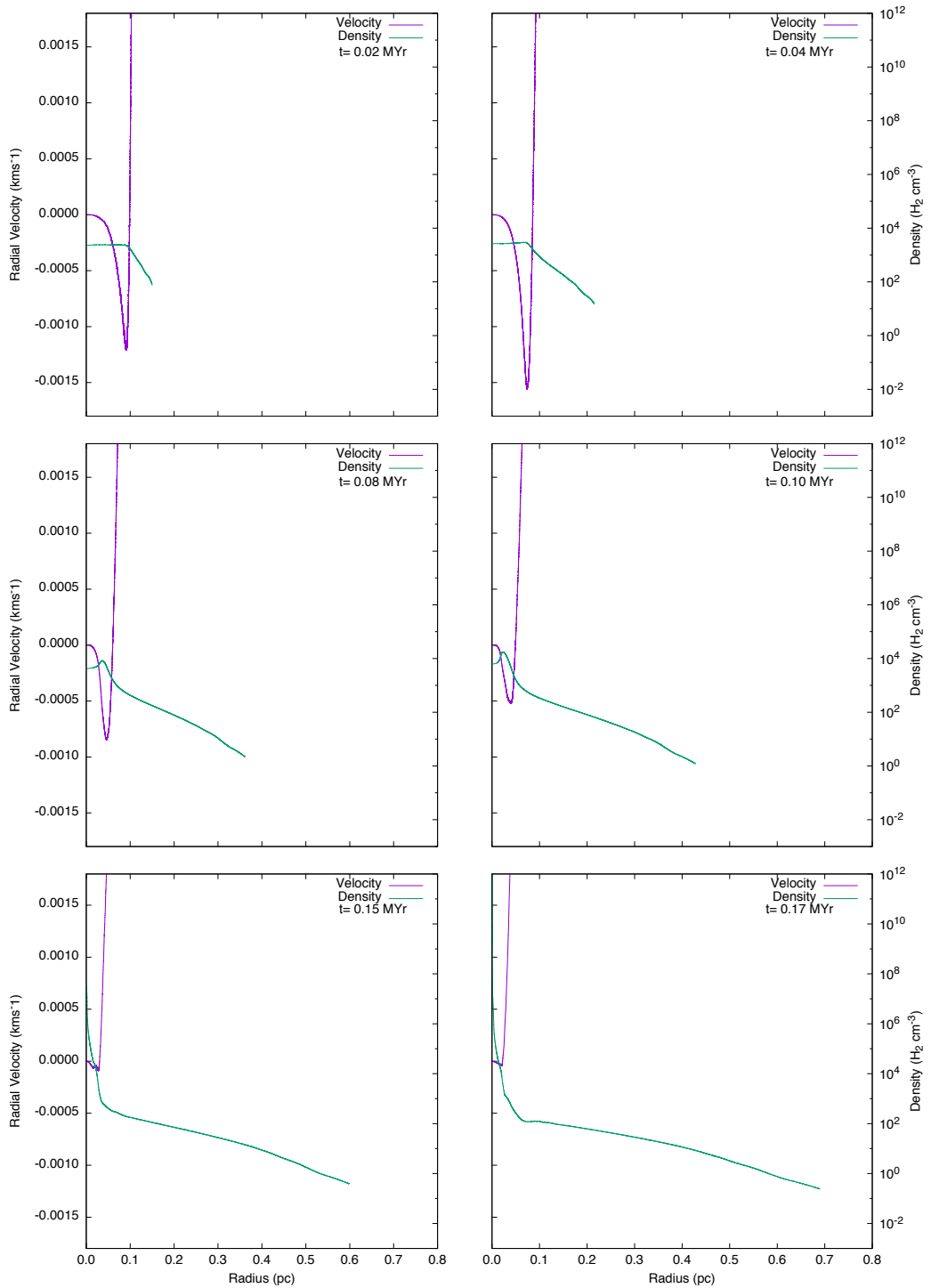
Figure B.98: FUV radiation = 100 G_0. Six snapshots showing radial velocity (purple line) and density (green line) for a cloud with an initial density of 1000 cm^{-3}, a mass of 3 M$_\odot$ and a radius of 0.24 pc.
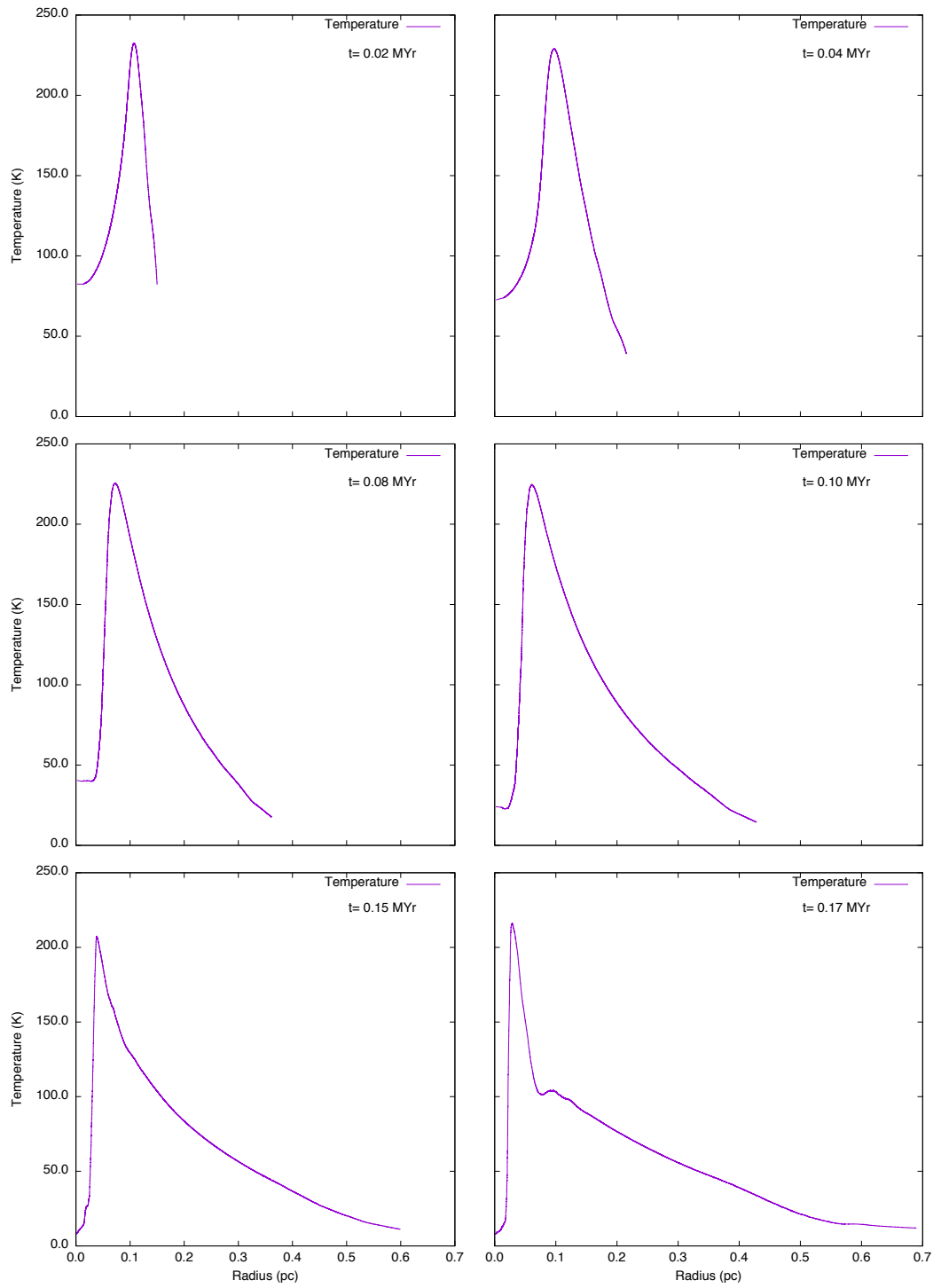
Figure B.99: FUV radiation = 100 G_0. Six snapshots showing temperature (purple line) for a cloud with an initial density of 1000 cm^{-3}, a mass of 3 M$_\odot$ and a radius of 0.24 pc.
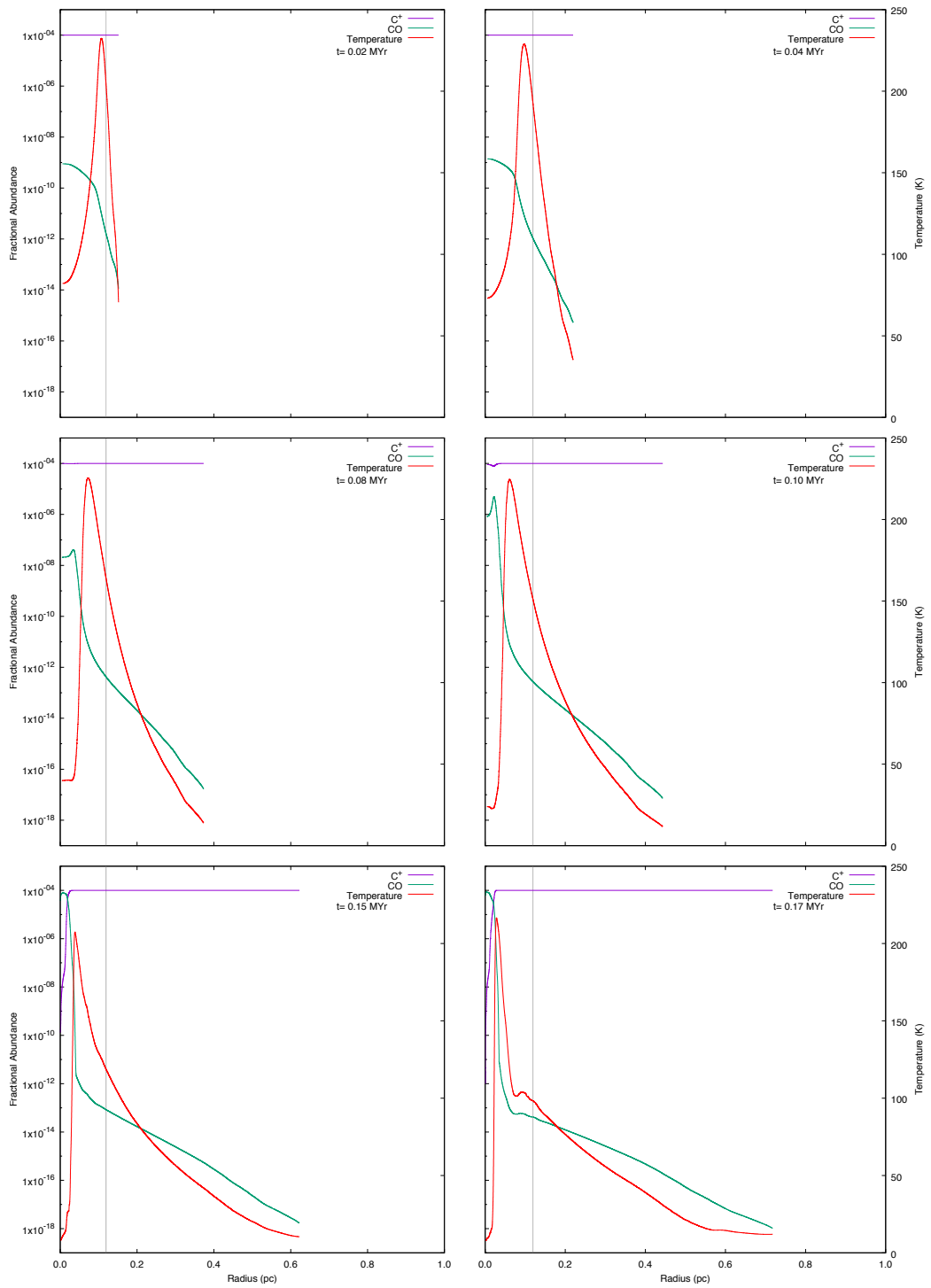
Figure B.100: FUV radiation = 100 G_0: six snapshots showing the chemical abundances of CO and C$^+$ for a cloud with an initial density of 1000 cm^{-3}, a mass of 3 M$_\odot$ and a radius of 0.24 pc.
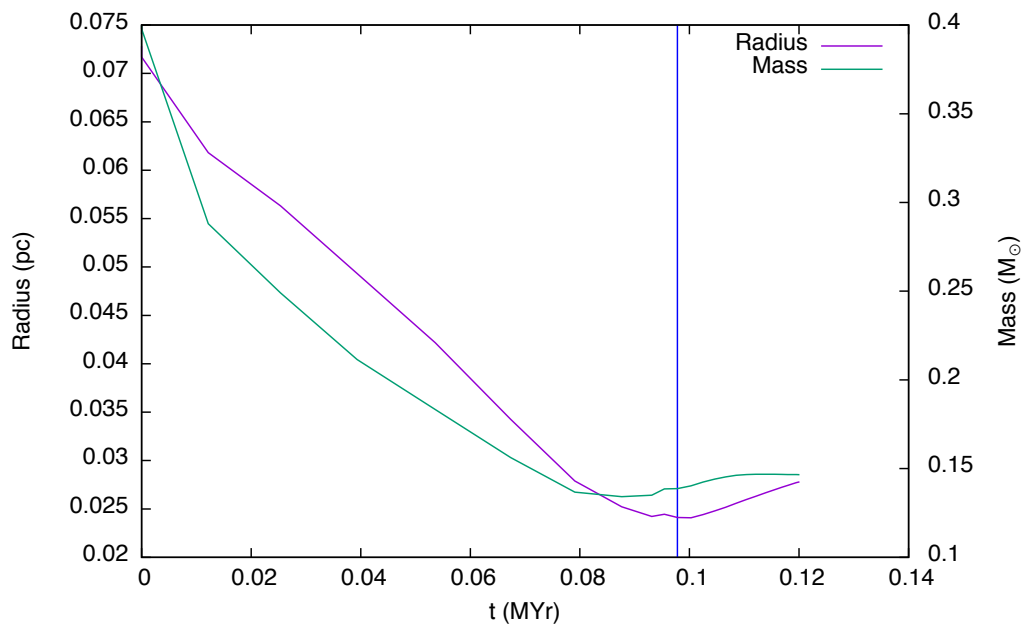
Figure B.101: FUV radiation $= 100$ G_0. The time evolution of a cloud with an initial density of 2000 cm^{-3}, a mass of 0.7 M$_\odot$ and a radius of 0.12 pc is shown in this graph. The cloud radius (purple line) is taken to be the zero crossing point of radial velocity and the mass (green line) is taken to be that which lies inside the radius. The blue vertical line denotes the time at which the high density peak first forms. This is the minimum cloud mass which collapses for the selected values of density and FUV flux.
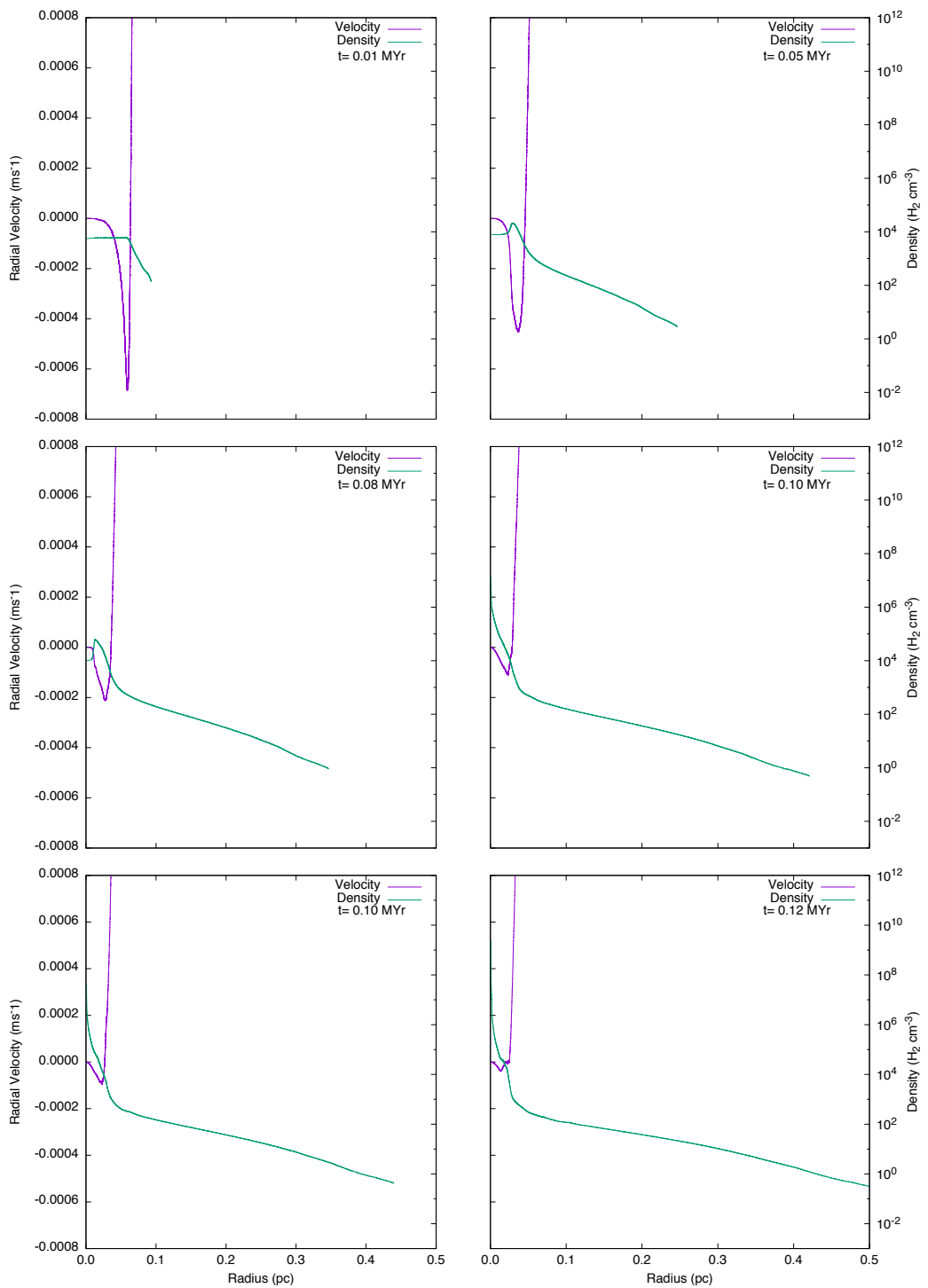
Figure B.102: FUV radiation = 100 G_0. Six snapshots showing radial velocity (purple line) and density (green line) for a cloud with an initial density of 2000 cm^{-3}, a mass of 0.7 M$_\odot$ and a radius of 0.12 pc.

Figure B.103: FUV radiation $= 100$ G_0. Six snapshots showing temperature (purple line) for a cloud with an initial density of 2000 cm^{-3}, a mass of 0.7 M$_\odot$ and a radius of 0.12 pc.

Figure B.104: FUV radiation = 100 G_0: six snapshots showing the chemical abundances of CO and C^+ for a cloud with an initial density of 2000 cm^{-3}, a mass of 0.7 $M_\odot$ and a radius of 0.12 pc.

Figure B.105: FUV radiation = 100 G_0. The time evolution of a cloud with an initial density of 5000 cm^{-3}, a mass of 0.4 M$_\odot$ and a radius of 0.07 pc is shown in this graph. The cloud radius (purple line) is taken to be the zero crossing point of radial velocity and the mass (green line) is taken to be that which lies inside the radius. The blue vertical line denotes the time at which the high density peak first forms. This is the minimum cloud mass which collapses for the selected values of density and FUV flux.

Figure B.106: FUV radiation = 100 G_0. Six snapshots showing radial velocity (purple line) and density (green line) for a cloud with an initial density of 5000 cm^{-3}, a mass of 0.4 M$_\odot$ and a radius of 0.07 pc.
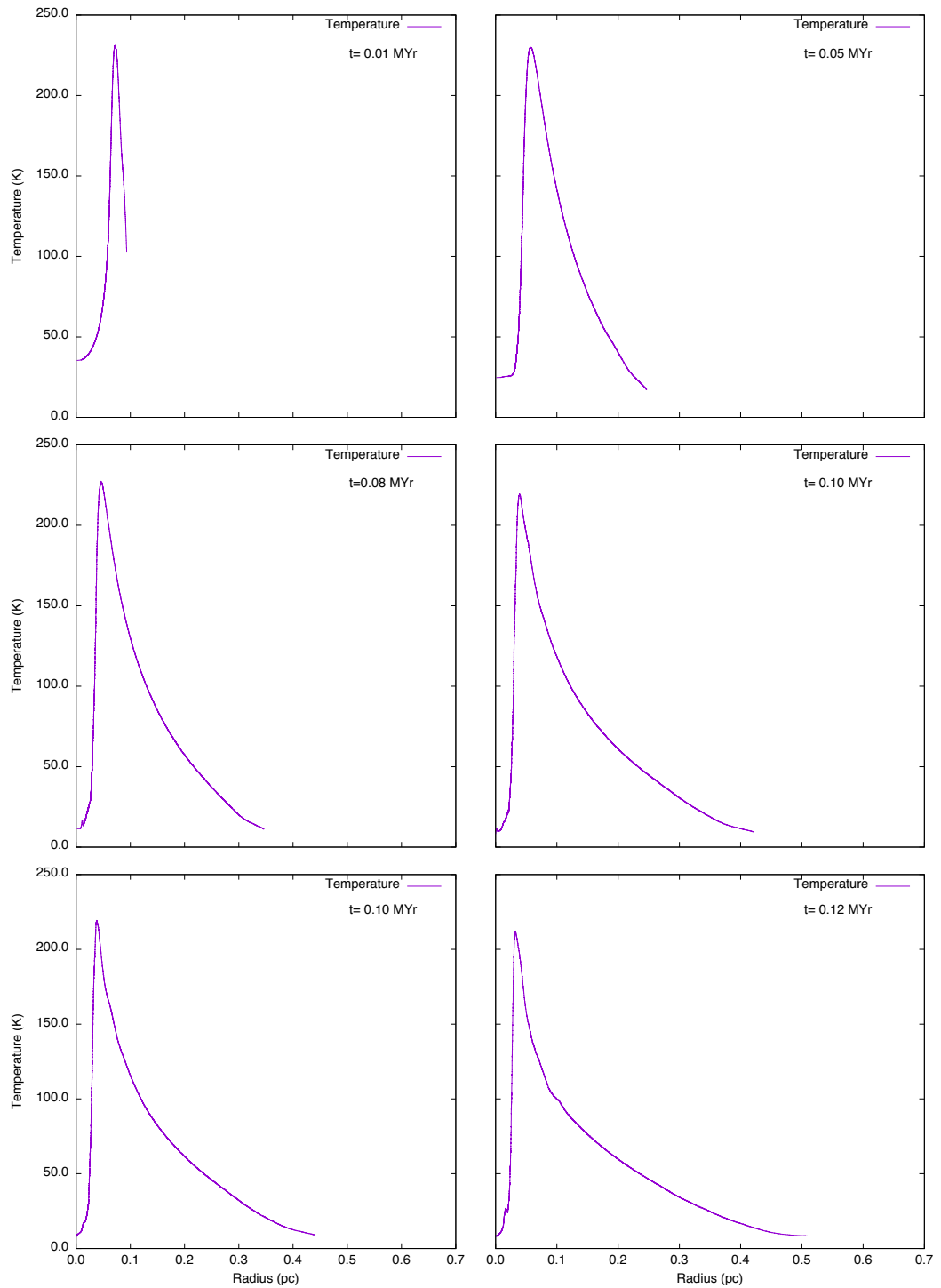
Figure B.107: FUV radiation $= 100\ G_0$. Six snapshots showing temperature (purple line) for a cloud with an initial density of 5000 cm^{-3}, a mass of 0.4 M$_\odot$ and a radius of 0.07 pc.
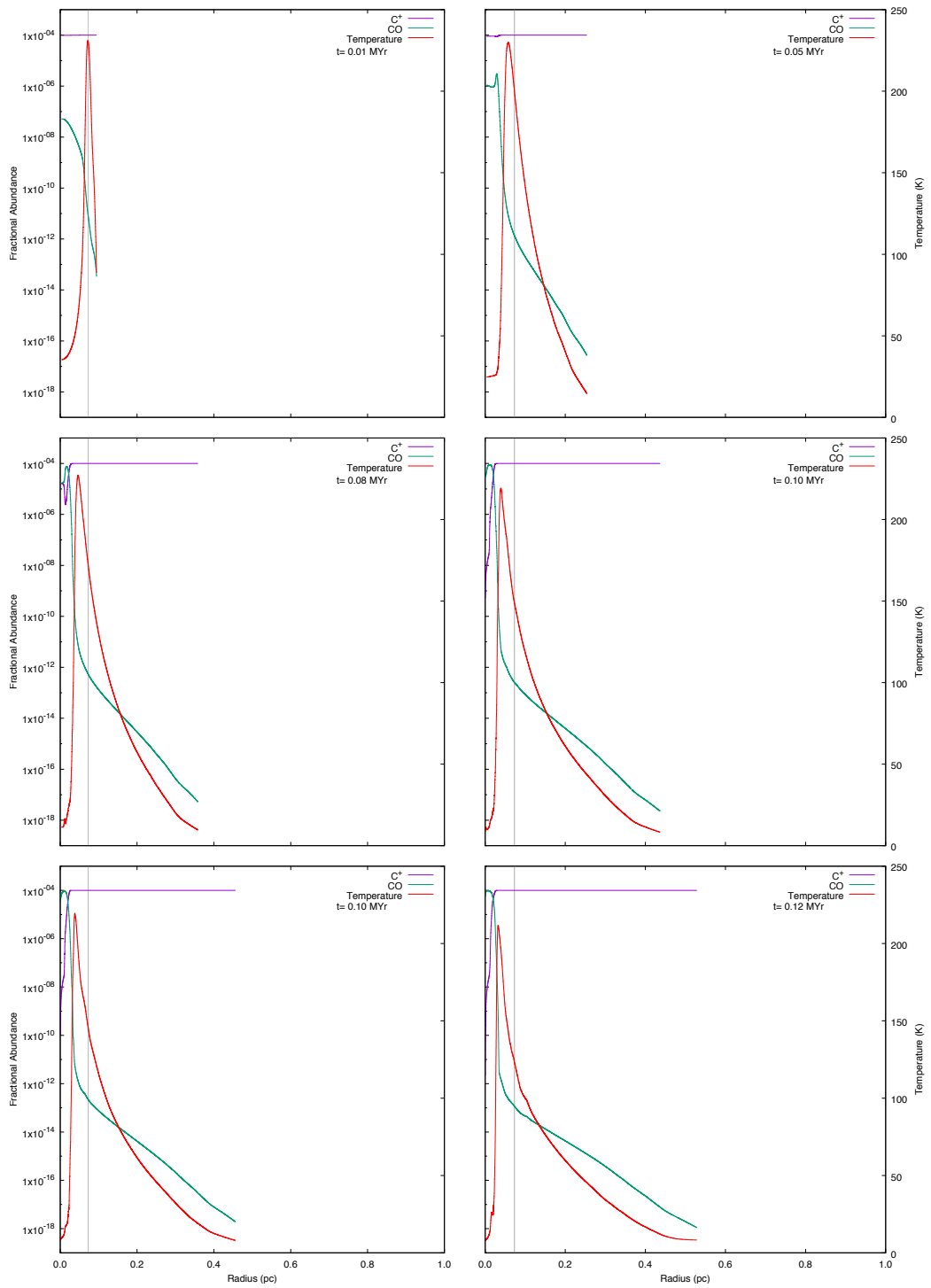
Figure B.108: FUV radiation $= 100$ G_0: six snapshots showing the chemical abundances of CO and C^+ for a cloud with an initial density of 5000 cm^{-3}, a mass of 0.4 $M_\odot$ and a radius of 0.07 pc.
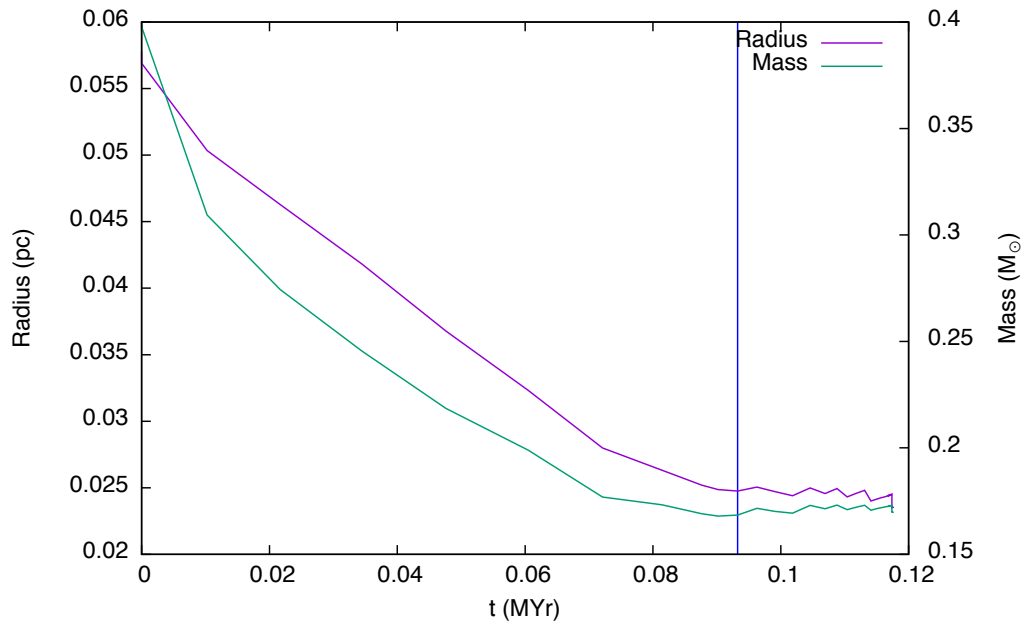
Figure B.109: FUV radiation = 100 G_0. The time evolution of a cloud with an initial density of 10000 cm^{-3}, a mass of 0.4 M$_\odot$ and a radius of 0.06 pc is shown in this graph. The cloud radius (purple line) is taken to be the zero crossing point of radial velocity and the mass (green line) is taken to be that which lies inside the radius. The blue vertical line denotes the time at which the high density peak first forms. This is the minimum cloud mass which collapses for the selected values of density and FUV flux.
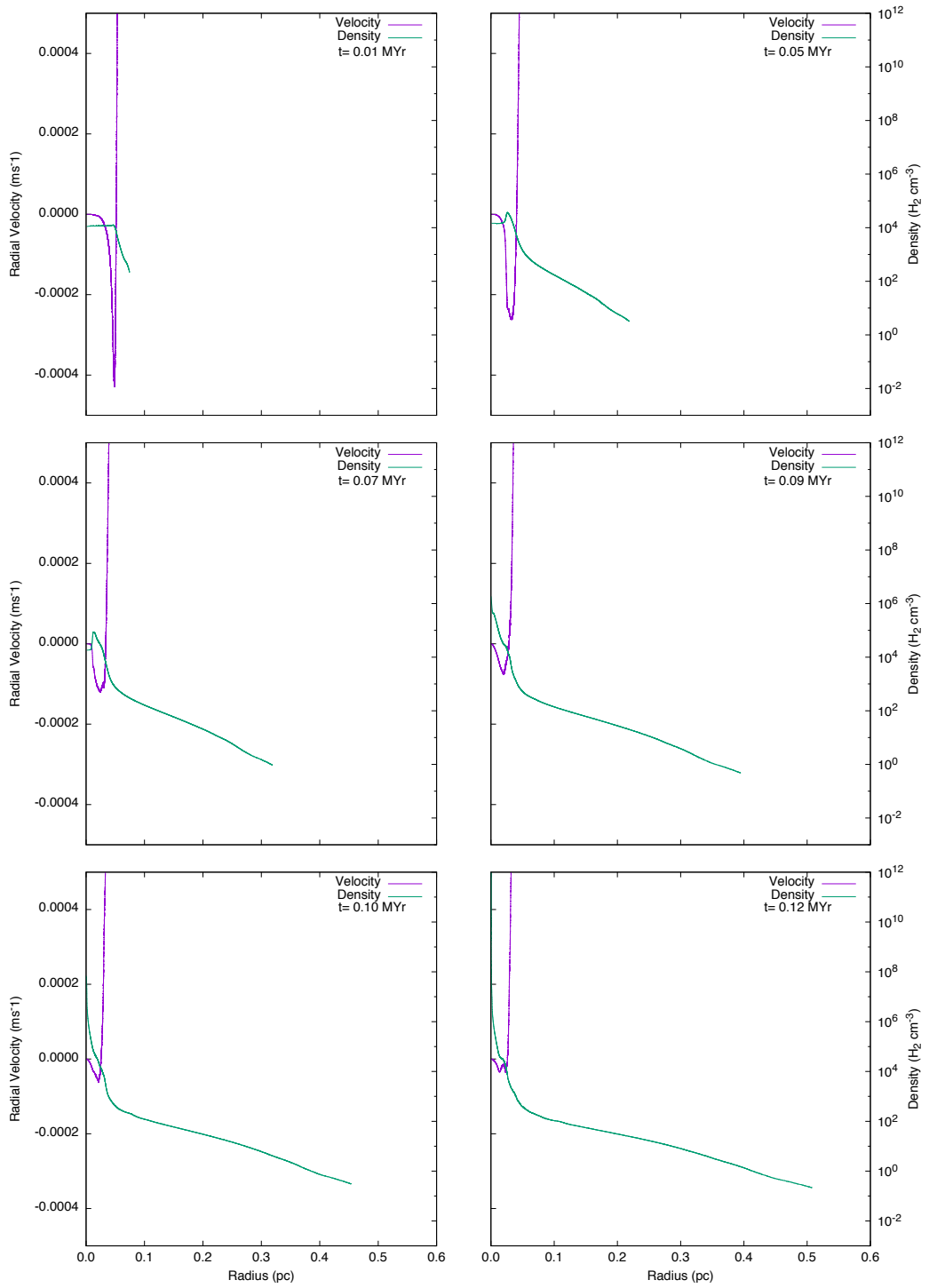
Figure B.110: FUV radiation $= 100 \ G_0$. Six snapshots showing radial velocity (purple line) and density (green line) for a cloud with an initial density of 10000 cm^{-3}, a mass of 0.4 M$_\odot$ and a radius of 0.06 pc.
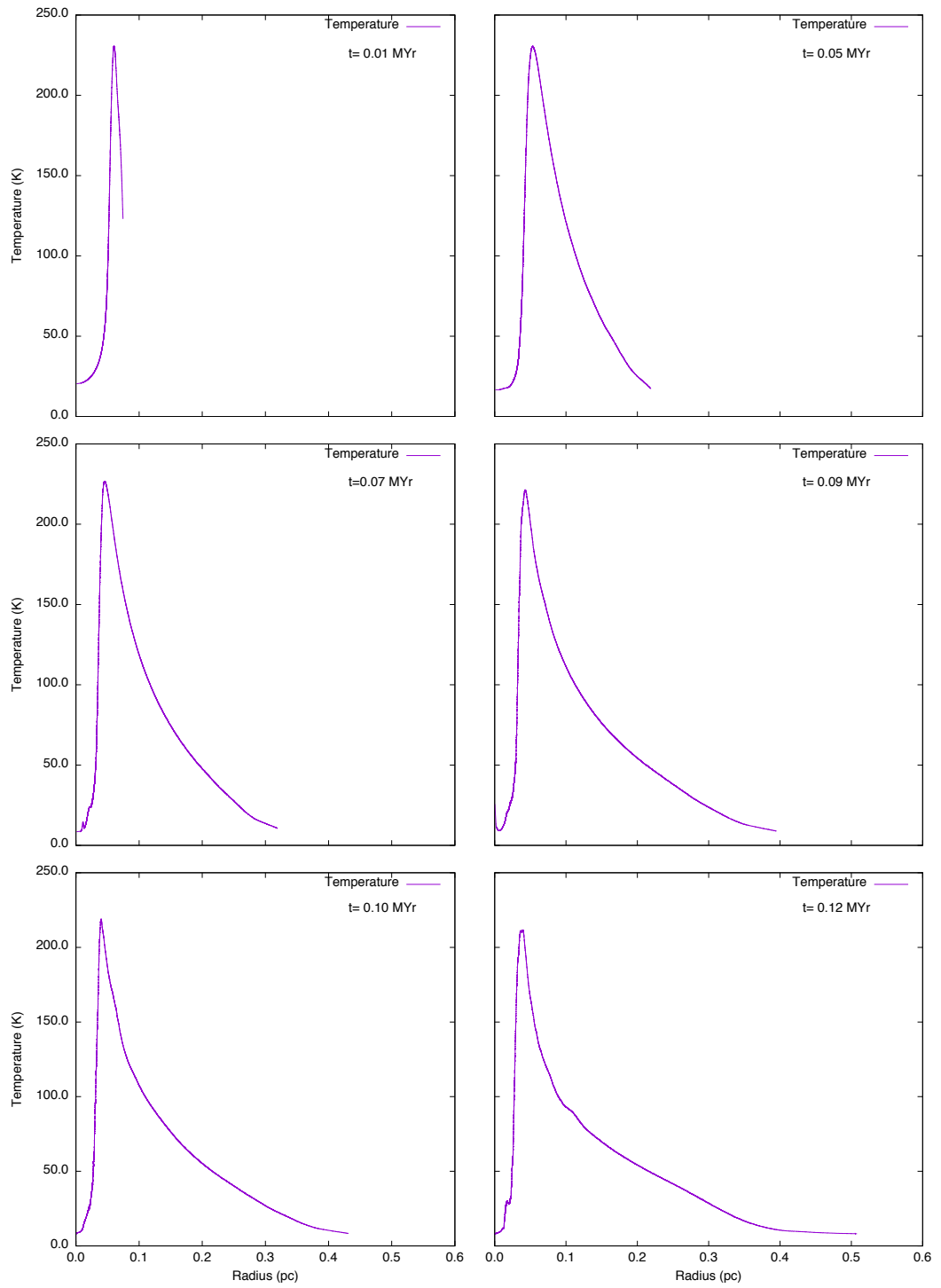
Figure B.111: FUV radiation $= 100$ G_0. Six snapshots showing temperature (purple line) for a cloud with an initial density of 10000 cm^{-3}, a mass of 0.4 M$_\odot$ and a radius of 0.06 pc.
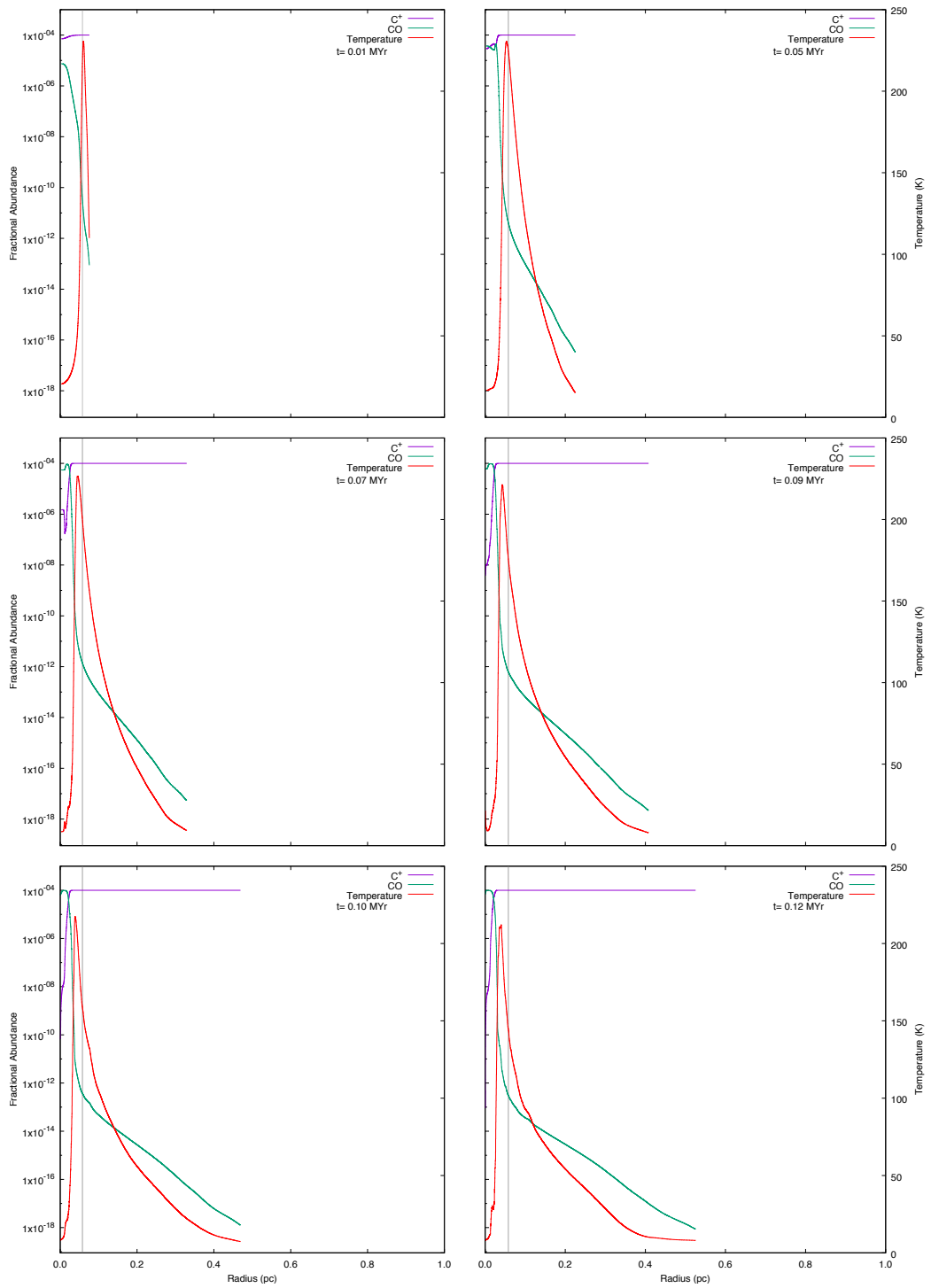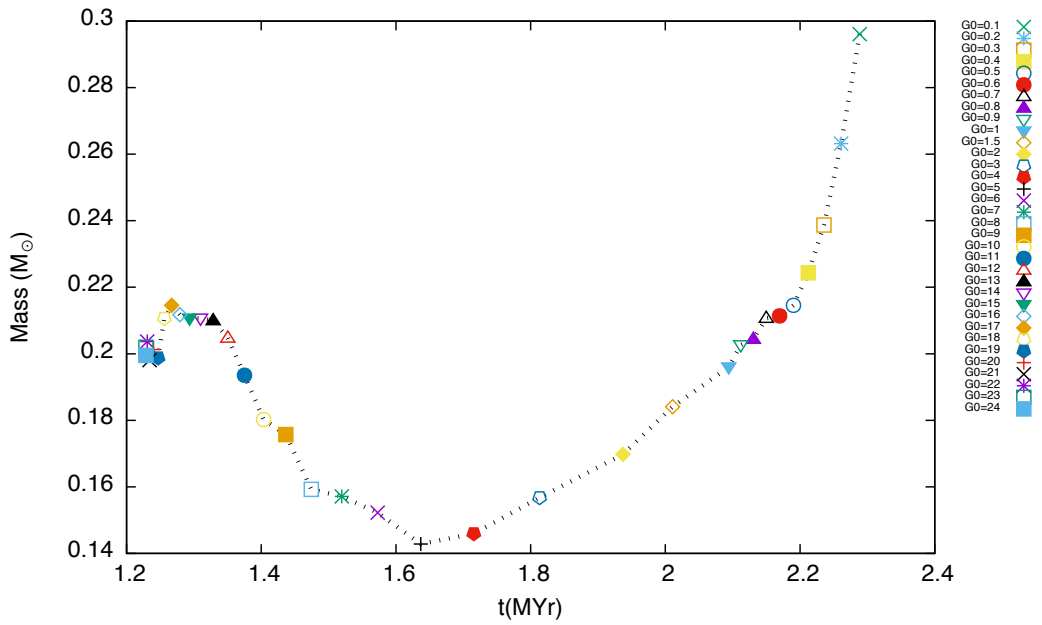
Figure B.112: FUV radiation = 100 G_0: six snapshots showing the chemical abundances of CO and C^+ for a cloud with an initial density of 10000 cm^{-3}, a mass of 0.4 $M_\odot$ and a radius of 0.06 pc.
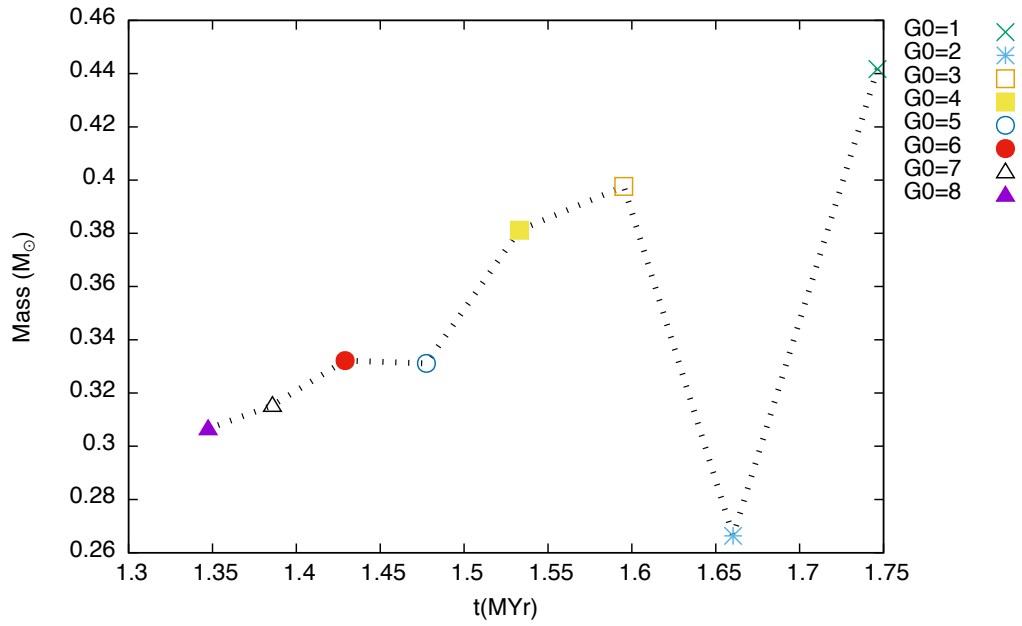
CHAPTER C

FURTHER WORK

Figure C.1: The initial condition of the cloud is $35M_{\odot}$, $n_i = 200$ cm^{-3} with different strengths of FUV. The protostar seed mass is calculated as mass greater then 10^7cm^{-3} which is shown to respect with time of the formation of the seed.

Figure C.2: The initial condition of the cloud is $35M_\odot$, $n_i = 300$ cm^{-3} with different strengths of FUV. The protostar seed mass is calculated as mass greater then 10^7cm^{-3} which is shown to respect with time of the formation of the seed.
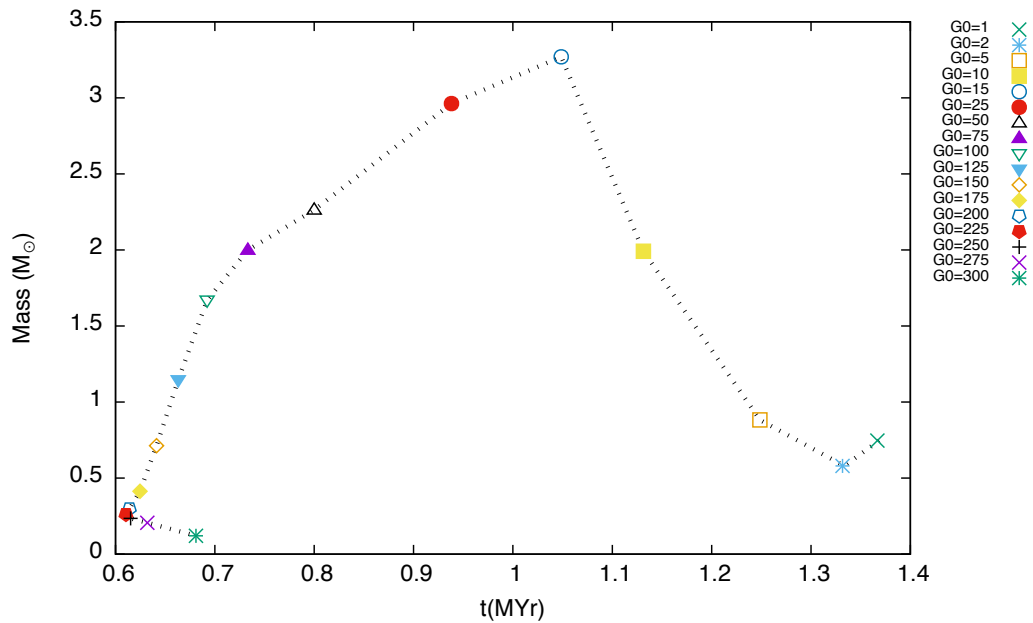

Figure C.3: The initial condition of the cloud is $35M_\odot$, $n_i = 500$ cm^{-3} with different strengths of FUV. The protostar seed mass is calculated as mass greater then 10^7cm^{-3} which is shown to respect with time of the formation of the seed.
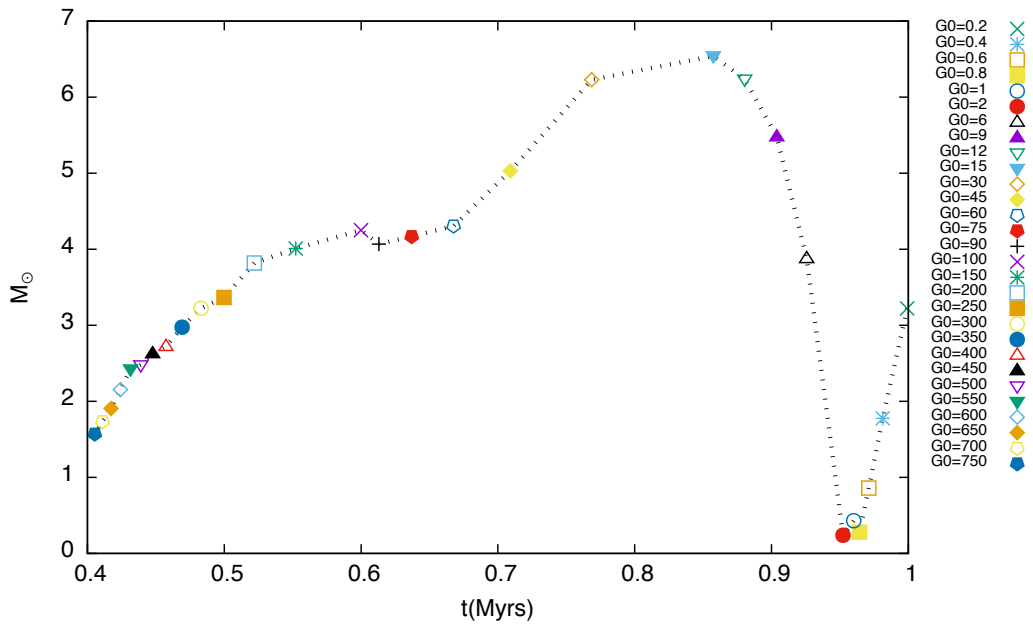
Figure C.4: The initial condition of the cloud is $35M_\odot$, $n_i = 1000$ cm^{-3} with different strengths of FUV. The protostar seed mass is calculated as mass greater then 10^7cm^{-3} which is shown to respect with time of the formation of the seed.